# 18TH INTERNATIONAL SYMPOSIUM on SPACE TERAHERTZ TECHNOLOGY

# ISSTT 2007

## MARCH 21-23, 2007

## CALIFORNIA INSTITUTE OF TECHNOLOGY

## PASADENA . CALIFORNIA . USA

www.isstt2007.caltech.edu

# PROCEEDINGS

CALIFORNIA INSTITUTE OF TECHNOLOGY 1891

*Proceedings of the*

# EIGHTEENTH INTERNATIONAL SYMPOSIUM ON SPACE TERAHERTZ TECHNOLOGY

**March 21-23, 2007**

**California Institute of Technology**
**Pasadena, California, USA**

Edited by Alexandre Karpov

# Preface

The 18th International Symposium on Space Terahertz Technology was held at campus of California Institute of Technology, Pasadena, California, USA on March 21-23, 2007. The Symposium has been attended by about 140 scientists and engineers from USA, European Union, Russia, Japan and China. The symposium organizers would like to thank all the authors and participants to make the symposium successful and enjoyable. Also we would like to thank California Institute of Technology for hosting this event on campus.

All the submitted papers have been included in the proceedings. The accepted abstracts have been used for other presentations. In total the seventy eight (78) presentations have been made, where the 56 have been oral and 22 posters. The breakdown of the presentations in terms of the technology category is as follows:

| | |
|---|---|
| HEB | 6 |
| SIS | 17 |
| Local Oscillators | 8 |
| Direct Detectors | 13 |
| Terahertz Systems | 10 |
| Optics and measurement techniques | 10 |
| Schottky mixers | 4 |
| Components | 5 |
| Backend | 5 |

The 19th International Symposium on Space Terahertz Technology will be held on April 28-30, 2008 at SRON in Groningen, Netherlands. Contact ISSTT2008@SRON.nl

The 20th International Symposium on Space Terahertz Technology will be held in spring of 2009 at University of Virginia / NRAO, Charlottesville, VI, USA. http://www.nrao.edu/meetings/ISSTT2009

Alexandre Karpov

## Session 1 Terahertz Systems 1 Chair Tom Phillips

## Session 2 SIS mixers I Chair Edward Tong

## Session 3 Local Oscillators Chair Imran Mehdi

## Session 4 Direct Detectors I Chair Jonas Zmuidzinas

---

**Poster session** **Chairs: Peter Siegel and Ghassan Yassin**

## Session 5 Direct Detectors II (KID) Chair Boris Karasik

## Session 6 HEB mixers Chair Jian-Rong Gao

## Session 7 Optics and waveguides Chair Paul Goldsmith

## Session 8 THz receivers and backend Chair Karl Jacobs

## Session 9 Terahertz Systems II Chair Raymond Blundell

## Session 10 SIS mixers II Chair Alexandre Karpov

## Session 11 Novel devices and measurements Antti Raisanen

## Session 12 Schottky mixers and detectors Tom Crowe

# SOFIA: An Observatory for THz Science and Technology

Eric E. Becklin[*a], Sean C. Casey[a], and Xander Tielens[b]

[a] Universities Space Research Association, NASA MS 211-3, Moffett Field, CA 94035-1000
[b] Code SST, NASA Ames Research Center, MS 245-1, Moffett Field, CA 94035-1000

## ABSTRACT

The Stratospheric Observatory for Infrared Astronomy (SOFIA) is the next generation of airborne astronomical observatories. Funded by the U.S. and German space agencies with an expected operational lifetime of 20 years, SOFIA is scheduled for science flights beginning in late-2009. The observatory consists of a 747-SP aircraft modified to accommodate a 2.5-meter infrared telescope within an open port cavity. Academic and government laboratories spanning both the U.S. and Germany are developing science instruments for SOFIA. With an evolving suite of state-of-the-art technologies, SOFIA will explore the emission of astronomical sources with an unprecedented level of angular resolution (θ[arc-seconds] = 0.1 x wavelength [μm]) and spectral line sensitivity over a core frequency range of 1 – 10 THz (i.e. wavelengths of 30 – 300 microns). On April 26, 2007, the first test flight of the heavily modified SOFIA aircraft was achieved in Waco, Texas. The current status of SOFIA is available from the observatory web site at http://sofia.arc.nasa.gov and is updated frequently.

Keywords: SOFIA, airborne astronomy, far-infrared, instruments

## 1. INTRODUCTION

The Stratospheric Observatory For Infrared Astronomy (SOFIA) along with the Spitzer and Herschel observatories are the U.S. and European premier astronomical programs for infrared and submillimeter astronomy. SOFIA, a joint project of NASA and the German Space Agency (DLR) is a 2.5-meter telescope in a Boeing 747-SP aircraft designed to make sensitive infrared measurements of a wide range of astronomical objects (Erickson and Davidson 1995, Becklin 1997, Casey 2004). It will fly at and above 12.5 km, where the telescope will collect radiation in the wavelength range of 0.3 μm to 1.6 mm. The SOFIA science program is being developed and operated for NASA and DLR by the Universities Space Research Association (USRA).

The telescope and 20% of operations will be supplied by Germany through contracts with DLR. In Germany, the University of Stuttgart has been awarded the contract to run the Deutsches SOFIA Institut (DSI). Science communities in the U.S. and Germany have the responsibilities for the development of the science instruments to be installed on the SOFIA telescope. In the U.S., science instrument teams are selected and funded through an a peer review and ranking of the proposals received.

## 2. SCIENCE OPERATIONS

SOFIA will see first light in 2009, and is planned to make more than 120 scientific flights per year of at least 8 to 10 hours in duration. SOFIA is expected to operate for at least 20 years, primarily from NASA's Dryden Flight Research Center in Edwards, California, but occasionally from other bases around the world, especially in the Southern Hemisphere. SOFIA will fly above 12.5 km, where the typical precipitable water

[*] contact: ebecklin@sofia.usra.edu; telephone: (650)604-2114; NASA MS 211-3, Moffett Field, CA 94035-1000

column depth is less than 10 μm. A graphic comparison of the typical transmission at mountaintop and aircraft altitudes is shown in Figure 1. It is clear that, except for a few very narrow bands in the mid-infrared that are completely blocked by telluric $CO_2$, the atmosphere at aircraft altitudes is mostly transparent at infrared and submillimeter wavelengths. In particular, THz frequencies (30 – 300 microns) are strongly blocked at typical Mauna Kea-type water vapor values (ZH2O ~ 1 mm).

The SOFIA Science and Mission Operations Center (SSMOC) will be located at NASA's Ames Research Center in Moffett Field, CA and is currently operated by USRA under contract to NASA. The SOFIA Program expects to support approximately 50 investigation teams per year through a peer reviewed proposal process.

In early-1997, NASA acquired the SOFIA aircraft, the 'Clipper Lindbergh', from United Airlines. The telescope and support structure was developed by DLR and delivered to NASA in late-2002. The first ground-based observations with the SOFIA telescope were in mid-2004. The first flight of the modified aircraft was on April 26, 2007 and is shown in Figure 2. With most U.S. and German science instruments nearing completion, the first science flights are expected in early-2009.

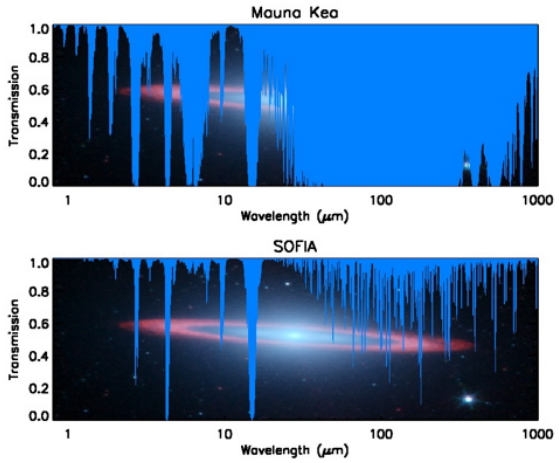


**Figure 1. The comparison of atmospheric transmission at THz frequencies between ground based and airborne facilities. Note that THz observations (1 – 10 THz) are completely blocked by the effects of atmospheric water vapor.**


**Figure 2. The first test flight of the SOFIA aircraft occurred on April 26, 2007 in Waco, Texas after nearly ten years of development. Open door test flight are expected in 2008 with science flights beginning in 2009.**

## 3. SOFIA'S TELESCOPE AND FIRST GENERATION INSTRUMENTS

Mounted in the aft section of the aircraft, the SOFIA telescope is stabilized in-flight by a three-axis gyroscope package coupled to a magneto-torque motor drive via a tuned servo-system. Guide camera and strain gauges provide low frequency corrections for close-loop tracking on celestial sources. The primary mirror is finished to provide quality images at optical wavelengths. The portside telescope cavity door is typically closed for take-off and landings so as the keep the aluminized mirror surface as clean as possible (and of moderately low emissivity). The door is opened at altitude and is articulated to track the telescope's range of motion in elevation (20 – 60 degrees). A secondary mirror drive provides both chopping and scanning motions. The top-level characteristics for SOFIA are listed in Table 1.

Table 1. SOFIA Characteristics

| | |
|---|---|
| Nominal Operational Wavelength Range | 0.3 to 1600 microns |
| Primary Mirror Diameter | 2.7 meters |
| System Clear Aperture Diameter | 2.5 meters |
| Nominal System f-ratio | 19.6 |
| Primary Mirror f-ratio | 1.28 |
| Telescope's Unvignetted Elevation Range | 20 – 60 degrees |
| Unvignetted Field-of-view Diameter | 8 arc-minutes, 13 arc-minutes at optimum focus |
| Maximum Chop Throw on Sky | ± 4 arc minutes (unvignetted) |
| Diffraction-Limited Wavelengths | > 15 microns |
| Recovery Air and Optical Temperature in Cavity | 240 K |
| Image Quality of Telescope Optics (at 0.6 microns) | 1.0" on-axis (80% encircled energy) |
| Optical Configuration | Bent Cassegrain, chopping secondary and flat folding tertiary |
| Chopper Frequencies | 1 to 20 Hertz for 2-point square-wave chop |
| Pointing Stability | < 2.0" rms for first-light |
| Pointing Accuracy | = 0.5" if on-axis Focal Plane tracking<br>= 3" if on-axis Fine-Field tracking |
| Total Emissivity of Telescope (goal) | 15% at 10 microns with dichroic tertiary<br>10% at 10 microns with aluminized tertiary |
| Chopped Image Quality due to coma for ± 4' chop throw | = 9.1" for 80% encircled energy diameter<br>= 5.8" for 50% encircled energy diameter |

A total of nine instruments have been selected and are now under development. SOFIA's first generation instruments cover the full wavelength range from the visible to the near, mid, and far-infrared and submillimeter and, in spectral resolution terms, range from imagers with narrow photometric bands, to moderate resolution spectrometers geared towards studies of broad dust and molecular features, to high resolution instruments capable of velocity-resolved gas phase line studies. The discovery space of SOFIA's first generation instrument suite is illustrated in Figure 3.

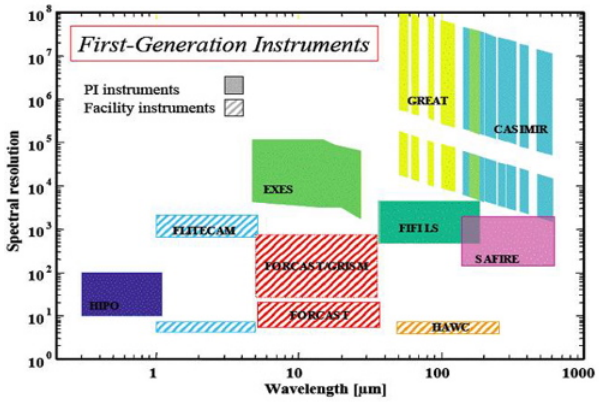


**Figure 3. The phase space of wavelength coverage versus spectral resolution for SOFIA's first generation instrument suite. The instruments GREAT, CASIMIR, and SAFIRE are discussed in this symposium.**

The operational parameters of the first generation instruments are listed in Table 2 below. SOFIA science instruments are either principal investigator class or facility class. In particular, the current suite includes three Facility Class Science Instruments (FSI): HAWC, FORCAST, and FLITECAM. Facility class instruments are maintained and operated by the science staff of the SSMOC for the general science community. In addition, there are six Principal Investigator Class (PI) Science Instruments, which will be maintained and operated by the PI teams at their home

institutions. General investigators will be able to propose for these instruments in collaboration with the PI teams. Two of the PI Class instruments (FIFI-ls and GREAT) are being developed in Germany.

Table 2: SOFIA First Light Instruments

| PI | Institution | Name | Type of instrument |
|---|---|---|---|
| E. Dunham | Lowell Observatory | HIPO | High-speed Imaging Photometer for Occultations 0.3-1.1 μm |
| I. McLean | UCLA | FLITECAM | Near-IR Camera 1-5 μm; GRISM $R$ = 2,000 |
| J. Lacy | Univ. of Texas | EXES | Echelon spectrometer 5-28μm; $R = 10^5$, $10^4$, or 3,000 |
| T. Herter | Cornell Univ. | FORCAST | Mid IR Camera 5-40 μm |
| D. A. Harper | Univ. of Chicago | HAWC | Far IR Bolometer Camera 50-240 μm |
| A. Poglitsch | MPE, Garching | FIFI-LS | Field Imaging Far IR Line Spectrometer 4-210 μm; $R \cong 2{,}000$ |
| S. Moseley | NASA GSFC | SAFIRE | Imaging Fabry-Perot Bolometer Array Spectrometer 145-655 μm; $R$ = 1,000-2,000 |
| R. Güsten | MPIfR, KOSMA | GREAT | Heterodyne Spectrometer 60-200 μm $R = 10^4$-$10^8$ |
| J. Zmuidzinas | Caltech | CASIMIR | Heterodyne Spectrometer 200-600 μm $R = 10^4$-$10^8$ |

An obvious disadvantage of an airborne mission compared to a space-based mission is the much higher background. Nevertheless, SOFIA will be about an order of magnitude more sensitive than the IRAS space mission and of course will have a factor >5 better spatial resolution due to its larger telescope aperture. At high spectral resolution, SOFIA will match or be more sensitive than the ISO space mission. In addition, no space-based mission is presently envisioned with a spectral resolution exceeding 3,000 in the "home" (the 3 to 150 μm range) of many of the important atomic and ionic fine structure lines as well as ro-vibrational transitions of many simple molecules, including $H_2O$, $CH_4$, and $C_2H_2$.

However, a great strength of an airborne astronomy program is that science instruments can be regularly exchanged between flight opportunities. In addition, compared to space-based missions, much larger and more massive instruments can be flown. Likewise, mission constraints such as heat dissipation or power consumption are of less concern for airborne platforms than for satellites. The SOFIA instrument program takes full advantage of these differences. SOFIA's first generation instrumentation is technically very diverse.[1]

Another advantage of an airborne observatory, as compared to a space-based mission, is the ability to rapidly incorporate improvements in technology and other instrument upgrades. In this way, instrumentation can quickly react to the latest technological innovations. At frequencies of 1 – 10 THz (30 – 300 microns), technology is still rapidly improving and major advances in detector sensitivity and array size can be expected over SOFIA's 20-year lifetime. The SOFIA program plans to support a technology development and new instrumentation program that will essentially provide an entirely new instrument complement (and thus an entirely new mission) every ~10 years. Given the cost of new space-based instrumentation and the

[1] Details on all SOFIA science instrument are available from: http://www.sofia.arc.nasa.gov/Science/instruments/sci_instruments.html .

rapidly evolving capability at THz frequencies, a modest level of funding for new SOFIA instruments expects to yield a bountiful science return to NASA, DLR, and the at-large astronomical community.

## 4. THZ SCIENCE WITH SOFIA

As illustrated in Figure 4, SOFIA will be able to contribute to a wide variety of science topics. These focus on the formation of stars and planetary systems, the characteristics of dwarf-planets at the edge of our Solar System and what they tell us about the origin and evolution of the solar system, the death of stars and the enrichment of galaxies by their ashes, the black hole in the center of our galaxy, and the role of star formation and black hole activity in the nuclei of starburst galaxies. Below, we discuss in more detail some of the first THz science that may be done with SOFIA.

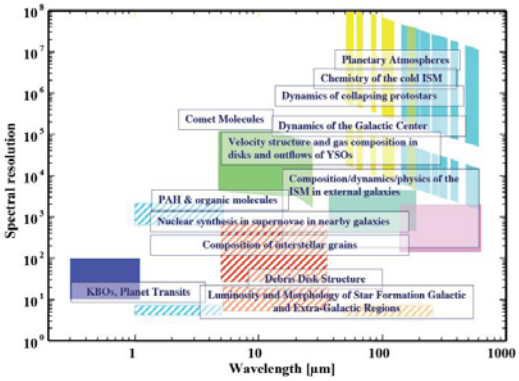


**Figure 4. An overlay of SOFIA science with the phase space of the observatory's first generation instrument suite.**

### 4.1. The ISM of Galaxies

The interstellar medium (ISM) plays a central role in the evolution of galaxies as the birthsite of new stars and the repository of old stellar ejecta. The formation of new stars slowly consumes the ISM, locking it up for millions to billions of years. As these stars age, the winds from low mass, asymptotic giant branch stars (AGB) and high mass, red supergiants (RSG), and supernova explosions inject nucleosynthetic products of stellar interiors into the ISM, slowly increasing its metallicity. This constant recycling and associated enrichment drives the evolution of a galaxy's visible matter and changes its emission characteristics. To understand this recycling, we have to study the physical processes of the ISM, the formation of new stars, the injection of mass by evolved stars, and their relationships on a galaxy-wide scale. Dust and gas play a major role in these processes and hence SOFIA with its wide wavelength coverage and high spectral resolution capabilities is destined to play a dominant role in this field.

Of specific importance are the atomic fine structure lines of [OI] at 63 and 145 μm and of [CII] at 158μm. These lines are bright in regions illuminated or shocked by massive stars and their outflows. The GREAT instrument on SOFIA will be the only means to resolve these lines at the sub-km/s level and hence probe in detail the physical conditions in these regions as well as their kinematics.

### 4.2. The Interstellar Deuterium Abundance

Deuterium was formed in the Big Bang; its abundance provides strong constraints on the physical conditions during the first few minutes of the universe's expansion. As stars form, deuterium is lost due to nucleosynthesis when material is cycled through stellar interiors in the course of galactic chemical evolution. Deuterium is thus potentially a key element for probing the origin and evolution of the universe as well as the star formation history of the universe. The 3 THz (100 μm) channel on GREAT is designed to measure the ground state transition of HD, the main reservoir of deuterium in molecular clouds, at sub-km/s resolution. HD will be seen in emission in the warm gas associated with photodissociation regions and interstellar

shocks, and in absorption toward bright background sources. Observations of a wide sample of sources will probe the cosmologically important D abundance and its astration by nuclear burning in stars throughout the galaxy. SOFIA is the only observatory with the appropriate wavelength coverage and spectral resolution required for this study (see Güsten 2005).

### 4.3. THz (Far-Infared and Submillimeter) Surveys

Following the spectral studies of ISO (e.g. van Dishoeck and Tielens, 2001) and Spitzer (e.g. Watson et al, 2004), and in line with the spectral surveys proposed for Herschel (e.g. Schilke et al, 1997), SOFIA will likely also develop its own spectral surveys program. Using the first light heterodyne instruments, spectral line surveys can be made to reveal many new lines in the broad atmospheric window of SOFIA not covered by Herschel. With spectral line sensitivities similar to the CSO, many new lines should be observed for the first time in the 1.3 - 1.5 THz region and the 2 - 5 THz region

## 5. SUMMARY

The Stratospheric Observatory for Infrared Astronomy (SOFIA) will be the premier platform from which to make astronomical observations at THz frequencies for the next twenty years. With the ability to deploy new and updated instruments, the observatory will play an important role in addressing a variety of astrophysical problems well into the 21st century.

## 6. ACKNOWLEDGMENTS

We thank the entire SOFIA team for much tireless and continued work on the SOFIA project. We would especially like to thank Tom Greene, Rolf Güsten, John Lacy, and Matt Richter for putting together parts of several of the science cases described in this paper.

## 7. REFERENCES

Becklin, E. E., "The Stratospheric Observatory for Infrared Astronomy (SOFIA)", in the *Proceedings of the ESA Symposium "The Far Infrared And Submillimetre Universe"*, pp. 201-206, ESA SP-401, Grenoble, France, August 1997.

Casey, S. C., "The SOFIA program: astronomers return to the stratosphere", in *Advances in Space Research*, p 560 – 567, 34, 2004.

Erickson, E. F. and Davidson, J. A., "SOFIA: The Future of Airborne Astronomy", in *Proceedings of the Airborne Astronomy Symposium on the Galactic Ecosystem: From Gas to Stars to Dust*, edited by M. R. Haas, J. A. Davidson, and E. F. Erickson, vol. 73, Astronomical Society of the Pacific, San Francisco, CA, 1995.

Güsten, R., The Interstellar Deuterium Abundance, *http://www.sofia.usra.edu/Science/science_cases/index.html*, 2005.

Schilke, P., Phillips, T. G., and Mehringer, D. M. First Wide Band Submillimeter Line Surveys, in: Wilson, A. (Ed.), The Far Infrared and Submillimeter Universe, pp. 73-80, (1997).

van Dishoeck, E. F. and Tielens, A. G. G. M. Space-borne Observations of the Life Cycle of Interstellar Gas and Dust, in: Bleeker, J. A. M., Geiss, J., and Huber, M. C. E. (Eds.), The Century of Space Science, pp. 607-646, 2001.

Watson, D. M. et al. Mid-infrared spectra of class I protostars in Taurus. Astrophys. J. Supplement Series 154, 391-395, 2004.

# Spectroscopy with the Herschel Space Observatory

Paul F. Goldsmith

NASA Herschel Project Scientist
Jet Propulsion Laboratory, California Institute of Technology

***Abstract* — Submillimeter astronomy from space offers many advantages, due to completely avoiding the attenuations and noise from the Earth's atmosphere. For spectroscopy in the 60 to 670 micron range, the Herschel Space Observatory offers important new capabilities in terms of angular resolution, sensitivity, and over much of this range, for high spectral resolution observations. Herschel builds on the success of two earlier space missions devoted to submillimeter spectroscopy: SWAS and Odin. In this paper, I briefly highlight the results from those missions. I then discuss the capabilities of the three instruments on the Herschel Space Observatory, known by their acronyms HIFI, SPIRE, and PACS, focusing on spectroscopic observations. I conclude with a short summary of some of the astrophysical highlights that may be anticipated when Herschel is operational, which should be about 6 months after launch, currently scheduled for September 2008.**

***Index Terms* — submillimeter spectroscopy, far-infrared spectroscopy, spectrometers**

## I. THE EARTH'S ATMOSPHERE

The submillimeter spectral range may be defined as the decade in wavelength shortwards of 1mm, thus covering the range of 1000 μm to 100 μm. This is also referred to by some as the far-infrared, although that term generally includes wavelengths as short as a few tens of microns. The primary impediment to astronomy in the 1000 μm to 100 μm wavelength region, whether referred to as the submillimeter or far-infrared, is the earth's atmosphere. Both in terms of the absorption, and also due to variability and inhomogeneities, the atmosphere is a real obstacle. Water vapor is the primary culprit, and only at the highest, driest sites is the amount of water low enough to provide reasonable transmission at the most favorable wavelengths. These "atmospheric windows" fall between strong rotational transitions of the water molecule, but at frequencies near the transition frequencies themselves, the atmosphere remains opaque even from airplane altitudes. This situation, shown in Figure 1, means that while good astronomy can be done in submillimeter windows, to get good coverage **throughout** the submillimeter range, one has to go into space.

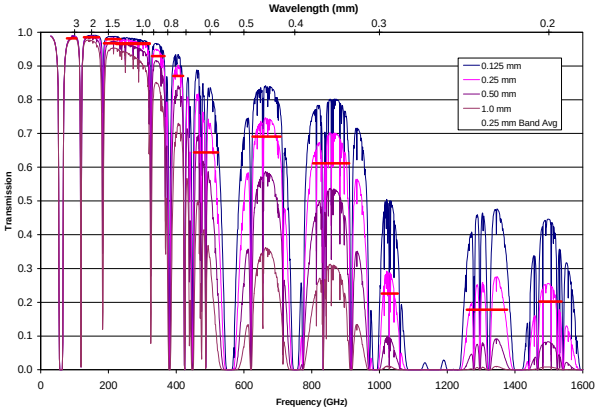


Figure 1 – Atmospheric transmission at millimeter and submillimeter wavelengths for different values of atmospheric precipitable water vapor. The different ALMA bands are indicated by the horizontal lines. The spectral regions with essentially zero transmission coincide with strong rotational transitions of $H_20$, with the exception of the ranges blocked by the $O_2$ lines near 60 GHz and that obscured by the single line near 118 GHz.

Submillimeter astronomy can be done from the ground, but this does require a high altitude site. Until the present, this has primarily meant Mauna Kea, in Hawaii, where the Caltech Submillimeter Observatory (CSO), James Clerk Maxwell Telescope (JCMT), and the Submillimeter Array (SMA) are located. There is a growing movement to utilize the high Chajnantor plateau in northern Chile, where the APEX, RLT, Nanten, and ASTE telescopes are sited, where the Atacama Large Millimeter Array (ALMA) is under construction, and where the Cornell Caltech Atacama Telescope (CCAT) will be located. Getting above most of the water vapor has been possible with airborne telescopes, notably the Kuiper Airborne Observatory (KAO), and the Stratospheric Observatory for Infrared Astronomy (SOFIA) which should be operational in a few years. Many of these instruments are described in other talks in this conference, and the best additional sources of information about their capabilities are their respective web sites.

## II. SUBMILLIMETER ASTRONOMY FROM SPACE – THE PATHFINDER MISSIONS: SWAS & ODIN

Submillimeter astronomy from space offers the following important advantages:

- access to the full spectral range, which is essential to obtain an unbiased inventory of molecules in astronomical sources and to determine the spectral energy distribution (SED) of dust in cool molecular clouds;
- ability to observe key species totally blocked by the earth's atmosphere, notably $H_2O$ and $O_2$;
- superior calibration accuracy due to the absence of large and variable atmospheric attenuation;
- lower noise due to absence of short-term atmospheric fluctuations, particularly important for broadband (continuum) observations;
- better system stability due to the absence of atmosphere and also diurnal local temperature variations.

The above considerations were key factors in the decision to develop two previous missions dedicated to high resolution submillimeter spectroscopy. Other space missions, including the Infrared Space Observatory (ISO) and the Infrared Astronomy Satellite (IRAS) observed in the short wavelength portion of the submillimeter. ISO had moderate resolution spectrometers, while IRAS did not carry out spectroscopic observations. The Submillimeter Wave Astronomy Satellite – SWAS (NASA) and the Odin satellite (Swedish space agency together with other European space agencies) utilized heterodyne receivers with phase locked local oscillators and mixers, an IF amplifier chain, and acousto-optical and digital spectrometers for spectral analysis. As such, the signal path is very similar to that found in ground-based radio astronomy systems [1].

SWAS was a relatively simple system with few tuning adjustments. The front end had an ambient temperature calibration load, and a nutuating secondary for rapid beam switching on the sky. However, most observations were carried out by position switching, that is, by repointing the entire spacecraft at 30s intervals, alternating between the "source" and "reference" positions. This was efficient due to the very rapid slewing and acquisition (using a star tracker) of the satellite resulting from its relatively large gyros and good control system (see Figure 2). The system stability was excellent, due to careful thermal design, and a number of very long integrations were carried out which achieved noise levels consistent with those expected from the radiometer equation and the noise temperature.

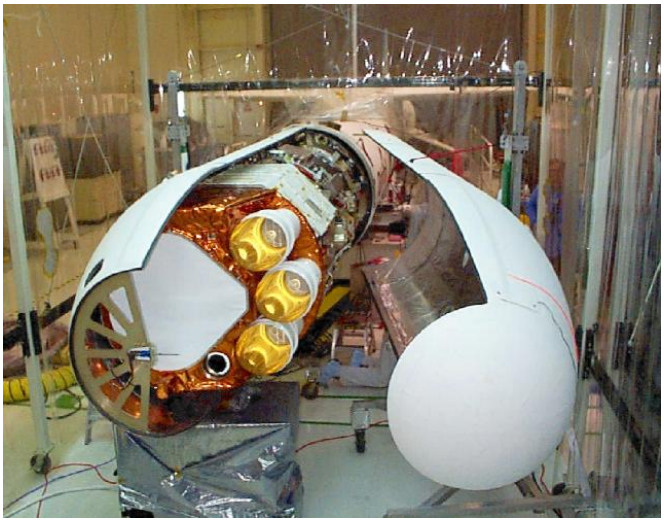

Figure 2 – SWAS spacecraft being readied for launch by Pegasus XL rocket. The woven teflon film covers the elliptical aperture on the left. Three Winston cone radiators which passively cool the front end to ~ 170 K are on the right, and the star tracker aperture is visible at lower middle.

The SWAS front end included two Schottky diode second harmonic mixer receivers operating in opposite linear polarizations. The local oscillator, which was essentially fixed tuned, was provided by frequency-tripled Gunn oscillators. The choice of IF and LO frequencies resulted in the 487.25 GHz 3,1 – 3,2 transition of $O_2$ being in the lower sideband of receiver 1, and the $^3P_1$ – $^3P_0$ 492.16 GHz transition of CI being in the upper sideband. For receiver 2, the 550.93 GHz transition of $^{13}CO$ was in the lower sideband, and the 556.94 GHz $1_{10}$ – $1_{01}$ transition of $H_2O$ was in the upper sideband. The outputs from both receivers were frequency diplexed into an acousto-optical spectrometer which devoted 350 MHz bandwidth to each spectral line. By retuning the Gunn oscillator, receiver 2 could be configured to observe the $H_2{}^{18}O$ isotopologue of water. The front end was passively cooled to ~ 170 K and system noise temperatures were 2200 – 2500 K DSB for the four primary lines of interest.

The SWAS satellite operated extremely well from its launch in December 1998 through July 2004 when it was put into hibernation. SWAS carried out large-scale surveys of neutral carbon (CI) and the J = 5 – 4 transition of $^{13}CO$ in many giant molecular clouds. These provided a great deal of information on their structure and density. But the greatest effort was spent observing the ground state transition of water, which of course cannot be observed from the ground. While $H_2O$ can readily be detected in warm regions, its abundance relative to $H_2$ was found to be typically a factor of 100 below that predicted by models of interstellar chemistry. A collection of

the early scientific results from SWAS can be found in [2]. Along with this, the $O_2$ line was not detected, and the limits in a wide range of sources [3] showed that this species, which was anticipated to be a major reservoir of oxygen in dense interstellar clouds, was again a factor ~ 100 less abundant relative to $H_2$ than had been anticipated.

These SWAS results indicated that our ideas about chemistry in dense clouds would have to be modified. Naturally, there was some surprise and controversy about the low abundance of water and molecular oxygen. However, not long after SWAS results were published, the Odin satellite was launched. Odin was considerably more complex than SWAS having several different receivers, widely tunable local oscillators, and a digital autocorrelation spectrometer as well as an acousto-optical spectrometer [4]. Also, Odin's primary reflector was 1.1m in size compared to the 0.54 x 0.68 m elliptical primary mirror employed by SWAS, giving a smaller beam. The Odin satellite was designed to carry out observations of the earth's atmosphere as well as astronomy, and thus could look "down" as well as "up". The front end was cooled by a mechanical cooling system rather than by passive radiators as was SWAS. The latter system could thus not look towards the earth without dramatically upsetting the thermal balance of the receiver system.

Odin's results on water and molecular oxygen were largely consistent with those of SWAS. In particular, water lines were again found to be very weak, and the abundance of this species low. Odin confirmed this by observing the rare $H_2{}^{18}O$ isotopologue of water (Figure 3), and from this astronomers concluded that the fractional abundance of $H_2O$ relative to $H_2$ is only 1–8 $x10^{-8}$ [5]. One of the possible explanations is that oxygen atoms stick to dust grains, are then hydrogenated to water, which remains on the grain surfaces as water ice. The result is a deficiency of oxygen in the gas phase, and that which remains tends to be in the form of carbon monoxide, leading to much reduced abundances for other oxygen-containing species, notably water and molecular oxygen [6]. There are other competing theories including circulation of material between cloud edges and well-shielded interior. This is just one of the areas that will be addressed by the Herschel Space Observatory.

## III. THE HERSCHEL SPACE OBSERVATORY

The Herschel Space Observatory (HSO) can be considered to be a second-generation submillimeter spectroscopy facility for astronomy. This does not mean that it can only do spectroscopy. In fact, two of its instruments together cover the entire 60 μm to 500 μm range for broadband photometry, using imaging arrays of detectors. The purpose of this paper is, however, to focus on the spectroscopic capabilities of Herschel. General information about the satellite, as well as the capabilities of the three focal plane instruments can best be found on the web, at http://herschel.esac.esa.int/ and http://www.ipac.caltech.edu/Herschel/.

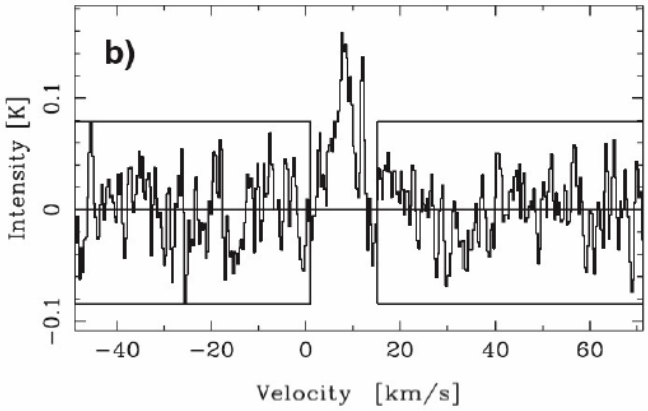


Figure 3 – Odin detection of $H_2{}^{18}O$ in Orion [5]. This very weak line confirms the low abundance of gas phase water in quiescent molecular clouds.

The HSO has a 3.5 m diameter primary reflector, which is passively cooled to ~ 70 K. This low temperature is made possible by the HSO's orbit – it will be near the L2 Lagrange point, 1.5 million km farther away from the sun than is the earth, along the line from the sun to the earth. This orbit gives good thermal stability as well as low thermal pickup from the earth. The instruments in the Herschel focal plane are cooled to 2 K by liquid helium, and some of the detectors are cooled to sub-Kelvin temperatures by additional refrigeration stages. Herschel is scheduled to be launched in September 2008 by an Ariane V rocket, which in a dual launch, will also take the Planck spacecraft into orbit.

Herschel has three focal plane instruments which operate as spectrometers. They are

HIFI: Heterodyne Instrument for the Far Infrared, a high resolution heterodyne spectrometer covering 157 μm to 212 μm and 240 μm to 625 μm;

SPIRE: Spectral and Photometric Imaging Receiver, an imaging Fourier Transform spectrometer covering 200 μm to 670 μm;

PACS: Photoconductive Array Camera and Spectrometer; grating spectrometer with image slicer covering 60 μm to 210 μm.

This set of instruments is particularly interesting purely from the point of view of technology as they cover almost the complete gamut of existing technology in terms of detectors

and achieving spectral resolution. In the next sections, I will briefly discuss each of the three Herschel instruments.

*A. HIFI*

HIFI uses two mixers operating in orthogonal linear polarizations at each frequency. To cover the very large frequency range, there are 7 bands, and for each the local oscillator is divided into a high frequency and low frequency unit. The mixers in the five lowest frequency bands (480 – 1250 GHz) are Superconductor Insulator Superconductor (SIS) mixers and in the two highest frequency bands (1410 – 1910 GHz) are Hot Electron Bolometer (HEB) mixers. Providing a broadly tunable local oscillator was a major technical challenge for HIFI. It is realized by a chain starting with a relatively conventional frequency synthesizer at K-band, which is then frequency tripled to W-band. From there, different combinations of frequency doublers and frequency triplers multiply the frequency by factors between 6 and 24 to obtain the power required to pump the pair of mixers operating at the desired submillimeter frequency.

The IF from the SIS mixers is in the range 4 to 8 GHz, and that from the HEB mixers covers 2.4 to 4.8 GHz. The HIFI mixers are cooled to 2 K, and each mixer is followed by a low noise amplifier at a temperature of 15 K. Further amplification is followed by frequency conversion for the HEB channels, and the signals from the selected band are sent to the ambient temperature spectrometer subsystem.

Spectral analysis is carried out by two different subsystems. Each is doubled to provide independent analysis for each linear polarization. The wideband system (WBS), based on an acousto-optical spectrometer, first divides the signal into 4 1GHz-wide sub bands. These are sent to four Bragg cell transducers in a collimated laser beam. The diffracted energy is collected by a CCD readout which has 4 lines of detectors - one for each of the 4 sub bands. Each linear array provides 1000 pixels with 1 MHz nominal channel separation, and noise bandwidth slightly greater than 1 MHz. Thus, there is a total of 8000 spectral channels in the two polarizations from the wideband spectrometer system. At the highest HIFI frequency, the 2.4 GHz IF bandwidth corresponds to a velocity range of 380 km/s and the channel width corresponds to a velocity range of 0.16 km/s. At the lowest frequency, the 4 GHz IF bandwidth corresponds to 2500 km/s, and the resolution is 0.6 km/s. HIFI thus has a maximum fractional frequency coverage of 0.008, which is adequate for individual lines even in active galaxies. For line surveys, numerous observations with different local oscillator settings will be required.

The velocity resolution of the wideband spectrometer is not quite adequate for observations of quiescent regions in the interstellar medium. To enable this science a high resolution narrow band system (NBS) based on a digital autocorrelation spectrometer, is included. The NBS can provide resolutions as fine as 0.125 MHz, corresponding to a maximum velocity resolution of 0.08 km/s. This high resolution data covers up to 235 MHz of frequency, which can be moved within the bandpass of the WBS, to examine a particular spectral line in more detail, for example. The NBS can also provide somewhat lower frequency resolution over bandwidths up to 500 MHz.

HIFI noise temperatures represent impressive progress, especially given that this is in a space-qualified system which has had to undergo rigorous testing and is capable of nearly autonomous operation. The double sideband (DSB) noise temperature for the SIS systems increases approximately linearly from 50 K at 480 GHz to 1000 K at 1250 GHz. These values are the average over the 4 GHz IF band. For the HEB mixers, noise temperatures are somewhat higher, but the primary variation is as a function of IF frequency rather than RF frequency: typical values are 1000 K and 2.4 GHz and 2000 K at 4.8 GHz IF frequency.

The HIFI system optics includes a chopper which can make the operating receiver look at one of two temperature-controlled absorbing loads for calibration. It can also switch the beam between two positions in the focal plane, which has the effect of introducing an angular offset of 3’ for the beam on the sky. Each of the 7 HIFI bands points to a different position on the sky, and that only one band can be used at any one time. Thus, the telescope pointing must correct for the band that has been selected, while the data can be taken by moving the entire telescope between the “source” and “reference” position at a relatively slow rate, by rapid beam switching using the focal plane chopper, or by frequency switching. The actual performance of these various observing modes will be proven only during the verification phase once the satellite is on orbit. Additional HIFI information can be found in [7].

*B SPIRE*

The SPIRE instrument has largely separate sections for photometry and spectrometry. The most complete and up to date information can be found at http://www.spire.rl.ac.uk/ and in [8]. SPIRE spectroscopy is based on the Fourier Transform Spectrometer (FTS). An input wavelength range is determined by an input filter, and power within this range is processed by a dual-beam interferometer, with the interferogram being taken over a selected path length difference. An off-line Fourier Transform of the interferogram yields the power spectrum of the input signal. This basic system has been used in many astronomical (and other) spectrometers, and has the advantage that the entire frequency range is analyzed simultaneously. Thus, at low resolution, this can be used to measure the spectral energy distribution (SED) of continuum emission from dust grains. At higher resolution, individual spectral lines can be observed.

A limitation of the FTS in the submillimeter is that the restricted path length difference (in cm) that can be achieved implies a maximum spectral resolution (in $cm^{-1}$). For SPIRE, the highest resolution of 0.04 $cm^{-1}$ corresponds to a modest fractional resolution, as indicated in Figure 4. This resolution is adequate to obtain the integrated intensity in spectral lines, but only for external galaxies with relatively large line widths will any lines be resolved. Nevertheless, the fact that the entire bandpass is analyzed simultaneously makes SPIRE a powerful tool for diagnostics of galaxies, as well as for objects such as the giant planets in our solar system which have pressure broadened spectral lines.

An important advantage of the FTS is that a number of beams corresponding to different directions on the sky can propagate through the spectrometer simultaneously. In the case of the SPIRE FTS there are two detector arrays. For the short wavelength band covering 200 μm to 325 μm, there are 37 detectors in a hexagonal close packed array. For the long wavelength band covering 315 μm to 670 μm there are 19 detectors. Each detector, which is a germanium spider web bolometer, is coupled to the telescope with an individual feed horn. The result is that the array samples essentially every other diffraction limited beam on the sky. The long wavelength horns are larger than those for the shorter wavelength band, and the two are arranged so that 13 of the beams look at the same direction in the sky in each band. This imaging capability obviously speeds up mapping of extended objects dramatically. Special techniques using the beam steering mirror included in SPIRE will be available to make fully Nyquist-sampled maps of modest size. Larger regions will be mapped by a combination of telescope pointing and scan mirror motion. Several of the projects already proposed for SPIRE involve spectral maps of extended regions in the Milky Way and other galaxies.

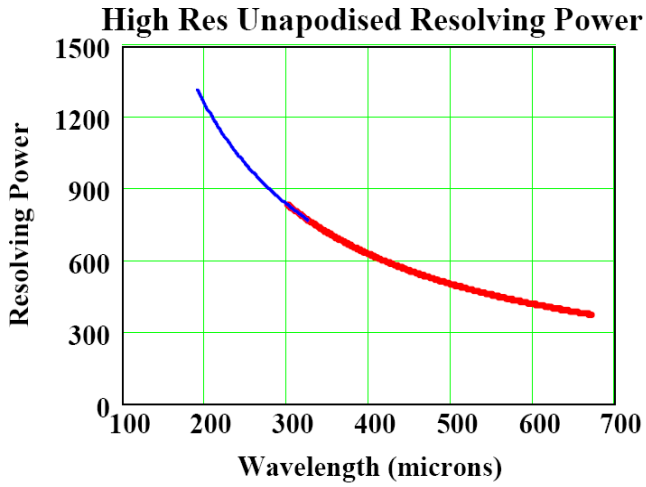


Figure 4. SPIRE resolving power (λ/Δλ) as a function of wavelength with highest spectral resolution.

The sensitivity of the SPIRE spectrometer system is fairly uniform as a function of wavelength. For an integration time of 1 hr, a 5σ limit is ~$3x10^{-17}$ W $m^{-2}$ in units of integrated flux density.

*C. PACS*

PACS, like SPIRE, has independent units for photometry and spectroscopy. They cover approximately the same wavelength range but use different types of detectors. Additional information about PACS can be found in [9] and at http://www.mpia.de/PACS/index_B.html. The PACS spectrometer is based on a diffraction grating. In this instrument, an image slicer takes a 5x5 array of 9.4" pixels on the sky and reimages them onto a 25 element line, which is effectively the input slit to the grating. The grating sends light in different directions according to wavelength, but it does this for each of the 25 spatial elements along the slit. The detector arrays have 16 spectral elements by 25 spatial elements. Each detector is a Ge:Ga bolometer, unstressed for shorter wavelengths and stressed for longer wavelengths. Since different wavelength ranges can be diffracted in different orders, one can observe in two wavelength ranges simultaneously. These are 65 – 85 μm and 130 μm – 210 μm, or 85 μm – 130 μm and 130 μm – 210 μm.

The resolution of the PACS spectrometer depends on wavelength (in part due to different orders being used in different ranges), varying from 3000-4000 at the short wavelength end to 1000-2000 at the longest wavelengths. These are high enough that some spectral lines in active regions, such as the Galactic Center, may be resolved, and

emission lines from nearby galaxies almost certainly will mostly be spectrally resolved.

PACS sensitivity varies considerably as a function of wavelength as shown in Figure 5. As is the case for SPIRE, PACS gains an impressive advantage in spectroscopy of

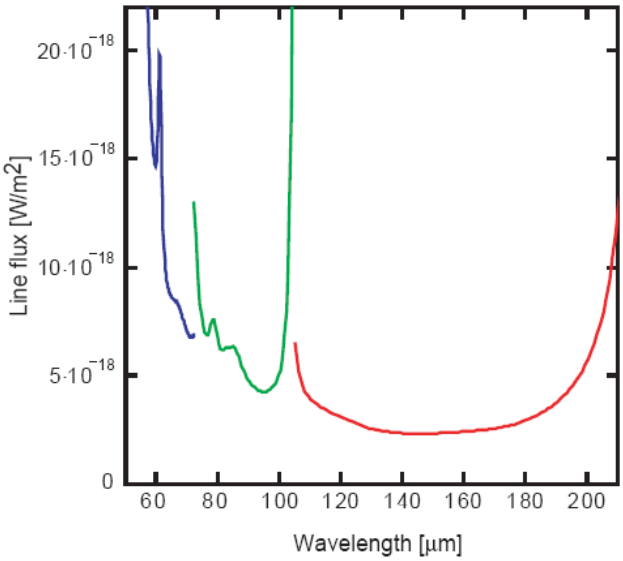


extended sources since 25 spatial pixels are observed

Figure 5. PACS sensitivity in terms of 5σ integrated line flux limit achievable in 1 hr integration. From [9].

simultaneously. At the relatively short PACS wavelengths, even though the spectrometer detector pixels correspond to a beam size larger than determined by diffraction, the 9.4" beams are quite small, and many interesting sources will definitely be spatially extended. Thus there are a number of mapping modes for exploiting PACS.

## IV. HERSCHEL SCIENCE

Due to the large wavelength coverage, the greatly improved sensitivity compared to past submm missions, and the great variety of frequency resolution and types of observation that can be carried out, it is impossible to give fair treatment to all the astronomy that has already been proposed to be done with Herschel, and that likely will be carried out. I here give only a few selected highlights, focusing on the types of observations that can be carried out in the general category of "Herschel Spectroscopy."

One of the key goals of Herschel spectroscopy is to study molecules in the interstellar medium, as well as in solar system objects and the atmospheres of evolved stars. Many molecules have their rotational transitions in the millimeter and submillimeter regions. The most abundant of these is carbon monoxide, and the lowest rotational transitions are shown in Figure 6. While the lower transitions can be well studied from the ground at millimeter wavelengths, at the temperatures characteristic of star forming regions in the Milky Way and other galaxies, as well as in protoplanetary disks and the solar system, the strongest transitions will be in the submillimeter/far infrared, exactly the region covered by Herschel. As seen in Figure 6, the different Herschel instruments together cover CO transitions with upper level quantum number between 4 and 43. This wide range will allow extremely good use of CO as a diagnostic of physical conditions in a very wide range of environments, as well as being optimal to trace gas in regions with very different physical conditions.

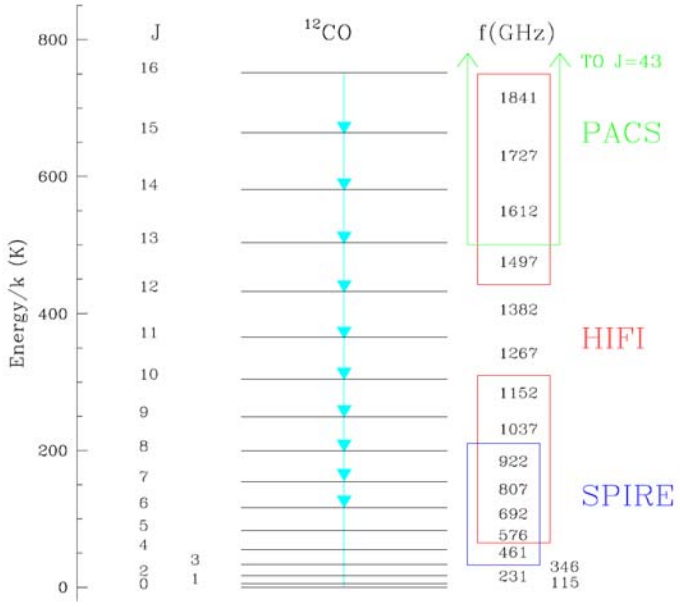


Figure 6. Lower rotational energy levels and transitions of the carbon monoxide molecule, with indication of which can be observed with which Herschel instrument.

Another target for Herschel spectroscopy will be fine structure lines – the transitions which arise from interaction of spin and orbital angular momentum in atoms. Two of the most important atomic species with submillimeter fine structure lines are carbon and oxygen. The term schemes along with key spectroscopic information are shown in Figure 7. Neutral carbon has been observed with some difficulty from the ground, but has also been studied using telescopes in stratospheric aircraft, and with the SWAS and Odin satellites. However, almost all of this work has been done on the lower frequency (492 GHz) transition, but both fine structure lines

will be observable with Herschel HIFI. Observing the two transitions together will greatly increase our ability to disentangle optical depth and excitation effects, making possible a much more accurate determination of the CI abundance, which is a very important issue for modeling of molecular cloud structure.

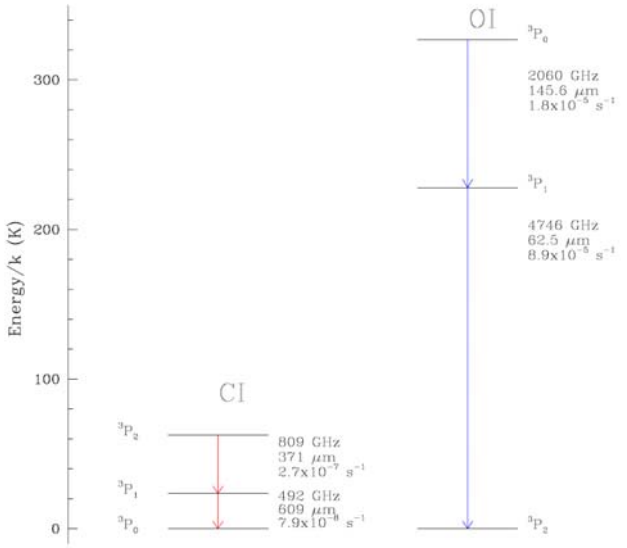


Figure 7. Fine structure transitions of atomic carbon and atomic oxygen.

Atomic oxygen has been observed using the ISO satellite. It is one of the most important cooling lines in photon dominated regions, and is seen throughout the Milky Way and other galaxies. The PACS system will give astronomers dramatically enhanced capability to observe OI, although emission and absorption features in the Milky Way will not be spectrally resolved.

Other important spectral lines for Herschel include fine structure transitions of ionized species, particularly carbon and nitrogen. Again in the PACS range, these lines are crucial for understanding the thermal balance in regions around massive young stars. Herschel projects will be targeting CII and NII lines in a variety of regions ranging from nearby ionized regions to distant galaxies.

## V. CONCLUSIONS

The first generation of space missions for submillimeter spectroscopy, SWAS and Odin, had a great impact on our ideas about interstellar chemistry and the structure of molecular clouds. Herschel, with a far larger primary reflector, and instruments with far greater sensitivity and frequency coverage, will certainly produce many more surprises, as well as filling in our knowledge about the solar system, molecular clouds and star formation, and galaxies near and far. The three instruments, considered as spectrometers, are so different from one another that they make almost a textbook on different ways to build a spectrometer. HIFI has only a single spatial pixel, but extremely broad coverage combined with high frequency resolution. SPIRE and PACS are both imaging spectrometers, but operate very differently. SPIRE covers a large frequency range with modest resolution, while PACS observes a narrow wavelength range at any moment, but offers moderate frequency resolution, sufficient to resolve spectral lines in some situations. HIFI and SPIRE can observe many lines simultaneously, while PACS observes a single line. We certainly anticipate that these disparate spectrometers will together have a great impact on astrophysics starting about two years from now.

## ACKNOWLEDGEMENT

I thank Gary Melnick, PI of the SWAS mission, for providing graphics of hardware and scientific results. The research described in this (publication or paper) was carried out at the Jet Propulsion Laboratory, California Institute of Technology, under a contract with the National Aeronautics and Space Administration. This research has made use of NASA's Astrophysics Data System.

## REFERENCES

[1] G. J. Melnick et al. "The *Submillimeter-Wave Astronomy Satellite*: Science Objectives and Instrument Description," Astrophys. J., 539, pp. L77-L85, 2000.

[2] Special issue of The Astrophysical Journal dedicated to SWAS, Astrophys. J., 539, pp. L77 – L153, 2000.

[3] Paul F. Goldsmith et al., "$O_2$ In Interstellar Molecular Clouds," Astrophys. J., 539, pp. L123-L127, 2000.

[4] U. Frisk et al., "The Odin Satellite I. Radiometer design and test," Astron. Astrophys., 402, pp. L27-L34, 2003.

[5] A.O.H. Olofsson et al., "Odin water mapping in the Orion KL region," Astron. Astrophys., 402, pp. L47-L54, 2003.

[6] E. Bergin et al. "Implications of *Submillimeter-Wave Astronomy Satellite* Observations for Interstellar Chemistry and Star Formation," Astrophys. J., 539, pp. L129-L132, 2000.

[7] T. deGraauw et al., "The Herschel-Heterodyne Instrument for the Far-Infrared," Proc. SPIE, 2006.

[8] M. Griffin et al. "Herschel-SPIRE: design, performance, and scientific capabilities," Proc. SPIE, vol. 6265, pp. 62650A-1 – A12, 2006.

[9] A. Poglitsch et al., "The Photodetector Array Camera and Spectrometer (PACS) for the Herschel Space Observatory," Proc. SPIE, vol. 6265, pp. 62650B-1 – B12, 2006.

# The Cornell Caltech Atacama Telescope

Simon J. E. Radford[a], Riccardo Giovanelli[b], Thomas A. Sebring[b], Jonas Zmuidzinas[a]
[a] California Institute of Technology, 320-47, Pasadena, CA 91125
[b] Center for Radiophysics and Space Research, Cornell University, Ithaca, NY 14853

**ABSTRACT**

Cornell University, the California Institute for Technology, and the Jet Propulsion Laboratory are jointly studying the construction of a 25 m diameter telescope for submillimeter astronomy on a high mountain in northern Chile. This Cornell Caltech Atacama Telescope (CCAT) will combine high sensitivity, a wide field of view, and a broad wavelength range to provide an unprecedented capability for deep, large area, multi-color submillimeter surveys to complement narrow field, high resolution studies with ALMA. CCAT observations will address fundamental themes in contemporary astronomy, notably the formation and evolution of galaxies, the nature of the dark matter and dark energy that comprise most of the content of the universe, the formation of stars and planets, the conditions in circumstellar disks, and the conditions during the early history of the Solar system. The candidate CCAT site, at 5600 m in northern Chile, enjoys superb observing conditions. To accommodate large format bolometer cameras, CCAT is designed with a 20 arcmin field of view. CCAT will incorporate closed loop active control of its segmented primary mirror to maintain a half wavefront error of 10 μm rms or less. Instrumentation under consideration includes both short (650 μm–200 μm) and long (2 mm–750 μm) wavelength bolometer cameras, direct detection spectrometers, and heterodyne receiver arrays. The University of Colorado, a Canadian university consortium, and the UK Astronomy Technology Centre on behalf of the UK community are pursuing participation in the CCAT consortium. When complete early in the next decade, CCAT will be the largest and most sensitive facility of its class as well as the highest altitude astronomical facility on Earth.

## 1. INTRODUCTION

Led by pioneering research at the CSO, the JCMT, and other telescopes, submillimeter astronomy has made tremendous advances in the last twenty years. Two notable examples are the discovery of a population of optically inconspicuous but submillimeter luminous galaxies in the early universe with the SCUBA camera (Holland et al. 1999) and the recognition the integrated intensity of the far IR and submillimeter radiation in the universe equals the intensity at optical wavelengths (Hauser & Dwek 2001). At the same time, the size of background limited bolometer arrays for submillimeter observations is increasing rapidly, doubling every couple of years. These cameras, which are well suited to high sensitivity, wide field surveys, will soon outstrip the capabilities of existing telescopes. Bolometer arrays are complementary to the heterodyne technology used in interferometers, such as ALMA. Finally, meteorological and radiometric studies in the high Andes of northern Chile have identified superb sites there, better than Mauna Kea, for ground based submillimeter astronomy.

These factors have motivated Cornell University, the California Institute for Technology (Caltech), and the Jet Propulsion Laboratory (JPL) to jointly study the construction of a 25 m telescope for submillimeter astronomy on a high mountain in northern Chile. With a 20 arcmin field of view, this Cornell Caltech Atacama Telescope (CCAT; Figure 1) will emphasize sensitive wide field observations with large format bolometer cameras. CCAT will have a larger aperture, better quality optics, a larger field of view, and a better site than existing telescopes. By identifying an abundance of sources for later detailed study, CCAT's large area surveys will complement the narrow field, high spectral and spatial resolution capabilities of ALMA. The CCAT feasibility and concept design study (Sebring et al. 2006a) was completed at the end of 2005 and the project received a

Fig. 1. CCAT at 5600 m on Cerro Chajnantor, Chile (concept view).

strong endorsement from an independent review committee in 2006 January. The CCAT consortium is now expanding and the project plan aims for initial observations in 2012.

## 2. SCIENCE HIGHLIGHTS

Although hydrogen and helium make up over 98% of the baryonic matter in the Universe, in many cases it is the heavier elements, notably carbon, oxygen, silicon, and iron that allow us to discover and study distant objects. These elements form complex molecules and small dust particles that in many astrophysical environments obscure optical and ultraviolet photons and radiate predominantly at submillimeter wavelengths. Many of the most powerful and interesting phenomena in the universe, from star forming regions in our own galaxy to entire starburst galaxies in the early universe, are shrouded by dust and are completely inaccessible with optical observations. This makes submillimeter observations a particularly valuable probe of many astrophysical sources.

As well as being substantially larger and more sensitive than existing submillimeter telescopes, CCAT will be the first large submillimeter telescope designed specifically for wide field imaging. Hence it will provide an unparalleled ability to address key astronomical questions by mapping large areas of the sky. Science highlights include:

*Galaxy formation and evolution:* CCAT will detect hundreds of thousands of submillimeter starburst galaxies from the era of galaxy formation and assembly 10–12 billion years ago ($z$ = 2–4) and will probe the earliest bursts of dusty star formation as far back as $z \sim 10$, less than 500 million years after the Big Bang. These observations will investigate the star formation history of the early universe, including the evolution of the population, the luminosity distribution, and the clustering of these galaxies.

*Dark Matter and dark energy:* CCAT's high resolution images of the Sunyaev-Zel'dovich effect in hundreds of clusters of galaxies will illustrate in detail how clusters form and evolve and will aid the determination of the dark energy equation of state and other cosmological parameters from SZ survey catalogs.

*Star Formation:* CCAT will provide the first complete census of cold, dense Galactic molecular cores that collapse to form stars. In nearby clouds, CCAT will detect 0.08 $M_{\odot}$ cores, smaller than the lowest mass stars.

*Protoplanetary and debris disks:* CCAT will survey nearby young star clusters to determine the prevalence and evolution of protoplanetary and debris disks. In conjunction with high resolution ALMA imaging, CCAT observations will study disk structure.

*The Kuiper belt:* Beyond Neptune, the Kuiper belt is a relic containing a record of the processes active in the early solar system, i. e., the accretion, migration, and clearing phases. CCAT will determine basic physical data – sizes and albedos – for hundreds of Kuiper belt objects, helping to anchor models of planet formation in the early solar system.

## 3. TELESCOPE SITE

Over the past decade, several groups have evaluated conditions for submillimeter astronomy at sites at and above 5000 m in the Atacama region of northern Chile (Radford & Holdaway 1998; Giovanelli et al. 2001). The measurements demonstrate these sites enjoy excellent observing conditions with extremely low atmospheric water vapor content. Observing conditions are considerably better than Mauna Kea and are comparable to the Antarctic plateau. As a result several telescopes have already been established in the vicinity of the village of San Pedro de Atacama, notably the international ALMA project now under construction on the 5000 m Chajnantor plateau. Furthermore, conditions on the peaks surrounding the ALMA site are even better, particularly when thermal inversions trap much of the water vapor below the mountain summits. Under these circumstances, the transmission in the submillimeter (350 μm and 450 μm) windows is excellent and limited transmission exists even in windows up to 150 μm (Marrone et al. 2005).

Of the several peaks reasonably close to ALMA, Cerro Chajnantor (5600 m) has been selected as the candidate CCAT site. Other projects are also interested in this mountain, which lies within the recently expanded CONICYT science preserve, and the University of Tokyo has constructed a road to the summit area. For CCAT, the candidate location is a small shelf about 150 m northeast and 50 m below the summit ridge (Figure 2). This location is shielded from the prevailing westerly winds and is not visible from San Pedro. In 2006 May an autonomous instrument suite was deployed to assess observing conditions at the candidate CCAT site. The data are freely available (www.submm.org/site). Meteorological measurements show the candidate CCAT site is extremely dry and experiences typical wind speeds a bit lower than at the ALMA site, which is a pleasant surprise. Two tipping radiometers, one at the candidate CCAT site and

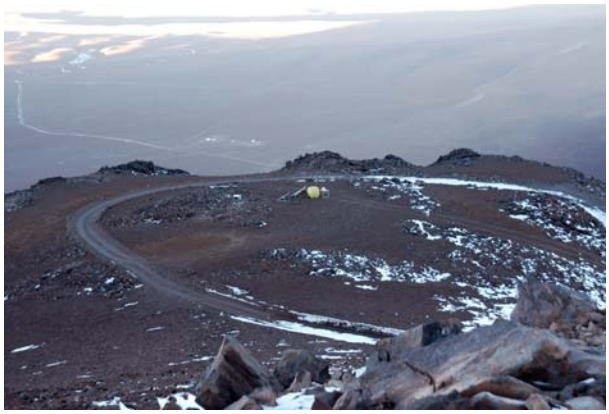

Fig. 2. View to the northeast over the CCAT site and meteorological equipment at 5612 m near the summit of Cerro Chajnantor. The existing ASTE and NANTEN2 telescopes are visible on the plateau 800 m below.

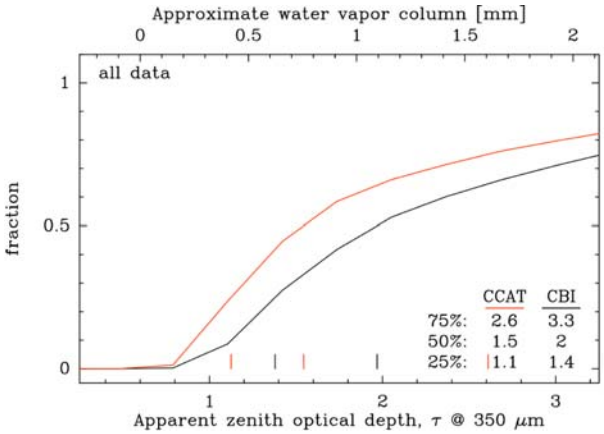


Fig. 3. Cumulative distributions of simultaneous measurements of the apparent submillimeter (350 μm) optical depth at the CCAT candidate site (5610 m) and at the CBI (5050 m) for 2006 May–2007 April. The CCAT site enjoys significantly better conditions than the CBI or ALMA, almost as much better as ALMA enjoys compared with Mauna Kea.

one at the CBI on the ALMA plateau (5050 m) for reference, simultaneously measure the atmospheric transparency at 350 μm. These comparative measurements show the submillimeter transparency, which is largely determined by the water vapor column, is significantly better at the CCAT candidate site than at ALMA (Figure 3). Observing conditions at the CCAT site are excellent, almost as much better than ALMA as ALMA is better than Mauna Kea.

## 4. TELESCOPE DESIGN

For CCAT, the primary technical requirements are a large aperture (25 m), a wide field of view (20'), high efficiency at submillimeter (> 200 μm) wavelengths, accurate offset pointing (better than 0.3" rms), and agile scanning performance. High aperture efficiency demands high quality optics, namely a half wavefront error ≤ 10 μm rms for all the principal optical surfaces together. Relative to its size, CCAT requires an optical quality substantially better than any existing radio telescope. Fundamental limits on specific stiffness and thermal stability mean this level of performance is not likely possible with a passive telescope design, even with a carbon fiber structure. To meet this challenge, therefore, the CCAT design (Sebring et al. 2006a, 2006b) incorporates closed loop active control of the primary mirror, where the relative positions of the mirror panels are sensed and then controlled with actuators. Although a few radio telescopes (CSO, GBT, Noto) use open loop control to correct for gravitational distortions with look up tables and several optical telescopes (e. g., Keck) successfully use closed loop control of segmented primary mirrors, CCAT will be the first radio telescopes to implement a closed loop active primary mirror.

### 4.1 Optical design

For optimum performance over the full field of view, CCAT has a Ritchey Chrétien design (Cortés-Medellín & Herter 2006). To allow rapid exchanges, the instruments will be mounted at the Nasmyth foci behind the primary mirror and outside the elevation bearings. These foci are inside the outer diameter of the primary mirror to keep the secondary mirror size, the back focal distance, and the dome size small. Two bent Cassegrain foci are also available on the tipping structure for small science or telescope diagnosis instruments. The primary focal ratio, *f*/0.4, is typical for a radio telescope. Across the field of view, the image quality is excellent. Although the optimal focal surface is curved, short wavelength, wide field instruments can accommodate this curvature either with corrective coupling optics or with a segmented detector array.

### 4.2 Primary mirror

The primary mirror is comprised of 210 keystone shaped panels arranged in seven rings. The panels, with maximum dimensions of 1.6 m × 1.9 m, are kinematically mounted at just three points. To meet the telescope's overall wavefront error specification, the surface accuracy tolerance for the panels is ≤ 5 μm rms including manufacturing errors and thermal and gravitational deformations. Preliminary analysis indicates several sandwich technologies can meet the requirements, including carbon fiber skins with aluminum honeycomb cores (Martin et al. 2006), molded lightweight borosilicate glass (Strafford et al. 2006), and electroformed nickel skins with aluminum honeycomb cores (Valsecchi 2003). In all these technologies, the reflecting surfaces are replicated from precision mandrels and, in the cases of carbon fiber or glass, coated with aluminum. A bolted truss, most likely made of steel for cost reasons, supports the primary mirror panels and actuators. Because such a truss is neither stiff nor thermally stable enough to maintain the necessary accuracy, active control of the panel positions is required.

### 4.3 Active mirror control

Although the success of the Keck and other optical telescopes shows closed loop active control of a segmented primary mirror is feasible, applying the technique in the technical and financial context of a radio telescope poses some challenges. Edge sensors will be used to measure the relative displacements and dihedral angles of adjacent primary mirror panels. These measurements are very effective for controlling small scale, panel to panel scale mirror distortions. Unfortunately, however, they are comparatively insensitive to large scale deformations of the entire telescope, such as focus, astigmatism, etc., that will be introduced by varying gravitational loads and thermal gradients. Moreover, because the edge sensors and actuators are physically displaced but coupled through the panels, thermal and gravitational distortions of individual panels, even if radiometrically insignificant, can adversely affect the overall mirror alignment. Hence supplemental metrology systems, such as laser rangefinders or angle sensors, are under consideration. Preliminary models indicate the active control system will work, although many details remain to be settled. Shearing interferometry observations of planets (Serabyn 2006), which have been successfully used at the CSO for many years, will be used for initial alignment of the mirror panels and for calibration of the active control system.

### 4.4 Secondary and tertiary mirror

The 2.6 m diameter secondary mirror and 1.9 m × 2.7 m tertiary mirror will be made with the same technology as the primary mirror panels. Because they are unique optics, they may be figured individually rather than replicated from a mandrel. The secondary mirror will be mounted on a five axis hexapod and will probably have a nutator for rapid beam switching during spectroscopic observations. The tertiary mirror rotates to direct the beam to any of the four foci.

### 4.5 Mount

Designs for the optics and the telescope mount were developed together. The concept mount design (Finley et al. 2006) has hydrostatic azimuth bearings with journals mounted on a cylindrical pier and radial runout controlled by a central pintle bearing. Two diametrically opposed pairs of geared motors drive against a large helical gear mounted on the inside diameter of the azimuth journal. The much lighter elevation stage uses rolling element bearings and a pair of geared motors driving a helical gear sector. To allow the full 20 arcmin field of view to pass through to the instruments, the elevations bearings have large (> 1 m diameter) apertures. Tape encoders with multiple read heads are used on both axes. Preliminary servo control models indicate the telescope will meet the stringent requirements for pointing accuracy and scanning motions. To meet the challenge of accurate pointing, an auxillary optical or near IR telescope will be used to measure the mount characteristics. Then submillimeter observations will establish the radiometric pointing. Closed loop guiding in the near IR with the auxillary telescope is also under consideration.

### 4.6 Dome

To reduce the adverse influence of wind loads and solar heating on telescope quality and pointing and to provide shelter for science instruments and telescope staff, CCAT will be enclosed in a dome. For a 25 m telescope, the smallest dome that permits free movement of the telescope inside is about 42 m in diameter. Parametric assessment of several dome types (Loewen et al. 2006) concluded a calotte design offers significant mechanical advantages and will be cheaper to build and to operate. The calotte design achieves all sky pointing with two rotation stages, a conventional azimuth stage parallel to the ground and a second stage inclined about 38° to the vertical. This design is balanced about both rotation axes and features a fixed circular aperture, which provides good protection from the wind. The nearly continuous spherical shell lends itself to efficient space frame construction. An interior shutter rotates independently to meet the

aperture near the horizon. Compared with other dome types, the calotte design is lighter, exhibits less and more uniformly distributed stress throughout the structure, and is balanced about both axes.

### 4.7 Facilities

On the mountain, the telescope facility (Terán et al. 2006) includes a control room, an office area, a computer and electronics room, and an instrument preparation lab. Because of the high altitude, these working spaces will have oxygen enrichment to enhance the safety, comfort, and productivity of observers and telescope staff. Portable supplemental oxygen will be used for exterior work during operations and during all phases of construction. Separate outbuildings house mechanical equipment such as chillers, compressors, etc., to minimize vibration and heat loading in the telescope enclosure. A lower altitude (2500 m) support facility near San Pedro will provide housing for telescope staff as well as a remote control room, offices, and instrument workshops.

## 5. INSTRUMENTATION

In recent years, large format bolometer arrays for submillimeter astronomy have developed rapidly. CCAT is specifically designed to take advantage of these developments and the primary science objectives emphasize wide field imaging and surveys. Hence the initial plan for facility instruments (Stacey et al. 2006) features two large format bolometer cameras, one for submillimeter wavelengths, 200–620 μm, and the other for near millimeter wavelengths, 740–2000 μm. Spectrometers, both direct detection and heterodyne, are also under consideration and existing, previous generation instruments developed for other facilities, will be brought to CCAT to enhance the scientific yield of the cameras. Although existing instruments cannot accomplish all the primary CCAT science objectives, they will provide important supplementary capabilities, especially in the early years of operation. Looking to the future, foreseeable instrument developments will extend the CCAT science return for many years.

### 5.1 Direct illumination cameras

At short submillimeter wavelengths the leading camera technology is directly illuminated TES silicon bolometers, exemplified by SCUBA2 (Holland et al. 2006b), now approaching initial deployment on the JCMT. When complete, SCUBA2 will simultaneously observe two bands, 450 μm and 850 μm, with 5120 pixels each. On CCAT, SCUBA2 would Nyquist sample a 2.7′ × 2.7′ field of view at 450 μm. By the time CCAT begins observations, SCUBA2 will have been in use for several years and will be a proven instrument, making it ideal for telescope commissioning. In addition, SCUBA2 would take advantage of the excellent observing conditions at CCAT to make very valuable science observations, in its own right, especially at 450 μm.

To follow SCUBA2, the concept for a short wavelength camera (SWCam) has 32,000 directly illuminated TES silicon bolometers spaced to Nyquist sample a 5′ × 5′ field of view (FoV) at 350 μm. The detector array is made of 25 edge butted 32 × 40 pixel subarrays of the type now produced for SCUBA2. Mesh filters, well matched to the atmospheric windows and mounted in a wheel immediately behind the Lyot stop, select the observing wavelength. Transmissive optics with diamond antireflection coated germanium lenses couple the array to the telescope focus. To ease the operations support requirements, the camera will use closed cycle cryogenics with pulse tube coolers followed by $^4$He and $^3$He or ADR stages.

### 5.2 Antenna coupled cameras

For wavelengths beyond the niobium superconducting energy gap ($2\Delta \approx 725$ GHz ≈ 410 μm), it is possible to construct antenna coupled pixels with lithographed superconducting microstrip. These phased array pixels allow precise beam formation and simultaneous multicolor observation. Recently a small camera demonstrating this technique has been deployed to the CSO (Schlaerth et al. 2007). In the long wavelength camera (LWCam) concept, each pixel has 16 slot dipole antennae with 16 taps on each slot. The signals are summed in a binary tree combiner and microstrip bandpass filters separate the frequency bands, providing simultaneous multicolor observations. For detectors, both TES bolometers and MKID resonators are under consideration. In total, there are 45,000 pixels with the central 10′ field Nyquist sampled at 850 μm and the entire 20′ × 20′ field of view covered at the longer wavelengths. To insure minimum optical loading, the camera is coupled to the telescope with reflective optics.

### 5.3 Direct detection spectrometers

Moderate spectral resolution, broadband, direct detection spectrometers would be valuable on CCAT for determining the redshift of distant galaxies, for example, or for line surveys in nearby galaxies. A current instrument is Zspec (Earle et al.

2007), which uses the WaFIRS architecture with a Roland grating in a parallel plate waveguide and an array of bolometers to achieve a resolving power of 200–400 over the entire 185–305 GHz atmospheric window. For CCAT, a similar design could cover the 350 μm and 450 μm windows simultaneously. Moreover, laboratory studies of flexible dielectric waveguides suggest multiobject instruments are possible, albeit with considerable development.

### 5.4 Heterodyne cameras

Novel packaging techniques and advances in digital signal processing now permit the construction of moderate scale heterodyne spectrometer arrays, such as the 64 pixel, 350 GHz SuperCam (Groppi et al. 2007). For CCAT, a preliminary concept is a 128 pixel, 650 GHz array with a 2–4 GHz bandwidth.

## 6. CONSORTIUM AND SCHEDULE

In 2005, Caltech, Cornell, and JPL carried out the CCAT feasibility and concept design study. Concurrently, the UK Astronomy Technology Centre proposed a similar concept (Holland et al. 2006a). At present these institutions, along with the University of Colorado and the Universities of British Columbia and of Waterloo, are establishing a CCAT consortium to pursue construction and operation of the telescope. Other institutions have also expressed interest in the project. The present development schedule aims for initial observations in 2012 and full operation in 2014, concurrent with the start of full ALMA operations.

## 7. SUMMARY

The Cornell Caltech Atacama Telescope will be a significant new facility for submillimeter astronomy, especially for sensitive wide field surveys. The high, dry site enjoys superb observing conditions. The telescope's combination of large aperture, high quality optics, and wide field will be unequalled. CCAT will provide a platform for instruments that take maximum advantage of rapidly developing detector technology. The concept telescope design builds on successful prior telescopes and the proposed technologies are largely within the state of the art. Several institutions are establishing a consortium to construct and operate the telescope.

## REFERENCES

Cortés-Medellín, G., & Herter, T., 2006, Proc. SPIE 6267, 2F
Earle, L., et al., 2006, Proc. SPIE 6275, 10
Finley, D. T., Reese, E. O., Hermann, K. G., Gienger, A., Sebring, T. A., 2006, Proc. SPIE 6267, 2P
Giovanelli, R., et al., 2001, PASP 113, 803
Groppi, C., et al., 2007, Proc. 18th Int. Symp. Space Terahertz Tech.
Hauser, M. G., & Dwek, E., 2001, ARAA 39, 249
Holland, W. S., et al., 1999, MNRAS 303, 659
Holland, W. S., et al., 2006a, Proc. SPIE 6267, 2E
Holland, W. S., et al., 2006b, Proc. SPIE 6275, 1E
Loewen, N., Brzezik, W., Halliday, D. J., & Sebring, T., 2006, Proc. SPIE 6267, 2J
Marrone, D. P., et al., 2005, Proc. 16th Int. Symp. Space Terahertz Tech., astro-ph/0505273
Martin, R. N., Romeo, R. C., & Kingsley, J. S., 2006, Proc. SPIE 6273, 0P
Radford, S. J. E., & Holdaway, M. A., 1998, Proc. SPIE 3357, 486
Schlaerth, J., et al., 2007, Proc. 18th Int. Symp. Space Terahertz Tech.
Sebring, T. A., et al., 2006a, Cornell Caltech Atacama Telescope Feasibility Concept Design Study, www.submm.org
Sebring, T. A., Giovanelli, R., Radford, S., & Zmuidzinas, J., 2006b, Proc. SPIE 6267, 75
Stacey, G. J., et al., 2006, Proc. SPIE 6275, 1G
Strafford, D. N., DeSmitt, S. M., Kupinski, P. T., & Sebring, T. A., Proc. SPIE 6273, 0R
Terán U., J., Neff, D. H.; Sebring, T., 2006, Proc. SPIE 6267, 3G
Valsecchi, G., et al., 2003, Proc. IEEE Ant. Prop. Soc. Intl. Symp., 1, 124

# The Submillimeter Array

Raymond Blundell

*Harvard Smithsonian Center for Astrophysics*
*60 Garden Street*
*Cambridge MA02138 USA*

The Submillimeter Array, a collaborative effort between the Smithsonian Institution and the Academia Sinica Institute of Astronomy and Astrophysics, was largely completed by November 2003, when scheduled science observations began. At that time the array consisted of eight six-meter diameter antennas equipped with receivers designed to operate in the atmospheric windows around 230, 345 and 650 GHz.

During the past three years a number of improvements and upgrades have been made to the array which now performs nightly astronomical observations on a routine basis. These upgrades will be discussed as well as plans for short-term improvements.

# Construction of a Side-Band-Separating Heterodyne Mixer for Band 9 of ALMA

F. P. Mena, J. W. Kooi, A. M. Baryshev, C. F. J. Lodewijk, R. Hesper, W. Wild, and T. M. Klapwijk.

***Abstract*—In this article we present the design, modeling and construction of a side-band-separating (2SB) heterodyne receiver for the frequency range from 600 to 720 GHz that corresponds to band 9 band of ALMA. The characteristics of this receiver present a significant improvement over the current double-side-band (DSB) configuration currently under development. The core of the mixer consists of a quadrature hybrid, two LO injectors, two superconductor-insulator-superconductor (SIS) junctions, three signal-termination loads, and two IF filtering systems. All these parts were modeled and optimized prior construction. Our 2 mixer exploits waveguide technology and has been constructed in the split-block technique. We used state-of-the-art CNC micromachining which permitted us to obtain the small dimensions required for this frequency range. The constructed receiver presents a good performance but we suggest various ideas for further improvement.**

***Index Terms*— Astronomy, submillimeter wave mixers, superconductor-insulator-superconductor devices.**

## I. Introduction

THE Atacama Large Millimeter Array (ALMA) is the largest radio astronomical enterprise ever proposed. Currently, it is under construction and it is expected to be operational by 2012 [1] Each of its constituting antennas will be able to hold 10 heterodyne receivers covering the spectroscopical windows allowed by the atmospheric transmission at the construction site, the altiplanos of the northern Chilean Andes. In contrast to the side-band-separating (2SB) receivers being developed at low frequencies, double-side-band (DSB) receivers are being developed for the highest two spectroscopical windows (bands 9 and 10). Despite of the well known advantages of 2SB receivers, they have not been implemented at the highest-frequency bands as the involved dimensions for some of the RF components are prohibitory small. However, the current state-of-the-art micromachining technology has proved that the complicated structures necessary for this development are attainable [2]. Here we report the design, modeling, realization, and characterization of a 2SB mixer for band 9 of ALMA. The performance is excellent and satisfies the ALMA specifications. However, further improvement can be achieved.

This work was supported in part by NOVA, the Netherlands Research School for Astronomy, and the FP6 Radionet AMSTAR program of the European Union.

F. P. Mena, A. M. Baryshev, R. Hesper, and W. Wild are with the Netherlands Institute for Space Research and the Kapteyn Institute of the University of Groningen, Landleven 12, 9747AD Groningen, The Netherlands.

J. Kooi is with the California Institute of Technology, MS 320-47 Pasadena, California 91125, USA

C. F. J. Lodewijk and T. M. Klapwijk are with the Kavli Institute of Nanoscience, Delft University of Technology, Lorentzweg 1, 2628 CJ Delft, The Netherlands.

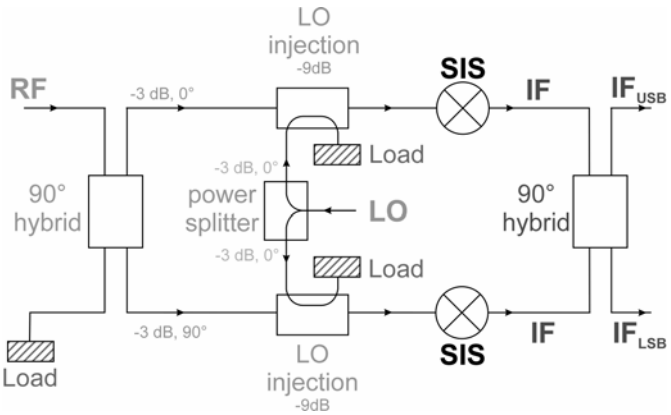


Fig. 1. Scheme of the chosen configuration for our 2SB mixer.

## II. Design and Modeling

From a variety of possible 2SB schemes, we have selected the configuration shown in Fig. 1. A 90° hybrid has been selected over its 180° counterpart despite of the superior fundamental and intermodulation product suppression capabilities of the latter. This is justified as the intrinsic parasitic capacitance of SIS junctions naturally suppresses intermodulation products and higher harmonics. Moreover, a 90° hybrid is simpler and, thus, easier to implement at these high frequencies [3].

We have opted for waveguide technology for the construction of the RF components and planar stripline for the IF filtering and matching parts. The current design follows previous work proposed for the balanced and correlation receivers at CSO [3]. Each one the RF components and the planar IF system (Figures 2 and 3) were modeled independently using commercial microwave-analysis software [4]. The dimensions of every RF component were selected for an optimal performance in the 600–720 GHz range. On the other hand, the IF signal is intended to cover 4–8 GHz.

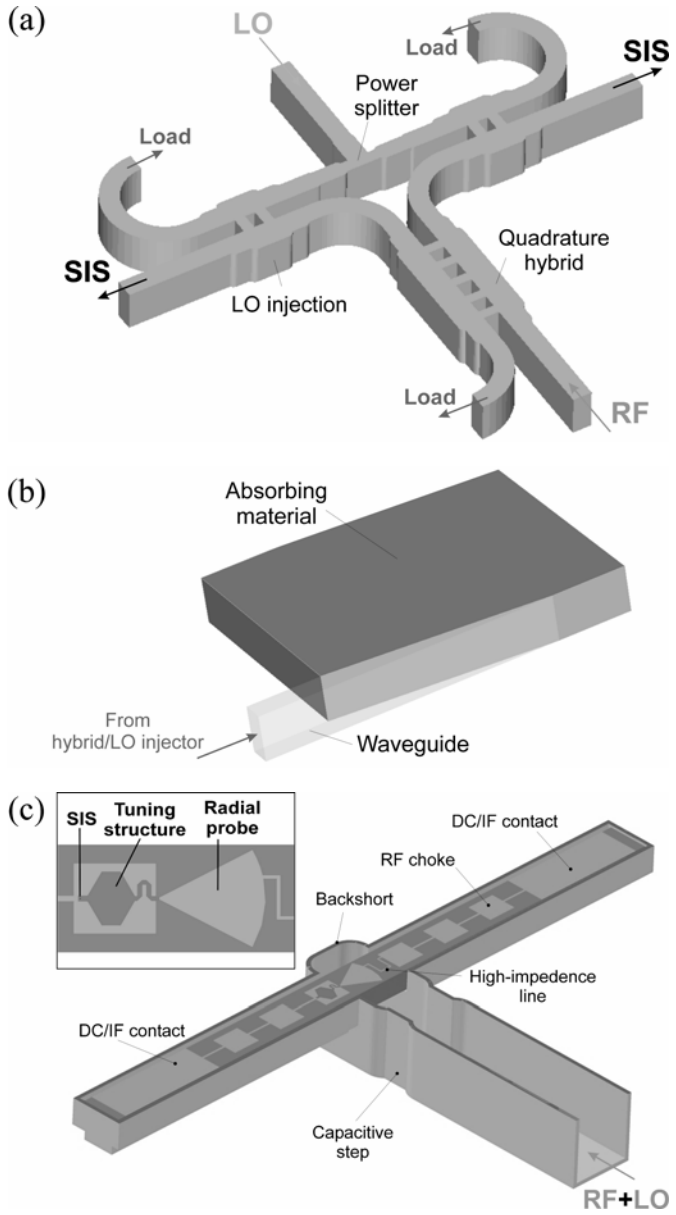


Fig. 2. Design of the various RF components: (a) Core of the 2SB mixer. (b) Signal termination load. (c) Waveguide to microstrip transition. The transversal dimensions of the waveguide are 145× 310 mm$^2$.

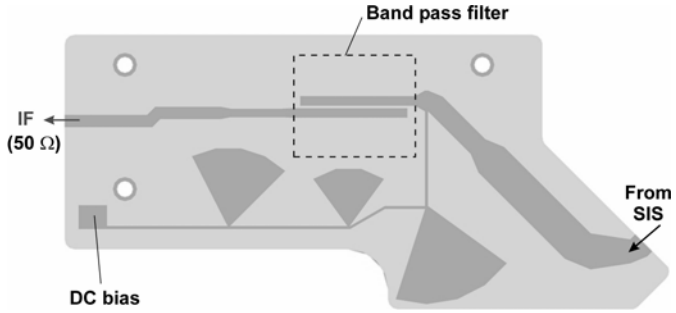


Fig. 3. IF configuration. The dashed line shows the positioning of a cutout bellow the substrate needed for the 3-9 GHZ band pass filter.

### *A. RF components*

In Fig. 3 we show the proposed concepts for the different RF components. The design of the power divider, LO injectors, and quadrature hybrid are based on a narrow bandwidth split block version developed for the ALMA project at lower frequencies [5]. However, at variance with that previous work, the waveguide width (b-dimension) of the present hybrid and the LO injectors has been increased by a 32.5% to maximize the thickness of the branch lines (Fig. 2) [3]. Every one of these components was simulated and optimized using commercial software. The results, summarized in Fig. 4a, show a rather flat response of the devices in our frequency window.

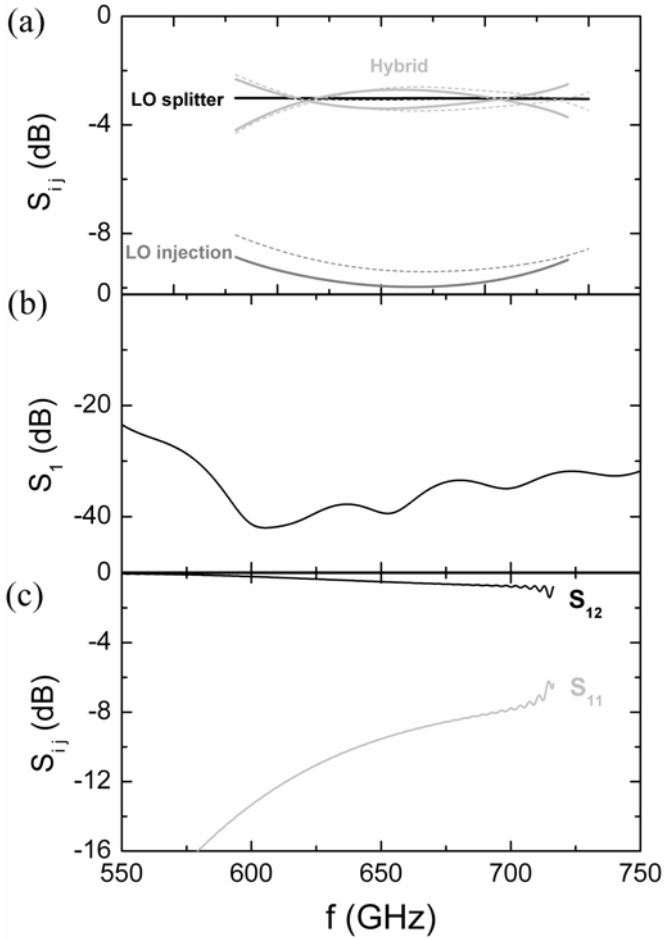


Fig. 4. Results of the electromagnetic modeling of the different RF components: (a) S-parameters between the input and output of the the 90° hybrid, LO splitter, and LO injector as designed, solid lines, and as constructed, dashed lines. (b) Reflection coefficient of the signal termination load. (c) Coupling efficiency and return loss of the waveguide-microstrip transition.

Although several configurations have been proposed for the signal termination loads [5]–[6], we have selected a rather novel and simple configuration which is appropriate for the small dimensions involved in the present work. The design, presented in Fig. 2(b), consists of a cavity at the end of the waveguide partially filled with an absorbing material. The geometry we are presenting here is relatively easy to make as the largest dimension is designed parallel to the splitting plane of the block. Extensive simulations of this configuration have been presented elsewhere [7]. The loads show a good performance, as demonstrated by the reflection coefficient [Fig. 4(b)], if Eccosorb MF112 [8] is used as absorbing

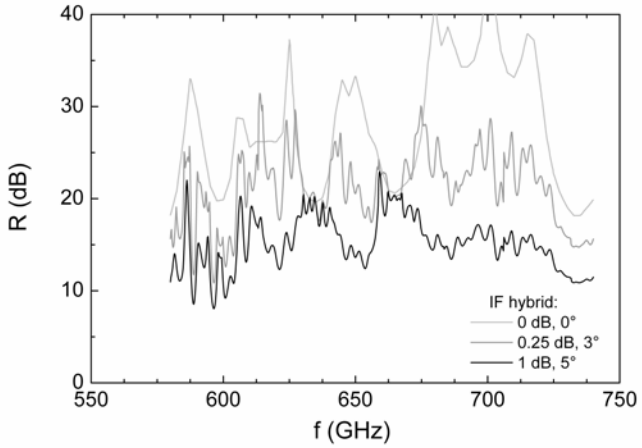


Fig. 5. Calculated sideband ratio assuming a perfect IF hybrid (light gray line) and with a amplitude and phase imbalances of 0.25 dB and 3° (gray line), and 1 dB and 5° (black line).

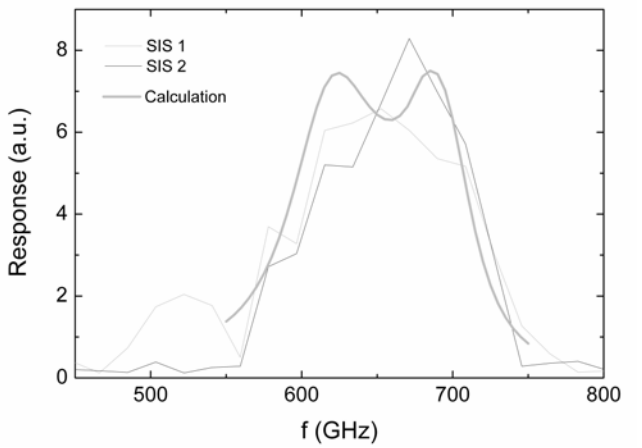


Fig. 6. Calculated and measured response of the fabricated SIS junctions. The response was measured through the RF port.

material. When the cavity is terminated at the point where the wedged part ends, large resonances appear. They can be easily damped by adding extra absorbing material. Moreover, it has also been shown [7] that this approach is pretty robust as various possible mounting errors have little influence in the overall performance.

We use a full height waveguide-to-microstrip transition to couple the incoming signal to the thin-film tuning structure of the SIS junction. The proposed structure is shown in Fig. 2(c). We have opted for a configuration that crosses the waveguide but in this case care must be taken in the way the DC bias return line meanders across the waveguide as this structure is prone to setup modal resonances. Therefore, we selected a design similar to the one proposed by Risacher et al. [9]. An important modification is that we have added a capacitive step in front of the radial probe as it improves the overall performance [10]. For the RF choke we selected the popular "rectangular" structure. The calculated coupling efficiency and return loss, between the waveguide and the tip of the radial probe, are presented in Fig. 4(c).

Given the calculated S-matrices of the different RF components, we used an S-matrix circuit simulator to calculate the sideband ratio of the complete RF core. The

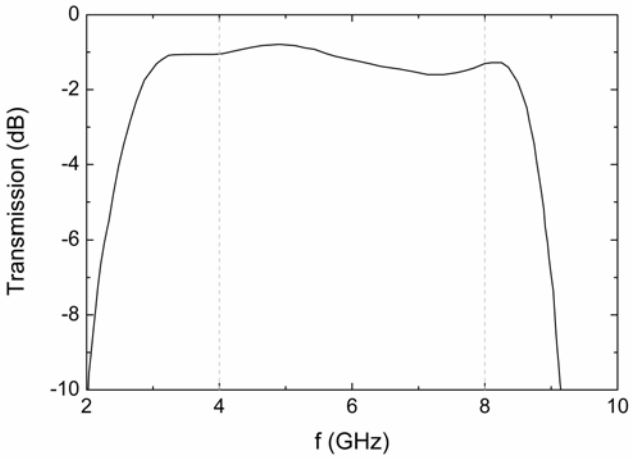


Fig. 7. Calculated transmission between the input and output ports of the IF structure presented in Fig. 3.

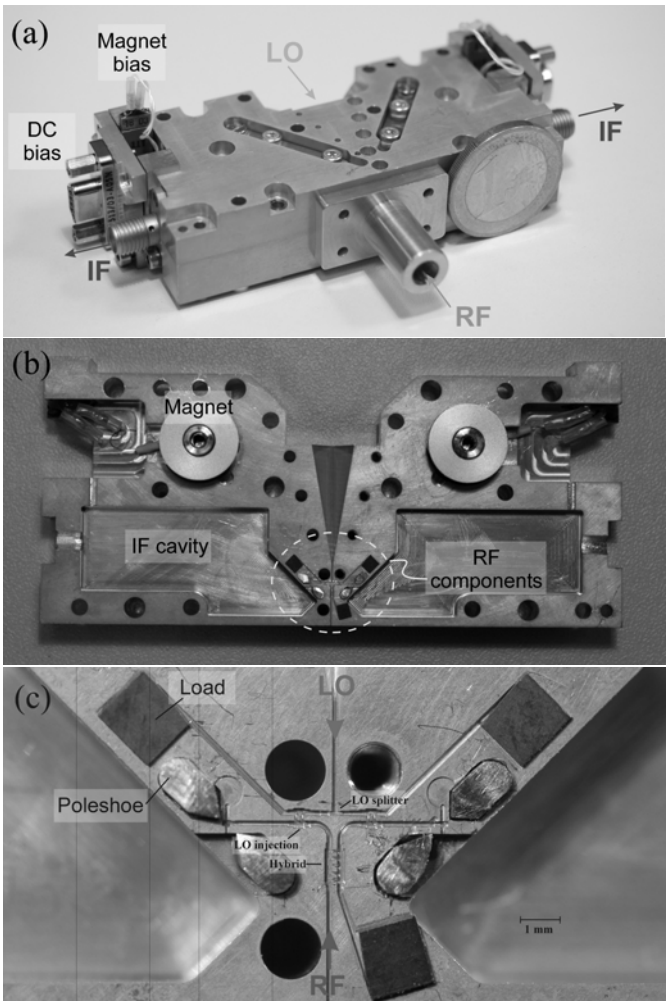


Fig. 8. Constructed 2SB block and its different components: (a) Closed 2SB block. (b) Upper half. (c) Close-up of the RF components.

results are given in Fig. 5. If a perfect IF hybrid is assumed, which will set the upper limit, a sideband ratio above 20 dB is expected across the whole band. However, the characteristics of the IF hybrid are far from ideal. We, therefore, have repeated the calculations assuming some amplitude and phase imbalance which will lower the 2SB performance.

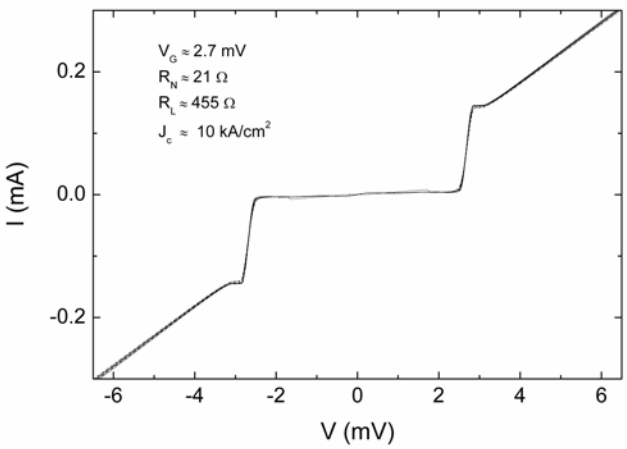


Fig. 9. IV curves of 8 different junctions. The average values of gap voltage ($V_G$), normal resistance ($R_N$), leakage resistance ($R_L$), and critical current density ($J_C$) are shown.

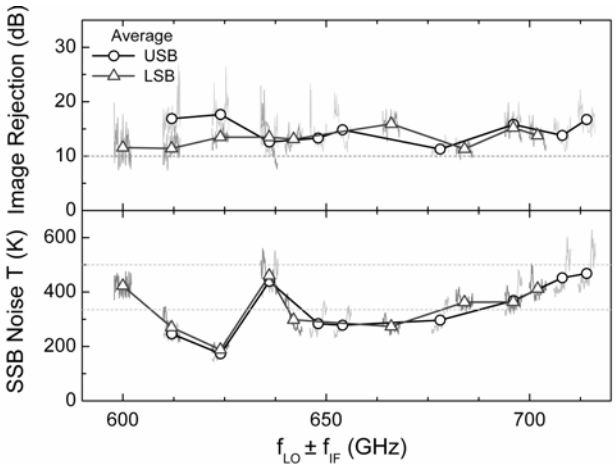


Fig. 10. Single sideband noise temperatures (bottom panel) and image rejection ratios (upper panel) at different LO frequencies. Dashed horizontal lines represent ALMA specifications for these two parameters.

### *B. SIS junction and tuning structure*

Based in our successful experience with the development of DSB receivers for band 9 of ALMA, we have opted for a single Nb/$AlO_x$/Nb junction devices as detection elements for our receiver (for fabrication details, see Section III-B). Although junctions using AlN as barrier have intrinsic better properties [11], we have selected the former as, at the moment, its fabrication process is much more reliable. The reasons for which the single junction approach is preferred are twofold. First, it permits an easier suppression of the Josephson currents across the junction and, second, it allows less effort in finding reasonably matched mixers.

Given the resistance-area product, $R_nA$, of $AlO_x$ junctions (~20 $\Omega.\mu m^2$), we have selected the area of the SIS junction to be 1 $\mu m^2$ [12]. The resulting SIS impedance has to be matched with the impedance at the radial probe tip which is calculated through the electromagnetic simulation described in the previous Section. The matching is obtained by a multi-section stripline made of Nb as shown in the inset of Fig. 2(c). For a given stripline geometry, it is possible to calculate the total transmission from the radial probe tip and the SIS junction using the microscopic theory of superconductivity in the dirty limit and standard transmission line theory [13]. The geometrical parameters where changed as to get a good coverage of band 9. The result of the calculation is shown in the thick solid line of Fig. 6.

### *C. Planar IF filtering and matching*

To facilitate reliability and modeling, we have opted for a planar IF filtering and matching design (Fig. 3). This is a compact unit containing the IF match, DC-break, bias tee, and EMI filter. The advantage of such planar structure has been demonstrated and used in various astronomical instruments [3]. It has to be noted that, for this filter to work, the ground plane directly underneath the filter has to be removed. Previous to fabrication, the dimensions were optimized for a good performance in the 4 to 8 GHz frequency range. In Fig. 7, we show the calculated performance of the IF circuit. As shown in there, the transmission is expected to be greater than −2dB in the range of interest and the complex impedance limited to a small region.

## III. CONSTRUCTION

### *A. Waveguide block*

We have constructed the mixer in a split-block as demonstrated in Fig. 8. We have used conventional machining for the large features and CNC micromachining for the small RF features [2]. Both parts of the block were made of copper which is gold platted afterwards with a thickness of ~2 μm. The fabricated unit is rather compact (8×2×3 $cm^3$). It contains all the RF components, the IF filtering board, the DC biasing circuit, and the magnetic probes needed to suppress the Josephson currents in the SIS junctions. A closer inspection of the fabricated block shows that all the waveguides and cavities are approximately 5 μm wider than designed. The reason appears to be the gold plating process as it etches away the copper that makes the block. However, the erosion is rather uniform through the entire block. To determine what the influence of this situation will be, we have repeated the simulation process with the measured dimensions (dashed lines in Fig. 4a). It is clear that our design is pretty robust as long as the symmetry is maintained.

### *B. SIS junctions*

The SIS devices were fabricated on a quartz substrate. First, a Nb monitor layer is deposited, after which an optically defined ground plane pattern of Nb/Al/$AlO_x$/Nb is lifted off. Junctions are defined by e-beam lithography in a negative e-beam resist layer and etched out with a SF6/O2 reactive ion etch (RIE) using $AlO_x$ as a stopping layer. The junction resist pattern is subsequently used as a lift off mask for a dielectric layer of $SiO_2$. A Nb/Au top layer is deposited and Au is etched with a wet etch in a KI/I2 solution using an optically defined mask. Finally, using an e-beam defined top wire mask pattern, the layer of Nb is etched with a SF6/O2 RIE, finishing the fabrication process. This process renders a high yield and good reproducibility as demonstrated by the IV plots of 8

junctions (out of a sector containing 20 junctions) shown in Fig. 9.

## IV. MIXER CHARACTERIZATION

### *A. Band coverage*

The direct response, as function of frequency, of both SIS junctions contained in our mixer has been measured using a home-made Fourier transform spectrometer. The results are presented in Fig. 6. Both junctions present good band coverage and are in good agreement with the predicted response. The good agreement is obtained despite the fabrication errors discussed in the previous Section since those errors do not modify dramatically the impedances at the probe tip [Fig. 4(a)].

### *B. Noise temperature and sideband ratio*

Noise temperatures ($T_{rx}$) were measured using the conventional Y-factor method. As described in [14], the same setup was slightly modified to determine the sideband ratios (R) $T_{rx}$ and R for both output bands were determined at several LO pumping frequencies and recorded as function of IF frequency. The results are summarized in Fig. 10. Both quantities are rather close to ALMA specifications as indicated by the horizontal dashed lines of Fig. 10. For $T_{rx}$, 80% of the band should not exceed 335 K while all points should below 500 K [15]. The image rejection ratio, on the other hand, should always be above 10 dB.

Although the noise temperature complies with ALMA specifications, it is obvious from Fig. 10 that the IF response presents a rather steep increase at high IF frequencies. The most probable reason is a mismatch between the SIS impedance and the IF unit. Further work has to be done in this aspect to improve the noise temperatures.

The obtained image rejection ratios are in close agreement with the modeling prediction given in Fig. 5 if an amplitude and phase mismatches of 1 dB and 5° in the IF hybrid are considered. These, indeed, are the experimental values obtained at 77 K [16]. It has to be noted that the hybrid used is a commercial one that has been optimized for operation at ambient temperature [17]. It is reasonably to argue that mismatches of 0.25dB and 3° can be obtained by optimization of the design at low temperatures. In that case, an improvement of ~7 dB is expected (Fig. 5).

## V. CONCLUSIONS

In this article we have presented the design, modeling, and realization of a side-band-separating mixer that covers the frequency range of ALMA band 9. A full test of the mixer was also presented demonstrating that complies with ALMA specifications. However, further improvement can be achieved if the IF system is optimized and AlN-barrier SIS junction technology is used.

## REFERENCES

[1] ALMA web site, http://www.alma.nrao.edu/.
[2] Radiometer Physics GmbH, http://www.radiometer-physics.de/.
[3] J. Kooi et al., "Heterodyne Instrumentation Upgrade at the Caltech Submillimeter Observatory", SPIE, Millimiter and submillimiter detectors for Astronomy II, vol. 332, pp. 5498, 2004.
[4] Microwave Studio, http://www.sonnetusa.com/.
[5] S.M.X Claude et al., "Design of a Sideband-Seperating Balanced SIS Mixer Based on Waveguide Hybrids", Alma Memo 316, 2000.
[6] A. R. Kerr et al., "MF-112 and MF-116: Compact Waveguide Loads and FTS Measurements at Room Temperature and 5 K", Alma Memo 494, 2004.
[7] F. P. Mena and A. Baryshev, "Design and Simulation of a Waveguide Load for ALMA-band 9", Alma Memo 513, 2005.
[8] G. A. Ediss et al., "FTS Measurements of Eccosorb MF112 at Room Temperature and 5 K from 300 GHz to 2.4 GHz", Alma Memo 273, 1999.
[9] C. Risacher et al., "Waveguide-to-Microstrip Transition with Integrated Bias-T", IEEE Micro. and Wire. Comp. Lett., vol. 13, pp. 262, 2003.
[10] J. Kooi et al., "A Full-Height Waveguide To Thin-Film Microstrip Transition With Exceptional Rf Bandwidth And Coupling Efficiency", Int. J. Ir. & Mm. Waves, vol. 24, pp. 261, 2003.
[11] J. Kawamura et al., "Very high-current-density Nb/AlN/Nb tunnel junctions for low-noise submillimeter mixers". Appl. J. Phys. 76, pp. 2119, 1996.
[12] A. R. Kerr and S.-K. Pan, "Some Recent Developments In The Design Of Sis Mixers", Int. J. Ir. & Mm. Waves, vol. 11, pp. 1169, 1990.
[13] C. F. J. Lodewijk et al., "Improved design for low noise Nb SIS devices for Band 9 of ALMA (600 - 720 GHz)", Conf. Proc. 16th ISSTT, pp. 42, 2005.
[14] A. R. Kerr, S.-K. Pan, and J. E. Effland, "Sideband Calibration of Millimeter-Wave Receivers", ALMA Memo 357, 2001.
[15] W. Wild and J. Payne, "Specifications for the ALMA Front End Assembly," http://www.cv.nrao.edu/~awootten/mmaimcal/.
[16] S. Mahieu, Institut de RadioAstronomie Millimétrique, France, private communication, Jan. 2006.
[17] Advanced Technical Materials Inc., http://www.atmmicrowave.com/.

# SIS Mixer for 385 – 500 GHz with On-Chip LO injection

Raquel Monje, Victor Belitsky, Christophe Risacher, Vessen Vassilev and Alexey Pavolotsky

Group for Advanced Receiver Development (GARD), Department of Radio and Space Science with Onsala Space Observatory, Chalmers University of Technology, SE 41296 Gothenburg, Sweden

## ABSTRACT

We present the design and first experimental results of a 385-500 GHz fixed-tuned double sideband (DSB) receiver based on a superconductor-insulator-superconductor (SIS) junction mixer with on-chip LO injection circuitry. At high frequency, branch waveguide couplers are difficult to manufacture with required accuracy as the branches (slots) become extremely narrow. In order to solve this problem, we propose a coupler integrated onto the mixer chip and fabricated together with the SIS junction and the tuning circuitry. The on-chip LO directional coupler is made of superconducting lines with slot lines in the ground plane. Thus, the coupler is integrated into conventional SIS junction fabrication steps, benefiting from the processing accuracy better than 0.5 μm by using optical lithography only. Furthermore, the mixer design includes a novel component, an ellipse termination for the idle LO port, made of thin-film resistive material. This termination gives very broadband performance using a compact area. Moreover, it is very tolerant to the sheet resistivity of the film, geometry and does not require any physical grounding [1]. The mixer is to be used at the Atacama Pathfinder EXperiment (APEX) telescope in Chile [2].

***Keywords:*** SIS mixer, waveguide probe, directional couplers, E-probe, substrate-based coupling structure.

## 1. INTRODUCTION

The Atacama Path Finder EXperiment (APEX) [2] is a 12 m telescope; it is a prototype antenna of the Atacama Large Millimeter Array (ALMA) [3]. APEX is placed in Cerro Chajnantor in the Chilean Atacama desert, at an altitude of about 5000 m. The site is one of the best places for submillimeter astronomy on the Earth because of the extremely low content of water vapour. For spectroscopy studies APEX will house single pixel heterodyne receivers covering the frequency range of 211 GHz up to 1.5 THz and heterodyne arrays consisting of 7 x 2 pixels CHAMP+ [4] operating at 650 and 850 GHz.
The work presented here is part of our development for APEX band 3 (385 – 500 GHz), a sideband separation SIS mixer with 4-8 GHz IF output. This technology provides better sensitivity for spectral line observation than double sideband (DSB) [5]. Besides, DSB observations may lead to spectral line-confusion or degrade the system noise temperature and the receiver sensitivity with strong atmospheric absorption bands falling into the image band. This is a driving reason to choose this technology considering that some of the important molecules for this band are very close to telluric absorption line, as in the case of deuterated water, HDO, with its fundamental transition frequency at 465 GHz.

## 2. MIXER DESIGN

### 2.1 Mixer Chip Design

The mixer design integrates several novel RF components in the same substrate, making the design very compact and innovative. The mixer chip comprises a waveguide-to-microstrip transition with integrated bias-T; two hammer-type chokes; a 50-Ohm LO probe; an on-chip - 16 dB directional coupler for the LO injection and an ellipse termination for the idle port of the coupler.
The RF probe couples the input waveguide signal to the SIS junction while having an isolated port at the opposite side of the substrate, where the IF signal can be extracted and DC current can be injected to bias SIS junctions, minimizing its influence

on the performance of RF [6]. The RF probe is shaped using a combination of rectangular and radial probe in order to achieve a broadband matching between the waveguide and the probe output. A low impedance probe is important for the matching of the SIS junction with typical impedance at RF of ~ 5 – 10 Ω. According to our HFSS simulations [7], the impedance observed at the microstrip (output of the probe) is approximately 35 Ω [8]

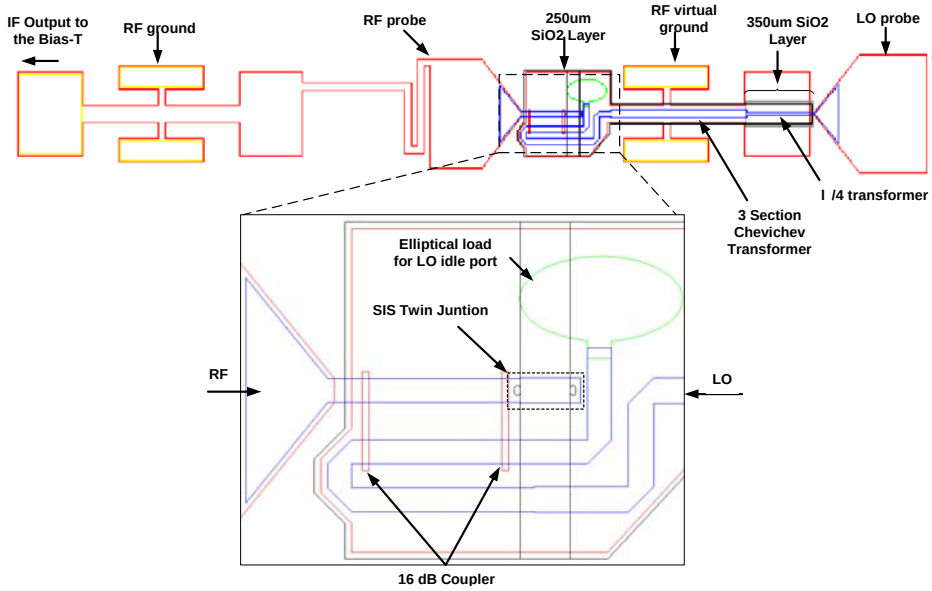


**Fig. 1.** Drawing of the mixer chip design for APEX Band 3 (385 – 500 GHz). The quartz substrate containing the RF and LO probe and two hammer type choke to provide RF ground and IF port. A zoom view of the 16 dB coupler with the tuning circuitry and the twin junctions.

The LO is fed through a waveguide-to-microstrip probe at the opposite side of the substrate and is coupled to the RF signal through a - 16 dB directional coupler, see Figure 1. The 50 Ohm LO probe impedance is transformed into a 9 Ohm - impedance of the coupler- by a quarter of wavelength transformer followed by a three sections Chebishev transformer.
The on-chip LO directional coupler is placed on the same dielectric ($SiO_2$ with $\varepsilon_r = 3.74$) as the SIS junction and the RF tuning circuitry. The coupler consists of two parallel superconducting lines coupled via lumped links - two perforations forming slot-lines in the ground plane. This way, the RF signal coming from the waveguide-to-microstrip probe is coupled to the LO signal and directed to the SIS twin junctions while the idle port of the LO coupler is terminated with an elliptical termination [1].
In order to match the complex impedance of the SIS junction to the nearly real impedance of the signal source (probe), the capacitance $C_j$ of the junction should be resonated out at RF. The use of photolithography to define the junction area limits us to use relative large junction area (~ 3 $\mu m^2$). For a given critical current density, the SIS capacitance is of the order of 300 fF. The tuning circuitry uses two junctions connected through a short line, equivalent to an inductance, $L_t$, at RF. A quarter of wavelength transformer transforms the impedance of the probe into the RF impedance of the twin junctions [9]. The tuning circuitry provides a power matching better than -10 dB over the band of interest [8].

### 2.2. Mixer Block Design

The double sideband mixer block, shown in Figure 2 top-left, is fabricated using Copper-Tellurium alloy, which is easier to machine. A very thin layer of gold (2 μm) is plated to allow bonding with gold wires and to protect the block from corrosion. The DSB mixer block consists of two parts; the mixer back piece where the mixer chip is placed together with the DC circuitry and IF output (see Figure 2 top-right); and the intermediate piece containing the waveguides for the RF and LO signal injection. Those parts are manufactured by direct milling, using the split-block technique. Figure 3 shows the sideband separation mixer block which consists of two mixer back pieces, being common for the DSB and 2SB design, whereas the intermediate waveguide piece will be substituted with a unit containing the LO in-phase power divider and a 3 dB 90 degrees waveguide hybrid for the RF signal in order to achieve sideband separation using quadrature scheme [8]. This

intermediate piece is intended to be fabricated by using copper micromachining, an innovate technology developed at GARD and successfully used for the APEX T2 [10].
The mixer chip is placed in a 65 µm-deep channel milled in the mixer back piece with a 10 µm x 120 µm air-gap underneath the substrate. The use of suspended microstrip increases the cut-off frequency of the substrate channel and allows increasing its width. The substrate dimensions are 1200 µm x 150 µm x 65 µm, one bond wire connects the ground of the mixer chip to the mixer block. The IF circuitry made on alumina substrate is integrated in the mixer block. It comprises a bias-T and 20 Ohm-to-50 Ohm IF transformer. Three bond wires connect the mixer chip to the IF circuitry, which tune out the IF capacitance of the SIS and tuning circuitry lines. The DC circuitry for the SIS biasing is placed on the back side of the mixer block pieces.

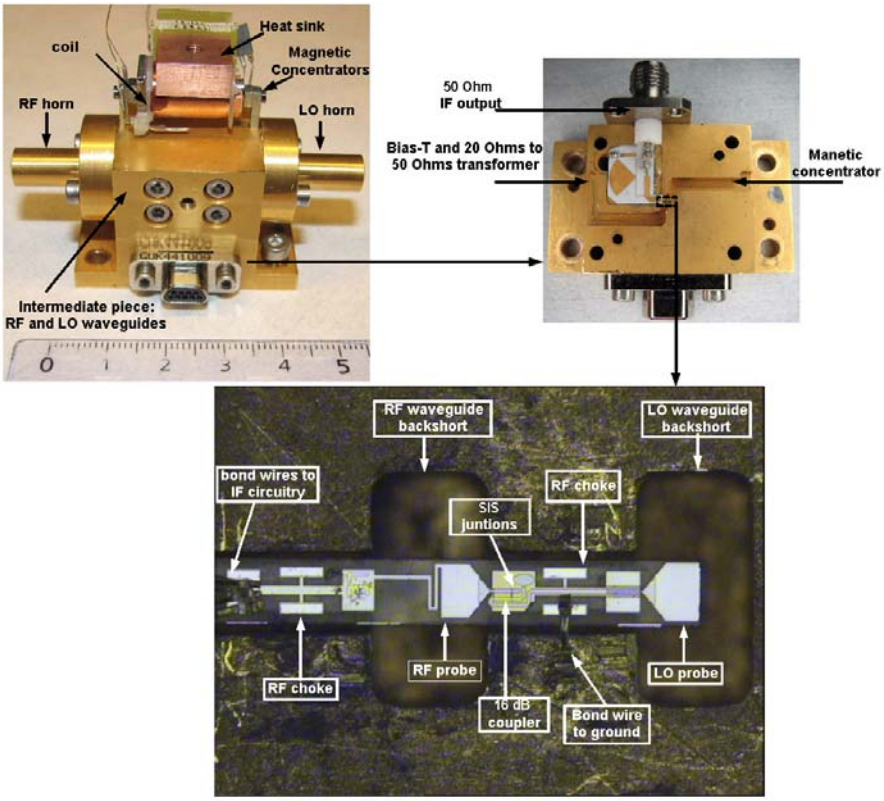


**Fig. 2.** Top left picture shows the DSB mixer block: two magnetic iron concentrators guide the magnetic field from an external coil to the vicinity of the junctions; Top right picture of the mixer back piece containing the mixer chip, the bias-T and the 20 to 50 Ohm transformer and the DC circuitry in the back side, this piece is compatible with the 2SB mixer; bottom centered picture of an optical microscope view of the mixer chip.

## 3. MEASUREMENTS

### 3.1. Measurement setup

The laboratory test measurements are performance in a liquid helium Oxford Instrument cryostat. The mixer uses a corrugated horn followed by a cold Teflon lens with a focal distance of 25 mm. The vacuum window is a 1.5 mm high density polyethylene (HDPE) window with anti-reflecting grooved surface optimized for these frequencies. We use a 200 µm Zitex film as infrared filters. The local oscillator is a multiplier chain (x36) from VDI and is quasioptically injected at the opposite side of the RF window with the help of a combination of horns and a Teflon lens of 36 mm focal distance.

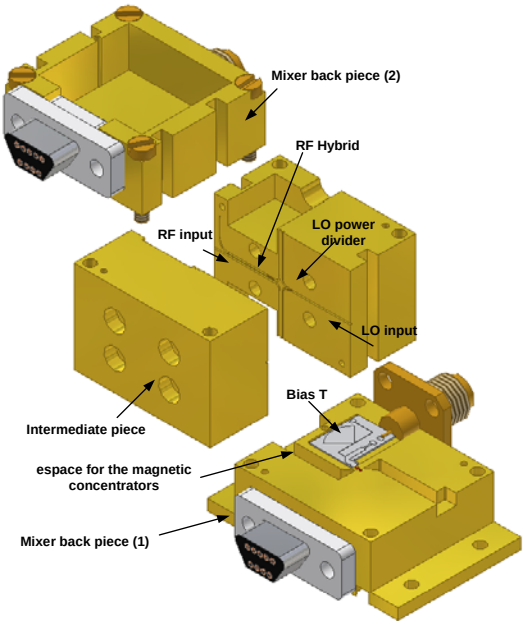


**Fig. 3.** Drawing of the 2SB mixer block. The mixer block consists of two mixer back pieces where the mixer chip is placed together with the DC input and IF output, and two intermediate pieces containing the LO power divider and the RF3dB 90° hybrid.

### 3.2. Noise temperature performance and diagnosis

The noise temperature measurements were performed with the Y factor technique using a hot (293 K) and a cold load (77 K) placed in front of the input window. Figure 4 shows the measured uncorrected receiver noise temperature.

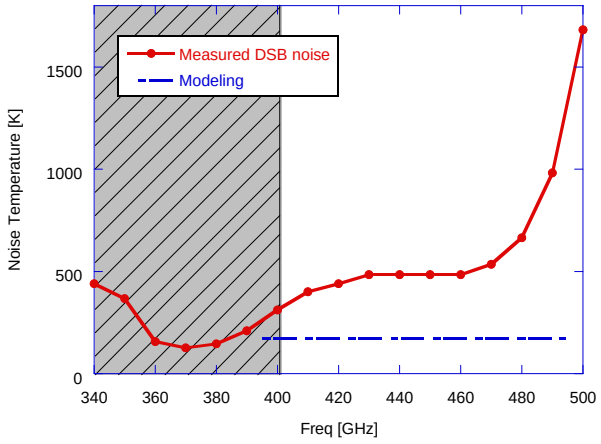


**Fig. 4.** Measured DSB receiver noise temperature.

The measured noise is almost five times greater than the noise expected through modeling for this mixer. A possible reason for such disagreement with the design expectations is thought to be due to high RF losses originated from the ground perforations for the on-substrate LO injection circuitry. The slots cause weak-links – areas where the line gets thinner than two times the London penetration depth, loosing superconductivity properties- in the strip counter layer and detune the circuitry resulting in the frequency-dependent mismatch. Figure 5 illustrates different points where we can have such weak links, e.g. at the probe-to-microstrip transition, where the probe (made of Nb line of 350nm) is deposited over quartz substrate and it is connected to the microstrip line placed over a $SiO_2$ layer of 250 nm. In such places, the line is thinner than on flat surfaces and, hence, might have structural defects acting as weak-links. Figure 5 shows how this effect appears in the DC IVC and IF power.

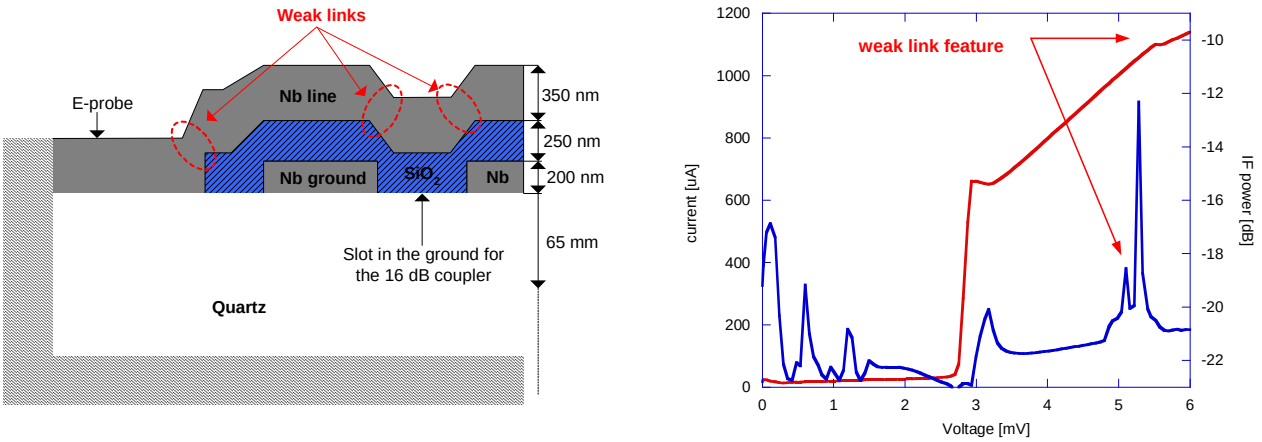


**Fig. 5**.Left picture shows a cross section of a mixer chip; right picture shows the DC measurements of the IVC (red curve) and IF power (blue curve).

A new iteration of the wafer has been produced adding Nb patches in those critical regions on top of the counter Nb layer (referred as Nb line on Figure 5 left), increasing the thickness of the lines in the discontinuity areas. DC features at the IVC and IF power were no longer detected, nevertheless, no significant changes in the noise performance were measured. These results indicates that discontinuities on the lines still introduce extra parasitic inductance in the mixer RF tuning circuitry, coming from possible cracks in the transitions areas or from regions where the Nb top layer get closer to the ground layer. Currently, a new study is been carrying out to planarize the ground-plane by filling the perforations with $SiO_2$ to avoid any RF effects due to discontinuities in the strip layer.

## 4. CONCLUSIONS

In this paper, we present the design and first measurements of a DSB fixed-tuned SIS mixer for APEX band 3 (385-500 GHz). The mixer design introduces novel components such as a waveguide probe with integrated bias-T, allowing to extract IF signals and to inject DC current, and an on-chip integrated LO injection circuitry employing a high-performance ellipse termination for the directional coupler idle port. All these components are fabricated together with the SIS junction and the tuning circuitry. The first measurements show perfect functionality of the LO injection over the entire mixer band 385-500 GHz, while we have measured a higher noise than the expected especially at the higher frequency band. The analysis of the measurements results point out to imperfections in the manufacturing of the chips, that produced weak links or cracks in the top Nb line and introduce extra parasitic inductance, which at these frequencies could affect the tuning circuitry considerably and therefore, increase the conversion losses of our mixer.

## ACKNOLEDGEMENTS

The authors would like to acknowledge D. Henke, GARD, for very interesting and useful discussions. Dr. D. Meledin, GARD, for assisting in the mixer block design and Prof. H. Olofsson, Director of Onsala Space Observatory for his support. APEX Project is funded by the Swedish Research Council and the Wallenberg Foundation by their respective grants. Part of this work was supported by EU FP6 AMSTAR Program.

## REFERENCES

1. R. R. Monje, Vessen V. Vassilev, Alexey Pavolotsky and Victor Belitsky, “High Quality Microstrip Termination for MMIC and Millimeter-Wave Applications” IEEE MTT-S International Microwave Symposium, June 12-17, 2005, Long Beach, California
2. APEX homepage at Onsala: http://www.oso.chalmers.se/oso/apex/index.html
3. R.S.Booth, “ALMA, the Atacama Large Millimetre Array”, European Space Agency, (Special Publication) SP-451, pp. 107-114, May 200. See also ALMA project in ESO homepage: http://www.eso.org/projects/alma/index.html.

4. Champ + homepage at: http://www.strw.leidenuniv.nl/~champ+/
5. P. R. Jewell and J. G. Mangum, “System temperatures single versus double sideband operation and optimum receiver performance”, International Journal of Infrared and Millimeter Waves, Vol. 20, No 2, pp. 171-191, May 1999.
6. Christophe Risacher Vessen Vassilev, Alexei Pavolotsky and Victor Belitsky, “Waveguide-to-microstrip transition with integrated Bias-T”, IEEE Microwave and Wireless Components Letters, Vol.13, No. 7, July 2003, pp. 262–264.
7. HFFS, High Frequency Structure Simulator version 5.6, Agilent Technologies.
8. R. R. Monje, V. Belitsky, V. Vassilev, A. Pavolotsky, I. Lapkin, ”A 385-500 GHz SIS Mixer for APEX Telescope”, proceeding of the SPIE Millimeter and Submillimeter Detector for Astronomy, eds. J. Zmidzinas, W. S. Holland, S. Withington, W. D. Duncan, 6275, pp 19.
9. Belitsky V. , Tarasov M.A., "SIS Junction Reactance Complete Compensation", IEEE Trans. on Magnetic, 1991, MAG- 27, v. 2, pt. 4, pp. 2638-2641.
10. A. Pavolotsky, D. Meledin, C. Risacher, M. Pantaleev, V. Belitsky, “Micromachining approach in fabricating of THz waveguide components”, Microelectronics Journal 36 (2005), pp. 683-686.

# Development of 1 THz SIS mixer for SOFIA

A. Karpov, D. Miller, J. A. Stern*, B. Bumble*, H. G. LeDuc*, J. Zmuidzinas

California Institute of Technology, Pasadena, CA 91125, USA
* MDL, Jet Propulsion Laboratory, Pasadena, CA 91109, USA

## Abstract

We report the development of a low noise and broadband SIS mixer aimed for 1 THz channel of the Caltech Airborne Submillimeter Interstellar Medium Investigations Receiver (CASIMIR), designed for the Stratospheric Observatory for Far Infrared Astronomy, (SOFIA). In the SIS mixer are used the Nb/AlN/NbTiN junctions with the Josephson critical current density of about 40 KA/cm $^2$. The mixer is built using a double-slot quasi-optical design and covers a 250 GHz band centered at 1 THz. The minimum measured receiver noise is about 353 K (Y=1.50). The receiver noise may be reduced using a higher level of LO power. The developed mixer will allow building a receiver with the noise temperature approaching 250 K in 1 THz band and having a broader operation band compared to the previously reported.

## Introduction

The Earth atmosphere is nearly opaque at the Terahertz frequencies and one has to use the orbital or sub orbital platforms for astronomical observations in THz band. The Stratospheric Observatory for Far Infrared Astronomy (SOFIA) [1] is an example of such sub orbital platform. The observatory is based at a 747 Boeing flying a 2.5 meter telescope at an altitude up to 14 km. A high cost of SOFIA operation and a limited observation time is making the sensitivity of the detectors, and thought the speed of the detection, a vital priority in this project.

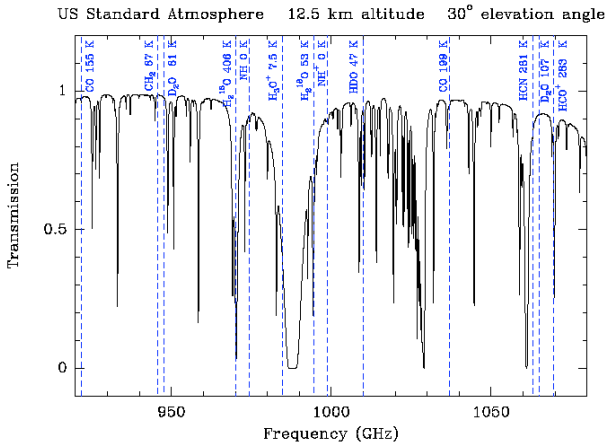


Fig.1 The atmospheric transmission in 0.9 – 1.1 THz band of SOFIA observatory flying at 12 km altitude with telescope at 30 degree elevation angle calculated using ATM [2]. A number of interesting molecular lines is located at the frequencies with nearly ideal (90-95%) transmission of the atmosphere. The atmospheric background noise is below the quantum limit of the heterodyne receivers.

An example of transmission of the atmosphere for SOFIA flying at 12 km altitude and for the telescope elevation angle of 30 degree is presented in fig. 1. The transmission has been calculated using ATM model [2]. Outside of relatively narrow absorption lines of the earth atmosphere the transmission may be as good as 95 - 90%, resulting in the atmospheric background noise temperature as low as 15-30 K. The quantum

limit of the noise of a DSB heterodyne receiver is about $T_N=h\nu/2k\approx$ 24 K at 1 THz [3] and this noise level is comparable with the atmospheric background noise. Therefore the development of a receiver approaching the quantum limit of sensitivity in 1 THz band may substantially improve the capability of SOFIA.

## SIS mixer design

We developed a SIS mixer using a high critical current density Nb/AlN/NbTiN junctions with the normal state resistance to area product $R_NA$= 6 Ohm μm$^2$ [4]. The two SIS junction circuit is coupled to the double slot antenna. We are using epitaxial Nb ground plane and a gold wire layer to form the matching circuit of the SIS mixer.
Due to a low resistivity of the epitaxial Nb film of about 0.2 μOhm cm, the loss in the mixer circuit is relatively low. Another advantage of the design using epitaxial Nb ground plane instead of NbTiN is a much better tolerance to the manufacturing errors. The 1 THz frequency is well above the gap frequency of Nb $F_{gNb}$=700 GHz, and so at 1 THz Niobium behaves as a normal metal. Therefore at 1 THz a microstrip circuit made off Nb has no reduction of the speed of propagation of the signals related to the kinetic inductance. A manufacturing error in length or in positioning of the circuit parts is leading to an error in the phase length of the circuit elements. The error is smaller if Nb ground plane is used instead of NbTiN. This advantage may be particularly important for development of multybeam receivers, where a big number of identical mixer is required.
The mixer housing design is presented in the fig.2 a. It is similar to one used in our work on 1.2 THz SIS mixer [5]. The mixer housing consist of the base frame, of the IF and DC bias board, and of the IF and DC connectors. A Silicon lens with the mixer chip on it back side is fixed in a hole at the front plane of the mixer housing. The mixer chip layout is in the figure 2 b. It is a twin SIS junction circuit coupled to a double-slot planar antenna.

The model prediction of the mixer on-chip coupling is presented in fig. 3. For modeling we used the SUPERMIX [6] software package. The predicted mixer response is centered at 1 THz and should be about 250 GHz wide. The measured FTS response matches well the model prediction (fig. 3).

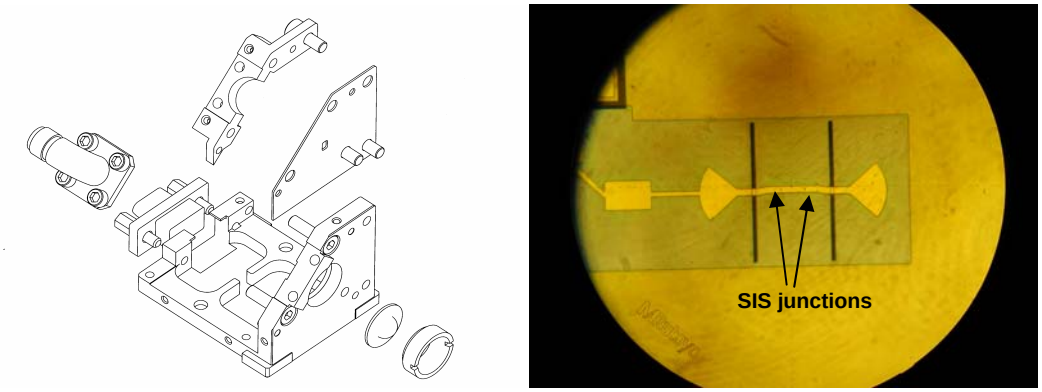


a) b)

Figure 2 a) The mixer housing of a 1 THz SIS mixer developed for SOFIA. It is similar to one used in our work on 1.2 THz SIS mixer [5]. The mixer housing consist of the base frame, IF and DC bias board, IF and DC connectors. A Silicon lens with the mixer chip on it back side is fixed in a hole at the front plane of the mixer housing. b) The 1 THz mixer chip layout. The mixer has a twin SIS junction circuit coupled to a double-slot antenna.

## Experiment

The test receiver used in our experiment consists of an Infrared Laboratories LH-3 cryostat, of the local oscillator, and of the bias electronics. The cryostat vacuum window is in Mylar 12 μm thick. An infrared filter made of Zitex is located at the 77 K stage of the cryostat. The local oscillator power is coupled to the mixer beam using a Mylar beam splitter 13 micron thick. The intermediate frequency range is 4 GHz –

8 GHz and the IF amplifier noise is about 3 K. During the test the physical temperature at the mixer block was about 2 K.

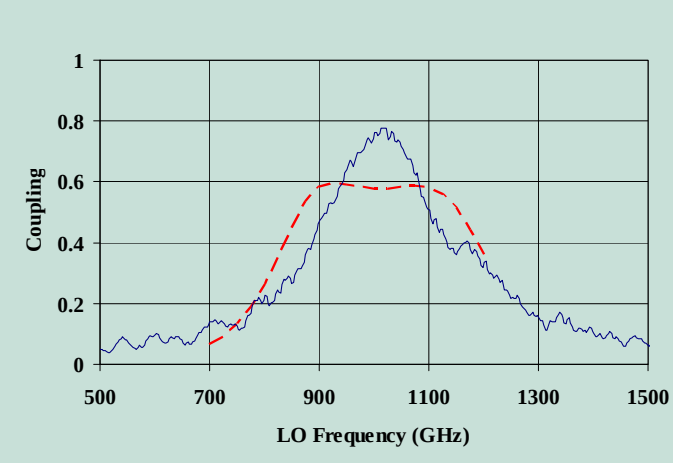


Figure 3. The model prediction of the 1 THz mixer on-chip coupling (dashed line) and the measured FTS response (continues line). The measured FTS response matches well the model prediction.

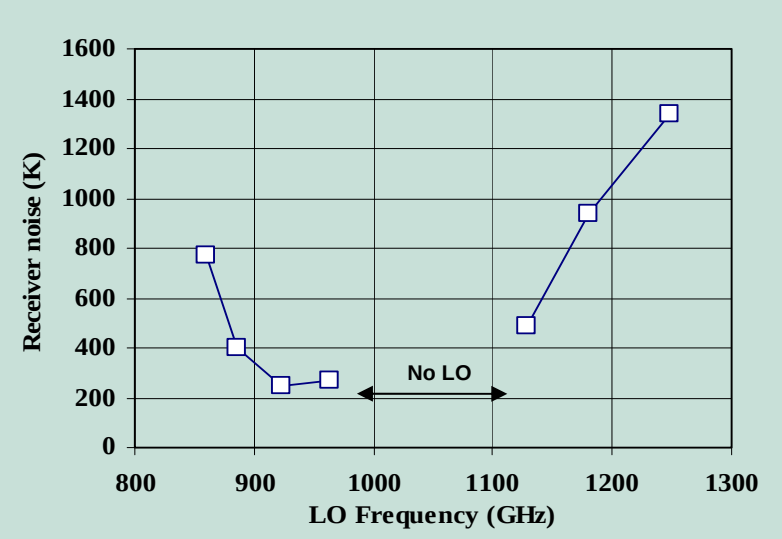


Figure 4. The measured receiver noise corrected for the loss in the LO injection beam splitter. The receiver band is about 250 GHz and it is centered at 1 THz. The break in the curve corresponds to the band with no LO available. The minimum receiver noise corrected for the loss in LO coupler is about 250 K.

We used the Y-factor method for the measurement of the receiver double sideband noise. The ambient temperature and the liquid-nitrogen cooled loads are used as the reference signal sources. The minimum measured receiver noise temperature is $T_{REC}$=353 K (Y=1.50) at 924 GHz. The receiver noise corrected for the loss in the 13 μm thick Mylar beam splitter is presented in the fig. 4. In a good agreement with the mixer design requirements the measured receiver bandwidth is about 250 GHz and is centered at 1 THz frequency. The minimum receiver corrected noise temperature is 250 K. We had no LO coverage for some part of the receiver band.

The level of available LO power was limiting the receiver sensitivity. An example of the receiver performance as a function of LO power level is presented in the fig. 5. The receiver noise and the mixer conversion gain are plotted as a function of the Local Oscillator induced DC current, The SIS junction bias voltage was fixed at V=2.12 mV and the LO frequency was 964 GHz. The receiver noise is corrected for the loss in the 13 μm thick LO beamsplitter. It is visible that the conversion gain and the mixer noise may be improved at a higher level of LO power (fig. 5).

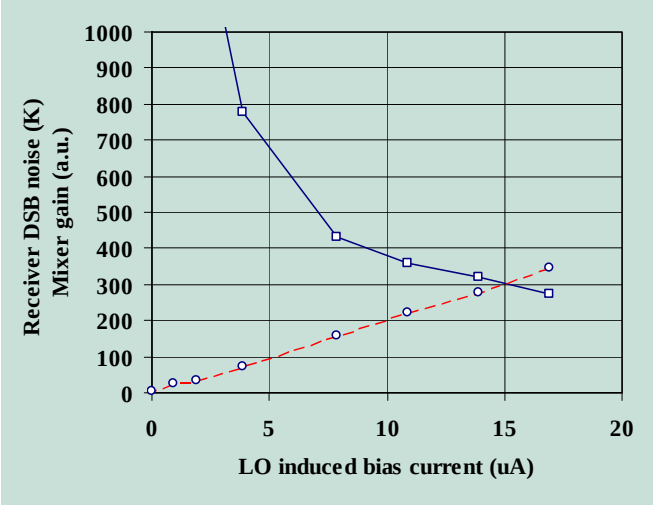


Figure 5. The receiver noise and the mixer conversion gain are plotted as a function of the Local Oscillator induced DC current. The SIS junction bias voltage is fixed at V=2.12 mV and the LO frequency is 964 GHz. The receiver noise is corrected for the loss in the LO beam splitter. It is visible that the conversion gain and the mixer noise may be improved at a higher level of LO power.

## Conclusion

We developed a broad-band low noise SIS mixer for 1 THz channel of CASIMIR instrument of Stratospheric Observatory for Far Infrared Astronomy (SOFIA). The mixer band of operation is 0.875 – 1.125 THz, about 250 GHz wide. The minimum DSB receiver noise measured in our test receiver is 353 K (Y=1.50). The receiver noise corrected for the loss in the LO injection beam splitter is 250 K. The Local Oscillator power level in our test was below an optimal level, and the mixer performance may be improved using more LO power. The developed mixer appears to be a prospective element for construction of a low-noise heterodyne receiver for SOFIA.

## Acknowledgment

This work is supported by SOFIA USRA instrument development program.
The authors would like to thank Imran Mehdi (JPL) for the loan of 1 THz local oscillator.

## References

1. E. E. Becklin, “Stratospheric Observatory For Infrared Astronomy (SOFIA)”, in *Space telescopes and instrumetst, Proc. of SPIE*, Vol. 3356, Mar. 1998. pp. 492-499. 1998.
2. J. R. Pardo, J. Cernicharo, and E. Serabyn, "Atmospheric Transmission at Microwaves (ATM): An Improved Model for mm/submm applications", *IEEE Trans. on Antennas and Propagation*, 49/12, 1683-1694 (2001).
3 A.R. Kerr, M.J. Feldman, and S.-K. Pan, “Receiver noise temperature, the quantum noise limit, and the role of zero-point fluctuations”, in *Proceedings of 8th International Symposium on Space Terahertz Technology*, March. 25-27, 1997, pp. 101-111.
4. B. Bumble, H. G. LeDuc, J. A. Stern, and K. G. Megerian “Fabrication of Nb/Al-Nx/NbTiN Junctions for SIS mixer applications, *IEEE Trans. on Applied Superconductivity*, Vol. 11, No. 1, pp. 76-79, 2001.
5. A. Karpov, D. Miller, F. Rice, J. A. Stern, B. Bumble, H. G. LeDuc, J. Zmuidzinas, “Low Noise SIS Mixer for Far Infrared Radio Astronomy”, in *Millimeter and Submillimeter Detectors for Astronomy II, Proceedings of SPIE*, Vol. 5498, October 2004, pp. 616-621.
6. J. Ward, F. Rice, G. Chattopadhyay, J. Zmuidzinas, “Supermix”, in *Proc. of the 10th Int. Symp. on Space THz Tech*., March 16-18, pp. 268-280, 1999.

# Performance and modeling of 700 GHz SIS finline mixers

Paul K. Grimes, Ghassan Yassin, Stafford Withington and Karl Jacobs.

***Abstract*—SIS mixers using finline waveguide to microstrip transitions show a number of advantageous features, particularly in providing a broadband, fixed impedance feed to the SIS mixer tuning circuit. The large chip area and insensitivity to mixer block machining tolerances simplifies the assembly of the mixer, as well as allowing more advanced mixer designs to be fabricated on a single chip. Finline SIS mixers have shown good performance in the 230 and 350 GHz bands[1][2], and we have also previously reported results from two finline SIS mixers in the 600-720 GHz band[3][4], obtaining best receiver noise temperatures of ~250 K.**

**In this paper we present results from several finline mixers in the 600-720 GHz band, using both variants of our original 3-stage Chebyshev filter tuned single junction mixers and new Belitsky tuned mixers. These dual junction tuned mixers show significantly better performance than our previously reported results, with receiver noise temperatures below 200 K.**

**We present detailed SuperMix simulations of the receiver performance and compare these with measured results. We find good agreement between simulations and measured performance can be achieved by introducing a small amount of attenuation in the RF circuit of the mixer. We also present simulations of the IF bandwidth of finline mixers, and suggest a method by which this can be greatly improved.**

## I. Introduction

Superconductor-Insulator-Superconductor (SIS) mixers are commonly used as coherent detectors in millimeter and sub-millimeter wave astronomy, and are the basis of the most sensitive receivers at frequencies up to a 1 THz. Modern niobium based SIS mixers achieve sensitivities comparable to the quantum limit at frequencies up to the superconducting energy gap of niobium (680 GHz). However, above the gap losses in the niobium transmission lines become significant, while losses in other components of the receiver also increase, and so careful analysis and design of the complete receiver system is required to achieve the best possible performance.

In this paper we report results from seven finline SIS mixers operating in the 600-720 GHz band, i.e. across the superconducting energy gap of niobium. While finline mixers have a number of important advantages, the long length of niobium superconducting transmission line that makes up the finline taper means that losses may be very large at frequencies above the superconducting gap. We have therefore used experimental techniques and numerical simulations to separate the various contributions to the receiver performance, with the aim of determining the performance of the finline tapers across the superconducting energy gap.

P. Grimes and G. Yassin are with the Dept. of Physics, University of Oxford, Denys Wilkinson Building, Keble Road, Oxford, OX1 3RH, UK.
S. Withington is with the Dept. of Physics, Cavendish Laboratory, Madingley Road, Cambridge, CB3 0HE, UK.
K. Jacobs is with KOSMA, I. Physikalisches Institut, University of Cologne, 77 Zülpicher Strasse, 50937, Köln, Germany.

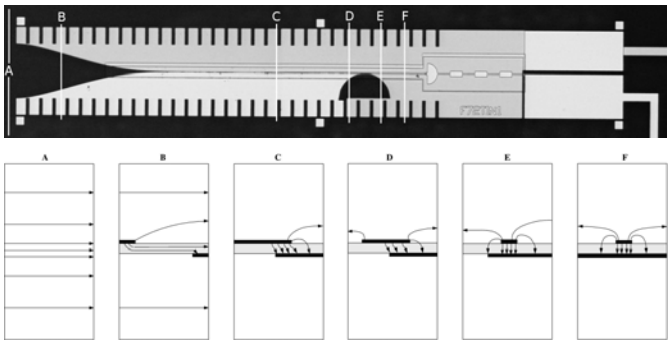


Fig. 1. (Top) A 700 GHz finline mixer chip. The finline taper runs from the left to center of the chip, and the mixer tuning circuit, RF block and bond pads are on the right (Bottom) Cross-sections through the finline taper, showing the metallization and the E-field lines. The finline taper gradually transforms the waveguide mode at A through unilateral finline (B) to antipodal finline (C), before transitioning from antipodal finline to microstrip (D-F).

Finline tapers have been successfully used on many mm-wave superconducting detectors, including our previously reported 230 and 350 GHz SIS mixers and a 700 GHz balanced mixer. We have also recently designed finline tapers for the 100 GHz TES detectors for Clover[5], and a 230 GHz cold electron bolometer. We have demonstrated that these tapers provide a broadband mixer feed that does not require a complex mixer block or any mechanical tuning and provide a large substrate area that is suitable for high levels of integration. Once the RF signal has passed to the microstrip output of the finline taper, the waveguide surrounding the chip can be removed, allowing great flexibility in processing the RF signal and in extracting IF signals from the chip.

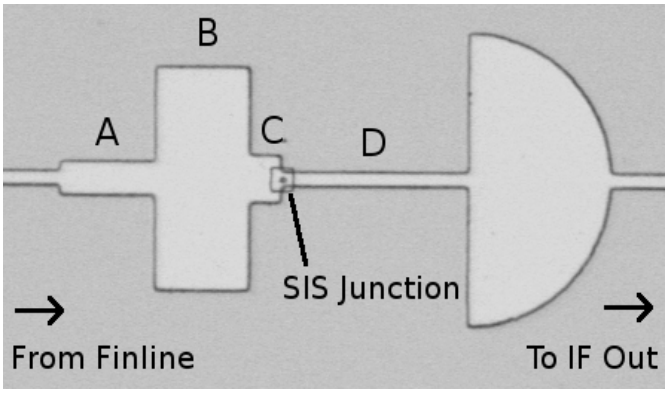


Fig. 2. The 3-stage Chebyshev tuned mixer and radial RF-choke design. Typical dimensions are: **A** 7 x 26 μm, **B** 46 x 24 μm, **C** 10 x 6.5 μm and **D** 3 x 39 μm.

## II. The 700 GHz Finline Mixer Design

### A. Mixer chip

The mixer chip (Fig. 1) is deposited in five steps, using four UV lithography masks. First a Nb-AlOx-Nb trilayer is deposited (200 nm, 10 nm, 100 nm). The junction is then defined by reactive ion etching, and the first SiO dielectric layer (200 nm) is evaporated using the same photoresist mask. A second layer of SiO is deposited to thicken the dielectric layer to 425 nm. Finally the 400 nm Nb wiring layer (with a 25 nm Au protection layer on top) is sputtered, forming the upper fin, mixer wiring and bond pads.

The mixer is deposited on a 225 µm fused quartz (infrasil) wafer, which is diced and then lapped to 45-60 µm thickness on a dicing saw after fabrication. A triangular taper is diced onto the front of the mixer chip to prevent reflections from the front of the mixer chip.

The finline taper consists of two niobium fins deposited on the quartz mixer chip, that gradually extend from the walls of the E-plane of the waveguide until they overlap at the centre of the waveguide. The fins are separated in the overlap region by a 0.425 µm layer of evaporated SiO. Once the fin overlap is large enough that fringing effects can be ignored, the top fin is tapered away from the wall to form the wiring layer of the output microstrip and mixer circuit, before the lower fin (the lower layer of the trilayer) is extended across the waveguide to form the ground plane of the microstrip (Fig. 1).

The finline taper is designed using a mixture of transverse resonance and spectral domain analysis as the inputs to an optimum taper method. Details of the electromagnetic design have already been reported[6].

The 20 Ω microstrip feeds the mixer tuning circuit, containing the SIS junction(s). A second microstrip carries IF signals from the output of the mixer tuning circuit to bond pads at the end of the chip. DC bias signals are also applied to the SIS junction via these bond pads and microstrip.

Results from mixers using two different types of tuning circuits are presented in this paper. The first design tested consists of a 3-section microstrip Chebyshev transformer (Fig. 2) that transforms the 20 Ω input microstrip impedance to the 20 Ω plus 65 fF capacitance of the SIS junction. This circuit was optimized using Sonnet em suite to maximize the RF coupling to the SIS junction.

The second circuit (Fig. 3) uses a two junction (or "Belitsky"[7]) tuning circuit, consisting of two SIS junctions separated by a length of microstrip, and with a quarter-wave section of microstrip to match the 20 Ω input microstrip to the 10 Ω normal resistance of the two parallel SIS junctions. The capacitance of one junction, transformed by the microstrip section, cancels out the capacitance of the second junction[8]. This circuit was optimized using SuperMix[9] to give the maximum conversion gain across a broad RF bandwidth. In both circuits the IF signal from the junction is readout via a radial stub RF choke to prevent RF signal leaking into the IF circuit.

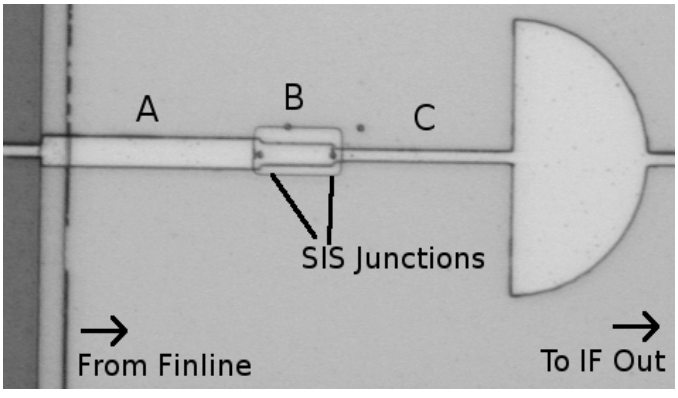


Fig. 3. The dual junction tuned mixer and radial RF-choke design. Typical dimensions are: **A** 7 x 48.5 µm, **B** 5 x 15.5 µm and **C** 3 x 39 µm.

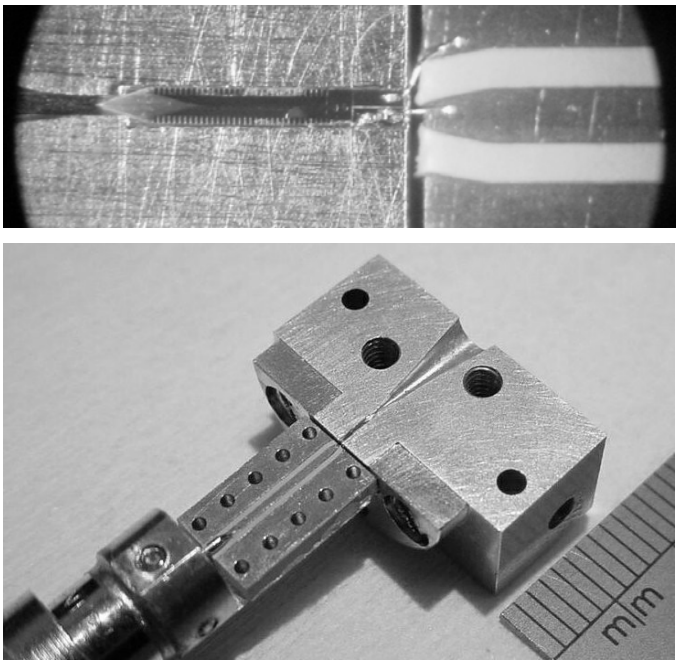

Fig. 4. (Top) The mixer chip mounted in the split mixer block and bonded to the CPW IF board. (Bottom) One half of the split mixer block, showing the SMA connector, IF board, mixer chip and Pickett-Potter horn.

### B. Mixer block

The split mixer block is directly machined in aluminum in two halves, joined along the E-plane of the 160 µm by 320 µm waveguide. The mixer chip is superglued into a pair of 60 µm

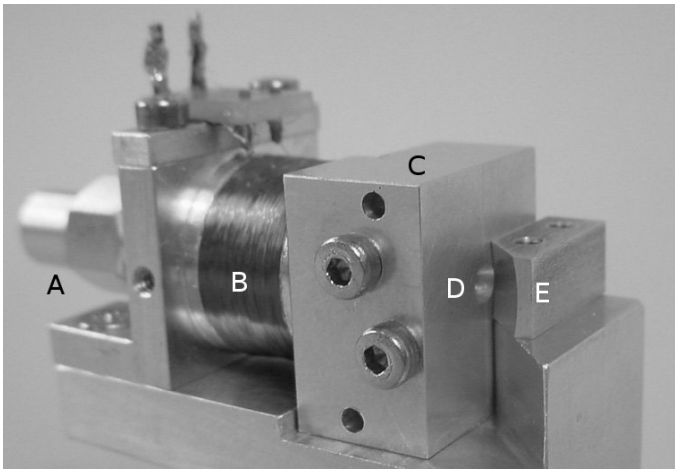


Fig. 5. The assembled mixer block and support jig. Visible components include: **A** SMA connector, **B** electromagnet, **C** split mixer block, **D** horn aperture and **E** offset parabolic reflector.

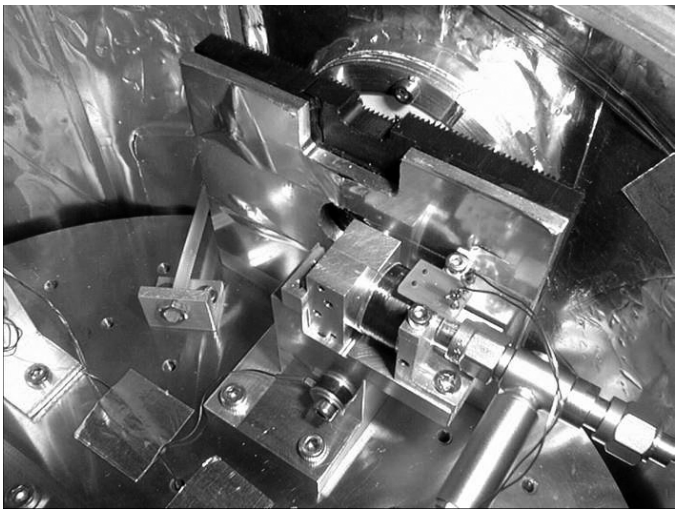

Fig. 6. The mixer assembled into the He4 cryostat. The horn-reflector aperture is to the top left of the mixer block, point through the circular aperture in the TK RAM shield. The Zitex IR filter can be seen over the top of the shield.

wide by 60 µm deep grooves machined into the waveguide walls in one half-block (Fig. 4).

The mixer is fed by a Pickett-Potter Horn Reflector (PPHR) antenna[3] directly machined in two halves into the mixer block, with the offset parabolic reflector (used to correct the spherical phase cap) mounted onto the jig holding the mixer block (Fig. 5). This feed is relatively simple to machine, and provides a good radiation pattern across the mixer band.

The mixer chip is bonded to a short section of co-planar waveguide on RT/Duroid 6010LM that carries the IF and bias signals to an SMA connector mounted on the back of the mixer block (Fig. 4). A superconducting electromagnet mounted coaxially with the IF board and mixer chip is used to suppress the Josephson current in the SIS junction (Fig. 5).

### *C. Test receiver*

Experimental investigation of the mixer performance was carried out by mounting the mixer block in an IR labs He4 wet cryostat, looking out through a thermal filter consisting of 4 thin layers of Zitex and through either a resonant 610 um HDPE vacuum window or a 2.5 mm thick HDPE window with corrugated antireflection grooves machined into the surface. A small area of Thomas Keating RAM tiles with an aperture around the beam are positioned between the mixer block and the thermal filters to help prevent standing waves (Fig. 6). For most of the measured data in this paper, the cryostat was cooled to below 2.4 K by pumping on the helium bath.

The IF and bias signals are separated in a Radiall 0-12 GHz bias tee. The IF signal is then amplified by a Berkshire 4-6 GHz cryogenic LNA with a nominal noise temperature less than 4 K, before being passed out of the cryostat to the warm IF electronics, consisting of a 4.2-5.8 GHz bandpass filter, two amplifiers and a diode power detector.

LO power was provided by a RPG Gunn diode, doubler, tripler chain providing up to 330 µW across a 600-720 GHz band. The LO beam is focused by an offset parabolic mirror and then coupled to the mixer via a 8.5 µm or 18 µm Mylar beam splitter.

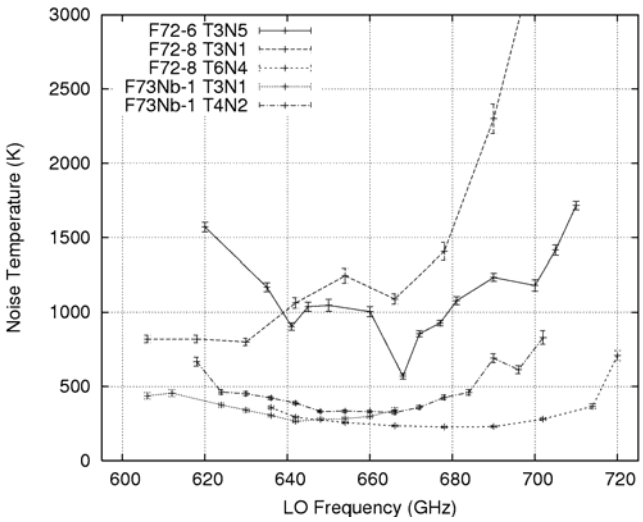


Fig. 7. Measured noise performance for five 3-stage Chebyshev transformer tuned mixers. All of these measurements were carried out at a physical temperature of 2.5 K.

## III. Measured Performance

Five 3-stage Chebyshev tuned devices (from 3 fabrication batches) and two dual junction tuned devices (from the final fabrication batch) were selected for testing on the basis of their measured IV curves. Devices with suitable normal resistances, low subgap leakages and Fiske resonances close to the expected values were chosen for full RF testing. Noise and gain performance of these devices is given in Figs. 7-10.

Noise performance was determined using the Y-factor method with 77 K and 297 K Eccosorb loads, while conversion gain was determined by comparing the IF output power for the two loads, after calibrating the gain of the IF chain using the unpumped SIS junction biased above the gap as a noise source. No corrections have been applied to receiver noise temperatures, and the Rayleigh-Jeans

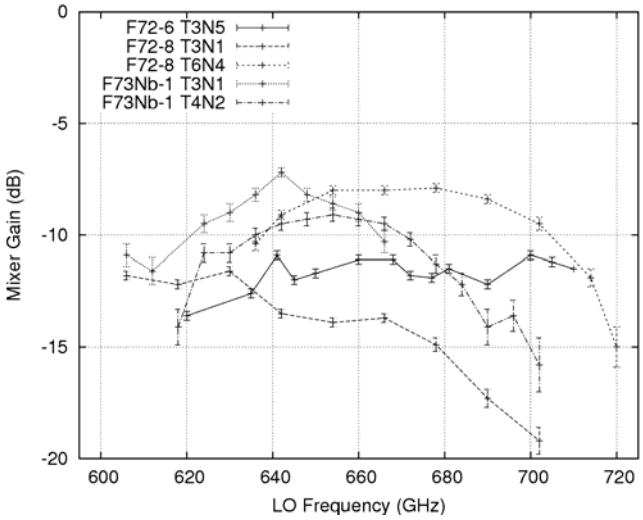


Fig. 8. Measured conversion gain for the five 3-stage Chebyshev transformer tuned mixers of Fig. 7. The IF system gain is calibrated, and the conversion gain referred to front of the IF amplifier by using the unpumped SIS junction, biased well above the gap, as a noise source.

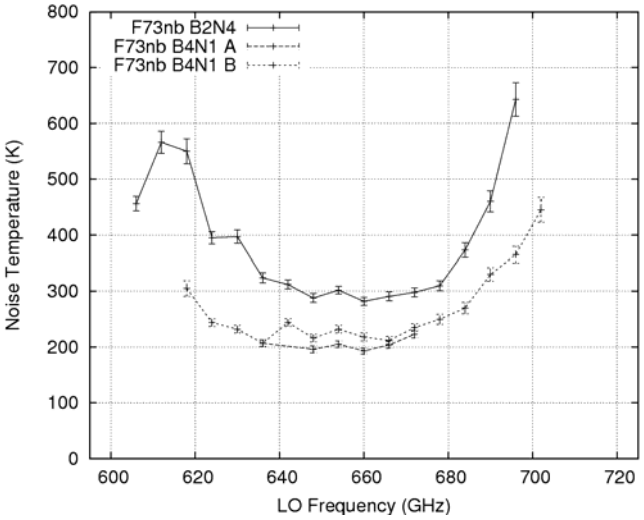


Fig. 9. Measured noise performance for two dual junction tuned mixers. Device F73nb-1 B4N1 was measured twice, with significantly better performance recorded over a reduced frequency range on the first attempt.

approximation is used in determining load powers, leading a to slight overestimation of the receiver noise.

Of the five Chebyshev tuned devices, the first two devices tested (F72-6 T3N5 and F72-8 T3N1) were deliberately chosen because they were tuned above 700 GHz and below 620 GHz respectively, in order to give reasonable direct detection sensitivity for measuring the Pickett-Potter horn reflector antenna radiation pattern at the edges of the band. The heterodyne performance of these devices was measured using an older cryogenic IF LNA, with a noise temperature of ~10 K. As expected, the performance of these devices is compromised by both the poor tuning and noisier IF chain. These devices were tested using the corrugated Dewar window. In subsequent tests, better performance was obtained with the thin resonant Dewar window, and this window was used for all other results.

The other three devices tested were all well tuned, and were

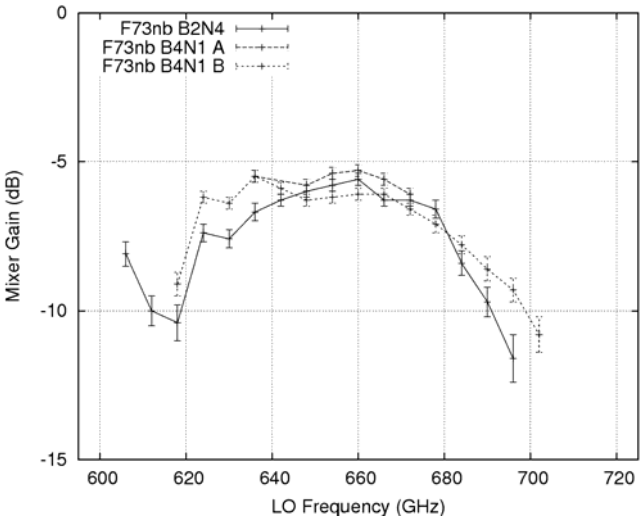


Fig. 10. Measured conversion gain for the two dual junction tuned mixers of Fig. 9. Again, device F73nb-1 B4N1 showed significantly better performance over a narrow frequency range in the first experiment.

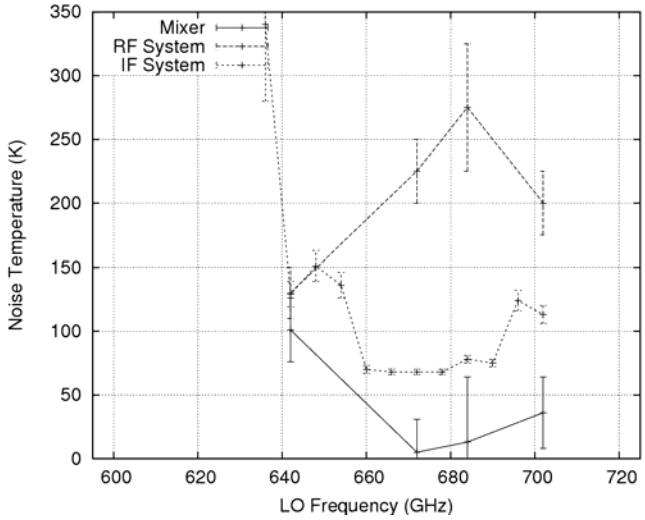


Fig. 11. Measured contributions from receiver components to the total receiver noise for device F72-8 T6N4. The IF noise is estimated from the measured conversion gain and IF amplifier input noise temperature (both measured directly for the bare amplifier, and as part of the receiver system, using the method of [10] ), while the RF side noise contribution is estimated at selected frequencies using the intersecting lines method[11]. The remaining system noise is assigned to the mixer itself.

tested using the IF amplifier described in II.C. All of these devices showed conversion gains between -8 and -10 dB and noise temperatures below 400 K across the centre of the LO band, with best values of -8 dB and 250 K for F72-8 T6N4 between 666 and 690 GHz. The performance below 640 GHz for all devices is limited by the available LO power, while at the top edge of the band the performance is limited by both the available LO power and by the above gap losses in the finline and mixer tuning circuit.

For the best device (F72-8 T6N4), the intersecting lines method was used at selected frequencies to estimate the noise contribution of from the RF circuits and optics, while the measured conversion gain was used to estimate the IF system contribution to the noise. The results of this analysis are shown in Fig. 11 and suggest that the noise of the receiver is dominated by losses in the RF circuit and/or optics.

The two dual junction devices tested show better conversion gain and noise performance than the single junction devices, with best values of -5.3 dB and 196 K for device F73nb-1 B4N1 at 660 GHz.

The direct coupling and heterodyne bandwidth of these two devices is significantly wider than for the single junction devices, making it much easier to couple LO power. However both devices are still under-pumped at frequencies below 624 GHz. The performance of device F73nb-1 B4N1 was significantly better during a preliminary test at the centre of the band than when the full LO band was measured during a second experiment, probably due to a change in the test receiver optics between the two experiments.

## IV. Simulations of Receiver Performance

Caltech's SuperMix simulation library[9] was used to model the performance of the complete receiver. The receiver

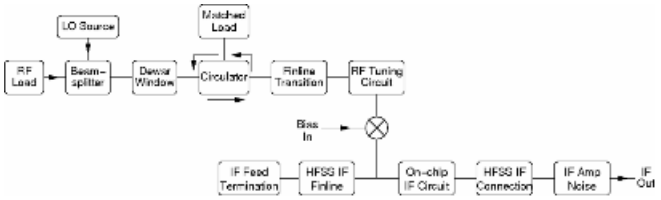


Fig. 12. SuperMix circuits used to simulate the performance of the complete 700 GHz finline test receiver. The top circuit consists of RF frequency components, while the lower circuit consists of the IF components.

is modeled using the RF and IF circuits shown in Fig. 12. The RF circuit consists of the hot/cold load, LO source (with 300 K sideband noise temperature), beamsplitter, Dewar window, finline transition and the mixer tuning circuit. The finline transition is modeled as a circulator with matched load to provide input matching and a length of superconducting microstrip to model the above gap losses. The IF circuit includes the IF representation of the mixer chip circuits, finline taper and bondwire connection to the IF board CPW line, as well as a constant noise temperature due to the IF amplifier.

### *A. Component modeling*

Several new classes were created within SuperMix to allow the whole receiver system to be modeled. The main two components required were 2 and 3 port models of a dielectric slab placed within the free space beam. These components were used to represent the HDPE resonant window and the Mylar beamsplitter, and can represent a dielectric slab at an any angle to the beam in either parallel or perpendicular polarization. The scattering parameter calculations for these components were derived from the reflection and transmission properties given by Goldsmith[12]. A basic check of the model was carried out by calculating the transmission through the Dewar vacuum window and comparing this with FTS measurements of the window, which showed good agreement.

The effect of the finline taper is included in the simulations using two methods. For RF signals only the above gap losses of the finline are modeled by including a length of superconducting microstrip, chosen to match the decrease in conversion gain above the gap. For IF signals the finline is modeled using Ansoft's HFSS electromagnetic simulation software. HFSS is also used to model the bondwire connections between the mixer chip and the IF CPW

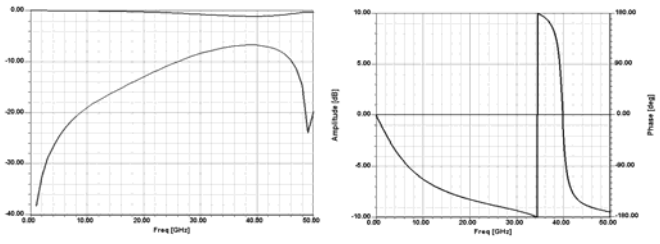

Fig. 13. (Left) Magnitude of HFSS simulated scattering parameters for the bondwire connection between the mixer chip and the IF board for IF frequencies up to 50 GHz. (Right) Magnitude and phase of the IF signal reflected from the finline taper as a function of IF frequency. The finline appears as an open circuit at 0 and 40 GHz, and as a short circuit at 34 GHz.

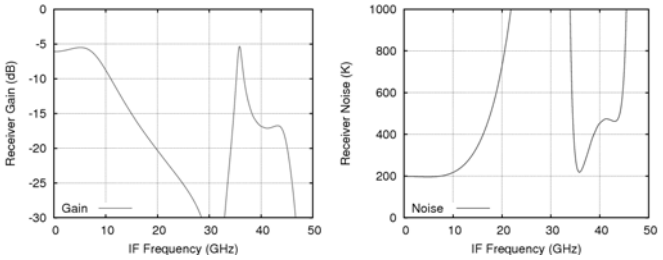


Fig. 14. SuperMix simulated performance of device F73nb-1 B4N1 as a function of IF frequency. The variation in performance is dominated by the effect of the phase of reflections from the finline taper.

connection board. The response of these two IF components are shown Fig. 13.

At IF frequencies, the finline taper is perfectly reflecting (as the IF signals are below the cut-off frequency of the waveguide), the but the point along the finline at which this reflection occurs is strongly frequency dependent, as the cut-off frequency is tapered along the finline. This gives a frequency dependent phase change in the reflection. Simulating the mixer performance as a function of IF frequency (Fig. 14) shows that this property of the finline taper limits the IF bandwidth of the mixer to around ~8-10 GHz, but has little effect below this frequency.

### *B. Receiver performance modeling*

A number of parameters are varied in the SuperMix model to fit the simulated mixer performance to the measured performance. These parameters are: LO power (assumed to be that required to give optimum conversion gain), junction capacitance (chosen to give correct shape to the gain at subgap frequencies), and the length and gap voltage of the microstrip representing the finline (chosen to give the correct slope and frequency turn-over point at high frequencies). An additional attenuation at variable temperature is included in the RF circuit (between the Dewar window and the finline) to fit the overall conversion gain and receiver noise temperature.

These parameters were independently fitted to the measured performance of the best devices of each type (F72-8 T6N4, Fig. 15 and F73nb-1 B4N1, Fig. 16.). The performance of these devices can be fitted using similar parameters in both simulations. These parameters are given in Table. 1.

From these results, it appears that there is an additional RF loss of -2.5 to -3.5 dB in the receiver, with an effective temperature of 100-120 K. Obviously this may be made up of several components, at different points in the system, and may not only be in the RF system of the receiver.

TABLE I
FITTED SIMULATION PARAMETERS

| Quantity | Fitted Values |
|---|---|
| Junction capacitance | 65-72 fF |
| LO power | 10-12 μW |
| LO sideband temperature | 300 K |
| Finline equivalent length | 600 μm |
| Finline gap voltage | 2.77 mV (670 GHz) |
| RF Attenuation | -2.5 - -3.5 dB |
| RF Attenuator Temperature | 100-120 K |

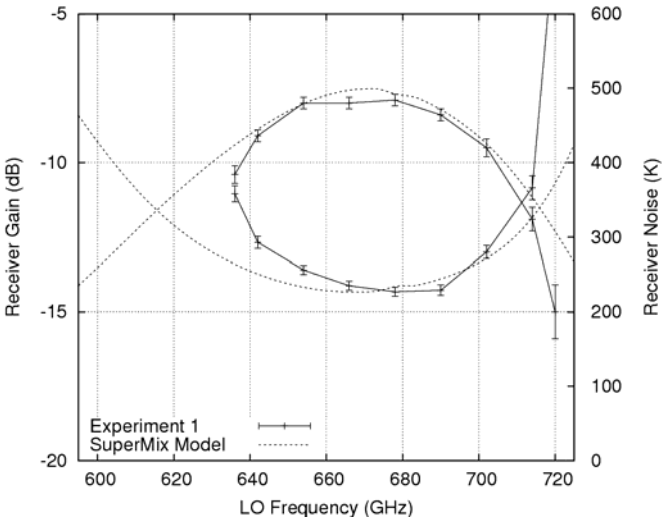


Fig. 15. Comparison of measured data for Chebyshev tuned device F72-8 T6N4 and SuperMix simulated receiver performance.

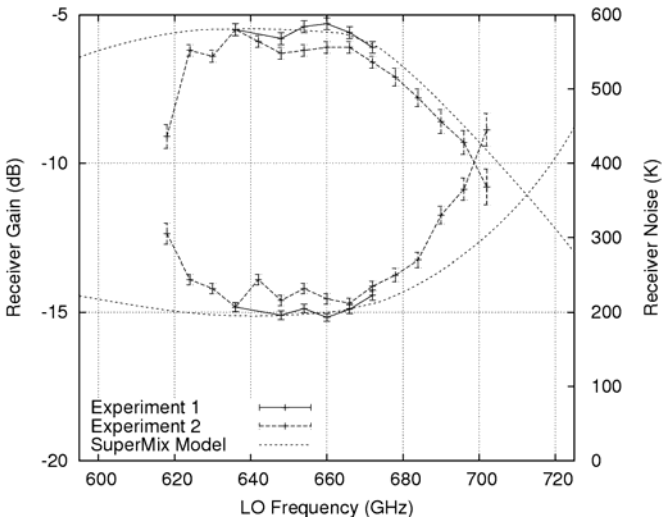


Fig. 16. Comparison of measured data for dual junction tuned device F73nb-1 B4N1 and SuperMix simulated receiver performance.

We suggest several possible sources for this attenuation: losses in the Mylar beamsplitter due to water vapor absorbed in the lab environment; attenuation in the IR filters on the 77 K shield of the Dewar; and losses in the IF board, bias tee and coax used to connect the mixer chip to the IF amplifier.

## V. Conclusions and Future Prospects

We have measured several 700 GHz finline mixers using two different tuner designs, and obtained best uncorrected receiver noise temperatures of 250 K and 196 K for each design. The performance of these receivers has been extensively modeled, and good agreement can be obtained between the measured and simulated performance if an extra ~3 dB of attenuation is included in the RF system of the mixer.

We have demonstrated that finline mixers can be operated at frequencies approaching the superconducting gap of niobium. More work will be required to extend operation above the superconducting gap, such as shortening the taper using a more rigorous method of taper design, and/or employing NbTiN films in the taper. Thinner substrates will also substantial improve the performance.

Finally we would like to emphasize that back-to-back finline transitions are ideal for realizing balanced and image separating mixer designs, in which the signal is fed from one finline and the LO from the other. The large substrate area allows the required hybrids to fabricated on-chip, in elegant planar circuits. We have already designed and fabricated a balanced finline mixer based on this concept (Fig. 17)[13] and testing of these devices is currently in progress.

## References

[1] G. Yassin, R. Padman, S. Withington, K. Jacobs and S. Wulff, "A broad band antipodal finline mixer for astronomical imaging arrays", Electron. Lett., vol. 33, pp. 498.

[2] G. Yassin, S. Withington, M. Buffey, K. Jacobs and S. Wulff, "A 350-G Hz SIS antipodal finline mixer", IEEE Trans. Microwave Theory and Tech., 48, p. 662, 2000.

[3] P. Kittara, P. K. Grimes, G. Yassin, S. Withington, K. Jacobs, and S. Wu lff, "A 700 GHz antipodal finline mixer fed by a Pickett-Potter horn-reflector antenna", IEEE Trans. Microwave Theory and Tech., 52, p. 2352, 2004.

[4] P. K. Grimes, P. Kittara, G. Yassin, S. Withington and K. Jacobs, "Investigation of the performance of a 700 GHz finline mixer", Proc. 14th Int. Symp. Space THz Tech., Tucson AZ, 2003.

[5] D. M. Audley *et al*, "Prototype finline-coupled TES bolometers for CLOVER", Proc 17th Int. Symp. Space THz Tech., Paris, 2006.

[6] C.E. North, G. Yassin and P.K. Grimes, "Rigorous analysis and design of finline tapers for high performance millimetre and submillimetre detectors", Proc. 17th Int. Symp. Space THz Tech., Paris, 2006.

[7] V.Y. Belitsky and M.A. Tarasov, "SIS junction complete reactance compensation", IEEE Trans. Magn., 27, pp 2938-2641, 1991.

[8] J. Zmuidzinas, H. G. LeDuc, J.A. Stern and S.R. Cypher, "Two-junction tuning circuits for submillimeter SIS mixers", IEEE Trans. Microwave Theory and Tech., 42, p. 698-706, 1994.

[9] J. Ward, F. Rice, G. Chattopadhyay and J. Zmuidzinas, "SuperMix: A flexible software library for high-frequency circuit simulation, including SIS mixers and superconducting elements", Proc. 10th Int. Symp. Space THz Tech., 1999.

[10] D.P. Woody, R.E. Miller and M.J. Wengler, "85-115 GHz receivers for radio astronomy", IEEE Trans. Microwave Theory and Tech., 33, p. 90-95, 1985.

[11] R. Blundell, R.E. Miller and K.H. Gundlach, "Understanding noise in SIS receivers", Int. J. Infrared Millimeter Waves, 13, p. 3-14, 1992

[12] P.F. Goldsmith, "Quasioptical systems: Gaussian beam quasioptical propagation and applications", John Wiley & Sons, Inc., 1997.

[13] P.K. Grimes, G. Yassin, K. Jacobs and S. Withington, "A 700 GHz single chip balanced SIS mixer", 16th Int. Symp. Space THz Tech., Gothenburg, 2005.

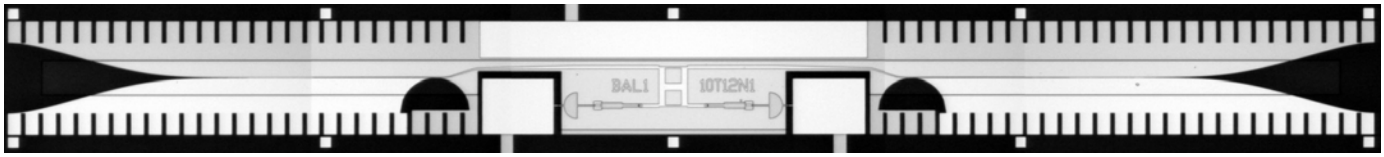

Fig. 17. A 700 GHz single chip balanced SIS mixer, based on back-to-back finline tapers. The RF and LO signals are fed via the two finline tapers and combined in microstrip quadrature hybrid at the center of the chip.

# Tolerance Analysis of THz-Range Lens-Antenna and Balanced SIS Mixers

Andrey V. Uvarov, Sergey V. Shitov, Oleg V. Koryukin, Maksim A. Bukovski, Yoshinori Uzawa, Takashi Noguchi, Matthias Kroug, Masanori Takeda, Zhen Wang and A. N. Vystavkin

***Abstract*—Effects caused by imperfection of extended hemispherical immersion lens-antenna are studied numerically at 865 GHz. Elliptical and aplanatic focusing regimes are tested in combination with double-slot and double-dipole feeds for their aperture efficiency in the presence of multiple misalignment factors, which include possible phase and amplitude asymmetry of complimentary SIS tuning circuit. A new balanced lens-antenna SIS mixer is analyzed for its aperture efficiency with respect to an IF bandwidth of 4-12 GHz. Experimental data on lens-antenna SIS mixers with epitaxial NbN-AlN-NbN tunnel junctions is presented.**

***Index Terms*—lens-antenna, aperture efficiency, quasioptical mixer, SIS mixer, balanced mixer, NbN tunnel junction**

## I. Introduction

The primary cases to use the immersion lens-antenna are as following: i) a large-chip integrated circuit containing a printed antenna (ex. [1], [2]); ii) a densely packed array of printed antennas (imaging array) fabricated on the same chip (ex. [3]) or iii) need for a very broadband (multi-octave) reception that is not possible with waveguides. The low-noise performance of a lens-antenna THz-band mixer employing SIS junctions has been demonstrated quite some time ago [4], [5]. The most attractive feature of the lens-antenna technology is that the size of quasioptical chips is not dependent on frequency; the chips are easier to process and can be handled with much less caution. Numerical models are often based on perfect symmetry of the structure and accuracy of its parameters. However, this cannot be always achieved at submillimeter wavelength. The accuracy of mechanical (optical) parts and their alignment are limited usually by a few micrometers. The misalignment of the lithography process is typically up to half-micron. The required accuracy of SIS junction size must be often better than 50 nm. This list does not include yet some random defects of the structure and slight changes in properties of sputtered materials, which are difficult to detect. Since we are aiming the option development of balanced/quasioptical mixers for ALMA Band-10 (787-950 GHz), many precise components are used, and the tolerance analysis is of great interest for understanding possible restriction on design/performance of our mixers. This report is focused on analysis of the following specific problems of the symmetry-based SIS mixers:

- Beam distortion of a lens-antenna mixer due to positioning error of the antenna with respect to the immersion lens.
- Beam distortion due to amplitude and phase errors caused by photolithography misalignment.
- Beam distortion due to unequal size and impedance of two junctions of a twin-SIS mixer and/or due to inequality of two twin-mixers of a balanced lens-antenna mixer.
- Beam tilt due to unequal phase of two IF output signals of a balanced QO mixer.

The feasibility of the research is not limited to the single-element mixer; its results (and methods) can be applied to a single-lens imaging array for analysis of its off-axis pixels.

## II. Calculation Method and Criteria

The beam has been calculated using a technique of well-known Kirhoff-Hugens' diffraction integral taken over the curved surface of the lens. We have analyzed two cases of focusing of a spherical lens-antenna: elliptical (synthesized) and aplanatic. The printed (lithographic) double-slot antenna and the double-dipole antenna with back-reflector were tested as feeds of the lenses. First we calculated amplitude and phase at two vibrators of a double-element antenna. The far-field beam of the antennas was then calculated assuming a sinusoidal current distribution along the antenna vibrators. The refracting surface of a silicon lens was assumed laying in the far-field. The matching (anti-reflection) coating is attached to the lens surface. No effects of internal reflection are taken into account. The tolerance margins were set as follows: i) off-axis misalignment of antenna (X- or Y-offset) up to 10 μm; ii) on-axis offset (Z-offset) up to 20 mm; iii) lithographic masks offset up to 1 μm; iv) difference in $R_n$ for twin-SIS up to 20% in

Manuscript received April 30, 2007. This work was supported in parts by the ALMA-J Office, National Astronomical Observatory of Japan, and by ISTC project #2626.

Andrey V. Uvarov is with the Institute of Radio Engineering and Electronics, Russian Academy of Sciences, Moscow, 125009, Russia (phone: +7-495-2032505; fax: +7-495-2038414; e-mail: uvarov@hitech.cplire.ru ).

Sergey V. Shitov is with the National Astronomical Observatory of Japan, Mitaka, Tokyo 181-8588, Japan, and with the Institute of Radio Engineering and Electronics, Russian Academy of Sciences, Moscow 125009, Russia (phone: +81-422-343879; fax: +81-422-343864; e-mail: s.shitov@nao.ac.jp ).

Oleg V. Koryukin, Maksim A. Bukovski and A. N. Vystavkin are with the Institute of Radio Engineering and Electronics, Russian Academy of Sciences, Moscow 125009, Russia (e-mails: koryukin@hitech.cplire.ru , maksim.bukovski@rambler.ru , vyst@hitech.cplire.ru ).

Yoshinori Uzawa, Takashi Noguchi and Matthias Krough are with the National Astronomical Observatory of Japan, Mitaka, Tokyo 181-8588, Japan (e-mails: y.uzawa@nao.ac.jp , t.noguchi@nao.ac.jp , matthias.kroug@nao.ac.jp ).

Masanori Takeda and Zhen Wang are with the National Institute of Information and Communication Technology, Kobe, 651-2492 Japan (e-mail takeda@po.nict.go.jp , wang@nict.go.jp ).

mixer configurations as in [4], [5]; v) off-axis position of the anti-reflection coating up to 10 μm. As the result the excitation power ratio of two antennas up to 2.3 and phase shift up to 15 degrees are used.

To compare different combinations of lenses and antennas, we used the following well-known integral criteria [6]: the spillover efficiency

$$\varepsilon_s = \frac{\int_{\Omega_0} |E|^2 \cdot d\Omega}{\int_{4\pi} |E|^2 \cdot d\Omega}, \quad (1)$$

( $\Omega_0$ is the solid angle of sub-reflector) and the taper efficiency

$$\varepsilon_t = \frac{\left| \int_{\Omega_0} E \cdot d\Omega \right|^2}{\int_{\Omega_0} |E|^2 d\Omega \cdot \int_{\Omega_0} d\Omega} \quad (2)$$

yielding the full aperture efficiency as

$$\varepsilon_{ap} = \varepsilon_s \cdot \varepsilon_t . \quad (3)$$

## III. Two-Element Feed in Aplanatic and Elliptical Focus

The beam and phase patterns of a spherical lens in elliptical regime of focusing shown in Fig. 1(a) and Fig. 1(b) are in reasonable agreement with [7], [8]. The Gaussian impurity of the beam (sidelobes at -18…-20 dB) can be a serious problem within an optical system with numerous limiting apertures. Fortunately, there is no need in intervening optics between the mixer and the sub-reflector of the ALMA telescope, if such lens-antenna is used. Since the Gaussian fit of the nominal beam is good down to the edge of the sub-reflector at -10 dB (Fig. 1a), the beam of the telescope will be essentially the same as the sub-reflector were illuminated with a corrugated horn antenna. Note that the joint result of all misalignments is rather similar to tilt of the beam that can be compensated by mechanical rotation of the mixer block for about 0.6 degree. The phase error across the beam is less than 1/16 of the wavelength (Fig. 1b) thus being below the RMS accuracy of the telescope dish.

The results of aplanatic focusing are presented in Fig. 2(a) and Fig. 2(b). Strong diffraction effects are clearly seen within the main lobe along with essentially larger phase slope. The summary of criteria (1)-(3) presented in Table 1 shows faster degradation of the beam efficiency for the case of aplanatic focusing, but it remains higher than elliptical one. However, the aplanatic focus, unlike elliptical one, does not maintain the constant beam-width, so its correction (if any) cannot be a simple rotation. Some concerns are arising from the fact that intervening optics is necessary for the aplanatic lens-antenna. We do not analyze this problem here.

The aperture truncation analysis presented in Fig. 3 is using a few Gaussian beams of different half-power width (20, 30 and 60 degree) as they were launched by the feed located in the point of elliptical focus. It is obvious that much better Gaussisity (and beam efficiency) can be achieved, if the synthesis of a narrow-beam printed antenna is possible.

Fig. 4(a) and Fig. 4(b) demonstrate the difference between double-dipole and double-slot feed antennas. The far-field pattern of the double-dipole antenna, calculated inside the silicon lens in presence of misalignments, shows its better stability and potentially lower truncation level than for the double-slot antenna. This can be explained by the doubled number of elements of the array-antenna due to image provided by the back reflector.

## IV. Balanced Quasioptical Mixer

The layout of the new balanced quasioptical SIS mixer is presented in Fig. 5. The mixer employs two double-slot antennas, which are crossing each other in the areas of minimum *rf* current [9]. We have confirmed with CST MWS software that the beam quality (shape and efficiency) of the cross-slot antenna is generally the same as presented in Fig. 1. Each antenna receives one of two orthogonal polarizations, the LO and the signal. The signal beam is coupled from two vertical slots into twin-SIS mixers, Mixer 1 and Mixer 2, exciting them in anti-phase. The LO power is combined from two horizontal slots using a RF balun, then split in half and supplied to the mixers in-phase. This prevents coupling of LO power to the signal beam and vice versa. The LO balun is simulated providing phase shift of 180±14º across the band as presented in Fig. 6. Since the phase slope of the RF balun is small, the essential tilt of the LO beam can hardly be expected across the RF band. To combine signals from two mixers within 4-12 GHz IF bandwidth, the optimization of the half-wave balun is made. It is important to note here that the antenna beam pattern of the balanced quasioptical mixer will be formed via interference of two IF signals, since they preserve the RF phase information.

Assuming the dynamic resistance of SIS mixers Rd = 290 Ω the optimum balun characteristic impedance is found as 135 Ω, and its length is 4206 μm. The characteristics of the IF balun circuit are presented in Fig. 7 and Fig. 8. Resulting beam properties are shown in Fig. 9 as a set of far-field beam patterns and in Fig. 10 as a plot of integral efficiencies.

## V. Experimental Quasioptical Mixer Result

Along with numerical studies on relatively complex quasioptical balanced SIS mixers, we designed a simpler double-slot antenna mixer [10], which is aiming to facilitate the general development of SIS structures including waveguide mixer for ALMA Band-10. Simulation predicted $T_{RX}$ below 200 K (DSB) for such a mixer, if a good-quality Nb-$AlO_x$-Nb twin-junction is implemented into a NbTiN/$SiO_2$/Al microstrip. Since now we got samples with epitaxial NbN twin-SIS junction ($R_nA$ = 18, A = 0.5 μm$^2$) implemented into NbN/$SiO_2$/Al microstrip made in NiCT [11]. This type of SIS mixer is being studied for the first time. The mixer chip of size 2,45 mm x 2.45 mm x 0.3 mm made of MgO ($\varepsilon_{MgO}$ = 9.6) was mounted with a 10-mm diameter silicon lens ($\varepsilon_{Si}$ = 11.7), which

does not have any anti-reflection coating, in the elliptical focusing position, $L_{ext}$ = 1.95 mm. The IF chain was connected to the mixer block with a 15-cm coaxial cable followed by a 4-8 GHz isolator. The noise temperature of the IF chain was estimated with the mixer's shot noise being about 10-15 K within the 4-8 GHz IF band. The measured mixer gain was -15 dB including optical losses of about 3.5 dB and resistive loss in the SIS tuning circuit of 3 dB. Correcting for the optics loss, we got noise temperature referenced to the (cold) antenna of the mixer of about 400 K as shown in Fig. 11. Using Tucker's theory [12] we calculated the available gain of the mixer as -7 dB. This value is about 1.5 dB larger than our experimental estimate. This discrepancy can be explained with losses due to combined effect of long bonding wires (1.5-2 mm) and relatively long coaxial cable. The noise of the SIS mixer is estimated as 130 K that can be explained by presence of the multiple Andreev reflection [13]. The experiment has verified the effective magnetic field penetration depth of the tuning circuit NbN(200 nm)/$SiO_2$(250 nm)/Al(350 nm) being about 300 nm.

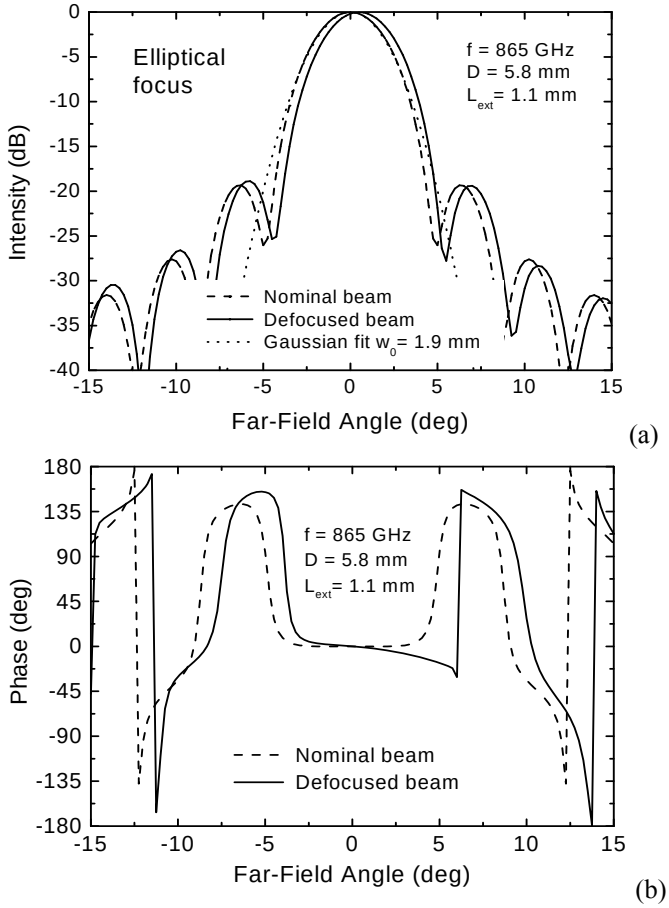


Fig. 1. E-plane beam patterns of double-slot lens-antenna (vibrator length, L = 100 μm, distance between two vibrators, W = 54 μm) calculated for elliptical focusing position (extension from center, $L_{ext}$ = 1100 μm) for case of combination of misalignment factors listed in Table 1. (a) Effect of beam tilt. (b) Distortion of phase characteristic.

TABLE I.
MISALIGNMENT FACTORS AND THEIR EFFECT ON BEAM EFFICIENCY OF THE LENS-ANTENNA TWIN-SIS MIXERS.

| | Elliptical focus | | Aplanatic focus | |
|---|---|---|---|---|
| | Nominal position of feed | Mask offset 1 μm SIS area 20% Y-offset 10 μm Z-offset 20 μm ARC offset 10 μm | Nominal position of feed | Mask offset 1 μm SIS area 20% Y-offset 10 μm Z-offset 20 μm ARC offset 10 μm |
| Spillover efficiency (1) | 80.2% | 79.8% | 85.8% | 85.0% |
| Taper efficiency (2) | 87.2% | 86.6% | 93.3% | 92.5% |
| Aperture efficiency (3) | 69.9% | 69.1% | 80.1% | 78.7% |

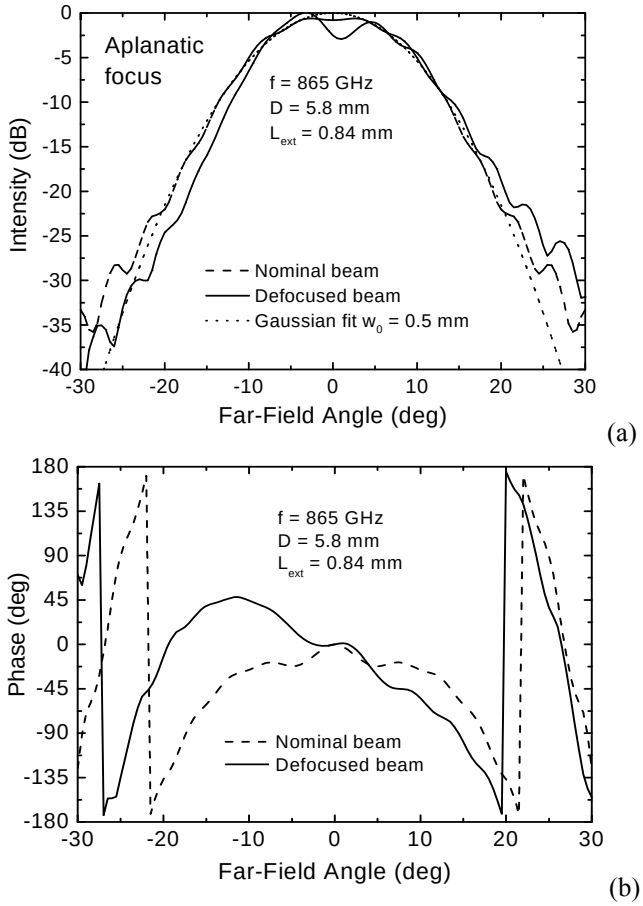


Fig. 2. E-plane beam patterns under the same conditions as Fig. 1, but the antenna is placed in aplanatic focusing position ($L_{ext}$ = 840 μm): (a) effect of tilting and narrowing the beam; (b) distortion of phase characteristic.

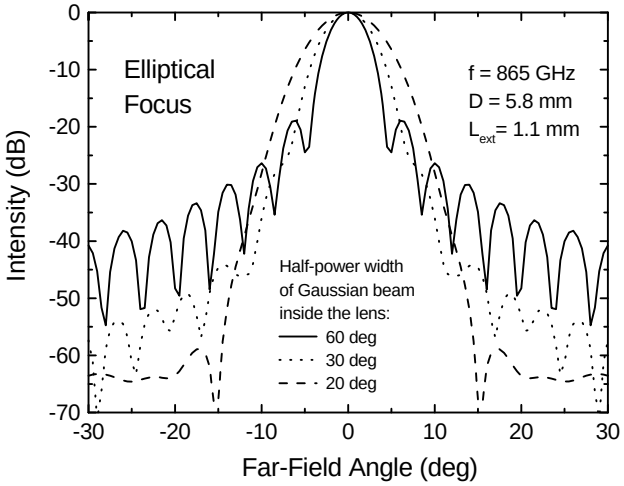


Fig. 3. Dependence of the lens-antenna beam on the beam-width of the feeding source. The gaussian beam launcher is combined with extended ($L_{ext}$=1100 μm) hemispherical immersion lens diameter 5.8 mm made of silicon. Note that the beam-width and sidelobe level are dependent on illumination angle of the lens.

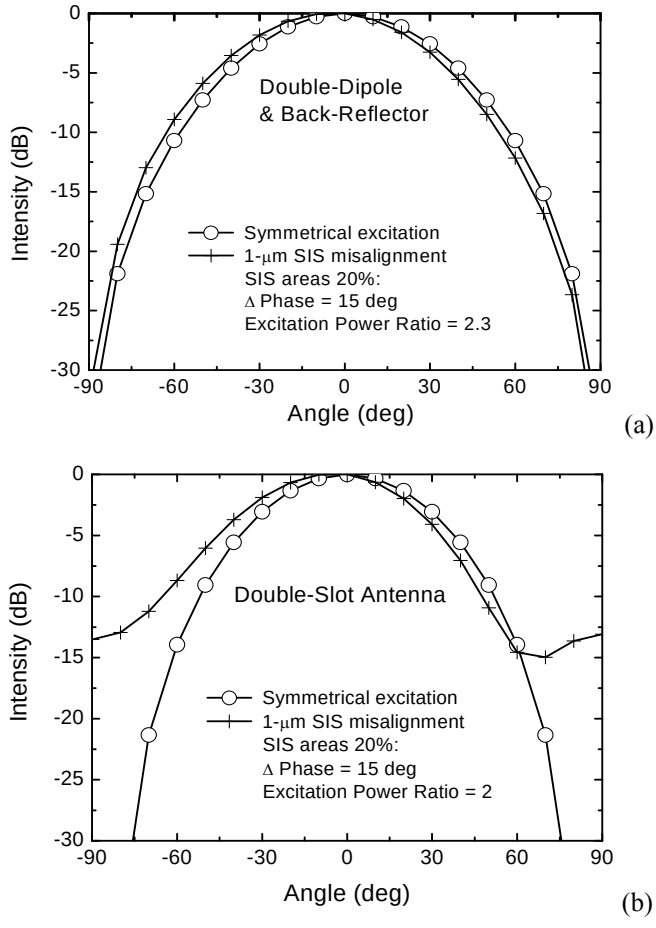


Fig. 4. Calculated illumination inside the silicon lens by (a) double-dipole antenna with back-reflector (L = 42 μm, W = 34 μm, distance to reflector 23 μm) and (b) double-slot antenna (L = 100 μm, W = 54 μm).

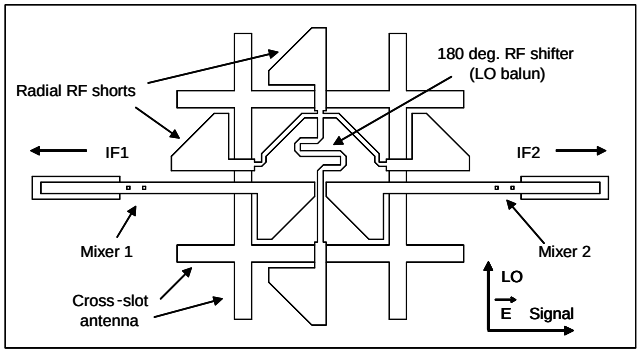


Fig. 5. Layout of the lens-antenna balanced SIS mixer. The output signals IF1 and IF2 are essentially anti-phased and must be combined at the output of an IF balun (not shown). The balun phase delay may change across IF band the 4-12 GHz IF band that may cause some tilt of the beam of the printed antenna array.

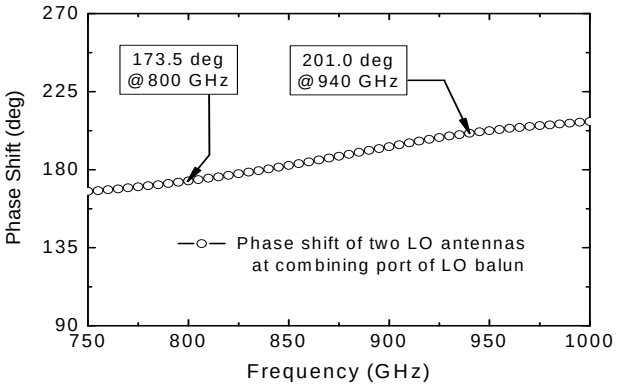


Fig. 6. Phase characteristic of 180-degree RF shifter (LO-balun) circuit of the quasioptical balanced mixer from Fig. 5.

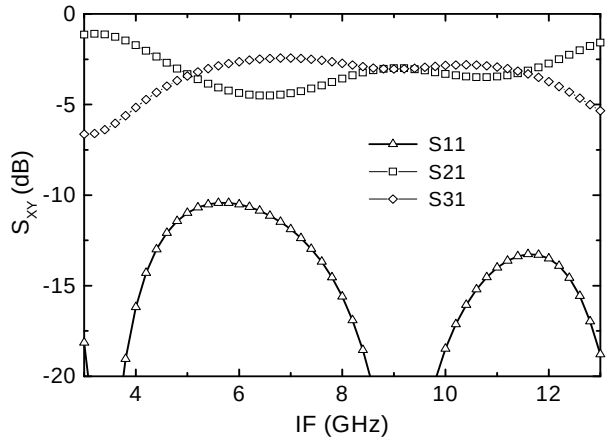


Fig. 7 Amplitude characteristics of an optimized 4-12 GHz IF balun (L = 4206 μm, $Z_0$ = 135 Ω) of the quasioptical balanced SIS mixer from Fig. 5: $S_{11}$ stands for reflection at the combining point connected to IF amplifier $Z_{in}$= 50 Ω, $S_{21}$ and $S_{31}$ are transmission coefficients from IF ports of the two mixers.

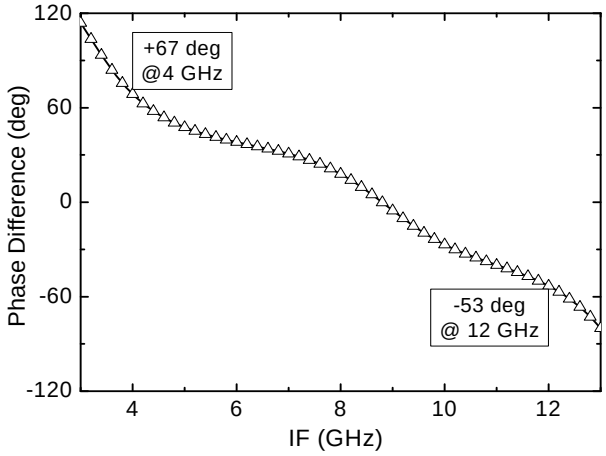


Fig. 8 Phase characteristics of an optimized 4-12 GHz IF balun of the quasioptical balanced SIS mixer from Fig. 5

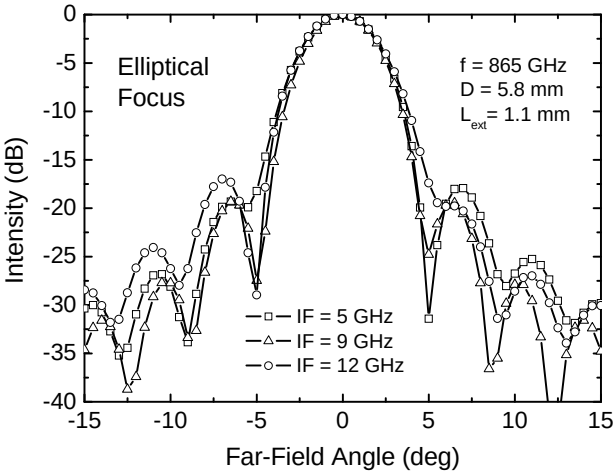


Fig. 9 Beam profiles calculated for a balanced quasioptical SIS mixer from Fig. 5 within IF-band 4-12 GHz.

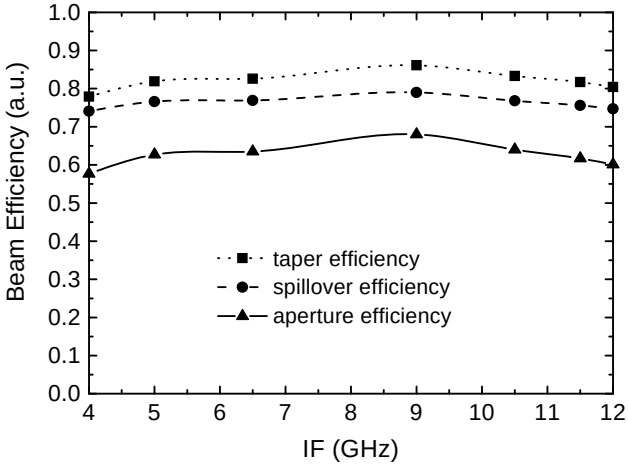


Fig. 10 Beam efficiency calculated for a balanced quasioptical mixer from Fig. 5 at 865 GHz. Note that the beam of the two-antenna array is defined for a balanced mixer by the interference of two signals at the output of the IF balun circuit.

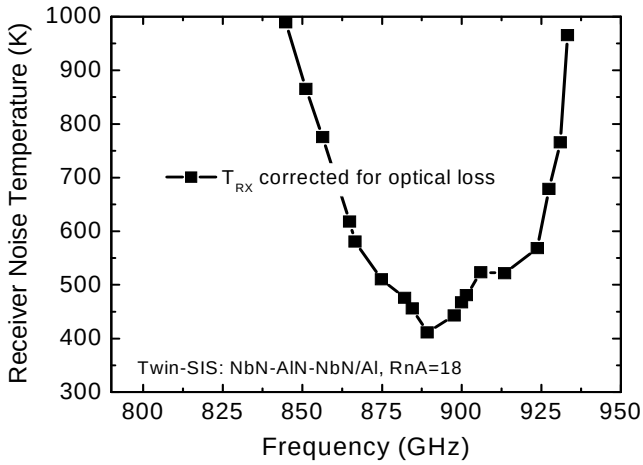


Fig. 11 Preliminary result on noise temperature (DSB) of quasioptical double-slot antenna receiver (L=100 μm, W=54 μm) in elliptical focusing position (D=10 mm, $L_{ext}$=1950 μm). The main goal of this test device is to attain parameters of a particular circuit with epitaxial NbN SIS junctions [11].

## VI. Conclusions

The tolerance analysis has demonstrated that the behavior of a lens-antenna is dependent on the type of focusing (elliptical vs. aplanatic) and on the antenna-feed design (double-slot vs. double-dipole with back-reflector). Misalignment of the lens feed with respect to the optical axis brings the greatest beam distortion, and the effect of multiple misalignments can be characterized as the tilt of the beam with a few percent drop of the integral beam efficiency. It looks possible in most cases to correct the beam tilt by the mechanical rotation of the lens-antenna mount about its phase center. For doing this correction efficiently, no near-field intervening optics is desirable in front of the lens-antenna. In spite of the better integral efficiency of the aplanatic focusing, the combined effect of the misalignment and the intervening optics (accounting for its loss) can be a source of additional beam distortion that has to be studied in more details.

The numerical study of the new balanced quasioptical mixer demonstrates that reasonable stability of its beam over an IF band of 4-12 GHz can be achieved with a relatively simple balun circuit.

The noise temperature of 400 K (DSB, corrected for optical loss) is demonstrated at 890 GHz for a new double-slot antenna SIS mixer employing epitaxial NbN twin-SIS junction and Al-wiring. This result is verified with Tucker's theory being limited by the quality of the IV-curve and by loss in the $NbN/SiO_2/Al$ tuning circuit. To understand the relatively high noise of the NbN SIS mixer, the effect of multiple charge transfer (Andreev reflection) has to be taken into account.

We hope that present research can help in separating the problems of effective utilization of lens-antennas into two groups: i) beam distortions caused by the design of a lens-antenna itself and ii) distortions arising from properties of the extended optical path including effects of truncating apertures, ghost reflections, etc.

## ACKNOWLEDGMENT

Authors thank M. Ishiguro, T. Hasegawa, J. Inatani, T. de Graauw, H. Matsuo, M. Candotti, S. E. Bankov and J. Zmuidzinas for encouragement and many fruitful discussions.

## REFERENCES

[1] S. V. Shitov, O. V. Koryukin, Y. Uzawa, T. Noguchi, A. V. Uvarov, I. A. Cohn, "Development of balanced SIS mixers for ALMA Band-10," Presented at 17th International Symposium on Space Terahertz Technology, Paris, France (May 10-12, 2006).

[2] V. P. Koshelets, S. V. Shitov, "Integrated Superconducting Receivers" Superconductor Science and Technology, vol. 13, pp. R53-R69, 2000.

[3] A. N. Vystavkin, S. V. Shitov, A. G. Kovalenko, A. V. Pestriakov, I. A. Cohn, A. V. Uvarov, "Arrays of TES direct detectors for supersensitive imaging radiometers of 1.0–0.2 mm waveband region", Invited talk, Proceedings #WPP264 of European Space Agency, Seventh International Workshop on Low Temperature Electronics, WOLTE-7, Noordwijk, the Netherlands, pp. 101-108, 21-23 June 2006.

[4] M. Bin, M. C. Gaidis, J. Zmuidzinas, T. G. Phillips, H. G. LeDuc, "Low-noise 1 THz niobium superconducting tunnel junction mixer with normal metal tuning circuit," Appl. Phys. Lett., vol. 68, pp. 1714–1716, 1996.

[5] S. Shitov, B. Jackson, A. Baryshev, A. Markov, N. Iosad, J. Gao, T. Klapwijk, "A low-noise double-dipole antenna SIS mixer at 1 THz," Physica C, vol. 372, no. 1, pp. 374–377, 2002.

[6] Paul F. Goldsmith, "Quasioptical Systems: Gaussian Beam Quasioptical Propagation and Application", IEEE Press, 1997.

[7] D. Filipovic, S. Gearhart, and G. Rebeiz, "Double-slot antennas on extended hemispherical and elliptic silicon dielectric lenses," *IEEE Trans. Microwave Theory Tech.*, vol. 41, pp. 1738–1749, Oct. 1993.

[8] M. J. M. van der Vorst. Integrated lens antennas for submillimetre-wave applications. PhD thesis, ISBN 90-386-1590-6. Technical Univ. of Eindhoven, Netherlands, Apr. 1999.

[9] G. Chattopadhyay, F. Rice, D. Miller, H. LeDuc, J. Zmuidzinas, "A 530-GHz balanced mixer," IEEE Microwave Guided Wave Lett., vol. 9, no. 11, pp. 467-469, Nov. 1999.

[10] S. V. Shitov, T. Noguchi, T. Matsunaga, T. Tamura, A. V. Uvarov, I. A. Cohn, T. Hasegawa, "A SIS mixer for ALMA band 10: development concept", Presented at 16th International Symposium on Space Terahertz Technology, Conference Proceedings ISSTT 2005, May 2-4, Gothenburg, Sweden, pp. 165-168, 2006.

[11] Y. Uzawa, Z. Wang, A. Kawakami, "Terahertz NbN/AlN/NbN mixers with Al/SiO/NbN microstrip tuning circuits," Appl. Phys. Lett., vol. 73, no. 5, pp. 680–682, 1998.

[12] J. R. Tucker and M. J. Feldman, "Quantum detection at millimetre wavelengths," Rev. Mod. Phys., vol. 57, no. 4, pp. 1055–1113, 1985.

[13] Y. Uzawa and Z. Wang, "Coherent multiple charge transfer in a superconducting NbN tunnel junction," Phys. Rev. Lett., vol. 95, pp. 017002-1-017002-4, July 2005.

**Development of Multiplier Based Sources for Frequencies up to 2 THz**

T.W. Crowe, D.W. Porterfield, J.L. Hesler, W.L. Bishop, G.S. Schoenthal,
D.S. Kurtz and K. Hui

Virginia Diodes Inc., Charlottesville, VA 22902

A primary challenge in creating the next generation of submillimeter-wave receiver systems for space science is generating the required local oscillator power. Broad-band performance and power levels suitable for array receivers are required. Also, the sources must be suitable for use at remote installations. This means they should be compact, reliable, electronically tunable and maintenance free. This talk will focus on our continuing development of terahertz sources with emphasis of "turn-key" operation, enhanced tuning bandwidth and output frequency to 1.9 THz.

Virginia Diodes has developed a series of broadband frequency multipliers based on integrated diode circuits. A tripler to the WR0.5 waveguide band has recently been demonstrated. An amplifier/multiplier chain with this component, shown in Fig. 1, generates 1 – 3 uW of power at room temperature within the 1.8 – 1.9 THz band. Most importantly, it is extremely easy to use and requires no mechanical tuning or user controlled bias adjustments.

This talk will summarize the performance of this system, as well as a range of other terahertz sources that offer exceptional performance as well as unprecedented ease of use.

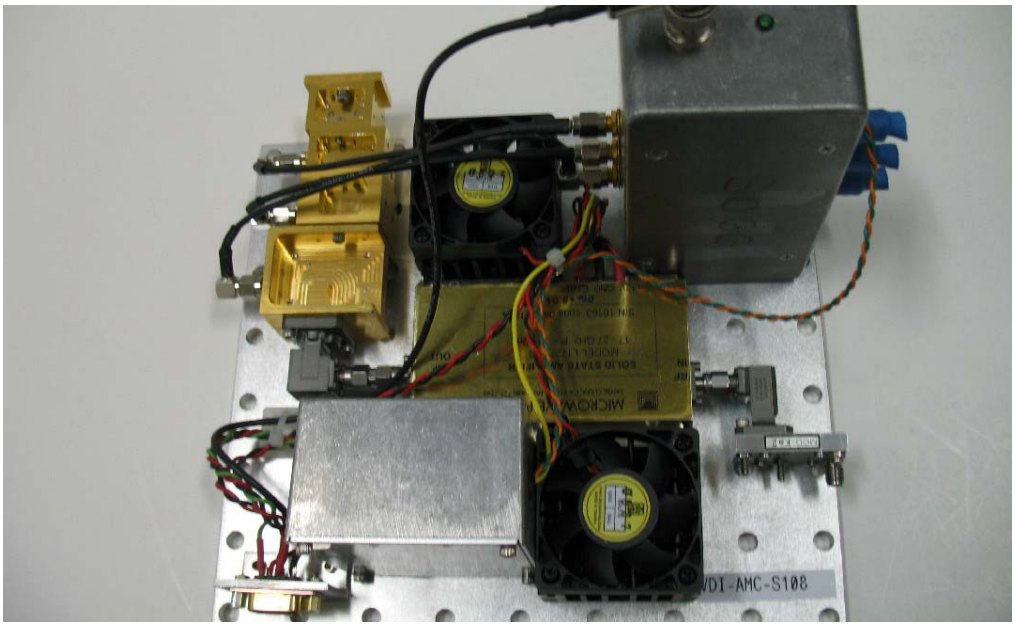


*Fig. 1: A 1.9 THz amplifier/multiplier chain consisting of a low frequency coaxial input, an input doubler (~13GHz, PMP), a power amplifier (MPI) and a chain of VDI multipliers (x2x2x2x3x3). It generates useful power from 1.8 – 1.9 THz (1-3uW), has no mechanical tuners and requires no user controlled bias adjustments.*

# A 780-950GHz Frequency Tripler for Radio Astronomy

Alain Maestrini [1+3], Charlotte Tripon-Canseliet [1], John S. Ward [2], John J. Gill [2], Erich Schlecht [2], Goutam Chattopadhyay [2] and Imran Mehdi [2]

[1] LISIF - Université Pierre et Marie Curie, 4 place Jussieu, case 252, 75252 Paris cedex 5

[2] Jet Propulsion Laboratory, California Institute of Technology,
MS 168-314, 4800 Oak Grove Drive, Pasadena, CA 91109

[3] LERMA, Observatoire de Paris, 61 avenue de l'Observatoire, 75014 Paris

*Abstract*— We report on the design and fabrication of a fix-tuned wide bandwidth balanced frequency tripler working in the 780-950 GHz band. The multiplier features four GaAs Schottky planar anodes in a balanced configuration integrated on a few micron thick membrane. The multiplier is bias-able and is designed for 15 mW of input power. However, for the preliminary RF tests presented in this paper, the 780-950 GHz tripler was pumped by a chain of two cascaded fixed-tuned balanced doublers able to deliver 4-10.5 mW in the band 273-320 GHz when pumped by a 120-150 mW solid-state source. Due to the limited bandwidth of the driver chain, only tests at frequencies above 820 GHz have been performed. A dual-chip version of the wideband six-anode 260-340GHz frequency tripler presented in [1] is currently in the process of being fabricated and should replace soon the current driver.

Room temperature measurements show a conversion efficiency above 1% across the 820-950 GHz band with a peak conversion efficiency of 3.6% at 820 GHz. The output power is above 100 µW from 820 GHz to 935 GHz and falls to 40µW at 950 GHz with a maximum of 325 µW of output power at 852 GHz. Predictions are in close agreement with these measurements, thus, the multiplier is expected to cover frequencies below 820 GHz (which is actually the peak efficiency) down to 870 GHz once a broader-band driver is assembled. During the measurements all the bias voltage of all three multipliers were kept constant therefore the local oscillator chain was very easy to operate (it was fix-tuned and fix-biased).

[1] Alain Maestrini, Charlotte Tripon-Canseliet, John S. Ward, John J. Gill, and Imran Mehdi, "A High efficiency Multiple-Anode 260-340 GHz Frequency Tripler", to appear in the proceedings of the 17th International Conference on Space Terahertz Technology, Paris, 10-12 May 2006.

This work was primary supported by the Jet Propulsion Laboratory, California Institute of Technology and by the University Pierre et Marie Curie-Paris6 and the Observatory of Paris.

# Maximizing SNR in LO Chains for ALMA Single-Ended Mixers

Eric W. Bryerton, Matthew A. Morgan, Dorsey L. Thacker, and Kamaljeet S. Saini

## I. Abstract

**This paper describes the design methodology used to develop local oscillators for the ultra-sensitive single-ended sub-millimeter wave mixers used in ALMA. Recent results of the ALMA LO system are presented, showing little or no noise added to the receiver. Measurements of excess amplitude noise from ALMA LO prototypes in the development phase are also shown. A design methodology is presented for suppressing amplitude noise in LO chains, using examples from different ALMA bands. We conclude with recommendations for future sub-millimeter LO systems.**

## II. Introduction

THE Atacama Large Millimeter Array (ALMA) telescope currently under construction on the Atacama plateau in northern Chile will have at least 66 antennas and will cover 30 to 950 GHz in ten bands using dual-polarized heterodyne receivers. Currently, all bands under construction use single-ended SIS mixers. In a single-ended mixer, noise on the sidebands of the LO is downconverted into the IF and is indistinguishable from the desired IF signal. It therefore is equivalent to an increased mixer noise temperature. The amount of noise downconverted to the IF is equal to the LO power used to pump the mixer divided by the signal-to-noise-ratio (SNR) of the LO.

In this paper, we briefly outline the early development of the ALMA local oscillator drivers, primarily in regards to addressing amplitude noise. Measurements of early prototypes showed considerable amplitude noise originating from the LO. Further measurements at several receiver bands along with some simple calculations and models indicated a few key steps to take to suppress this noise contribution. The current LO design, taking into account these findings, is presented with measurement examples showing minimal receiver noise contributions. We then concentrate on two remaining potential problem areas, which can be very difficult to fully eliminate in broadband LO systems.

## III. Design and Development

A block diagram of the band 6 (211-275 GHz) ALMA LO system is shown in Fig. 1 as being representative of the ALMA LO system. Noise is introduced into the system predominately from each of the amplifiers in the chain. The YIG tuned oscillator module also contains an amplifier.

The first LO prototypes employed discrete connectorized modules for each of the amplifiers, multipliers, and filters following the YTO with SMA adapters and coaxial cable in between the components. The first WR-10 power amplifiers used in these prototypes used the MMICs and packages developed by the HIFI project [1]. The output power of these initial chains had very large ripples as might be expected from all the mismatches and cable lengths. A more critical problem with such an arrangement was the resulting sideband noise. Fig. 2 shows the measured receiver noise when using this LO. The receiver noise with this LO wildly varies with both LO frequency and across the 4-12 GHz IF band. This is a result of the long mismatched lengths between all the components in the LO chain. Focusing on only two LO frequencies only one GHz apart (250 and 251 GHz) in Fig. 3, it is seen how much the noise contribution can vary over a small frequency range.

The authors are with the National Radio Astronomy Observatory, Charlottesville, VA 22903-4602 USA (phone: 434-296-0336; fax: 434-296-0324; e-mail: ebryerto@nrao.edu).

The Atacama Large Millimeter Array is an international astronomy facility. ALMA is an equal partnership between Europe and North America, in cooperation with the Republic of Chile, and is funded in North America by the U.S. National Science Foundation in cooperation with the National Research Council of Canada, and in Europe by the European Southern Observatory and Spain. ALMA construction and operations are led on behalf of North America by the National Radio Astronomy Observatory, which is managed by Associated Universities, Inc., and on behalf of Europe by ESO.

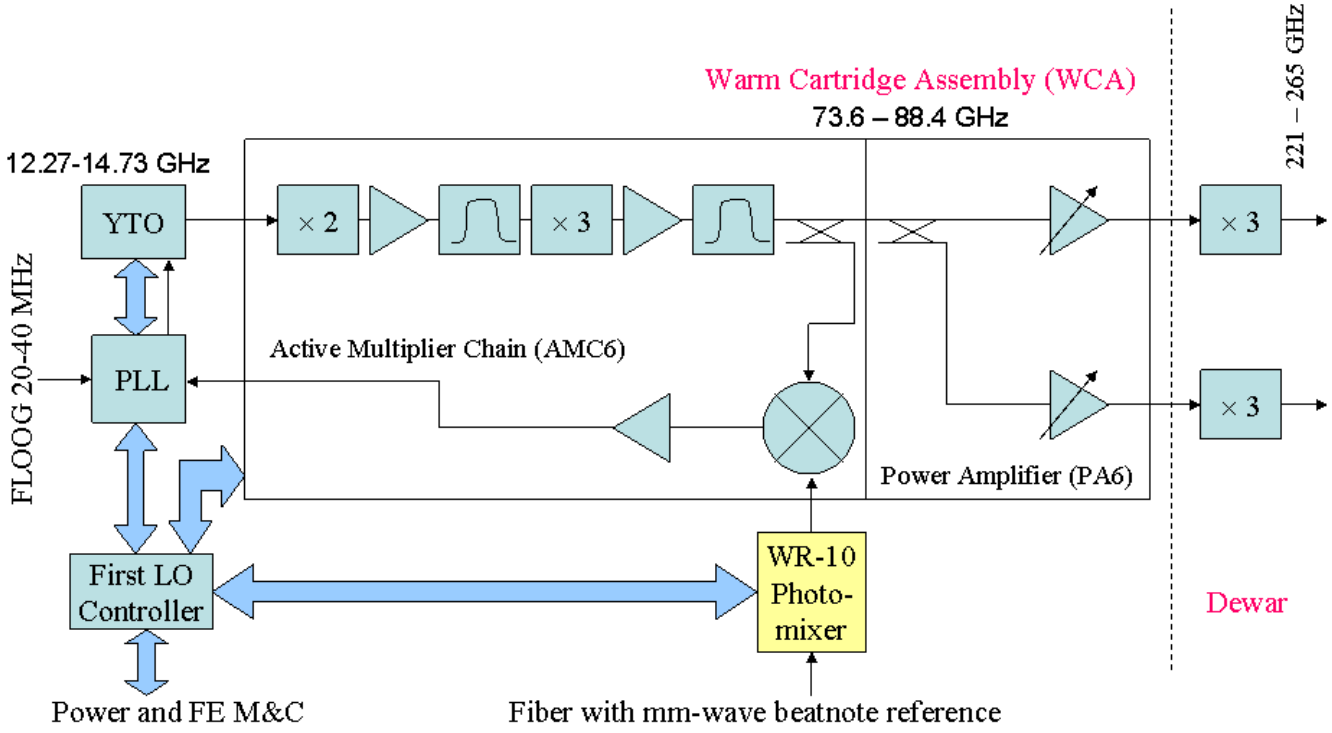


**Fig. 1 Block diagram of local oscillator (LO) for ALMA Band 6 (211-275 GHz).**

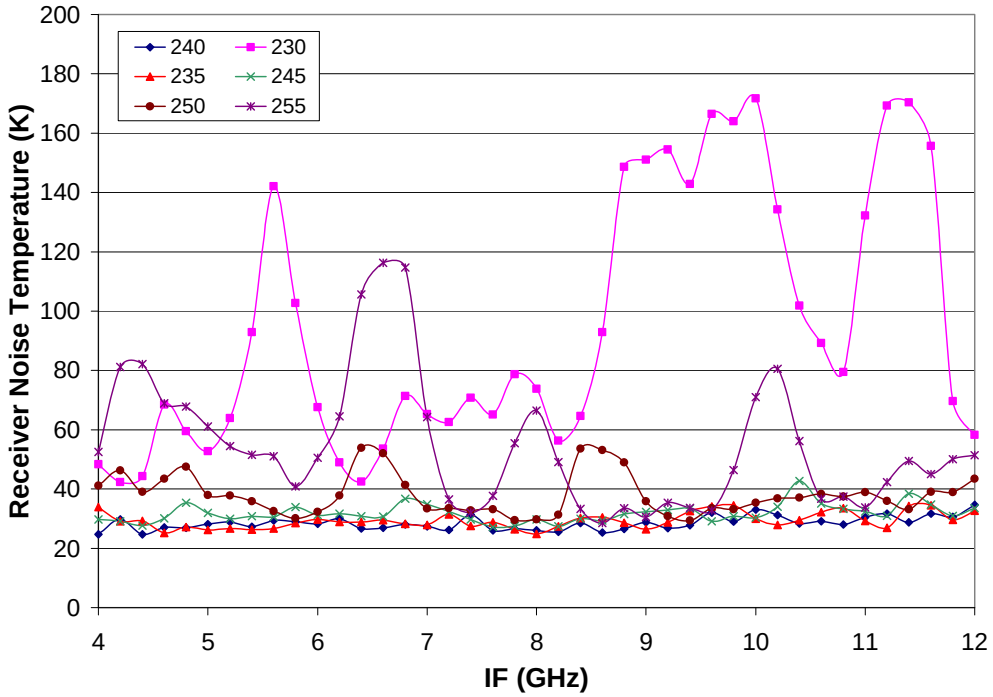


**Fig. 2 Measured receiver noise temperature of a prototype ALMA Band 6 (211-275 GHz) mixer with a prototype LO driver at LO frequencies of 230, 235, 240, 245, 250, and 255 GHz.**

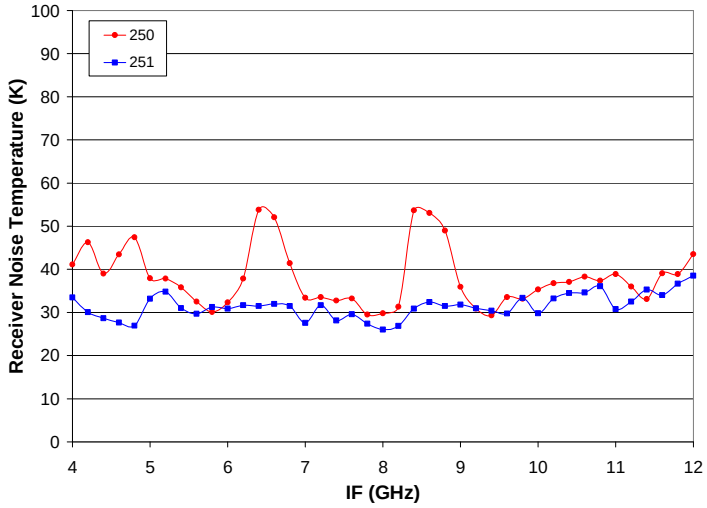


**Fig. 3 Measured receiver noise temperature of a prototype ALMA Band 6 (211-275 GHz) mixer with a prototype LO driver at LO frequencies of 250 and 251 GHz.**

Based on these and other early measurements, a set of guidelines for maximizing SNR in LO chains was developed. These are: (1) modest saturation of amplifiers (3-5 dB gain compression); (2) bandpass filters after each multiplication where possible; (3) integration as much as possible to minimize mismatch and standing waves; (4) properly pumped frequency multipliers.

Using these guidelines, highly integrated LO modules were designed and built. An example of one of these is shown in Fig. 4. This is an Active Multiplier Chain (AMC) module used for ALMA band 6. To minimize the effects of mismatch, the amplifier, multiplier, and filter functions are all integrated on MMICs and interconnected with 0.002" bond ribbons. Up to about 45 GHz, commercial-off-the-shelf (COTS) MMICs were available. Above that frequency, wideband MMIC multipliers and amplifiers are still not available commercially and had to be developed. We therefore developed a set of custom MMICs using a few different processes. First of all, multiplier and mixer MMICs from 60-145 GHz were designed and tested with the UMS Schottky process [2]. 5-section coupled-line bandpass filters were designed and fabricated on 0.003" Alumina. Alumina microstrip-to-waveguide transitions are used based on the design in [3]. Power amplifier MMICs were developed in both 0.1 μm GaAs pHEMT [4] and 0.1 μm InP HEMT [5] processes.

Receiver noise measurements from the highest ALMA band currently being built (band 9, 602-720 GHz) are shown in Fig. 5. These are measurements carefully comparing this LO to a Gunn oscillator based LO, showing no noticeable difference. These noise measurements are performed using the band 9 mixer test set, not the actual band 9 receiver. The noise of the actual band 9 receiver is much lower [6].

## IV. Modeling of AM and PM Noise Sidebands

In a LO chain consisting of a cascade of amplifiers and multipliers, the white noise introduced by each amplifier is half AM and half PM, since the noise in any given sideband is uncorrelated with the noise in the other sideband. A single-sideband (SSB) pure noise signal can be decomposed into four components, an AM and PM component of equal magnitude at each sideband. The AM components are in phase with the LO signal and the PM components are in quadrature with the carrier. Therefore in one sideband, the AM and PM components cancel, and in the other sideband, they add coherently [7,8].

A single-ended mixer is sensitive only to the AM noise components. This is easy to see in the frequency domain, since the two sidebands downconverted to the same IF add in phase, so that the AM components add coherently at the IF, while the PM components cancel each other. Note this is also true for a sideband-separating mixer (SSM), since in a SSM the sidebands of the LO are not separated.

It is therefore necessary to concentrate on propagation of the AM noise components. The AM noise is limited and suppressed in a saturated amplifier. This was experimentally shown in [9] and can be understood intuitively and modeled by looking at the input-output response of the amplifier:

$$\frac{SNR_{out}}{SNR_{in}} = \frac{\left(P_{out} \big/ P_{in}\right)}{\left(dP_{out} \big/ dP_{in}\right)} \tag{1}$$

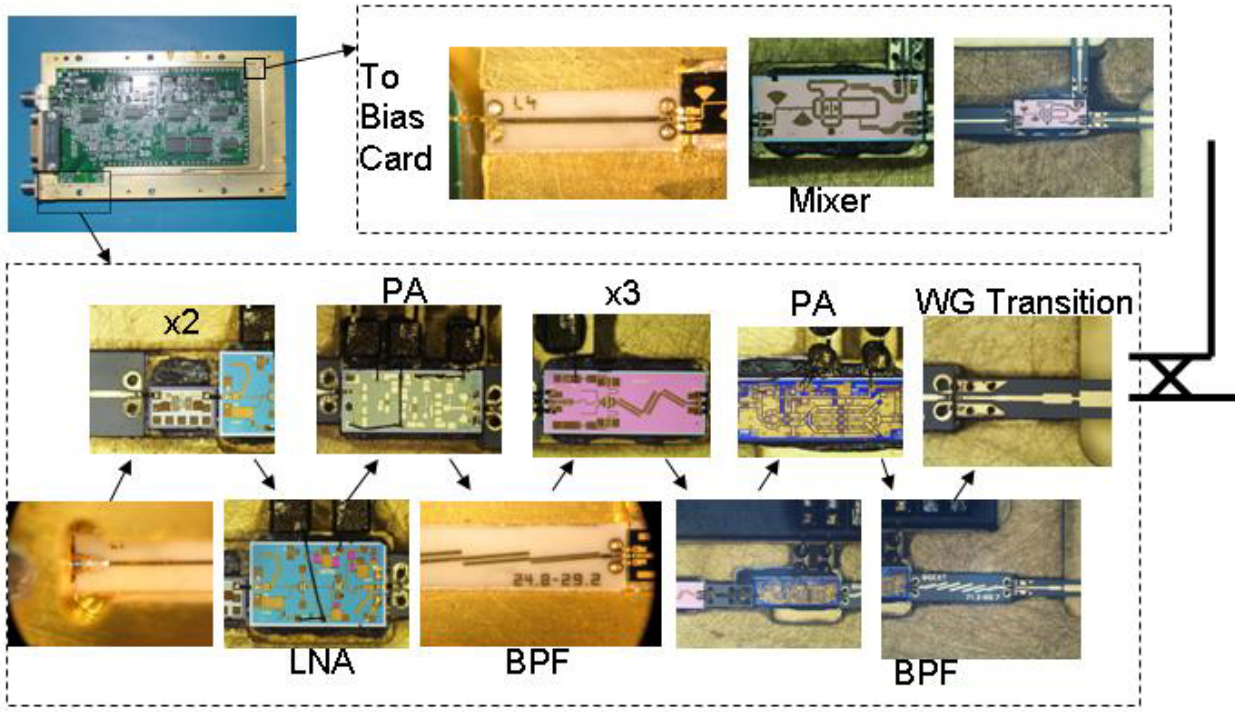


**Fig. 4 Photograph of Active Multiplier Chain (AMC) module for LO driver of ALMA 211-275 GHz receiver. Substrate and MMIC areas are expanded and shown in detail.**

To determine $dP_{out}/dP_{in}$, either the output power can be measured at very finely spaced input power levels or a polynomial function can be fitted to the measured $P_{out}$ versus $P_{in}$ curve and the derivative can then be calculated from that polynomial. A typical SNR improvement of 6-10 dB is obtained at a moderate level of gain compression (3-5 dB). PM noise is not, however, suppressed in a saturated amplifier since, to the first order, the phase response does not depend on input power.

In a multiplier, assuming it is properly pumped, the AM contribution to SNR remains constant since the output power is linearly dependent on input power. PM noise contribution to SNR is increased by the square of the multiplication factor. The consequence therefore of a cascade of amplifiers and multipliers is to decrease the AM noise and increase the PM noise, such that by the end of the cascade, the noise is dominated by PM. Since the single-ended mixer is only sensitive to AM noise and not to PM noise, the downconverted IF contains little noise contributions from the LO chain and does not contribute to overall receiver noise.

## V. Potential Problems

### *A. Underpumped multipliers*

AM noise in a properly pumped multiplier does not increase, as explained in the previous section. However, if the multiplier is operated with a low input power, the amplitude of the output signal is no longer linearly, but exponentially, dependent on the input signal. For example, the ALMA band 7 LO was designed to provide 25-100 uW LO power. However, less than 10 uW is required at most frequencies, meaning that, absent a cold attenuator after the final tripler, the tripler must be operated in its underpumped mode. Using Eq. (1) and the measured output versus input power response of the tripler, the AM noise enhancement is calculated to be 6-10 dB. The result is seen in Fig. 6. By adding a cold attenuator after the final LO tripler before the mixer, the multiplier was required to be pumped harder to give the same pump power to the mixer, reducing the amplitude noise contributed by the LO to a minimal amount. This effect was also seen in the ALMA Band 9 (602-720 GHz) LO, causing an increase in receiver noise over a small frequency range. By using a thinner beamsplitter, thereby increasing the required drive power to the multiplier, the excess noise disappeared.

The solution seems simple—avoid underpumping multipliers. However, in broadband systems, this can be quite difficult to achieve in practice. First of all, sub-millimeter wave power sources are typically designed for maximum power and system designers are hesitant to specify a lower power level than what is achievable, since receiver systems at these wavelengths have traditionally been LO starved. Secondly, for wideband systems, it is difficult to maintain relatively flat power versus frequency. If the LO power is not sufficiently flat across the band, then in order to have sufficient LO power at the weakest part of the band, the strongest part of the band will need to be underpumped.

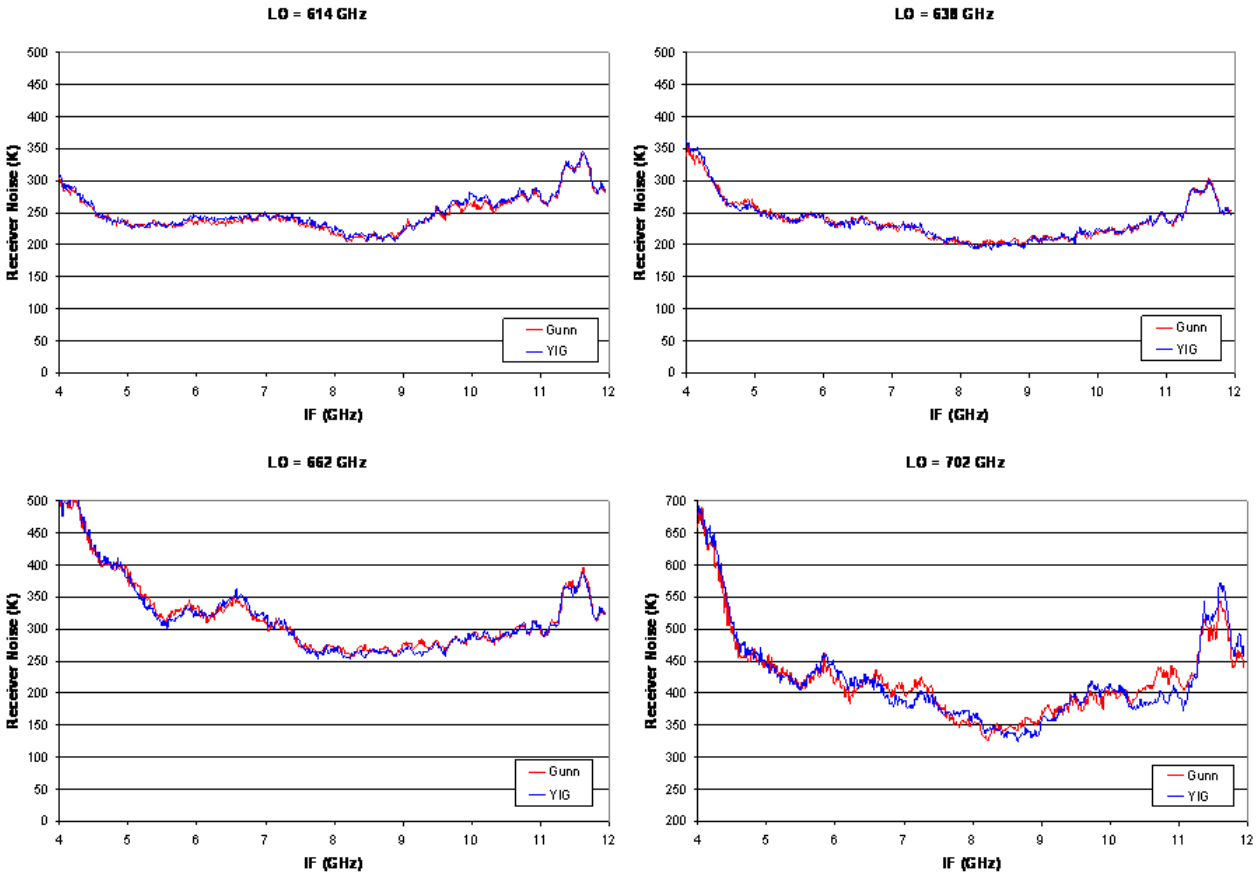


**Fig. 5 Measured receiver noise of a Band 9 (600-720 GHz) ALMA mixer with the ALMA LO versus Gunn oscillator LO for LO frequencies of 614, 638, 662, and 702 GHz.**

### *B. PM-AM conversion*

Since the PM component of the noise dominates as the noise progresses through the chain of amplifiers and multipliers, even a small amount of PM to AM conversion at the end of the chain can cause a large increase in the AM noise, which will then negatively impact receiver noise.

It is instructive to look at PM-AM conversion in the frequency domain. AM modulation appears as double sideband (DSB) modulation where the two sidebands are in phase with one another with respect to the carrier. PM modulation shows up as DSB modulation where the two sidebands are opposite in phase with respect to the carrier. SSB modulation is therefore equal parts AM and PM where the AM and PM components are correlated with each other in such a way as to cancel each other out in one of the sidebands. [7,8]

The introduction of any element which has an amplitude or phase response which differs at one sideband from the other will therefore cause conversion from AM to PM and vice versa. For example, consider a signal with only PM modulation, and therefore double sideband. Passing this signal through a filter with rejects completely one sideband while passing the carrier and other sideband, essentially generating a single sideband modulation, converts half the PM modulation to AM modulation, since a single sideband modulation is half AM and half PM. This can be generalized for any level of amplitude or phase imbalance.

## VI. Conclusions and Recommendations

Recommended guidelines for maximizing the SNR in sub-millimeter LO chains are: (1) modest saturation of amplifiers; (2) integration as much as possible to minimize mismatch and standing waves; (3) properly pumped frequency multipliers; and (4) bandpass filtering where, to avoid PM-AM conversion, the best approach is to filter both sidebands as high in frequency as possible, after as many amplifier stages as possible. This final point requires the bandwidth of the final amplifier stage to be less than the lowest IF. Besides moving to a higher IF band, this leads the design toward lower-frequency, higher-power final amplifiers, saturated and filtered, followed by a higher order multiplier chain.

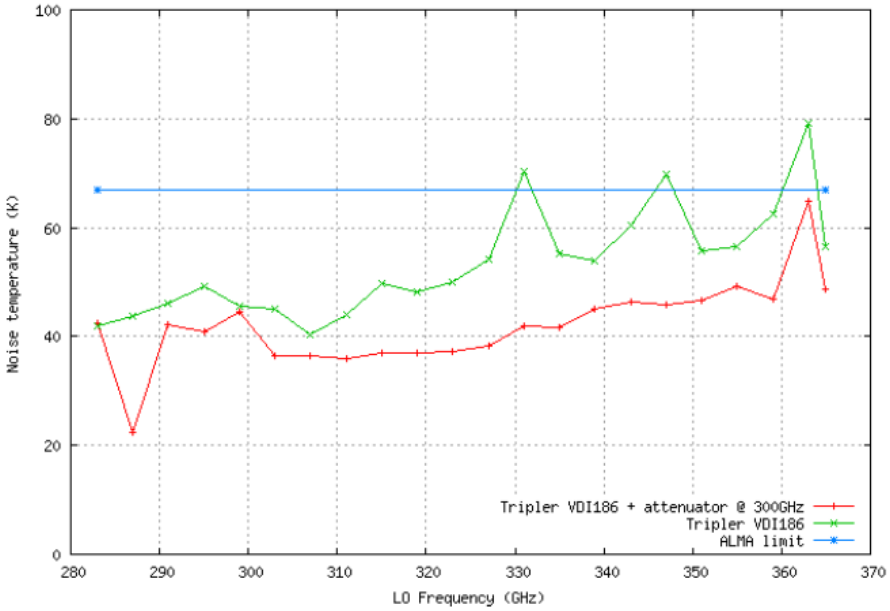


**Fig. 6 Measured receiver noise of an ALMA Band 7 (275-370 GHz) mixer with an ALMA LO driver with and without an attenuator between the final LO tripler and mixer [10].**

## ACKNOWLEDGMENTS

We would like to acknowledge all the ALMA cartridge groups, whose receiver noise measurements were all used to understand and solve the problems of LO sideband noise. This includes: (Band 3) Herzberg Institute of Astrophysics (HIA), (Band 6) National Radio Astronomy Observatory (NRAO), (Band 7) Institut de Radioastronomie Miliimetrique (IRAM), (Band 9) Space Research Organization of the Netherlands (SRON), (Bands 4, 8) National Astronomy Observatory of Japan (NAOJ). We would also like to acknowledge the Jet Propulsion Lab (JPL), particularly Todd Gaier and Lorene Samoska, for their support in development of the power amplifier MMICs used in the LO drivers.

## REFERENCES

[1] L. Samoska, T. Gaier, A. Peralta, S. Weinreb, J. Bruston, I. Mehdi, Y.C. Chen. H.H. Liao, M. Nishimoto, R. Lai, H. Wang, and Y.C. Leong, "MMIC power amplifiers as local oscillator drivers for FIRST," in *UV, Optical, and IR Space Telescopes and Instruments, Proceedings of SPIE* vol. 4013 (2000), pp. 275-284.

[2] M. Morgan, E. Bryerton, P. Cesarano, T. Boyd, D. Thacker, K. Saini, and S. Weinreb, "A millimeter-wave diode MMIC chipset for local oscillator generation in the ALMA telescope," *IEEE MTT-S Symp. Dig.*, pp. 1587-1590, Long Beach, CA, June 2005.

[3] Y. Leong and S. Weinreb, "Full band waveguide-to-microstrip probe transitions," *IEEE MTT-S Symp. Dig.*, vol. 4, pp. 1435-1538, Anaheim, CA, June 1999.

[4] M. Morgan and S. Weinreb, "A W-band monolithic medium power amplifier," IEEE MTT-S Symp. Dig., vol. 1, pp. 133-136, Philadelphia, PA, June 2003.

[5] L. Samoska, E. Bryerton, M. Morgan, D. Thacker, K. Saini, T. Boyd, D. Pukala, A. Peralta, M. Hu, and A. Schmitz, "Medium power amplifiers covering 90-130 GHz for the ALMA telescope local oscillators," *IEEE MTT-S Symp. Dig.*, pp. 1583-1586, Long Beach, CA, June 2005.

[6] A. Baryshev, "Performance of ALMA band 9 receiver series," *Proc. of the 18th Intl. Symp. on Space THz Tech.*, Pasadena, CA, April 2007.

[7] R. Scott, C. Langrock, and B. Kolner, "High-dynamic range laser amplitude and phase noise measurement techniques," *IEEE Journal on Selected Topics in Quantum Electronics*, vol. 7, no. 4, July/Aug 2001, pp. 641-655.

[8] F. Walls, "Correlation between upper and lower sidebands," *IEEE Trans. on Ultrasonics, Ferroelectrics, and Frequency Control*, vol. 47, no. 2, pp. 407-410, Mar. 2000.

[9] N. Erickson, "AM noise in drivers for frequency multiplied local oscillators," *Proc. of the 15th Intl. Symp. on Space THz Tech.*, Apr 2004.

[10] B. Jammet, B. Lazareff, F. Mattiocco, D. Maier, "Investigation of excess noise of band 7 SIS mixers pumped with NRAO AMC and VDI tripler," IRAM Technical Report, May 5, 2006.

# Beam patterns of distributed feedback surface-plasmon THz quantum cascade lasers

J.N. Hovenier[1] S. Paprotskiy[1,a], J.R. Gao[1,2], P. Khosropana[2], T.M. Klapwijk[1], L. Ajili[3], M. A. Ines[3], and J. Faist[3]

[1] Kavli Institute of NanoScience, Delft University of Technology, Delft, The Netherlands
[2] SRON Netherlands Institute for Space Research, Utrecht/Groningen, The Netherlands
[3] Institute of Physics, University of Neuchâtel, Neuchâtel, Switzerland

Correspondence: J.R. Gao@tnw.tudelft.nl

THz quantum cascade lasers (QCLs) become the choice of solid-state local oscillators (LO) beyond 2 THz because of their frequency coverage, compactness, high power efficiency, and narrow linewidth. They have been successfully demonstrated as LO in laboratory's tests using a hot/cold load.[1] Until now only QCLs based on Fabry-Perot cavity have been investigated as LO, including their beam patterns. However, to perform a spectroscopic measurement, QCLs with a stable single–mode emission at a precisely designed wavelength are desirable. For this purpose, a distributed feedback (DFB) structure, which is based on the first order Bragg gratings incorporated into the waveguide, needs to be introduced into QCLs.

Here we report the first beam pattern measurements of 3.4 THz DFB surface plasmon QCLs. The beam patterns are known to be crucial for coupling the radiation to a mixer.

The QCLs used are developed by University of Neuchâtel[2]. The active region is based on a bound-to-continuum design, while the DFB structure is based on strongly coupled surface grating fabricated with wet etching and metal coverage. Two QCLs with ridge widths of 100 μm or 200 μm have been studied and both lase in single-mode at 3.4 THz. To measure the far-field beam patterns, we use a similar setup as for the metal-metal waveguide QCLs[3], but with a reduced surface area of the pyroelectric detector to improve the angular resolution. We found that the beams follow nearly the diffraction limit, if measured with a poor angular resolution and a coarse scanning. However, we observed the interference patterns, characterized by a strong modulation in the intensity with a (intensity) minimum in the pointing direction of the laser, if measured with a relatively high angular resolution and a fine scanning. We also notice that the interference patterns behave in a very much different way as in metal-metal waveguide QCLs[3,4], suggesting a different physical origin. Such beam patterns make heterodyne mixing using the DFB QCLs and an NbN HEB mixer extremely challenging.

[a] On leave from Institute of Radio Engineering and Electronics, Russian Academy of Sciences, 103907 Moscow, Russia.

[1] J. R. Gao, J. N. Hovenier, Z. Q. Yang, J. J. A. Baselmans, A. Baryshev, M. Hajenius, T. M. Klapwijk, A. J. L. Adam, T. O. Klaassen. B. S. Williams, S. Kumar, Q. Hu, and J. L. Reno, Appl. Phys. Lett. **86**, 244104 (2005).
[2] L. Ajili, M.A. Ines, J. Faist, H. Beere, D. Ritchie, G. Davies, and E. Linfield (in preparation)
[3] A. J.L. Adam, I. Kašalynas, J.N. Hovenier, T.O. Klaassen, J.R. Gao, E.E. Orlova, B.S. Williams, S. Kumar, Q. Hu, and J. L. Reno, Appl. Phys. Lett. **88**, 151105(2006)
[4] E.E. Orlova, J.N. Hovenier, T.O. Klaassen, I. Kašalynas, A. J.L. Adam, J.R. Gao, T.M. Klapwijk, B.S. Williams, S. Kumar, Q. Hu, and J. L. Reno, Phys. Rev. Lett. **96**, 173904(2006).

# Development and Design of a 340 GHz Photomixer Source

Biddut Banik, Josip Vukusic, Syed Mahmudur Rahman, Henrik Sunnerud and Jan Stake

***Abstract*— We present the design of an InGaAlAs/InP uni-traveling-carrier photo-diode (UTC-PD) at mm-wave frequencies up to 340 GHz. The photo diode epitaxy is optimized using a quasi-3D software implementing the hydrodynamic semiconductor equations, for which an output power of 3 mW at 340 GHz was simulated. An equivalent circuit of the UTC-PD has been fitted to experimental $S_{11}$ measurements up to 67 GHz. Finally, an optimized antenna coupled UTC-PD with choke filter has been designed. This MMIC circuit is intended for photomixing, with output power at 340 GHz.**

***Index Terms*— Photomixer, terahertz source, uni-traveling carrier photo-diode**

## I. Introduction

The increasing demand for sources in the THz frequency regime has prompted a numerous number of electrical and optical schemes for the generation of sub-mm waves. Photomixing, being one of these schemes, relies on the nonlinear mixing of two closely spaced laser wavelengths generating a beat oscillation at the difference frequency, as exemplified in Fig.1. One of the benefits of using this method is the wide tunability of the output frequency. The 350 GHz [1] band has interesting applications for remote sensing of atmospheric gases, which needs a local oscillator (LO) for sensitive detection. By using a laser fed LO source the signal can be easily distributed by fiber optics and can be used in antenna networks for instance.

In the recent years, there has been an increasing interest in the Uni-Traveling-Carrier Photodiode (UTC-PD) for photomixing, photo receivers, microwave and mm-wave generation, fiber-optic communication systems and wireless communications. UTC-PDs offer several advantages over PIN-PDs. A UTC-PD uses only electrons as the active carriers and hole transport does not directly affect the diode response and output saturation. UTC-PDs have become very promising by demonstrating output powers of 20 mW at 100 GHz [2]

Manuscript received June 21, 2007. This work was supported by the Swedish Foundation for Strategic Research (SSF).

Biddut Banik, Josip Vukusic, Syed Mahmudur Rahman and Jan Stake are with the Physical Electronics Laboratory, Dept. of Microtechnology and Nanoscience, Chalmers University of Technology; SE-41296, Göteborg, Sweden (e-mail: biddut.banik@mc2.chalmers.se).

Henrik Sunnerud is with the Photonics Laboratory, Dept. of Microtechnology and Nanoscience, Chalmers University of Technology; SE-41296, Göteborg, Sweden (e-mail: sunnerud@chalmers.se).

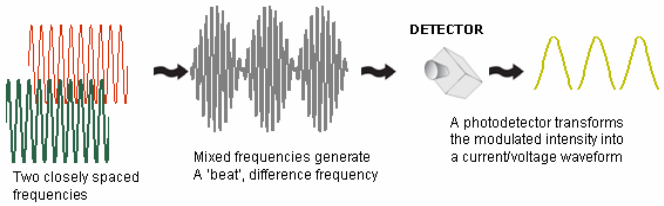


Fig.1. By shifting the laser wavelength slightly we can achieve wide tunability of our electrical output

and 25 μW at 1 THz [3].

We report our research results based on the InGaAlAs/InP uni-traveling-carrier photo-diode (UTC-PD) at lower frequencies (<60 GHz) extending up to 340 GHz. Our research goal encompasses realization of compact and tunable THz sources by photomixing and integration of the photomixer with antennas.

## II. Uni-Traveling Carrier Photo-Diode

### A. Working Principle

Electron-hole pairs are generated when the light is absorbed in a photo diode. For the conventional PIN-PD this occurs in the undoped, intrinsic region. This results in an approximately equal length of transport for both holes and electrons. Because of the significantly larger mass of the holes these limit the speed of the device. In a UTC-PD on the other hand, the light is absorbed in the p-doped region thereby significantly shortening the distance to the p-contact for the holes. In this way we also avoid the build-up of holes that would at some point screen the acceleration field normally present in the device. Fig.2 shows a comparison between the operational principles of the PIN-PD and the UTC-PD. In the conventional PIN-PD, under a high-excitation condition the band profile changes as photo-generated carriers are accumulated in the absorption layer. This in turn decreases the electric field and drastically reduces the carrier velocity and results in output current saturation. In the case of the UTC-PD, the space charge consists of only electrons whose velocity at overshoot is much higher than that of holes, even for the decreased electric field, and thus postpones current saturation. In UTC-PDs, high electron mobility in the depletion layer can be maintained at a relatively low electric field or even with the built-in field of the *p-n* junction. This enables high-speed operation of the UTC-PD without applying any bias voltage. The device thereby offers higher operation current and lower

operation voltage [4].

We can see from Fig. 2 that UTC-PDs have separate absorption and depletion regions. The absorption layer and the depletion layer thicknesses in the UTC-PD structure can therefore be independently designed. This means that a very thin absorption layer can be used for higher bandwidth without sacrificing the RC charging time. On the other hand, in the PIN-PD the RC charging time becomes significantly larger when the absorption layer thickness is excessively reduced to decrease the carrier transit time.

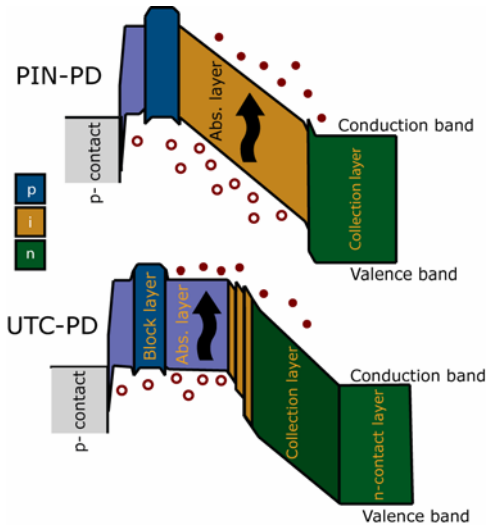


Fig.2. Schematic band diagrams of a PIN-PD and an UTC-PD [5]

This work features InGaAlAs/InP UTC-PD devices for which InGaAs is the absorbant and 1.55 μm is the operating wavelength. By using this standard telecommunications wavelength we have a wide spectrum of relatively inexpensive, high performance equipment at our disposal.

### *B. Device Fabrication*

The fabrication of the InGaAlAs/InP UTC-PD's is initiated by growth of the material layering by our in house molecular beam epitaxy (MBE) system. To fabricate the devices standard III-V processing techniques are used. This includes photolithography UV/DUV, E-beam evaporation, contact annealing, wet etching, dry etching and electroplating. To facilitate efficient light collection by the bottom illuminated devices the substrate is thinned by lapping and polishing. This is followed by $Si_3N_4$ anti-reflection coating. Fig. 3 shows SEM photograph of two fabricated UTC-PDs of different sizes with air-bridges.

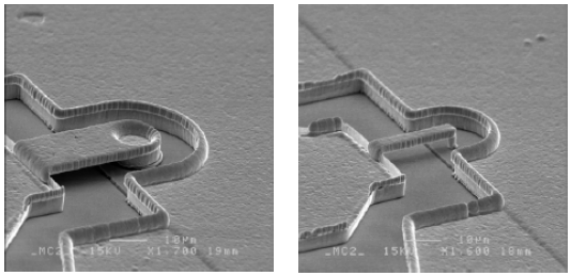

Fig.3. SEM photograph of the fabricated UTC-PDs with a detector diameter of 20 μm and 3 μm respectively.

### *C. Device characterization*

Fabricated devices with 8-17 micron diameters and 220 nm absorption layer widths were characterized. These devices had a 50 Ohm coplanar waveguide leading up to the device itself. The photo-diodes were excited by 1 ps pulses with a 50 MHz repetition frequency. By simultaneously probing the open end of the waveguide using a 70 GHz sampling oscilloscope we were able to estimate the 3-dB bandwidth of the UTC-PDs. The upper graph of Fig. 4 shows an example of the sampled impulse response for an 8 micron device. Because of the frequency dependent losses from the bias-T, cables and probes a significantly lower 3-dB bandwidth was measured. By compensating for the influence of the measurement setup, as seen in the lower graph of Fig. 4, we arrived at an expected 3-dB bandwidth of 60 GHz for these devices.

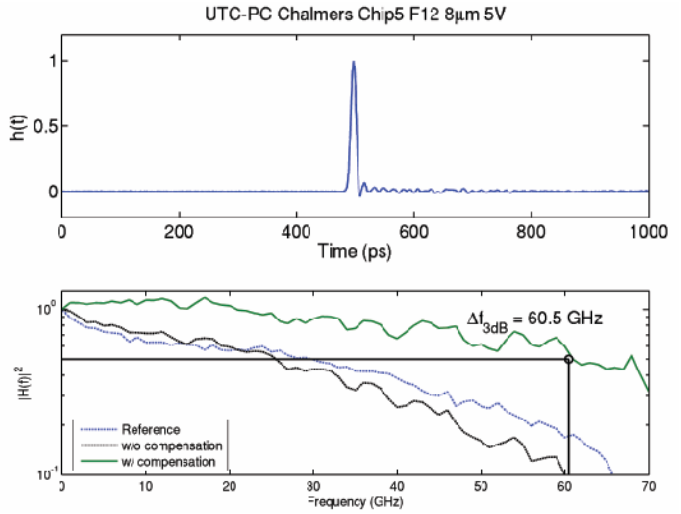


Fig.4. (upper) impulse response from an 8 mm UTC-PD. (lower) Fourier transform of the impulse response with the bandwidth limitations of the measurement setup included

Fig. 5 shows the 3-dB bandwidth for different power injection levels. We can see that the detector response saturates at pulse energies above 1 pJ. Also, we can note that 10 V reverse bias is more successful in sweeping the large number of electrons through the device. As discussed earlier, the large number of generated carriers distort the acceleration field. But by applying a high external voltage we

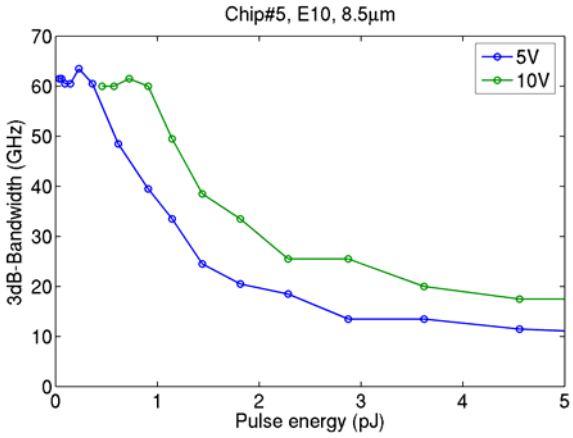


Fig.5. 3-dB bandwidth versus input pulse energy of an 8 micron device with a 220 nm absorption layer

counteract this distortion and the onset of the saturation can be postponed.

### D. Equivalent Circuit

In order to understand the impedance behavior of the photo detector we have compared measured s-parameters with an equivalent circuit model. This will allow us to estimate the device impedance when scaling down the detector area for higher frequencies.

In principle, the equivalent circuit of a UTC-PD can be realized as a current source $I_{UTCPD}$ in parallel with a very high resistance $R_{UTCPD}$ and capacitance $C_{UTCPD}$. The fabricated UTC-PD devices have a short strip of coplanar waveguide (CPW) leading up to them to accommodate the measurement probes. The equivalent circuit for UTC-PD and CPW, shown in Fig. 6 (a), is modeled in Advanced Design System (ADS). The CPW is modeled as a cascade of series inductance $L_{CPW}$ and shunt capacitance $C_{CPW}$. Fig. 6 (b) shows the $S_{11}$ plot attained by simulation and measurement from 10 GHz to 67 GHz.

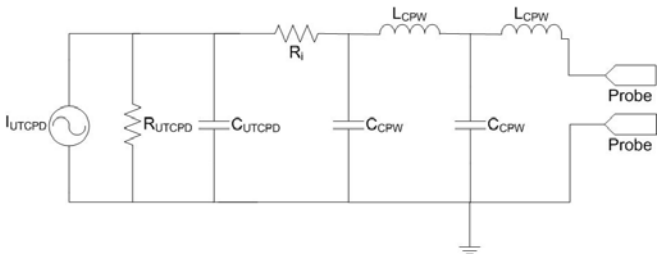


(a)

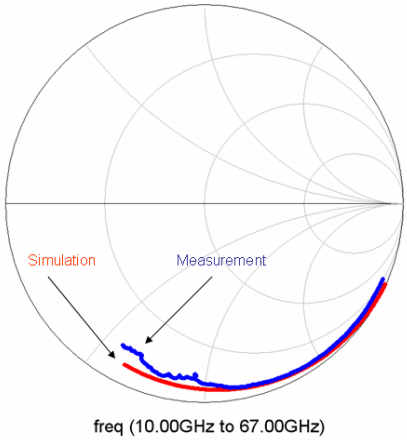


(b)

Fig.6. (a) Equivalent circuit of the UTC-PD (b) simulation and measurement results ($S_{11}$).

## III. Epitaxial Modeling

To optimize the UTC-PDC epitaxial layering for the task at hand, we implemented a quasi-3D model using a commercial TCAD software [6]. Fig. 7 shows the graphical user interface describing the epitaxial layering of the device.

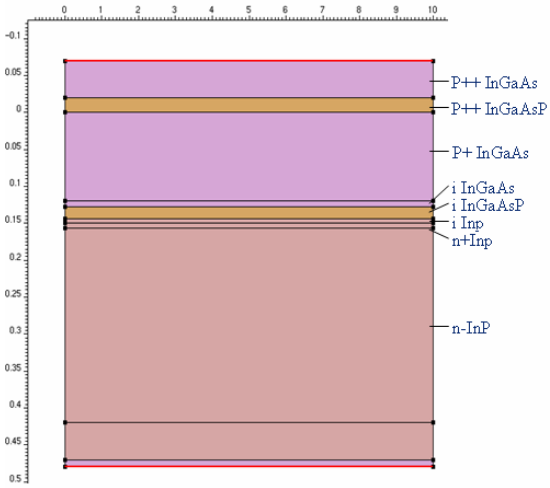


Fig.7. Graphical user interface of the TCAD software with the layer compositions marked

These calculations use the hydrodynamic model to model the carrier transport through the photo-detector. In this way we take into account the velocity overshoot in the device. Fig. 8 (a) shows the difference in electron velocity between the conventional drift diffusion (DD) and the hydrodynamic (HD) model. Since the carrier transport in the UTC-PD is predominantly governed by electrons the significant discrepancy between the DD and HD model will influence the simulation results. Fig. 8 (b) shows the energy band diagram under different optical injection levels. We can see that above some injection level the carrier accumulation impairs the acceleration field in the collector region and thereby saturates the detector response.

This is also evident in Fig. 9 (a) in which the detector responsivity has been plotted against different optical input powers. We can see that at some point saturation effects limit the amount of power that the UTC-PD can handle. Note also the difference between the DD and the HD model. Since the DD model doesn't include velocity overshoot effects it clearly underestimates the power handling of the device.

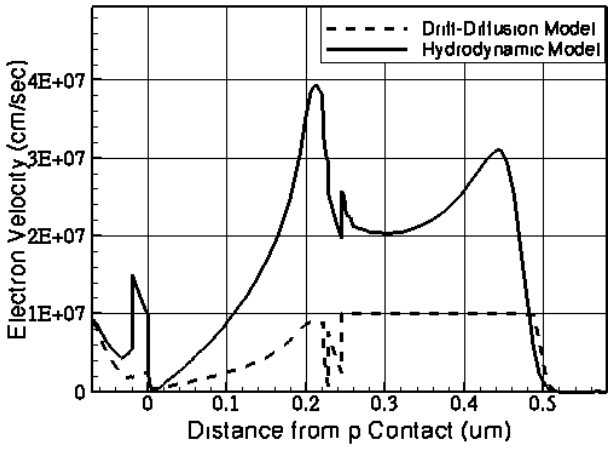


(a)

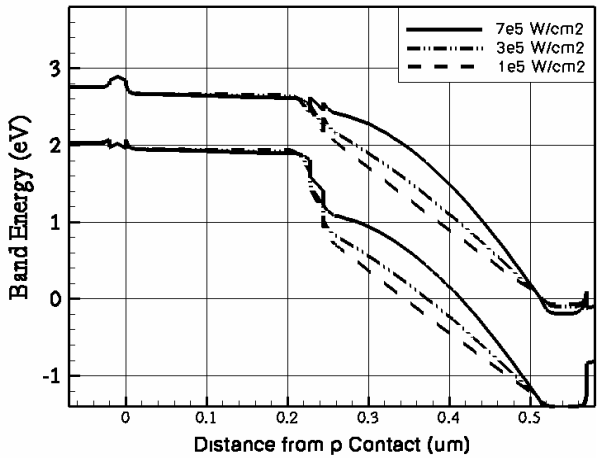


(b)

Fig.8. (a) Electron velocity distribution across the UTC-PD (b) Energy band-diagram for different optical injection levels calculated using the HD model

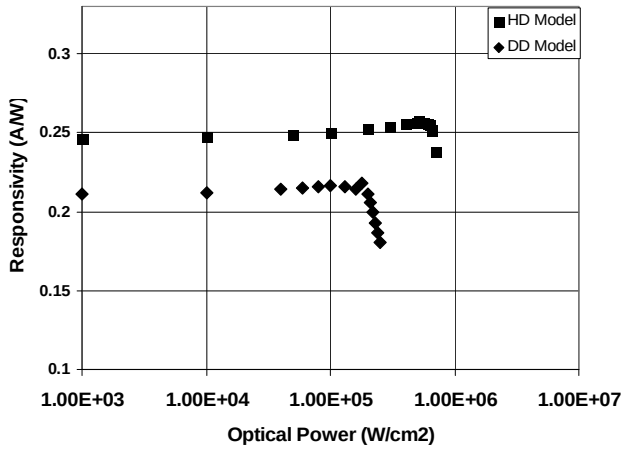


(a)

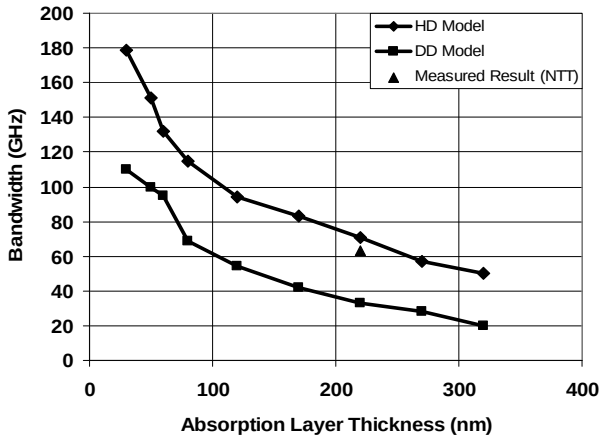


(b)

Fig.9. (a) Responsivity at different optical input powers (b) Bandwidth for different absorption layer thicknesses

Fig. 9 (b) shows a comparison between the DD and the HD model bandwidths for different absorption layer thicknesses. Again we can see that the bandwidth is underestimated by the DD model because of the inability to predict the velocity overshoot. An experimental result has also been included in the graph for comparison at 220 nm absorption layer thickness.

## IV. Layer Optimization Example

Our goal is to design and optimize a 340 GHz photomixer. So we can therefore use the implemented software to change layer thicknesses of our epitaxy to maximize the output power. In this case we have chosen to vary the collection and absorption layer thickness. The positions of these layers are shown in Fig. 10. An optical pulse train with 340 GHz frequency and at different power levels was fed into the device to mimic photomixing. Fig. 11 (a) shows the resulting output power when varying the absorption layer thickness for a fixed (263 nm) collection layer thickness. We can see that a thickness of ~38 was optimum. By keeping the absorption layer constant (38 nm) we then varied the collection layer thickness. This is presented in Fig. 11 (b), where we can see that the optimum collection layer thickness was 140 nm.

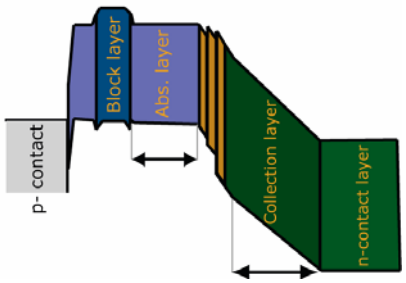


Fig.10. Simulations varying the absorption and collection layer widths

The trade off in this case is between long carrier transit time for a thick collection layer and the high capacitance (RC-constant) for a thin collection layer. We can note that the maximum output power is slightly above 3 mW. In these calculations we have not included any losses in the outcoupling of the radiation. Also, this optimization was done without any thermal analysis, which may limit the manageable input power.

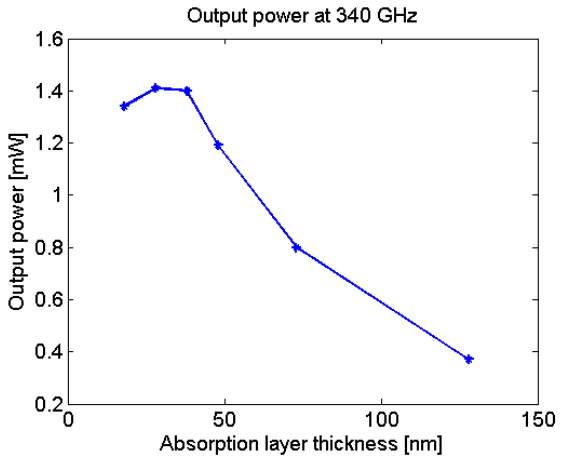


(a)

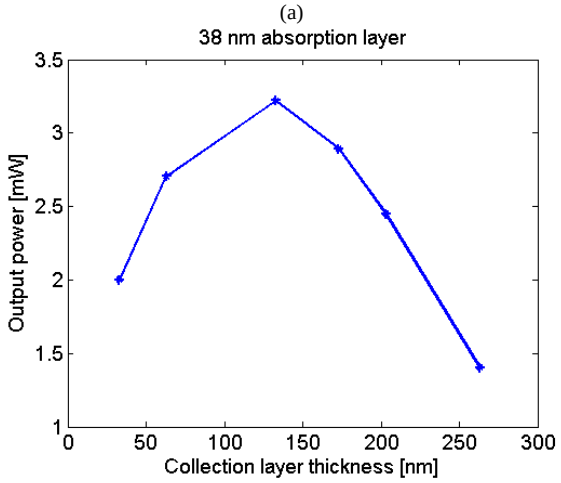


(b)

Fig.11. (a) Optimization of the absorption layer thickness s (b) Optimization of the collection layer thickness

## V. Antenna Design

Due to the benefits of THz technology in various applications such as security and imaging systems, photomixing with UTC-PDs have proven to be an attractive solution for THz generation. A convenient approach for the realization of a THz emitter is to integrate the photo detector with an antenna.

As shown in [7], the THz output power from a photomixer is proportional to the antenna impedance. For UTC-PD-antenna integration, different types of antennas such as bowtie, log-spiral and log-periodic antenna have been reported. However, the impedance of those broadband antennas is relatively low [8-11]. Resonant antennas such as dipole and slot antennae offer relatively high impedance at the resonant frequency [11, 12]. Photomixing with resonant twin-dipole and twin-slot antennae has also been reported [13].

Twin-dipole antennas provide symmetric near-Gaussian beam pattern. Another advantage of twin-dipole antennas is that the high directive gain reduces the reflection loss at the surface of a silicon substrate lens. Twin-dipole antennas offer the flexibility of inductance tuning by adjusting the length of the transmission line connecting the photoconductive gap and the antenna. This feature enables us to cancel the capacitance of the photoconductive gap and thereby reducing the bandwidth limiting RC- constant

Compared to microstrip lines and coplanar waveguides, coplanar stripline (CPS) provides higher characteristics impedance [14] and hence suitable for designing antennas with higher impedance. Our goal was to design an antenna for the UTC-PD which can be monolithically integrated, offers higher antenna impedance and thus provides higher power.

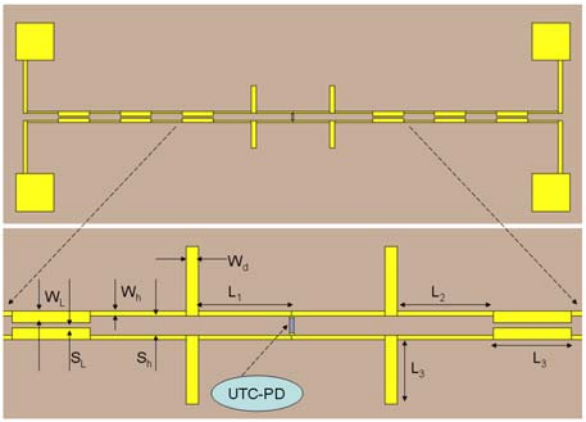


Fig.12. 340 GHz UTC-PD antenna with choke filter and biaspads

Therefore, a twin-dipole CPS antenna on 150 µm thick InP substrate with gold conductor (2 µm thick) was designed having choke filters and biaspads [15]. Fig.12 shows the center-fed twin-dipole antenna and the corresponding design parameters. In the design, the dimensions were $W_h$ = 5 µm, $S_h$ = 20 µm. At first the Hi Z – Low Z choke filter was designed and optimized in Ansoft HFSS by varying $L_3$.

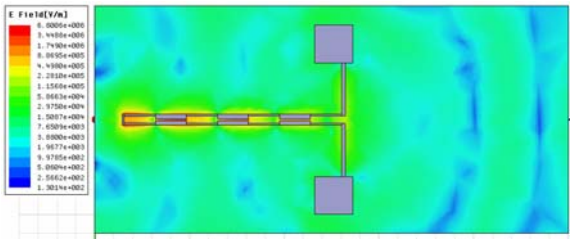

(a)

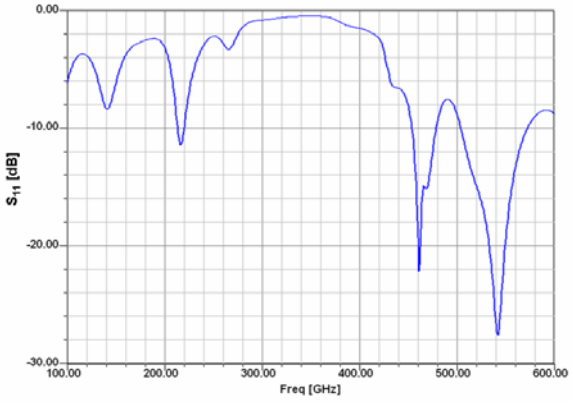


(b)

Fig.13. (a) E-field distribution through Hi Z – Low Z steps of the choke filter (b) return loss of the choke filter, resonance at 340 GHz

Fig.13 (a) illustrates the E-field distribution through the Hi Z- Low Z choke filter. Fig.13 (b) shows the return loss of the choke filter. After optimization, a pronounced resonance is observed at 340 GHz where the real part of the input impedance becomes very high and effectively acts as an open circuit. Therefore, at 340 GHz the choke filter provides very high return loss, as can be seen in Fig. 13 (b).

The UTC-PD antenna was then optimized to attain higher input impedance at 340 GHz by varying $W_d$, $L_1$, $L_2$ and $L_3$. Fig. 14 (a) illustrates the E-field distribution through the antenna. Fig. 14 (b) shows the input impedance of the antenna and a pronounced resonance is observed at 340 GHz.

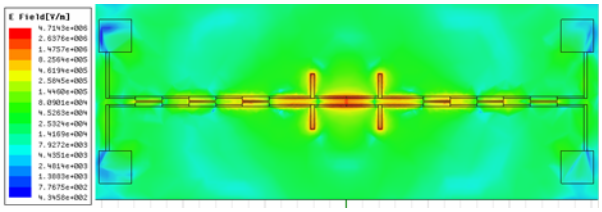

(a)

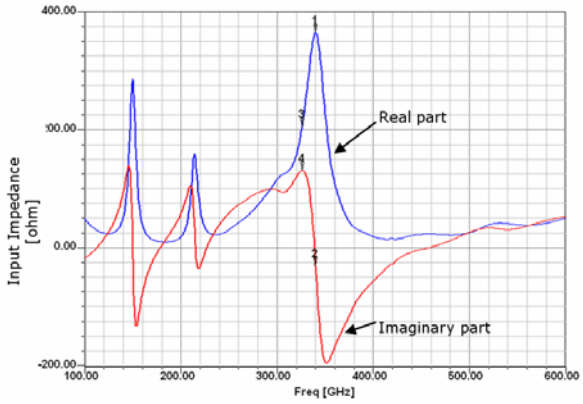


(b)

Fig.14. (a) E-field distribution through the twin-dipole antenna (b) Input impedance of the antenna, resonance at 340 GHz

The optimized antenna design, hence, will enable us to eradicate the RC limitation that arises from UTC-PD capacitance. This capacitance can be extracted from the equivalent circuit fit of the s-parameter measurements. The high input impedance of the antennae will maximize the THz output power from the photomixer.

## VI. Conclusion

We have presented experimental results on UTC-PDs for frequencies up to 67 GHz. This included impulse response and S-parameter measurements. An equivalent circuit was fitted to these results. This was followed by a design methodology for optimizing the output power from a UTC-PD at 340 GHz. The design of the epitaxial layering showed the possibility for ~3 mW of output power. After a short discussion of antenna alternatives the twin-dipole antenna was chosen as the most suitable to integrate with the UTC-PD. The layout of the antenna was then designed to accommodate UTC-PD biasing and optimal impedance matching.

## References

[1] H. Smith, R. Hills, S. Withington, J. Richer, J. Leech, R. Williamson, H. Gibson, R. Dace, B. Barker, R. Baldwin, H. Stevenson, P. Doherty, D. Molloy, V. Quy, C. Lush, S. Hales, B. Dent, I. Pain, B. Wall, P. Hastings, B. Graham, T. Baillie, K. Laidlaw, R. Bennett, I. Laidlaw, W. Duncan, M. Ellis, R. Redman, B. Wooff, K. Yeung, J. Fitzsimmons, L. Avery, D. Derdall, D. Josephson, A. Anthony, R. Atwal, T. Chylek, D. Shutt, P. Friberg, N. Rees, R. Philips, M. Kroug, T. Klapwijk, T. Zijlstra, and P. G. Ananthasubramanian, "HARP-B: A 350GHz 16-element focal plane array for the James Clerk Maxwell telescope," *Proceedings of SPIE - The International Society for Optical Engineering*, vol. 4855, pp. 338-348, 2002.

[2] H. Ito, T. Nagatsuma, A. Hirata, T. Minotani, A. Sasaki, Y. Hirota, and T. Ishibashi, "High-power photonic millimetre wave generation at 100 GHz using matching-circuit-integrated uni-travelling-carrier photodiodes," *Optoelectronics, IEE Proceedings*, vol. 150, pp. 138-142, 2003.

[3] C. C. Renaud, M. Robertson, D. Rogers, R. Firth, P. J. Cannard, R. Moore, and A. J. Seeds, "A high responsivity, broadband waveguide uni-travelling carrier photodiode," *Electronics Letters*, vol. 40, pp. 1297-8, 2004.

[4] H. Ito, S. Kodama, Y. Muramoto, T. Furuta, T. Nagatsuma, and T. Ishibashi, "High-speed and high-output InP-InGaAs unitraveling-carrier photodiodes," *IEEE Journal of Selected Topics in Quantum Electronics*, vol. 10, pp. 709-27, 2004.

[5] T. Ishibashi, T. Furuta, H. Fushimi, S. Kodama, H. Ito, T. Nagatsuma, N. Shimizu, and Y. Miyamoto, "InP/InGaAs uni-traveling-carrier photodiodes," *IEICE Transactions on Electronics*, vol. E83-C, pp. 938-49, 2000.

[6] www.synopsys.com.

[7] M. Tani, O. Morikawa, S. Matsuura, and M. Hangyo, "Generation of terahertz radiation by photomixing with dual- and multiple-mode lasers," *Semiconductor Science and Technology*, vol. 20, pp. 151-63, 2005.

[8] E. R. Brown, K. A. McIntosh, K. B. Nichols, and C. L. Dennis, "Photomixing up to 3.8 THz in low-temperature-grown GaAs," *Applied Physics Letters*, vol. 66, pp. 285-7, 1995.

[9] K. A. McIntosh, E. R. Brown, K. B. Nichols, O. B. McMahon, W. F. Dinatale, and T. M. Lyszczarz, "Terahertz photomixing with diode lasers in low-temperature-grown GaAs," *Applied Physics Letters*, vol. 67, pp. 3844-6, 1995.

[10] S. Verghese, K. A. McIntosh, and E. R. Brown, "Highly tunable fiber-coupled photomixers with coherent terahertz output power," *IEEE Transactions on Microwave Theory and Techniques*, vol. 45, pp. 1301-9, 1997.

[11] I. S. Gregory, C. Baker, W. R. Tribe, I. V. Bradley, M. J. Evans, E. H. Linfield, A. G. Davies, and M. Missous, "Optimization of photomixers and antennas for continuous-wave terahertz emission," *IEEE Journal of Quantum Electronics*, vol. 41, pp. 717-728, 2005.

[12] I. S. Gregory, W. R. Tribe, B. E. Cole, M. J. Evans, E. H. Linfield, A. G. Davies, and M. Missous, "Resonant dipole antennas for continuous-wave terahertz photomixers," *Applied Physics Letters*, vol. 85, pp. 1622-4, 2004.

[13] S. M. Duffy, S. Verghese, A. McIntosh, A. Jackson, A. C. Gossard, and S. Matsuura, "Accurate modeling of dual dipole and slot elements used with photomixers for coherent terahertz output power," *IEEE Transactions on Microwave Theory and Techniques*, vol. 49, pp. 1032-8, 2001.

[14] D. Zhengwei, G. Ke, J. S. Fu, F. Zhenghe, and G. Baoxin, "CAD models for asymmetrical, elliptical, cylindrical, and elliptical cone coplanar strip lines," *IEEE Transactions on Microwave Theory and Techniques*, vol. 48, pp. 312-16, 2000.

[15] H. Ito, F. Nakajima, T. Furuta, and T. Ishibashi, "Continuous THz-wave generation using antenna-integrated uni-travelling-carrier photodiodes," *Semiconductor Science and Technology*, vol. 20, pp. 191-8, 2005.

# Noise and responsivity measurements in Hot-Electron Direct Detectors

Boris Karasik[*,1], David Olaya[#], Jian Wei[#], Sergey Pereverzev[#], Michael Gershenson[#], Jonathan Kawamura[*], William McGrath[*], and Andrei Sergeev[§]

[*] Jet Propulsion Laboratory/California Institute of Technology, 4800 Oak Grove Dr., Pasadena, CA 91109, USA
[#] Dept. of Physics & Astronomy, Rutgers University, 136 Frelinghuysen Rd., Piscataway, NJ 08854, USA
[§] Dept. of Electrical Engineering, SUNY at Buffalo, 332D Bonner Hall, Buffalo, NY 14260, USA

We present the current progress and the test results for the hot-electron transition-edge devices of nanoscale size operating at ~ 0.1-0.4 K. The ultimate goal of this work is to develop a submillimeter Hot-Electron Direct Detector with the noise equivalent power NEP = $10^{-18}$-$10^{-20}$ W/Hz$^{1/2}$ operated at ~ 0.3 K for the moderate resolution spectroscopy and CMB studies on future space telescope (e.g., SAFIR, SPECS, SPICA, CMBPol) with cryogenically cooled (~ 4-5 K) mirrors.

Using the shadow mask evaporation technique we fabricated nanoscale Ti bridges with Nb Andreev contacts. The devices were fabricated on a Si wafer and did not rely on the thermal insulation due to the membrane support normally required in conventional bolometers. The thermal conductance in our devices is set by the electron-phonon coupling, which is very weak in disordered metals at subKelvin temperatures. From the electrical measurements, the thermal conductance was found to be ~ 2 fW/K at 300 mK and ~ 0.1 fW/K at 40 mK. If the thermal fluctuation noise is dominant in the devices then such a uniquely low thermal conductance should provide the NEP required for most demanding applications.

The measurements involving detection of single NIR photons ($\lambda$ = 1550 nm) allowed for determination of the bolometer thermal time constant (electron-phonon relaxation time) being of 20 μs at 200 mK and a few μs at 370 mK. The latter measurements were hindered by the limited SQUID bandwidth (100 kHz). A broadband 1 MHz SQUID is being set up for future experiments on single photon detection.

The output electrical noise measured in the devices in the voltage-bias mode was dominated by the thermal energy fluctuations (phonon noise). This was an indication that the responsivity was sufficiently high (i.e., the superconducting transition was steep enough).

The very low NEP and the high speed are a unique combination not found in other detectors. This would allow for a very high data rate in an application, though more work is needed to develop an adequate read-out/multiplexing electronics for this type of detector. Beside the extremely low phonon-noise NEP, the nanobolometers have a very low electron heat capacitance. This makes them promising as detectors of single FIR photons for the moderate resolution spectroscopy above 1 THz where the background photon arrival rate is less than the detector speed.

This research was carried out in part at the Jet Propulsion Laboratory, California Institute of Technology, under a contract with the National Aeronautics and Space Administration. The research at Rutgers University and SUNY at Buffalo was supported by a NASA grant.

[1] E-mail: boris.s.karasik@jpl.nasa.gov

# Development of a Large Format Fully Sampled Bolometer Camera for 2 mm Wavelength

Dominic J. Benford[1], Johannes G. Staguhn[1,2], Christine A. Allen[1], Troy J. Ames[1], Ernest D. Buchanan[1,3], Stephen F. Maher[1,4], S. Harvey Moseley[1], Elmer H. Sharp[1,5], Edward J. Wollack[1]

1 – NASA / Goddard Space Flight Center, Greenbelt, MD 20771 USA
2 – University of Maryland, College Park, MD 20742 USA
3 – AdNet Systems, Rockville, MD 20852 USA
4 – SSAI, Lanham, MD 20706 USA
5– GS&T, Greenbelt, MD 20770 USA

## ABSTRACT

The 2 mm (150 GHz) atmospheric window enables unparalleled ground-based observations of the earliest active dusty galaxies in the universe. We have undertaken the development of a bolometer camera, GISMO (the Goddard-IRAM Superconducting 2-Millimeter Observer), which will obtain large and sensitive sky maps at this wavelength. The instrument will be used at the IRAM 30 m telescope, where we hope to have a trial observing run in Summer 2007. The innovative element in this camera is its 8×16 fully sampled planar array of multiplexed superconducting transition edge sensor bolometers. This array is based on our recently demonstrated Backshort Under Grid architecture, designed to be scaled to kilopixel arrays with high sensitivity (of around $4 \cdot 10^{-17}$ W/√Hz at $T_C$~450 mK). A compact cryogenic optical system provides a wide field of view of almost 2′×4′, enabling GISMO to be very efficient at detecting sources serendipitously in large sky surveys, while retaining diffraction-limited imaging performance. GISMO will provide significantly greater imaging sensitivity and mapping speed at this wavelength than has previously been possible. The major scientific driver for the instrument is to detect dust emission from high-*z* ULIRGs and quasars. The instrument provides an important portion of the spectrum of high redshift galaxies at the Rayleigh-Jeans part of the dust emission spectrum, even at the highest redshifts. Models of galaxy evolution predict that GISMO will serendipitously detect one galaxy in every four hours of observing blank sky, and that one quarter of these galaxies will be at a redshift of $z > 6.5$.

## 1. BACKGROUND

A key observational tool in the study of the evolution of the universe out to cosmological distances is to observe the (redshifted) thermal emission from interstellar dust in galaxies. The most distant astronomical objects known to date are luminous, dusty galaxies at redshifts *z*~6, a time when the universe was less than one Gyr old. At this epoch, the reionization of the universe was still not completed. These dusty galaxies all experience a phase of violent star formation, and a large number of them are seen to host luminous active nuclei (quasars) – processes that ultimately will reionize the universe. One of the major scientific pursuits for understanding the formation of structure in the universe is to learn about the physics of the formation of these galaxies. We would like to understand the relationship between the star formation and quasar activity with their corresponding feedback mechanisms in these objects. The bulk of the total luminosity of both processes in these dusty galaxies is redshifted into the submillimeter and millimeter regime and therefore can be efficiently observed at these wavelengths.

## 2. GISMO: A 2 MM BOLOMETER CAMERA FOR THE IRAM 30 M TELESCOPE

At NASA's Goddard Space Flight Center we are now building the bolometer camera GISMO (Goddard-IRAM Superconducting 2-Millimeter Observer), optimized for operating in the 2 mm atmospheric window. We have negotiated an opportunity to operate the instrument on the IRAM 30 m telescope on Pico Veleta in Spain (Baars et al. 1987). The instrument is primarily aimed at surveying the first dusty galaxies in the universe. The camera is built around an

8□×□16 pixel array of 2 mm pitch, close-packed superconducting Transition Edge Sensor (TES) bolometers which will be described in more detail in the following chapter. In this section, we discuss the scientific motivation for GISMO.

Continuum measurements of galaxies at long wavelengths are well suited to determining the luminosity and star formation rate in these objects (for a review see, e.g., Blain et al. 2002). Observations with GISMO will complement existing 850 μm – 1.25 mm SEDs of high redshift galaxies at the Rayleigh-Jeans part of the dust emission spectrum, even at the highest redshifts. In particular at redshifts of $z$>5 sky-background-limited bolometric observations at 2 mm are highly efficient as compared to observations at shorter (sub)millimeter wavelengths. Figure 1 demonstrates this by showing a plot of the 1.2 mm/2.0 mm flux density ratio versus redshift for template LIRGs and ULIRGs with luminosities ranging between $L_{FIR} = 10^{11}$ $L_\odot$ and $L_{FIR} = 10^{14}$ $L_\odot$. With GISMO operating at 2 mm wavelength, three atmospherical windows will then be available for efficient continuum observations of the high-$z$ universe: 2mm with GISMO; 1.2 mm with MAMBO (Kreysa et al. 2002) and Bolocam (Glenn et al. 2003); and soon 0.85 mm with SCUBA-2 (Holland et al. 2006). With the availability of three (sub)millimeter colors the accuracy in the determination of photometric redshifts and absolute luminosities for those objects will be improved. GISMO's pixel separation of 2 mm corresponds to an angular separation of 14" on the sky, or ~λ/D (only slightly beam oversampled) at 2 mm wavelength and the telescope diameter of 30 m. With this spatial sampling GISMO will be very efficient at detecting sources serendipitously in large sky surveys, while the capability for diffraction limited observations is preserved (Bernstein 2002). Dithering will be used to recover the full angular resolution provided by the telescope. Figure 2 shows our model predictions for the cumulative dark sky galaxy number counts versus flux for GISMO. Using the sensitivity numbers shown in Table 1 we find that we expect one 5σ galaxy detection on the blank sky in 4 hours of observing time, with the probability of 1 in 4 that it is at a redshift $z$ > 6.5. Since the current highest quasar redshift is $z$=6.42 (Willott, McClure & Jarvis 2003), GISMO will be a powerful surveyor of the highest redshift universe.

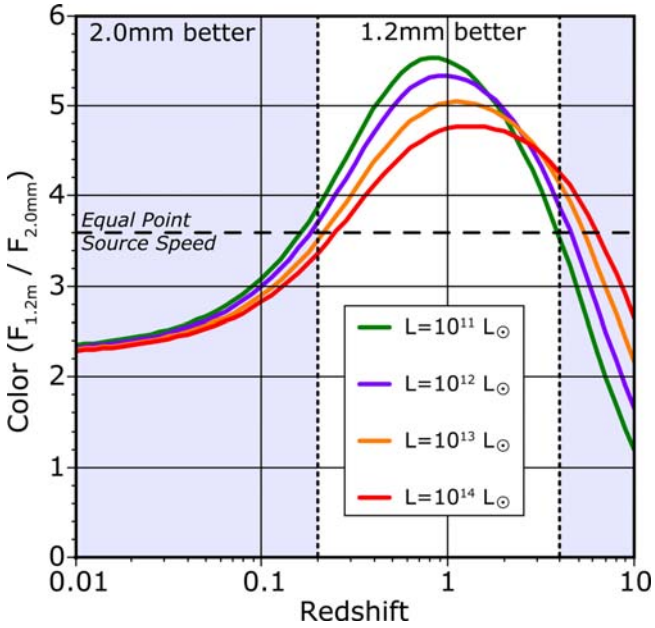


Figure 1. The modeled color (flux density ratio) between 1.2mm and 2.0mm as a function of redshift shows a significant change around redshifts of $z$~1. For typical observing conditions, the color that provides equal point source signal-to-noise in equal integration time at both wavelengths us around 3.6 (dashed line). At typical galaxy luminosities, the plot shows that observations at a wavelength of 2.0mm are more sensitive than 1.2mm for detecting both local ($z$<0.2) and very high redshift ($z$>4) galaxies. When field of view is taken into account, the 2.0mm band is always favorable to the 1.2mm band.

The 2 mm spectral range provides a unique low background window through the earth's atmosphere (see Figure 3 and Table 1 which show sky parameters for Pico Veleta). However, in order to obtain close to sky background limited performance for a bolometer camera with 20% bandwidth operating at 2 mm wavelength, detectors with a noise

equivalent power (NEP) of ≈$4 \cdot 10^{-17}$ W/√Hz or better are required to keep bolometer excess noise below 25%. A camera achieving this sensitivity can then conduct efficient observations of the earliest active dusty galaxies in the universe.

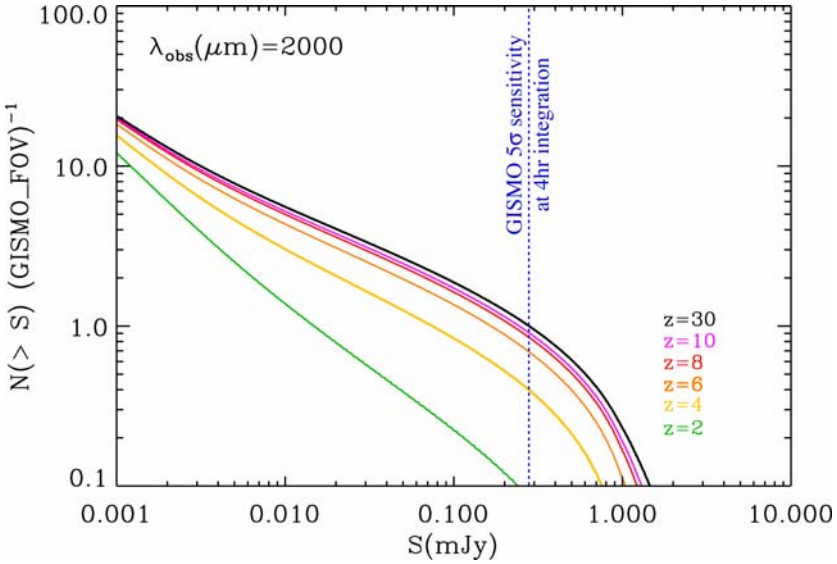


Figure 2. Model predictions for the cumulative dark sky galaxy number counts versus flux for GISMO. Each curve gives the number of sources per GISMO field of view at a redshift of less than the cutoff that is brighter than the indicated flux density.

Table 1. Typical winter and summer sky background at Pico Veleta.

| Frequency (GHz) | Sky Emissivity | Sky Noise (W/√Hz) | NEFD (mJy/√Hz) |
|---|---|---|---|
| 150 (2mm) | 0.08 (Winter) | $5.5 \cdot 10^{-17}$ at Zenith | 3.3 |
| 250 (1.2mm) | 0.16 (Winter) | $2.4 \cdot 10^{-16}$ at Zenith | 14 |
| 150 (2mm) | 0.22 (Summer) | $1.4 \cdot 10^{-16}$ at 30° El. | 10.5 |
| 250 (1.2mm) | 0.45 (Summer) | $6.0 \cdot 10^{-16}$ at 30° El. | 61 |

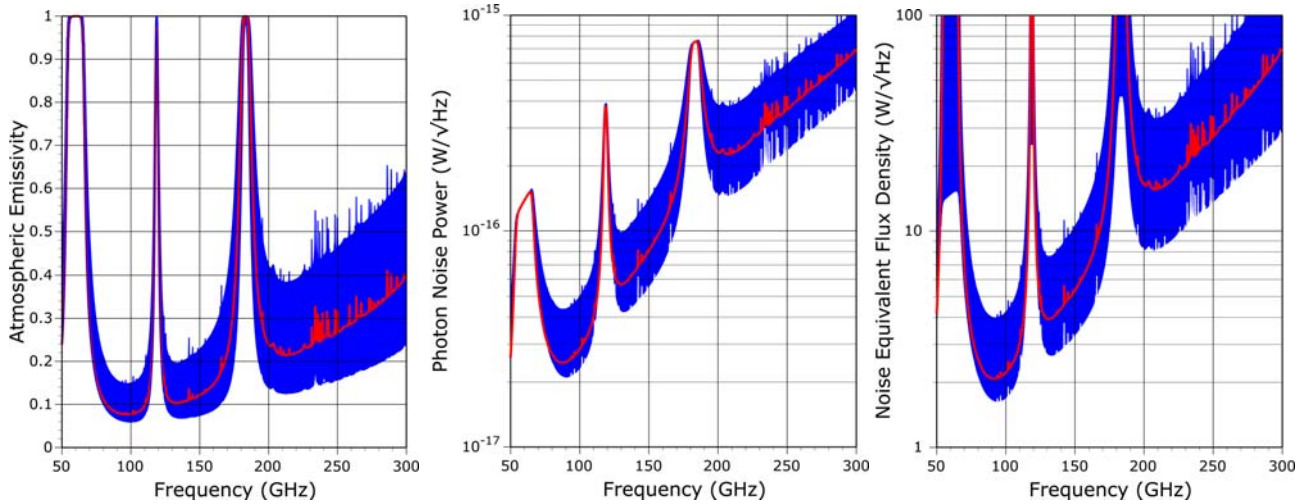


Figure 3. (Left) Modeled atmospheric emissivity as a function of frequency, showing a range of conditions between at the zenith in winter and at 30° elevation in summer; (Center) atmospheric photon noise for these conditions; (Right) noise equivalent flux density.

Other scientific projects for GISMO include – but are far from being limited to – large scale surveys of dust in protostellar clouds and galactic and extragalactic star forming regions.

## 3. DETECTORS: THE BACKSHORT-UNDER-GRID (BUG) ARRAY

We have developed a new type of two-dimensional planar bolometer array architecture, which separates the absorber and the backshort production, allowing a straightforward way to provide detector arrays for a wide range of wavelengths (Allen et al. 2006). The Backshort Under Grid (BUG) approach is comprised of a large array of thin membrane absorbers with leg thermal isolation (Figure 4, left). These photos show an enlargement of one pixel which shows the integrated Transition Edge Sensor (TES) bolometer in more detail. The normal metal "Zebra" structure on the Mo/Au thermistor, which is used to suppress excess noise (Staguhn et al. 2004), is clearly visible in this image. An 8□×□16 array will be used in GISMO. Figure 4 (center) shows an image of this BUG array, fabricated in our group at NASA/GSFC.

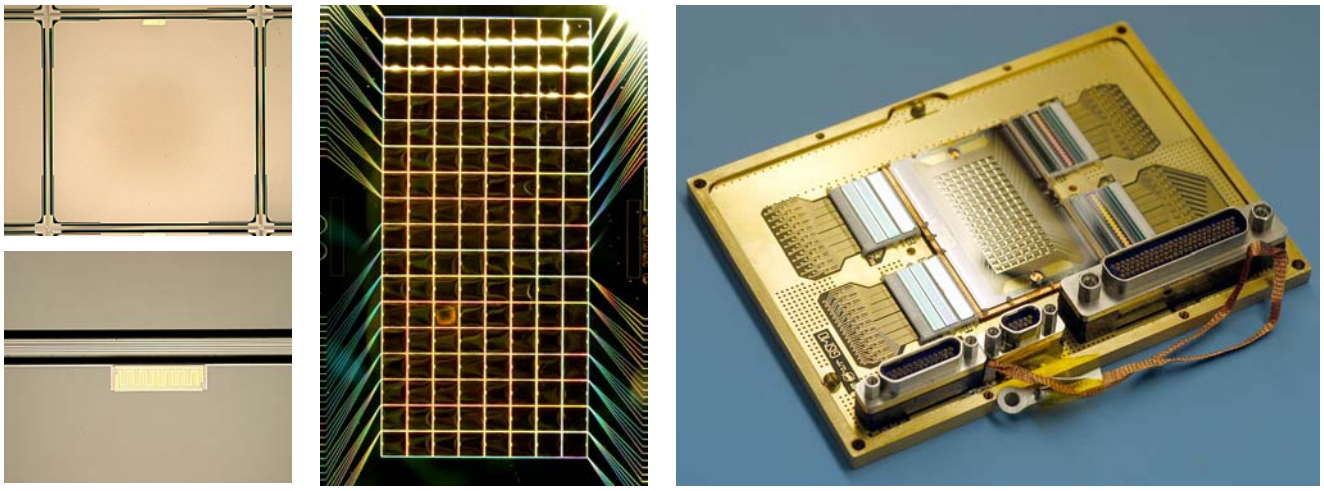

Figure 4. (Left): These photos detail the individual bolometer construction, including the eight thermal isolation legs and the thermistor with interdigitated noise suppression normal metal bars; (Center): Photograph of the completed 8□×□16 array of 2mm-pitch pixels; (Right): The GISMO detector package, providing four readout columns each with a (from outside to inside) SQUID multiplexer chip, Nyquist Inductor chip, and Shunt chip; the micro-D connectors at the lower edge set the overall size of the box, which is around 88 mm × 120 mm.

The TES arrays are read out by four 32-channel SQUID time-domain multiplexers provided by NIST/Boulder (deKorte et al. 2003). Both the readout electronics (Forgione et al. 2004) and the IRC control and data acquisition software (Ames & Case 2003) are used in other instruments such as the MUSTANG 3 mm bolometer camera for the Green Bank Telescope (Dicker et al. 2004). The complete array package with biasing shunt resistor chips, Nyquist inductor filter chips, and SQUID multiplexer chips, is shown in Figure 4 (right).

Individual bolometer characteristics were determined by precise measurements on small witness sample of four bolometers each. The phonon noise equivalent power (NEP) of the bolometers is $4.2 \cdot 10^{-17}$ W/√Hz, which is comfortably less than the expected sky noise of ~$8 \cdot 10^{-17}$ W/√Hz (Figure 3). A reduction in the transition temperature (the tested device has $T_C = 459$ mK) could be used to further improve the detector noise without any modification of the array design, since the GISMO refrigerator – a $^3$He/$^4$He system (from Chase Cryogenics, www.chasecryogenics.com) with a base temperature of below 260 mK – will allow the operation of bolometers with $T_C$ of below 400 mK). However, this reduction in noise is accompanied by a reduction in saturation power, and for instrument validation under mediocre weather conditions and lower elevations, a saturation power of well above 20 pW is needed; given this, a $T_C$ of at least 430 mK is required, allowing only 15% reduction in phonon noise.

We measured an electrothermal feedback time constant, $\tau_{etf}$, of about 50 μs ($F_{TES} \sim 3.5$ kHz). The detector circuit contains a Nyquist inductor which is chosen such that the detector integrates for a full readout cycle of the multiplexer (typically the frame rate is set to around 10 kHz). A measured noise spectrum of a representative bolometer was published by Staguhn et al. (2006). The measured in-band noise of the device on at two bias points is less than 20\%

above the fundamental phonon noise limit. Only the out-of-band (>3 kHz) excess noise is higher than this value. This noise is suppressed by the Nyquist filter and therefore does not degrade the overall performance.

In recent optical tests, a small aperture was placed in the cryostat to limit power on the detectors (in part to enable viewing of a room-temperature blackbody without saturation). This also provided a variation in the power on each detector. A current-voltage curve taken on many detectors simultaneously is then representative of a family of such curves taken on a single device taken at many different illuminations. In Figure 5 we show a family of simultaneous measurements, both in bias current vs. voltage and bias power vs. voltage. Note that the current is very nearly hyperbolic (i.e., constant power) when on the superconducting transition, whereas the current is highly linear (i.e., constant resistance) when in the normal regime. The measured resistances of all bolometers has a distribution that is approximately Gaussian with a standard deviation of 2%. Due to the aperture, the powers on the transition vary; under the assumption that the saturation power of 30 pW is identical for each detector (which is approximately true), the optical power is then just the difference between this and the measured bias power for each detector, or 13 to 20 pW.

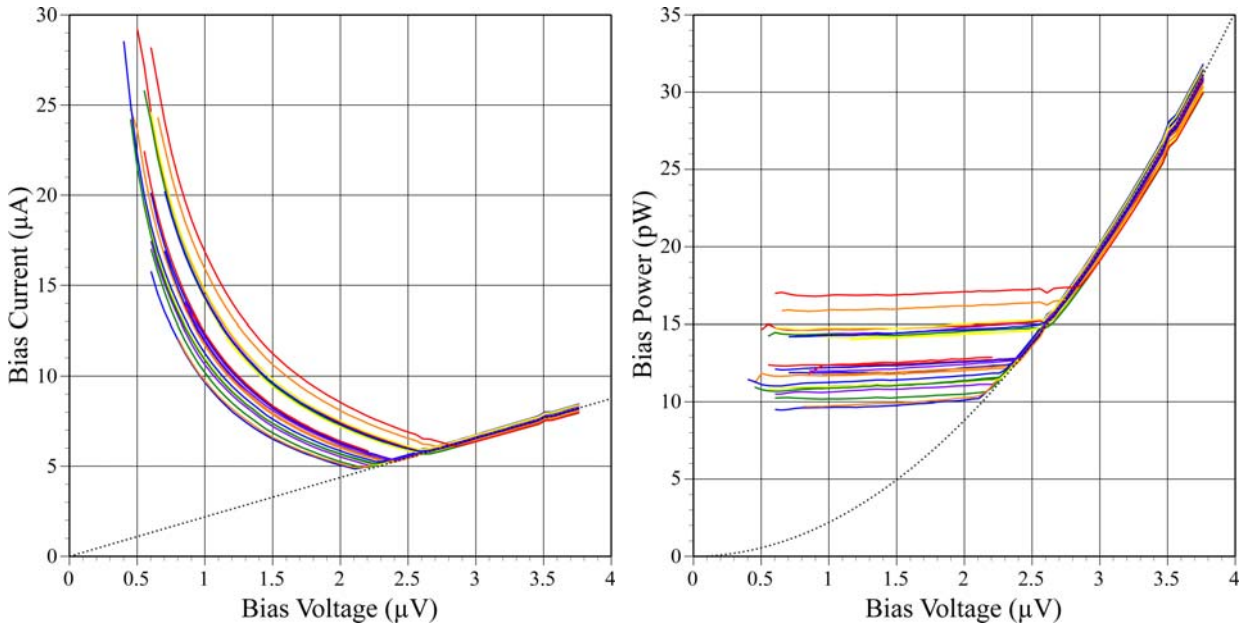


Figure 5. (Left) Measured current vs. bias voltage for an array of bolometers; (Right) Calculated bias power vs. bias voltage. Note that the detectors were illuminated by different powers, and hence the curves do not overlap.

Initial optical tests used an internal blackbody calibration source to illuminate the bolometers. A representative graph of the received power as a function of the illuminator temperature is shown in Figure 6. The curve can be fit to the expected power of the blackbody and is nearly linear, with a typical $R^2$ of >0.98 and an offset of always <1 pW. Further optical testing was conducted with the cryostat window open, to verify the beam outside the cryostat and to look for modulated signals from the far field. In Figure 6 is a time series of several detectors as one of us (EHS) waved his hand in the beam. Quantitatively, the beam appears to be of the correct size and with a ~20% hot spillover component consistent with diffraction around the internal aperture.

## 5. SUMMARY

We have built a 2 mm bolometer camera for the efficient detection of extremely high redshift galaxies. The camera is currently undergoing a variety of optical performance tests and or goal is the deployment of GISMO at the IRAM 30m telescope for trial observations in late 2007.

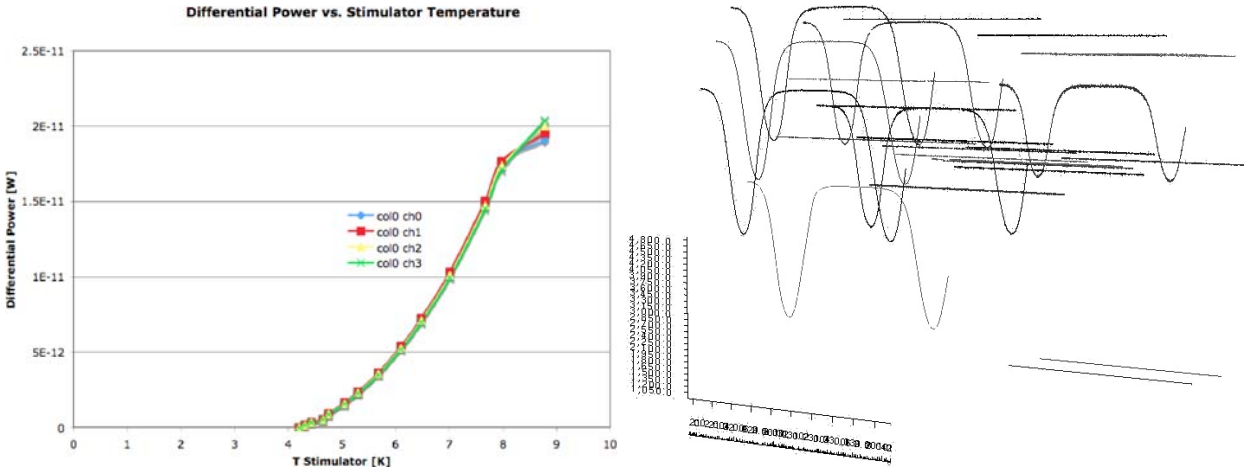


Figure 6. (Left) Detector optical power for several bolometers as a function of blackbody illumination temperature; (Right) Time series of the optical response to a warm source waved into and out of the beam (negative indicates more power).

## REFERENCES


Allen, C.A., Benford, D.K., Chervenak, J.A., Chuss, D.T., Miller, T.M., Moseley, S.H., Staguhn, J.G., Wollack, E.J., 2006, Nuc. Inst. & Meth. Phys. Res. A, 559, pp.522-524; *"Backshort-Under-Grid arrays for infrared astronomy"*

Ames, T.J. & Case, L., 2003, Proc. SPIE #4857, pp.73-84; *"Distributed framework for dynamic telescope and instrument control"*

Baars, J.W.M., Hooghoudt, B.G., Mezger, P.G. & de Jonge, M.J. 1987, A&A, 175, pp.319-326; *"The IRAM 30-m millimeter radio telescope on Pico Veleta, Spain"*

Bernstein, G. 2002, PASP, 114, pp.98-111; *"Advanced Exposure-Time Calculations: Undersampling, Dithering, Cosmic Rays, Astrometry, and Ellipticities"*

Blain, A.W., Smail, I., Ivison, R.J., Kneib, J.-P. & Frayer, D.T. 2002, PhRep, 369, pp.111-176; *"Submillimeter Galaxies"*

de Korte, P.A.J., Beyer, J., Deiker, S., Hilton, G.C., Irwin, K.D., Macintosh, M., Nam, S.W., Reintsema, C.D., Vale, L.R. & Huber, M.E. 2003, RSI, 74, pp. 3807-3815; *"Time-division superconducting quantum interference device multiplexer for transition-edge sensors"*

Dicker, S.R., Abrahams, J.A., Ade, P.A.R., Ames, T.J., Benford, D.J., Chen, T.C., Chervenak, J.A., Devlin, M.J., Irwin, K.D., Korngut, P.M., Maher, S.F., Mason, B.S., Mello, M., Moseley, S.H., Norrod, R.D., Shafer, R.A., Staguhn, J.G., Talley, D.J., Tucker, C., Werner, B.A. & White, S.D. 2006, Proc. SPIE #6275, pp. 62751B; *"A 90-GHz bolometer array for the Green Bank Telescope"*

Forgione, J.B., Benford, D.J., Buchanan, E.D., Moseley, S.H., Rebar, J. & Shafer, R.A. 2004, Proc. SPIE #5498, pp. 784-795; *"Enhancements to a superconducting quantum interference device (SQUID) multiplexer readout and control system"*

Glenn, J., Ade, P.A.R., Amarie, M., Bock, J.J., Edgington, S.F., Goldin, A., Golwala, S., Haig, D., Lange, A.E., Laurent, G., Mauskopf, P.D., Yun, M. & Nguyen, H. 2003, Proc. SPIE #4855, pp.30-40; *"Current status of Bolocam: a large-format millimeter-wave bolometer camera"*

Holland, W., MacIntosh, M, Fairley, A., Kelly, D., Montgomery, D., Gostick, D, Atad-Ettedgui, E, Ellis, M, Robson, I., Hollister, M., Woodcraft, A., Ade, P., Walker, I., Irwin, K., Hilton, G., Duncan, W., Reintsema, C., Walton, A., Parkes, W., Dunare, C., Fich, M., Kycia, J., Halpern, M., Scott, D., Gibb, A., Molnar, J., Chapin, E., Bintley, D., Craig, S., Chylek, T., Jenness, T., Economou, F. & Davis, G. 2006, Proc. SPIE #6275, pp.62751E; *"SCUBA-2: a 10,000-pixel submillimeter camera for the James Clerk Maxwell Telescope"*

Kreysa, E., Gemünd, H.-P., Raccanelli, A., Reichertz, L. A. & Siringo, G. 2002, AIPC, 616, 262; *"Bolometer arrays for Mm/Submm astronomy"*

Staguhn, J.G., Benford, D.J., Chervenak, J.A., Moseley, S.H., Jr., Allen, C.A.; Stevenson, T.R.; Hsieh, W.-T., 2004, Proc. SPIE #5498, pp. 390-395; *"Design techniques for improved noise performance of superconducting transition edge sensor bolometers"*

Staguhn, J.D., Benford, D.J., Allen, C.A., Moseley, S.H., Sharp, E.H., Ames, T.J., Brunswig, W., Chuss, D.T., Dwek, E., Maher, S.F., Marx, C.T., Miller, T.M., Navarro, S. & Wollack, E.J. 2006, Proc. SPIE #6275, pp.62751D; *"GISMO: a 2-millimeter bolometer camera for the IRAM 30 m telescope"*

Willott, C. J., McLure, R. L. & Jarvis, M. J. 2003, ApJ, 587, pp. L15-L18; *"A $3\times10^9$ $M_{solar}$ Black Hole in the Quasar SDSS J1148+5251 at z=6.41"*

# Design Constraints on Transition Edge Sensor Pixels for Filled Arrays

J. A. Chervenak, C. A. Allen, D. Benford (NASA GSFC)
M. Niemack, J. Lau, T. Marriage, S. Staggs (Princeton U.)

We report on bolometer performance including noise and bandwidth of superconducting transition edge sensors (TES) on pixels suitable for close-packed, two-dimensional arrays. The electrothermal circuit of a TES consists of the superconducting sensor and wiring intimately coupled to a photon absorber that is thermally isolated from a heat sink held at the operation temperature of the instrument. In our case, the sensor is a Mo/Au bilayer with Mo/Nb wiring, the absorber is a shallow implanted layer or Bi film covering a silicon membrane, and the thermal isolation is micromachined constrictions in the thin (1-1.5 μm) membrane. Such a focal plane consists of metallized features making up the TES, the absorber coupled region, and vacuum gaps or supporting frame. Efforts to minimize these reflecting (TES) and transmissive (frame/gap) regions relative to the size and pixellation of the absorbing region compete with mechanical constraints as well as demonstrable electrical performance. Pixel designs for the Millimeter Bolometer Array Camera for the Atacama Cosmology Telescope and other receivers require high-speed, low-noise bolometers that can operate above 300 mK and fill the focal plane with absorber-coupled silicon membrane. Our collaborations have explored the phase space for integration of all-silicon absorbing focal planes with metallic detector components for 90 to 280 GHz imaging. We describe the results obtained during this pixel optimization. As possible, we generalize our study to TES designs for anticipated performance of direct-coupled focal planes operated at other bath temperatures and sensitive at other frequencies.

# Responsivity and Noise Measurements of Zero-Bias Schottky Diode Detectors

Jeffrey L. Hesler and Thomas W. Crowe

Virginia Diodes, Inc., Charlottesville, VA 22902, www.VADiodes.com

***Abstract* — Schottky barrier diodes can be used as direct detectors throughout the millimeter- and submillimeter-wave bands. When the diodes are optimized to have a low forward turn-on voltage, the detectors can achieve excellent frequency response and bandwidth, even with zero-bias. This paper reports on the characterization of VDI's zero-bias Schottky detectors. Responsivity typically ranges from 4,000 V/W at 100 GHz to 400 V/W at 900 GHz and each detector achieves good responsivity across the entire single-moded bandwidth of the input rectangular waveguide. Under low power operation the detectors achieve a measured noise-equivalent-power (NEP) of about 1.5x10$^{-12}$ W/√Hz, even without signal modulation. Such high sensitivity is expected for any zero-bias diode detector with high responsivity when there is no incident RF power; since only thermal noise can be generated under this condition. However, as the input power is increased, excess noise is generated. This noise typically has a 1/f power spectrum and is commonly known as flicker noise. Flicker noise becomes increasingly important as the input power is increased and signal modulation is generally required to achieve maximum sensitivity. The signal-to-noise of the VDI zero-bias detectors has been carefully measured as a function of input power and modulation rate. This data allows the user to understand the sensitivity of the detector under real operating conditions, and is therefore far more useful than the simple measurement of detector NEP with zero RF power, which is commonly quoted in the literature for new diode detector designs.**

***Index Terms* — Terahertz detectors, zero-bias detectors, noise-equivalent power, flicker noise.**

## I. Introduction

This article describes the characterization and measurement of the responsivity and noise properties of zero-bias Schottky detectors that have been developed at Virginia Diodes, Inc. The Schottky diode detector has a long history of use for the detection of power at mm- and submm-wavelengths [1]. Diode detectors can operate at ambient or cryogenic temperature and have an extremely fast response time compared with other room temperature detectors, such as Golay cells, pyroelectric detectors, or bolometers [2,3]. An important factor in considering the usefulness of all diode detectors is the excess noise sources beyond thermal and/or shot noise, such as 1/f or flicker noise. Although zero-bias diodes cannot generate significant excess noise at very low input power levels, as the input power is increased the flicker noise also increases and eventually becomes the dominant noise mechanism. Thus, characterization of the detector requires measurement of the diode's noise properties across the range of input power levels over which it will be used.

VDI's Schottky diode detectors use rectangular waveguide housings and the entire circuit is optimized for operation over the full single-moded waveguide band without any mechanical tuners. Their responsivity typically ranges from about 4,000 V/W at 100 GHz to 400 V/W at 900 GHz. The primary goal of this investigation has been to characterize the sensitivity of the VDI zero-bias detectors. Thus, this paper describes measurements of the diode's noise properties over a wide range of input power levels. The diode responsivity, NEP and signal-to-noise ratio (SNR) are presented.

## II. Diode I-V Characteristics

The VDI detector diodes are planar Schottky barrier diodes fabricated in a flip-chip configuration using the basic process described in [4]. This configuration, as shown in Fig. 1, allows for a low parasitic contact that is mechanically rugged and repeatable. The measured I-V of a WR-10 detector diode is shown in Fig. 2. In order to determine the theoretical voltage responsivity of the diode a least-squares curve fit was made between the measured data and the exponential Schottky diode I-V equation [5]. The measured and curve-fit data for the WR-10 diode near zero-bias are shown in Fig. 3. The least-squares curve fit parameters for this diode were determined to be $I_{sat}$=11 μA, Rs=19 Ω, Ideality Factor, η=1.13. The zero-bias junction resistance, dV / dI = $V_o$ / $I_{sat}$, is 2.6 kΩ; where $V_o = \eta kT/q$.

The intrinsic voltage responsivity of the diode can be determined from the diode I-V equation, as [6]

$$R_v = \left. \frac{-\frac{d^2V}{dI^2}}{\frac{dV}{dI}} \right|_{I=0} = \frac{1}{I_{SAT}} \qquad (1)$$

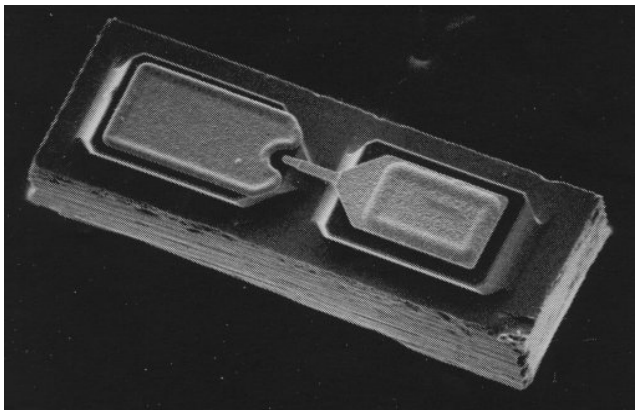

Fig. 1. Scanning electron micrograph of a planar Schottky barrier diode. Chip dimensions approximately 180x80x40 µm.

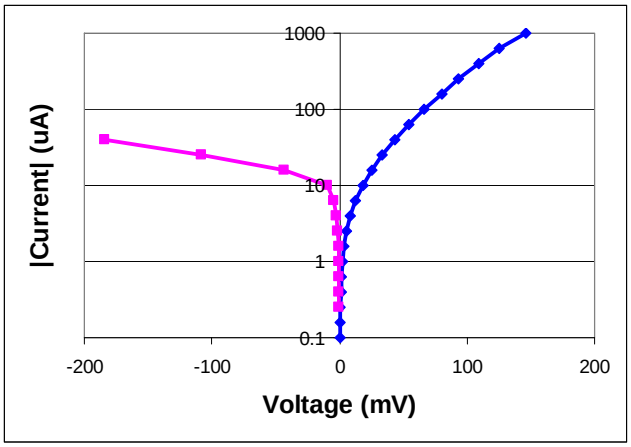


Fig. 2. The measured current-voltage characteristic of the zero-bias flip-chip WR-10 Schottky detector diode.

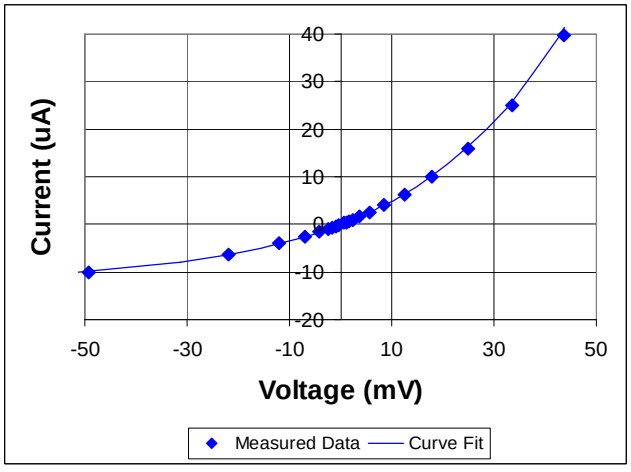


Fig. 3. Curve fit of exponential diode I-V of WR-10 detector diode to measured data near zero bias. Curve fit parameters Isat=11 µA, Rs=19 Ω, Ideality, η=1.13.

## III. MEASUREMENTS OF DETECTOR RESPONSIVITY

Measurements over the WR-10 frequency band were made of the voltage responsivity of the detector diode discussed in the previous section. The responsivity is shown in Fig. 4. The input power to the detector was kept in the range from 3-5 µW, which insured that the detector was operating in the square-law region. A WR-10 directional coupler was used to set the input power into the detector and to thereby eliminate the effect of standing waves on the measurement. The measured responsivity matches well with the predicted value of 6,500 V/W, indicating that the diode capacitance has only a small effect in this frequency range.

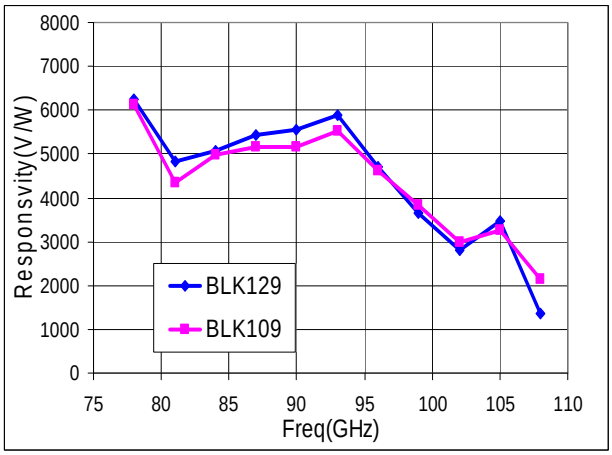


Fig. 4. Measured responsivity of two WR-10 ZBD detectors. The RF power was kept in the square-law region, and ranged from 3-5 µW over the band.

## IV. NOISE MEASUREMENTS OF SCHOTTKY DIODES IN THE LOW SIGNAL REGIME

As a start to understanding the noise properties of these detectors, measurements were made of their zero-bias noise properties. The test configuration consisted of a low noise operational amplifier (input noise 3.2 nV/√Hz) with a gain of 100 followed by a Tektronix TDS744 digital oscilloscope. In order to verify the accuracy of the system, the noise properties of 1 kΩ to 10 kΩ resistors were measured, and the measurements agreed with theoretical predictions to within 10%. Next, the thermal noise of a model WR-6.5ZBD detector was measured. This detector has a measured zero-bias junction resistance of 1.8 kΩ. As shown in Fig. 5, the measured noise was found to correspond to that of a noisy resistor with the same resistance.

When the detector is used to measure small signals, this thermal noise will be the dominant noise source. Thus, the measured noise voltage and responsivity can be used to calculate the NEP of the detector for low input power levels. The result for the WR-6.5ZBD detector, is shown is Fig. 6. The low power NEP varies from about 1.5 to 2 pW/√Hz across the detector band.

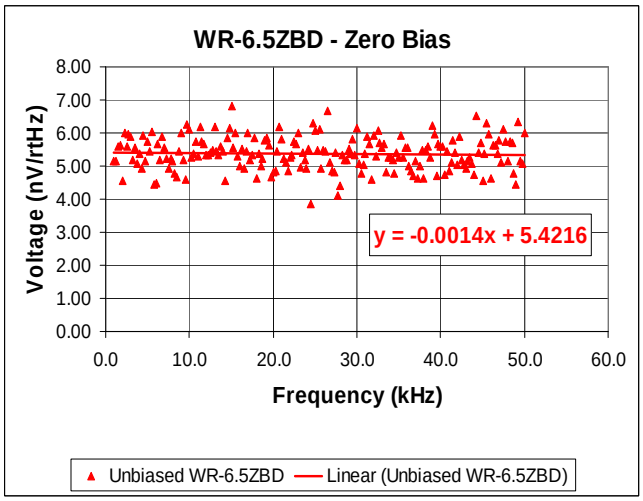


Fig. 5. The measured noise of a WR-6.5ZBD with no applied bias or RF power. The curve fit noise voltage of 5.4 nV/√Hz corresponds to the noise from a 1.8 kΩ resistor, which equals the measured junction resistance for this detector.

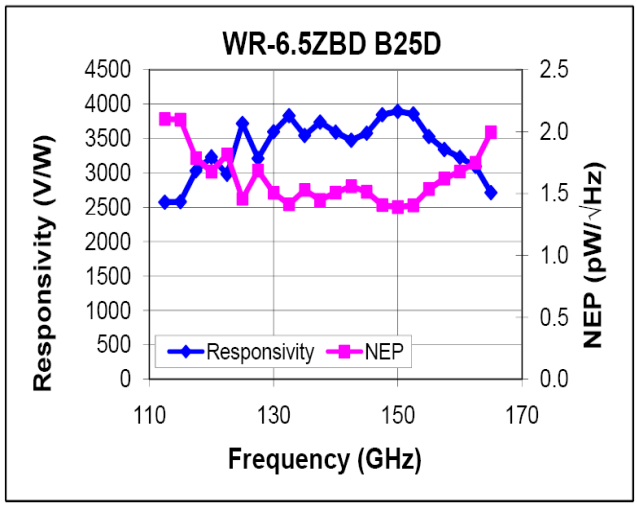


Fig. 6. The noise equivalent power of a WR-6.5ZBD calculated from the measured noise at zero-bias with no RF power and the measured responsivity as a function of frequency across the waveguide band of the detector.

## V. DYNAMIC RANGE OF SCHOTTKY DETECTORS

In order to characterize the performance of the WR-6.5ZBD under applied RF power, its noise properties were measured for varying levels of applied signal power. The measurement setup described in the previous section was used, with the addition of a DC block after the detector to avoid saturating the low-noise amplifier. The measured curves for applied power ranging from -18 dBm to -2 dBm are shown in Fig. 7. As is shown by the curve fits, the measured noise matches the expected 1/f shape.

Using the measured noise characteristics we can determine the effect of the flicker noise on the detector signal-to-noise as the applied power is increased. As was shown in Fig. 7, the flicker noise factor increases roughly linearly with the applied power. Figure 8 shows the measured signal-to-noise for the WR-6.5ZBD for modulation rates ranging from 10 Hz to 100 kHz. The top curve (blue) shows the signal-to-noise for an ideal square-law device without 1/f noise and ignoring saturation effects at large signal levels. The next curve (pink) shows the effect of detector saturation, which acts to lessen the S/N improvement as the input power is increased. The three remaining curves show the actual S/N of the detector as a function of input power and modulation rate. For very low modulation rates (~10Hz) the S/N saturates at rather low input powers, about -40 dBm. However, for 100kHz modulation the impact of the noise is greatly reduced resulting in improved S/N for detector operation at high signal levels.

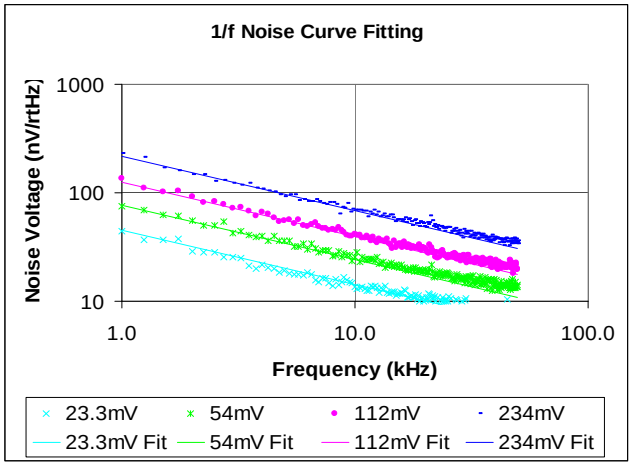


Fig. 7. The measured noise of a WR-6.5ZBD for varying levels of detected signal. The applied power levels were: -18 dBm for Vdet=23 mV, -13 dBm for Vdet=54 mV, -8 dBm for Vdet=112 mV, and -2 dBm for Vdet=234 mV.

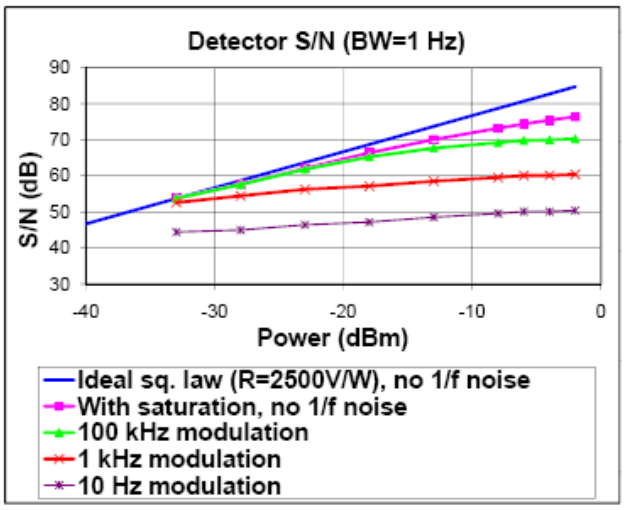


Fig. 8. The WR-6.5ZBD signal-to-noise ratio as a function of the applied signal power (-40 dBm to 0 dBm) and the signal modulation rate (100 kHz, 1 kHz, and 10 Hz). This measured data is compared to two ideal cases without excess noise, first assuming ideal square-law response and second including diode saturation effects.

## VII. Conclusion

Measurements of the responsivity and noise properties of VDI's zero-bias detectors have been performed. These detectors have been demonstrated to be extremely fast devices ($\tau << 1$ nS) with broad operational bandwidth and high sensitivity. At small signal levels they have excellent NEP; approximately 1.5 pW/√Hz near 150 GHz; rising to approximately 20 pW/√Hz at 800 GHz. This low-signal NEP could be significantly improved by optimizing the signal coupling to the detector over a narrower frequency band. However, the detector is perhaps more useful for general applications when the coupling is optimized across the full waveguide band.

In large signal applications the flicker noise becomes increasingly significant; and thus modulation is required to achieve optimal sensitivity. The effect of diode saturation and flicker noise on the signal-to-noise ratio of the detectors, as a function of modulation, has been investigated and the results were depicted in a convenient graph.

These results have confirmed that measurements of the NEP of diode detectors at very low power levels is not sufficient to characterize their performance in the broader range of applications where higher power levels are likely to be encountered.

## Acknowledgement

The development of the zero-bias detectors was initially supported by two ARO SBIR contracts (DAAD19-02-C-0013, W911NF-04-C-0141). These noise measurements were supported by a NASA/JPL SBIR (NNC06CA22C).

## References

[1] H. C. Torrey and C. A. Whitmer, Crystal Rectifiers. vol. 15, M.I.T. Rad. Laboratory Ser. New York: McGraw-Hill, 1948.
[2] P.R. Griffiths and J.A. de Haseth, 'Fourier Transform Infrared Spectrometry', Wiley Interscience, New York, 209–212 (1986).
[3] P. R. Griffiths and C. C. Homes, 'Instrumentation for far-infrared spectroscopy', Handbook of Vibrational Spectroscopy, Volume 1 - Theory and Instrumentation, Wiley, New York, 2001.
[4] W.L. Bishop, E. Meiburg, R.J. Mattauch, T.W. Crowe and L. Poli, A Micron-Thickness, Planar Schottky Diode Chip For Terahertz Applications With Theoretical Minimum Parasitic Capacitance, 1990 IEEE MTT-S Int. Mic. Symp. Digest, pp. 1305-1308, May 1990
[5] S.M. Sze, Physics of Semiconductor Devices, Second Ed., John-Wiley & Sons, New York, 1981.
[6] A.M. Cowley and H.O. Sorenson, "Quantitative Comparison of Solid-State Microwave Detectors," MTT-14, No. 12, pp. 588-602, Dec 1966.

# An Antenna Coupled Cold-Electron Bolometer for High Performance Cosmology Instruments

Leonid Kuzmin[1], Ghassan Yassin[2], Stafford Withington[3] and Paul Grimes[2]
[1] Chalmers University of Technology, S-41296 Gothenburg, Sweden,
[2] Oxford University, United Kingdom
[3] Cambridge University, United Kingdom

*Abstract*— **The newly emerging CMB polarization experiments (eg CLOVER, EBEX) employ detectors comprising transition-edge sensors (TES). The detectors will operate at temperatures of approximately 100 mK and will be read out by time division or frequency multiplexed SQUID amplifiers. Although detectors are expected to deliver impressive sensitivity, future space B-mode experiments (eg B-Pol) can benefit greatly from an increase in sensitivity, much higher saturation power, and flexibility in their realization on planar substrates.**

**In this paper we describe a Cold-Electron Bolometer (CEB), which is a serious candidate for the next space cosmology missions. We analyze the suitability of various devices for the 70 GHz channel of the proposed B-Pol polarimeter. The detector may also be of interest to ground-based experiment as a result of the simplicity of its integration to planar circuit technology. The Capacitively Coupled CEB is a planar antenna-coupled superconducting detector with high sensitivity and high dynamic range. The CEB can meet noise requirements with both SQUID and JFET readouts. The SQUID readout can be used the same as for TES bolometers with typical SQUID sensitivity of 0.5 pA/Hz$^{1/2}$. An attractive realisation of the detector at millimetre wavelengths is to fabricate the CEB directly connected to the antenna on a planar substrate. The proper matching can be achieved by fabrication of an absorber strip of resistance equal to the wave impedance of the antenna.**

**Three variants of the CEB concept have been considered. The optimum realization of a CEB with SIN and SN tunnel junctions gives noise less than photon noise with SQUID readout. Estimations of the CEB noise with a JFET readout (at 300 K and 4.2 K) has shown an opportunity to realize background-limited performance for realistic power loading. Matching to a JFET is best obtained by using the SCEB (with weak superconducting absorber), and choosing a voltage bias in the flat region of the IV curve with very high dynamic resistance. This configuration can gives photon noise limited performance with JFET readout over a wide range of optical loading levels. Another possibility for matching to a JFET is a current-biased series array of CEBs with normal metal absorbers, connected in parallel for HF signal.**

**The antenna-coupled CEB bolometer is easy to couple to a wide range of planar antennae systems, either on bulk or membrane substrates. Applicability of the CEB to B-Pol and similar space missions looks very promising for all of the frequency bands and with both JFET and SQUID readout schemes.**

*Index Terms*— Cold-Electron Bolometer, SIN tunnel junction, Josephson junction, Andreev contact, SQUID readout

Manuscript received October 3, 2007. L. Kuzmin is with the Chalmers University of Technology, 412 96 Gothenburg, Sweden (phone: +46 31 7723608; fax: +46 31 7723471; e-mail: Leonid.Kuzmin@ mc2.chalmers.se).

## I. Introduction

Recent Cosmology experiments have discovered that the Universe consists mainly of mysterious Dark Energy and Dark Matter [1]. Indeed, in 2006, a Nobel Prize was awarded for the experimental observation of anisotropies in the Cosmic Microwave Background (CMB) radiation, and the subsequent realization that the expansion of the Universe is controlled by unknown forces [2]. There are several cosmology instruments (B-Pol [3], BOOMERanG, [4], CLOVER [5], EBEX, BICEP, QUIET,) that are being designed to measure the polarization state of the Cosmic Microwave Background (CMB), in particular the *B*-mode polarization, which is generated by primordial gravitational waves.

It is well known, however, that ground-based experiments are severely limited by atmospheric noise even at best sites. Consequently, space-borne CMB polarization instruments are now being planned both in the USA and Europe. A European consortium has already been assembled to design the next ESA CMB cosmology instrument. An expression of interest has recently submitted to ESA, as part of the Cosmic Vision Call, to support a medium-scale space mission called B-Pol [3] .

A new generation of detectors is needed for these advanced telescopes, and these detectors must achieve sensitivities better than $\sim 10^{-18}$ W/Hz$^{1/2}$. One of these technologies is the Capacitively Coupled Cold-Electron Bolometer (CEB) [6]-[8]. The CEB can be used with both JFET [9] and with SQUID readout [6],[8]. The JFET readout has been used for the latest astronomy missions, and the SQUID readout and multiplexing has been developed for TES (Transition-Edge Sensor) bolometers [10,11]. Overall, the goal is to achieve, with a CEB read out by a JFET or SQUID, a noise-equivalent power that is less than the photon noise of the CMB radiation.

The CEB is a planar antenna-coupled superconducting detector with high sensitivity and high dynamic range. It operates through electron cooling by SIN tunnel junctions, and with strong electrothermal feedback [6]. To achieve noise matching to the estimated in-flight optical power load, different concepts of the CEB, with SQUID and JFET readouts, must be analyzed. In this paper, we analyze an optimal configuration having one SIN junction and an Andreev SN contact, and SQUID readout. We also analyse a SCEB with a superconducting absorber, and a parallel/series array of CEBs with JFET readout for the 70 GHz channel of B-Pol.

To increase the CEB efficiency in voltage-biased mode, for current readout, an optimal configuration with a capacitively coupled SIN junction and an Andreev SN contact [12] has been selected (Fig. 1). This concept has been invented to improve the noise properties by increasing the responsivity of the CEB with SQUID readout. An important feature of the design is that the volume of the normal metal is partly squeezed due to the proximity effect of the superconducting electrode of the Andreev contact. This squeezing further increases the efficiency of the electron cooling without degrading the HF coupling.

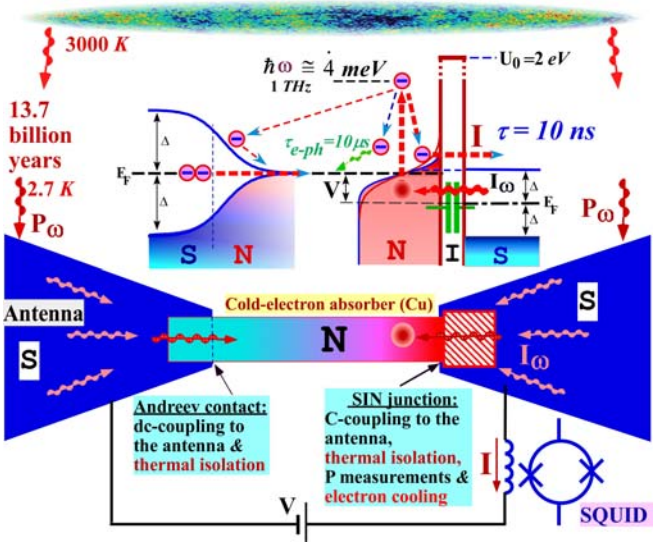


Fig 1. Schematic of the optimal Cold-Electron Bolometer (CEB) with capacitive coupling to the antenna and a SQUID readout. The CEB comprises a planar superconducting antenna and an absorber coupled through the capacitance of an SIN tunnel junction, and an SN Andreev contact. The SIN tunnel junction is used also for electron cooling, and for reading out the signal with a SQUID.

Detection using this device is obtained by allowing the incoming signal to pass from the antenna to the absorber through the capacitance of a tunnel junction and an Andreev contact. RF matching is realized by the resistance of a normal absorber, which is independent of the tunnel junction parameters.

The concept is based on *direct electron cooling* of the absorber, which provides strong *negative electrothermal feedback* for the signal. This feedback is analogous to the TES [10,11], but artificial dc heating is replaced by *direct electron cooling* to a minimum temperature. This innovation can lead to a major breakthrough in realizing supersensitive detectors. The noise properties of this device are improved considerably by decreasing the electron temperature. The loop gain of the electrothermal feedback can exceed 1000. The response time is reduced, by electrothermal feedback, to 10 ns compared to the intrinsic e-ph time constant of 10 μs.

The CEB in voltage-biased mode allows a substantial increase in the dynamic range, by removing incoming power from the absorber. The current flowing through the tunnel junction is readout by a SQUID, which intrinsically has a high dynamic range. The CEB with one SIN junction and one Andreev contact has almost twice the responsivity of the traditional CEB with two SIN junctions in series.

## II. Model

In what follows we shall use the basic concept of the CEB with strong electrothermal feedback due to electron cooling. This structure has been analyzed in detail in Ref. [6],[13]. The operation of CEB can be described using the heat balance equation:

$$P_{cool}(V,T_e,T_{ph})+\Sigma\Lambda(T_e^5-T_{ph}^5)+\frac{V^2}{R_j}+I^2R_{abs}+C_\Lambda\frac{dT}{dt}=P_0+\delta P(t) \quad (1)$$

Here, $\Sigma\Lambda(T_e^5 - T_{ph}^5)$ is the heat flow from the electron to the phonon subsystems in the absorber, $\Sigma$ is a material constant, $\Lambda$ is the volume of the absorber, $T_e$ and $T_{ph}$ are, respectively, the electron and phonon temperatures of the absorber; $P_{cool}(V,T_e,T_{ph})$ the cooling power of the SIN tunnel junction; $C_\Lambda = \Lambda\gamma T_e$ is the specific heat capacity of the absorber; Rj the subgap resistance of the tunnel junction; Rabs the resistance of the absorber; $P(t)$ the incoming rf power. We can separate Eq. (1) into the time independent term,

$\Sigma\Lambda(T_{e0}^5 - T_{ph}^5) + P_{cool\,0}(V,T_{e0},T_{ph}) = P_0$, and the time dependent term,

$$(\partial P_{cool}/\partial T + 5\Sigma\Lambda T_e^4 + i\omega C_\Lambda)\delta T = \delta P\,. \quad (2)$$

The first term, $G_{cool}=\partial P_{cool}/\partial T$, is the cooling thermal conductance of the SIN junction that gives the negative electrothermal feedback (ETF); when it is large, it reduces the temperature response $\delta T$ because cooling power, $P_{cool}$, compensates the change of signal power in the bolometer. The second term, $G_{e-ph} = 5\Sigma\Lambda T_e^4$, is electron-phonon thermal conductance of the absorber. From Eq. (2) we define an effective complex thermal conductance which controls the temperature response of CEB to the incident signal power

$$G_{eff} = G_{cool} + G_{e-ph} + i\omega C_\Lambda \quad (3)$$

In analogy with TES [11], the effective thermal conductance of the CEB is increased by the effect of electron cooling (negative ETF).

Here we assume that the SIN tunnel junction is voltage-biased, and the current is measured by a SQUID [6],[12]. The sensitivity of the device is then characterized by the current responsivity $S_I$, which is the ratio of the current change and the change in the power load of the bolometer,

$$S_I=\frac{\partial I_\omega}{\partial P_\omega}=\frac{\partial I/\partial T}{G_{cool}+G_{e-ph}+i\omega C_\Lambda}=\frac{\partial I/\partial T}{G_{cool}}\frac{L}{(L+1)[1+i\omega\tau]} \quad (4)$$

where $L = G_{cool}/G_{e-ph} >> 1$ is ETF gain and

$$\tau = C_\Lambda/G_{e-ph} = \tau_0/(L+1) \quad (5)$$

is an effective time constant, $\tau_0 = C_\Lambda/G_{e-ph}$ ($\cong 10\mu s$ at 100 mK).

The strength of the electrothermal feedback is estimated as:

$$L(\omega) = \frac{G_{cool}}{G_{e-ph}(1+i\omega\tau)} = \frac{\partial I/\partial T}{G_{cool} + G_{e-ph} + i\omega C_\Lambda} \quad (6)$$

Noise properties are characterized by the *NEP*, which is the sum of three different contributions:

$$NEP^2_{total} = NEP^2_{e-ph} + NEP^2_{SIN} + \delta I^2 / S_I^2 \quad (7)$$

$$NEP^2_{e-ph} = 10 k_B \Sigma \Lambda (T_e^6 + T_{ph}^6) \quad (8)$$

is the noise associated with electron-phonon interaction; $NEP^2_{SIN}$ is the noise of the SIN tunnel junctions, and the last term $\delta I^2/S^2_I$ is the noise of an amplifier (SQUID): $\delta I$, is expressed in pA/Hz$^{1/2}$.

The noise of the SIN tunnel junctions, $NEP^2_{SIN}$ , has three components: shot noise $2eI/S^2_I$, the fluctuations of the heat flow through the tunnel junctions, and the anticorrelation term between these two processes [13],[14].

$$NEP^2_{SIN} = \delta P_\omega^2 - 2\frac{\delta P_\omega \delta I_\omega}{S_I} + \frac{\delta I_\omega^2}{S_I^2} \quad . \quad (9)$$

This anticorrelation is a form of the electrothermal feedback discussed earlier by Mather [15].

## III. The CEB with SIN tunnel junction and SN contact and SQUID readout

The analysis of the Cold-Electron Bolometer (CEB) shows that the optimal configuration of the bolometer in voltage-biased mode is a CEB with a single SIN Junction and an Andreev SN contact [12]. Any use of a double junction in

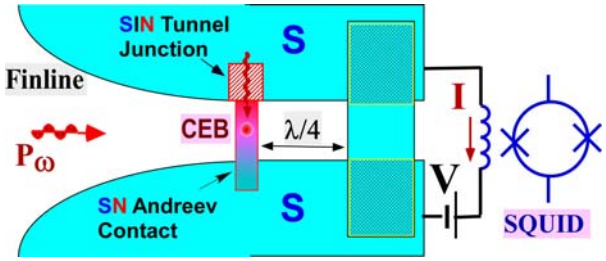


Fig. 2. A Cold-Electron Bolometer (CEB) coupled to a finline antenna with SQUID readout.

voltage-biased mode [6,8] would lead to the splitting power between two junctions and a degradation of responsivity. The optimal readout is a SQUID, and voltage bias.

We have analyzed the concept of an optimal cold-electron bolometer for 70 GHz channel of B-Pol polarometer in the presence of the typical power load ($P_0$ = 0.2 pW per polarization component) [3].

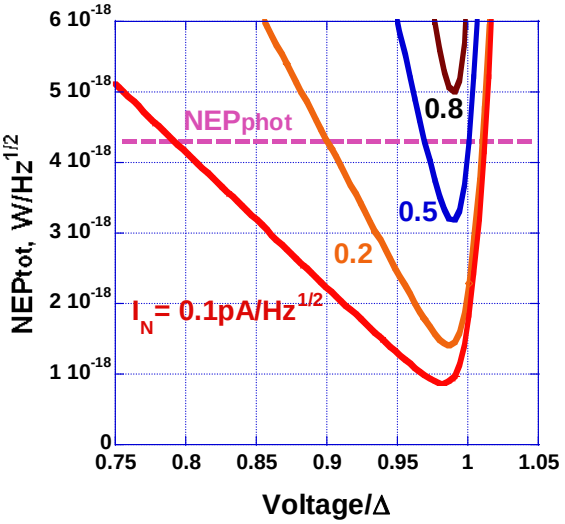


Fig. 3 Total NEP of the CEB with SIN tunnel junction for the 70 GHz channel, with a SQUID noise current from 0.1 pA/Hz$^{1/2}$ and 0.8 pA/Hz$^{1/2}$. R=0.2 kOhm, S=2μm$^2$, Vol=0.03um$^3$, power load $P_0$ = 0.2 pW, T=100 mK. The NEPphot= 4.3*10$^{-18}$ W/Hz$^{1/2}$ is shown by dashed line.

Photon noise: $NEP_{phot} = \sqrt{2P_0 * hf}$ . (10)

For the 70GHz channel, NEPphot= 4.3*10$^{-18}$ W/Hz$^{1/2}$.

Fig. 3 shows the results of a simulation of a CEB with a single SIN junction, with realistic parameters for the tunnel junction and absorber, and values of SQUID noise from 0.1 pA/Hz$^{1/2}$ to 0.8 pA/Hz$^{1/2}$. The level of NEPphot has been achieved for SQUID noise lower than 0.5 pA/Hz$^{1/2}$

## IV. The SCEB with SIS' and Josephson junctions in *voltage-biased mode* with JFET readout

We shall now discuss a second scheme, which matches the moderate dynamic resistance of the CEB (~1÷10 kOhm) to the high noise equivalent resistance of a JFET (~1 MΩ). To achieve noise matching to a JFET, a Cold Electron Bolometer with a weak Superconducting absorber (SCEB) has been proposed [9]. In voltage-biased mode, with a voltage higher than the difference gap, an SIS´ junction has a considerably increased dynamic resistance that is used to suppress voltage noise of JFET. However, the use of two series tunnel junctions is not optimal for voltage-biased mode [12]. A CEB with an SIS´ junction and a SS´ Andreev-type contact (similar to optimal bolometer with SIN and SN contacts [12]) could solve this problem, but would bring complicated 3-layer technology.

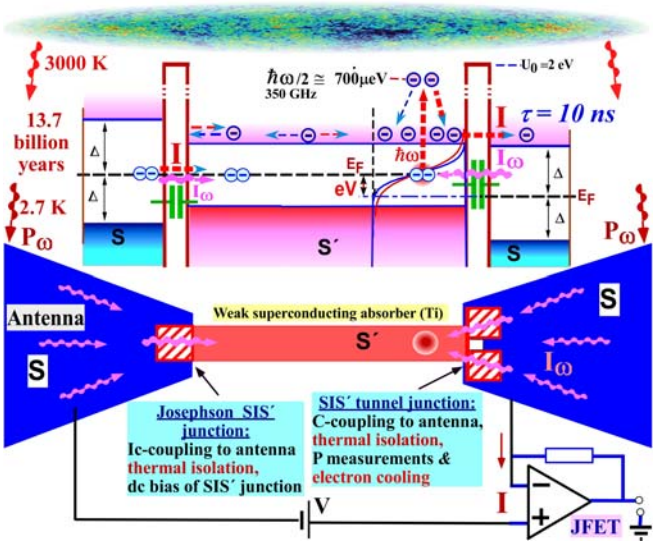


Fig 4. Schematic of a Superconducting Cold-Electron Bolometer (SCEB) with SIS´ and Josephson Tunnel Junctions and a JFET readout [16]. The SIS´ junction is used for capacitive coupling to the antenna, thermal isolation, electron cooling and dc readout by a JFET. The Josephson junction is used for dc and RF contacts, and for thermal isolation. SIS´ junction is made in a loop geometry for easy suppression of a critical current by a weak magnetic field.

A novel concept of a Superconducting Cold-Electron Bolometer (SCEB) with SIS´ and Josephson tunnel junctions (Fig. 4) has been proposed recently [16]. The main innovation in comparison with previous concepts of the CEB in voltage-biased mode is the effective use of a Josephson junction for dc and RF contacts, and for thermal isolation. The SIS´ junction (for RF coupling, thermal isolation, electron cooling and dc readout) is proposed in a loop geometry for suppressing the critical current by a weak magnetic field. A remarkable feature of this concept is that the critical current of the Josephson junction is not completely suppressed by a weak magnetic field. As a result, a robust two layer technology can be used in fabrication of both the SIS´ and Josephson tunnel junctions simultaneously. In this paper we analyzed a realization of the SCEB for the 70 GHz channel of B-POL.

For RF coupling we have chosen a 4-probe antenna in circle waveguide with direct connection of SCEBs to the antenna (Fig. 5a) [16]. In contrast to a previous concept of the SCEB with coplanar lines [9], the RF region is strictly limited by the circular waveguide area. The optimal point for the CEB is shown in the diagram, where the RF current is greatest. The problem of DC bias of an SIS´ junction could be solved by introducing one more Josephson junction at the right end of the absorber (Fig. 5b). Two opposite SCEBs are connected in parallel, for each polarization, by dc leads, and measured by JFET in voltage-biased mode. The optimal bias point of SIS´ junction is between the difference and sum gaps where the I-V curve has increased dynamic resistance (Fig. 6). For the JFET noise, 3 nV/Hz$^{1/2}$ & 5 fA/Hz$^{1/2}$, the effective noise impedance is around 600 KOhm. The suppression of the JFET voltage noise is important for this realization. Current noise in a JFET are rather low, at the level of 5fA/Hz$^{1/2}$. The high noise impedance of a JFET amplifier is one of the reasons why a low-ohmic TESs [9,10] cannot be matched with JFETs.

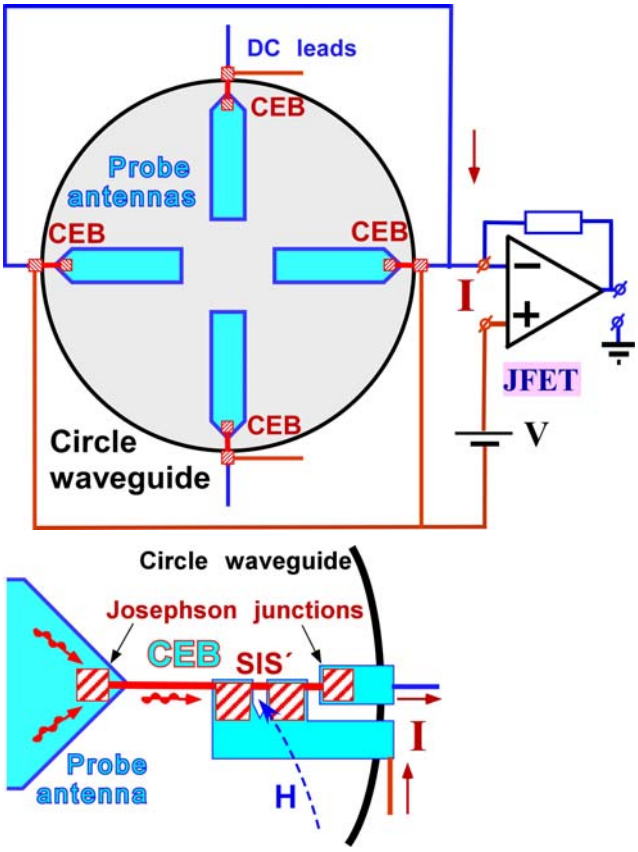


Fig 5. a) Direct connection of CEBs to a 4-probe antenna in a circular waveguide [16]. CEBs in opposite probes are connected in parallel for each polarization. b) A detail of the CEB connected to a probe antenna with an additional Josephson junction for dc bias supply.

For the analysis we use a previous concept of the CEB with strong electrothermal feedback, due to electron cooling [6,8,13], and with a superconducting absorber [9]. For an optical power load of $P_0$ = 0.2 pW per polarization for the 70 GHz channel of B-Pol, the photon noise is NEPphot = 4.3*10$^{-18}$ [3].

Figure 3 shows simulations of the different contributions to

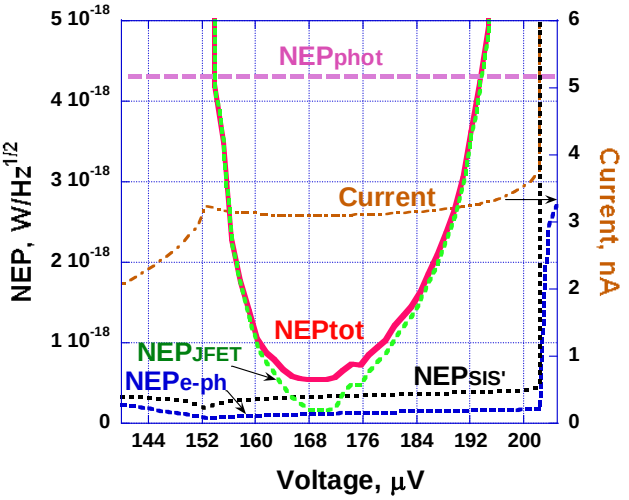


Fig. 6. NEP components of the SCEB with JFET readout for $I_{JFET}$=5 fA/Hz$^{1/2}$, $V_{JFET}$=3 nV/Hz$^{1/2}$, R=1 kOhm, $\Delta$=0.02μm$^3$, power load $P_0$ = 0.2 pW per polarization. IV curve is shown for estimation of a high dynamic resistance of the junctions. The NEPphot= 4.3*10$^{-18}$ W/Hz$^{1/2}$ is shown by dashed line.

the total NEP of the bolometer. We see that for a range of bias voltage from 155 μV to 195 μV, the total NEP of the SCEB is well below the photon noise: $NEP_{tot} < NEP_{phot}$. The range of voltages from 155 μV to 170 μV is not recommended for use because, due to negative slope the IVcurve, the operating point would be unstable. In addition, the $NEP_{tot}$ of the SCEB is dominated at the optimum point by the shot/heat noise of the detector, $NEP_{SIS'}$, (9) corresponding to the background limited mode of operation. Equation (9) includes the effect of the noise reduction of SIS′ tunnel junction due to the anticorrelation term. The final noise, $NEP_{SIS'}$, is less than noise components. The effect is stronger than for SIN junction noise [12] due to the well-defined level of the quasiparticle energy just near the superconducting gap.

## V. The CEB Array with SIN Tunnel Junctions in *Current-Biased Mode* with JFET Readout

An alternate mode of CEB operation is a novel concept employing a parallel/series array of CEBs with SIN Tunnel Junctions, for effective matching to a JFET amplifier [17] (Fig. 7). Previous analysis of a single current-biased CEB with JFET readout showed that the JFET input voltage noise limits the sensitivity [9]. The main reason is the degradation of voltage responsivity under high optical power load. The main innovation of the CEB array is the distribution of power between N series CEBs, and summarizing the increased response from the array. Effective distribution of power is achieved by a parallel connection of CEBs, which couple to the RF signal through additional capacitances (Fig. 7b). The response is increased because the CEB is sensitive to the level of power, and the power is decreased N times for the individual CEBs, with a proportional decrease of absorber overheating.

The high sensitivity of the CEB for small power loads has been analyzed theoretically [6,8,13], and demonstrated experimentally [18]. In this paper we analyze a realization of the CEB array for the 70 GHz channel of B-Pol. For RF coupling we analyze a system with the direct insertion of the CEB arrays into a 4-probe antenna inside a circular waveguide (Fig. 7). The system is similar to the previous 4-probe system with SCEBs (Fig. 5), with the replacement of the SCEBs by the CEB arrays, and with the replacement of the parallel connection to a series connection of opposite CEBs. The problem of DC biasing the CEB arrays can be solved by interconnecting opposite probes by a narrow strip with very high inductive impedance (Fig. 7a). A small isolation layer should be placed between strips in the centre of the waveguide. Two opposite CEB arrays are connected in series to get two-times higher response for each polarization. The voltage response is measured by a JFET amplifier in a current-biased mode. The main purpose of this concept is to match the total dynamic resistance of the array to the noise impedance of a JFET (~0.6 MΩ). The power should be divided between the CEBs in the array to increase the responsivity due to lower overheating and moderate electron cooling.

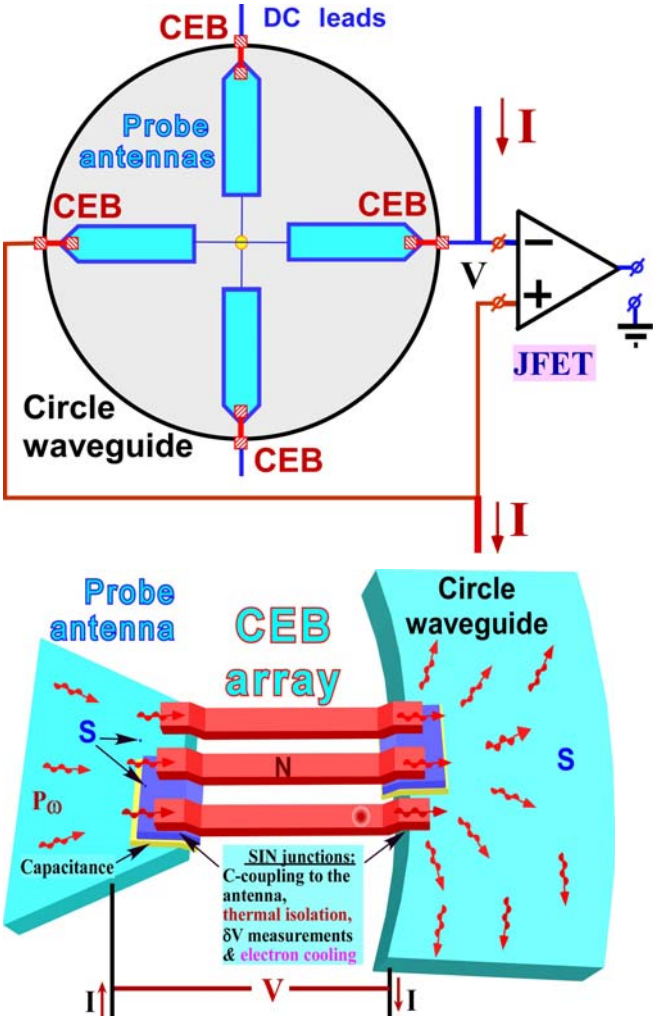


Fig 7 a) Direct connection of CEBs to a 4-probe antenna in circlar waveguide [17]. CEBs in opposite probes are connected in series by a narrow strip for each polarization. b) Each probe is really connected to an array of CEBs with series connection for DC and parallel for RF (schematically shown as a single CEB in the top figure). For RF the CEBs are connected in parallel by additional capacitances between superconducting islands and antenna.

The operation of a CEB array can be analyzed using the heat balance equation for a single CEB [13] taking into account power distribution between the N bolometers. The responsivity $S_V$ is described by the voltage response to an incoming power

$$S_V = \frac{\delta V_\omega}{\delta P_\omega} = \frac{\partial V / \partial T}{G_{e-ph} + 2G_{SIN} + i\omega C \Lambda} \qquad (10)$$

The second term

$$G_{SIN} = \frac{\partial P_{SIN}}{\partial T} - \frac{\partial P_{SIN}}{\partial V}\left(\frac{\partial I}{\partial T} / \frac{\partial I}{\partial V}\right) \qquad (11)$$

is the cooling thermal conductance of the SIN junction, $G_{SIN}$, which gives some electron cooling and help to avoid overheating of the absorber.

Noise properties are characterized by the noise equivalent power (*NEP*), which is the sum of three contributions:

$$NEP_{tot}^2 = N * NEP_{e-ph}^2 + N * NEP_{SIN}^2 + NEP_{JFET}^2. \qquad (12)$$

Here $NEP_{e\text{-}ph}$ is the same electron-phonon noise as in Eq. 8. $NEP_{SIN}$ is the noise of the SIN tunnel junctions. The SIN noise has three components: the shot noise $2eI/S2I$, the fluctuations of the heat flow through the tunnel junctions and the correlation between these two processes [13-15]:

$$NEP^2_{SIN} = \frac{\delta I^2_\omega}{(\frac{\partial I}{\partial V} S_V)^2} + 2\frac{< \delta P_\omega \delta I_\omega >}{\frac{\partial I}{\partial V} S_V} + \delta P^2_\omega \quad (13)$$

Due to this *correlation* the shot noise is increased at 30-50% in contrast to the CEB in voltage-biased mode (9) where strong *anti-correlation* decreases the shot noise.

The last term is due to the voltage $\delta V$ and current $\delta I$ noise of a JFET, which are expressed in nV/Hz$^{1/2}$ and pA/Hz$^{1/2}$:

$$NEP^2_{JFET} = (\delta V^2 + (\delta I * (2Rd + Ra) * N)^2) \Big/ S_V^2 \quad (14)$$

The strong dependence on N, decreasing this noise is included in the responsivity $S_I$, which is proportional to N.

The estimations were made for the 70 GHz channel of BPol.

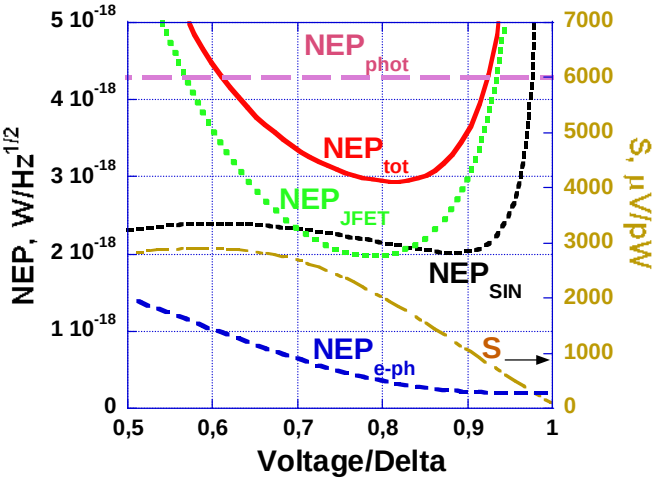


Fig. 8. NEP components of the array of 10 CEBs with JFET readout at 70 GHz with power load of 0.2 pW for $I_{JFET}$=5 fA/Hz$^{1/2}$, $V_{JFET}$=3 nV/Hz$^{1/2}$, R=4 kOhm, $\Lambda$=0.03μm$^3$, T=100 mK.

We have simulated arrays of CEBs with different numbers of CEBs, from 1 to 14, to achieve a low NEP with JFET readout. Fig. 8 shows typical results of an NEP simulation for the optimal array of 10 CEBs. We see that for a range of normalized voltage from 0.62 to 0.93, the total NEP of the CEB array is less than the photon noise. At the optimum point, background limited performance is realized (the total noise is determined by the noise of SIN junctions, $NEP_{SIN}$, (13) due to background power load).

The dependence of the noise components on the number of bolometers is shown in Figure 9. The total NEP decreases to a level less than photon noise for a number of CEBs larger than 6 (3 for each probe). It is achieved mainly through the suppression of the JFET noise component due to the increased responsivity (10). Figure 9 demonstrates a strong linear increase of the responsivity proportional to N when the number of bolometers is increased. The noise of the JFET (14) is proportionally decreased, which is the main goal of this realization. Around the optimum point (N=10) the $NEP_{JFET}$ is less than $NEP_{SIN}$ , which is a manifestation of background-limited operation. The $NEP_{SIN}$ increases proportionally to √N (according to eq. 6), but decreases due to a decrease of the heat flow (and current) and an increase of the responsivity S. These two effects approximately compensate each other, and $NEP_{SIN}$ is not very sensitive to the number of the bolometers. The most surprising result is that the NEPeph (8) is not increased proportionally to the number of bolometers when the total volume of absorber is increased proportionally to N. The reason is due to a compensation of this dependence by some decrease in Te that is in the 6$^{th}$ power for NEPeph (8).

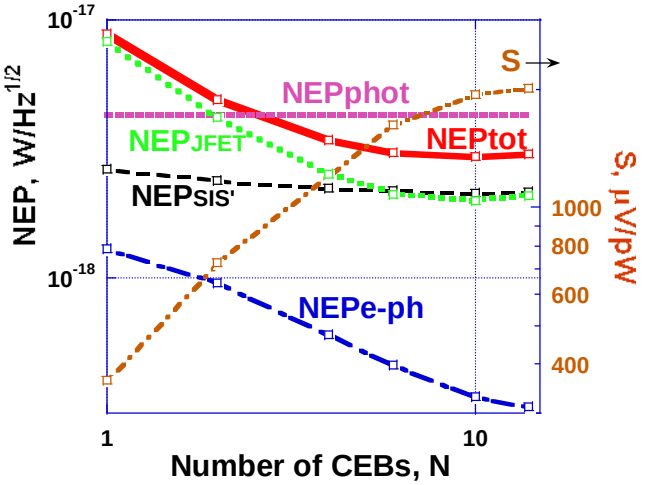


Fig. 9. NEP components and photon NEP in dependence on the number of CEBs in a series array. The parameters of CEBs are the same as in Fig. 8. The responsivity S is shown for illustration of the effect of the CEB number.

*Optimal number of CEBs in series array.* The optimal number is determined mainly by the power load Po and the volume of absorber $\Lambda$. The general rule of array design is the following: the number of bolometers, N, should be increased to split Po between bolometers up to the point when $P_0/N = P_{ph}$ , where $P_{ph} = T^5_{ph}\,\Sigma\Lambda$. The phonon power is determined by only one parameter, the volume of the absorber, $\Lambda$. There is no need to increase the number of bolometers more than this figure because the optical power loading in each bolometer becomes less than the power from phonons. Responsivity is saturated after this level.

## VI. Conclusion

We have analyzed several variations of the concept of a Cold-Electron Bolometer (CEB) with an SIN (Superconductor-Insulator-Normal Metal) or SIS´ (Superconductor-Insulator-Weak Superconductor) tunnel junctions for realization of the requirements of future space projects. These concepts give unique opportunities to achieve NEPs less than photon noise for any optical power loading with standard JFET or SQUID readouts. Three variants of the CEB concept have been considered for the 70 GHz channel of B-Pol. The first optimal solution is a CEB with SIN and SN tunnel junctions which gives noise less than photon noise with SQUID readout.

For matching the device to a JFET readout we have analyzed the SCEB (with weak superconducting absorber) choosing a voltage bias in the flat region of the IV curve with very high dynamic resistance. This configuration can give background

limited performance with total noise considerably less than photon noise. Another concept for matching with JFET readout is a current-biased series array of CEBs with normal metal absorbers, connected in parallel for the RF signal. This concept has also demonstrated total noise less than the background photon noise.

Several variants of RF coupling of CEBs to finline and a 4-probe antenna have been proposed. We have shown that the CEB is an ideal antenna-coupled bolometer that can be easily integrated to any antenna system on a bulk or membrane substrate. Applicability of the CEB to BPol and similar space missions looks very promising for the whole range of frequency bands, and with both JFET and SQUID readout.

The authors would like to thank Paolo de Bernardis, Philip Mauskopf and Dmitri Golubev for interesting discussions. The work was supported by SNSB and STINT Swedish agencies.

## REFERENCES

[1] C. Seife, BREAKTHROUGH OF THE YEAR 2003: "Illuminating the Dark Universe", *Science*, vol. 302, pp. 2038-2039, Dec. 2003.

[2] *2006 Nobel Prize in Physics* for discovery of the blackbody form and anisotropy of the cosmic microwave background radiation.

[3] B-Polarization Satellite Proposal for Detecting Primordial Gravitational waves from Inflation. ESA, June 2007. http://www.b-pol.org/

[4] BOOMERANG - balloon telescope: Measurements of CMB Polarization, http://oberon.roma1.infn.it/boomerang/b2k/

[5] G. Yassin et al., "CLOVER- A Novel Instrument for Measuring the CMB Polarization", Proc. of the 15th Int. Symposium on Space Terahertz Technology, pp 152-160, UMASS, USA (2004).

[6] L. Kuzmin "Ultimate Cold-Electron Bolometer with Strong Electrothermal Feedback", *Proc. of SPIE conference "Millimeters and Submillimeter Detectors"*, 5498, p 349, Glasgow, June 2004.

[7] L. Kuzmin "On the Concept of a Hot-Electron Microbolometer with Capacitive Coupling to the Antenna", Physica B: Condensed Matter, 284-288, 2129 (2000).

[8] L. Kuzmin D. Golubev "On the concept of an optimal hot-electron bolometer with NIS tunnel junctions". Physica C 372-376, 378 (2002)

[9] L. Kuzmin, P. Mauskopf, and D Golubev, "Superconducting Cold-Electron Bolometer with JFET Readout for OLIMPO Balloon Telescope". *Journal of Physics: Conference Series (JPCS)*, Volume 43, pp. 1298-1302 (2006).

[10] K. Irwin. Applied Physics Letters, 66, (1995) 1998

[11] A. Lee, P. Richards, S. Nam, B, Cabrera, K. Irwin, *Applied Physics Letters*, 69, (1996) 1801.

[12] L. Kuzmin, "Optimal Cold-Electron Bolometer with an SIN Tunnel Junction and an Andreev Contact". Proc. of the 17th Int. Symp. On Space Terahertz Technol., ISSTT-2006 (Paris, May 2006).

[13] D. Golubev and L. Kuzmin. Nonequilibrium theory of the hot-electron bolometer with NIS tunnel junction. *Journal of Applied Physics*. 89, 6464-6472 (2001).

[14] S. Golwala, J. Johum, and B. Sadoulet, Proc. of the 7 Int. Workshop on Low Temperature Detectors, July 1997, Munich, pp 64-65.

[15] J. C. Mather, Appl. Opt. 21,1125 (1982).

[16] Leonid Kuzmin, "A Superconducting Cold-Electron Bolometer with SIS´ and Josephson Tunnel Junctions", Journal of Low Temperature Physics, 151, pp. 292-297 (2008).

[17] Leonid Kuzmin, "Array of Cold-Electron Bolometers with SIN Tunnel Junctions for Cosmology Experiments", Journal of Physics: Conference Series (JPCS), 97, 012310 (2008).

[18] I. Agulo, L. Kuzmin and M. Tarasov, "Noise Characterization of the Cold-Electron Bolometer", subm. to Applied Physics Letter (2007).

# Recommendations for Waveguide Interfaces to 1 THz

J.L. Hesler, A.R. Kerr, W. Grammer, and E. Wollack

***Abstract* — The existing waveguide interface standards are generally found to be unsatisfactory above 110 GHz. An improved interface is proposed which is backward-compatible with the MIL-DTL-3922/67C standard and most of its higher-frequency variants. As there are currently no standard waveguide bands above 325 GHz, an extended set of bands is recommended for operation to 1100 GHz.**

***Index Terms* — Waveguides, millimeter-wave waveguides, rectangular waveguides, submillimeter-wave waveguides, standards.**

## I. Introduction

The existing waveguide interface standards above 110 GHz, from WR-8 (90-140 GHz) to WR-3 (220-325 GHz), have long been known to have significant limitations. Over the years, efforts to modify and improve the standards have been made at companies such as Aerowave, Agilent (HP), Custom Microwave, Flann, Maury Microwave, Millitech, and Oleson Microwave Laboratories, as well as at various research institutions [1-3]. These efforts lead to the creation of competing and often incompatible interface standards. Furthermore, for frequencies above 325 GHz there are no universally supported waveguide standards at present, although at least one new set has been suggested [4].

In the 1960s and early 1970s, the industry wrestled with standardization issues remarkably similar to those under discussion today. As organizations developed interfaces to meet their own needs, multiple flange variants were developed complicating progress toward a universal standard [5]. This anarchy persisted until the 1975 release of MIL-F-3922/67B, which specified round millimeter-wave flanges for use through 110 GHz. Most notable in that specification was the explicit definition of the alignment pins and pin-holes. Several studies have shown that the flange works as designed through 110 GHz [1]. Used with WR-15 and smaller waveguides, the 0.750" diameter flange is commonly called the "750-round" flange (round flanges are still often referred to by their outdated 1950s AN nomenclature: UG-383, UG-385, UG-387). The current version of the Military Specification is MIL-DTL-3922/67C. Above 110 GHz, the so-called *mini-flange*, MIL-F-3922/74, was specified to operate up to 325 GHz (WR-3), but with experience it was found to have poor repeatability, as well as being difficult to machine. The community became dissatisfied with the mini-flange, preferring instead variations of the 750-round flange with tightened tolerances. Different groups developed different variants of this standard, with a resulting loss of cross-compatibility. For these reasons, it is important to establish a new standard which allows the development of compatible components for the THz community.

This paper presents recommendations for a standard waveguide interface and also a set of frequency bands for use from 110 to 1100 GHz. These recommendations are based in large part on work carried out for the multi-national ALMA project [6]. The interface has been successfully implemented for substantial numbers of both passive and active waveguide components at frequencies ranging from 31- 950 GHz. A number of factors in the choice of a waveguide interface are discussed, including tolerances, interface size and pattern, backward compatibility, English vs. metric units, and the use of anti-cocking flanges. For frequencies above 325 GHz, we propose defining waveguide bands in a manner consistent with the existing set of overlapping waveguide bands specified in MIL-DTL-85/3C.

## II. Goals of a Waveguide Interface Standard

The main reason for developing a waveguide interface standard is to ensure compatibility of components from different groups. The following features and goals are desirable:

1) Repeatable operation to ~1 THz with low reflection.
2) Backward compatiblility with existing interfaces and waveguides below 325 GHz.
3) Ease of machining.
4) Applicability to extruded waveguide and to electroformed and machined blocks.
5) Asexual, to avoid the need for male and female flanges.
6) Anticocking, but should not require surface relief on machined blocks.

### *Backward Compatibility*

Over the past 30+ years, a large amount of waveguide hardware has been developed for 75-325 GHz using either the 750-round flange or the mini-flange. In that time, laboratories have accumulated many components while manufacturers have made a substantial investment in tooling (fixtures, mandrels, jigs, *etc*.) to produce these parts, and in inventory. Because of this broad infrastructure, backward compatibility is an important practical consideration when developing a new interface standard. While backward compatibility may not be possible with all variations of the old interface, it should not

J. L. Hesler is with Virginia Diodes Inc., Charlottesville, VA 22902

A. R. Kerr and W. Grammer are with the National Radio Astronomy Observatory, Charlottesville, VA 22903

E. Wollack is with the Goddard Space Flight Center, Greenbelt, MD 20771

The National Radio Astronomy Observatory is a facility of the National Science Foundation operated under cooperative agreement by Associated Universities, Inc.

be ruled out; rather, the cost benefits of backward compatibility (not having to replace existing equipment) must be weighed against the potential performance advantages of a new but incompatible interface. The waveguide and interface standards proposed here are compatible with most existing hardware, and as such offer an appropriate path forward.

One important aspect of backward compatibility is the use of metric as opposed to English units. From a scientific viewpoint it would be desirable to have a metric interface standard, but backward compatibility precludes this. For this reason, the interface and waveguide sizes proposed here are based on English units.

## III. Waveguide Interface Recommendation

A diagram of the proposed waveguide interface is shown in Fig. 1. This interface is an extension of MIL-DTL-3922/67C interface with tightened tolerances and anti-cocking characteristics. A number of factors must be considered.

*Interface Tolerancing*

The tolerancing of the interface, particularly the alignment pins and pin-holes, is crucial to accurate mating of two waveguides, and thus to minimizing the reflection at the interface. However, there is a tradeoff between interface alignment, machinability, mating force, and binding at the interface. The common use of drilling jigs for manufacturing waveguide interfaces sets limits to the achievable angular alignment of the pins, and so interfaces made using drilling jigs are likely to be limited to use below 325 GHz. By using CNC machines to fabricate the interface as an integral part of a waveguide component it is possible to maintain tighter tolerances, thus minimizing reflections at higher frequenices. In order to provide the greatest flexibility, a multi-tiered tolerancing scheme is proposed, as specified in the *Tiered Tolerancing Table* in Fig. 1. The tightest tolerances, labeled *Submm*, represent the strictest tolerance specification that can reasonably be achieved using a standard high-precision CNC milling machine.

By using the waveguide interface misalignment simulations described in [1], we can link the tolerances given in Fig. 1 to a worst-case reflection due to interface misalignment. Table 1 shows the calculated return loss for the three tolerancing schemes. As can be seen in the table, even the tightest tolerance yields only marginal worst case performance at 825 GHz (7 dB return loss). This is an indication of the practical limit of a machined interface: to achieve a satisfactory return loss near 1 THz is extremely difficult. To date, above ~1 THz, nearly all devices have avoided waveguide interfaces by using integral feedhorns to couple power into or out of the component.

*Alignment Pins*

No changes are proposed to the pin originally specified in the MIL-F-3922/67B interface. The waist shown in the drawing was found to improve the grip of the dowel when it is pressed inplace, and so it should be retained.

One additional consideration related to the pin is its height above the plane of the interface. In general, the pin height should be minimized to reduce binding and to ease the angular tolerance. However, the pin must also be tall enough to keep the interface in place while the screws are being engaged. As a compromise, a pin height of 0.156" above the interface face is recommended, as in MIL-DTL-3922/67C.

*Annular Recess and Relief Around Pin Holes*

The annular recess is used to minimize the contact area of the interface and thus to ensure greater pressure in the vicinity of the waveguide aperture while preserving the anti-cocking nature of a flat flange without a central boss. At sub-millimeter wavelengths, a gap of only a few microns between flange faces can introduce significant loss and reflection, and the annular recess also helps to avoid gaps caused by bumps

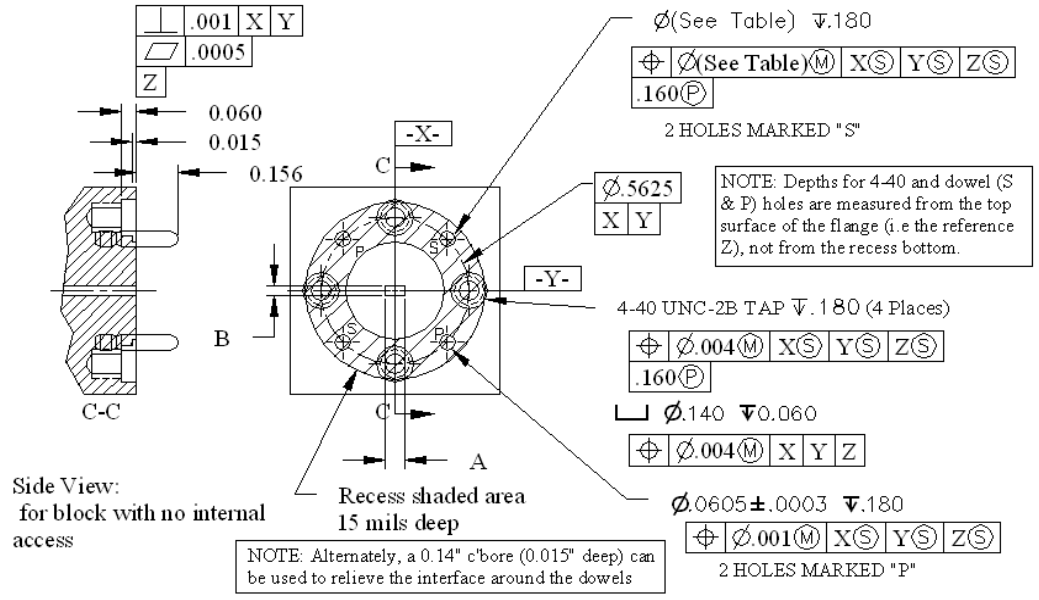


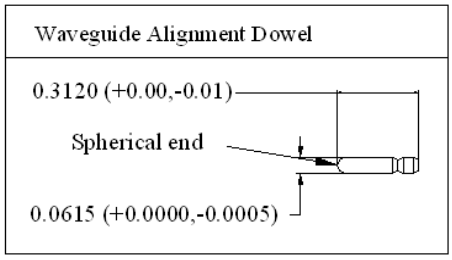


| Tiered Tolerancing Table (for Slip Fit Dowel Holes) | | |
|---|---|---|
| Submm | Ø.0635 +.0003 -.0000 | Ø.001Ⓜ |
| WR-3 | Ø.0640 +.0005 -.0000 | Ø.001Ⓜ |
| WR-10 | Ø.0645 +.001 -.0000 | Ø.002Ⓜ |

Figure 1. Drawing of the recommended waveguide interface from WR-10 to WR-1.0.

on the mating surfaces from metal displaced when the alignment pins are pressed in place (after inserting the pins, the flange surface can not be lapped). The proposed 0.015" deep annular recess provides the necessary relief.

Because of the complexity of machining the annular recess, the simpler alternative of a 0.14" counterbore (0.015" deep) around the pin holes may be preferred, and this is included in the interface drawing as an option.

*A Miniature Interface*

At millimeter and submillimeter wavelengths, the geometry of the 750-round interface can force a component to be larger than required electrically. For this reason, it is desirable to have an alternative miniature interface, preferably one which fits within the proposed interface so that parts with miniature interfaces can be tested using components with the larger standard interface. Such a miniature interface, shown in Fig. 2, has been developed at NRAO for use in the ALMA project. Similar in size to the mini-flange, it is asexual, and has no screw or pin holes in the E-plane, a desirable characteristic for split-block waveguide components.

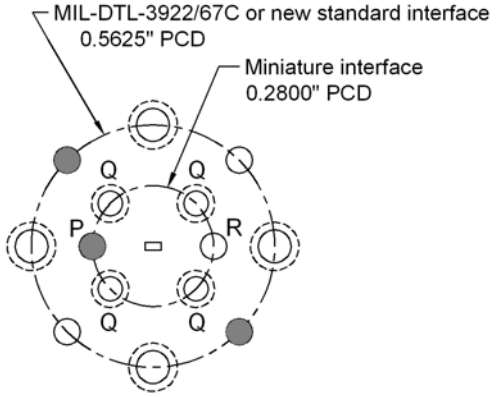


Figure 2: The Grammer miniature interface fits within the larger MIL-DTL-3922/67C pattern. Each side of the interface contains one captive pin (P) and a clearance hole (R) for the mating pin. The bolt holes (Q) can be either #2-56 or M2. Tolerancing for the miniature interface should follow that of the proposed larger interface.

**TABLE 1: PIN AND PIN-HOLE DIMENSIONS AND TOLERANCES**

| | Submm | WR3 Tol | WR10 Tol |
|---|---|---|---|
| | (in.) | (in.) | (in.) |
| Min. Pin Diameter | 0.061 | 0.061 | 0.061 |
| Max. Pin Diameter | 0.0615 | 0.0615 | 0.0615 |
| Min. Hole Diameter | 0.0635 | 0.064 | 0.0645 |
| Max. Hole Diameter | 0.0638 | 0.0645 | 0.0655 |
| Pin Tolerance Range (PLTZF) | 0.001 | 0.001 | 0.001 |
| Hole Tolerance Range (PLTZF) | 0.001 | 0.001 | 0.002 |
| Pin Tolerance Range (FRTZF) | 0.001 | 0.001 | 0.001 |
| Hole Tolerance Range (FRTZF) | 0.001 | 0.001 | 0.002 |
| Maximum Total Offset | 0.0024 | 0.0028 | 0.0038 |
| Fit Tolerance | 0 | 0.0005 | 0 |
| | | | |
| | Frequency of Min Return Loss Due to Misalignment (GHz) | | |
| | Submm | WR3 Tol | WR10 Tol |
| Minimum RL (23 dB) at | 275 | 240 | 176 |
| Minimum RL (7 dB) at | 825 | 720 | 528 |

## IV. WAVEGUIDE BANDS

The current standard series of waveguide bands starts in the microwave region at 320 MHz (WR-2300), and extends in two overlapping series to 325 GHz (WR-3), as specified in MIL-DTL-85/3C. If the number following the dash in the WR-## nomenclature is divided by 100, the result is the waveguide broad-wall width in inches (certain band designations, particularly the higher frequency ones, have been rounded for convenience). In order to cover many decades of frequency, the lower frequency series is extended by decades. So, for example, there are waveguide bands at 2.2-3.3 GHz (WR-340), 22-33 GHz (WR-34), and 220-325 GHz (WR-3), with broadwall widths of 3.4", 0.34", and 0.034". This progression can be continued upwards, as shown in Table 2 starting at WR-10 and extending to 1100 GHz. In order to avoid confusion caused by rounding of the band numbers, we have added an extra significant digit, and thus WR-3 becomes WR-3.4 in this nomenclature.

**TABLE 2: CURRENT AND PROPOSED WAVEGUIDE BANDS**

| Proposed Band Designation | EIA Band Designation | Internal Dimensions (mils) | Internal Dimensions (mm) | Frequency Range (GHz) | TE(10) Cutoff (GHz) |
|---|---|---|---|---|---|
| WR-10 | WR-10 | 100 x 50 | 2.540 x 1.270 | 75.0 - 110.0 | 59.0 |
| WR-8 | WR-8 | 80 x 40 | 2.032 x 1.016 | 90.0 - 140.0 | 73.8 |
| WR-6.5 | WR-6 | 65 x 32.5 | 1.651 x 0.826 | 110.0 - 170.0 | 90.8 |
| WR-5.1 | WR-5 | 51 x 25.5 | 1.295 x 0.648 | 140.0 - 220.0 | 116 |
| WR-4.3 | WR-4 | 43 x 21.5 | 1.092 x 0.546 | 170.0 - 265.0 | 137 |
| WR-3.4 | WR-3 | 34 x 17 | 0.864 x 0.432 | 220.0 - 330.0 | 174 |
| WR-2.8 | n/a | 28 x 14 | 0.711 x 0.356 | 265.0 - 400.0 | 211 |
| WR-2.2 | n/a | 22 x 11 | 0.559 x 0.279 | 330.0 - 500.0 | 268 |
| WR-1.9 | n/a | 19 x 9.5 | 0.483 x 0.241 | 400.0 - 600.0 | 311 |
| WR-1.5 | n/a | 15 x 7.5 | 0.381 x 0.191 | 500.0 - 750.0 | 393 |
| WR-1.2 | n/a | 12 x 6 | 0.305 x 0.152 | 600.0 - 900.0 | 492 |
| WR-1.0 | n/a | 10 x 5 | 0.254 x 0.127 | 750.0 - 1100.0 | 590 |

In certain circumstances it is necessary to use a waveguide band which overlaps standard bands. In practice, the choice of a non-standard band may be dictated by a scientific application (e.g., an atmospheric window or a group of molecular lines) or by a particular component (e.g., a frequency multiplier whose output range does not fit within a standard band). In such cases, the proposed WR-## nomenclature is easily modified by the user with results which are immediately clear to other engineers.

## V. Discussion and Future Development

The proposed waveguide interface and set of waveguide bands cover 110 GHz to 1.1 THz. They are compatible with existing standards while offering greater precision and repeatability. For more than five years they have been used successfully for hundreds of components made for the multi-national ALMA project. However, the relatively poor return loss at the highest frequencies leaves much to be desired. It has been suggested [7] that alignment tolerances could be tightened significantly by using shorter alignment pins. By reducing the protrusion of the pin above the plane of the interface from 0.156" to 0.070", a pin hole diameter of 0.0625" could be used with a pin tolerance range of 0.0005". This would improve the worst-case return loss below 1.1 THz to 10 dB.

The effect of the specified interface flatness on loss and return loss is not well understood. Non-flat flange pairs could be investigated, either experimentally or by electromagnetic simulation, to determine the necessary flatness tolerance.

## VI. Acknowledgment

The authors thank Leon Kozul of Aerowave Inc. and Neal Erickson of the University of Massachusetts, Amherst, for their helpful comments and suggestions.

## References

[1] A.R. Kerr, E. Wollack, and N. Horner, "Waveguide Interfaces for ALMA Instrumentation," ALMA Memorandum 278, 9 Nov. 1999. http://www.mma.nrao.edu/memos/html-memos/alma278/memo278.pdf.

[2] A. R. Kerr, L. Kozul and A. A. Marshall, "Recommendations for Flat and Anti-Cocking Waveguide Interfaces," ALMA Memo 444, National Radio Astronomy Observatory, Charlottesville VA 22903, 6 Jan 2003. http://www.mma.nrao.edu/memos/html-memos/alma444/memo444.pdf.

[3] E. Schlecht, "High frequency interfaces," JPL Internal Report, LO Subgroup, 13 Aug 2001.

[4] J. S. Ward, "New Standards for Submillimeter Waveguides," Proc. 17th Int. Symp. on Space THz Tech., Paris, May 2006.

[5] T. N. Anderson, "Status Report on International Millimeter Waveguide Flange Standards," IEEE Trans. Microwave Theory Tech., vol. MTT-11, no. 9, pp. 427-429, Sept. 1963.

[6] ALMA is the *Atacama Large Millimeter and submillimeter Array* http://www.alma.nrao.edu/.

[7] N. R. Erickson, private communication, July 2007.

# A Low-Loss Dielectric Waveguide Structure for Terahertz Applications

**Daryoosh Saeedkia[1], Mohammad Neshat[1], Suren Gigoyan[2], and Safieddin Safavi-Naeini[1]**
[1]*Department of Electrical and Computer Engineering, University of Waterloo, 200 University Ave West, Waterloo, ON, Canada N2L 3G1*
[2]*Institute of Radio physics & Electronics, Ashtarak, Armenia 378410*

The most challenging issue in designing dielectric waveguide structures is to achieve high efficiency coupling into and out of the waveguides. The coupling efficiency becomes more important at the millimeter-wave and terahertz frequencies, where the available power from the sources is limited. In this paper, we present a dielectric waveguide structure with extremely low return loss and insertion loss at the millimeter-wave and terahertz frequencies. The proposed structure consists of a dielectric waveguide made of high dielectric constant and low loss materials, such as Alumina, high-resistive silicon, and GaAs, located above a dielectric support substrate, such as Teflon and Plexiglas. The power is coupled into and out of the waveguide by means of two metallic rectangular waveguides without any horn type extensions, which makes the metallic waveguide structure easy to fabricate and low-cost. Both the waveguide and the substrate are linearly tapered at the input and output ends to increase coupling efficiency and decrease losses due to reflection and scattering at the discontinuities. The taper length is optimized to have maximum coupling efficiency. The dielectric waveguide is designed to be single mode at the given frequency range in order to minimize the dispersion and to have maximum overlap between the field distribution inside the rectangular waveguide and that of the dielectric waveguide. The designed structures are simulated by the Ansoft HFSS software, a commercial full-wave electromagnetic simulator based on finite element method (FEM). Fig. 1 shows the $S_{11}$ and $S_{21}$ parameters of the designed structure for the frequency range of 95-104 GHz. The dielectric waveguide is made of Alumina with $\varepsilon_r$=9.8 and the loss tangent of $\tan\delta = 1.5\times10^{-4}$ and high-resistive silicon with $\varepsilon_r$=11.65 and the loss tangent of $\tan\delta = 2\times10^{-3}$. The dielectric support substrate is made of Teflon with $\varepsilon_r$=2.08 and the loss tangent of $\tan\delta = 6\times10^{-4}$. The dimensions of the waveguide are $a = b = 0.4$ mm, $L = 20$ mm, and $t = 5$ mm. The return loss is less than -20 dB over a 7 GHz bandwidth and the insertion loss is less than 0.9 dB.

Shown in Fig. 2 are the $S_{11}$ and $S_{21}$ parameters for the frequency range of 400-465 GHz. At this frequency range, the loss tangent for Alumina is $\tan\delta = 6\times10^{-4}$ and for high-resistive silicon is $\tan\delta = 1\times10^{-3}$. The dimensions of the waveguide are $a = b = 0.15$ mm, $L = 20$ mm, and $t = 2$ mm. The structure shows 65 GHz bandwidth, over which the return loss is less than -24 dB and the insertion loss is less than 0.6 dB for Alumina waveguide and less than 1.3 dB for silicon waveguide.

The measurement and characterization of the device is under way.

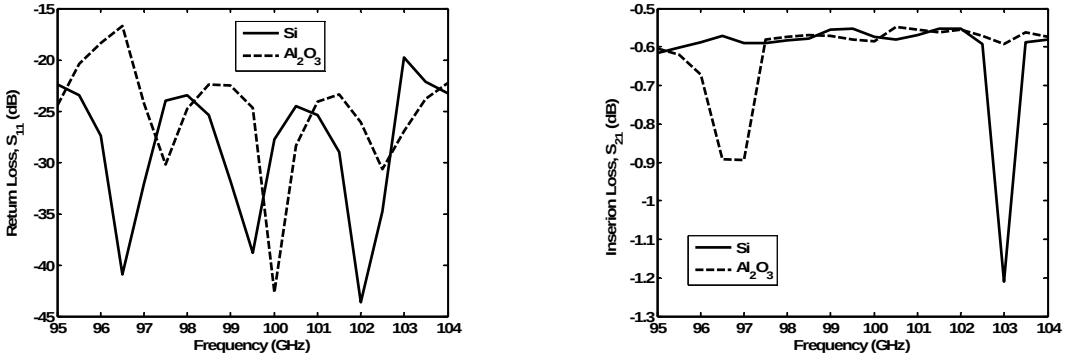


(a) (b)

Fig. 1 (a) Return loss (b) insertion loss of dielectric waveguide made of Alumina and Silicon for 95-104 GHz

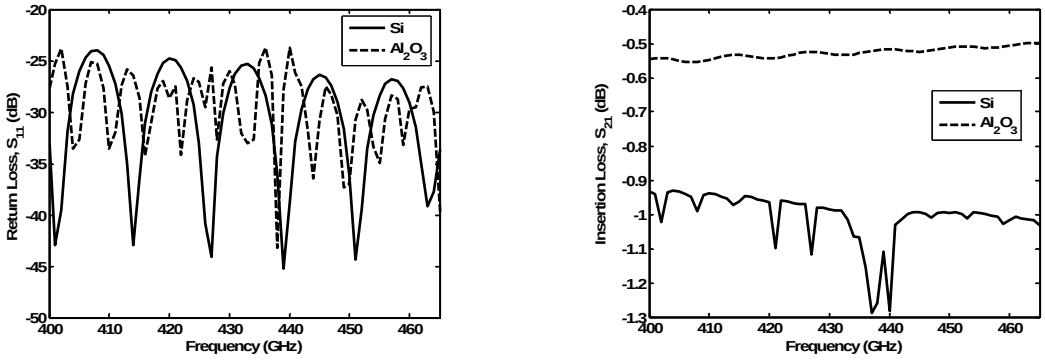


(a) (b)

Fig. 2 (a) Return loss (b) insertion loss of dielectric waveguide made of Alumina and Silicon for 400-465 GHz

# Large bolometers arrays with NbSi sensors for future space experiments

F. Pajot [1], Y. Atik [1], C. Evesque [1], S. Lefranc [1], B. Leriche [1], J-P. Torre [1], B. Bélier [2], N. Marsot [2], L. Dumoulin [3], L. Bergé [3], M. Piat [4], E Bréelle [4], D Prêle [5], A. Benoit [6], C. Hoffmann [6], T. Durand [6], P. Camus [6], D. Santos [7], F-X. Désert[8], Yong Jin [9], M Giard [10]

[1] *CNRS-IAS Bât. 121, Université Paris Sud-11, F- 91405 Orsay, France*
[2] *CNRS-IEF Bât. 220, Université Paris Sud-11, F- 91405 Orsay, France*
[3] *CNRS-CSNSM Bât 104, Université Paris Sud-11, F- 91405 Orsay, France*
[4] *CNRS-APC 10 rue Alice Domon et Léonie Duquet, 75205 PARIS cedex 13, France*
[5] *CNRS-LISIF 3 rue Galilée Site "Saint Raphael", F-94200 Ivry sur Seine, France*
[6] *CNRS-Institut Néel 25 avenue des Martyrs, F-38042 Grenoble, France*
[7] *CNRS-LPSC 53 avenue des Martyrs, F-38026 Grenoble, France*
[8] *CNRS-LAOG Observatoire de Grenoble, BP53, F-38041 Grenoble cedex 9, France*
[9] *CNRS-LPN Site Alcatel, Route de Nozay, F-91460 Marcoussis, France*
[10] *CNRS-CESR 9 avenue du Colonel Roche, F-31028 Toulouse, France*

**Email :** francois.pajot@ias.u-psud.frAbstract

*The submillimeter and millimeter space astronomy will require higher sensitivity instrument for the future missions. Large bolometer arrays filling the telescopes focal planes are a promising solution to this sensitivity increase.*

*New techniques in microelectronics allow to build such arrays of detectors using collective processes. We present here the developments led in France of bolometers arrays using NbSi alloy thermometers. NbSi films can be made either high impedance or superconducting. We describe the manufacturing process of the array and the tests perspectives.*

## 1. Introduction

The submillimeter and millimeter wavelength range is entering a new era with the launch to come of the Planck and Hershel space missions. The observations from above the atmosphere, opaque excepted for a few windows of the spectrum, will give unprecedented access to the studies of the interstellar medium, the galaxies, the large structures of the universe and the cosmic microwave background (CMB).

The design of present space missions dedicated to submillimeter and millimeter broadband or low spectral resolution observations is based on direct detectors limited by the photon noise of the incoming radiation in a diffraction limited beam. Bolometers are the most sensitive detectors for this purpose. They are associated to feedhorns and arranged in groups covering a fraction only of the focal plane area. The advantage of well defined beams is therefore counter-balanced by the loss of a large fraction of the collected photons. This is the case in the HFI/Planck and SPIRE/Herschel instruments.

Among the topics that will need further observations following these two missions, the study of the inflation phase of the universe will require large improvements of sensitivity in the measurement of the CMB polarized emission. The ESA Cosmic Vision and NASA Beyond Einstein programs includes missions dedicated to these measurements.

An increase factor of 10 to 100 is required in sensitivity with respect to current instruments. It cannot be obtained by increasing the integration time, already counted in years for a whole sky survey. The only solution is a full coverage of the focal plane by large contiguous detector arrays of 10 000 pixels or more, with individual pixel NEPs below $10^{-17}$ $WHz^{-1/2}$.

We present here a french collaborative effort in the developpement of such arrays. The DCMB (Développement Concerté de Matrices de Bolomètres) R&D program is supported by CNES (Centre National d'Etudes Spatiales), the CNRS (Centre National de la Recherche Scientifique) and the participating Universities.

The subsystems concerned by the R&D program are: the thermal architectures of the bolometers arrays, the thermometers, the coupling with the optical radiation and the readout electronics. Two types of thermometers are beeing studied, based on Niobium Silicon alloys: high impedance (Anderson isolator) or superconducting [1].

## 2. Arrays manufacturing

### 2.1 Thermal architecture

The thermal architectures is developped in common for both types of thermometers in the microelectronics facility IEF/MINERVE of Paris Sud-11 University at Orsay. Two architectures have been designed, a 204 pixels array and an 23 pixels array. The former (fig. 1) will be used in a millimeter camera for the 30m IRAM telescope on Pico Veleta (Spain).

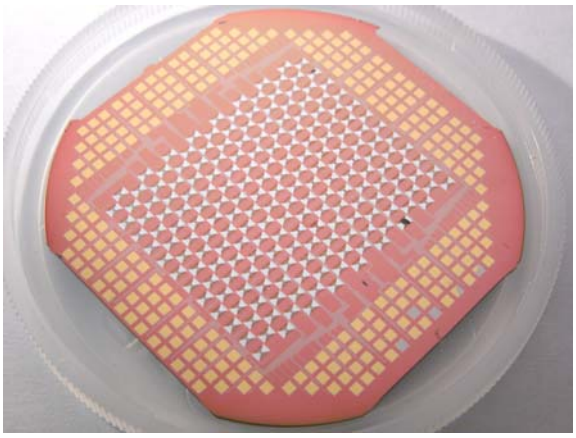

*Figure 1: 204 pixels array architecture*

The later (fig. 2) is designed to be used in the Olimpo balloon program with a feedhorn array in front of the detctors.

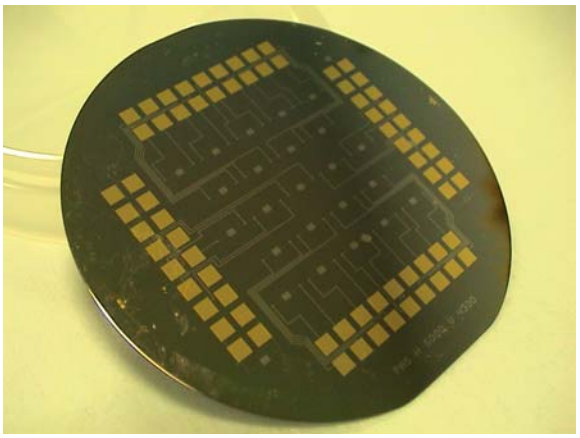

*Figure 2: 23 pixels array architecture (thermometers only)*

### 2.2 Thermometers

The two types of thermometers studied are based on Niobium Silicon alloys. These are high impedance (Anderson isolator) [2] or superconducting (Nb fraction larger than 0.13). The thermometric sensor is composed of a film of NbSi co-evaporated by irradiating two targets of Nb and Si simultaneously.

In the case of the superconducting sensor, the mixing ratio *x* of the 100 nm thick $Nb_xSi_{x-1}$ thermometer is adjusted in order to obtain the goal transition temperature. In order to lower (below 1 Ω) the average resistance of the film at the middle of the superconducting transition, an interleaved comb geometry is used for the Nb electrodes (fig. 3). A typical NbSi thermometer (10 mm x 10 mm) transition curve was previously measured [3]. The design is scaled down to 0.8 mm x 0.8 mm for the 23 pixels array (fig. 2).

Nb and NbSi are deposited in dedicated evaporators and co-evaporators of CSNSM/Orsay.

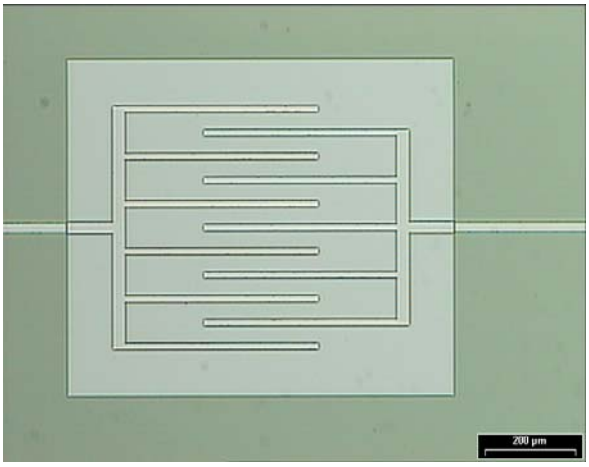


*Figure 3: NbSi superconducting thermometer. The leads comb structure is Nb, and the square NbSi.*

### 2.3 Microfabrication process

The steps of microfabrication of the superconducting bolometers are as follows:

1. Deposition of membranes material by PECVD ($SiO_2$ + $Si_3N_4$: SiO2/SiN/SiO2 = 290/230/100 nm)
2. $Nb_xSi_{1-x}$ co-evaporation (x=15.55%, 1000 Å)
3. Nb evaporation (500 Å)
4. Au evaporation
5. Silicon deep etching

### 2.4 Readout

Multiplexed readout will be performed using HEMT for the high impedance thermometers, and using a 4K SiGe ASIC associated with SQUIDs for the superconducting thermometers. Developpement of the ASIC is described by D. Prele et al. (this conférence). SQUIDs mux and amplifiers procurement is currently in discussion with Supracon (Jena).

### 2.5 Coupling with radiation

The 204 pixels array includes an antenna pattern associated to a dissipator for the coupling with the incoming radiation [4]. For the first realisation of the superconducting array, the radiation will be absorbed by a standard resistive layer or a grid adapted to the vacuum impedance. The long term goal is to couple to the incoming radiation by means of antenna [5].

## *3.* Test perspectives

Tests and characterisation of the high impedance arrays are described in [1]. The test setup for the superconducting array is under development. NbSi alloy is a new material for TES design, it requires a full characterisation and validation before using it to produce large arrays. The uniformity of the superconducting transition temperature and slope will be measured on a 23 pixels array for which only the thermometers are built (fig. 3). In parallel, we will characterize the noise properties of a single NbSi superconducting thermometer. The test setup is based on a commercial SQUID system from Star Cryoelectronics, and a 300 mK mini-fridge and a thermal stage regulated between 300 and 500 mK.

## 4. Conclusion

While the high impedance arrays are mostly validated and characterized, the development of superconducting arrays is starting and its testing phase is only beginning Once this phase is passed, we will be able to continue the integration of a complete array of superconducting bolometers with optical coupling.

## References

[1] M. Ukibe et al., *"Fabrication of large NbSi bolometer arrays for CMB applications"*, Nuclear instruments & Method in physics research **559** (2006) pp 554-556.

[2] Camus Ph. et al, "*Low temperature NbSi thin film bolometers on Silicon Nitride membranes low temperature for bolometer applications*", NIMA A **444** (2000) pp. 419-422.

[3] S. Lefranc et al., *"Superconducting NbSi thermometers for use in TES devices"*, Nuclear instruments & Method in physics research **559** (2006) pp 468-470.

[4] D. Rauly et al., ISSTT 2006 conference

[5] C.L. Kuo, J.J. Bock et al., *Antenna-coupled TES bolometers for CMB polarimetry*, Proc. SPIE **6275** (2006), p 1

# A Quantum-limited Submillimeter Mixer with an Inhomogeneous Distributed SIS Junction Array

Wenlei Shan, Shengcai Shi, Yutaro Sekimoto and Takashi Noguchi

***Abstract*—Heterodyne mixing performance of a waveguide SIS mixer with inhomogeneous distributed junction (DJ) array composed of 3 SIS junctions is experimentally investigated at 375-500GHz. Quantum-limited noise temperature of 3-DJ mixer is demonstrated. Besides its low noise temperature, the mixer conversion gain of 3-DJ mixer is found to be more uniform over RF band than that of a PCTJ (parallel-connected twin junctions) mixer. The FTS (Fourier transform spectrum) response indicates a broad RF bandwidth of the 3-DJ mixer that is limited by the bandwidth of waveguide probe instead of mixer's tuning circuit.**

***Index Terms*—SIS mixers, Submillimeter wave, Distributed junction array, Noise temperature, Gain flatness.**

## I. Introduction

The RF bandwidth of an SIS mixer is restricted by the bandwidth of antenna (waveguide probe) or the tuning circuit used for tuning out the geometric capacitance of tunnel junction. The bandwidth of waveguide probe can be as wide as 30% and be much wider in the case of quasi-optical mixer. The bandwidth of tuning circuit, usually the actual threshold of overall bandwidth, is determined by the quality factor of a resonator-like tuning circuit composed of a microstrip inductive line and the capacitive tunnel junctions. The quality factor Q is proportional to the frequency and inversely proportional to the current density $Q \sim \omega/Jc$. Therefore, the current density must be high in order to achieve broad RF band at submillimeter range. However, Jc cannot exceed the fabrication limit around $10kA/cm^2$ when the conventional $Nb/AlO_x/Nb$ technique is employed. At 500GHz the Q factor is normally larger than 5, determining a relative RF bandwidth about 20%.

Mixer designs involving multi-junctions (N>2) or SIS non-linear transmission lines are found to have broader RF bandwidth even with relatively low Jc. These designs characterized by distributed mixing with either SIS tunnel microstrip line [1][2][3][4] or parallel-connected multi-junctions [5][6][7][8] or a combination of above two [9]. Most of these designs have demonstrated wide RF bandwidth within submillimeter range as predicted by theoretical calculation. Noise temperature as low as 5 times of quantum limits at 4.2K bath temperature has been achieved at 600GHz band by using a half-wavelength SIS non-linear microstrip line of a width 0.55μm [3] and at 200GHz band with an inhomogeneous 5-DJ mixer [7]. These designs are potentially useful in some applications that require wide-band fix-tuned mixers at low device impedance such as integrated receiver with built-in FFO (flux flow oscillator).

In contrast to SIS non-linear microstrip lines, lumped DJ arrays allow large-size junctions that can be easily fabricated with conventional photolithography. An inhomogeneous DJ array composed of junctions with different dimensions non-uniformly located along a microstrip transmission line is predicted to be more efficient and therefore less noisy than a homogenous DJ array [10]. In this paper we present a measurement result of 3-DJ mixer that demonstrates an overall receiver noise temperature as low as 3 times of quantum limits at 4.2K at frequencies ranging from 375 to 500GHz and with 4-8GHz IF. Correcting for the contribution from IF chain and RF optics, the mixer noise is found to be about one quantum limit. The result indicates that the quantum-efficient mixing can be achieved with distributed mixing scheme. The RF bandwidth (in sense of noise temperature) of PCTJ is found to be similar to 3-DJ at this frequency range since the current density is rather high. However, the gain fluctuation of 3-DJ is found to be much smaller, reflecting a uniform signal coupling between source and detector over the RF band. This feature is beneficial for actual radio telescope to achieve good linearity of backend.

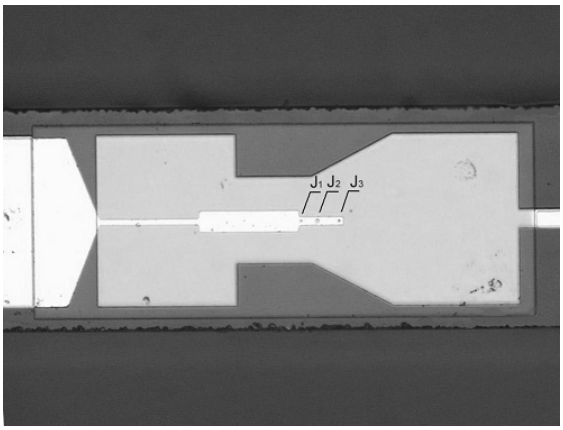


Fig.1 Inhomogeneous 3-DJ array Mixer

This work was supported in part by the NSFC under Contracts No. 20030001-10390163 and No. 10303008, and CAS under Contract No. KJCX2-SW-T2.

Wenlei Shan and Shengcai Shi are with the Purple Mountain Observatory, National Astronomical Observatories of China, Nanjing, 210008, China. (phone: +86-25-8333-2204; email: shawn@nro.nao.ac.jp; scshi@pmo.ac.cn)

Yutaro Sekimoto and Takashi Noguci are with National Observatory of Japan, Mitaka-shi, 181-8588, Japan (e-mail: sekimoto.yutaro@nao.ac.jp ; Takashi.Noguchi@nao.ac.jp).

TABLE I
PARAMETERS OF EACH DESIGN

| Design | Junction Index | Junction Size (um) | Tuning Index | Tuning Length (um) |
|---|---|---|---|---|
| PCTJ | | | | |
| | $J_1$ | 1.5 | $L_{1,2}$ | 14.0 |
| | $J_2$ | 1.5 | | |
| 3DJ | | | | |
| | $J_1$ | 1.4 | $L_{1,2}$ | 10.0 |
| | $J_2$ | 2.0 | $L_{2,3}$ | 11.4 |
| | $J_3$ | 1.4 | | |

The junction is numbered form left to right in Fig. 1. $L_{m,n}$ indicates the tuning distance between junction m and n.

## II. MIXER DESIGN

The first step of inhomogeneous DJ design is to determine the junction sizes and the length of microstrip line between adjacent junctions in order to achieve minimum return loss within a certain RF bandwidth. In principle wideband matching theory [11] can be applied for this purpose. Under the condition of available junction fabrication process, however, the application of this design method is impeded by the strong limitations on junction size, current density and linewidth of microstrip line. On this account, a random searching algorithm is employed to get minimum spreading of impedance over the frequency range 375-500GHz. For a 3-element DJ there are 5 variables listed in Tab.1 as well as some indirect parameters such as Jc and linewidth of strip. These variables are confined to certain limits. For example, the junction size limit is set to be 1.5~2.2um (for easy fabrication with a contact mask-aligner) and the current density less than 10kA/cm$^2$. The SIS junction is modeled by a combination of a capacitance and a resistance connected in parallel. The specific capacitance of SIS junction is supposed to be a function of current density and the resistance is the junction's small-signal resistance that is close to its normal resistance. A 5-dimension Sobol quasi-random sequence is [12] firstly employed to find a rough range and then a fine searching in a narrowed range is performed. In fact there are many solutions satisfying the goal of the optimization for the reflection coefficient. From those solutions, the best one is decided by carrying out a mixing performance calculation with our simulation software based on quantum mixing theory with a 5-port approximation.

The 3-DJ mixer is shown in Fig. 1 and the parameters in Table I , where PCTJ design is also listed for comparison. The normal resistances of PCTJ, 3-DJ are 8Ω and 3.7Ω respectively. The input impedances of 3-DJ and PCTJ are plotted in a Smith chart (Fig. 2) normalized by their normal resistance. Since the impedance difference of probe feed and 3-DJ is quite large, we incorporate a two-section impedance transformer, which is superior to a single section transformer because of its wider bandwidth.

A waveguide-microstrip probe is optimized in a half-reduced waveguide to achieve nearly frequency-independent impedance within 385-500GHz at the probe's feed point [13]. The feed-point impedance can be reduced to 30Ω by means of adding one section of impedance transformer and reducing the height of waveguide to half. With doing so, the matching of the low-impedance DJ over a wide frequency band is facilitated.

## III. MEASUREMENT RESULTS AND DISCUSSION

The 3-DJ mixers are measured in a 4-K Gifford-McMahon/Joule-Thomson mechanical cryocooler. An isolator with a built-in bias-T, inserted between the SIS mixer and a 4-8GHz low noise amplifier, is cooled to 4K to reduce the thermal noise injection from its terminated port. An off-axis ellipsoidal mirror with an edge-taper of 30dB is put on the 4K stage to refocus the beam from the diagonal horn onto an external hot (300K) /cold (liquid nitrogen) load. A 100μm-thick polyimide film is used as the vacuum window while a 150μm-thick Zitex sheet cooled at the 70K stage blocks the infrared radiation. A 12.5μm-thick polyimide film is used as a beam splitter, coupling the LO signal generated by a Gunn oscillator followed by two Schottky-diode doublers with a factor of -15dB.

Typical IV curves as well as IF responses are plotted in Fig. 3. The receiver noise and conversion gain of 3-DJ is plotted in Fig. 4 as a function of LO frequency between 376GHz and 496GHz. The performance of a PCTJ is also shown for comparison. It is worth noting that the PCTJ is fabricated on the same wafer and measured in the same mixer block. Both

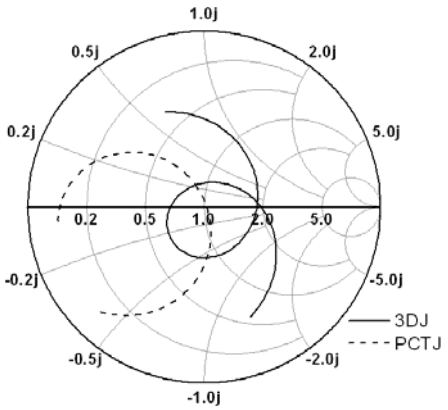


Fig. 2 Impedances of input port of PCTJ, 3DJ in 300-600GHz

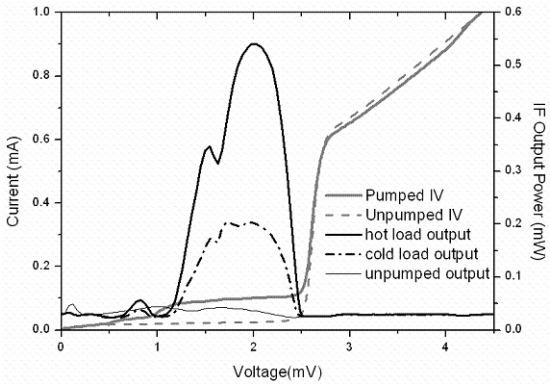


Fig.3 IV curves and IF output measured at 386GHz.

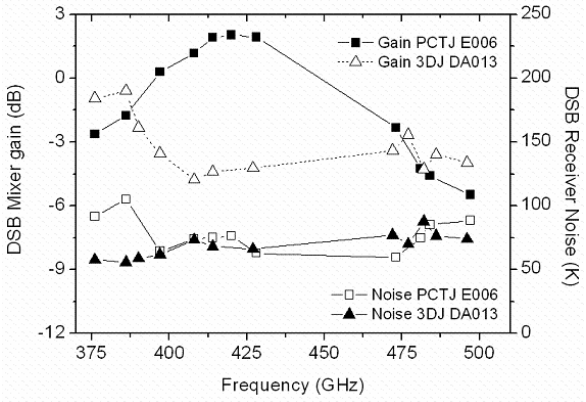


Fig.4 Comparison of receiver noise and gain of 3-DJ and PCTJ as a function of LO frequency.

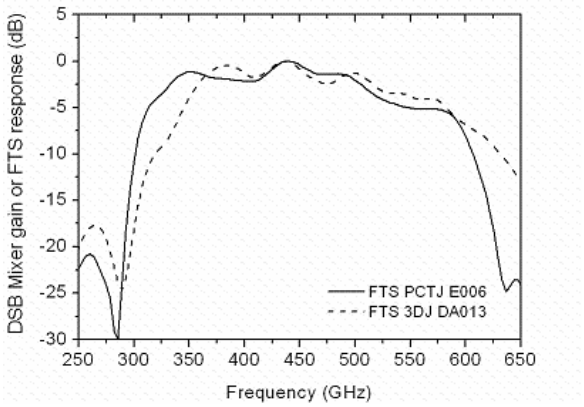


Fig. 5 The FTS responses of 3-DJ and PCTJ

mixers demonstrate excellent low noise temperature over the whole RF band from 375 to 500GHz.

A noise breakdown of the whole DSB receiver system at 427GHz is shown in Table II. The contributions of RF insertion loss and input noise from optics are estimated by theoretical calculation. The mixer noise is finally calculated to be 21.5K (about one quantum limit $hf/2K_B$ , where $h$ is the Planck's constant, $f$ is the frequency and $K_B$ is the Boltzmann's constant) at this frequency. Since several ellipsoidal focusing mirrors at signal path also introduce loss and noise, which are not included in this calculation, the mixer noise should be even smaller and close to zero-point fluctuation limit, which is half of a quantum limit.

Due to the limitation of LO frequency coverage, the performances of both mixers are compared to each other in wider frequency range by measuring their FTS (Fourier Transform Spectrum) responses. The FTS spectrums in Fig.5 shows a similar response bandwidth of 3-DJ and PCTJ. The lower cutoff frequency is caused by waveguide cutoff frequency. The upper cutoff frequency about 600GHz is found to be coincident with that of waveguide probe, which is simulated with a 3D EM simulation software Ansoft HFSS.

The measured noise temperatures of 3-DJ and PCTJ in frequency range 375-500GHz are quite similar. It is difficult to judge which one is superior to the other in sense of noise. However, Fig. 4 shows that 3-DJ has a more uniform conversion gain in measured frequency range. This should be attributed to uniform signal coupling efficiency that we aim to realize. Flat conversion gain has some advantages. For example, when the noise from IF chain is large, a mixer with uniform conversion gain results in uniform overall receiver noise temperature over the RF band. Large gain variation may also cause non-linearity problems of the backend of a radio telescope if no compensation is made to regulate the IF output. DJ mixers with flat gain can thus avoid such problems and improve the reliability.

One of the disadvantages of DJ SIS mixer is their relatively large LO power assumption, which is almost inversely proportional to the device normal resistance. It may limit their application in Terahertz regime since LO power is usually quite weak unless sub-micro size junction is adopted. Another disadvantage of DJ mixer is its relatively large junction capacitance that reduces the IF bandwidth. To study the influence of junction capacitance on the IF response, we measure the mixer's conversion gain as a function of intermediate frequency shown in Fig. 6. The 3dB IF bandwidth of 3-DJ narrower than that of PCTJ is indeed observed. Such a problem can be partly solved by inserting IF matching circuit that tunes out junction capacitance at certain IF frequency. However, the total IF bandwidth is still limited by the quality factor calculated at IF. In turn, small junctions are required to reduce the geometric capacitance to achieve

TABLE II
NOISE BREAKDOWN OF DSB RECEIVER SYSTEM AT 427GHZ

| Element | $T_{in}$ (K) | Gain(dB) | $T_{front}$ (K) |
|---|---|---|---|
| IF amplifier | 5.2 | | 12.1 |
| IF Isolator | 4.2 | 0 | 9.8 |
| SIS mixer | <21.5 | -3.12 | <24.5 |
| IR filter | 0.18 | -0.18 | 0.2 |
| Dewar window | 4.9 | -0.25 | 5.1 |
| Beam splitter | 9.6 | -0.13 | 9.6 |
| Receiver | | | 61.3 |

The four columns show the element name, input noise, gain and equivalent noise referred to the receiver input respectively.

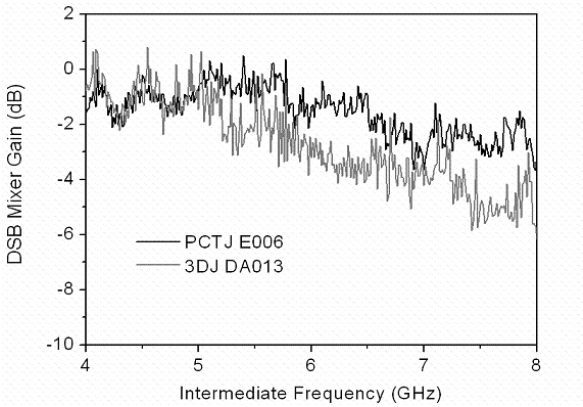


Fig. 6 Mixer conversion gain of 3-DJ and PCTJ as a function of intermediate frequency from 4 to 8GHz.

wide IF bandwidth.

## IV. Conclusion

An inhomogeneous 3-DJ SIS mixer is designed to have a uniform signal coupling in the frequency ranging from 375 to 500GHz. The corrected noise temperature of 3-DJ SIS mixer is close to one quantum limit approaching theoretical minimum. Such a noise performance is comparable with a PCTJ mixer that is fabricated on the same wafer and mounted in the same mixer block. The 3-DJ SIS mixer demonstrates a uniform conversion gain over the measured RF band in contrast to the PCTJ, gaining advantages in some applications requiring gain flatness. The 3-DJ SIS mixer has a broad RF bandwidth (about 40%) measured from its FTS response. In this specific case, the RF bandwidth is determined by waveguide probe instead of tuning circuit.

## References

[1] C. E. Tong, R. Blundell, B. Bumble, J. Stern, and H. G. LeDuc, "Quantum limited heterodyne detection in superconducting nonlinear transmission lines at submillimeter wavelength," *Appl. Phys. Lett.*, vol. 67, pp. 1304–1306, Aug. 1995.

[2]C.-Y.Tong, Raymond Blundell, Krikor G. Megerian, Jeffrey A. Stern, and Henry G. LeDuc, "A 650 GHz Fixed-tuned Waveguide SIS Distributed Mixer With No Intefrated Tuning Circuit," IEEE Trans. On Applied Superconductivity, Vol. 13, No. 2, 680-683, June 2003.

[3] Cheuk-yu Edward Tong, Raymod Blundell, "Quantum-limited Mixing in a Transformer-coulpled SIS Resonator for the 600GHz Frequency Band, " thirteenth International Symposium on Space terahertz Technology, Harvard University, March, 2002.

[4] Y. Uzawa, A.Kawakami, S.Miki, and Z.Wang, "Performance of all-NbN quasi-optical SIS mixers for the terahertz-band," IEEE Trans. Appl. Supercond.,Vol. 11, pp183-186, 2001.

[5] S.-C. Shi, T. Noguchi, and J. Inatani, "Performance of SIS mixers with distributed junction arrays," in *Proc. 8th Int. Space Terahertz Technol. Symp.*, Boston, MA, Mar. 1997, pp. 81–90.

[6] S. C. Shi, T. Noguchi, J. Inatani, Y. Irimajiri, and T. Saito, "Experimental results of SIS mixers with distributed junction arrays," *IEEE Microwave Guided Wave Lett.*, vol. 8, pp. 381–383, Nov. 1998.

[7] M. Takeda, T. Noguchi, and S.-C. Shi, "Predicted performance of superdonductor–insulator–superconductor mixers with inhomogeneous distributed junction arrays," *Jpn. J. Appl. Phys.*, vol. 39, no. 9A, pp. 5095–5098, Sept. 2000.

[8] Masanori Takeda and Takashi Noguchi, " A 200-285GHz Waveguide SIS Mixer With an Inhomogeneous Distributed Junction Array," IEEE Trans. On Microwave Theory and Techniques, Vol. 50, No.11, 2618-2623, Nov. 2002.

[9] Yoshinori Uzawa, Masanori Takeda, Akira Kawakami, and Zhen Wang, "Design and Analysis of an ALL-NbN SIS Mixer Using a Tuning Circuit With Two Half-Wavelength Distributed Junctions," IEEE Trans. On Applied Superconductivity, Vol. 13, No.2, 688-691,June 2003.

[10] M. Takeda, T. Noguchi, and S.-C. Shi, "Predicted performance of superdonductor–insulator–superconductor mixers with inhomogeneous distributed junction arrays," *Jpn. J. Appl. Phys.*, vol. 39, no. 9A, pp. 5095–5098, Sept. 2000.

[11] Wideband Circuit Design by H.J. Carlin and P.P. Civalleri CRC Press, 1997

[12] Sobol, I. M. The distribution of points in a cube and the approximate evaluation of integrals, *USSR Comput. Math. Math.Phys.* 7, 4, 86-112, 1967.

[13] Wenlei Shan, Takashi Noguchi, Shengcai Shi and Yutaro Sekimoto ,"Design and Development of SIS Mixers for ALMA Band 8", *IEEE Trans. Applied Superconductivity*, Volume 15, Issue 2, June 2005 Page(s):503 - 506

# 2.5THz multipixel heterodyne receiver based on NbN HEB mixers

S.Cherednichenko*[a], V.Drakinskiy [a], J.Baubert[b], B.Lecomte[b], F.Dauplay[b], J.-M.Krieg[b], Y.Delorme[b], A.Feret[b], H.-W.Hübers[c], A.D.Semenov[c], G.N.Gol'tsman[d],

[a] Chalmers University of Technology, Department of Microtechnology and Nanoscience, SE-41296, Gothenburg, Sweden

[b] Observatoire de Paris, LERMA, 77, Avenue Denfert-Rochereau, 75014, Paris, France.

[c] German Aerospace Center (DLR), Institute of Planetary Research, 12489 Berlin, Germany.

[d] Physical Department, State Pedagogical University of Moscow, 119891 Moscow, Russia.

*serguei.cherednichenko@mc2.chalmers.se ; http://www.chalmers.se/mc2/EN/laboratories/microwave-terahertz

**ABSTRACT**

A 16 pixel heterodyne receiver for 2.5 THz has been developed based on NbN superconducting hot-electron bolometer (HEB) mixers. The receiver uses a quasioptical RF coupling approach where HEB mixers are integrated into double dipole antennas on 1.5μm thick $Si_3N_4$/ $SiO_2$ membranes. Spherical mirrors (one per pixel) and backshort distance from the antenna have been used to design the output mixer beam profile. The camera design allows all 16 pixel IF readout in parallel. Measurements of the mixers sensitivity and the input RF band are presented, and compared against calculations.

# High current-density aluminum-nitride tunnel barriers grown by plasma nitridation from a remote plasma source.

T. Zijlstra, C. F. J. Lodewijk, D. N. Loudkov and T. M. Klapwijk
Kavli Institute of Nanoscience, Faculty of Applied Sciences
Delft University of Technology
Lorentzweg 1, 2628 CJ Delft, The Netherlands

High current-density tunnel-junctions are needed to achieve wide band operation of sub-millimeter mixers. Aluminum-oxide barriers have an upper limit (Kleinsasser et al[1]) of 20 kA/cm$^2$ , beyond which excessive sub-gap leakage emerges. Aluminum-nitride has been introduced by Shiota et al[2] as a suitable alternative, allowing higher current densities for similar thicknesses. Various encouraging results have been obtained, but the control turned out to be unsatisfactory (Bumble et al[3]). Unlike thermally grown aluminum-oxide the nitridation is conducted in a nitrogen plasma with a mixture of chemically active species of various energies. Most barriers to date have been grown in a parallel plate reactor in which the aluminum is in direct contact with the plasma. Very high current-densities (54 kA/cm$^2$) have been reached in barriers deposited by reactive sputter deposition by Wang et al[4]. An alternative nitridation-method has been introduced by Kaul et al[5] in which a Kaufmann ion source is used to generate a controlled ion flux.

Here we report on aluminum-nitride tunnel barrier growth using an inductively coupled plasma source (Weiler et al[6]). Such a source permits the control of the fraction of atomic nitrogen[7] in the total ion flux, while also allowing energies as low as a few eV. Therefore we are able to distinguish between pure chemical processes and ion-implantation processes in the barrier growth. Tunnel junctions with critical current-densities as high as 70 kA/cm$^2$ have been made successfully. We have realized ten batches of which the electrical characteristics respond systematically to variations in the process parameters. Typical devices have been implemented for potential use in ALMA Band 9 mixers[8].

Standard bilayers of niobium (100 nm) and aluminum (7 nm) have been used. The growth chamber is equipped with a COPRA source from CCR[9]. A comparison is made of growth at two different positions with respect to the source, leading to different growth rates. We find, counter-intuitively, that with increasing atomic nitrogen pressure the barrier thickness-growth decreases. We conjecture that an increase in molecular recombination reduces the density of active atomic nitrogen on the surface.

---

[1] A. W. Kleinsasser, W. H. Mallison and R. E. Miller, IEEE Trans. Applied Superconductivity **5**, 2318 (1995)
[2] T. Shiota, T. Imamura and S. Hasuo, Appl. Phys. Lett. **61**, 1228 (1992)
[3] B. Bumble, H. G. LeDuc, J. A. Stern and K.G. Megerian, IEEE Trans. Applied Superconductivity, **11**, 76 (2001)
[4] Z. Wang, A. Kawakami, and Y. Uzawa, Appl. Phys. Lett. **70**, 114 (1997)
[5] A. B. Kaul, A. W. Kleinsasser, B. Bumble, H. G. LeDuc and K. A. Lee, J. Mater. Res. **20**, 3047 (2005)
[6] M. Weiler, K. Lang, E. Li, J. Robertson, Appl. Phys. Lett. **72**, 1314 (1998)
[7] T. Czerwiec, F. Greer, and D.B. Graves, J.Phys. D: Appl. Phys. **38**, 4278 (2005)
[8] C.F.J. Lodewijk, T. Zijlstra, D.N. Loudkov, T.M. Klapwijk, F.P. Mena, and A.M. Baryshev, this conference.
[9] See T. W. Cecil, R. M. Weikle, A. R. Kerr and A. W. Lichtenberger, Applied Superconductivity Conference (2006) for related work.

# Integration and performance of the flight configuration SIR on TELIS

P. Yagoubov, G. de Lange, R. Hoogeveen

National Institute for Space Research, SRON, the Netherlands

V. Koshelets

Institute of Radio Engineering and Electronics, IREE, Russia

G. Wagner, M. Birk

Institute for Remote Sensing Technology, DLR, Germany

TELIS (Terahertz and submm Limb Sounder) is a three-channel balloon-borne heterodyne spectrometer for atmospheric research.

We present design and experimental results of the 500 - 650 GHz channel. It is based on a phase-locked Superconducting Integrated Receiver (SIR), on-chip combination of a low-noise SIS mixer and a superconducting Flux Flow Oscillator acting as Local Oscillator.

The SIR channel has been thoroughly tested and recently integrated into the TELIS instrument.

We will present experimental results of the completely integrated flight configuration SIR channel, including noise performance, (DSB NT below 300 K), beam pattern, system stability tests and gas cell measurements using flight electronics and backend spectrometer.

# Development of high-Q superconducting resonators for use as Kinetic Inductance detectors

*J. Baselmans, S.J.C. Yates, R. Barends, J.N Hovenier, J.R. Gao, and T.M. Klapwijk*

One of the greatest challenges in the development of future radiation detectors for space applications is the fabrication of large detector arrays, which should have background limited sensitivity in combination with many pixels with a multiplexed readout. Within this context we have started the development of Microwave Kinetic Inductance Detectors (MKID's) [1], which have the potential to fulfill both requirements. The heart of every pixel of a MKID detector array is an extremely high Q superconducting quarter wavelength microwave thin film resonator. Many resonators, each with slightly different resonance frequency, can be read out simultaneously using 1 single microwave low noise amplifier coupled to room temperature electronics enabling, in principle, arrays with $10^5$ pixels. We present measurements of thin film Coplanar waveguide (CPW) resonators, made from Aluminum on high dielectric substrates such as Si and Sapphire. We use an adiabatic demagnetization cooler (ADR) with a mechanical pulse tube cooler as cryogenic system. We have measured the electrical noise equivalent power (NEP) of several resonators made in different batches using sputter deposition and wet etching. The resonators are typically 3 μm wide and several mm long, with resonance frequencies between 3 and 8 GHz. The film thicknesses of the devices are 100 nm or 280 nm. We obtain a NEP ~ $1 \cdot 10^{-17}$ W/Hz$^{1/2}$ at frequencies of about 0.5kHz. At lower frequencies the NEP increases due to increasing phase noise from the resonators.

[1] Peter K. Day, Henry G. LeDuc, Benjamin A. Mazin, Anastasios Vayonakis & Jonas Zmuidzinas, NATURE 425, 817 (2003).

# SUPERCONDUCTIVE PARALLEL JUNCTIONS ARRAYS FOR SUBMM-WAVE LOCAL OSCILLATOR APPLICATIONS

**F. Boussaha[*], M. Salez[*1], J-G. Caputo[2], L. Loukitch[2], M. Chaubet[3]**

[*]LERMA, Observatoire de Paris, 77 avenue Denfert-Rochereau, 75014 PARIS – France
[1]Laboratoire des Solides Irradiés, Ecole Polytechnique, Route de Saclay, 91128 Palaiseau -France

[2]Laboratoire de Mathématique, INSA de Rouen, B.P.8, 76131 Mont-Saint-Aignan cedex – France

[3]CNES - BP 2220, 18 avenue Edward Belin, 31401 Toulouse Cedex 4 – France

We are developing Submillimiter-wave fully Integrated superconducting Receivers (SIRs) based on SIS mixer and SIS Multijunction operating as local oscillator. In deed, Multijunction-based FFOs may be an interesting alternative to LJJ-based FFOs in SIRs, allowing wide LO tunability, wide impedance matching bandwidths, and increased design flexibility and control of technological parameters. In this paper, we will present a numerical study of the Josephson electrodynamics in this kind of device and measurement results of output power from 5 junction array with current density of ~ 10 kA/cm² at submm-wave frequencies.

# The Impact of Standing Waves in the LO path of a Heterodyne Receiver

O.Siebertz, C.Honingh, T.Tils, C.Gal, M.Olbrich, R.Bieber, F.Schmuelling, R.Schieder

KOSMA, I. Physikalisches Institut, Universität zu Köln, Germany

## Introduction

Many observations of molecular lines in interstellar space or planetary atmospheres are affected by serious problems with standing wave patterns in the spectra. This becomes particularly nasty when studying broad extragalactic or pressure broadened atmospheric lines. When observing at THz frequencies these problems become more and more prominent due to the increased required bandwidth. Mostly, such patterns are attributed to reflections in the telescope optics, particularly from the sub-reflector in a Cassegrain telescope. But there are many other sources of standing waves in the quasi-optics of a heterodyne receiver. In this paper we describe the effect of reflections between mixer and local oscillator (LO) inside of a receiver. Some portion of the signal radiation becomes reflected by the mixer, and propagates partly to the LO with reduced amplitude due to the generally small reflectivity of the beam combiner. Nevertheless, although the power in one roundtrip becomes significantly reduced, there is still enough amplitude left, so that interference with the incoming signal radiation becomes visible.

The situation is depicted in Fig.1. In the figure the local oscillator and mixer reflectivity is indicated by the power reflection coefficients $r_L$ and $r_M$ respectively. The beam splitter reflects and transmits the power with coefficients r and t. The field of the LO at the mixer is composed of the superposition of all partial beams which are reflected back and forth between the LO and the mixer. Consequently, after summing up all partial beams, the total LO power coupled to the mixer is:

$$P_L = r \cdot P_{L0} \cdot A(\nu_L) \quad \text{with} \quad A(\nu) = [(1-u)^2 + 4 \cdot u \cdot \sin^2(2\pi s / c \cdot \nu)]^{-1}$$

$P_{L0}$ is the power of the LO itself as is incident on the beam splitter, and $\nu_L$ is the LO frequency. $A(\nu)$ is the Airy-function as is well known for optical resonators. $u = r \cdot \sqrt{r_M} \cdot \sqrt{r_L}$ is the roundtrip efficiency for the field amplitude within the cavity, $s$ is the optical path length between mixer and LO, and $c$ is the speed of light.

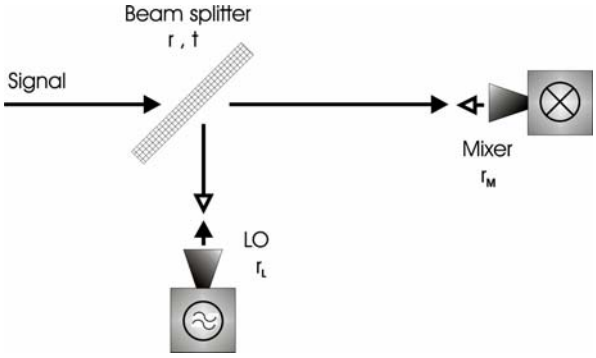


**Fig.1**
Beam path in a typical heterodyne setup

Due to the interference the LO power becomes periodically modulated as a function of frequency with a free spectral range $FSR = c/(2 \cdot s)$. The peak to valley ratio is given by:

$$PVR = (1+u)^2 / (1-u)^2$$

When assuming a LO-coupling of 10% and a reflection of 20% from mixer and LO, the resulting variation between peak and valley is 8%. This is a typical value one can easily verify by experiment when varying the distance between LO and mixer or the frequency of the LO.

The LO standing wave problem is a well known phenomenon, which confirms that there is usually an appreciable amount of reflection involved. But, what is mostly neglected, the consequences for the signal are as important. The signal power becomes also reflected within the mixer/LO cavity, and, similar as before, one finds for the signal power at the mixer:

$$P = t \cdot P_0 \cdot A(\nu_S)$$

with $\nu_S$ the signal frequency ($\nu_S = \nu_L \pm \nu_{IF}$) and $P_0$ the signal input power as is incident on the beam splitter. Consequently, there is also modulation of the detected signal power with frequency, which is due to the

effective filter characteristics of the mixer/LO cavity. With the assumed reflectivities above the signal gain is also modulated by 8% peak to valley, which is a lot more than one can expect from feedback effects due to reflections from the telescope optics or the calibration loads.

The signal power of a single sideband system, as seen with the calibration loads, is now given by

$$P_{Hot,Cold} = P_{Sys} + t \cdot P_{H,C} \cdot A(\nu_S)$$

with $P_H$ and $P_C$ the thermal emission from the hot- and cold-load, and $P_{Sys}$ the noise power of the system itself. This means that the y-factor, and the noise temperature accordingly, will depend on intermediate frequency like:

$$y(\nu_S) = P_{Hot}/P_{Cold} = [P_{Sys} + t \cdot P_H \cdot A(\nu_S)] / [P_{Sys} + t \cdot P_C \cdot A(\nu_S)] \approx 1 + t \cdot [P_H - P_C] / P_{Sys} \cdot A(\nu_L \pm \nu_{IF})$$

Consequently, y – 1 varies also by 8%, when assuming the same reflectivities as above.

With a dual sideband mixer the input to the mixer is the sum of the signal inputs from both sidebands, $P_l$ in the lower and $P_u$ in the upper sideband. The total power is then equivalent to:

$$P = P_{Sys} + t \cdot [P_l + P_u] = P_{Sys} + t \cdot [P_{l0} \cdot A(\nu_l) + P_{u0} \cdot A(\nu_u)] \quad \nu_u = \nu_L + \nu_{IF},\ \nu_l = \nu_L - \nu_{IF}$$

The two Airy-functions give rise to different gain factors for each sideband, which depend on the two signal frequencies $\nu_u$ and $\nu_l$. Their values vary with intermediate frequency, but in general differently for the two sidebands. If the cavity length $s$ happens to be a multiple of a quarter of the LO wavelength, both Airy-functions have identical values at all intermediate frequencies $\nu_{IF}$ so that both sidebands experience identical gain variations. (At this position the LO-power at the mixer is at minimum or maximum.) In this particular case the y-factor modulation is maximized. On the other hand, if the cavity length is an odd multiple of $\lambda_{LO}/8$, the ripples from both sidebands cancel each other nearly completely, and the y-factor modulation becomes minimized. This indicates that the appearance of the DSB-system noise temperature is strongly dependent on the actual LO tuning.

When observing spectra the problem is more intricate than it might appear, and this is due to the additional complication when calibrating a spectrum. A calibrated spectrum is usually evaluated from the ratio of two differences consisting of two measurements on sky (signal *S* and reference *R*) and two load measurements (hot load *H* and cold load *C*).

$$Signal \propto \frac{[S_l - R_l] \cdot A(\nu_l) + [S_u - R_u] \cdot A(\nu_u)}{[H_l - C_l] \cdot A(\nu_l) + [H_u - C_u] \cdot A(\nu_u)}$$

The problem is not visible, if a continuum signal is detected, which contributes equally in both sidebands, since the modulations $A(\nu)$ in the numerator and denominator cancel each other. This is different when observing lines signals in one sideband only, or when measuring S and R from different emitters, as is typical during atmospheric studies, while switching between sky and an internal load. Since the power differences *S*-*R* are different in the two sidebands, the modulating Airy-functions can not cancel, unless they are identical in both sidebands. Thus, the expression becomes dependent on intermediate frequency. In effect, the derived sideband efficiencies become modulated, and consequently, the calibration becomes uncertain. One should note that this problem arises only due to the fact that the calibration signal originates from both sidebands, but the signal does not. Only, if the two Airy-functions $A(\nu_l)$ and $A(\nu_u)$ are identical at all IF-frequencies (or proportional, if the mixer itself has different responsivities in the two sidebands), the calibration is unaffected, as is the case for a cavity length equal to a multiple of $\lambda_{LO}/4$. This means that it is best to maximize the ripple on the noise temperature in order to minimize the calibration error! Without this precaution, the variation of the sideband sensitivities can make it particularly difficult to disentangle complex signals which come from both sidebands, or, in general, to compare the strength of different lines with high confidence.

## Experimental setup

The standing wave related effects were investigated using the development models of the WBS (**W**ide **B**and **S**pectrometer) and of the band-2 mixer of the HIFI instrument (**H**eterodyne **I**nstrument for the **F**ar-**I**nfrared) for the ESA cornerstone mission "Herschel" [1], which both have been fabricated at KOSMA. The spectrometer is an acousto-optical spectrometer (AOS), which is based on a recent development of a so called "Array-AOS" [2,3]. It provides 4 input bands between 1.6 and 2.6 GHz each at a resolution of approximately 1 MHz per pixel. The full coverage of the IF bandwidth of the mixer (4 to 8 GHz) is achieved by frequency converters in the IF processor which splits the input band into four identical AOS bands. The mixer is a fixed-tuned SIS Nb-AlO-NbTiN waveguide mixer for the range between 600 and 825 GHz (see e.g. [1]). Coupling of LO power to the mixer is provided by means of a tilted polarizing grid. A gas-cell, filled with Formaldehyde ($H_2CO$) at a pressure of some ten mTorr, is positioned between

the mixer and two calibration loads (see Fig.2). The rotational molecular transitions are chosen for full saturation of the absorption in the center of the lines. Although $H_2CO$ has not a very dense rotational spectrum it has the advantage that the permanent dipole moment is very high and that it exhibits strong transitions over the full frequency range of the HIFI instrument between 500 GHz and 1.9 THz (see e.g. [5]).

The primary goal of the experiments was to analyze standing wave problems in a typical heterodyne receiver setup (see Fig.2). For this the spectrum is observed while detecting the emissions from the two calibration loads through the cell; a hot load at ambient temperature and a cold load at liquid Nitrogen temperature. A chopper wheel behind the cell switches between the loads at a rate of 0.8 Hz. The spectrometer is synchronized to the chopper, and for each measurement 100 such cycles are averaged in order to improve the signal to noise ratio. Before starting these integrations a "Zero-measurement" - $Z(v_i)$ - is performed for an identification of the zero level of the spectrometer itself.

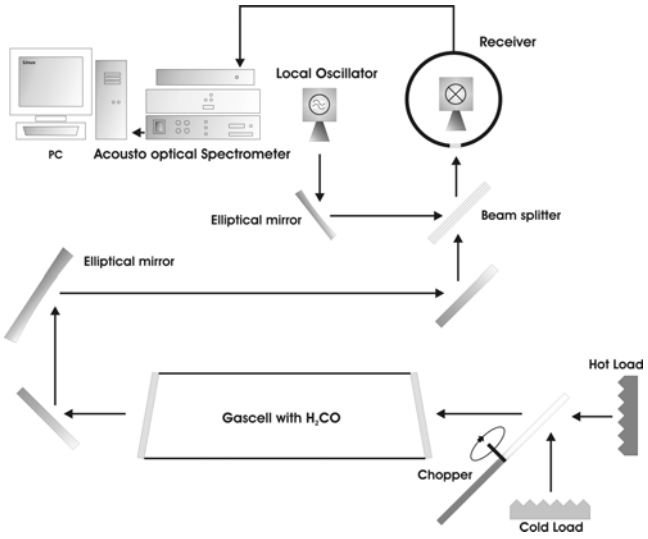


**Fig.2** Lay-out of the gas-cell test set-up

Four data sets are taken: two with filled cell against hot and cold load, and another two with empty cell. When dividing the difference of the first two by the difference of the second one obtains a calibrated spectrum with

$$Q_{u,l}(\nu) = 1 - \gamma_{u,l} \cdot (1 - e^{-\tau(\nu)})$$

$\gamma_{u,l}$ are the two sideband efficiencies, and we have used: $\gamma_u+\gamma_l+\gamma_0 = 1$. $\gamma_0$ stands for any other response like direct detection or harmonic response of the mixer. $\tau(\nu)$ is the frequency dependent optical depth of the line signal. A too small value of $\tau$ prohibits a precise determination of the sideband efficiency, since its exact value is usually unknown. Therefore, strong absorption lines (or long cells) are required so that the exponential vanishes. At the same time, there should be enough spectrometer bandwidth to cover some portion in the spectrum, which is free of molecular emission. The calibration accuracy can then be estimated from the resulting value of $Q$, which is supposed to be unity. Ideally, at sufficient optical depth, one obtains a precise value of the sideband efficiencies in the line centers:

$$Q_{u,l} = 1 - \gamma_{u,l}$$

With two molecular lines one can determine now each of the sideband efficiencies, and it is clear that the sum of both, $\gamma_u$ and $\gamma_l$, should be smaller than or equal to unity. How much it deviates depends on the amount of undesired response of the mixer. When positioning two saturated lines, one in the upper and the other in the lower sideband, at the same IF-frequency, $Q$ should reach a value of 0, unless there is significant amount of direct detection. This is an excellent method to determine direct detection of HEBs for example.

## Experimental Results

The first goal during the experiments was to verify the existence of a signal standing wave between mixer and LO. For most of the following experimental results the LO coupling to the mixer was chosen fairly high (≈ 20%) in order to show the effects very clearly. Fig.3 indicates how significant the gain ripple can become. Depicted is the y-factor minus 1, which is derived from a cold and a hot load measurement with the empty gas-cell in the optical path. It is evident that a strong standing wave pattern with more than 10%

ripple is present. The period of the pattern corresponds exactly to the distance between mixer and LO (~ 27 cm). The two curves in the figure represent the outcome at two different LO positions separated by a quarter of a wavelength, which changes the phase of the pattern by π. This is a perfect confirmation that the signal standing wave originates from reflections at the local oscillator. The pattern is superimposed with the variation of the system noise temperature across the IF band, therefore there is additional structure in the spectrum.

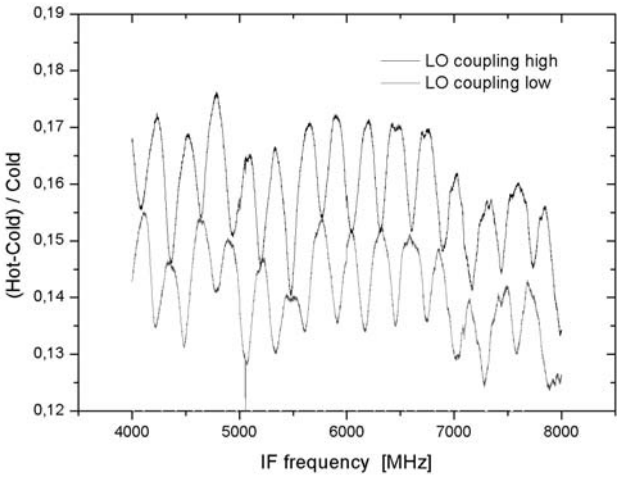


**Fig.3** Standing wave pattern visible in the y-factor during gas-cell measurements with empty cell. The LO frequency is about 668.5 GHz The two curves represent the results at two LO positions separated by a quarter of the LO wavelength.

When calibrating the spectra, the ripple vanishes, since the same structure is present in both, the signal and the calibration measurements. Thus, a uniform baseline is the result (see figures below). But, any change of the LO position for example during the time needed for a complete observing cycle (signal, reference, hot, and cold load) will make parts of it visible. From this it becomes evident that the stability of the LO position and frequency is decisive for the appearance of ripple structures in the spectra. In consequence, the stability of the complete system as seen with Allan variance tests for example becomes negatively affected.

The strong variability of the sideband responses of the mixer is visible in Fig.4. There are two pressure broadened molecular lines, one in each sideband, which are rather different in amplitude indicating some significant differences in sideband sensitivity of the mixer itself. Plotted are the lines seen for three different lengths of the mixer/LO cavity, which has also direct consequences for the LO power coupled to the mixer. In order to compensate for the changes in noise power output the mixer bias is adjusted for similar operating conditions. The amplitude of the lines varies significantly while the sum of the two sideband efficiencies γu and γl is not even close to "1", as would be expected. The result is a clear proof that there is large uncertainty for the sideband response which is obviously caused by different influence of the standing wave on the two sideband efficiencies. In the presented case the amplitudes of the two lines vary by as much as 20%. Similar observations were made when tuning the LO-frequency.

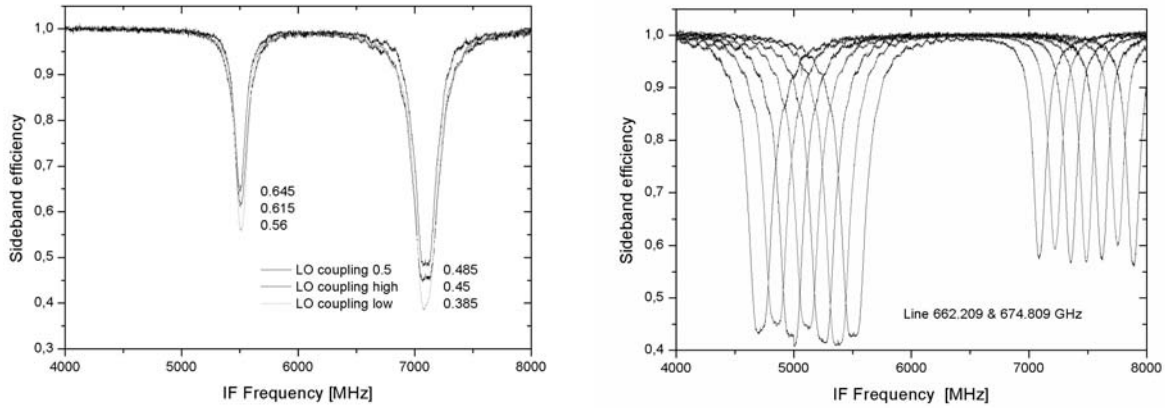


**Fig.4 Left:** Line pair at 662.209 GHz – lower sideband (right line) – and 674.809 GHz – upper sideband (leftline) – observed at different LO positions. Note that the numbers provided in the plot represent the values of 1-γ. R**ight:** Same line pair (positions are reversed) at different LO frequencies. The line amplitudes appear dependent on LO tuning.

In order to verify that the setup is not responsible for the differences, we tuned the LO so that the two lines appear at exactly the same intermediate frequency. The result is shown in Fig.5. Since the value of $\gamma_u+\gamma_l$ should be close to unity, a value near zero is expected at the peak of the combined lines. The deviation from this value is a good measure for the accuracy of the measurements. Part of the remaining 0.8 % signal at line center may be due to some minor amount of direct detection of the mixer, but a small contribution due to incomplete saturation is also possible (see Eq.(5)). In general one can conclude that the overall accuracy of the efficiency measurements is better than 1%, and that the effects on the calibration are definitely real.*-

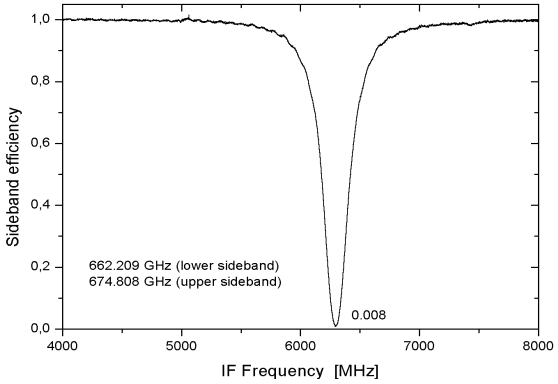


**Fig.5** Mixer response with the two lines of Fig.4 at identical intermediate frequency. The total response is 99.2%, which is very close to the theoretical value. This verifies that the lines seen in Fig.4 and 5 are fully saturated, and that the large difference in response between the sidebands is real and most likely caused by the mixer itself

## Con**clusions**

Our observations have confirmed that a major portion of baseline ripple in the spectra of heterodyne receivers can be attributed to standing waves in the mixer/LO cavity. The amplitude of the ripple structures depends directly on the coupling efficiency of the LO into the signal path. If one can afford to waste huge amounts of LO-power, minimum coupling should be used. Nevertheless, a coupling of 1% (r=0.01) causes still ripples in the range of 1% peak to valley. The situation is slightly worse when using a grating as beam splitter, since the polarization effects increase the problems. Much more troublesome is a Martin-Puplett diplexer! Exactly in IF-band center, where the diplexer should have maximum signal transmission, is no reflection of signal to the LO. But at the band-edges, if one octave of IF-band is used, the uncertainty of the sideband calibration can exceed ±20%, when using the same reflection coefficients for mixer and LO as above. This is due to the fact that a Martin-Puplett provides 25% reflectivity for the signal towards the LO at the band edges. The problem is rather difficult to handle, since the amplitude of the efficiency modulation is now dependent on IF-frequency, so that it is tricky to correct for during data analysis.

A ripple-free system would require that the calibration is also done with single sideband calibration loads. A single sideband filter helps, but it is important to implement a cold termination of the reflected sideband. This removes the ripple on the sideband efficiency because one calibrates now correctly with load signal from one sideband only, but the ripple on the system noise temperature remains. With a warm termination the situation deteriorates, because the radiation from a warm termination of the sideband filter co-adds to the signal of the calibration loads resulting in very different contributions from both sidebands. Good experience is made with sub-harmonically pumped mixers, because there is no possibility for the signal reaching the LO. Another and very practical way is to use a Fabry-Perot type diplexer, which does not allow any signal coupling to the LO (see e.g. [6]). But, similar as with a Martin-Puplett, the LO has maximum standing wave dependent on the coupling efficiency of the Fabry-Perot.

The LO standing wave itself is difficult to remove. A quarter-wave plate together with a linear polarizer can be useful, since it acts as an optical isolator for the reflected power. If it is placed in front of the LO, the signal and LO standing wave are both suppressed, but half of the LO power is wasted. Unfortunately, with simple quarter-wave plates or an equivalent grid/mirror arrangement the isolation is frequency dependent. One therefore has no full isolation at all signal frequencies. But isolation in the range of at least 15 dB is always possible (see e.g. [7]). It might be a bit tedious to tune the isolator for each new LO frequency, but it is probably worthwhile. An alternative method is to use a path-length modulator in front of the mixer or LO. If the modulation is fast enough and has sufficient amplitude, the ripple is effectively averaged out. The introduced LO-power modulation might be nasty, but, when synchronizing sampling time with modulation frequency, it should be possible to remove those effects. If a polarizing grid or a Martin-Puplett is used for LO-coupling, one has to be careful when using polarizing components for isolation. It requires some additional analysis to do it properly.

**References**

[1] Th.de Graauw, F.P.Helmich; Proc. of `The Promise of the Herschel Space Observatory', symposium held 12-15 December 2000 in Toledo, Spain, eds. G.L.Pilbratt, J.Cernicharo, A.M.Heras, T.Prusti, R.Harris, ESA SP-460, pp. 45-51, 2001

[2] J.Horn, O.Siebertz, F.Schmülling, C.Kunz, R.Schieder, G.Winnewisser; Exper.Astron. 9, 17-38 (1999)

[3] R.Schieder, O.Siebertz, F.Schloeder, C.Gal, J.Stutzki, P.Hartogh, V.Natale, Proc. of "UV, Optical, and IR Space Telescopes and Instruments", J.B.Breckinridge, P.Jakobsen Eds., SPIE 4013, 313-324, (2000)

[4] I. López-Fernández, J.D. Gallego, C. Diez, A. Barcia, J.M. Pintado, Proc. of "Astronomical Telescopes and Instrumentation" Conference: "Millimeter and Submillimeter detectors", Waikoloa (Hawaii, USA) on August 22-28 2002 SPIE 4855 (2002)

[5] The Cologne Database for Molecular Spectroscopy CDMSH; S. P. Müller, S. Thorwirth, D. A. Roth, and G. Winnewisser, Astronomy and Astrophysics 370, L49–L52 (2001)

[6] F.Schmuelling, B.Klumb, M.Harter, R.Schieder, B.Vowinkel, G.Winnewisser; Appl.Opt. 37, 5771 (1998)

[7] K.Eigler, R.Schieder, B.Vowinkel; 16th Int. Conference on Infrared and Millimeter Waves, Conf.Digest, Lausanne, SPIE 1576 (1991)

# THz direct detector with 2D electron gas periodic structure absorber.

D. Morozov[a], P. Mauskopf[a], I. Bacchus[a], M. Elliott[a], C. Dunscombe[a], M. Hopkinson[b], M. Henini[c]
[a]School of Physics and Astronomy, Cardiff University, 5 The Parade, CF24 3AA, UK
[b]Department of Electronics and Electrical Engineering, University of Sheffield, S10 2TN, UK
[c]School of Physics and Astronomy, University of Nottingham, NG7 2RD, UK

## ABSTRACT

We describe the performance of a direct detector that uses the high mobility 2D electron gas (2DEG) formed at the AlGaAs/GaAs interface as a frequency selective absorber. The 2DEG mesa-structure is etched to form a planar periodic structure with resonant absorption properties in the submm - THz region. Electrons in the 2DEG are heated by incoming radiation above the lattice temperature and the temperature of the hot electrons is measured by Superconducting - 2DEG - Superconducting (S-2DEG-S) tunnel junctions. The estimated noise equivalent power for such a detector at 100 *mK* is in order of $10^{-18}$ $W/Hz^{1/2}$. In this paper we present the spectral measurements and simulated results of absorption properties at 4.2 *K* for a resonant mesa geometry. The thermal conductance and time constant of 2D electrons are studied at 450 *mK*-4.2 *K*. We measure an electron-phonon conductance on the order of $10^{-17}$ *W/K* per electron at 450 *mK* which gives a low value of heat conductance 2DEG relative to normal metal absorbers due to the low 2DEG electron density. These devices have a combination of sensitivity and speed which makes them possible candidates for the components in future astrophysical THz instruments.

## 1. INTRODUCTION

The development of high sensitivity direct detectors for mm-Thz radio-astronomy has been a field of active interest for a few decades. Transition Edge Sensors (TES) [1], normal metal - insulator - superconducor tunnel junctions (NIS) [2, 3] and cold electron bolometers (CEB) [4, 5, 6, 7] are some of the technologies which have achieved extremely low value of *NEP*. Microbolometers like NIS and CEB detectors make use of the thermal isolation between electrons and phonons in normal metal absorbers with submicron dimensions to detect THz radiation. The two-dimensional electron gas in AlGaAs/GaAs heterojunctions at 4.2 *K* and lower temperatures is weakly coupled to the lattice and the hot electron effect in the 2DEG can also be used to make a sensitive bolometric detector in THz range. The 2DEG electron mobility ($\mu$) and density ($n_s$) can be set at optimal values during the semiconductor heterostructure's growth process so that a 2DEG will have up to $10^5$ times lower thermal conductivity per unit area than a normal metal absorber with the same DC resistance. The lower thermal conductivity allows detector designs of greater than sub-micron size, facilitating construction. These advantages make 2DEG detectors good candidates for filled arrays of ultra-sensitive bolometers with free-space absorbers.

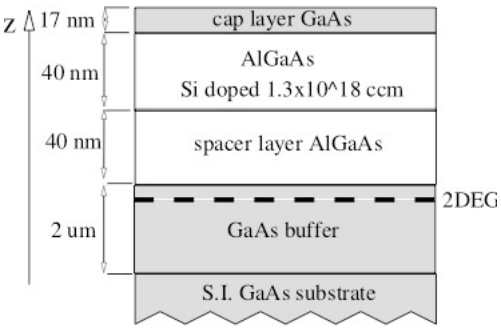


*Figure 1: Heterostructure*

In this paper we present low temperature transport measurements of 2DEG properties (thermal and electrical) and the design and measurements of a periodic absorber structure. We incorporate this absorber into a simple 2DEG HEB where the electron temperature is determined from the DC resistance of the 2DEG. We measure the sensitivity of this device at 4.2 K and compare it with estimates from DC IV curves. The sensitivity of the 2DEG HEB is limited by the slope of the resistance vs. temperature curve for the 2DEG. Finally we analyze a proposed detector consisting of a 2DEG as a radiation absorber and S-2DEG tunneling contacts as a thermometer to measure electron temperature of the 2D electrons.

## 2. SAMPLES AND EXPERIMENTAL TECHNIQUES

The heterostructures were grown by molecular - beam epitaxy and have the layer structure shown in fig. 1. We primarily used material from two growth runs, one from Nottingham University (NU03) and one from the University of Sheffield (S8).

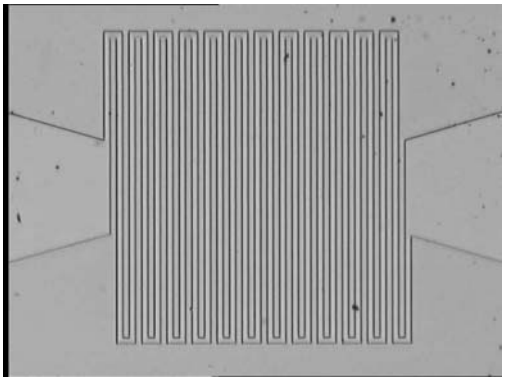

*Figure 2: Optical microscope picture of the meander type detector.*

The fabrication process for the devices included the following steps. First, mesas were formed by wet etching with $H_2SO_4/H_2O_2/H_2O$ etch solution. Then ohmic contacts were deposited by thermal evaporation of AuGe-Ni-Au and patterned in a "lift-off" process followed by thermal annealing in a $N_2$ gas atmosphere at $\approx 400^oC$ for 1 minute. We fabricated a variety of mesa geometries from the heterostructure wafer material. Hall bar devices were used to measure the thermal and electrical properties of the 2DEG. The mobility and electron density of 2D electrons at 4.2 *K* were found by measuring of Shubnikov-de-Haas oscillations period and amplitude with constant applied electrical power. For the heterostructures used in this study we measured $\mu$ =1.6 x $10^6$ $cm^2/Vs$ and $n_s$ = 1.8 $10^{11}$ $cm^{-2}$.

The absorber/detector design consisted of a meander geometry with ohmic contacts at either end. The path of the meander was 20 $\mu m$ wide with a filling factor of 50%. It covered an area of 1x1 $mm^2$ and is shown in fig. 2. For optical tests of HEB detector with the meander absorber we used a simple setup with a blackbody radiation source with temperature $T_{bb}$ = 800 *K*. The detector was mounted in an integrating cavity behind a Winston horn and thermally mounted on the cold stage of an cryostat at the base temperature close to 4.2 *K*. To block 300 K thermal radiation low-pass mesh filters with cut-off frequencies of ≈ 9 *THz* were placed at the 4 *K* and 77 *K* stages. The detector block with the horn inside the cryostat is shown in fig. 3. The power from the blackbody source was estimated to be $P_s \approx 3.1$ *nW* in the bandwidth of the filter in front of the detector. For the spectral measurements, the detector was placed at the output of a scanning Fourier Transform Spectrometer.

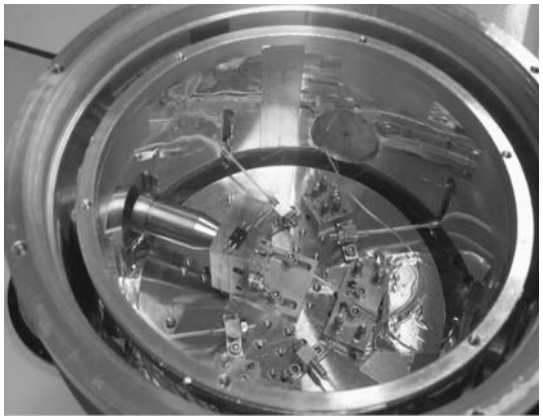

*Figure 3:Picture of the detector block with Winston horn inside the cryostat.*

## 3. EXPERIMENT AND DISCUSSION

We characterized the electrical and thermal properties of the 2DEG meander from the *R*(*T*) and using *IV* curves measured at different base temperatures. We obtained values for $(1/R)dR/dT$ and $G_{th}$ at 4.2 *K* and 450 *mK* in agreement with the values measured in the Hall bars. These parameters are listed in table 1.

Optical tests of the meander-type detector gave us the results shown in fig. 4. The maximum value of $S_V \approx 233 V/W$ occurred at bias current $I_b = 10 \mu A$ and $NEP \approx 8.9 \times 10^{-11} W/Hz^{1/2}$. An electical *NEP* can be calculated from DC measurements using $S_V = I_b(dR/dT)/G_{th}$ and taking into account that noise has contribution from Johnson and phonon noise [8]. Calculated values were $S_V \approx 270 V/W$ and $NEP \approx 3 \times 10^{-11} W/Hz^{1/2}$. This indicates that the peak optical efficiency of the detector is about 30%. The time constant of the detector ($\tau$) is estimated using a calculated value for the heat capacity of the electrons $C_e$ and the measured $G_{th}$ as $\tau = C_e/G_{th}$. To show the predicted performance of the same detector operated at *T*=450 *mK* we estimate the responsivity, *NEP* and time constant using the DC electrical characterisation. Experimental and theoretical data for different detector temperatures is given in table 2.

*Table 1:Experimental data of the DC electrical and thermal transport.*

| Sample | $(1/R)dR/dT$ $K^{-1}$ per square<br>4.2 *K* | $(1/R)dR/dT$, $K^{-1}$ per square<br>450 *mK* | $G_{th}$ , *W/K*<br>4.2 *K* | $G_{th}$ , *W/K*<br>450 *mK* |
|---|---|---|---|---|
| NU03 | $75.2 \times 10^{-3}$ | $3.2 \times 10^{-3}$ | $1.5 \times 10^{-15}$ | $1.1 \times 10^{-17}$ |
| S8 | $46.9 \times 10^{-3}$ | $3.1 \times 10^{-3}$ | $4.14 \times 10^{-14}$ | $1.2 \times 10^{-16}$ |

*Table 2:Meander detector performance DC biased at $I_b$ = 10 $\mu$A*

| *T, K* | $S_V$, *V/W* | *NEP, W/Hz$^{1/2}$* | $\tau$, *ns* |
|---|---|---|---|
| experim. 4.2 *K* | 233 | 8.9 x $10^{-11}$ | 0.94 |
| model 4.2 *K* | 270 | 3 x $10^{-11}$ | ≈1 |
| model 450 *mK* | 6 x $10^{3}$ | 2.5 x $10^{-14}$ | ≈100 |

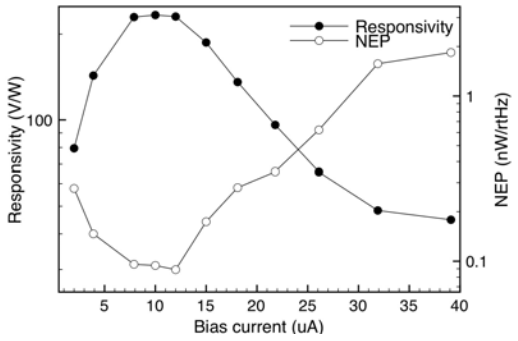


*Figure 4:Responsivity and NEP for the meander type HEB detector.*

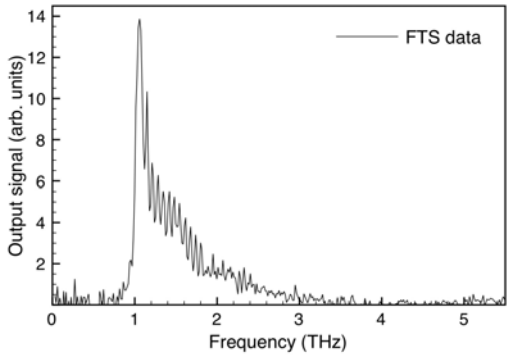


*Figure 5: FTS spectrum of the meander detector.*

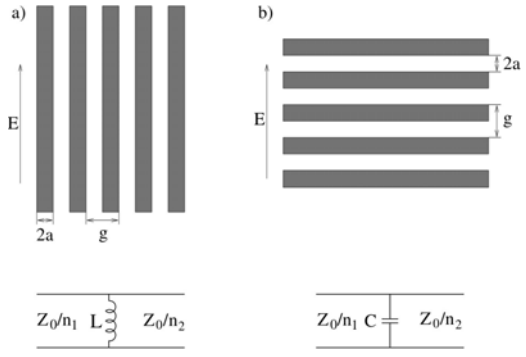


*Figure 6:(a) Inducive and (b) capacitive strip periodic structures and their equivalent electric circuits.*

Spectral measurements of the detector response have been made using a Fourier Transform spectrometer. The maximum detector response was in a narrow frequency range close to 1 *THz*. The dependance of the detector output signal on the frequency of the incident radiation is shown in fig. 5. The selectivity of the input signal frequency can be explained in terms of resonant absorption in periodic grid structures [9, 10]. Let us briefly discuss the model behind the resonance properties of periodic grid structures. The basic structures include inductive and capacitive gratings and they are shown on fig. 5 as well as corresponding equivalent circuits. The reactance of an inductive grid will be [9]:

$$\frac{X_l}{Z_0} = \frac{g}{\lambda} \ln \csc \frac{\pi a}{g}, \qquad (1)$$

where $Z_0$ = 377 Ohm is the free space impedance, $\lambda$ is the free space wavelength. Similarily, the reactance of a capacitive grid will be:

$$\frac{X_c}{Z_0} = \frac{-2}{n_1^2 - n_2^2} \left( \frac{4g}{\lambda} \ln \csc \frac{\pi a}{g} \right)^{-1}, \qquad (2)$$

where $n_1$ and $n_2$ are dielectrics refractive indices. Here we assume the equivalent electric circuit with capacitance and inductance in series. For a real structure one should also include resistance $R_0$ in the above model (see fig. 7). The transmittance through the shunted circuit is given by [9]:

$$T = \frac{4 n_1 n_2 \left( (R_0 / Z_0)^2 + (X / Z_0)^2 \right)}{\left(1 + (n_1 + n_2) R_0 / Z_0\right)^2 + (n_1 + n_2)^2 (X / Z_0)^2}, \quad (3)$$

here, $X = X_l + X_c$ is the full reactance of the circuit shown on fig. 7. In general this circuit will have a resonant absorption feature at a wavelength close to the periodicity of the structure $\lambda_0 \approx g$ in free space $n_1 = n_2 = 1$. But in the case of a 2DEG situated close to the surface of a GaAs with $\varepsilon$ =12.9 the absorption resonance will shift to longer wavelengths $\lambda \approx 300\ \mu m$. Using equations (1), (2) and circuit simulator we obtained absorption spectrum shown in fig. 8 for radiation at normal incidence to the device. The projected pattern from the meander will appear smaller at larger incidence angles thereby spreading the resonant absorption towards higher frequencies.

A high performance detector based on a high mobility 2DEG requires the separation of the 2DEG absorber and the electron temperature thermometer. Using the 2DEG resistance as an indicator of the electron temperature [11, 12] limits both the

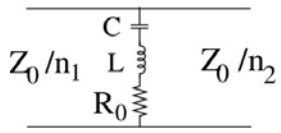


*Figure7:Equivalent circuit for meander type detector*

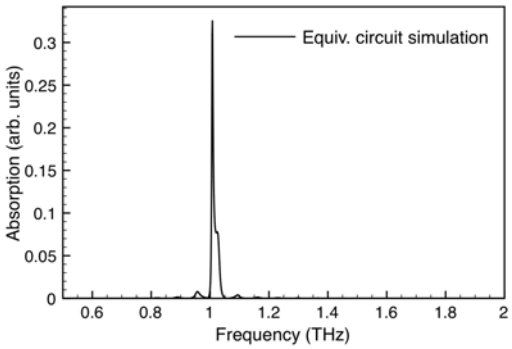


*Figure 8: Simulated absorption spectrum*

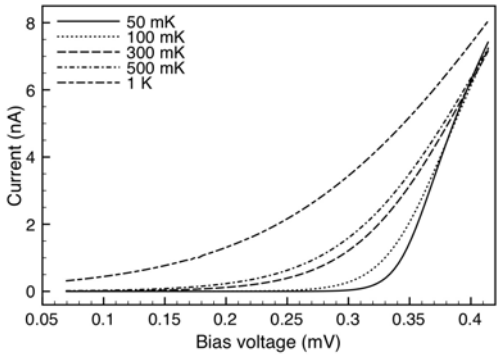


*Figure 9: Computed I-V curves for the detector with two S-2DEG-S junctions at different temperatures*

responsivity and the *NEP* due to weak $R(T)$ dependence of the 2DEG at liquid $^4$He temperatures. A 2DEG detector with a higher $dR/dT_e$ would have the advantages of both a low $G_{th}$ absorber and high responsivity thermometer. We propose to use a 2DEG-Superconductor junction as a thermometer to read out $T_e$ similar to Rowell and Tsui [13]. Tunnel junctions could be made by forming Schottky barriers in the interface between GaAs and superconducting contacts. We simulated a detector which has a 2DEG as a radiation absorber and two aluminum superconducting contacts with tunnel barriers as a thermometer. According to [2, 3] the tunneling current through the contact is given by:

$$I = \frac{1}{2eR_N}\int_{\Delta}^{\infty}\frac{1}{e^{(E-eV)/k_BT_e}+1}\frac{E}{\sqrt{E^2-\Delta^2}}dE, \quad (4)$$

where $R_N$ is the normal state resistance of the junction, $\Delta$ is the energy gap of the superconductor and $V$ is the bias voltage. For $(\Delta - eV) > k_BT$ the above equation simplifies to:

$$I \approx I_0 e^{-(\Delta-eV)/k_BT} \quad (5)$$

with $I_0 = (2eR_N)^{-1}\sqrt{2\pi\Delta k_BT}$. The junction can be current-biased such that the temperature responsivity $dV/dT$ is $\approx -(k_B/e)\ln(I_0/I)$ [2, 3].

Calculated IV curves for different temperatures are shown in fig. 9. Values of $R_N$ =5 *kOhm* and $2\Delta(0)_{Al}$ = 0.348 *meV* have been used [14]. Using the computed IV curves we estimate the detector performance. The assumed area of the absorber is 60 $\mu m^2$ and the operating temperature $T$ = 100 *mK*. At bias current $I_b$ = 0.4 *nA* the voltage response is $dV/dT \approx 287\ \mu V/K$, $S_V \approx 5.7 \times 10^9$ *V/W* and *NEP* $\approx 1.5 \times 10^{-18}$ *W/Hz*$^{1/2}$. For the estimation of *NEP* shot noise, Johnson noise and phonon noise contributions have been taken into account. In this type of detector at 100 *mK* shot noise contribution is dominant.

## 4. CONCLUSION

We report the experimental results of spectral measurements of a 2DEG absorber, electrical and thermal properties of the 2DEG at low temperatures. We also have measured performance of a 2DEG HEB as a direct detector of THz radiation at 4.2 *K*. We model the coupling of THz radiation to the 2DEG using a quasi-optical theory of periodic structures. This model reproduces the observed spectral response but it does not take into account the contribution of the kinetic inductance in the 2DEG as part of the equivalent circuit. Using these results, we estimate the *NEP* of a detector consisting of a 2DEG absorber and S-2DEG thermometer operating at 100 *mK* to be in order of $10^{-18}$ *W/Hz*$^{1/2}$.

This work is supported by a rolling grant from the Particle Physics and Astronomy Research Council (PPARC).

## REFERENCES

[1] J. Zmuidzinas and P. Richards, "Superconducting detectors and mixers for millimeter and submillimeter astrophysics," *Proceedings of the IEEE* **92**, pp. 1597–1616, October 2004.

[2] M. Nahum and J. M. Martinis, "Ultrasensitive-hot-electron microbolometer," *Appl. Phys. Lett.* **63**, pp. 3075–3077, 1993.

[3] M. Nahum, T. M. Eiles, and J. M. Martinis, "Electronic microrefrigerator based on a normal-superconductor tunnel junction," *Appl. Phys. Lett.* **65**, pp. 3123–3125, 1994.

[4] D. Golubev and L. Kuzmin, "Non-equilibrium theory of a hot electron bolometer with normal metal-insulator-superconductor tunnel junction," *Jour. App. Phys.* **89**, pp. 6464–6472, 2001.

[5] L. Kuzmin and D. Golubev, "On the concept of an optimal hot-electron bolometer with nis tunnel junctions," *Physica C* **372-376**, pp. 378–382, 2002.

[6] L. Kuzmin, "Superconducting cold electron bolometer with proximity traps," *Micro. Elect. Engn.* **69**, pp. 309–316, 2003.

[7] D.-V. Anghel and L. Kuzmin, "Capacitively coupled hot-electron nanobolometer as far-infrared photon counter," *Appl. Phys. Lett.* **82**, pp. 293–295, January 2003.

[8] P. L. Richards, "Bolometers for infrared and millimeter waves," *Jour. App. Phys.* **76**, pp. 1–24, July 1994.

[9] L. B. Whitbourn and R. C. Compton, "Equivalent-circuit formulas for metal grid reflectors at a dielectric boundary," *Applied Optics* **24**(2), pp. 217 – 220, 1985.

[10] R. Ulrich, "Far-infrared properties of metallic mesh and its complementary structure," *Infrared Physics* **7**, p. 65, 1967.

[11] J. X. Yang, P. Agahi, D. Dai, C. F. Musante, W. Grammer, K. M. Lau, and K. S. Yngvesson, "Wide-bandwidth electron bolometric mixers: a 2DEG prototype and potential for low-noise THz receivers," *IEEE Trans. on Micr. Theo. and Techn.* **41**, pp. 581–589, 1993.

[12] J. X. Yang, J. Li, C. F. Musante, and K. S. Yngvesson, "Microwave mixing and noise in the two-dimensional electron gas medium at low temperatures," *Appl. Phys. Lett.* **66**, pp. 1983–1985, 1995.

[13] J. M. Rowell and D. C. Tsui, "Hot electron temperature in InAs measured by tunneling," *Phys. Rev. B* **14**, pp. 2456–2463, 1976.

[14] D. Morozov, I. Bacchus, P. Mauskopf, M. Elliott, C. Dunscombe, M. Henini, and M. Hopkinson, "High sensitivity terahertz detector using two-dimensional electron gas absorber and tunnel junction contacts as a thermometer," *Proc. SPIE* **6275**, p. 62751P, 2006.

# A High Power Frequency Tripler for 100 GHz

Tomas Bryllert, Josip Vukusic and Jan Stake

***Abstract*—We present a high-power frequency tripler for 100 GHz. The tripler - that is based on a single HBV diode - produces >200 mW of output power with a 3-dB bandwidth of 6%. This is the highest output power ever recorded for an HBV based multiplier irrespective of output frequency. The module features an ultra-compact waveguide block design and a microstrip matching circuit on high-thermal-conductivity AlN to improve the power handling capability.**

***Index Terms*—Heterostructure Barrier Varactor, HBV, multiplier, high power, aluminium nitride, THz source**

## I. Introduction

Most of the systems operating at THz frequencies today use single pixel receivers. There is however a lot of work invested to expand these systems to arrays of receivers, both to improve the scanning speed for radio telescopes and to do real-time imaging in other applications. As the number of pixels increase the demand for local oscillator power will increase – which is the issue we address in this work.

The Heterostructure Barrier Varactor (HBV) is a device well suited to produce high power levels at THz frequencies. The fact that several varactors can be stacked on top of each other during epitaxy allows for fabrication of diodes with high power handling capability while keeping the devices electrically small. In this work we present a circuit that can handle >1 W of input power with a single diode. Another feature that favors the use of HBVs in THz frequency multipliers is that the devices have a symmetric C-V characteristic which will produce only odd harmonics of the fundamental frequency; this simplifies the circuit design for higher order multipliers (x3, x5). Both triplers and quintuplers based on HBV diodes have been demonstrated at low THz frequencies by different groups [1-6]. In this work we present state-of-the-art results from a high output power frequency tripler at 111 GHz. Initially we describe the design and fabrication of the tripler which is followed by a report of the measurement results.

## II. High Power HBV diodes

We have fabricated HBV diodes out of InGaAs/InAlAs/AlAs on a InP S.I substrate. This material system offers high electron mobility (InGaAs) as well as a high conduction band offset in the varactor - resulting in low leakage current. The epitaxy consists of three stacked diode structures, and the diode is then fabricated with four series connected mesas (fig 1). This diode geometry gives a total of twelve varactor barriers, with a DC breakdown voltage of >40 V (fig 2).

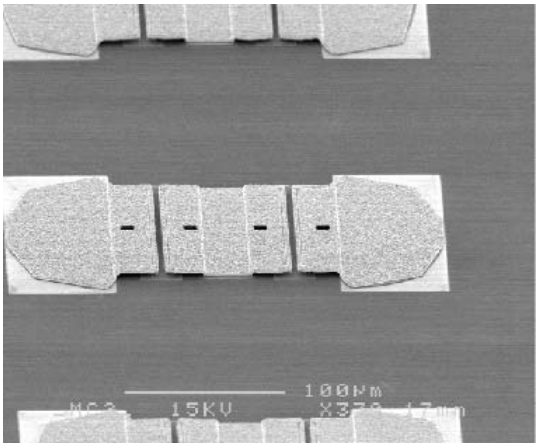


Fig. 1. SEM image of a high-power HBV diode on chip.

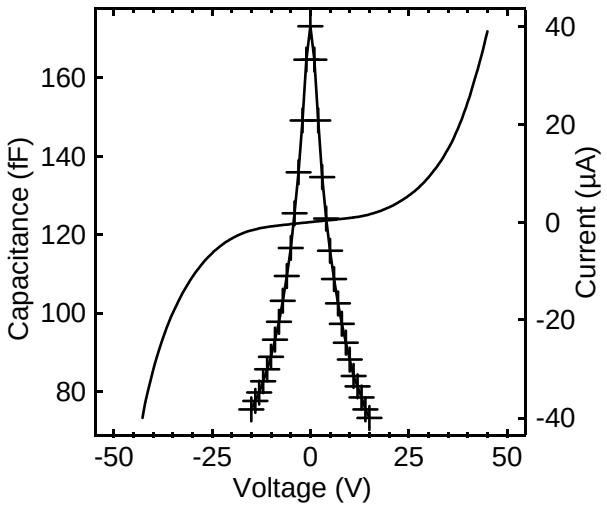


Fig. 2. DC characteristics of a high-power HBV diode with a mesa area of 1000 $\mu m^2$.

## III. Multiplier design

The HBV diode is flip-chip soldered onto a microstrip circuit that contains the impedance matching elements and waveguide probes. The microstrip circuit is then mounted in a waveguide block with waveguide input/output interfaces (WR22/WR10). One of the ambitions of the work was to make a design that was reliable and reproducible – therefore care was taken to minimize the number of manual steps in the

fabrication and mounting. No DC electrical connection between the microstrip circuit and the waveguide block was therefore used, and a new layout of the block was introduced as described below.

### *A. Waveguide block*

The waveguide block was machined in brass and electroplated with 2 µm of gold. The block is split in a plane perpendicular to the input- and output waveguides as seen in figure 3. This layout results in a very compact circular block only 6 mm thick and 30 mm in diameter.

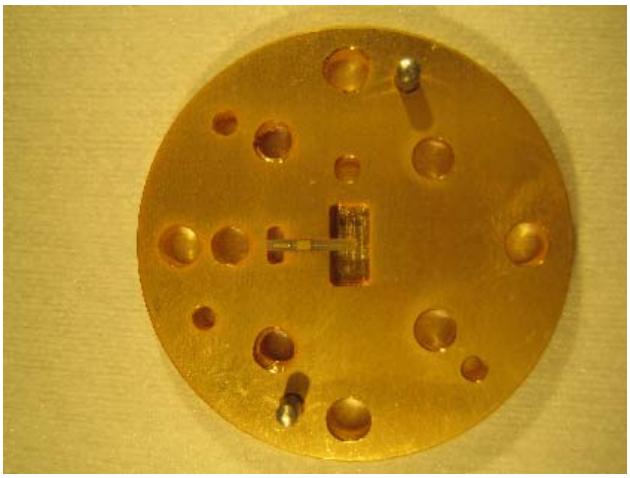

Fig. 3. One half of the waveguide block with a microstrip circuit mounted.

The two block halves are milled from one side only which gives simple and accurate machining. The microstrip matching circuit – including the HBV diode - is located in a channel connecting the input- and output waveguides. There are no mechanical tuners in this design.

### *B. Microstrip circuit*

The microstrip circuit was fabricated on an AlN substrate to improve the power handling capability (AlN has a high thermal conductivity ~ 170 W/mK). No DC connection between the waveguide block and the circuit was used since simplicity was one of the design objectives. This also means that open waveguide probes were used both on the input and on the output side.

The optimum embedding impedances were extracted from harmonic balance simulations using the Chalmers HBV device model [7]. These impedances were then implemented using a quarter wave transformer and an inductive line for the fundamental frequency, and an open-stub stop-filter in combination with the output probe for the third harmonic (fig 4).

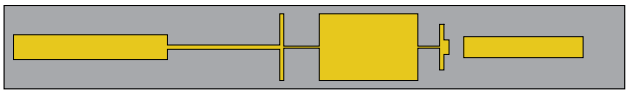

Fig. 4. The microstrip circuit showing the different matching elements and the input/output probes.

No power is generated at the second harmonic because of the symmetric capacitance-voltage characteristics of the HBV diode, which means that this harmonic does not have to be considered in the circuit design. The microstrip circuit was mounted in the waveguide block with glue.

## IV. RESULTS

The input signal to the multiplier was provided by a HP83650B frequency synthesizer followed by a Spacek power amplifier. To avoid having power reflected back from the multiplier to the power amplifier a waveguide isolator was inserted as shown in figure 5.

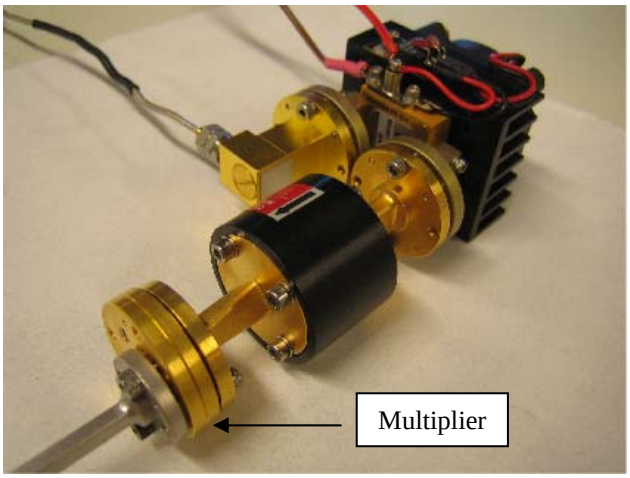


Fig. 5. Measurement setup showing power amplifier, isolator and multiplier.

The output power was measured using an Erickson PM2 power meter.

In figure 6 the output power is shown as a function of frequency at an input power of 1 W. A maximum conversion efficiency of 20% is measured at 111 GHz output frequency and the 3-dB bandwidth is 6%.

In figure 7 the output power is plotted as a function of input power showing a maximum output power of 240 mW.

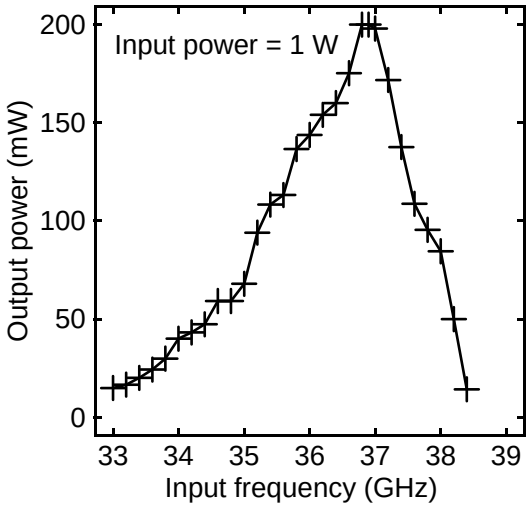


Fig. 6. Output power as a function of input frequency. The maximum conversion efficiency is 20% and the 3dB bandwidth is 6%

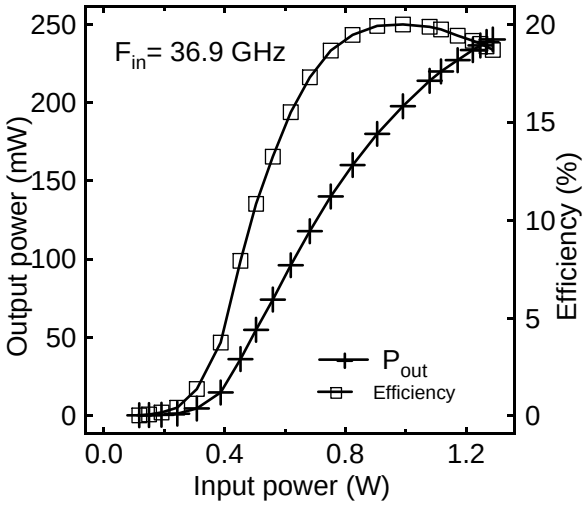


Fig. 7. Output power as a function input power. The maximum output power is 240 mW.

## V. Conclusion

A high power frequency tripler to 111 GHz using a single HBV diode has been designed and fabricated. 240 mW of output power and a conversion efficiency of 20% have been measured. The fixed-tuned 3-dB bandwidth was 6%. A new design of the waveguide block has been presented that makes the machining of the block simple and reliable. The microstrip circuits are also designed for reliable mounting with no DC connection to the block.

## Acknowledgment

The authors would like to thank Carl-Magnus Kihlman for fabricating the waveguide block and Mahdad Sadeghi for the growth of epi-material.

## References

[1] J. Vukusic, T. Bryllert, T. A. Emadi, M. Sadeghi, and J. Stake, "A 0.2-W Heterostructure Barrier Varactor Frequency Tripler at 113 GHz" *IEEE Electron Device Lett.*, vol. 28, no. 5, May 2007.

[2] X. Melique, A. Maestrini, R.Farre, P. Mounaix, M. Favreau, O. Vanbesien, J.-M Goutoule, F. Mollot, G. Beaudin, T. Narhi, D. Lippens, "Fabrication and performance of InP-based heterostructure barrier varactors in a 250-GHz waveguide tripler" *Microwave Theory and Techniques, IEEE Transactions on*, vol. 48, no 6, June 2000 pp.1000 – 1006.

[3] T. David, S. Arscott, J.-M. Munier, T. Decoopman, G. Beaudin, and D. Lippens, "Monolithic integrated circuits incorporating InP-based heterostructure barrier varactors" *IEEE Microw. Wireless Compon. Lett.*, vol. 12, no. 8, pp. 281–283, Aug. 2002.

[4] Q. Xiao, J. L. Hesler, T. W. Crowe, R. M. Weikle II, F. Duan, and B. S. Deaver, "High-efficiency heterostructure-barrier-varactor frequency triplers using AlN substrates" *Proc. IEEE MTT-S Int. Microw. Symp. Dig.*, Jun. 12–17, 2005, pp. 443–446.

[5] Q. Xiao, Y. Duan, J. L. Hesler, T. W. Crowe, and R. M. Weikle II, "A 5-mW and 5% efficiency 210 GHz InP-based heterostructure barrier varactor quintupler" *IEEE Microwave and Wireless Comp. Lett.*, vol. 14, pp. 159-161, Apr. 2004.

[6] T. Bryllert, A. Olsen, J. Vukusic, T. A. Emadi, M. Ingvarson, J. Stake and D. Lippens, "11% efficiency 100 GHz InP-based heterostructure barrier varactor quintupler" *Electron. Lett.*, vol. 41, no. 3, pp. 131–132, Feb. 3, 2005.

[7] M. Ingvarson, J. Vukusic, A. Ø.Olsen, T. A. Emadi, and J. Stake, "An Electro-Thermal HBV Model" *Proc. IEEE MTT-S Int. Microw. Symp. Dig.*, Jun. 12–17, 2005, pp. 1151-1153.

# High Output Power Low Noise Amplifier Chains at 100GHz

F. Maiwald, R. Lin, R. Dengler, S. Smith, J. C. Pearson, I. Mehdi, T. Gaier, J. Crowley*

Jet Propulsion Laboratory, California Institute of Technology, Pasadena, CA 91109, USA

* Currently working at MIT Lincoln Laboratory.

***Abstract* — Low noise amplifier (LNA) chains at 100GHz were constructed to be used as highly sensitive detectors in the development of the Haystack Ultra-wideband Satellite Imaging Radar (HUSIR). Three separately packaged MMICs are combined to provide a highly sensitive millimeter-wave detector. The LNA chip is a 0.1 micron InP based chip [1]. This is followed by 0.1 micron GaAs based driver and power amplifier MMICs [2]. This combination provides more than 50dB of gain over a frequency range of 90 to 100GHz with 50K noise temperature when measured at 20K ambient temperature. This chain provides enhanced functionality for the Haystack Ultra-wideband Satellite Imaging Radar (HUSIR).**

***Index Terms* — ground based radar, high gain amplifier, direct detector, millimeter waves, InP HEMT LNA, high power GaAs MMICs.**

## I. Introduction

The primary function of HUSIR will be to track and image satellites for the U.S. Space Command. To improve the imaging capabilities of HUSIR, wideband and sensitive W-band receivers are required. One of the key-components would be W-band LNAs optimized for these receivers, when cooled to 20K.

The W-band MMIC LNAs [1] and MMIC driver amplifiers [2] that have been used in this study were originally developed for ground-based and space-born radio astronomy. In this study those LNAs and amplifiers were utilized to construct sensitive receiver chains with high gain and low noise temperature. Four LNA chains with comparable performance were characterized. The measured results are presented and guidelines for a safe RF input power range are provided.

## II. LNA CHAINS

The LNA chains were tested in a cryostat capable of reaching temperatures below 20K by using two Watts cooling power generated from a closed cycle helium refrigerator. The input and output of the chains were connected to calibrated WR-10 waveguides which include 12.7 micrometer thick vacuum windows made of Mylar. A U-shaped bracket made of copper provided optimal thermal contact to the cold-head. An active temperature controller using calibrated Si-diodes was utilized to keep the temperature variation on the LNA below 0.1K. In order to minimize the thermal conduction of the bias connections, seven duo-twist phosphor bronze wires from Lake Shore, each with 0.127mm diameter and 30cm length, were thermally connected to the 70K stage of the cold-head.

Figure 1 shows a complete LNA chain before it was installed into the cryostat. The noise temperature of the LNA MMIC was less than 50K with more than 20dB gain in the targeted frequency band from 92 to 100GHz at 20K operation temperature.

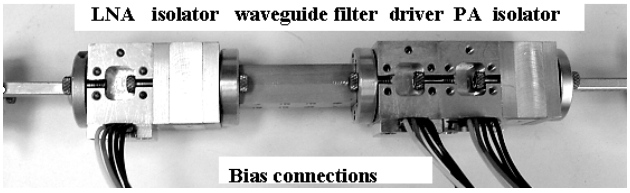


Figure 1: On the left side the input waveguide was attached to the LNA, followed by a WR-10 isolator and a very narrow banded waveguide filter (both made by Millitech). A driver and power amplifier stage provided sufficient system gain. A WR-10 isolator was attached on the output (right side). The total dimensions of the assembled chain were 20x20x160 mm.

A compact and low loss WR-10 isolator was implemented in order to reduce the impedance mismatch between the output of the LNA and the narrow-band WR-10 waveguide filter. Impedance matching at the output was achieved by a second isolator. The bandwidth of the WR-10 filter was designed to cover 92 to 100GHz with 80dB rejection outside the band (Figure 2). The cut-off condition of the waveguide at low frequencies naturally provides for the rejection, but at high frequencies it was necessary to implement a Chebyshev filter with 80dB rejection out of band. Additional rejection at frequencies greater than 103GHz was provided by the roll-off slope of 1.1dB/GHz from the power amplifier when integrated in the LNA chain. Impedance matching at the output was achieved by a second isolator. In Figure 2 the band-pass of the prototype filter is displayed. It was initially tuned too low at room temperature. When the filter was cooled

to 20K the band shifted upward by 0.5GHz. In order to properly adjust the bandwidth of the filter an appropriately designed shim was introduced between the two block halves. When shaving off or adding material between the split blocks the first-order effect was that the band-pass could be adjusted and the second-order effect was that the bandwidth could be adjusted.

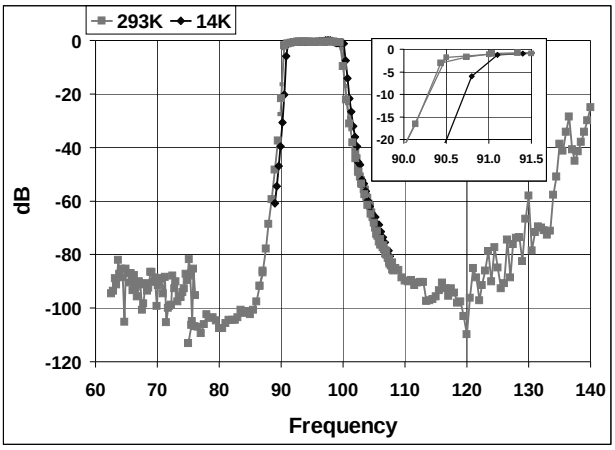


Figure 2: Measured band-pass characteristic of the prototype w/g filter at 300K and at 20K. The total power was determined with a calorimeter from Neal Erickson [3] (0.1microwatt to 200mW) and a vector network analyzer.

## III. RF INPUT POWER LEVEL

A major concern in radar applications, aside from reliability [4, 5], is that high RF power may leak into the front-end of the LNA chain. Therefore the minimum RF level that would cause damage needs to be determined. An indirect method is to observe the MMIC for changes in the DC bias conditions after the RF is removed. In this study, three different LNA chips from the same wafer were exposed to excessive RF powers at 20K in order to determine the maximum safe RF input power. The RF power was increased in steps and applied for at least five minutes to allow thermal heating to stabilize. Some of the measured DC bias conditions under increasingly higher applied RF powers are presented in Figure 3. At each increment, the bias conditions were compared to the initial recorded values without applied RF in order to check for permanent damage.

The biases of the LNA were separated as follows: Each LNA MMIC contained 4 FET stages each with two 2x20 micrometer fingers. The first and second stages were biased with a single gate power supply (Gate 1) and the third and forth stages were biased with an independent supply (Gate 2). All of the drains were biased together.

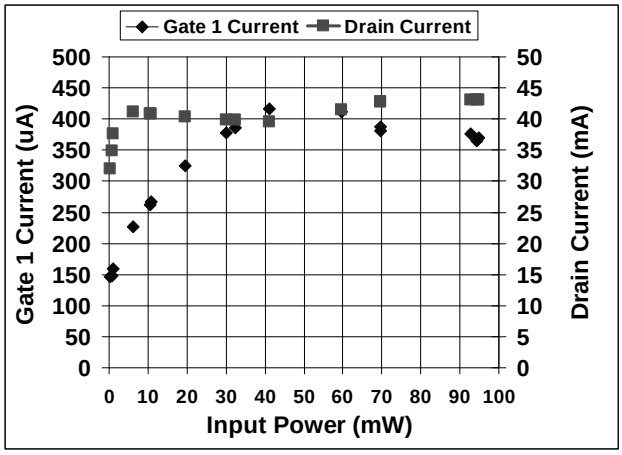


Figure 3: Measured bias conditions while RF was applied. Displayed are the changes in gate 1 bias current and drain current on one of the three LNAs when exposed to high RF input power. Permanent damage was observed above 40mW levels. No changes on gate 2 were observed.

The effect of high RF input power was detected on the drain current much earlier than at the gate 1 current. This is a result of small changes in the gate bias condition causing large changes of the drain current. The change in drain current at 0.5mA was in most cases nearly two times that of the initially measured bias conditions without RF applied. At these high RF levels the LNA did not contribute to the gain anymore because it was saturated already at a fraction of a microwatt. A maximum drain current was observed at RF levels around 10mW. When the RF power was increased above 10mW the current decreased by 10%. At RF levels above 40mW, permanent changes in the bias parameter were detected. The slope of the gate 1 current remained close to zero until the RF reached 1mW. Above this value the gate current increased nearly monotonically to more than a factor of 2 from the initial value. However, no change on gate 2 was observed down to the microampere level. This indicates that mostly the first two stages of the LNA were impacted by the applied RF.

The degradation of noise temperature was measured on one LNA only. It was confirmed that the noise temperature of the LNA degraded in concert with the changes in DC condition at levels above 40mW RF input power.

Additionally it was investigated whether RF power applied to the LNA at zero bias voltages would impose risk to the device. The induced currents for this condition were 240uA on gate 1 and 1mA on the drain at 20mW input power. The nominal bias conditions were used as the base-line to compare the actual measurements at each increment of RF power. No change was detected when a

RF level of 20mW was applied over 48 hours. In addition, the bias conditions were verified at 0.1mW, 0.2mW, and 0.3mW output power. Any change in input coupling on the first FET would have indicated a change from the initial bias values. However no changes in bias were detected.

The test confirmed that the LNA device would survive in an emergency "bias-supply-off" state, probably due to mismatching of the incident power when no bias voltage is applied. These results show that the LNA is much more robust than anticipated and that the incident RF power can be monitored even under saturation by monitoring the drain current for input power levels below 0.5mW and by the gate current for higher RF levels. These currents could be used as indicators of the applied power level even if the LNA is saturated.

In order to budget sufficient margin, it is not recommended to expose the LNA to RF levels above 10mW when biased at nominal conditions, assuming that 6dB de-rating is sufficient to maximize the LNAs life time. At this RF level the calculated power per micrometer gate length (2x20micrometer) was 250uW/um. Further investigations need to be performed to determine the effect of pulsed RF power to the LNA.

## IV. State-of-the-art performance

Optimal performance of the LNA chains was obtained by trading-off noise temperature, gain, 1dB compression point, and DC power consumption. A number of iterations on the combination of LNA, driver, and power amplifier were performed to satisfy most of the trade-off conditions. The performance of the final configuration of the four LNA chains was measured and the results are displayed in Figures 4-6.

The driver and power amplifier drains dominated the power consumption. Thermal dissipation was minimized at the expense of the 1dB compression and the gain. In this case the gate voltage was reduced until the amplifiers became current starved where gain and compression are a rapid function of gate voltage which is called the region of pinch-off. Above this point the gain and compression improved marginally with increasing gate. This is the most efficient operation point for these amplifiers but the 1dB compression point was reduced by about 2dB and the gain by about 1.5dB. However, the thermal dissipation was reduced by 50% which was very important to reduce the required cooling power. The maximum allotted power dissipation was 2W but the power dissipation was 1W under nominal operation.

Optimum gain (~22dB) of the LNA was observed to occur at $V_d \approx 0.9$V. The contribution to the drain current from Gate 1 was 4-7mA and for Gate 2 it was 3-5mA when optimized for noise temperature and gain. Both gates had similar voltages when optimized. The driver amplifier (~15dB) had its best gain between $V_d = 2.2$ and 2.6V at 20K. Increasing the drain current by applying positive gate voltage improved the gain slightly in the 92-100GHz range. While the best performance was observed at the maximum current tested, it should be noted that the gain difference between 200mA and 300mA was less than 0.5dB. The power amplifier (~22dB) had its best gain at 2.2V at 20K. Increasing the drain current by applying positive gate voltage increased the gain until about 320mA was reached. There was less than 0.5dB loss in gain when the current was reduced to 250mA.

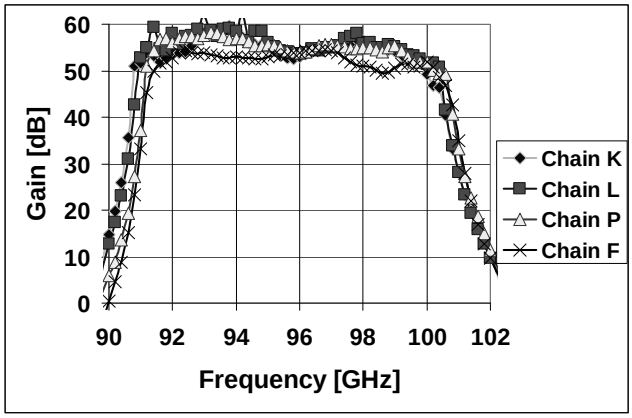


Figure 4: Measured gain of four LNA chains.

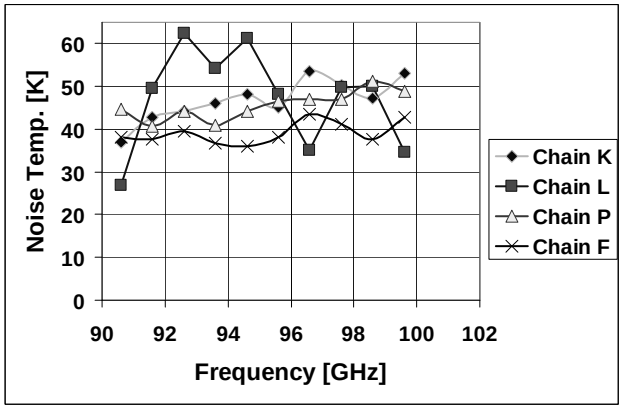


Figure 5: Measured noise temperature of four LNA chains.

In figure 5 the overall noise temperature is provided. The LNA noise dominates the noise temperature of the LNA chain. The driver and the power amplifier contributed approx. 10% to the noise temperature due to their noise figure of roughly 8dB. Excess noise had been observed in similar amplifiers

when biased higher than 3V with maximum rated current on the drain.

The 1dB compression point (see Figure 6) was limited by either the driver or the power amplifier depending on their operation point. The compression point was always increased with increasing drain voltage. In this study the best compression was at 3V for the driver and 3.2V for the power amplifier. Additionally, more drain current resulted in a slow increase in compression point. Typically the improvement was 0.2dB from the nominal current to the current limit. The measured 1dB compression point was observed to be between 10 to 16dBm.

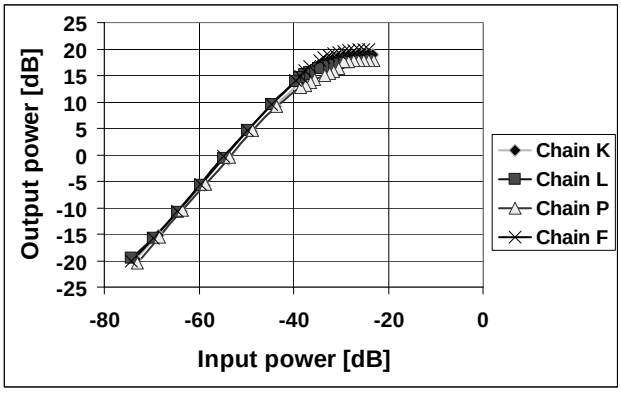


Figure 6: Measured 1dB compression point of four LNA chains at 96GHz.

## V. Conclusion

State-of-the-art MMICs that have been primarily designed and developed for astrophysics applications have been utilized to develop a wide-band low-noise millimeter-wave detector for radar. By optimizing low-noise and high-gain a compact chain that provides more than 50dB of gain with 50K of noise temperature has been demonstrated (at 20K). The 1dB compression point of a nominal chain is measured to be between 10 to 16dBm. Safe RF and operating conditions for these chains have been investigated for their utilization in radar applications.

## VI. Acknowledgement

The authors wish to acknowledge significant contributions from M. Soria-Price, A. Campbell, C. Flore-Helizon, and A. Peralta. Major contribution of critical components, including the WR-10 isolators and the WR-10 waveguide filters was provided by Millitech.

This research was carried out at the Jet Propulsion Laboratory, California Institute of Technology, and was sponsored by Defense Advanced Research Projects Agency (DARPA) through an agreement with the National Aeronautics and Space Administration. Opinions, interpretations, conclusions, and recommendations are those of the authors and are not necessarily endorsed by the United States Government.

## References

1. S. Weinreb, R. Lai, N. Erickson, T. Gaier, and J. Wielgus, "W-BAND INP WIDEBAND MMIC LNA WITH 30K NOISE TEMPERATURE," *IEEE MTT-S Digest*, pp. 101-104, Volume: 1, 13-19 June 1999.
2. H. Wang, L. Samoska, T. Gaier, A. Peralta, H.H. Liao, Y. C. Leong, S. Weinreb, Y.C. Chen, M. Nishimoto, R. Lai, "Monolithic power amplifiers covering 70-113 GHz," *IEEE Trans. Microwave Theory Tech*., vol. MTT-49, pp 9-16, Jan. 2001.
3. N. Erickson, "A Fast and Sensitive Submillimeter Waveguide Power Sensor," *Tenth International Symposium on Space Terahertz Technology*, pp. 501-507, Charlottesville, VA, 1999.
4. L. Samoska, K.Y. Lin, H. Wang, Y.H. Chung, M. Aust, S. Weinreb, and D. Dawson, "On the Stability of Millimeter-Wave Power Amplifiers," *IEEE International Microwave Symposium Digest 2002*, Vol. 1, pp.429-432.
5. Y.C. Chou, D. Leung, R. Lai, R. Grundbacher, D. Eng, J. Scarpulla, M. Barsky, P.H. Liu, M. Biedenbender, A. Oki, D Streit, "Evolution of DC and RF Degradation Induced by High Temperature Accelerated Lifetest of Pseudomorphic GaAs and InGaAs/InAlAs/InP HEMT MMICs," *40th Annual Int. Reliability Physics Symp*., Dallas, Texas, 2002 pp. 241-247.

# The Wide-Band Spectrometer (WBS) for the HIFI instrument of Herschel

O.Siebertz[1], F.Schmülling[1], C.Gal[1], F.Schloeder[1], P.Hartogh[2], V.Natale[3], R.Schieder[1]

[1] KOSMA, I. Physikalisches Institut, Univ. Cologne, Germany
[2] Max Planck Institut für Sonnensystemforschung, Katlenburg-Lindau, Germany
[3] IRA – INAF, Firenze, Italy

**Abstract**

The Wide Band Spectrometer (WBS) of The HIFI-instrument on Herschel consists of two Array-acousto-otpical spectrometers with 4 GHz total bandwidth each. The full bandwidth is composed of four 1 GHz sub-bands. The spectrometer includes an IF-processor, which splits the input band between 4 and 8 GHz into the AOS bands between 1.6 and 2.6 GHz. The spectrometers are stable with an Allan-variance minimum time of 500 seconds, and the gain linearity has been measured to better than ±0.3% maximum deviation from linear response. The total power consumption is 7 Watts for the AOS and 20 Watts for the IF-section. The spectrometers are fully space qualified and already in permanent use for system tests of the HIFI instrument during integration.

## Introduction

The HIFI instrument (Heterodyne Instrument for the Far Infrared) is one of the most complex heterodyne systems built for astronomy. It has 7 mixer bands covering the frequency range between about 490 and 1910 GHz nearly completely. For each band two mixers with crossed polarizations are implemented. The IF-bandwidth of most of the mixers is 4 GHz, which is spectrally analyzed by means of two acousto-optical spectrometers and/or two digital correlators. The WBS (Wide Band Spectrometer) is based on a recent development of an array acousto-otptical spectrometer [1], which provides four identical bands of 1 GHz bandwidth each at a frequency resolution of 1 MHz. Since spectrometers with 4 GHz instantaneous bandwidth at this kind of resolution do not exist, the frequency coverage is provided with a hybrid system, which splits the original band between 4 to 8 GHz into four identical bands between 1.6 and 2.6 GHz. We have built five WBS units: 1 development model (DM), 1 qualification model (QM), 2 Flight models (FM1 and FM2 for horizontal and vertical polarization mixers), and one spare model (SM).

## The spectrometer

A scheme of the WBS is shown in Fig.1. The spectrometer consists of two boxes, one optics unit (WBO) and one electronics unit (WBE). The electronics unit includes 4 AD-converters with 14 Bit each. In order to reduce differential non-linearity effects (DNL), a dither voltage is added to the ADC input, which is then digitally subtracted afterwards. This improves the DNL to that of a typical 16-Bit ADC, because the irregularities caused by the DNL are partly averaged out. The data are accumulated into custom designed ASICs, which are commanded via the command interface. In the IF section (WBI) the input band between 4 to 8 GHz is first amplified and then converted into 4 sub-bands between 1.6 and 2.6 GHz, which are then fed to the four transducers of the Bragg-cell in WBO. Variable attenuators are needed to adjust the gain for appropriate signal light levels on the CCD in WBO. A comb generator is built in for good frequency calibration of the spectrometer.

The principle of the optics of the array-AOS is shown in Fig.2. The laser output of approximately 35 mWatt is collimated by a collimation lens with an f-number of 0.5. The resulting parallel beam is then focussed by a cylindrical lens so that the light is well concentrated onto the narrow acoustic zone (~70 μm) in the Bragg-crystal. The beam is then split into four identical beams by a beam splitter. The beam distances match the distance between the four transducers in the Bragg-cell (1.6 mm). Behind the Bragg-cell the cross-polarized deflected light is passing a polarizer in order to avoid instabilities from scattered laser light. The following scan-lens focuses the light onto the CCD. The four signal beams are vertically sepa-

rated by means of a second cylindrical lens, which is positioned to match the location of the four resulting images with the four linear CCD lines, and to perfectly image the illuminated area in the Bragg-cell onto the CCD lines simultaneously. Since the signal beams cross between lens and CCD, a slit aperture is inserted at this position, which reduces the light scatter seen by each CCD line from the other areas in the Bragg-cell. This is extremely important because of stability problems due to the influence of laser speckles.

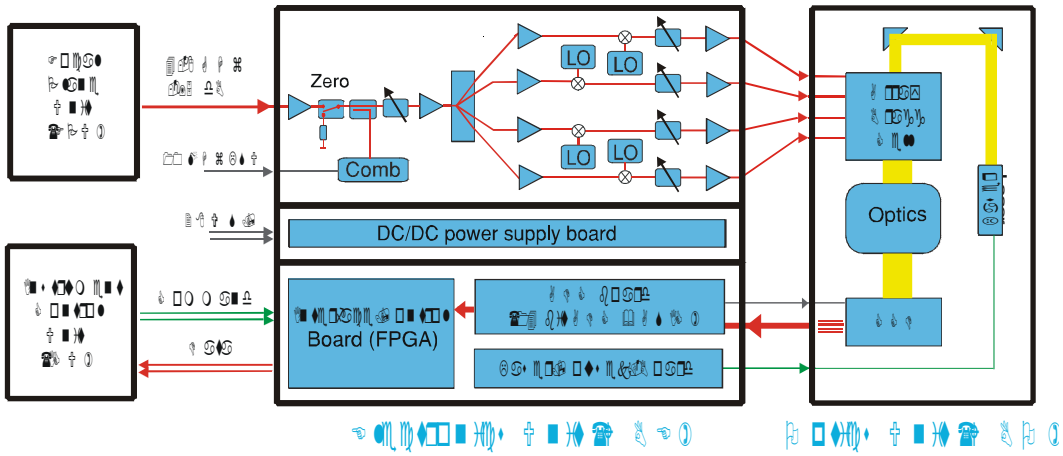


**Fig.1**: Scheme of the WBS

Since WBS is built for a space program with a lifetime of 4 years, the optics includes a second, redundant laser, which needs to be coupled to the system with low losses as well. Typically, a beam splitter is used for this purpose (see e.g. [2]), but it was important to make the optics as efficient as possible so that the additional 3 dB loss from an ordinary beam splitter was not acceptable. We therefore developed a special prism beam splitter, which accepts two laser beams at different input angles and provides identical output beams. The input and output facets of the prisms are oriented near Brewster angle so that negligible loss is introduced for both lasers at the same time. The accuracy for the prism assembly is very critical and it required several attempts to achieve satisfying results.

The requirements for the quality of the optics in an AOS are rather stringent since one has to deal with fully diffraction limited imaging. In order to avoid massive deterioration of the frequency resolution, the accuracy of all optical components must be better than $\lambda/10$ at a laser wavelength of 785 nm. This is a particular challenge for the collimation optics in front of the laser, which is difficult to fabricate because of the very small f-number. The imaging optics, which is a scan lens design, is also critical in this respect. When talking about imaging errors, it is clear that the orientation of the two cylindrical lenses in the system needs to be accurate within a few arc minutes. This requires very sophisticated alignment procedures, for which we investigated the far field patterns of the laser beams by means of a scanning linear CCD very carefully. At the same time, the accuracy of the position of the input laser beams must be accurate within 10 µm, and the input angle of the beams to the prism beam splitter needs to be within a few arc minutes as well. Again, this alignment is very critical.

Last, but not least, the whole assembly had be space qualified, meaning that it had to survive thermal cycling between –35 and +65 C, vibration test with 12 g rms, and shock test at 2000 g peak. The operating temperature of the mounting platform on the spacecraft was specified to +10 ± 5 C. It was also essential to include corrections for the absence of air, which has significant impact on the imaging in the optics unit. At the same time, degradations because of thermal expansion within a temperature range of 10 C (+10 ± 5 C) should not change the optical alignment within 20 µm or so. This needed a stress-free envelope of WBO, which we tried to ensure by grinding all mating surfaces of the cover and the base plate to an accuracy of a few µm, so that after combining the parts no visible change in performance due to stress deformation could occur.

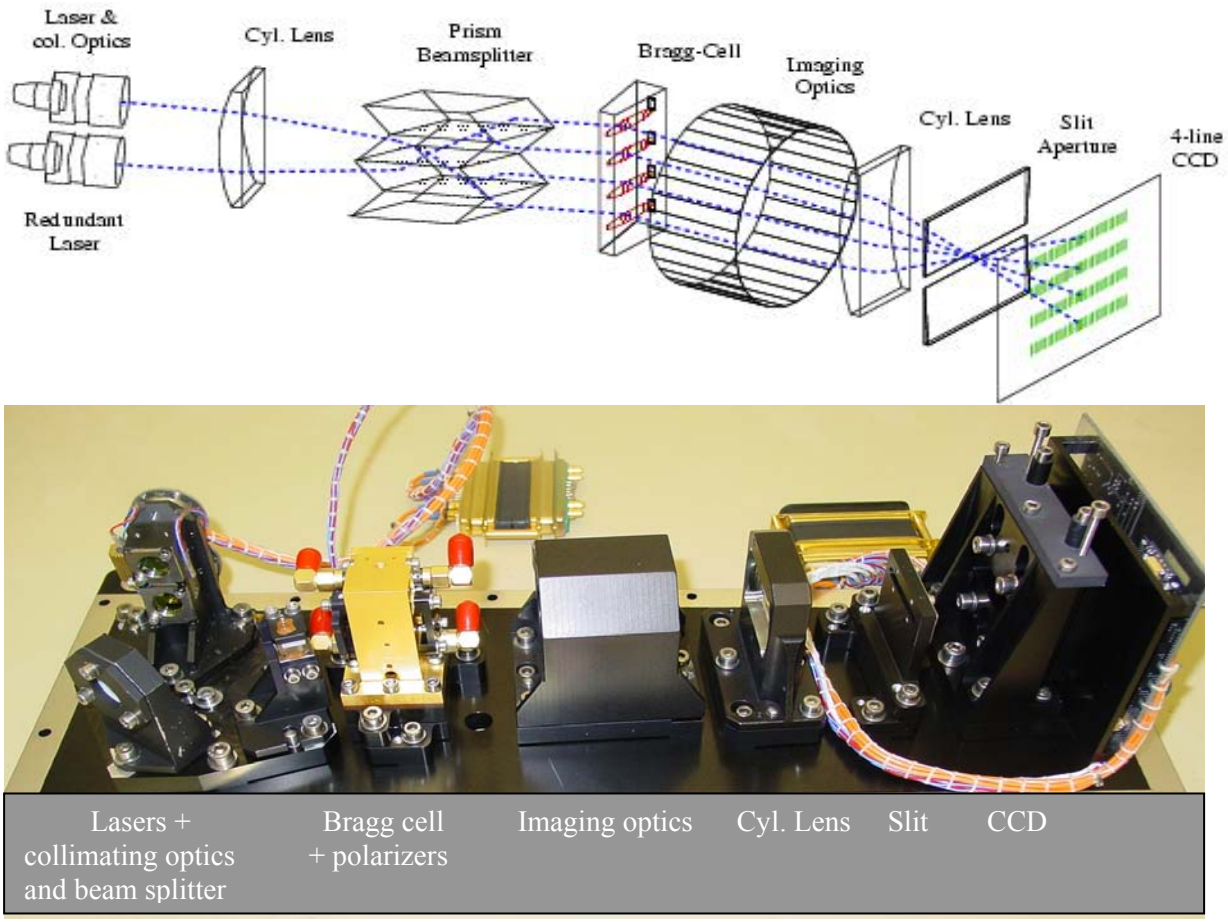


**Fig.2:** Scheme of the WBS optics and view of the hardware

As was mentioned before, the optical efficiency is rather decisive, because the required RF-power for sufficient illumination of the CCD needs to be as small as possible. This helps to keep the DC power for the final amplifiers in the IF-system at low level reducing the required DC power of the system. The focussing of the laser power onto the acoustic zones in the Bragg-crystal together with the perfect imaging of the illuminated area in the crystal onto the CCD gives an advantage in efficiency of more than one order in magnitude, in comparison to the SWAS AOS for example.

The stability of WBS is one of the most important parameters for WBS, since for a massive spacecraft like Herschel it is inevitable that switching between different positions on sky will cause substantial time delays. Therefore the Allan variance should still show near radiometric performance even at integration times above 100 seconds. This requirement is in conflict with the optical design, which is optimized for maximum efficiency, and is therefore extremely sensitive to alignment changes due to thermal drift for example. Therefore it was one of the most important interface requirements for the WBO to experience very little thermal fluctuations. The specification for the thermal interface to the spacecraft service module is one degree C per hour maximum gradient. Further increase of the thermal stability is achieved by reducing the thermal contact of WBO to the spacecraft base-plate.

### Test results

The specifications of WBS, as measured, are given in the table below. We consider the stability and the gain linearity as most important for the mission, but other parameters are important as well. In Fig.3 an Allan variance plot is depicted. Under best thermal conditions we have achieved an Allan variance minimum time near 500 seconds. This is calculated from the rms of the full 4 GHz spectrum and not from the

spectroscopic Allan-variance using two pixels only (see e.g. [3]). Under normal laboratory conditions it reduces to about 100 seconds. WBO is aligned for an operating temperature of the interface plate of about 10 C. Due to the additional thermal insulation the WBO operating temperature is raised from +10 C interface temperature to about +15 C. This was therefore the ambient temperature, at which the alignment procedures had to be done. Due to the very critical optical accuracy we had also to correct for the operating conditions under vacuum in orbit. This correction is achieved by means of an additional plane-parallel glass plate of 2 mm thickness in front of the CCD, which compensates for the shift of focus position between air and vacuum. This was finally verified during the thermal vacuum tests. The full 4 GHz baseline seen after 64 hours of integration at an On/Off switch cycle of 60 seconds is shown in Fig.4. The rms is very close to that predicted by the radiometer equation ($3.2 \cdot 10^{-6}$), when using a fluctuation bandwidth of 1.7 MHz (see Table).

| | |
|---|---|
| Total bandwidth | 4000 MHz in four sub-bands of 1000 MHz |
| Number of valid frequency pixels | 6910 |
| Resolution/fluctuation bandwidth | 1.1/1.7 MHz |
| Allan variance minimum time | > 200 sec |
| Frequency non-linearity | ±0.7 MHz |
| Power non-linearity | < 0.3 % |
| Noise dynamic range | 13 dB |
| Internal band-pass ripple | < 3 dB |
| Dimensions | 290x240x176 WBE, 400x170x130 WBO |
| Mass incl. harness | 12 kg (5.5 kg WBO 6.5 kg WBE) |
| Power consumption | AOS 7 Watt, IF-processor 20 Watt |
| Operating temperature | 10 ± 5 C at the interface (WBO) |

The noise dynamic range (NDR) of a spectrometer, which we specify as the input power range, within which the instrumental noise stays at less than 1 dB of the radiometric noise, is a serious concern for low noise mixer receivers with large IF-bandwidth. WBS has a specified NDR of about 10 dB, and we found a NDR up to 13 dB maximum. The main cause of spectrometer noise is shot noise of detected photo-elec-

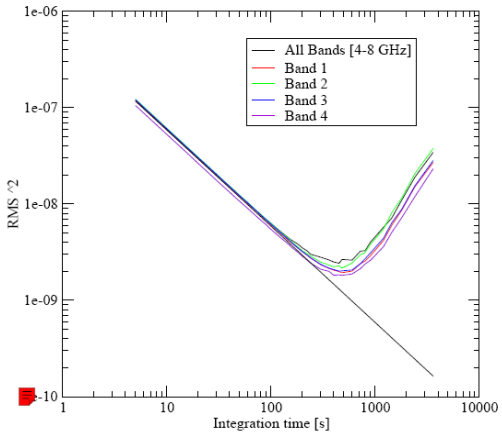


**Fig.3:**
Allan variance plot of WBS. Plotted are the rms-values of each of the 4 sub-bands and of the full 4 GHz band. They all are practically identical.

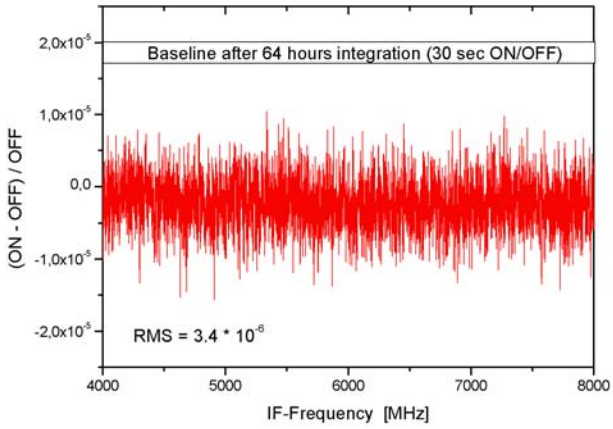


**Fig.4:**
Full 4 GHz baseline after long integration with WBS and a noise source. The rms matches the theoretical level of $3.2 \cdot 10^{-6}$ very closely ($B_{FI}$ = 1.7 MHz).

trons and read-out noise in the CCD. Significant parts of the NDR are already consumed by the gain ripple of the input and of the spectrometer and the power variations due to calibration load or signal power. The alignment of WBO as well as some equalization in WBI helped to reduce the instrumental gain ripple to better than 3 dB. One additional dB is already lost due to the necessity to stay safely below the saturation level of CCD and/or the AD-converter. Gain differences between the four sub-bands of WBO are taken care of by individual adjustable attenuators (±4 dB) in the IF. Therefore, only few dB are left as maximum

gain variations for all observations within each of the sub-bands. 3 dB power variations are expected as maximum signal variations on planets for example. This means that the maximum gain ripple from the mixer, cryogenic amplifiers is about 3 dB per 1 GHz when following the specification. This is a fairly tight requirement, which is not so easily met, but the increased NDR of WBS of 13 dB helps here a lot.

Gain linearity is an important property of any spectrometer. Non-linearity has consequences for the calibration accuracy, but is even more important for baseline ripple problems. In an AOS the major contributor to non-linearity is the CCD. Although photo effect should be precisely linear, it is very common that non-linearities of photo diodes, particularly in CCDs are problematic. The overall linearitiy of a CCD is strongly influenced by the amplitude and shape of the controlling pulses, and the applied voltages. In case of WBS, the situation became more complex, since it uses four linear CCD lines all operated in parallel on a single chip. The chip was cut out of a wafer taken from a normal linear CCD production line. After bonding and packaging we carefully investigated the properties of the chips. Since now four lines had to be driven in parallel instead of one only, we observed significant changes of the performance in comparison to single line chips. We therefore had to find out by experiment how the applied pulses and voltages had to be tuned. As a result, we have been able to verify a linearity of better than ±0.3% over the full NDR.

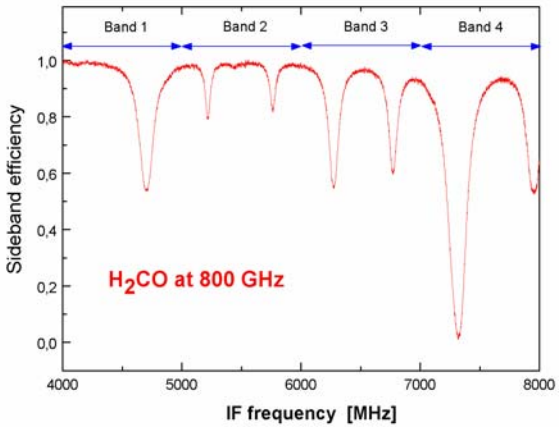


**Fig.5:**

Molecular line spectrum seen with WBS-QM through a gas-cell together with the Band 2 QM mixer of HIFI. The strong line to the right is the superposition of two saturated lines in both sidebands.

As an example, Fig.5 shows a 4 GHz spectrum of Formaldehyde at a frequency near 800 GHz, taken with the development model of WBS through a 35 cm long gas-cell. The mixer is a Band 2 mixer of HIFI, which was also developed at KOSMA. The lines are from both sidebands, and the strongest line at 7300 IF-frequency is a superposition of two saturated lines in both sidebands. Therefore, the response is 100% instead of only 50% for a line from one sideband only (see Poster P10 at this conference). The measurement took about 4 minutes and the signal to noise is nearly ideal. Note that there is practically zero baseline distortion. This is very satisfying when considering that the spectrum is the result of four independent measurements, HOT- and COLD-load seen through filled cell and HOT- and COLD-load seen through empty gas cell. The spectrum is the ratio of the differences of the two pairs of data. Very good power stability is demonstrated by the value of unity at absorption free frequencies. In particular, platforming is not visible, which confirms the excellent stability of the system.

## References

[1] A 4X1 GHz Array Acousto-Optical Spectrometer; J.Horn, O.Siebertz, F.Schmülling, C.Kunz, R.Schieder, G.Winnewisser; Exper.Astron. 9, 17-38 (1999)

[2] SWAS-AOS: The First Acousto-Optical Spectrometer in Space; J.Frerick, M.Klumb, R.Schieder, V.Tolls, G.Winnewisser, Proc. "Infrared Spaceborne Remote Sensing VII", M.Strojnik, B.F.Andresen Eds., SPIE 3759, 170-179 (1999)

[3] The Cologne Acousto-Optical Spectrometers; V.Tolls, R.Schieder, G.Winnewisser; Experimental Astronomy 1, 101 (1989)

# FFT spectrometer for (sub)mm radiometer applications

A. Emrich, M. Krus, J. Riesbeck
Omnisys Instruments AB, Gruvgatan 8, 421 30 Göteborg, Sweden

***ABSTRACT***

The FFT spectrometer is one of 5 types of spectrometers being considered for space based (sub)millimetre heterodyne systems. The advantages of the digital autocorrelation and FFT spectrometers compared to Chirp Transform, Acousto Optical and Filterbank spectrometers are; stability, compactness, high reliability and variability in bandwidth and resolution. FFT spectrometers based on the latest generation of FPGA devices now promise a cost effective alternative for low to medium bandwidth applications with high resolution requirements.

Omnisys has an FFT spectrometer design optimized for ground based applications. It follows the single Eurocard standard size and provides up to 2 GHz bandwidth and 1-4 inputs. With four inputs, the maximum processed bandwidth is 500 MHz.

Configurations with polyphase filtering, polarization processing and variable resolution over the processed band have also been tested. Results will be shown.

Omnisys FFT board provides 2 GHz processed bandwidth with a power budget of less than 20W. It seems possible to reduce this number to about 10-12 W in the short term for low power applications and to 5-7 W in a few years time.

A radiation tolerant design is in the pipeline. The main issue will be the power supply as providing a well conditioned 1.2 V rail with 8-10 A as well as 1.8, 2.5, 3.3 and 5 V will be a challenge with rad tolerant components.

For the SuperCAM imaging system, 16 boards will be used in two single height 19” crates to provide 64 spectrometers. It could be upgraded to provide 64 times 1 GHz by simply adding two crates. Test results will be shown in the conference.

In the picture to the right, we have 8 FFT boards providing up to 32 x 2048 channel spectrometers.

These can be housed in one single height 19” crate together with IF systems and embedded computers providing flexible interfaces to front-ends as well as flexible interfaces for switch synchronization, data readout and other forms of control. The default interface is 100 MBit/s Ethernet.

This is a breakthrough for future imaging applications as we can provide spectrometers for 5 kEuro each (in reasonable volume).

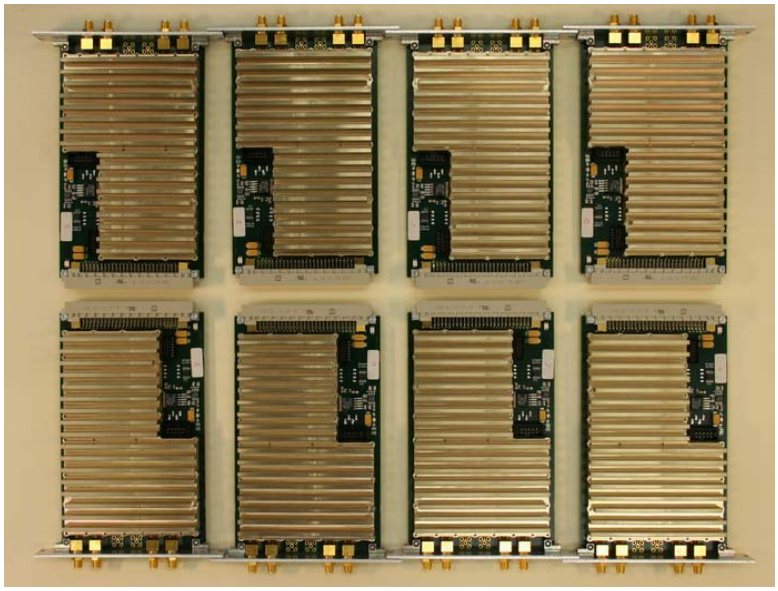

# Membrane Tip Probes for On-Wafer Measurements in the 220 to 325 GHz Band

Richard Campbell[1], Michael Andrews[1], Lorene Samoska[2], Andy Fung[2]

Abstract: We have developed a membrane-tip wafer probe for on-wafer measurements of passive structures, semiconductor devices and amplifiers in the 220 to 325 GHz WR-3 waveguide band. The probe provides the connection between an Oleson Microwave Labs Vector Network Analyzer (VNA) mm-wave extender head and on-wafer ground-signal-ground contacts. The probe has a section of WR-3 waveguide with a standard flange, a waveguide-to-coax transition with provisions for adjustment of both the E-field launch and back short. From the waveguide-to-coax transition, a short length of UT-013 coax connects to a thin-film membrane that includes a coax-to-microstrip transition and three wafer contacts manufactured photolithograpically using Cascade Microtech's thin-film process. The wafer contacts use the same mechanical structure and metallurgy as Cascade's Pyramid probe series, and are rated for millions of touchdowns with contact resistance of a few tens of milliohms even on aluminum pads.

Initial measurements on a pair of WR-3 probes and a standard calibration substrate with Cascade's 140 to 220 GHz VNA system suggest that loss is dominated by the length of waveguide between the coax-to-waveguide transition and the Oleson Microwave Lab mm-wave extender head. Measurements on the WR-5 band VNA are limited to the lower third of the WR-3 band. A second set of probes was built using significantly shorter waveguide sections. The original probes and short waveguide probes were then measured on the Jet Propulsion Labs WR-3 VNA system [1,2]. Loss through the longer probes was more than 5 dB from waveguide flange to probe tip, and loss through the short waveguide probes was near 2.5 dB for most of the WR-3 band, with increased loss above 300 GHz. Increased loss above 300 GHz is apparently due to poor contact with the back short during the measurements for the probe we tested.

Since the waveguide probes have electrically floating center contacts on the Ground-Signal-Ground membrane, we have also developed integrated bias Ts. To date, in-band performance of the bias Ts has only been measured on the WR-5 VNA, and the out-of-band performance measured using a DC to 110 GHz VNA.

[1]Cascade Microtech
2430 NW 206th Ave
Beaverton, OR 97006

[2]Jet Propulsion LaboratoryCalifornia
Institute of Technology, M/S 168-314
4800 Oak Grove Drive
Pasadena, CA 91109

This work was supported in part by the Jet Propulsion Laboratory, California Institute of Technology, under a contract with the National Aeronautics and Space Administration.

## Introduction to on-wafer probing of sub-mm wave circuits

Figure 1 illustrates how a pair of wafer probes is used to test a circuit. Figure 2 is a close-up sketch showing the parts of a wafer probe, and figure 3 is a photograph of a WR5 probe showing scale.

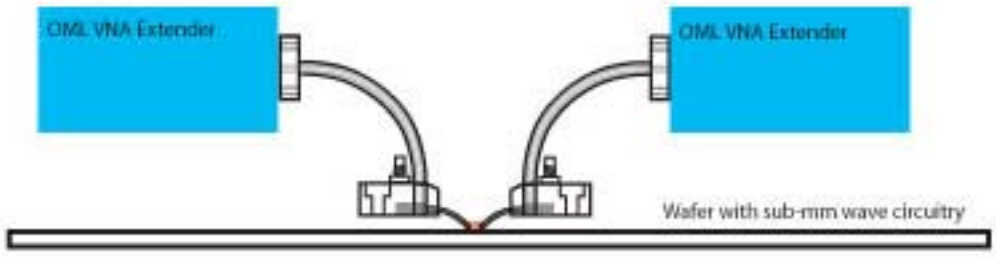


On Wafer Measurement using OML VNA Extenders and Wafer Probes

Figure 1

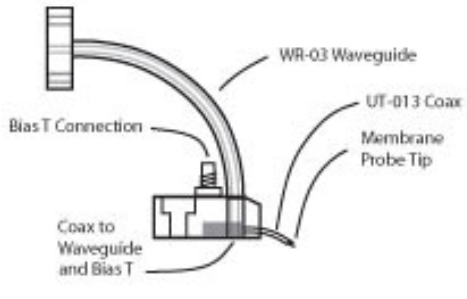



Probe Detail Sketch

Figure 2

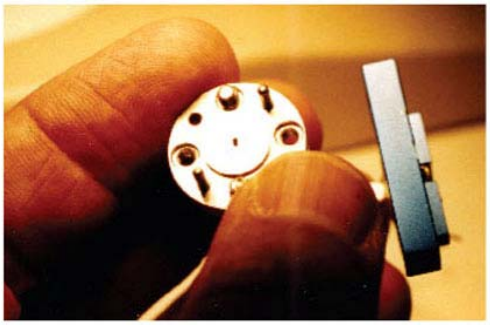

WR05 Probe Waveguide Flange

Figure 3

## Membrane Tip measurements and fabrication

The membrane probe tip and coax-to-membrane attachment were analyzed with basic theory and studied using a Modulated Scatterer Near-Field measurement system on X50 Scale Model at 6 GHz [3,4]. The measurements revealed high E-fields near the ground attachments to the outer coax connector that were reduced by reshaping the membrane. Figure 4 is a photograph of the X50 scale model of the original membrane. Figure 5 is a photograph of the top and bottom side of the thin-film membrane contact structure with 50 micron contact pitch. Note that the final membrane is shorter than the model. The membrane is fabricated in Cascade's thin-film process. The large structure on top with identification numbers is a handle that is removed after the tip is attached.

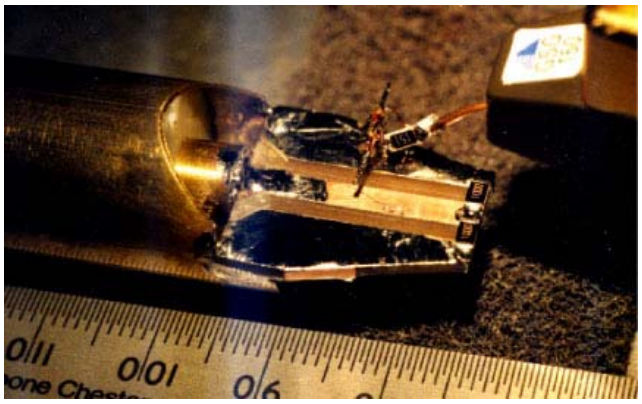

X50 Scale Model of 325 GHz Wafer Probe Tip

Figure 4

The Ground-Signal-Ground contacts and the metallization for attachment to the UT013 coax center and outer conductor may be seen clearly on the bottom of the membrane structures.

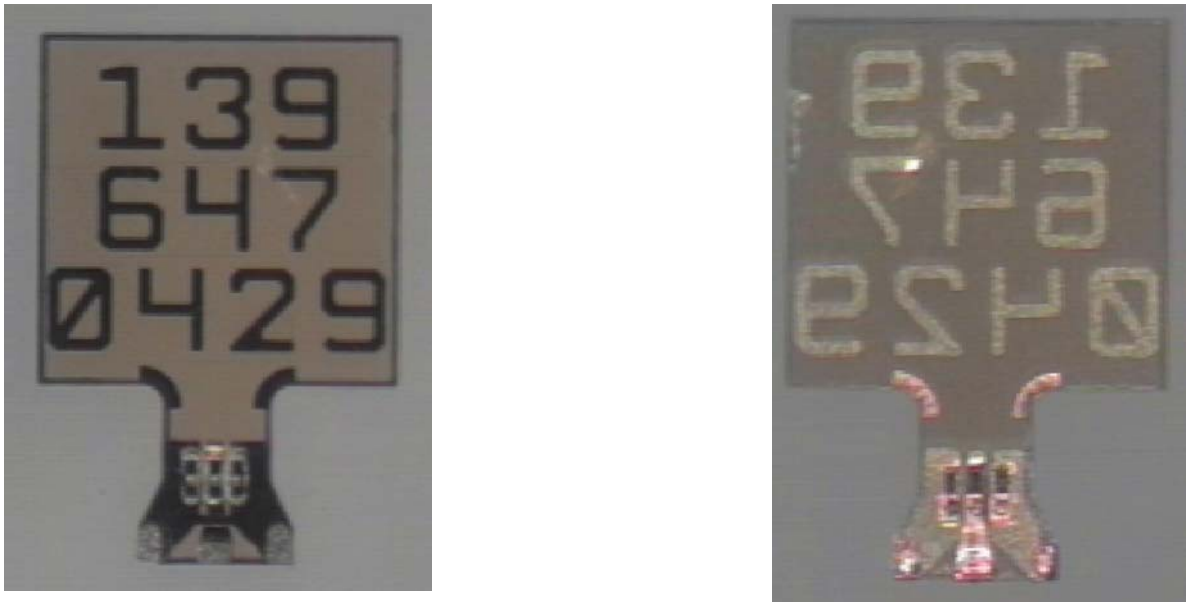


Top and Bottom Views of the Membrane Contact Structure

Figure 5

## One-Port Measurements

Four 325 GHz wafer probes were assembled at Cascade Microtech and measured on the JPL 325 GHz Network Analyzer. A waveguide cal was performed with the flange that connects to the probe as the reference plane. The first measurements were One-Port measurements, in which S11 is measured with the probe on a short, open and load. The round-trip loss through the probe can then be calculated from the S11 measurements. Two of the probes included bias Ts, and two used short waveguide sections. At 1mm wavelength, waveguide has considerable loss—on the order of 1 dB loss in 3 cm. Figures 6 and 7 show that the loss of a probe with 3 cm long waveguide is significantly lower than the loss of the probe with 7 cm long waveguide. Unfortunately, the back short on the waveguide-to-coax transition of the probe in figure 6 was not making good contact on one corner, and this resulted in degraded performance at high frequency.

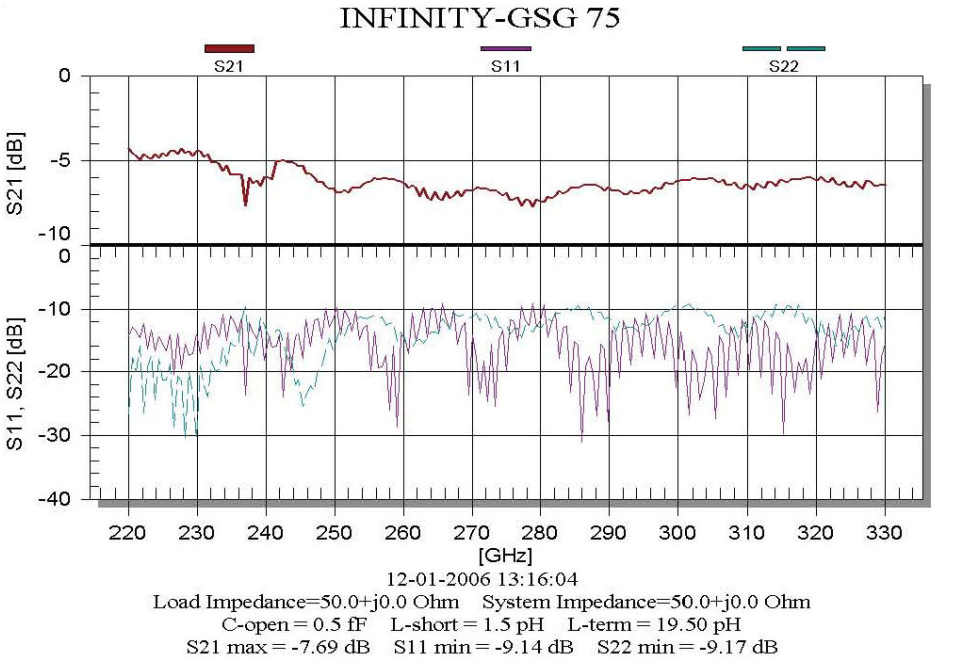


WR-03 Wafer Probe with 7 cm Long Waveguide

Figure 6

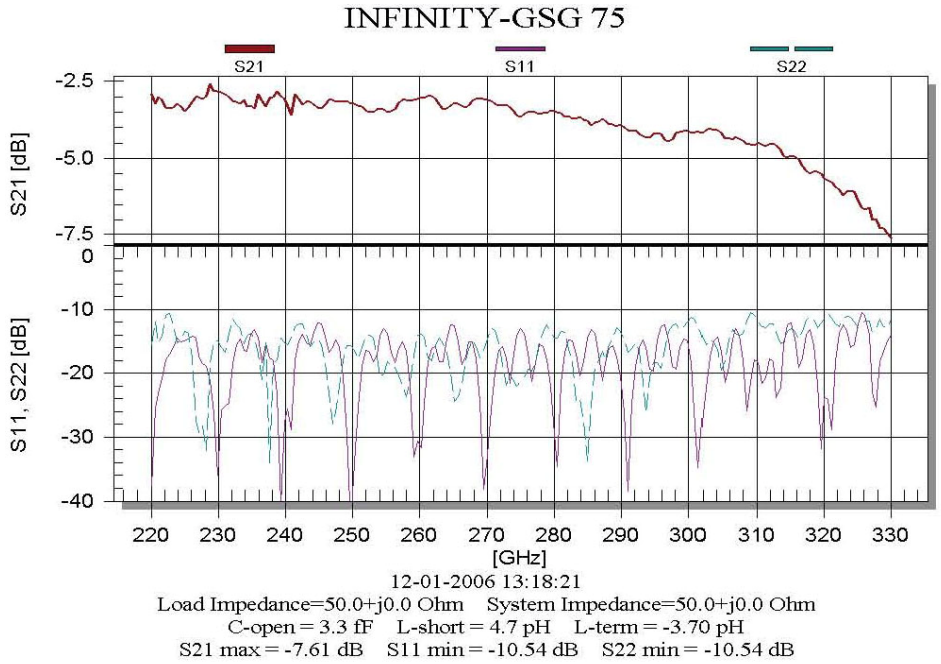


WR-03 Wafer Probe with 3 cm Long Waveguide

Figure 7

## Two Port Measurements

After the One-Port measurements were complete, we performed a two-port calibration of the 325 GHz Network Analyzer system and attempted a two-port measurement using the two probes measured in figures 6 and 7 and an standard substrate. The calibration did not hold during these measurements, but the raw data was stored. A stable cal and useful measurements were later obtained by processing the raw data using WinCal. Figure 8 shows the set of four S parameters obtained. Note that the through data S12 and S21 appears to be the sum of the two probe losses shown in figures 6 and 7, plus the additional loss of the CPW transmission line on the standard substrate.

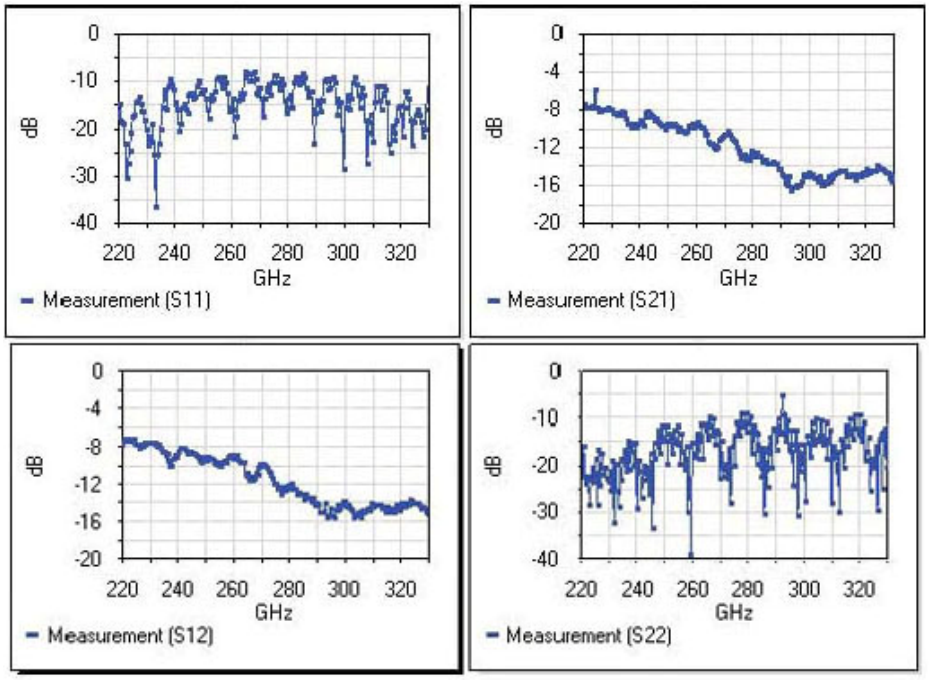


Two-Port Measurement Through the Probes in Figures 6 and 7

Figure 8

## Improvements

The initial measurements were encouraging. The bias T, which is a scaled version of the latest version used on Cascade's WR05 probes, worked well, with no resonances up through at least 325 GHz. It was clear that the waveguide should be as short as possible to minimize loss. The back short was mechanically improved. Several different tip configurations were tried, and the easily interchanged photolithographic membrane tip made it easy to modify contact pitch.

## Measurement of WR-03 Probes on WR-05 VNA System

Cascade Microtech does not currently have a 325 GHz VNA system, but there is some overlap between the WR03 and WR05 bands, so the improved WR03 probes were measured on Cascade's WR05 system after a WR05 waveguide cal. This is very instructive, as the WR03 waveguide cutoff is easily observed in the reflection and transmission data, and the upper frequency limit of the WR05 system is also clear. Figures 9 and 10 are two different WR03 probes with bias Ts measured in Cascade's WR05 system, from 180 to 240 GHz. As expected, the loss is high at the low end of the frequency range, and the VNA measurements become unreliable above the nominal band edge at 220 GHz.

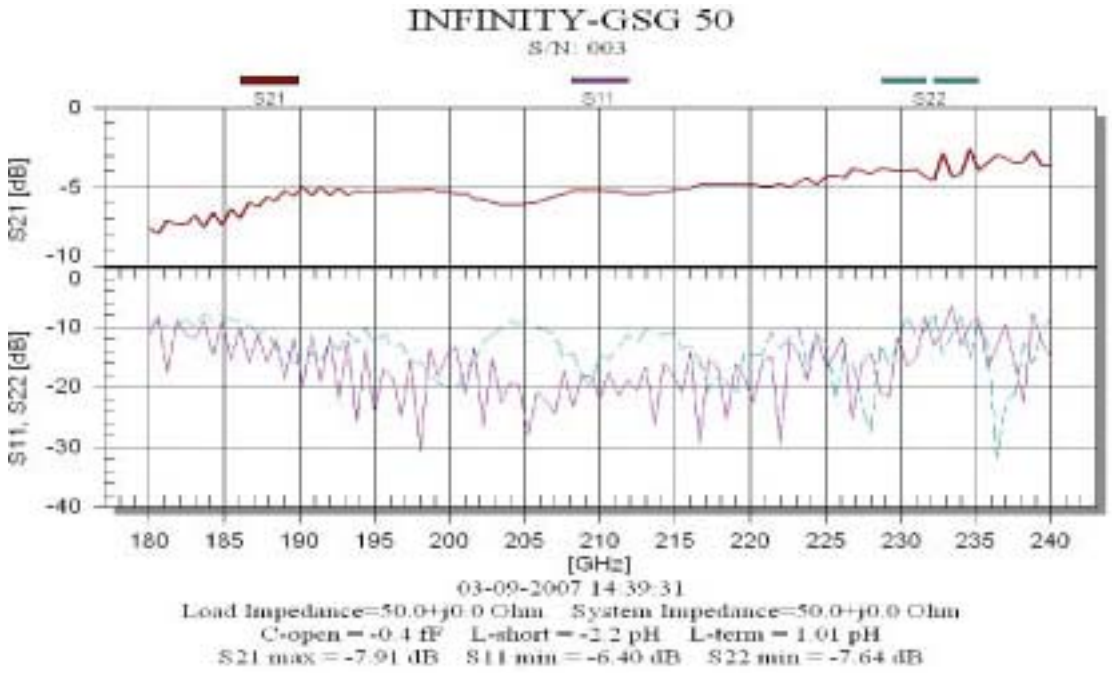


WR-03 Wafer Probe S/N003 on WR-05 System

Figure 9

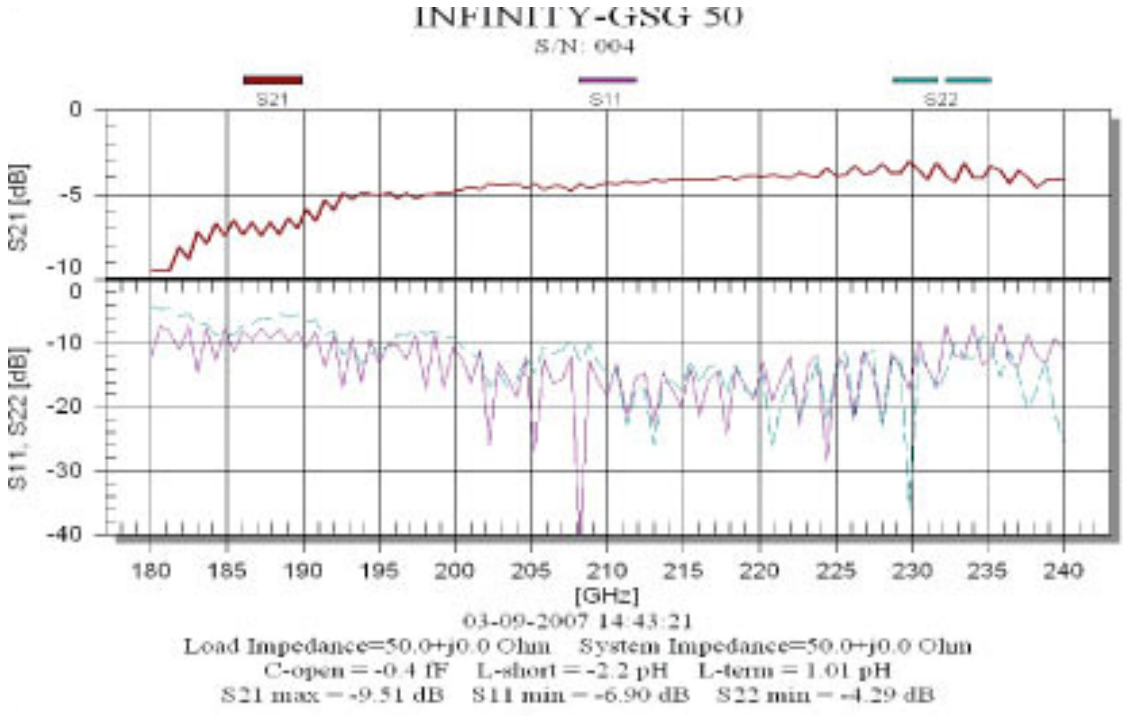


WR-03 Wafer Probe S/N004 on WR-05 System

Figure 10

The system was then calibrated using WinCal with the reference plane at the WR03 probe tips using a calibration standard substrate, and figures 11 and 12 are measurements of a 9 picosecond length of CPW transmission line after the WR03 probe tip cal. Figures 11 and 12 clearly show that the cal through the WR03 probe tips is unstable above 225 GHz on the WR05 system, but is clean and stable from 200 through 225 GHz.

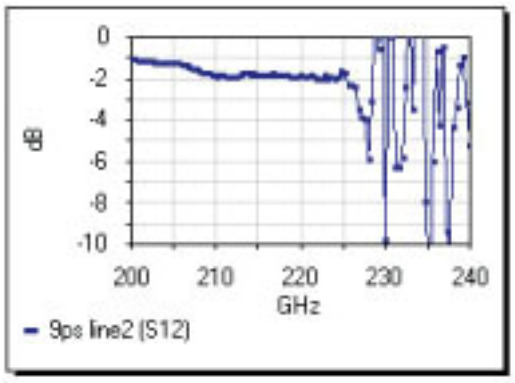


9 picosecond CPW Line Loss

Figure 11

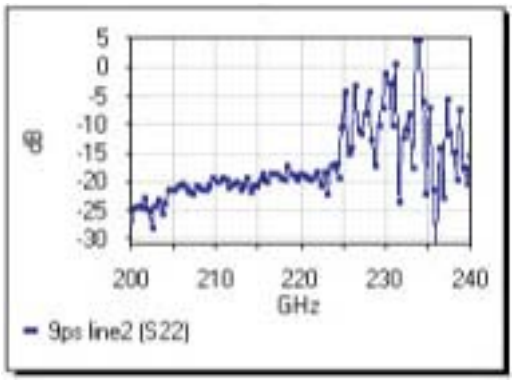


9 picosecond CWP Line Reflection

Figure 12

Conclusions

Photolithographic Membrane Tip Wafer Probes have been designed, built and measured for the 220 – 325 GHz WR-03 waveguide band. Example probes have been demonstrated with and without an integrated bias T on both the JPL 325 GHz VNA system and in the upper frequency range the Cascade Microtech 220 GHz VNA system. A calibration with the reference plane at the probe tips has been achieved on both systems, and the probes will next be used to evaluate active circuits similar to those reported in references 5-7.

References:

1. "Two Port Vector Network Analyzer Measurements in the 218-344 and 356-500 GHz Frequency Bands," Andy Fung, Douglas Dawson, Lorene Samoska, Karen Lee, Todd Gaier, Pekka Kangaslahti, Charles Oleson, Anthony Denning, Yuenie Lau, and Greg Boll, *IEEE Transactions on Microwave Theory and Techniques*, Dec. 2006, Vol.54, Issue 12, Part 2, Dec. 2006, pp.4507 - 4512.

2. "On-Wafer Vector Network Analyzer Measurements in the 220-325 GHz Frequency Band," A.K. Fung, D. Dawson, L. Samoska, K. A. Lee, C. Oleson, and G. Boll, *2006 IEEE MTT-S International Microwave Symposium Digest*, June 2006, San Francisco, CA, pp. 1931-1934.

3. R. Campbell, M. Andrews and Lynh Bui, “A 220 GHz Wafer Probe Tip with Reduced Stray Fields,” in Proceedings of the IEEE International Microwave Symposium 2005, Long Beach, CA, June 2005, pp. 651-654.

4. Richard L. Campbell, Michael Andrews, Timothy Lesher, and Chris Wai, “220 GHz Wafer Probe Membrane Tips and Waveguide-to-Coax Transitions,” in Proceedings of the European Microwave Conference 2005, Paris, FR, October 2005, pp. 1003-1006.

5. "Measurement of a 270 GHz Low Noise Amplifier with 7.5 dB Noise Figure," T. Gaier, L. Samoska, A. Fung, W.R. Deal, V. Radisic, X.B. Mei, W. Yoshida, P.H. Liu, J. Uyeda, M. Barsky, R. Lai, *IEEE Microwave and Wireless Components Letters, July 2007,* pp. 546-548.

6. "Demonstration of Sub-Millimeter Wave Fundamental Oscillators Using 35-nm InP HEMT Technology," V. Radisic, X.B. Mei, W.R. Deal, W. Yoshida, P.H. Liu, J. Uyeda, M. Barsky, L. Samoska, A. Fung, T. Gaier, R. Lai, *IEEE Microwave and Wireless Components Letters,* Vol. 17, Issue 3, March, 2007, pp. 223 - 225

7. "Demonstration of a Sub-Millimeter Wave Integrated Circuit (S-MMIC) using InP HEMT with a 35-nm Gate," W. R. Deal, S. Din, V. Radisic, J. Padilla, X.B. Mei, W. Yoshida, P.H. Liu, J. Uyeda, M. Barsky, T. Gaier, A. Fung, L. Samoska, R. Lai, *IEEE Compound Semiconductor Integrated Circuits Conference,* Nov., 2006, pp.33 - 36.

# SIDEBAND RATIO IN DOUBLE SIDEBAND RECEIVERS WITH A MICHELSON INTERFEROMETER

M. Romanini, A. M. Baryshev, R. Hesper, F. P. Mena, W. Wild

**Abstract—Terahertz heterodyne receivers typically use double sideband (DSB) mixers. The precise knowledge of the receiver sideband ratio (SBR) is a fundamental requirement for the calibration of the data taken with this type of receivers. At the moment the spectroscopic techniques developed for submillimeter analysis, such as Martin Pupplet interferometry[1] and Gas cell technique[2] rely on a calibrated filter system and suffer from inaccuracies caused by standing waves. Here, we present sideband ratio measurements of a submillimeter receiver in the 600-720 GHz band (ALMA Band 9) using a Michelson interferometer as input filter. The main requirement for this method is that the resolution must be high enough to allow distinguishing between the two side bands of the DSB receiver. The advantages of this method are, first, the simplicity of the experimental setup, and, second, the possibility to identify and calibrate out standing waves in the signal and local oscillator paths. In our procedure we use, in fact, exactly the same receiver configuration for both direct and heterodyne detections. Although the results are still preliminary, we have found a good agreement in the SBR measured with both configurations.**

***Index Terms*—Double sideband mixer, Michelson interferometer, sideband ratio.**

## I. INTRODUCTION

The millimeter and submillimeter regions of the electromagnetic spectrum are the most important ones for radio astronomy and for measurement of atmospheric molecules[3]. For the detection of these wavelengths, one of the most common methods is heterodyne detection. The purpose of a heterodyne receiver is to translate a signal at higher frequency to a lower frequency where it can be amplified more effectively. In a heterodyne receiver the incoming reference signal (RF) is combined, or "mixed", with a local oscillator (LO) signal at a frequency close to the reference signal frequency. The RF signal can be either above or below the LO frequency. These bands are called upper (USB) and lower (LSB) bands. The output of the receiver is the intermediate frequency (IF) corresponding to $f_{USB}-f_{LO}$ or $f_{LO}-f_{LSB}$. A double-sideband receiver has only one IF port and both signals are received in the same channel.

The accurate calibration of a heterodyne receiver requires knowledge of the sideband ratio (SBR), which is, the gain ratio between the upper and lower sideband frequencies. For an ideal double-sideband receiver the SBR is equal to one, but in practice the receiver response in the upper sideband may be different from that in the lower sideband. Hence it is very important to know the SBR at different LO frequencies to be able to recover, from a measured spectrum, the correct relative intensity of the various spectral lines.

Here we propose a new method to measure the SBR based on a Michelson interferometer. We investigate the relation between the direct and heterodyne mode to determine if the simple direct detection method is a reliable predictor of the SBR, and whether it can be used for the calibration of actual observations.

## II. EXPERIMENTAL SETUP

A block diagram of the instrumental setup is shown in Fig.1. The source consists of a glowbar lamp with a chopper in front of it for lock-in measurements. The first part of the setup consists of a Michelson interferometer. A beamsplitter (BS1) at the entrance of the Michelson interferometer is used to separate the light from the source into two beams. One beam is reflected off a fixed mirror and one off the moving mirror, whose motion is computer-controlled. Varying the position of the moving mirror changes the optical path of the second beam, thus introducing a time delay between the two beams. After the reflection from the mirrors, the beams are recombined, again through the beamsplitter BS1. The intensity of the recombined beam as a function of the path difference is the Fourier transform of the product of the spectral distribution of the source, the transmission of the optical medium and the spectral response of the detector. The maximum spectral resolution is defined as $\Delta\nu=c/2\Delta l$, where c is the light velocity and $\Delta l$ is the difference length path of the movable mirror. Since the resolution of a Michelson interferometer increases with increasing optical path difference, the maximum spectral resolution is achieved by using the entire distance over which the movable mirror can be displaced to measure only one side of the interferogram. If

M. Romanini is with the Kapteyn Astronomical Institute, University of Groningen, PO Box 800, 9700 AV, the Netherlands (e-mail: romanini@ astro.rug..nl).

A. M. Baryshev, R. Hesper, F. P. Mena, and W. Wild are with the Netherlands Institute for Space Research (SRON), Landleven 12, PO Box 800, 9700 AV, the Netherlands, and with the Kapteyn Astronomical Institute, University of Groningen, PO Box 800, 9700 AV, the Netherlands.

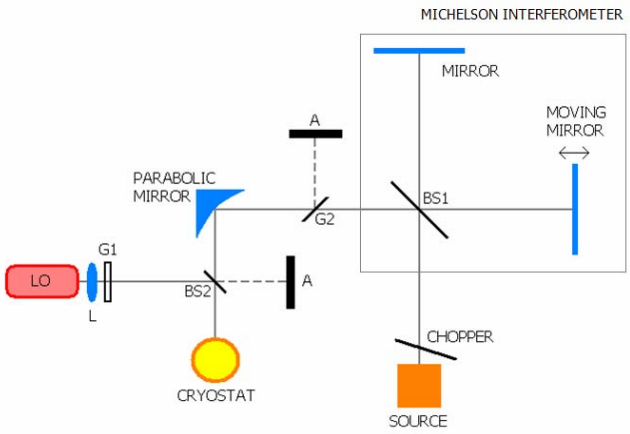


Fig. 1. Scheme of the heterodyne detection setup. *BS1* is the beamsplitter of the Michelson interferometer. The beam from *BS1* is coupled with the signal from the LO through beamsplitter *BS2*. *L* and *G1* are respectively a lens and a grid used to focalize and change the amplitude of the LO signal. The grid *G2* is used to reduce the standing waves from the LO as discussed in the text. The rejected beams are sent to absorber plates, *A*.

both sides of the interferogram are measured, the achieved resolution is half of the maximum resolution. In our Michelson interferometer the maximum spectral resolution achievable is 1 GHz, corresponding to a difference in path length of 150 mm.

When the receiver is used in direct detection mode, the recombined beam is sent to a parabolic mirror which focuses it into the cryostat where the receiver is located. In this way it is possible to obtain the frequency response of the receiver. In heterodyne detection mode, the beam from the parabolic mirror is coupled with the signal from the local oscillator using the beamsplitter BS2. We have performed the experiment in both detection modes using two different superconductor-insulator-superconductor (SIS) junctions, hereafter called mixer 1 and mixer 2. Both junctions are designed to operate in the 600–720 GHz band. Due to imperfections in the coupling between the incoming signal and the horn receiver, some LO signal can be reflected back into the Michelson interferometer forming standing waves. Since the LO signal is polarized, introducing a new grid (G2) can reduce these standing waves. We have done so during the heterodyne detection with mixer 2. By rotating G2 we can diminish the intensity of the standing waves.

## III. RESULTS AND DISCUSSION

We start presenting the data taken with mixer 1 which were obtained without the insertion of grid G2. First, we have measured the response of the mixer over the entire frequency range using the direct detection mode. This corresponds to the thick grey curve in Fig. 2a. The resolution in this mode is 18.75 GHz corresponding to a difference in path length of 8 mm. We have then characterized the mixer in heterodyne mode. This is achieved by coupling the LO signal at different LO frequencies to the RF signal. During heterodyne detection the LO frequency is varied from 597.6 GHz to 720 GHz in steps of 3.6 GHz. The LO signal power was kept constant over the whole frequency range. For these measurements we

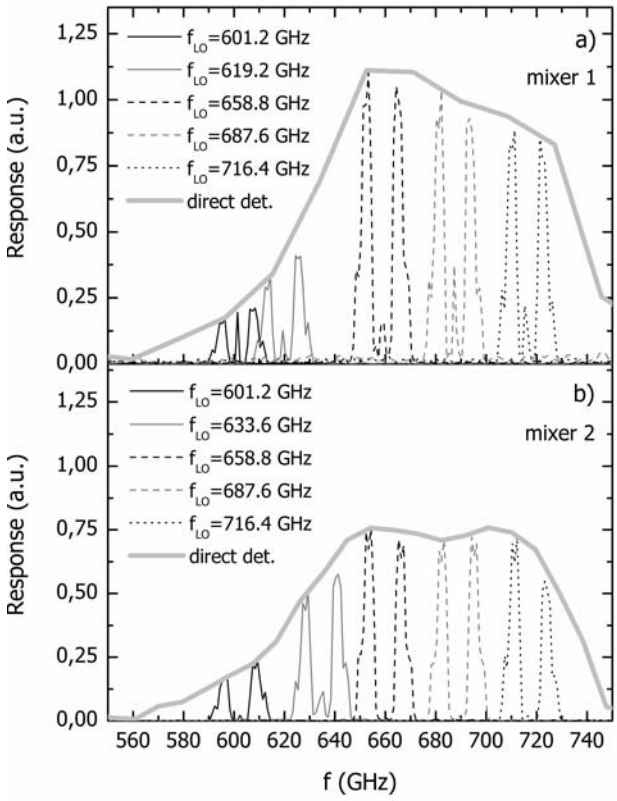


Fig. 2. Comparison between the direct response spectrum (thick grey line) and some heterodyne detection spectra at different LO frequencies (thin lines): a) with mixer 1 and without grid G2, b) with mixer 2 and the insertion of grid G2.

have used the entire path length of the Michelson interferometer in order to have the maximum spectral resolution (1 GHz). Examples of heterodyne spectra, acquired with different LO frequencies, are shown in the thin lines of Fig. 2a. In each spectrum two peaks can be clearly distinguished around the LO frequency, they correspond the LSB and USB bands. A third peak is visible between the two main features at exactly the LO frequency. These peak is originated by the standing waves from the LO that are reflected back in the interferometer.

Since the gain of the mixer is not constant for all measurements at different LO frequencies, each of the heterodyne spectra was normalized so that the intensity of one of the two sideband peaks coincides with the intensity of the direct response at the same frequency. With this procedure we can directly compare the full spectrum obtained with the direct detection mode and the heterodyne spectra at different LO frequencies. As it can be seen in Fig. 2a, the intensity ratio between the upper and lower sideband peaks follows closely the intensity profile of the direct spectrum.

The sideband ratio (SBR) is calculated for each LO frequency as the ratio between the integrals of the USB and LSB peaks. This is then compared with the SBR estimated from the direct detection response, defined as the ratio between the integrals of the direct-detection curve in the same frequency ranges of the USB and LSB peaks, respectively. The result of this comparison is reported in Fig. 3a. Each estimate is accompanied by the appropriate error bar. It can be seen that

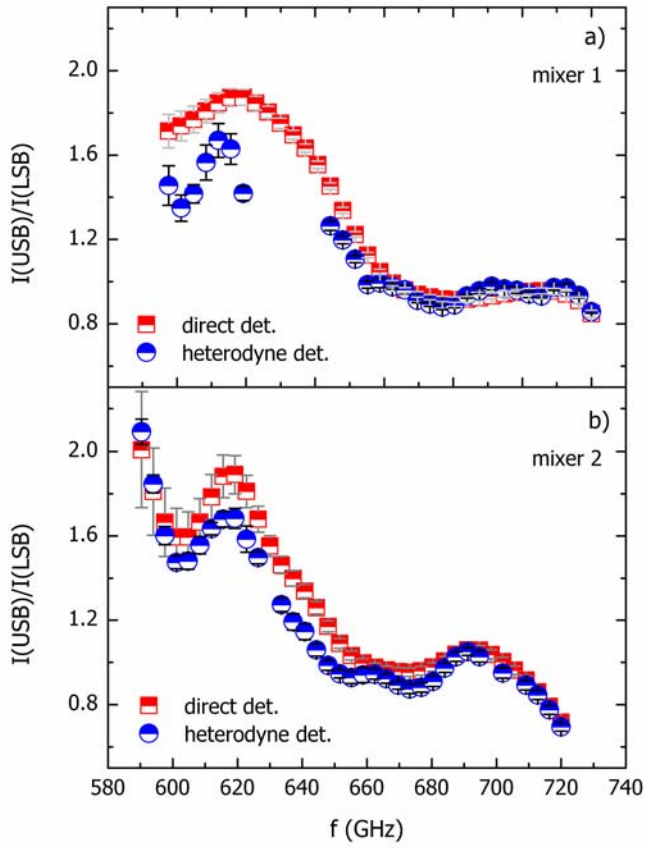


Fig. 3. Comparison between the measured SBR in heterodyne mode (ratio between the integrals of the USB and LSB peaks) and the estimated SBR from the direct detection response (ratio between the integrals of the direct detection curve in the same frequencies range of the USB and LSB peaks) a) with mixer 1 and without the grid G2, b) with mixer 2 and the insertion of the grid G2.

for both detection modes the SBR is in the expected range, *i.e.*, between 1.0 and 2.0[4] (corresponding to less than 3 dB), over the whole frequency spectrum.

From this first set of measurements it is seen that there are some differences between the SBR in the two different detections modes at frequencies below 640 GHz. The main reason is the presence of standing waves coming from the LO source as the pumping level changes with the position of the moving mirror in the Michelson interferometer. This effect is more pronounced at low frequencies since the coupling horn-incoming signal is also lower at these frequencies. The insertion of G2 solves almost completely this problem as discussed in Section II. Another problem is the low pumping level of the LO at some frequencies. An example of that is the lack of results between 620 and 640 GHz: the pumping level was not enough to generate a signal response at these frequencies. To overcome this difficulty, we have split the frequency range in two subranges, a low-frequency range from 590.4 GHz to 662.4 GHz and a high-frequency range from 666.0 GHz to 720 GHz. For each range we realigned the LO signal in order to optimize the pumping level. The heterodyne spectra were taken separately in these two frequency ranges, again in steps of 3.6 GHz. We performed a second set of measurements, with mixer 2, where these two changes were implemented. The results are shown in Fig. 2b. It is evident that the intensity of the central peak in each heterodyne spectrum has decreased. For mixer 2 we have also acquired a complete spectrum in direct mode. For this measurement we have increased the resolution to 9 GHz corresponding to a length path of 16 mm. This allows to increase the number of points in the direct spectrum and thus achieve a better estimate of the area under the curve for the evaluation of the SBR in direct mode. The spectra taken in these two configurations follow also quite well each other (Fig. 2b). What is more important, we found an almost perfect agreement between the SBR calculated from the two different detection modes (Fig. 3b).

## IV. CONCLUSIONS

We have presented a new simple experimental set up to measure directly the sideband ratio in heterodyne receivers. This set up uses a Michelson interferometer and a grid to filter out standing waves. We have applied this method to investigate the sideband ratio of two different double-sideband mixers when used in direct and heterodyne detection modes. A good agreement between these two modes has been found. However, a more thorough investigation of the relation between the direct and heterodyne mode is necessary, especially at low frequencies. We plan also to apply this method to the calibration of the sideband-separating mixer for Band 9 of ALMA recently developed at SRON.

## REFERENCES

[1] K. Kikuchi, Y. Fujii, J. Inatani, "Simple FTS measurement system for submillimeter SIS mixer", *Int. J. IR MM Waves*, 23, 1019, (2002).

[2] D. Teyssier et al., "A multi-path far-infrared and sub-millimeter gas cell for spectral tests of Herschel/HIFI", in *Proceedings of the 15th ISSTT,* 2004, session 7, paper 25.

[3] H. H. Davè, A. Dubey, S. Thampi, R. P. Singh, "Submillimeter wave science and applications", in *Proceedings of the 28th URSI General Assembly, 2005*, available online at: http://www.ursi.org/Proceeding/ProcGA05/pdf/JB2.4(0610).pdf.

[4] G. H. Tan, "Band 9 Cartridge technical specifications, FEND-40.02.09.00-002-A-SPE", ESO report, December 2003.

# Influence of substrates and buffer layers on the quality of NbN ultra thin film for THz HEB

B. Guillet, V. Drakinskiy, R. Gunnarsson, O. Arthursson, L. Méchin, S. Cherednichenko, Y. Delorme, J.M. Krieg

***Abstract*— In order to improve the crystalline quality of NbN ultra thin film for THz HEB applications, several buffer layers have been selected and investigated. The influence of the buffer layers on thermal boundary resistance of membrane-type Hot Electron Bolometer (HEB) devices and on their IF bandwidth is discussed. The influence of substrates and buffer layers on the quality of NbN ultra thin film has been studied by performing Atomic Force Microscopy (AFM) and low reflectometry measurements on NbN films on different substrates (3 µm SOI substrate and MgO buffered 3 µm SOI substrate). In particular, the physical properties (roughness and thickness) of NbN film layers have been carefully measured.**

## I. Introduction

NbN Hot Electron Bolometer (HEB) mixers are the device of choice for low noise heterodyne receivers for future astronomic and Earth's science space missions for the frequency range above 1 THz. Currently, the mixer noise temperature is approximately 10 to 15 times higher than the quantum limit ($h\nu/k_B$=48 K/THz, where $h\nu$ is the photon energy, and $k_B$ is the Boltzmann constant) [1,2,3,4] and the IF gain bandwidth on bulk substrate is up to 4.5 GHz [1,5,6].

The goal and motivations of this work is to fabricate a multipixel heterodyne receiver for 2.5 THz based on NbN superconducting hot-electron bolometer (HEB) mixers with quasi-optical design. The main membrane advantages are related to the RF and LO coupling efficiency. A 16 pixel heterodyne camera has already been built, which will be operated at 2.5 and 4.7 THz for deuterated hydrogen (HD) and neutral atomic oxygen (OI) lines observations, respectively [7].

This work was supported by ESA contract 16940, by the European Community's sixth Framework Program under RadioNet R113CT 2003 5058187, and by the MC2 ACCESS contract 026029.

B. Guillet was with LERMA Observatoire de Paris, 61 Avenue de l'Observatoire, 75014 Paris, France. He is now with GREYC (UMR 6072), ENSICAEN & Université de Caen Basse Normandie, 6 Bd Maréchal Juin, 14050 Caen, France. Corresponding author, phone: 0033231452693 fax: 0033231452698; E-mail: bguillet@greyc.ensicaen.fr.

V. Drakinskiy, R. Gunnarsson, O. Arthursson, and S. Cherednichenko are with Microtechnology and nanoscience (MC2), Chalmers University of Technology, 412 96 Göteborg, Sweden.

L. Méchin is with GREYC (UMR 6072), ENSICAEN & Université de Caen Basse Normandie, 6 Bd Maréchal Juin, 14050 Caen, France.

Y. Delorme and JM Krieg are with LERMA Observatoire de Paris, 61 Avenue de l'Observatoire, 75014 Paris, France.

The performances of NbN HEB mixer rely very much on the substrate the HEB is placed on (in contrast to SIS and Schottky mixers). As the result of the finite electron relaxation rate, the 3 dB HEB mixer gain bandwidth is limited by $f_{IF}=(2\pi\tau_{mix})^{-1}$ : $G(f)=G(0)/(1+(f/f_{IF})^2)$.

The gain bandwidth of NbN mixers is related to the « intrinsic » properties of the NbN material (the temperature derivative of the resistance, the electron-phonon interaction time, the electron and phonon thermal capacitances and the speed of sound), to the substrate (the film/substrate phonon transmission) and to the measurements setup (bias current, IF load resistance, etc.) [8].

Since the electron-phonon interaction time in NbN films is very short (~12 ps [9]), the limiting parameter of the hot electrons relaxation rate $\tau_{mix}^{-1}$ is the phonon escaping time (from the NbN film into the substrate). Figure 1 shows state of the art of the IF bandwidth using NbN mixers. Assuming that all these devices have the same thickness (expected thickness is 3.5 nm), the mixer gain bandwidth is related to the substrate or the buffer layer used. Most of the publications deal with HEB on bulk substrates but there are a few reports of how the HEB gain bandwidth is affected by replacing a bulk substrate by a thin membrane [7,10,11]. HEB devices (with 600 GHz design) have been fabricated on 1.4 µm thick $Si_3N_4/SiO_2$ stress-less membrane or $Si_3N_4/SiO_2$/bulk-Si. The difference of gain bandwidth measured between these two types of devices was not significant and was in the 0.6-0.9 GHz range [7,12]. These values are narrower than for NbN on bulk-Si [13]. The reduction of the gain bandwidth compared to bulk Si substrate is probably due to the material on which NbN is grown ($Si_3N_4/SiO_2$), and not to the membrane effect [12]. Nevertheless these values are sufficient for some radioastronomy applications.

Since a membrane is needed to reduce losses but it may be detrimental for epitaxial growth of NbN, there are two ways to increase the IF bandwidth of HEB devices. The first method is to put the HEB outside the membrane and place it on a bulk silicon surface by etching the $Si_3N_4/SiO_2$ buffer layer. Preliminary study has shown that a NbN film with a high Tc can be deposited on silicon surface after $Si_3N_4/SiO_2$ etching. Moreover a careful study of the interconnexions between the

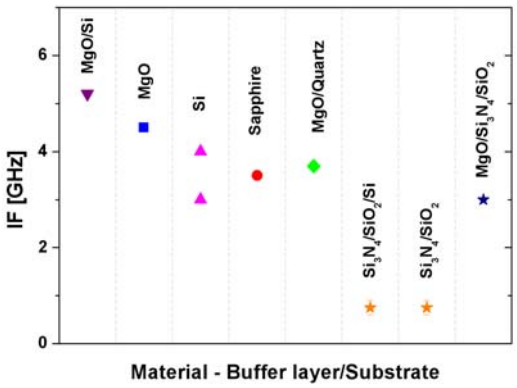


Fig. 1. State of the art of the IF bandwidth using NbN mixers (data taken from Refs. 5, 6, 7 and 12)

antenna on the membrane and the deported HEB mixer has to be done. The second way is to choose the "right material" for the membrane fabrication and NbN deposition. This technique is required in order to obtain epitaxial NbN thin films. Epitaxial thin films could exhibit similar properties as bulk material. So far it has not been thoroughly studied which buffer layers that are most suitable to get such films. The purpose of this work is to study the influence of various layers on NbN properties.

This paper presents some results of this « buffer layer approach ». Five different structures have been studied: NbN/$Si_3N_4$/$SiO_2$/Si, NbN/MgO/$Si_3N_4$/$SiO_2$/Si, NbN/SOI, NbN/MgO/SOI and NbN/MgO/Si. The NbN films on these differents structures have been deposited by dc reactive magnetron sputtering at Moscow State Pedagogical University.

## II. Structural Characterization of NbN Films

The choice of the most appropriate substrate for achieving the epitaxial growth of NbN is governed by several criteria [14]: *(i)* the lattice parameter mismatch between NbN and the substrate (or the buffer layer) has to be low (amorphous material is then prohibited); *(ii)* the NbN material and the substrate (or the buffer layer) have to be chemically inert; *(iii)* an ideal substrate would have a flat dense surface and be free of twins and other structural inhomegeneities; and *(iv)* the thermal expansion mismatch between NbN and the substrate (or the buffer layer) has to be low. Moreover the pressure and the substrate temperature during deposition have to be properly chosen in order to satisfy thermodynamical conditions during growth.

According to Table I, the most suitable material are 3C-SiC, $Al_2O_3$ and MgO. Their lattice mismatch with NbN material is approximately zero. $Si_3N_4$/$SiO_2$ buffer layer is not the most suitable substrate for achieving the epitaxial growth of NbN. The $Si_3N_4$ layer described here and used for the previous realisation of NbN HEB devices on membrane was amorphous. It is possible that the reduced IF bandwidth

TABLE I
Lattice Mismatch Between NbN Material and Different Possible Substrates or Buffer Layers

| Material | Lattice parameter [Å] | Lattice mismatch δ $\delta = (a_{substrate} - a_{NbN})/a_{substrate}$ |
|---|---|---|
| NbN | 4.39 – 4.42 | n.a. |
| $Si_3N_4$ | 7.59 | + 0.52 |
| Si | 5.43 | + 0.19 |
| $CeO_2$ | 5.41 | + 0.18 |
| YSZ | 5.14 | + 0.14 |
| $Al_2O_3$ | 4.76 | + 0.07 |
| 3C-SiC | 4.36 | - 0.01 |
| MgO | 4.20 | - 0.05 |

measured in NbN/$Si_3N_4$/$SiO_2$ devices was related to reduced quality of the NbN films.

Samples have been studied by x ray diffraction (XRD) in grazing 2θ configuration so that the signals from the substrate is minimized compare to those of the ultra thin film. Figure 2 shows the results for NbN/SOI and NbN/MgO/SOI. In the latter case all possible MgO orientations are observed indicating a polycrystalline MgO buffer layer. This was expected since the MgO layer was deposited at room temperature. In both cases reflections from the ultra thin NbN films are weak and no preferential orientation could be established, thus revealing the polycrystalline structure of NbN. The peaks are also quite wide compared to reflections from epitaxial layers.

## III. Thickness Measurements

The thicknesses have been investigated with a spectroscopical ellipsometer (from J.A. Woollam Co.), with x ray reflectometry, or with high-resolution transmission electron microscopy (HRTEM). The details of the modelling of the studied structures will be published seperately. The NbN exhibits a metallic behaviour in ellipsometry terms. The analysis also gives that the optical constants of the NbN are slightly different in the different samples, which may indicate that the stoichiometry of NbN could vary between the samples.

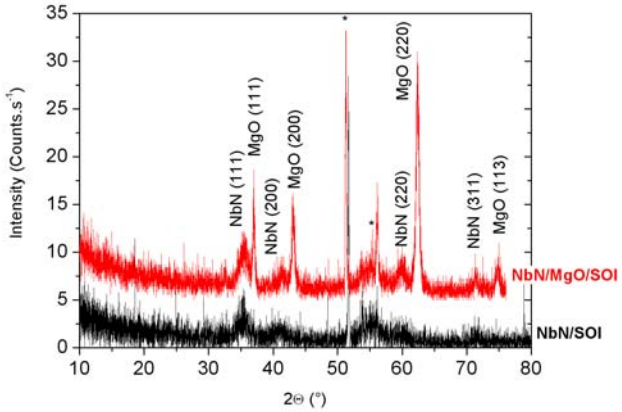


Fig. 2. XRD using grazing 2θ diffraction of 2 different samples: NbN/MgO/SOI and NbN/SOI. Peaks marked with * are parasitic signal from the instrument.

TABLE II
EXPECTED STRUCTURES COMPARED TO THE MEASURED THICKNESSES FOUND ELLIPSOMETRY TECHNIQUE FOR 3 DIFFERENT SAMPLES

| Samples | Expected structure | | Measured structure | |
|---|---|---|---|---|
| NbN/SOI | NbN | 3.5 nm ± 5% | NbN | 5.9 ± 0.4 nm |
| | | | $SiO_2$ | 6.7 ± 0.7 nm |
| | Si | 3 μm | Si | 2960.0 ± 0.3 nm |
| | $SiO_2$ (BOX) | 500 nm± 5% | $SiO_2$ (BOX) | 489.9 ± 1.1 nm |
| | Bulk-Si | 520 μm | Bulk-Si | |
| NbN/MgO/Si | NbN | 3.5 nm ± 5% | NbN | 7.8 ± 0.1 nm |
| | MgO | 200 nm | MgO | 206.7 ± 0.5 nm |
| | Bulk-Si | 520 μm | Bulk-Si | |
| *NbN/$Si_3N_4$/$SiO_2$/Si* | NbN | 3.5 nm ± 5% | NbN | 10.1 ± 0.1 nm |
| | $Si_3N_4$ | 600 nm± 5% | $Si_3N_4$ | 602 ± 1 nm |
| | $SiO_2$ | 800 nm± 5% | $SiO_2$ | 784.9 ± 1.1 nm |
| | Bulk-Si | 520 μm | Bulk-Si | |

TABLE III
PHYSICAL AND ELECTRICAL PROPERTIES OF DIFFERENT NBN SAMPLES

| Samples | Structural properties | NbN (3.5 nm expected) Thickness [nm] (method[b]) | Roughness [Å] (2×2 μm²) | $R_{300K}$ [Ω□] | $T_c$ [K] |
|---|---|---|---|---|---|
| *NbN on $Si_3N_4$/$SiO_2$/Si* | poly.[a] | 10.1± 0.1 (ellips.) | >9 | 660-700 | 8.3 |
| *NbN on MgO/$Si_3N_4$/$SiO_2$/Si* | poly.[a] | ~5-7 (TEM) | | 470-480 | 11.1 |
| *NbN on* SOI | poly.[a] | 5.9± 0.4 (ellips.) | 3 to 9 | 450-500 | 9.5 |
| *NbN on* MgO/SOI | poly.[a] | ~7 (X-ray) | ~5 | 500 | 10.2 |
| *NbN on* MgO/Si | poly.[a] | 7.8± 0.1 (ellips.) | | 250-255 | 13.0 |

[a]All the samples are polycrystalline.
[b]Method used: ellipsometry, HRTEM or x ray measurements

The SOI substrate exhibits a 3 mm silicon device layer (high resistivity), a buried oxide (BOX) 500 nm ± 5% thick and a 520 μm thick handle silicon wafer. Thin low stress $Si_3N_4/SiO_2$ membranes could be obtained with 0.6 μm thick $Si_3N_4$ buffer layer and 0.8 μm thick $SiO_2$ buffer layer.

As shown in Table II, the thicknesses from ellipsometry measurements are quite consistent with the substrate specifications. An important fact is that the measured NbN thickness is larger than expected for all samples. This thickness is between 5 to 10 nm and seems to be substrate dependent. Electrical properties of the NbN films and therefore of the devices are related to the quality and the thickness of the NbN film. For example, it is known that for a given substrate the critical temperature decreases with the thickness of the NbN film (thinner film gives lower critical temperature) [5]. Therefore, thickness measurements have to be considered important for the further development on devices based on such ultra thin films. Previously Gao *et al.* using HRTEM found a thicker NbN film than expected from deposition on bulk Si and on 3C-SiC buffer layer [15]. Moreover, ellipsometry revealed the presence of native silicon dioxide. A quite thick oxide (6.7 nm) has been measured on top of the SOI structure. One reason why this layer is much thicker than expected (1 to 2 nm usually) could be linked to the NbN deposition process that oxidises the Si surface. The vacuum is never perfect (oxygen remains) and the sample surface heats up to 800 °C during the deposition process. HRTEM measurement has to be done to check the thickness of the native silicon dioxide.

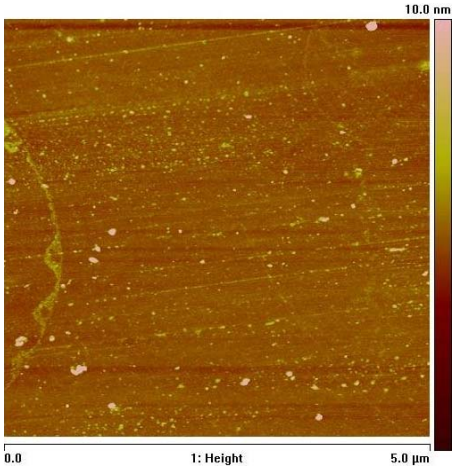

Fig. 3. AFM image of NbN/SOI sample: the associated rms roughness is 3 Å (5×5 μm² area).

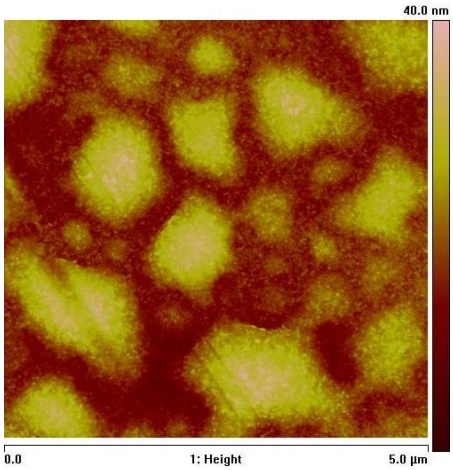

Fig. 4. AFM image of NbN/MgO/SOI sample: the associated rms roughness is 5 Å (5×5 μm² area).

## IV. SURFACE MORPHOLOGY

AFM measurements have been made on the films. The root mean square (rms) roughnesses are quite large compared to the NbN film thickness (Table III). The surface morphology is not homogeneous on a 5×5 μm² scale, which could cause problem for the HEB fabrication (cf. figures 3 and 4).

Table III gives the summary of the physical and electrical properties of the NbN films. The sheet resistance value at room temperature and the critical temperature for each sample are given. All the films are polycrystalline (from XRD and HRTEM analysis). Assuming that the NbN thickness is similar (around 6-7 nm), the MgO buffered bulk-Si seems to be the more promising: it gives a low sheet resistance and a high critical temperature.

## V. CONCLUSION

Physical and electrical properties of NbN ultra thin films with different buffer layers and different substrates have been measured and studied. We have demonstrated that several physical and electrical parameters of the NbN film depend strongly on the choice of buffer layers and substrates. Thickness and roughness seem to be the most sensitive parameters. Meanwhile, the thickness measurements on devices based on such ultra thin films have to be considered very carefully. There are still big technological challenges to achieve ultimate NbN ultra thin films and devices based on them.

## ACKNOWLEDGMENT

The authors thank KOSMA for providing SOI wafer, SIFCOM at ENSICAEN for x ray measurement and Oriel GmbH for help in ellipsometry analysis.

## REFERENCES

[1] S. Cherednichenko, M. Kroug, P. Khosropanah, A. Adam, H. Merkel, E. Kollberg, D.Loudkov, B. Voronov, G. Gol'tsman, H.-W. Huebers, and H. Richter, *Physica C*, vol. 372, p427, 2002

[2] J. Kawamura, R. Blundell, C.E. Tong, G.N. Gol'tsman, E. Gershenzon, B. Voronov and S. Cherednichenko, *Appl. Phys. Lett*., 70(12), p1619, 1997

[3] M. Kroug, S. Cherednichenko, H. Merkel, E. Kollberg, B. Voronov, G. Gol'tsman H.-W. Huebers and H. Richter,, *IEEE Trans. on Appl. Supercond.* Vol.11, n.11, p962-965, 2001

[4] A.D. Semenov, H.W. Huebers, J. Schubert, G. Gol'tsman, A.I. Elantiev, B. Voronov and G. Gershenzon, *J. Appl. Phys.*, 88 (11), p6758, 2000

[5] Y.B. Vachtomin, M.I. Finkel, S.V. Antipov, B.M. Voronov, K.V. Smirnov, N.S. Kaurova, V.N. Drakinskiy and G.N. Gol'tsman. *Proc. of 13th International Symposium on Space Terahertz Technology*, p259, 2002

[6] D. Meledin, P.-Y.E. Tong, R. Blundell, N. Kaurova, K. Smirnov, B. Voronov, and G.N. Gol'tsman, *IEEE Trans. Appl. Supercond.*, 13 (2), p164, 2003

[7] S. Cherednichenko, V. Drakinskiy, J. Baubert, B. Lecomte, F. Dauplay, J.M. Krieg, Y. Delorme, A. Feret, H.W. Hübers, A.D. Semenov and G. Gol'tsman, *Proc. SPIE*, vol. 6275, p62750, 2006

[8] A.D. Semenov, G.N. Gol'tsman, and R. Sobolewski, *Supercond. Sci. Technol.* 15, p1689, 2002

[9] Y.P. Gousev, G.N. Gol'tsman, A.D. Semenov, E.M. Gershenzon, R.S. Nebosis, M.A. Heusinger, and K.F. Renk, *J. Appl. Phys.*, 75, p3695, 1994

[10] J. Baubert, H. Merkel, M. Salez, P. Pons, S. Cherednichenko, B. Lecomte, V. Drakinskiy, G. Gol'tsman, B. Leone, *IEEE Trans. Appl. Supercond.*, 15, 2, p507, 2005

[11] P.P. Munoz,, S. Bedorf,, M. Brandt, T. Tils, N. Honingh and K. Jacobs, IEEE Microw. Wireless Comp. Lett., 16 (11), p606, 2006

[12] S. Cherednichenko, V. Drakinskiy, J. Baubert, B. Lecomte, J.M. Krieg, B. Voronov, G. Gol'tsman, and V. Desmaris, to appear in *J. Appl. Phys*

[13] H. Ekström, E. Kollberg, P. Yagoubov, G.N. Gol'tsman, E. Gershenzon, and K.S. Yngvesson, *Appl. Phys. Lett.*, 70 (24), 1997

[14] J.M. Philips, *J. Appl. Phys.*, 79, 4, p1829, 1995

[15] J.R. Gao, M. Hajenius, F.D. Tichelaar, B. Voronov, E. Grishina, T.M. Klapwijk, G. Gol'tsman, and C.A. Zorman, *Proc. of 16th International Symposium on Space Terahertz Technology*, 2006

# Reflection measurement of absorption coatings using 600-670 GHz vector network analyzer

A.M. Baryshev, W. Jellema, R. Hesper, W. Wild

***Abstract*—This article describes several aspects of ALMA band 9 cartridges: design, development and characterization. We give special attention to the characterization of the system. In this context, we present the noise measurements of the first eight cartridges with an emphasis on the extremely large IF bandwidth (4-12 GHz). The IF gain slope, receiver linearity and saturation, receiver beam pattern and cross polarization level measurements are also presented.**

***Index Terms* — Heterodyne detection, vector network analyzer, sub millimeter wavelengths, calibration, reflecometer, black body**

## I. Introduction

Vector network analyzers (VNA) are common tool in microwave and millimeter wave laboratories. The capability in measuring not only amplitude but phase response of the circuit under test is a valuable asset for investigating RF properties of various systems. Progress in electronically tunable submm solid state sources allows for using them to extend a frequency range of VNA into submm/THz frequencies [1], [2].

In this report we present a construction and measurement of a single port quasi-optical VNA covering in the range of 600-670 GHz. This VNA was then used for measurements of frequency and spatially resolved reflection response of a SiC/Stycast absorption coating which is used both in ALMA and HIFI. The ability of spatially resolving the reflected signal allows for discriminating against contributions of other components of a test set up, thus greatly improving the measurement accuracy.

A Mihelson interferometer quasi-optical configuration was used to create a single port reflectometer. An ALMA band 9 x6 warm multiplier assembly was used as a signal source and a subharmonicaly pumped superlattice device has been used as a detector. These components allow to achieve dynamic range of 60 dB without using cooled detector. A spatial resolution of about 3 mm has been demonstrated.

Manuscript received August 6, 2007. This work was supported in part by the research funding from the European Community's sixth Framework Programme under RadioNet R113CT 2003 5058187 JRA AMSTAR, and Netherlands Astronomy Research School (NOVA).

A.M. Baryshev, R. Hesper and W. Wild are with the SRON Netherlands Institute for Space Research and Kapteyn Astronomical Institute, Landleven 12, 9747 AD Groningen, The Netherlands, (E-mail:A.M.Baryshev@sron.nl).

W. Jellema is with the SRON Netherlands Institute for Space Research, Landleven 12, 9747 AD Groningen, The Netherlands.

## II. Layout of measurement system

### A. Quasi-optics layout

The reflectometer is made by using the Mihelson interferometer scheme as shown in fig. 1, 2. Green dashed lines represents the main path of the signal and the red dashed line represent a parasitic channel which can be calibrated out using a standard calibration load (”matched load”, and “short”) techniques. A 40 micron thick Mylar foil beam splitter was used which corresponds to a 3 dB reflected - transmitted signal ratio for the frequency of interest. Main polarization of set-up is vertical (perpendicular to optical table plane) and is set by a polarization of detector and transmitter diagonal horns.

An ALMA x6 multiplier prototype made by NRAO and VDI has been used as a signal source [alma]. It has 610-712 GHz frequency coverage and 40 microwatt of peak output power. Its beam has been formed by a diagonal horn and an HDP lens. The source has an additional WR-8 coupling waveguide port which allows to pick part of the signal before x6 multiplier to create a reference for phase/amplitude detection circuit.

A subharmonically pumped (n=30..35) superlattice electronic device (SLED) was used as detector. It is mounted in to detector block with integrated diagonal horn. Its SMA connector DC/IF input was also used to provide a sub harmonic LO signal at 16…20 GHz. The same type of

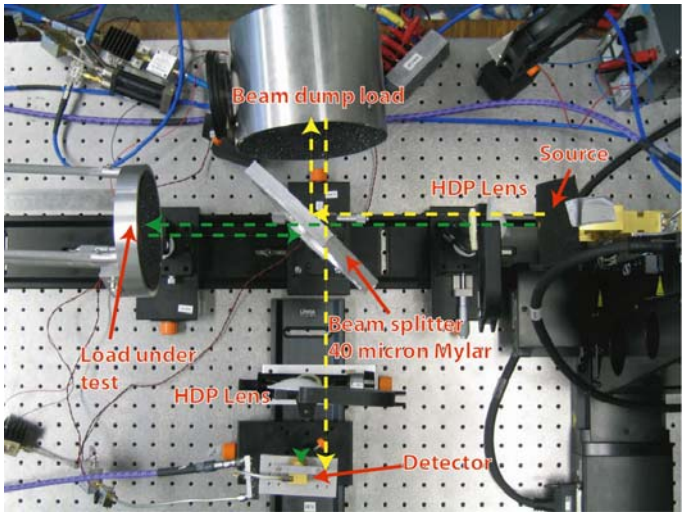


Fig. 1. Layout of single port quasi-optical VNA

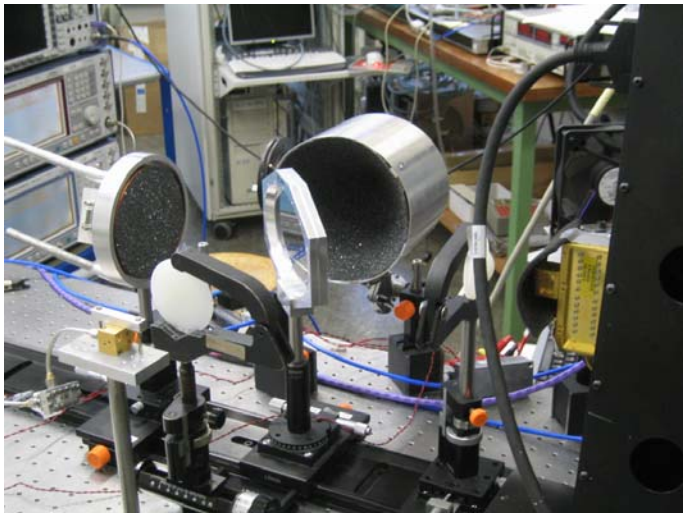

Fig. 2. Layout of the experiment in 3D.

detector was used in room temperature beam pattern measurements of ALMA band 9 optics [3].

The parasitic channel path of the interferometer shown in yellow line in fig. 1 has been terminated by a beam dump. The absorption coating has been made out of carbon loaded Stycast epoxy with SiC grains as the top layer [4]. Coating was deposited on the aluminum cone shape substrate (see fig. 2).

### B. *Phase and amplitude detection circuit*

The homodyne scheme similar to one used for ALMA [5] and HIFI [6] beam pattern measurements was used. A simplified signal diagram is presented in fig. 3. The source was driven by a frequency synthesizer S1. Another frequency synthesizer S2 was used both for pumping a detector SLED as well as Schottky mixer for creating reference system. Both S1 and S2 are Rohde & Schwartz SMP-20 type. The primary IF was 1 GHz. The IF signal of mixer M1 is amplified and multiplied by 6 to create a primary reference signal.

An additional mixer pair M3, M4 was used to take out coherent phase noise introduced by synthesizers S1 and S2 and allow for using extremely narrow detection bandwidth of 100 Hz. A Rohde & Schwartz microwave VNA in time sweep mode has been used as signal detection unit. Its internal reference oscillator was used as S3. All S1, S2 and S3 have been phase locked to each other.

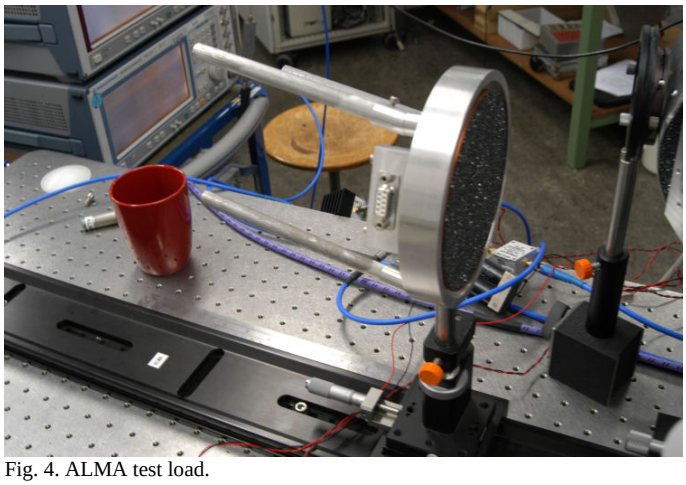

Fig. 4. ALMA test load.

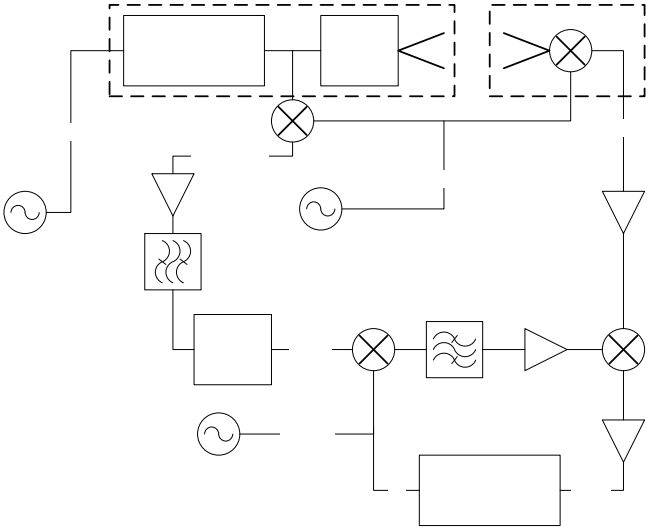

Fig. 3. Signal detection scheme

During measurements, for each point of signal frequency a oscillators S1 and S2 have been tuned such as the primary IF stays 1 GHz; output power of S2 is adjusted to maximize S/N at SLED detector and time sweep of VNA is taken. This procedure is repeated for each frequency following a table lookup procedure in control computer. It was found that frequency and output power setting repeatability is sufficient for doing frequency sweeps.

### C. *Calibration procedure*

A quasi-optical VNA calibration has been achieved by measuring amplitude and phase response of the system while two calibration loads were presented to its input beam. A flat mirror was mounted and presented a “short” calibration load. An absorber material sheet mounted at large distance in the input beam served as a “matched load” equivalent. Any consequent measured traces $A(f)$ were corrected by the calibration information as follows:

$$A_c(f) = \frac{A(f) - A_{load}(f)}{A_{short}(f) - A_{load}(f)},$$

where $A(f)$ is the complex measured response, $A_{load}(f)$ is matched load response, and $A_{short}(f)$ is a “short” response.

This calibration procedure is used for all the data presented in this paper. For creating a spatial response of test objects a Fourier transform of complex amplitude $A_c(f)$ is used to create complex spatial response $A_c(x)$.

### D. *ALMA 100 C test load*

ALMA 100 C test load is shown in fig. 4. It is made of a copper disk suspended in an aluminum case and provided with temperature sensor and resistive heater network for temperature control. Its surface is coated by a carbon loaded Stycast epoxy with SiC grains to provide an optimum

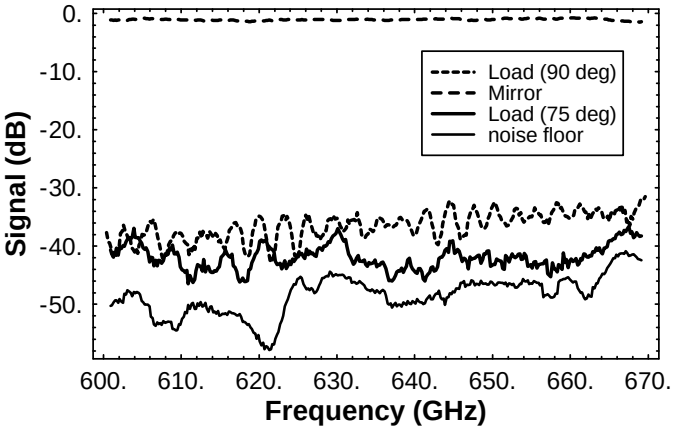


Fig. 4. Measured amplitude frequency response of strait load "Load (90 deg)", mirror, tilted load "Load (75 deg)" and noise floor of the system

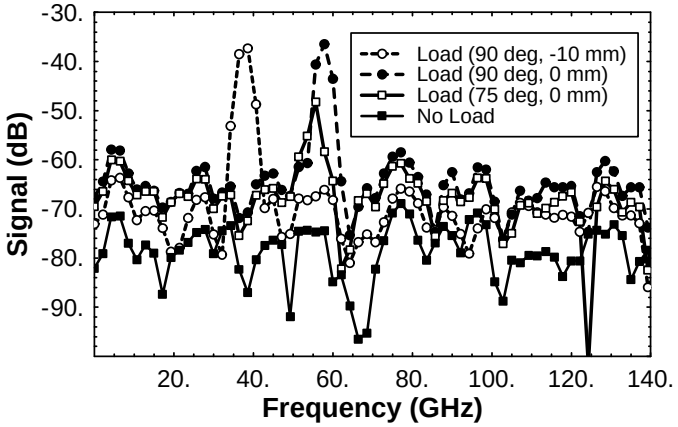


Fig. 5. Measured spatial response of different objects

absorption at submm frequencies. The same type of load was used in HIFI and ALMA band 9 receiver absorbers [4]. The goal of these measurements was to characterize the reflection coefficient of this type of absorber.

## III. Measurements and Discussion

### A. Frequency response

Fig. 4 shows measured amplitude frequency response of ALMA band 9 calibration load compared with the response of a flat mirror mounted at the load position. In order to investigate the specular/diffuse reflection, the load has been tilted by a 15 degree angle and measured again. The S/N leval of 50 dB has been achieved and load reflection of -33 dB across the frequency band has been demonstrated for specular reflection. If the load is tilted its reflection coefficient improves by 3-5 dB.

### B. Spatial response

A spatial response of ALMA calibration load is presented in fig. 5. It was obtained from the same measurement as in fig. 4 with an addition of a strait load which was shifted towards the VNA by 10 mm. As it is clearly seen from the fig. 5, reflection from the load can be resolved spatially with the accuracy of about 3 mm. The amplitude of the response corresponds to an average value in fig. 4.

Data shown in fig. 6, which corresponds to fig. 5 in the linear scale, demonstrates the ability of this method to spatially resolve the reflection even for relatively low level signal. It can also be seen in fig. 5 that response from tilted load is wider in distance space than response of the strait load as it is expected.

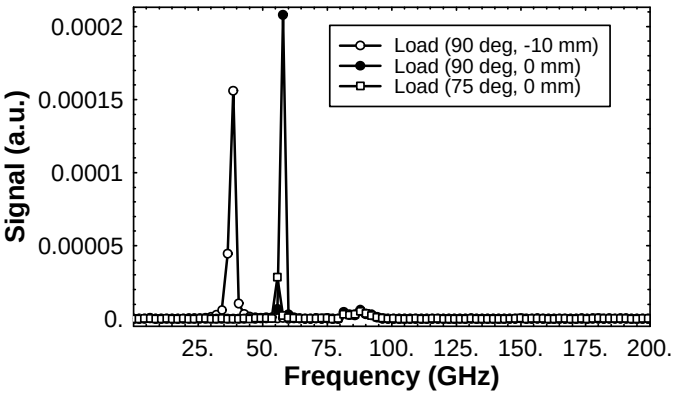


Fig. 6. Measured spatial response of different objects, linear scale. Data from fig. 5 is used.

## IV. Conclusion

We have demonstrated a quasi-optical single port vector network analyzer configuration over frequency range of 600-670 GHz with signal to noise ratio of about 60 dB. A spatial resolution of about 3 mm can be reached in this configuration allowing to analyze the reflection response of the device under test in greater detail.

Performance of ALMA test load was measured to be of -32 dB reflection level over 600-670 GHz which is localized at the surface of the load. The tilted load shows wider spatial response and approx 5 dB lower reflection signal amplitude.

## Acknowledgment

Authors would like to thank E. Bryerton, and J. Kooi for useful discussions.

## References

[1] E. Bryerton, K. Saini, M. Morgan, D. Thacker, "Development of Electronically Tuned Local Oscillators for ALMA", 30th Int Conf on Infrared and Millimeter Waves, Sept 2005.

[2] John Ward, Erich Schlecht, Goutam Chattopadhyay, Hamid Javadi, John Gill, and Imran Mehdi, "Local Oscillators from 1.4 to 1.9 THz", Proceedings, Sixteenth International Symposium on Space Terahertz Technology, Göteborg, Sweden, May 2005

[3] M. Candotti, A.M. Baryshev, N.A. Trappe, R. Hesper, J.A. Murphy, J. Barkhof, "Quasi-optical Verification of the Band 9 ALMA Front-End",Proc. Of 16th Int symp on Space Terahertz Technology, pp. 79-84, 2005

[4] M.C. Diez, T.O. Klaassen, K. Smorenburg; V. Kirschner, K.J. Wildeman, "Reflectance measurements on submillimeter absorbing coatings for HIFI", Proc. SPIE Vol. 4013, p. 129-139, 2000

[5] M. Carter, A.M. Baryshev, R. Hesper, S.J. Wijnholds, W. Jellema, T. Zijlstra, "Phase and Amplitude Antenna Measurements on an SIS Mixer Fitted with a Double Slot Antenna for ALMA band 9", Proc. of the Thirteenth Int. Symp. on Space Terahertz Technology, pp 515, 2002.

[6] W. Jellema, T.J. Finn, A.M. Baryshev, M. van de Vorst, S. Wittington, J.A. Murphy, W. Wild, "Phase-Sensitive Near-Field Measurements and Electromagnetic Simulations of a Double-Slot HEB Integrated Lens-Antenna Mixer at 1.1, 1.2 and 1.6 THz", Proc. of 16th Int Symp on Space Terahertz Technology, pp. 398-403, 2005

# Measurement of in-RF and out-RF band saturation of SIS mixer

A.M. Baryshev, F.P. Mena, R. Hesper, C.F.J. Lodewijk, D.N. Loudkov and T.M. Klapwijk

***Abstract*—In this article we answer experimentally the question of how much spurious signal power level (relative to LO power) can be tolerated by an SIS mixer. Spurious signals that are inside and outside of the signal sideband have been considered. It is demonstrated that about −20 dBc of in-RF-band spurious level can be tolerated. For out-of-RF-band spurious, on the other hand, a level of about −15 to −10 dBc can be tolerated depending on the frequency separation between the LO and the spurious signal.**

***Index Terms* — Heterodyne detection, saturation, spurious signals, SIS mixer, Local Oscillator, sub millimeter wavelengths**

## I. Introduction

THE instantaneous RF bandwidth of SIS-based mixers is limited by the relatively high capacitance of SIS junctions. Recently, significant progress has been achieved in extending the RF bandwidth of SIS mixers either using multiple junctions designs [1] or making use of high current density AlN barrier junctions [2], [3]. At the same time progress has been achieved in generating tuner-less LO power by all solid state sources [4]-[7]. These sources typically consist of microwave multipliers and amplifiers (F < 120 GHz) followed by a set of Schottky multipliers. Although providing enough power these sources often emit an unwanted combination of harmonic signals which can fall into the large RF band of state of the art SIS mixers and potentially disturb their nominal operation.

This article answers experimentally the question of how much spurious signal power (relative to LO power level) can be tolerated by an SIS mixer in two cases:

*1)* The spurious signal frequency falls in the input RF band of the mixer and it appears at the IF output, i.e. classical saturation by a narrow band signal. This case was previously discussed in [8], [9].

*2)* The spurious signal frequency falls in the instantaneous RF bandwidth of mixer but outside the input RF band and it does not appear at the IF output. This was discussed for lower frequency in [10].

In order to measure the tolerable spurious signal power level an experimental set-up has been created which allows to apply simultaneously two narrow band signals as well as a calibrated 300K/80K calibrator to an input of ALMA band 9 SIS mixer. Additionally, the output power of one of the narrow band sources can be varied by a rotating grid. The output power of the sources is strong enough that both can pump the SIS mixer and, thus, both can be calibrated with respect to each other.

We have performed standard hot/cold measurements while varying the power of one of the sources and using the other as LO. The frequency plan was such that a variable "spurious" signal source was kept fixed 642 GHz and several sets measurements were performed at different LO frequencies. It is demonstrated that about −20 dBc in-RF band spurious level can be tolerated. On the other hand, when out-of-RF-band is considered, about −15 to −10dBc can be tolerated depending on the frequency separation between the LO and the spurious signal.

## II. Measurement set-up and methods

### A. SIS mixer

An ALMA band 9 SIS mixer has been used in this work [11]. It uses a waveguide coupling scheme. An input F/2.5 signal beam is coupled to the main waveguide mode by means of a corrugated horn. A reduced size waveguide couples the RF signal to a single SIS junction fabricated on quartz substrate. An Nb-SiO2-Nb integrated tuning structure together with a fixed back short cavity tunes out the SIS junction's parasitic capacitance and provides an optimum input match.

The SIS junction is of the Nb-AlOx-Nb type with an area of approx 1 $\mu m^2$, an $R_nA$ value of 30 $\Omega\mu m^2$, a quality factor of 20 and a gap voltage of 2.8 mV at the physical temperature of 4.2 K. It was manufactured at TuDelft facilities following a standard SIS process [12]. The junction and integrated tuning circuit dimensions have been defined using e-beam lithography process. The Josephson effect noise has been suppressed during operation by means of a magnetic coil integrated into the mixer block.

### B. Receiver layout

The optics layout of the main experiment is shown in

Manuscript received May 1, 2007. This work was supported in part by the research funding from the European Community's sixth Framework Programme under RadioNet R113CT 2003 5058187 JRA AMSTAR, and Netherlands Astronomy Research Shool (NOVA)

A.M. Baryshev, F.P. Mena, R. Hesper, are with the SRON Netherlands Institute for Space Research and Kapteyn Astronomical Institute, Landleven 12, 9747 AD Groningen, The Netherlands, (E-mail:A.M.Baryshev@sron.nl)

C.F.J. Lodewijk, D.N. Loudkov and T.M. Klapwijk, Kavli Institute of Nanoscience, Faculty of Applied Sciences, Delft University of Technology Lorentzweg 1, 2628 CJ Delft, The Netherlands

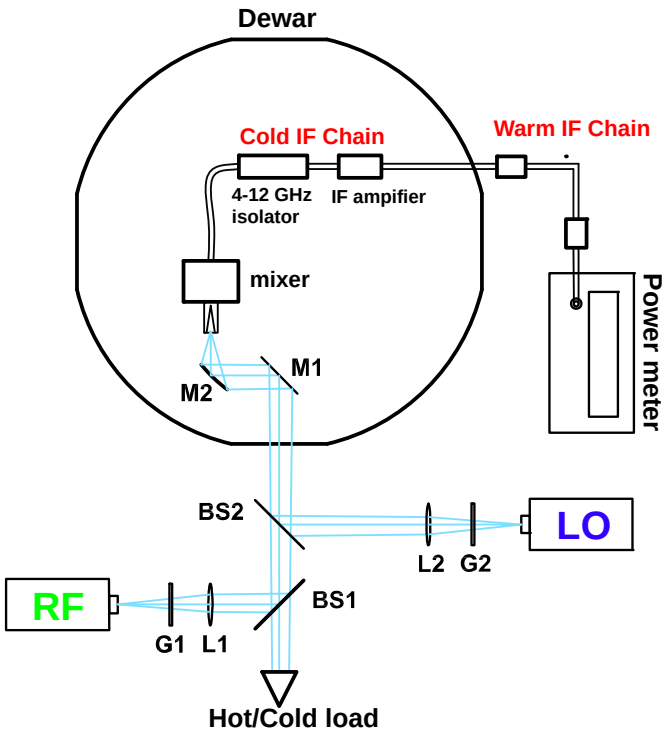


Fig. 1. Layout of the saturation experiment.

Fig. 1. A Gunn diode oscillator (100-120 GHz) followed by a Schottky diode doubler and tripler has been used to simulate a spurious signal. It has been coupled to the input beam by means of a 12 micron thick Mylar beam splitter (BS1) and a HDP lens (L1). The output frequency of the RF source has been fixed throughout whole experiment at 642 GHz and its output power adjusted regulated by means of a polarizing grid mounted in a computer controlled rotating fixture. The peak output power of several tens of microwatts can be regulated to approximately -40 dB relative power level referred to the input of the mixer.

An ALMA band 9 prototype has been used as a tunable frequency LO source. This LO is a combination of power amplifiers and frequency multipliers with a final stage of ×6 (integrated 2×3) multiplier with output frequency range of 600-712 GHz. This source has been made at NRAO in Charlottesville. The output power of the LO has been adjusted by a grid polarizer (G2) and coupled to a receiver beam by means of a 12 micron Mylar beam splitter (BS2) and a HDP lens (L2). It was possible to achieve an optimum pumping level of the SIS mixer throughout whole ALMA band.

RF and LO signals that pass through beam splitters or reflect from grids (G1, G2) were terminated in signal absorbers (not shown in the figure).

A switchable hot/cold load with temperature levels of 80 K (liquid nitrogen) and 300 K (room temperature) has been used to measure receiver noise temperature and gain under different conditions.

The SIS mixer, its associated cold optics (M1, M2) and cold IF components have been mounted in a vacuum space of a Infrared Labs HDL-8 liquid helium cryostat at 4.2 K. Two GoreTex® sheets of 1 mm thickness were used as 4 K and

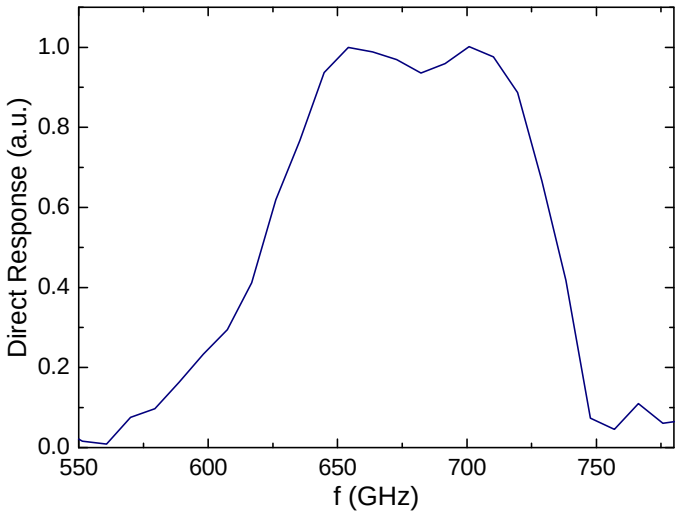


Fig. 2. Measured Fourier Transform Spectrometer response of SIS mixer showing an instantaneous bandwidth.

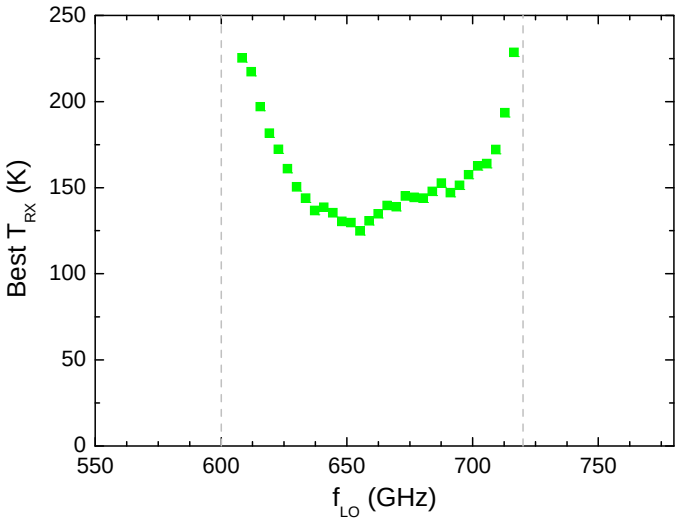


Fig. 3. Measured receiver noise temperature of SIS mixer. Measurements were done while RF source (see Fig. 1) was switched off.

80 K infrared filters and high performance anti-reflection coated quartz plate was used as vacuum window of the cryostat.

The cold IF coupling scheme uses a 4-12 GHz cryogenic isolator [13], and an InP type 4-12 GHz IF amplifier [14] of 30 dB gain and 4.6 K noise temperature. The warm IF chain consisted of two MITEQ IF amplifiers, a set of attenuators, a computer controlled tuneable YIG filter (with a bandwidth of 40 MHz) and an Agilent power meter. Particular care was taken to avoid saturation of the IF amplifier chain at all input conditions by choosing an appropriate attenuation level. This set-up allowed us to measure gain and noise temperature of the mixer versus IF frequency.

### *C. Experimental method and signal source power calibration*

During the experiment, the receiver was tuned first to a given LO frequency and an optimum pumping level was chosen. Then, for each RF spurious source power the receiver output power has been recorded as a function of IF frequency

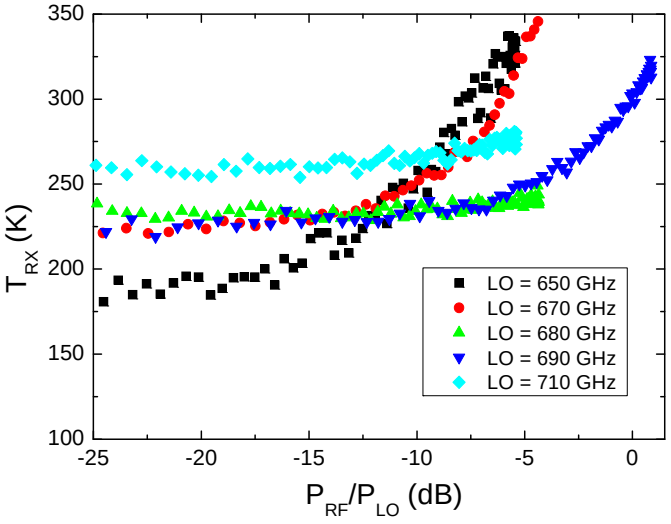


Fig. 4. Measured receiver noise temperature of SIS mixer vs. RF source power for several LO frequencies. Signal frequency was kept at 642 GHz.

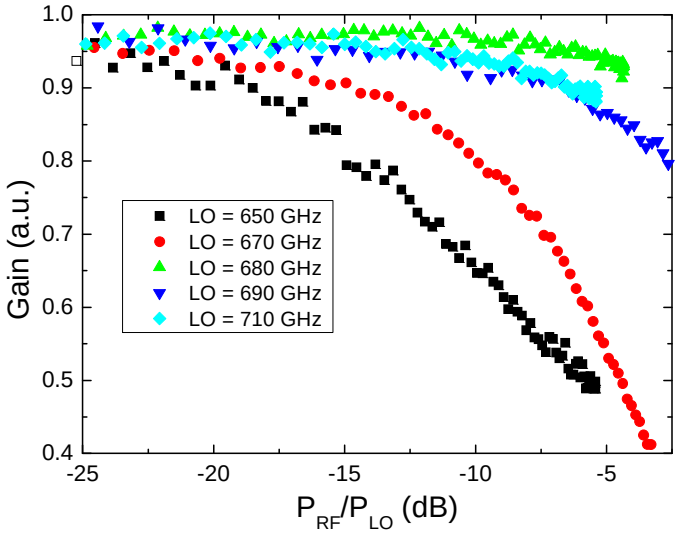


Fig. 5. Measured receiver gain of SIS mixer vs. RF source power for several LO frequencies. Signal frequency was kept at 642 GHz.

both for 80 K and 300 K black body loads at the input. This information permitted to calculate the receiver Y-factor, noise temperature and gain, which is then compared to an RF power off situation. The LO frequencies were chosen such that the spurious frequency fell in and out of the receiving sideband of the SIS mixer.

The RF source power referred to the SIS junction was calibrated by measuring the height of a 1st photon assisted tunneling step as function of the grid G1 rotation angle when LO source was off. The detected power has been calculated based on Tucker's theory and was in a good agreement with a cosine to the power fourth law, since both mixer and RF source are highly polarized. The maximum RF power was enough to pump the SIS mixer. The same method was used to measure the available LO power at the SIS junction at a given LO frequency. Using this method we can express the RF signal power in dBc relative to the LO power at the SIS junction at a given LO frequency. This allows us to exclude the influence of the frequency dependence of the input matching network throughput from consideration.

## III. Measurement Results and Dicussion

### A. Standard FTS and heterodyne characterization

A standard direct response of the mixer, as measured with a Fourier transform spectrometer, is presented in Fig. 2. It demonstrates good coverage of ALMA band 9 and an instantaneous RF coverage from 620 to 720 GHz. This response is typical for ALMA band 9 mixers of preproduction series design. The measured receiver noise temperature as function of the LO frequency with the RF source power set to zero is presented in Fig. 3. When compared with measurements performed within an ALMA band 9 cartridge, the noise temperature performance is worser as in the cartridge the LO source is at 80K. Nevertheless, these results demonstrate the adequate noise band coverage, and that this SIS mixers is good choice for further saturation level measurements.

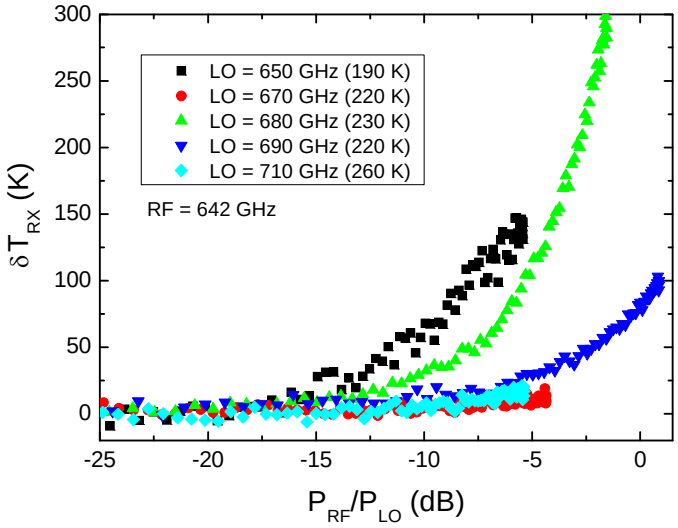


Fig. 6. Receiver noise temperature with receiver noise at zero RF power subtracted. Data are taken from fig. 4

### B. Saturation measurement results and discussion

Receiver noise temperature and gain as function of the RF signal power for different LO frequencies are shown in Figures 4 and 5 respectively. The respective LO frequencies are indicated on the inset. When $f_{LO}$ = 650 GHz, the response from the 642 GHz RF signal is present at an IF of 8 GHz. This IF frequency was excluded from the noise temperature and gain calculations. For other LO frequencies the RF frequency lies outside the nominal detection bandwidth. As it is demonstrated in Figs. 4-6 the receiver gain is the quantity which is the most sensitive to the presence of an RF signal. It becomes saturated for lower RF source powers than the receiver noise temperature and thus will be used as criteria for evaluation of allowable spurious signal power. The in-RF band spurious signal also has more effect (as can be intuitively expected) than the out-of RF band spurious signal. The –20 dBc in-RF band and –15 to –10dBc of out of RF band spurious signal relative power level can be tolerated in this

particular receiver, based on these experimental results.

One should note that noise temperature and gain calculations were done under the assumption that the mixer is pumped by a single LO source and signal from hot/cold is only converted to IF from the $f_{LO} \pm f_{IF}$ frequency range. However, as it can be seen from the power range (x-axis) of Figs. 4-6, the RF signal power can also be sufficient to pump the SIS mixer and, at these conditions, the RF signal is not a weak anymore and the SIS mixer operates under two LO signals simultaneously. This situation may give rise to a parasitic down conversion of frequencies around $f_{RF}$: $f_{RF} \pm f_{IF}$ which would modify our gain and noise temperature estimate. We believe, however, that this effect does not affect our conclusions as saturation effects begin to show already at relatively low RF power levels, where this parasitic down conversion is expected to be small. An additional narrow band low power signal source at frequency $f_{LO} \pm f_{IF}$ can be used to calibrate the strength of parasitic down conversion. We plan to carry out this experiment in the near future.

## IV. Conclusion

In conclusion, we have directly measured the power level of in-RF band and out-RF band spurious signals that can be tolerated by a single junction SIS mixer operating in the 600-720 GHz frequency range. An strong test signal was presented at the receiver input to simulate the presence of a spurious signal. Based on these experimental results, a −20 dBc of in-RF band and a −15 to −10dBc of out-of-RF band spurious signal relative power level can be tolerated in this particular receiver.

## Acknowledgment

Authors would like to thank E. Bryerton, W. Wild, B. Jackson and J. Kooi for useful discussions. This work has benefited from research funding from the European Community's sixth Framework Programme under RadioNet R113CT 2003 5058187 JRA AMSTAR.

## References

[1] J. Kawamura et al., "Very high-current-density Nb/AlN/Nb tunnel junctions for low-noise submillimeter mixers". J. Appl. Phys. 76, pp. 2119, 1996.

[2] C. F. J. Lodewijk, T. Zijlstra, D. N. Loudkov, T. M. Klapwijk, F. P. Mena, and A. M. Baryshev, "Wideband AlN-based SIS devices for frequencies around 700 GHz ", This conference.

[3] J. Kawamura, D. Miller, J. Chen, J. Zmuidzinas, B. Bumble, H. G. LeDuc, and J. A. Stern, "Very high-current-density Nb/AlN/Nb tunnel junctions for low-noise submillimeter mixers," *Appl. Phys. Lett.*, Vol. 76, 2119 (2000).

[4] G. Chattopadhyay, E. Schlecht, J. Ward, J. Gill, H. Javadi, F. Maiwald, and I. Mehdi, "An All Solid-State Broadband Frequency Multiplier Chain at 1500 GHz", IEEE Transactions on Microwave Theory and Techniques, vol. 52, no. 5, pp. 1538-1547, May 2004.

[5] John Ward, Goutam Chattopadhyay, Alain Maestrini, Erich Schlecht, John Gill, Hamid Javadi, David Pukala, Frank Maiwald, and Imran Mehdi, "Tunable All-Solid-State Local Oscillators to 1900 GHz", Proceedings, Fifteenth International Symposium on Space Terahertz Technology, Amherst, Massachusetts, 2004.

[6] John Ward, Erich Schlecht, Goutam Chattopadhyay, Hamid Javadi, John Gill, and Imran Mehdi, "Local Oscillators from 1.4 to 1.9 THz", Proceedings, Sixteenth International Symposium on Space Terahertz Technology, Göteborg, Sweden, May 2005.

[7] Eric W. Bryerton, S. K. Pan, Dorsey Thacker, and Kamaljeet Saini, "Band 6 Receiver Noise Measurements using a Pre- Prototype YIG-Tunable LO", ALMA MEMO #436

[8] A. R. Kerr, "Saturation by Noise and CW Signals in SIS Mixers", Presented at the 2002 International Symposium on Space THz Technology, Cambridge, MA, March 2002, ALMA MEMO 401, *http://www.alma.nrao.edu/memos/*

[9] S. Withington, P. Kittara, and G. Yassin, "Multitone quantum simulations of saturating tunnel junction mixers". J. Appl. Phys. 93, pp. 9812, 2003.

[10] L. R. D'Addario, "Saturation of the SIS mixer by out-of-band signals," *IEEE Trans. Microwave Theory Tech.*, vol. MTT-26, pp. 1103-1105, no. 6, June 1988.

[11] Baryshev *et al.*, "Development of a 0.6 THz SIS Receiver for ALMA", Proc of 12th Int. Symp. on Space Terahertz Technology, pp. 581-591, 2001

[12] M. Gurvitch, M.A.Washington and H.A. Huggins, Appl. Phys. Lett. 42, 472, (1983).

[13] PamTech, Passive Microwave Technology Inc, 4053 Calle Tesoro, Suite A, Camarillo, CA 93012

[14] Lauria, E.F., et al., "A 200-300 GHz SIS Mixer-Preamplifier with 8 GHz IF Bandwidth", ALMA memo #378, http://www.alma.nrao.edu/memos/htmlmemos/alma378/memo378.pdf

# Performance of ALMA band 9 receiver series

A.M. Baryshev, R. Hesper, F.P. Mena, B.D. Jackson, J. Adema, J. Barkhof, W. Wild, M. Candotti, M. Whale, C. Lodewijk, D. Loudkov, T. Zijlstra, T.M. Klapwijk

***Abstract*—This article describes several aspects of ALMA band 9 cartridges: design, development and characterization. We give special attention to the characterization of the system. In this context, we present the noise measurements of the first eight cartridges with an emphasis on the extremely large IF bandwidth (4-12 GHz). The IF gain slope, receiver linearity and saturation, receiver beam pattern and cross polarization level measurements are also presented.**

***Index Terms* — Heterodyne detection, saturation, spurious signals, SIS mixer, Local Oscillator, sub millimeter wavelengths**

## I. Introduction

The Atacama Large Millimiter Array (ALMA) project is a collaboration between Europe, North America, and Japan to build an aperture synthesis telescope consisting of at least 64 12-m antennas located at 5000 m altitude in Chile in its full configuration, ALMA will observe in 10 frequency bands between 30 and 950 GHz, and will provide astronomers with unprecedented sensitivity and spatial resolution at millimeter and submillimeter wavelengths. Band 9, covering 600-720 GHz, is the highest frequency band in the baseline ALMA project, and will thus offer the telescope's highest spatial resolution.

The ALMA Band 9 cartridge is a compact unit containing the core of a 600-720 GHz heterodyne receiver front-end that can be easily inserted into and removed from the ALMA cryostat present in every antenna. The core technologies of every cartridge include low-noise, broadband SIS mixers; an electronically tunable solid-state local oscillator; and low-noise cryogenic IF amplifiers. These components are built into a rigid opto-mechanical structure that includes a compact optical assembly mounted on the cartridge's 4K stage that combines the astronomical and local oscillator signals and focuses them into two SIS mixers as shown in Fig. 1.

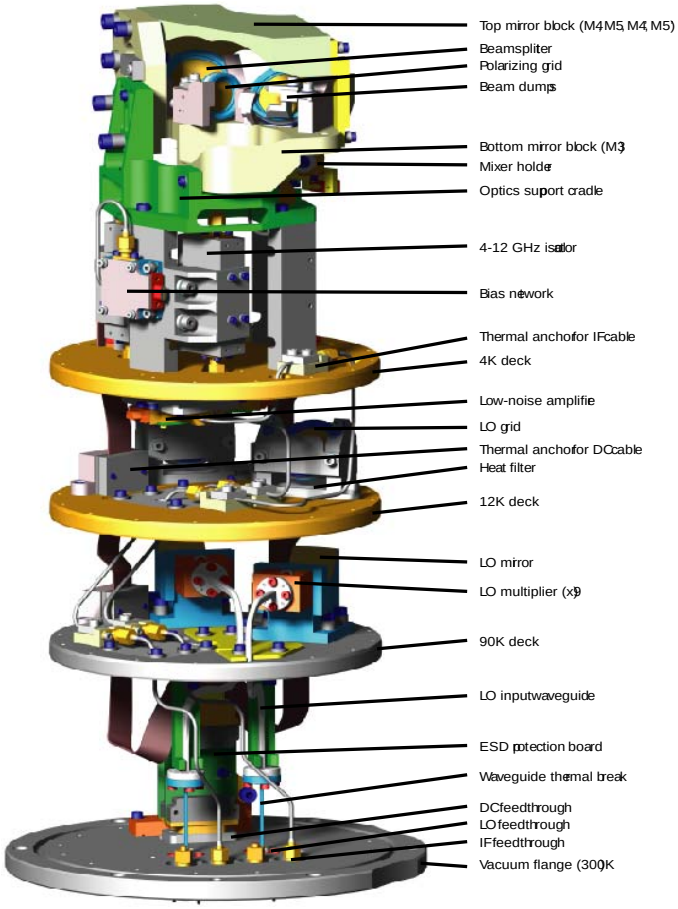


Fig. 1. Layout of the ALMA band 9 receiver..

In this article we present the noise measurements of the first eight receiver units with an emphasis on the extremely large IF bandwidth (4-12 GHz). The IF gain slope, receiver linearity and saturation, receiver beam pattern and cross polarization level measurements are also presented.

## II. Receiver Layout

### A. Overall layout

The ALMA band 9 receiver layout [1] is shown in Fig. 1. The receiver elements occupy four temperature levels. The temperature levels (4, 12, 90, and 300 K) are provided to the cartridge body from the main ALMA cooler and the cryostat cooling distribution system. The receiver insert (cartridge) can be placed into the main ALMA cryostat without disassembling the cartridge or the cryostat. The heat contact is

Manuscript received August 6, 2007. This work was supported in part by the research funding from the European Community's sixth Framework Programme under RadioNet R113CT 2003 5058187 JRA AMSTAR, and Netherlands Astronomy Research School (NOVA).

A.M. Baryshev, F.P. Mena, R. Hesper, J. Adema, J. Barkhof and W. Wild are with the SRON Netherlands Institute for Space Research and Kapteyn Astronomical Institute, Landleven 12, 9747 AD Groningen, The Netherlands, (E-mail:A.M.Baryshev@sron.nl).

B.D. Jackson is with the SRON Netherlands Institute for Space Research, Landleven 12, 9747 AD Groningen, The Netherlands.

M. Candotti, M. Whale are with National University of Ireland, Maynooth, Co. Kildare, Ireland

C.F.J. Lodewijk, D.N. Loudkov, T. Zijlstra and T.M. Klapwijk are with Kavli Institute of Nanoscience, Faculty of Applied Sciences, Delft University of Technology Lorentzweg 1, 2628 CJ Delft, The Netherlands.

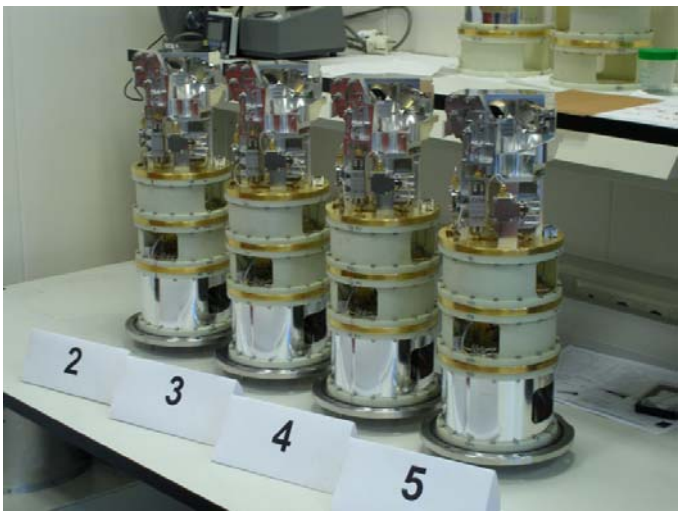

Fig. 2. Photograph of receiver cartridges #2-#5

provided by flexible heat links that only make contact when cryostat is cold and the mechanical support is made at the bottom of the cartridge assembly. The cartridge walls (not shown in figure) are made of fiber glass reinforced epoxy and the construction is rigid enough to maintain the beam orientation within required tolerances for all orientations of the ALMA antenna.

### B. Signal optics

The optics forming the main beam is all contained at the 4 K level. The SIS mixer beam is formed by a corrugated horn which is followed by two elliptical mirrors providing a frequency independent coupling between telescope and mixer. A linear wire grid is inserted between the mirrors to split the input beam in to two orthogonal linear polarizations. An additional elliptical focusing mirror and SIS mixer are used to receive the orthogonal polarization. The details and analysis of ALMA band 9 optics has been presented in detail previously [2]. The entire 4 K optics is arranged in a single CNC machined block that also contains part of the LO coupling optics. The relative position of mirrors is ensured by proper manufacturing tolerances of the mirrors themselves and mechanical fastening interfaces.

### C. Local oscillator arrangement

A quasi-optical LO insertion scheme was chosen for ALMA band 9 receiver. For each polarization channel an integrated ×3×3 Schottky diode multiplier (made by Virginia Diodes) is mounted on the 90 K stage. Its output beam is formed by a diagonal horn and is coupled by means of two elliptical mirrors: one is mounted on 90 K stage and another is mounted on 4 K stage. The LO beam is inserted into a signal beam just in front of a SIS mixer horn by means of a 6 micrometer thick Mylar® beam splitter (~4% coupling). Most of the LO output power is terminated into the black body absorbers mounted at 4 K level behind the beam splitters.

The ×3×3 multiplier is pumped by a microwave signal in the range of 67.7 to 79.1 GHz which corresponds to an output frequency range of 610 to 712 GHz. This signal is carried from a vacuum WR-12 waveguide flange at the 300 K base plate to a multiplier at the 90 K level by means of a gold plated stainless steel WR-12 waveguide. The pumping level of LO multipliers can be adjusted independently by a room temperature electronics providing optimal pumping level for each SIS mixers. The efficiency of this multiplier improves when it is cooled to 90 K compared to a room temperature and it provides 40 to 100 microwatts of output power across the band.

The room temperature driver for the LO system is made at National Radio Astronomical Observatory (NRAO) in Charlottesville. It is based on a YIG oscillator, its signal is multiplied ×3 and amplified by a power amplifier. Then it is split between two power amplifiers with electronically adjustable gain. These power amplifiers consist of several MMIC chips and use waveguide power combining technology. As a result, the output of these amplifiers is matched to WR-12 waveguide avoiding standing waves in the system. The output power level of this amplifier can be regulated anywhere in the range of 10 to 100 milliwats. Details of similar system can be found in [3].

### D. IF system

The band 9 cartridge IF system covers the frequency range from 4 to 12 GHz. The output of every SIS mixer is connected to a three stage InP IF amplifier made by YEBES via a cryogenic 4-12 GHz isolator made by Pamtec. The amplifier noise temperature is in the range of 4 to 6 K, the gain is around 30 dB and the power dissipation at 4 K is about 7 mW. The amplifier output is connected to a vacuum feedthrough interface (situated at the base plate) by a stainless steel cable which is anchored at the 4, 12 and 90 K levels. Finally, at room temperature, a gain-slope-corrected amplifier of 30 dB average gain is used to further boost IF output signal. A 3 dB gain slope across 4-12 GHz band is used to compensate for frequency dependent cable losses and mixer gain variation.

### E. SIS mixers

Two identical mixers blocks are used in the receiver system. They contain a corrugated horn, an all Nb SIS mixer with single Nb-$AlO_x$-Nb SIS junction. The mixers are of the

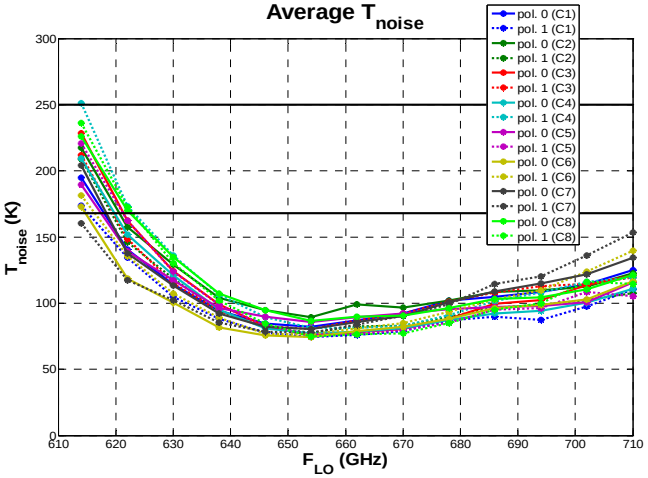

Fig. 4. Measured receiver noise temperature of SIS mixer vs. RF source power for several LO frequencies. Signal frequency was kept at 642 GHz.

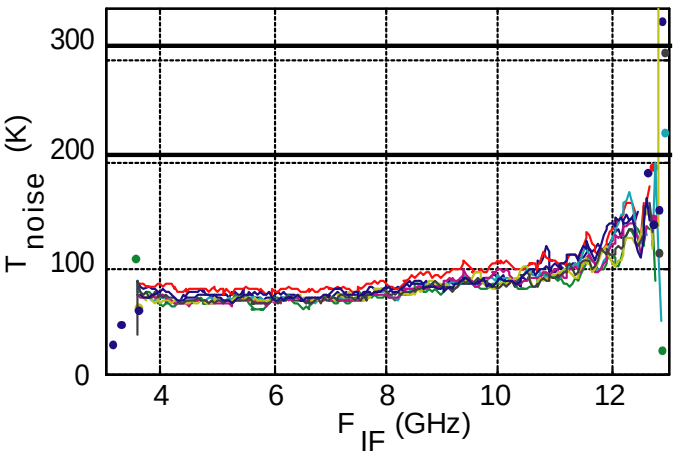


Fig. 5. Measured receiver noise temperature as a function of IF for four cartridges (#1..#4), for two polarization channels each, at 654 GHz LO frequency.

waveguide type and are described in detail in [4]. A superconducting coil is also mounted in the mixer holder to provide suppression of the Josephson effect. A typical operation current of 9 mA is required. A 500 Ohm resistor is built-in close to a SIS junction to be used to heat it up above the critical temperature and so remove any trapped magnetic field flux without dissipating much power. The system can return to operating conditions within 5 seconds.

### *F. Construction status*

A total of eight receiver units have been built and fully characterized to date. Two of them have been delivered to the ALMA integration center for further system test. Fig. 2 shows the photograph of four of the constructed units. A summary of the receiver performance will be presented in the following section.

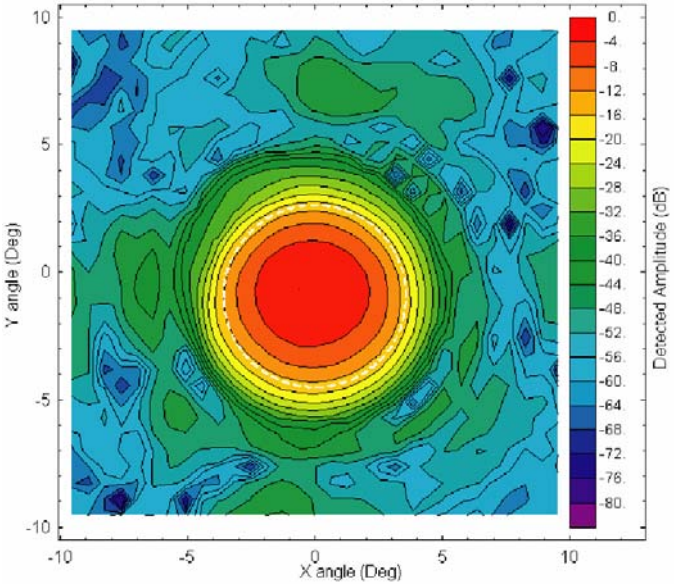


Fig. 6. Receiver beam in far field zone. Dashed line is the edge of the ALMA telescope secondary mirror.

## III. Demonstrated Receiver Perfomance and Discussion

In this section a summary of the receiver performance is presented: noise temperatures, IF gain variations, beam pattern, and saturation results. Measurement methods are also outlined.

### *A. Receiver Noise performance*

Noise performance of band 9 cartridge system has been evaluated using a dedicated measurement set-up which includes: a switchable hot/cold load with temperature levels of 80 K (liquid nitrogen) and 300 K (room temperature); a two channel IF system with YIG filters to analyze an IF response; a noise source to calibrate the IF system gain and a control computer with a control software. Most of the measurements can be done in batch mode without any operator's intervention.

During all performance measurements, the receiver was mounted in an ALMA test cryostat which provides the necessary temperature levels. The 4 K stage temperature was maintained by a software PID feed back loop at 4 K during all measurements.

A summary of the measured noise temperature as a function of IF is presented in Fig. 3. The data correspond to the eight built cartridges. The noise temperature is averaged across the IF band and is not corrected for receiver optics. Good repeatability between units has been achieved mainly due to an improved junction production (e-beam lithography) and junction mounting control. A major improvement in sensitivity has been achieved because by mounting the LO source at the 90 K temperature level, thus LO noise contribution is minimal.

Typical noise temperature dependences on IF are shown in Fig. 5 for four cartridges. Degradation of performance at around 12 GHz is due to a combination of several factors: SIS

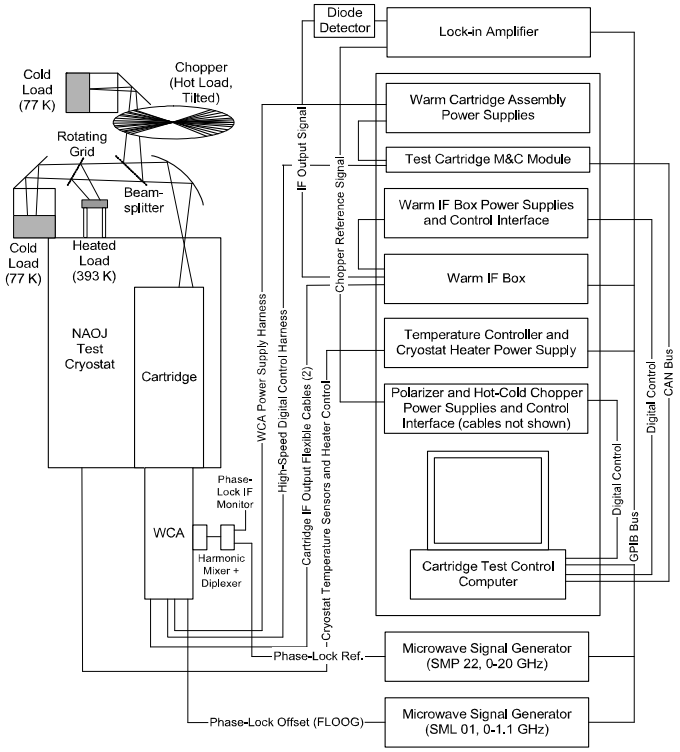


Fig. 7. Experimental layout for measurement of receiver saturation.

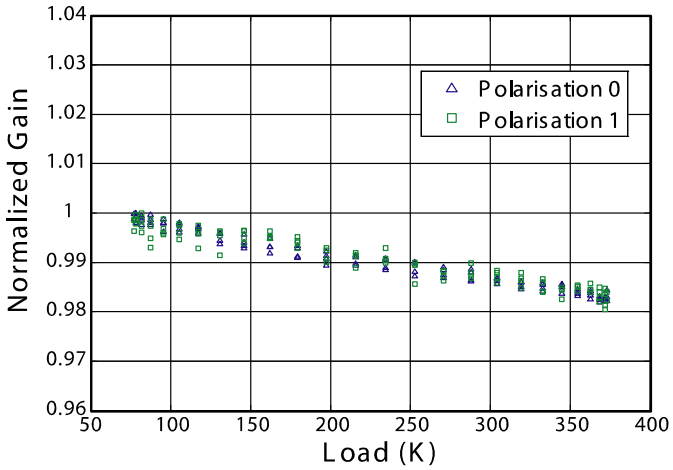


Fig. 8. Receiver small signal gain measured as a function of receiver input signal at 670 GHz LO frequency for two polarization channels.

mixer parasitic capacitance, degradation of 4-12 GHz isolator parameters and increase of noise temperature of cold IF amplifier. Nevertheless, an adequate 4-12 GHz IF band coverage has been achieved.

### *B. Receiver beam*

A typical receiver 2-D beam pattern is shown in Fig. 6. The far field plot has been obtained by a Fourier transform of near field data, which contains both phase and amplitude information. The near field measurement system was based on a method developed earlier [2]. The signal to noise ratio was about 70 dB which is adequate for determining reliably all beam parameters.

The secondary mirror edge illumination taper is found to be in the range of 12 to 14 dB compared to a design value of 12 dB and the beam direction is very close to a nominal 0.94° offset from vertical direction.

The total power of cross polarization signal was found to be about −17 dB relative to a power in the co-polar beam. This is above ALMA specifications but in agreement with physical optics calculations done in GRASP [2].

### *C. Receiver saturation by a 100° C black body radiation*

Special attention was given to measurements of receiver saturation/linearity. Calibration scheme of ALMA assumes that a 100° C black body will be used as one of the calibrators form band 9. It is important to be able to measure accurately a small signal receiver gain as a function of the input signal power.

The measurement layout is shown in Fig. 7. A small signal has been created by using a chopper wheel, covered by 300 K absorber, with an 80 K background liquid nitrogen load. This variable signal was inserted into receiver beam by means of a 14 micrometer thick Mylar beam splitter that has approximately 7 % coupling. A variable temperature load has been made of an additional 80 K liquid nitrogen absorber which is put into transmission arm behind a rotating linear polarizing grid. Signal reflected from the grid was terminated on the hot plate absorber which was kept at 100° C. By changing the angle of the grid one can present an input signal varying from 80 K to 373 K.

Receiver gain has been measured by using a fast Shottky diode power meter which was connected to a lock-in amplifier. The detection IF band of 4-12 GHz was determined by a band pass filter. Using large path length distances (0.8 m) and large IF detection bandwidth allowed us to average out standing waves that always exist in the experimental set-up, thus greatly improving the measurement accuracy compared to a single tone technique [5].

Signal from a lock-in amplifier was measured as a function of grid rotation angle for the range from 0° to 360° which resulted in passing through the same range of input temperatures four times. Input signal strength can be calculated from the grid angle using a $\mathrm{Cos}^2$ law. A typical measurement results are shown in Fig. 8. Receiver compression of less than 2 % has been observed for a 100° C load. Measured gain repeats well when passing the input power range several times which confirms that measurement accuracy is adequate. The measured value of gain does not depend on the level of liquid nitrogen in the load which confirms that this set-up is immune to the presence of moderate standing wave in the system.

## IV. Conclusion

In conclusion, we have manufactured and fully characterized eight units of ALMA band 9 receiver covering a 602 to 720 GHz input frequency range. All units demonstrated consistent receiver characteristics with the best measured noise temperature of all being 60 K. An improved measurement set-up has been created for measurements of gain saturation which has low measurement uncertainty due to averaging of receiver standing waves. Receiver gain compression below 2% has been demonstrated for 100° C load.

## Acknowledgment

Authors would like to thank E. Bryerton, and J. Kooi for useful discussions.

## References

[1] R. Hesper, B.D. Jackson, A.M. Baryshev, J. Adema, K. Wielinga, M. Kroug, T. Zijlstra, G. Gerlofsma, M. Bekema, K. Keizer, H. Schaeffer, J. Barkhof, F.P. Mena, A. Koops, R. Rivas, T.M. Klapwijk, W. Wild, "Design and development of a 600-720 GHz receiver for ALMA band 9", End",Proc. Of 16th Int symp on Space Terahertz Technology, pp. 110-115, 2005

[2] M. Candotti, A.M. Baryshev, N.A. Trappe, R. Hesper, J.A. Murphy, J. Barkhof, "Quasi-optical Verification of the Band 9 ALMA Front-End",Proc. Of 16th Int symp on Space Terahertz Technology, pp. 79-84, 2005

[3] E. Bryerton, K. Saini, M. Morgan, D. Thacker, "Development of Electronically Tuned Local Oscillators for ALMA", 30th Int Conf on Infrared and Millimeter Waves, Sept 2005.

[4] Baryshev *et al.*, "Development of a 0.6 THz SIS Receiver for ALMA", Proc of 12th Int. Symp. on Space Terahertz Technology, pp. 581-591, 2001

[5] A. R. Kerr, "Saturation by Noise and CW Signals in SIS Mixers", Presented at the 2002 International Symposium on Space THz Technology, Cambridge, MA, March 2002, ALMA MEMO 401, http://www.alma.nrao.edu/memos/

# Optical design of the submillimeter limb sounder TELIS

P. Yagoubov, A. Baryshev*, R. Hesper*

National Institute for Space Research, SRON, the Netherlands
*Kapteyn Astronomical Institute/SRON

V. Koshelets

Institute of Radio Engineering and Electronics, IREE, Russia

G. Wagner, M. Birk

Institute for Remote Sensing Technology, DLR, Germany

A. Murk

Institute of Applied Physics, University of Bern, Switzerland

TELIS (Terahertz and submm Limb Sounder) is cooperation between European institutes, DLR, RAL and SRON, to build a three-channel balloon-borne heterodyne spectrometer for atmospheric research. The optical front-end of the instrument consists of a dual-offset Cassegrain pointing telescope, calibration blackbody and relay optics, common for the three channels. Beam separation between the channels is performed quasioptically by a dichroic filter and a polarizer. After the splitting, the three beams enter liquid helium cooled cryostat, where each receiver has dedicated cold optics and mixer elements.

In this paper we present optical design and experimental results of the quasioptical 500 - 650 GHz channel for TELIS. It is based on a phase-locked Superconducting Integrated Receiver (SIR). The SIR chip is placed on the flat back surface of the elliptical silicon lens. Further shaping and relaying of the beam is done by means of reflective optics.

Design and validation of the optics, as well as estimation of optical components tolerances, have been performed using commercial software packages ZEMAX and GRASP.

In this paper we present experimental results of the amplitude-phase beam pattern measurements of the SIR cold optics performed at 620 GHz. We have also measured amplitude beam pattern of the complete instrument, including the telescope, using the compact range. Results of these tests will be presented at the conference.

# Superconducting microresonators for photon detection

J.Zmuidzinas, P. K. Day, J. Gao, J. Glenn, S. Golwala, S. Kumar, H. G. LeDuc,
B. A. Mazin, J. Schlaerth, and A. Vayonakis

California Institute of Technology, Pasadena, CA

The absorption of photons in a superconducting film breaks apart Cooper pairs and produces single-electron (quasiparticle) excitations, which may be detected using a lithographed resonator to obtain a sensitive measurement of the superconductor's surface impedance. This concept, under investigation at Caltech/JPL since 1999, provides the basis for sensitive, frequency-multiplexed detector arrays that are relatively simple to fabricate. Several methods are available for coupling the photon energy into the resonator, allowing operation from millimeter to X-ray wavelengths. At present, a prototype submillimeter multicolor array camera is being prepared for demonstration at the Caltech Submillimeter Observatory. The noise properties of the resonators have been studied carefully and should allow background-limited detection. Superconducting microresonators are now finding other applications, e.g. quantum computing experiments.

# Lumped Element Kinetic Inductance Detectors

Simon Doyle [a], Jack Naylon [b], Philip Mauskopf [a], Adrian Porch [b], and Chris Dunscombe [a]

[a] Department of Physics and Astronomy, Cardiff University, Queens Buildings, The Parade Cardiff CF24 3AA
[b] Department of Electrical Engineering, Cardiff University, Queens buildings, The Parade Cardiff CF24 3AA

## ABSTRACT

Kinetic Inductance Detectors (KIDs) provide a promising solution to the problem of producing large format arrays of ultra sensitive detectors for astronomy. Traditionally KIDs have been constructed from superconducting quarter-wavelength or half-wavelength resonator elements capacitivly coupled to a co-planar feed line. Photons are detected by measuring the change in quasi-particle density caused by the splitting of Cooper pairs in the superconducting resonant element. This change in quasi-particle density alters the kinetic inductance, and hence the resonant frequency of the resonant element. This arrangement requires the quasi-particles generated by photon absorption to be concentrated at positions of high current density in the resonator. This is usually achieved through antenna coupling or quasi-particle trapping. For these detectors to work at wavelengths shorter than around 500 μm where antenna coupling can introduce a significant loss of efficiency, then a direct absorption method needs to be considered. One solution to this problem is the Lumped Element KID (LEKID), which shows no current variation along its length and can be arranged into a photon absorbing area coupled to free space and therefore requiring no antennas or quasi-particle trapping. This paper outlines the relevant microwave theory of a LEKID, along with theoretical performance for these devices.

## INTRODUCTION

The principal of operation for any KID device is to measure the change in quasi-particle population within the volume of a superconducting film upon photon absorption. Any photon with an energy $hf > 2\Delta$, if absorbed will break apart Cooper pairs resulting in an excess quasi-particle population ($n_{qp}$). The result of this event is to alter the complex impedance of the film by increasing the kinetic inductance ($L_k$). In practice the variance in $L_k$ with change in quasi-particle density is very small and requires the film to be fabricated in to a high Q, microwave resonance circuit to sense this variation. In this regime we can monitor the change in phase of a fixed tone microwave probe signal centred on the resonant frequency. The variation in $L_k$ upon photon absorption is now scaled by Q, which can be of order $10^6$ for a low loss superconducting resonator operating well below the superconducting transition temperature of the film ($T_c$) [1]. The theoretical noise limit of these devices is governed by generation-recombination noise, which scales with temperature and film volume [2]. For a typical coplanar aluminium KID device operating at 100mK this noise is estimated to be around $10^{-20}$ W√Hz.

The approach to date for creating high Q microwave resonators from superconducting films for the purpose of photon detection has been to fabricate distributed half-wave or quarter-wave resonators from CPW geometries. For these devices to act as photon detectors power must be coupled in to area of high current density using antenna structures or quasi-particle traps [3]. In this paper we discuss the concept of a new idea for a lumped element KID which shows no current variation along its length and also serves as a free space absorber. This new approach provides an elegant solution to the problem of coupling THz radiation to the sensitive element of a KID device, combining the properties of the absorbing area, detection and readout elements of the KID.

## DISTRIBUTED KID DEVICES

In a resonant circuit fabricated from superconducting elements (L, C), varying the Cooper pair density in the superconductor will alter the resonant frequency $\omega_0$. The change in $\omega_0$ is proportional to $\alpha$ which is the ratio of kinetic inductance $L_k$ to normal inductance L ($\alpha = L_k/L$). A schematic of a quarter-wave KID is shown in fig (1). The resonant frequency for a quarter-wave KID constructed from a coplanar geometry can be approximated by:

$$f_0 \approx \frac{c}{4l\sqrt{\frac{1+\varepsilon_{sub}}{2}}} \qquad (1)$$

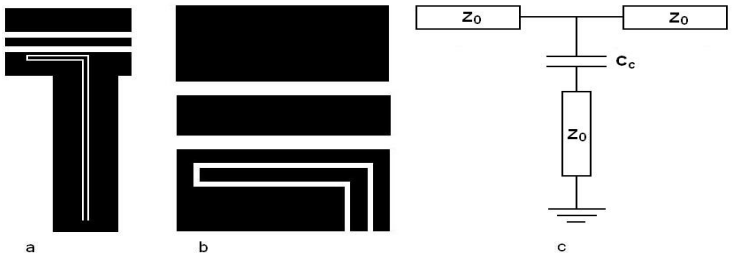


Fig 1, a) A schematic of a elbow coupled quarter-wave resonator. b) Close up of the elbow coupling section. c) Equivalent transmission line model.

Where $\varepsilon_{sub}$ is the substrate permittivity. Close to resonance the impedance of the quarter-wave section can be written as:

$$Z_{res} \approx \frac{Z_L}{g}(1 + 2jQ_u x) \tag{2}$$

Here $Z_L$ is the characteristic impedance of the resonance section, $Q_u$ is the unloaded quality factor, g is the coupling coefficient and *x* is given by $(\omega-\omega_0/\omega_0)$. The coupling coefficient is dependent on the coupling capacitance which is set by the geometry of the elbow section. The coupling is also set by $Q_u$ and the frequency at resonance.

$$g = \frac{2Q_u}{\pi}(\omega_0 C Z_L)^2 \tag{3}$$

The effect of g is to reduce the measured (loaded Q) $Q_L$ in such a way to give:

$$\frac{1}{Q_L} = \frac{1}{Q_u} + \frac{g}{2Q_u} \tag{4}$$

If the characteristic impedance of the resonant section is made to be the same as the characteristic impedance of the feed line then the power transmitted past the resonator at frequencies close to resonance can be calculated using a standard ABCD matrix approach [3] for a shunted impedance to ground giving

$$S_{21} = \left(\frac{2}{2+g}\right)\frac{1 + 2jQ_u^2 x^2}{1 + (4jQ_u x/2 + g)} \tag{5}$$

$$|S_{21}| = \left(\frac{2}{2+g}\right)\frac{1 + 4Q_u^2 x^2}{1 + (4Q_u x/2 + g)^2} \tag{6}$$

The change in phase close to resonance is given by the argument of $S_{21}$. For a quarter-wave resonator the resonant wavelength is fixed by geometry, the resonant frequency however is dependent on the line impedance which varies with kinetic inductance. From basic transmission line theory it can be shown that the change in resonant frequency upon changing $L_k$ is given by:

$$\Delta f = -\frac{1}{2}\frac{\alpha}{L_k} f_0 \Delta L_k \tag{7}$$

The change in resonant frequency is measured using a fixed tone microwave probe signal set equal to the resonant frequency $f_0$. As $f_0$ varies with photon absorption a shift in phase of the probe signal is observed. $\Delta L_k$ for a change in quasi-particle

density can be calculated by looking in the change in the complex component of the conductivity ($\sigma_2$). Using Mattis-Bardeen theory the change in $\sigma_2$ with the change in quasi-particle density yields the result for the change in phase of the probe signal with change in quasi-particle density:

$$\frac{d\theta}{dN_{qp}} = \left[ \sqrt{\frac{2}{\pi}} \cdot \frac{\hbar\omega I_0(\varsigma) - (2\Delta + \hbar\omega) I_1(\varsigma)}{\sqrt{\Delta k_B T (2\Delta + k_b T)}} \right] \frac{\alpha Q_L}{N_0 V} \tag{8}$$

where $\varsigma$ is given by

$$\varsigma = \frac{\hbar\omega}{2k_B T} \tag{9}$$

$N_0$ is the single spin density of electron states. $N_0$ for Niobium is $6.93 \times 10^{10}$ $\mu m^{-3}$ $eV^{-1}$ [4]. For Aluminium $N_0$ is $1.72 \times 10^{10}$ $\mu m^{-3}$ $eV^{-1}$, where V is the effective volume of the resonator. This effective volume accounts for the fact that only the areas of the film where current is flowing will be sensitive to pair breaking. $I_0$ and $I_1$ are modified Bessel functions. From (8) it is clear that in order to maximise the response of the device one needs to maximise $\alpha$ and $Q_L$ while minimising the film volume V.

## OPTICAL COUPLING TO A DISTRIBUTED KID

The current distribution along the length of a quarter-wave distributed KID follows a sine distribution with a current node at the coupling end of the line and a peak at the shorted end. This condition means that the response of a distributed KID to a pair breaking event will be position dependent, having a maximum at the shorted end and zero at the coupling end. For this reason optical power must be coupled in to the shorted end. There are two ways currently used to do this. The first is to take a KID fabricated from an Aluminium superconducting film with a bandgap of $2\Delta_{Al}$ and a Niobium antenna and microstrip line of band gap energy $2\Delta_{Nb}$ [5]. Coupling is achieved by running the microstrip line coupled to the antenna over the centre strip of the resonator using it as a ground plane. Any optical signal with photon energy $2\Delta_{Al} < E_{ph} < 2\Delta_{Nb}$ will now travel through the antenna and microstrip with very low loss. However once the signal reaches the KID it will break Cooper pairs in the resonator and be dissipated. This defines a band in which we can operate that is limited to be between the two bandgap energies of the resonator and antenna structure. Using an Aluminium KID with Niobium antenna sets this band to approximately 100 – 700 GHz.

Antenna coupled KIDs are limited by the bandgap energy of Niobium and therefore cannot be used for the detection of THz radiation. An alternative solution is to use a quasi-particle trap [5]. Here we use a superconducting film as an absorber and fabricate a KID from a superconductor with a lower bandgap energy to that of the absorbing film. The shorted end of the KID is placed in contact with the absorbing pad. Quasi-particles generated in the absorbing superconductor can now diffuse in to the KID, where owing to their higher energy will break further pairs and lose energy. The quasi-particle are now unable to diffuse back in to the superconducting absorber due to the energy gap created by the two materials. This method has been used to demonstrate the absorption of optical and X-ray photons [6] but will prove difficult to work for THz radiation. The reason for this is impedance matching. In order to get good coupling to free space the superconducting absorber must be of order $\lambda/4$ in size and have a normal impedance matched to that of free space. To impedance match to free space the films must be made thin to increase the sheet resistance, by doing this the diffusion length, *l* of the quasi-particles is reduced. Combined with the large absorber size it becomes very difficult to create a film of high enough quality to insure that the quasi-particles generated can diffuse in to the KID sensing element.

## THE LUMPED ELEMENT KID (LEKID)

One way of solving the problem of optical coupling THz radiation to a KID device is to use a lumped element resonator, which unlike its distributed counterpart shows no current variation across the device. This means the device itself can act as the absorber as well as the sensing element in a detector system. The device is based on a series LC circuit inductively coupled to a microstrip feed line. An example of a lumped element resonator is shown in fig (2).

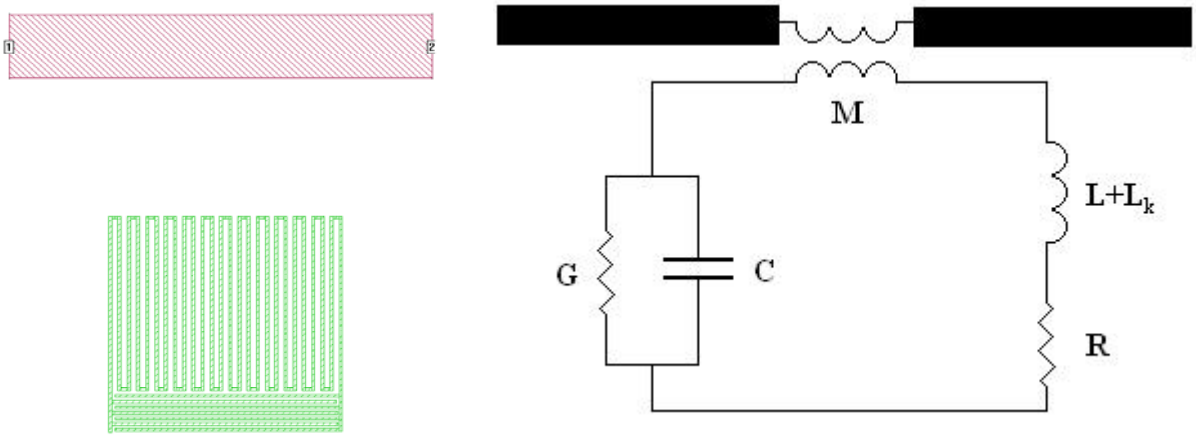


Fig 2: Left a schematic of a LEKID device showing the microstrip feedline (red) and resonant section (green). Right; the equivalent circuit of an inductively coupled LEKID device.

The inductor $L+L_k$ is formed from the self inductance of the meander, and the kinetic inductance of the superconducting film. The capacitor is formed from the interdigital structure connected to each end of the meander. The approximate resonant frequency of this device is simply:

$$\omega_0 = \frac{1}{\sqrt{LC}} \tag{10}$$

The impedance of the resonant section is given by:

$$Z_{res} = j\omega(L + L_k) - \frac{1}{j\omega C} + R \tag{11}$$

Around resonance an inductively coupled resonator with mutual inductance M, loads the feed line as if it were a lumped series impedance ($Z_{eff}$) on the feed line.

$$Z_{eff} = \frac{\omega^2 M^2}{Z_{res}} \tag{12}$$

As in the distributed case the scattering parameters about resonance can be found from a simple ABCD matrix approach. About resonance S21 is described by:

$$S_{21} = \frac{1}{1 + \frac{\omega^2 M^2}{2 Z_0 Z_{res}}} \tag{13}$$

Where $Z_0$ is the characteristic impedance of the feed line. Away from resonance $Z_{res}$ is very large hence and $S_{21}$ is unaffected by the presence of the resonator. At frequencies close to the resonant frequency the resonator begins to load the line and reduces $S_{21}$ reaching a minimum on resonance. As with the distributed KID we can define a coupling coefficient g.

$$g = \frac{M^2 Q_u}{Z_0 L}\omega \tag{14}$$

$Q_u$ for a series resonant circuit is given ωL/R [3]. In practice we want $Q_u$ to be as large as possible and therefore R to be as small as possible. R represents all the losses in the circuit, which are due to residual losses in the superconducting film brought about by quasi-particles as well as losses in the dielectric of the capacitor. We can rewrite $Q_u$ as:

$$Q_u = \frac{\omega L}{R_{qp} + 1/\omega C \cdot \tan\delta} \tag{15}$$

Here $R_{qp}$ is the residual quasi-particle loss and tanδ is the loss tangent of the capacitor. For an interdigital capacitor on sapphire at low temperatures tanδ is negligible so $Q_u$ is governed by $R_{qp}$. One additional mechanism of loss in this structure is through radiation. This loss would depend the geometry of the resonant element. $Q_L$ would now be written as

$$\frac{1}{Q_L} = \frac{1}{Q_u} + \frac{1}{Q_{rad}} \tag{16}$$

From the simulations performed radiation losses do not seem to be a problem for this structure, however $Q_{rad}$ can be reduced by placing the device in a closed box if radiation losses proved to be a problem. This clearly would not be suitable for a free space coupled detector, however the lid of this box could be replaced with a high pass filter reducing the radiation losses.

## SIMULATED RESPONSE

To determine the microwave response of a LEKID device we simulated several geometries using Sonnet EM. The device discussed from this point forward was designed on a 100μm thick sapphire substrate using a metal film with a real impedance 0.5μΩ/sq and a tanδ of $1 \times 10^{-6}$. These values are realistic for a superconductor of modest quality and have been compared with the results made from a measured distributed KID fabricated from a Tantalum film at 300mK. The mutual inductance and hence the $Q_L$ value is proportional to the distance of the resonator from the feed line. Fig (3) shows the simulated results of a resonator placed 200μm from the feed line. The $Q_L$ for this device was of order $10^5$ and had a phase slope dω/df of order 17000.

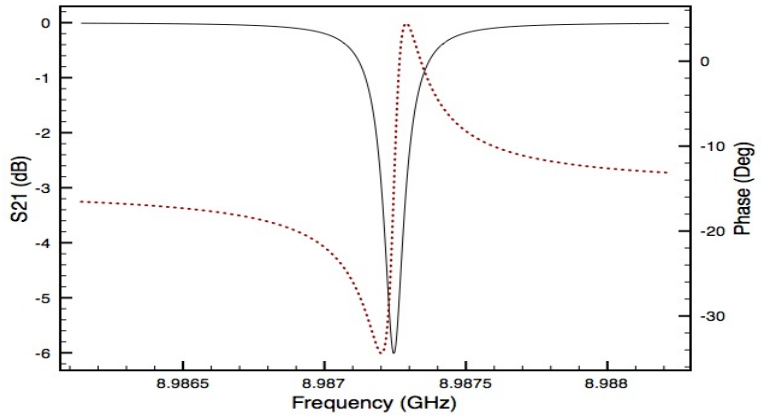


Fig 3, the simulated microwave response of a LEKID device

The response of this device to a change in quasi-particle density can be estimated in the same way as for a distributed KID using equation (8). An $\alpha$ value was calculated by performing a simulation on the meander structure alone to determine a value for the inductance of the meander section. $L_k$ was calculated using London theory and assuming that the current flow through the entire volume of the meander. This is a reasonable estimate if the film thickness is of order $2\lambda_L$ where $\lambda_L$ is the London penetration depth. Fig 4 shows the expected response of a typical LEKID device using a film thickness of 50nm fabricated from Aluminium and Niobium.

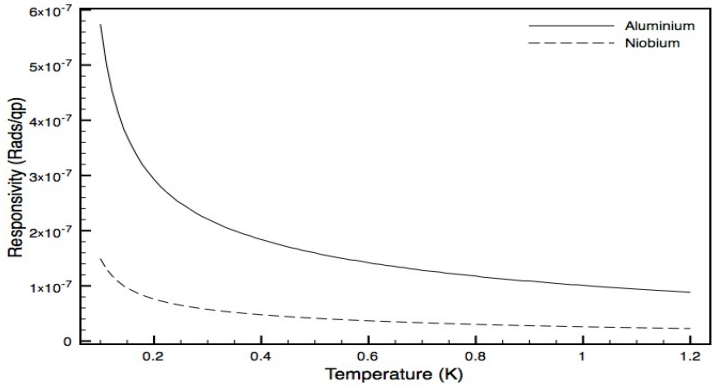


Fig 4, The predicted phase response to a single photon absorbed as a function of temperature for an Aluminium and Niobium LEKID device.

The results shown in fig (4) are comparable with the responsivity of a 50nm thick distributed KID with the same value of $Q_L$ operating at the same resonant frequency. The LEKIDs responsivity is lower by about a factor of 3. This is due to the LEKID geometry having a higher film volume at this resonant frequency.

The limiting noise of any KID device is governed by the generation recombination noise [2] and takes the form:

$$nep_{qp} = 2\Delta\sqrt{\frac{n_{qp}}{\tau_{qp}}} \tag{17}$$

This is the theoretical limit and will depend heavily on the film quality, which ultimately determines the number of quasi-particles at a given temperature ($n_{qp}$) and the quasi-particle life time at that temperature ($\tau_{up}$).

The current distribution across the device was also simulated to look for signs of the device resonating in distributed modes. For the typical geometries the distributed mode started appearing at around 30 GHz which is well out side the bandwidth of the readout electronics.

## 6. Optical coupling to a LEKID device

A HFSS simulation was performed on the meander section of the LEKID in the absence of a substrate. By tuning the thickness of the meander alone an absorption of 50% can be achieved over a broad range of frequencies. This is shown in fig (5). Due to the geometry of the meander the optical coupling of the LEKID devices simulated in this paper has a dependence on polarisation. The coupling to free space in the favored polarization is determined by the impedance the meander presents to an incoming photon. This impedance can be tuned by altering the film thickness or number of lines in the meander.

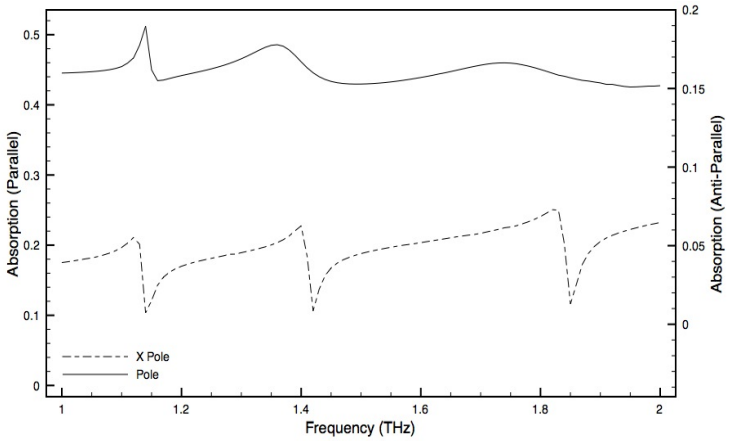


Fig 5, An HFSS simulation of the absorption of radiation with polarization parallel and anti-parallel to the meander absorbing structure in the absence of a substrate.

The presence of a substrate and ground plane behind the meander can be used to ones advantage by creating a λ/4 back-short. This in conjunction with a low loss anti-reflection coating can be used to maximise optical coupling. Using a quasi-optical analysis approach the optical coupling can be calculated to reach values close to 100% as shown in fig (6). An alternative approach is to remove some of the ground-plane of the device and illuminate the detector through the substrate. This approach has the advantage reducing the required impedance the meander needs to present to the incoming photon allowing for more leeway in the normal impedance of the of the meander structure. The approach also removes the need for a very low loss anti reflection coating, which would otherwise reduce the $Q_u$ of the resonator.

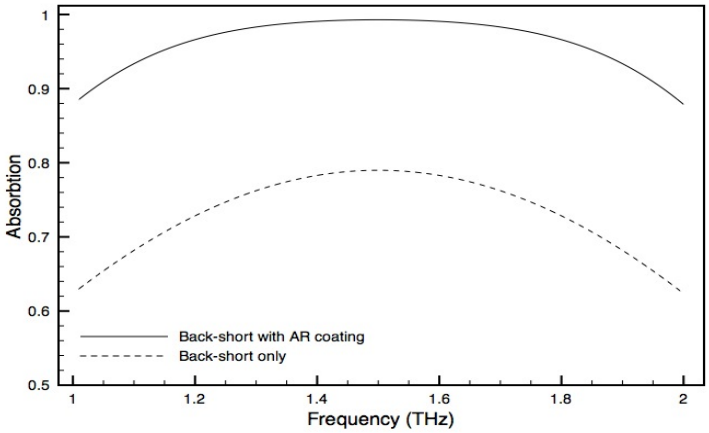


Fig 6, A Quasi-optical simulation showing the absorption of radiation with polarization parallel to the meander as a function of frequency in the presence of a substrate forming a λ/4 backshort.

## MULTIPLEXING

One of the major advantages with KID devices is there natural ability to multiplexing in the frequency domain. Changing the length of a distributed KID or changing the value of the interdigital capacitor of a LEKID alters the resonant frequency of the device. This enables many devices to be coupled to a single feed line. Using this approach one can excite all the KID devices coupled to a single line simultaneously by probing the line with a complex probe signal made up from the resonant frequency of each device. This probe signal can be constructed in software and then realised using digital to analogue converters

(DAC). In practice the complex probe signal is constructed at a lower frequency, which is then up converted using a mixer and local oscillator to the resonant frequency of the devices on the chip. Once the devices have been probed the signal can be mixed down using the same local oscillator and read in to an analogue to digital converter (ADC) for analysis. Both the DAC and DAC are available as "off the shelf" technologies providing a simple solution to reading out large arrays of KID detectors. This approach means as many as 10000 devices can be read out using only two coaxial lines connected to the detector array. This simplifies the cryogenics considerably and reduces the cold (4K) electronics to a single HEMT amplifier [5].

## 7. CONCLUSION

The LEKID device simulated in this paper demonstrates a promising solution to the problem of coupling THz radiation in to kinetic inductance sensing elements. We have demonstrated a comparable theoretical response to that of a distributed KID operating at a similar temperature and resonant frequency. The coupling of radiation to these devices shows a strong polarization response which can reach almost 100% if used in conjunction with a $\lambda/4$ backshort and anti-reflection coating. It is worth noting that due to the simplicity of the LEKID geometry means an entire array could be fabricated using a single lithographic step and etch along with two film depositions. The ease of processing is in striking contrast with competing detector technologies such as Transition Edge Sensors (TES) which require multiple fabrication steps.

## References

[1] P. K. Day. H. G. LeDuc, B. A. Mazin, A. Vayonakis and J. Zmuidzinas, "*A broadband superconducting detector suitable for use in large arrays*", *Nature*, Vol. 425, October 2003, pp. 817-821

[2] A. V. Sergeev, V. V. Mitin and B. S. Karasik, "*Ultrasensitive hot-electron kinetic-inductance detectors operating well below the superconducting transition*", *Appl. Phys. Lett*., Vol. 80, February 2002, pp. 817-819

[3] D. Pozar, *Microwave Engineering*, John Wiley, 2005 (Third edition)

[4] W. McMillan, "*Transition Temperatures of strong-coupled superconductors*", Phys. Rev vol.167, no2, pp. 331-344, 1968

[5] B. A. Mazin, "*Microwave kinetic inductance detectors*", Ph.D dissertation, California Institute of Technology, California, 2004

[6] B. A Mazin, et al "*A Position Sensitive X-ray Spectophotometer using Microwave Kinetic Inductance Detectors"*, arXiv:cond-mat/0610130v1 4 Oct 2006

## Acknowledgments

Discussions with: Mr Dmirty Morozov, Dr Gustav Teleberg, Dr Jochem Beselmans and Dr Stephen Yates

Work funded by PPARC rolling grant. Grant code:PP/D001048/1

# Terra Hertz imaging using superconducting kinetec inductance detectors:

*S.J.C.Yates, J.J.A. Baselmans, R. Barends, J.N. Hovenier, J.R. Gao and T.M. Klapwijk*

Superconducting Kinetec Inductance Detectors (KIDs) have significant advantages for building very large arrays of pixels (>1000), and have previously been proposed and prototyped for millimeter and x-ray detectors. Here we propose and discuss a simple detector scheme for (~2) THz imaging spectroscopy, suitable for a future mission like SPICA, so helping to take KID research from simple (KID) resonator characterization to full radiation detectors.

# A Millimeter/Submillimeter Microwave Kinetic Inductance Detector Camera for Multicolor Mapping

Jason Glenn[1], Peter K. Day[2], Sunil Golwala[3], Shwetank Kumar[3], Henry G. LeDuc[2], Benjamin A. Mazin[2], Hien T. Nguyen[2], James Schlaerth[1], Anastasios Vayonakis[3], & Jonas Zmuidzinas[2,3]

Microwave Kinetic Inductance Detectors (MKIDs) are sensitive, superconducting, Cooper-pair-breaking detectors. They lend themselves to elegant multiplexed readout using HEMT amplifiers and software-defined radio technology. Recently 16-pixel, two-color, antenna-coupled MKID arrays have been tested in the laboratory, demonstrating readiness for large-scale focal plane arrays for astrophysics. Additionally, MKID noise has been reduced to the BLIP level for 750 μm to 1.3 mm observations from Mauna Kea. Hence, we are building a four-band (750 μm, 850 μm, 1.1 mm, and 1.3 mm) MKID camera to make observations, first from the Caltech Submillimeter Observatory, and later from the Cornell-Caltech Atacama Telescope. The MKID camera will utilize an array of 600, four-color, antenna-coupled MKIDs, for a total of 2,400 channels, yielding a high survey mapping speed. We will report on a conceptual design for this camera and laboratory results from a small-scale demonstration camera[4]. A successful demonstration of large-scale MKID arrays will provide an alternative technology to transition-edge sensors (TESs) for SOFIA, the Beyond Einstein Cosmic Microwave Background Polarization Probe (CMBPol), and SAFIR.

[1]Center for Astrophysics and Space Astronomy, University of Colorado, 389-UCB, Boulder, CO 80309 (contact author: jglenn@casa.colorado.edu)
[2]Jet Propulsion Lab, 4800 Oak Grove Drive, Pasadena, CA 91109
[3]George W. Downs Laboratory of Physics, MC 320-47, California Institute of Technology, Pasadena, CA 91125
[4]This work is funded, in part, by a NASA APRA grant and a grant from the Moore Foundation.

# Quasiparticle lifetime in tantalum kinetic inductance detectors

R. Barends[1], J. N. Hovenier[1], J. R. Gao[1,2], T. M. Klapwijk[1],
J. J. A. Baselmans[2], S. J. C. Yates[2], Y. J. Y. Lankwarden[2], and H. F. C. Hoevers[2]

[1] Kavli Institute of Nanoscience, Delft University of Technology, the Netherlands.
[2] SRON Netherlands Institute for Space Research, Utrecht, the Netherlands.

The quasiparticle lifetime is a crucial parameter in achieving a background limited noise equivalent power for kinetic inductance detectors. We present measurements of the quasiparticle lifetime of 150 nm thick sputtered tantalum on silicon kinetic inductance detectors using optical pulses. We find that the quasiparticle lifetime saturates at low temperatures, increases to a maximum of up to 45 μs and subsequently drops with increasing temperature. We attribute this behavior to non-uniformity in the superconductor.

## Introduction

One of the greatest challenges for far infrared astronomy is the development of sensitive large cameras (>$10^4$ pixels), having a background limited sensitivity. To date no such detector exists. Recently kinetic inductance detectors (KIDs) have been proposed [1].

A KID consists of a superconducting microwave resonator and is a pair breaking detector; incident radiation breaks Cooper pairs into quasiparticles, changing the kinetic inductance of the superconductor, and thus the resonance frequency [2,3] and phase of the forward transmission.

This non-equilibrium process leads to an excess amount of quasiparticles above the superconducting gap depending on the rate of photon absorption and quasiparticle loss. The interplay between photon absorption, quasiparticle recombination, phonon trapping and local superconducting properties leads to an effective 'lifetime' of the quasiparticles [4,5]. The detectivity of KIDs and other pair breaking detectors such as superconducting tunnel junctions (STJs) depends crucially on this quasiparticle lifetime.

## Experiment

The measured phase response to an optical pulse can be seen in Fig. 1. The rise stems from the response time of the microwave resonator, which is a function of the loaded quality factor and resonance frequency. The exponential decay can be clearly characterized with a single decay time. Both the intensity and the pulse length are chosen to create a clearly observable response while staying in the linear regime.

The quasiparticle lifetime is known to depend on the choice of material [4]. We have opted for tantalum, because of its demonstrated lifetime and high critical temperature. A 150 nm tantalum layer is sputter deposited onto a HF-cleaned [100] Si wafer. Prior to tantalum deposition a 5 nm niobium seed layer is sputtered to promote growth of the tantalum alpha phase [6].

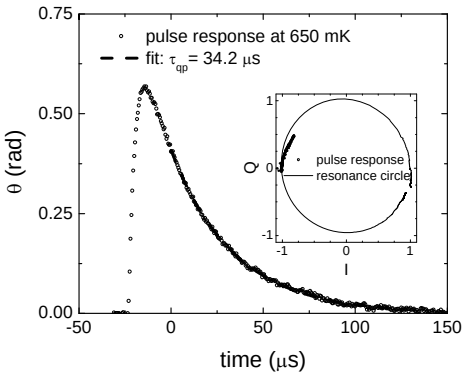


Fig. 1. The phase response to an optical pulse of 0.5 μs, the resonator response time is 3.7 μs. Both timescales are an order of magnitude smaller than the quasiparticle lifetime. The inset shows the response in the IQ plane, the resonator dip is slightly asymmetric.

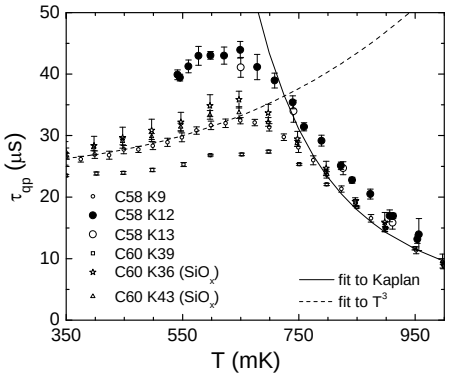


Fig. 2. The temperature dependence of the quasiparticle lifetime for different resonators in the frequency range of 4-6 GHz. With growing temperature, all show an increase in the lifetime until a maximum is reached after which an exponential decay takes over. The error bars are the standard deviation of multiple pulse responses. The lifetime of device K9 is fitted to a cubed temperature dependence and to a theoretical prediction of the recombination time using a gap of 0.27 meV [4].

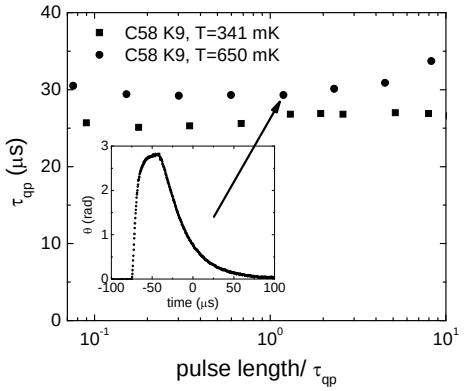


Fig. 3. The quasiparticle lifetime for different pulse lenghts. The excess quasiparticle number at the end of the pulse is related to the pulse length, being around an order smaller or larger than the lifetime. The inset shows the response for a pulse length equal to the lifetime.

Patterning is done using optical lithography and $CF_4/O_2$ reactive ion etching. The critical temperature is 4.4 K, its residual resistivity ratio is 3. The chip is partly covered with a 10 nm sputtered $SiO_x$ layer.

The devices are quarter wavelength CPW resonators and manifest as a circle in the polar plane of the forward transmission $S_{21}$. This resonance circle is normalized: it is shifted to the origin and given unity radius, in such a way that at resonance the imaginary part is zero and the real part is minus unity. This scaling allows the response of different KIDs to be compared. Using a signal generator, IQ mixer and 2-channel fast acquisition card the response can be monitored in time, see Fig. 1.

The chip is mounted in a sample box on a He-3 sorption cooler. A GaAsP LED having a rated response time of 10 ns acts as photon source for the optical pulse. The LED is placed at the 4K plate and is optically coupled to the sample box via a plexiglass fiber and illuminates the whole chip.

Due to the broad illumination and small resonator size the resonator and nearby ground plane is rather uniformly illuminated, leading to a homogeneous excitation of Cooper pairs and quasiparticles. This technique allows us to measure the quasiparticle lifetime without being limited by the outdiffusion of quasiparticles.

The quasiparticle lifetime is plotted versus temperature in Fig. 2 for several devices. When cooling down the quasiparticle lifetime increases until it reaches a maximum value at a temperature of 650 mK. Upon further cooling the lifetime starts to drop and seems to reach a saturation value around 350 mK. This feature is followed qualitatively by all devices. Quantitavely the lifetime at high temperatures and the saturation value of different devices lie closely together, however the maximum of the lifetime differs between 27 to 45 μs. Within this spread there is no significant difference in lifetime between resonators covered with a 10 nm $SiO_x$ layer, its presence does not significantly affect the lifetime. The $SiO_x$ layer leads to nearly a doubling of noise in covered resonators. The subject of noise will not be discussed in this article.

We find that the lifetime is independent of pulse duration, see Fig. 3. The lifetime does not change when the sample is shortly heated above the critical temperature. We have not observed a power dependence of the quasiparticle lifetime below the resonator saturation readout power. Near this power the quasiparticle lifetime decreases (not shown).

**Discussion**

The most striking feature is that the quasiparticle lifetime decreases with decreasing temperature for all devices below 650 mK. This represents a strong deviation from recombination theory for homogeneous superconductors [4], since the quasiparticle recombination time is expected to monotonically increase when cooling down and reaches values in the order of a second around 300 mK for bulk alpha phase tantalum, due to the exponential decrease in quasiparticle density.

The lifetime as depicted in Fig. 2 can be divided in three regimes: the saturation of the lifetime which is visible near 350 mK; the increase of the lifetime up to 650 mK which follows a $T^3$-dependence; and the subsequent decrease of the lifetime when heating up above 650 mK. The latter can be fitted to the theoretical prediction the recombination time [4], when using a superconducting gap of 0.27 meV, much smaller than that of bulk tantalum which is 0.67 meV.

Upon the absorption of optical photons, the high energy of the quasiparticles generated is quickly downconverted, mostly via electron-phonon scattering. In turn these phonons generate quasiparticles, leading to the photon energy being downconverted to a large number of excess quasiparticles near the superconducting gap [7]. The downconversion is too fast to be observed by the resonator due to the response time.

The quasiparticles recombine and emit phonons. As such, the effective lifetime is governed by the non-equilibrium quasiparticle and phonon densities and corresponding timescales, such as the recombination, Cooper pair breaking and phonon escape rate [5].

However in a superconductor where non-uniformities give rise to subgap states, quasiparticles can become trapped and become localized in a macroscopic depression of the order parameter or a single state. Non-uniformity can arise from vortices, trapped flux, magnetic impurities and metallic oxides. For example, niobium is known to have superconducting oxides with a critical temperature as low as 1.4 K [8], which could explain the choice of gap in the fit to Ref. 4. Detrapping can occur due to phonon absorption or scattering with a quasiparticle [9,10].

The fact that the maximum lifetime differs between devices at the same chip suggests the existence non-uniformity in the superconducting layer. The exact nature and origins of the traps in our devices is unknown. The reproducibility of the result after heating above the critical temperature rules out trapped flux.

We assume that the non-uniformity of the superconducting properties gives rise to an additional quasiparticle loss channel that is much faster.

Qualitatively, the increase in the lifetime with increasing temperature has been observed also in STJs [10]. The responsivity increases with a factor of two due to the lifetime up to around 600 mK, above which it decreases again. These junctions consist of two tantalum electrodes with an $Al/AlO_x$ barrier in between. Quantitatively, the value of the quasiparticle lifetime of up to 45 μs lies in the range of 5-80 μs which has been reported for tantalum in the literature [11-14].

The fact that similar results have been observed in tantalum devices with a dissimilar geometry and material composition suggests that the non-uniformity leading to our observation has a general character.

**Conclusion**

We have measured the quasiparticle lifetime in tantalum on silicon quarter wave KIDs using optical pulses for temperatures down to 350 mK. We find that the quasiparticle lifetime saturates at low temperatures around 25 μs, grows with increasing temperature and reaches a maximum value of up to 45 μs at a temperature of 650 mK, and drops at higher temperatures. There is no optical pulse length and readout power dependence of the lifetime and there is no significant difference between resonators covered with and without a 10 nm thick $SiO_x$ layer.

We attribute the low temperature behavior of the lifetime to quasiparticle traps arising from non-uniformity in the superconductor. The nature of these traps is unknown and deserves further attention.

The authors would like to thank P. Verhoeve and P. A. J. de Korte for stimulating discussions. The work is supported by RadioNet (EU) and the Netherlands Organisation for Scientific Research (NWO).

1. P. K. Day, H. G. LeDuc, B. A. Mazin, A. Vayonakis and J. Zmuidzinas, Nature **425**, 817 (2003).
2. S. Doyle, J. Naylon, J. Cox, P. Mauskopf, A. Porch, Proc. SPIE **6275,** 6275O1, (2006).
3. R. Barends, J. J. A. Baselmans, J. N. Hovenier, J. R. Gao, S. J. C. Yates, T. M. Klapwijk, and H. F. C. Hoevers, IEEE Trans. on Appl. Sup. (in press).
4. S. B. Kaplan, C. C. Chi, D. N. Langenberg, J. J. Chang, S. Jafarey and D. J. Scalapino, Phys. Rev. B **14**, 4858 (1976).
5. A. Rothwarf and B. N. Taylor, Phys. Rev. Lett. **19**, 27 (1967).
6. D. W. Face and D. E. Prober, J. Vac. Sci. Tech. A **5**, 3408 (1987).
7. A. G. Kozorezov, A. F. Volkov, J. K. Wigmore, A. Peacock, A. Poelaert and R. den Hartog, Phys. Rev. B **61**, 11807 (2000).
8. J. K. Hulm, C. K. Jones, R. A. Hein and J. W. Gibson, J. Low Temp. Phys. **7**, 291 (1972).
9. A. Poelaert, A. G. Kozorezov, A. Peacock and J. K. Wigmore, Phys. Rev. Lett. **82**, 1257 (1999).
10. A. G. Kozorezov, J. K. Wigmore, A. Peacock, A. Poelaert, P. Verhoeve, R. den Hartog and G. Brammertz, Appl. Phys. Lett. **78**, 3654 (2001).
11. T. Nussbaumer, P. Lerch, E. Kirk, A. Zehnder, R. Fuechslin, P. F. Meier, and H. R. Ott, Phys. Rev. B **61**, 9719 (2000).
12. P. Verhoeve, R. den Hartog, A. Kozorezov, D. Martin, A. van Dordrecht, J. K. Wigmore, and A. Peacock, J. Appl. Phys. **92**, 6072 (2002).
13. L. Li, L. Frunzio, C. M. Wilson, and D. E. Prober, J. Appl. Phys. **93**, 1137 (2003).
14. B. A. Mazin, B. Bumble, P. K. Day, M. E. Eckart, S. Golwala, J. Zmuidzinas, and F. A. Harrison, Appl. Phys. Lett. **89**, 222507 (2006).

# Development of HEB mixers for GREAT and for security screening

**A. Semenov, H. Richter, A. Smirnov, B. Günther, H.-W. Hübers**
**German Aerospace Center (DLR)**
**Rutherfordstrasse 2, 12489 Berlin, Germany**

**K. Il'in and M. Siegel**
**Institute of Micro- and Nanoelectronic Systems**
**University of Karlsruhe**
**Hertzstrasse 16, 76187 Karlsruhe, Germany**

**G. Gol'tsman**
**Physics department, Moscow State Pedagogical University,**
**M. Pirogovskaya 29, 119435 Moscow, Russia**

**V. Drakinskiy and H. Merkel**
**Department of Microtechnology and Nanoscience, Chalmers University of Technology**
**Fysikgrand 3, SE-41296, Gothenburg, Sweden**

**J. Karamarkovic**
**Faculty of Civil Engineering and Architecture, University of Nis**
**Aleksandra Medvedeva 14, 18000 Nis, Serbia**

We report the study on the quasioptical coupling efficiency and the gain bandwidth of NbN hot-electron bolometer mixers developed for the 4.7 THz channel of the German receiver for Astronomy at THz-frequencies (GREAT) and for security screening at subterahertz frequencies. Radiation coupling efficiency and directive properties of integrated lens antennas with log-spiral, log-periodic and double-slot planar feeds coupled to a hot-electron bolometer were experimentally studied at frequencies from 1 THz to 6 THz and compared with simulations based on the method of moments and the physical-optics ray tracing. For all studied antennas the modeled spectral dependence of the coupling efficiency fits to the experimental data obtained with both Fourier transform spectroscopy and noise temperature measurements only if the complex impedance of the bolometer is explicitly taken into account. Our experimental data did not indicate any noticeable contribution of the quantum noise to the system noise temperature. The experimentally observed deviation of the beam pattern from the model prediction increases with frequency and is most likely due to a non-ideality of the presently used lenses. Study of the intermediate frequency mixer gain at local oscillator (LO) frequencies between 2.5 THz and 0.3 THz showed an increase of the gain bandwidth at low LO frequencies that was understood as the contribution of the direct interaction of magnetic vortices with the radiation field. We have found that the non-homogeneous hot-spot model more adequately describes variation of the intermediate frequency bandwidth with the applied local oscillator power than any of uniform mixer models. The state-of-the-day performance of the GREAT 4.7-THz channel and the 0.8-THz security scanner will be presented.

# Highly Packaged HEB Receivers Using Three-Dimensional Integration

F. Rodriguez-Morales, S. Yngvesson, D. Gu, N. Wadefalk, K. Fu, C. Chan, J. Nicholson, and E. Gerecht

***Abstract*— We report a remarkable progress in the development of highly packaged heterodyne receivers using NbN HEB mixers and MMIC IF amplifiers. We are presenting a record IF noise bandwidth of 8 GHz (measured for a ∼700 GHz LO) using a lumped element matching network for the input of the IF pre-amplifier. Further, we describe the first three-dimensional (3–D) integration of a sub-millimeter mixer and its pre-amplifier using a simple vertical feed-through structure. Thereby, we achieve a volume shrinkage of at least 20 times, accompanied by a mass reduction of 15:1. These receivers bring promise for the implementation of large-format arrays for heterodyne terahertz sensing applications.**

## I. Introduction

HEB type terahertz heterodyne receivers employing NbN devices have been discussed since soon after the first ISSTT symposium. Several such receivers have been operated as ground-based astronomical observation systems and the HIFI instrument that is planned for launch in 2008 includes several HEB mixers [1]. So far no such system has used HEB heterodyne detectors in focal plane arrays, however, whereas arrays of direct detectors are commonly employed. Present HEB mixer receivers are not compact enough to be suitable for packaging in closely spaced arrays, and must be developed further, specifically with arrays in mind. Our group demonstrated the first prototype heterodyne focal plane assembly above 1 THz, a linear array of three elements [2]. Other (non-HEB) work on integrated mixer receivers has been documented in [3]–[5]. The present paper describes development of the HEB integrated receivers into even smaller units, with the final goal being the realization of a compact, multi-element two-dimensional (2–D) array. The immediate objective in the present study has been to develop methods for quantitative design of a receiver consisting of a quasi-optically coupled HEB device directly integrated in the same small block with an MMIC IF amplifier. For this purpose we first performed accurate broadband measurements and modeling of the impedance of the HEB device as a function of IF, and then used the model so obtained, together with CAD models for the MMIC amplifier and other circuit components for the design of several integrated receivers. By improving the broadband matching of the HEB to the MMIC we in one case demonstrated an 8 GHz receiver noise bandwidth. Further, our design methodologies have enabled us to significantly reduce the footprint of the integrated receivers using 2–D and 3–D packaging techniques [6].

This work was supported by NASA through the Langley Research Center under contract NAS1-01058 and CONACyT, Mexico. F. Rodriguez-Morales was with the University of Massachusetts, Amherst, MA 01003 USA. He is now with the Center for Remote Sensing of Ice Sheets (CReSIS), University of Kansas, Lawrence, KS, 66045 USA (e-mail:frodriguez@cresis.ku.edu); S. Yngvesson, J. Nicholson, and K. Fu are with the Dept. of Electrical and Computer Engineering, University of Massachusetts, Amherst, MA 01003 USA; D. Gu was with the Dept. of Electrical and Computer Engineering, University of Massachusetts, Amherst, MA 01003 USA, and is now with the National Institute of Standards and Technology, Boulder, CO 80305 USA; N. Wadefalk was with the RF and Microwave Group, California Institute of Technology, Pasadena, CA 91125 USA. He is now with the Microwave Electronics Laboratory Group, Chalmers University of Technology, SE-412 96 Göteborg, Sweden; C. Chan was with Holyoke Community College, Holyoke, MA 01040 USA. He is now with the Department of Electrical and Computer Engineering, University of Massachusetts, Amherst, MA 01003 USA; E. Gerecht is with the Dept. of Electrical and Computer Engineering, University of Massachusetts, Amherst, MA 01003 USA, and with the National Institute of Standards and Technology, Boulder, CO 80305 USA.

## II. Small Signal IF Impedance Characterization

We performed an extensive set of impedance measurements on several mixer devices fabricated from thin NbN film (3.5–4 nm thick[1]) sputtered on a 350 $\mu$m thick silicon substrate. The measurements were completed using an automatic network analyzer (ANA). The active NbN area was 0.4–0.5 $\mu$m long by 2 $\mu$m wide. We used various LO drive frequencies ranging from 694 GHz up to nearly 2 THz, which cover regions of the electromagnetic spectrum below and above the superconducting bandgap frequency of NbN for typical film parameters. The local oscillator source is the same $CO_2$-pumped far infrared laser system used in previous studies [8], [9]. The HEBs were quasi-optically coupled using monolithic log-periodic antennas in combination with a 4 mm diameter elliptical lens made of silicon. This antenna/lens configuration was designed to operate from 250 GHz to 3 THz. The IF frequency range covered by the ANA was 300 kHz to 8.5 GHz. This frequency range is sufficient to characterize the typical IF bandwidth for all phonon-cooled NbN HEB mixers developed to date. The measurements required an initial one-port short-open-load (SOL) calibration inside the cryostat. The calibration was done by putting each of the standards into the dewar in three consecutive thermal cycles and measuring the corresponding $S_{11}$ using the network analyzer. The power level from the network analyzer was -50 dBm. We designed a customized test vehicle to mount the devices under test (DUTs). This fixture provides the required biasing signals through a broadband resistor network constructed from quartz wire-bondable components. Fig. 1 shows an illustration of the experimental setup used for these measurements, including a picture of the broadband test fixture.

[1]The nominal thickness of the NbN film was given by the manufacturer (Moscow State Pedagogical University, MSPU) as 3.5 to 4 nm. Recent TEM measurements have yielded a thickness of 5–6 nm for similar films [7].

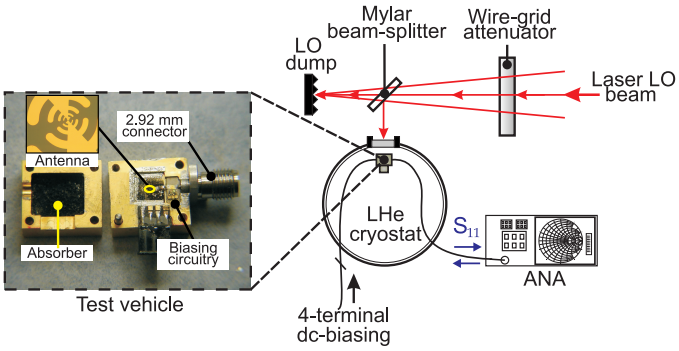


Fig. 1. Experimental setup for small signal IF impedance measurements.

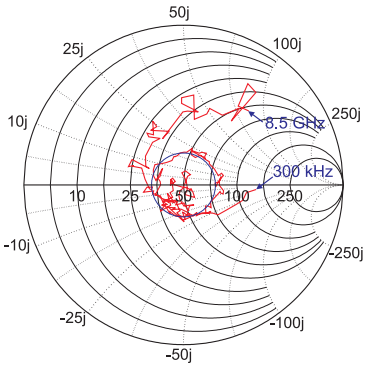


Fig. 2. Typical measured raw impedance data. The blue circle indicates constant standing wave ratio (SWR).

### A. Raw Impedance Data

Fig. 2 shows an example of the measured raw reflection coefficient for one specimen as obtained with the network analyzer. This is the actual source impedance seen by the low-noise amplifier at a particular operating point, including parasitic reactances in the circuit derived from the antenna structure, wire-bonds, transmission line transitions, etc. The HEB impedance (controlled by regulating the amount of incoming LO and dc power) determines the main contribution to the total input reflection coefficient of the IF LNA. However, parasitic reactances in the circuit should not be neglected when designing the appropriate input matching network for minimum noise. As will be discussed in the next section, data obtained in this fashion is very useful when designing integrated HEB-based down-converters.

### B. De-Embedded Impedance Data

The HEB IF small signal impedance was carefully de-embedded from the the measured reflection coefficient ($S_{11}$). The preceding SOL cryogenic calibration was used in combination with the S-parameters of two measured known loads (superconducting and normal state of the bolometer, respectively) to obtain a circuit model for the fixture parasitics. We then subtracted the effect of these parasitics from the measured data using standard computer aided design (CAD) tools. Using the de-embedded data we studied the impact of the LO frequency and biasing conditions in the IF impedance for the first time, providing substantially extended information beyond that obtained in previous measurements such as those presented in [7], [9]–[12]. The de-embedded impedance results were compared against two different models, namely the *Standard* model [10] and the Nebosis-Semenov-Gousev-Renk (NSGR) model [13]. These two formulations are convenient since analytical calculations can be performed of important microwave and terahertz parameters. They do not predict parameters such as conversion gain as accurately as the *hot-spot* model [14]–[16], however.

Fig. 3 shows and example of the fitting of the Standard and NSGR formulations with respect to the de-embedded experimental data for one of the DUTs (designated #D). The Standard model fits the experimental data quite well specially for 694 GHz, where the LO, dc, and microwave power are absorbed in same central hot-spot region of the device. The

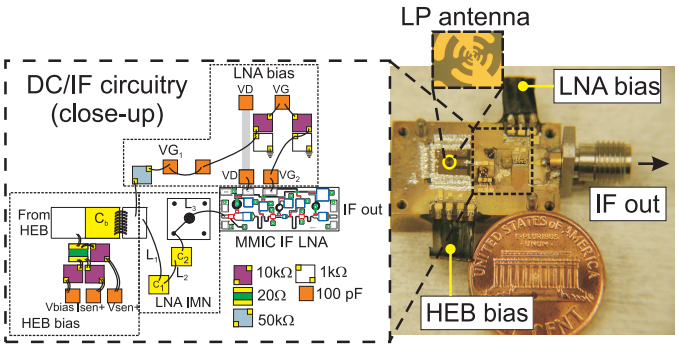


Fig. 5. Integrated receiver module with lumped-element mixer/LNA coupling.

NSGR model does also fit our measured data but requires the use of three time-constant parameters whereas the Standard model only needs one. The NSGR model has advantages in terms of physical interpretation of the time-constants. The interested reader is referred to ref. [17], where further information about our modeling efforts is provided along with additional measured data. We have shown empirically that the IF frequency dependence of the IF impedance, conversion gain, output noise and the receiver noise temperature for at least two devices are well modeled by the Standard model formulation (e.g. Fig. 4). We give experimental evidence of this statement being true for the IF frequency range required for practical integrated receiver design.

## III. Integrated Receiver Design

### A. Lumped Element Coupling

In order to realize the best trade-off between low-noise figure, wide bandwidth, and size; the coupling between the HEB mixer output and the HEMT IF LNA input needs to be studied. This analysis evidently requires the knowledge of the impedance presented by the HEB and surrounding circuitry, which was the center of our discussion in the previous section. Once this source impedance is known, an appropriate input matching network (IMN) can be designed to transform the HEB IF output impedance into the intended

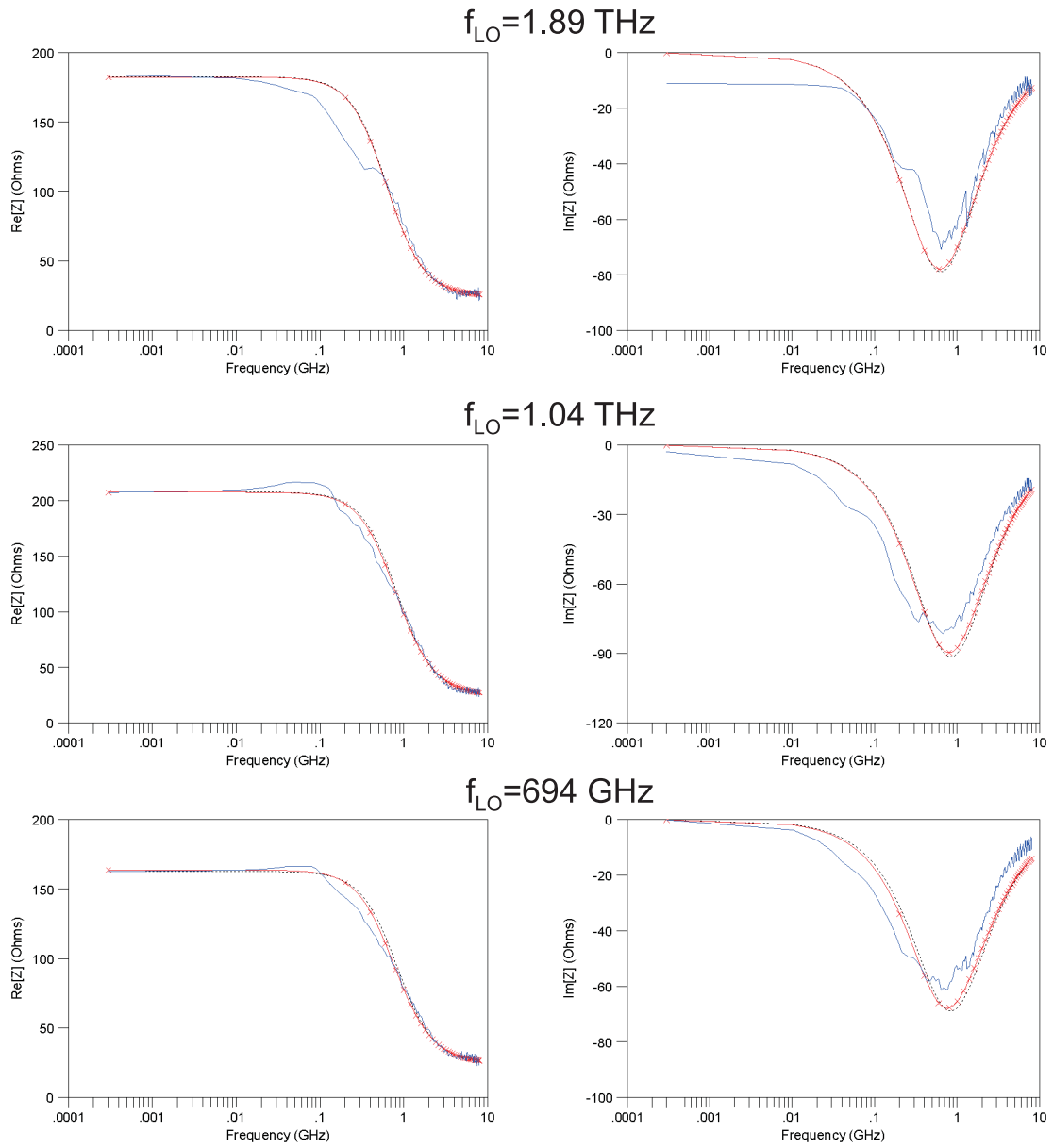


Fig. 3. Comparison of modeled versus de-embedded impedance of device #D measured for a fixed operating point (1 mV, 40 $\mu$A) for different LO frequencies: – Measured, -x- Modeled (NSGR), - - Modeled (Standard model).

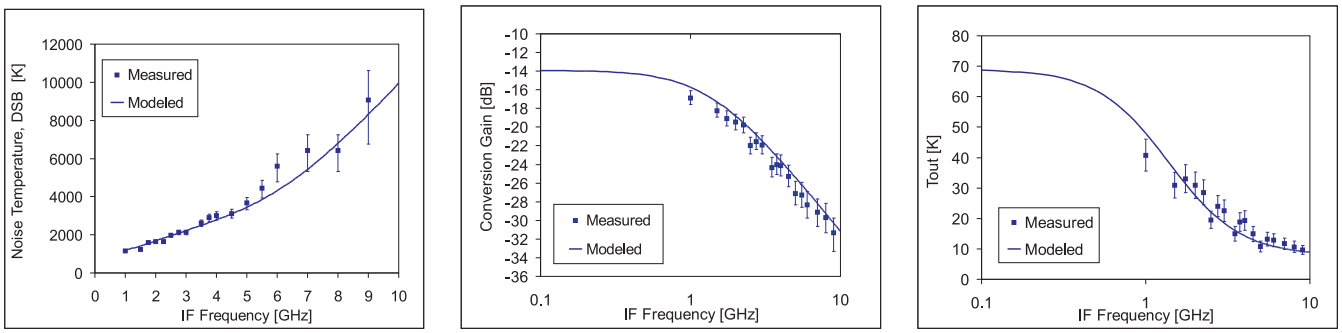


Fig. 4. Modeled versus experimental parameters as a function of IF frequency for a different sample (#C). This data was obtained for $f_{LO}$= 1.04 THz using an optimized lumped-element coupling circuit between the hot electron mixer and the IF amplifier. The empirical figures for the mixer conversion gain and output noise are estimated from the U-factor and the receiver noise temperature. The modeled curve is obtained using the methodology described in [17].

TABLE I

PERFORMANCE OF TWO MIXER SAMPLES MEASURED USING THE LUMPED-ELEMENT INTEGRATED RECEIVER MODULE

| Sample | LO [THz] | $T_{\mathrm{R,DSB}}$ [K] | $B_{\mathrm{eff}}$ [GHz] | $B_{\mathrm{N}}$ [GHz] |
|---|---|---|---|---|
| #C | 0.694 | 825 | 6 | 3.5 |
| | 1.04 | 1160 | 3.25 | 2.4 |
| | 1.89 | 3300 | 4.5 | 3.2 |
| | 2.50 | 4450 | 5 | 3.3 |
| #D | 0.694 | 1100 | 8 | 5.5 |
| | 1.04 | 1600 | 6 | 3.8 |
| | 1.89 | 2700 | 3.2 | 2.0 |

optimum source impedance $Z_{opt}$ required by the LNA.

Since the input impedance of a HEMT-based amplifier is mainly dominated by the gate-to-source capacitive reactance of the first transistor stage, the IMN should behave as a series inductor. One such IMN has already been successfully implemented by our group in the form of a multi-section microstrip transformer [18]. The use of a lumped-element matching network with wire-bonds as inductive elements to further reduce the down-converter size was proposed in previous editions of the ISSTT proceedings [8], [9]. As shown in Fig. 5, we have recently been able to successfully implement such a coupling circuit. The design methodology employed as well as the measured performance of this receiver implementation are discussed in great detail in [17]. In the proposed design methodology, we used the Standard model formulation for the mixer with parameters extracted from the impedance measurements, in combination with CAD models for the IF and dc circuitry to find theoretical estimates of the down-converter performance (e.g. Fig. 4). The estimations are self-consistent in the sense that they account for the noise produced by an MMIC LNA when an HEB is connected at its input, including fixture parasitics. Fig. 6 shows the variation of the double sideband receiver noise temperature, $T_{\mathrm{R,DSB}}$, as a function of IF frequency for two different operating points measured on sample #D. The biasing points were the optimum (1.5 mV, 35 $\mu$A) and (1.0 mV, 35 $\mu$A) using an LO frequency of 694 GHz. This plot shows a remarkable noise bandwidth of 8 GHz for the lowest-noise quiescent point. The narrower bandwidth observed at a slightly lower operating voltage agrees with the expected lower electron temperature, $\theta$, caused by a lower dc-power dissipated at bias point 2. We have also measured $T_{\mathrm{R,DSB}}$ for other LO frequencies (1.04 THz, 1.89 THz, and 2.5 THz) and other devices installed on the same down-converter block. As shown in Table I[2], the demonstrated noise and bandwidth[3] figures obtained are very competitive, in agreement with theoretical predictions.

[2]A different mixer sample (designated #C) was used for this comparative assessment.

[3]The receiver bandwidth performance was quantified in terms of the IF noise bandwidth, $B_{\mathrm{N}}$, and the effective IF bandwidth, $B_{\mathrm{eff}}$. $B_{\mathrm{N}}$ is the frequency at which $T_{\mathrm{R,DSB}}$ increases by a factor of two with respect to its lowest frequency value. $B_{\mathrm{eff}}$, is the bandwidth of an ideal receiver with perfectly sharp passband that yields the same output noise as the system being characterized [18].

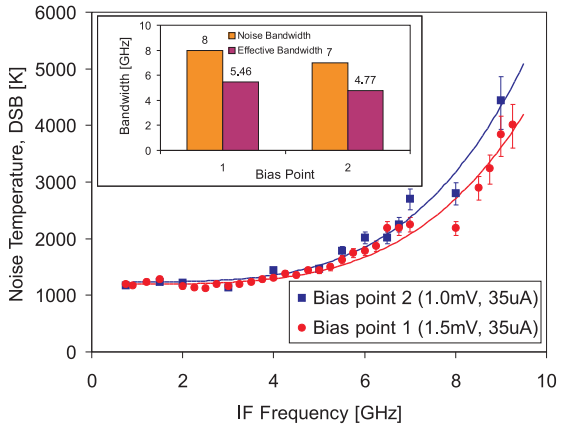


Fig. 6. Double-sideband receiver noise temperature measured at $f_{LO}$= 0.694 THz (sample #D) for two different bias points: i) 1.5 mV, 35 $\mu$A, and ii) 1.0 mV, 35 $\mu$A.

### *B. Three-Dimensional Integration*

We have mentioned that efficient receiver packaging techniques are essential to the development of close-fitting arrays. By far, the most efficient packaging scheme developed to date is three-dimensional integration. The benefits of 3-D packing have been thoroughly described in the literature (e.g. [19], [20]). We have recently explored the use of such techniques to realize an ultra-compact module with an HEB mixer and its corresponding IF amplifier stacked across the z-direction. A straightforward vertical microwave transition has been developed to convey dc and IF signals from the HEB mixer chip to the IF/DC circuitry, both of which are located on different planes. The transition provides impedance matched coupling between the coplanar waveguide (CPW) structure on the HEB chip and the microstrip-based MMIC IF LNA. The three-terminal vertical transition was designed based on ideas proposed within the electronic packaging community (e.g. [20]–[22]). We used full wave electromagnetic CAD tools (CST Microwave Studio) to simulate and optimize the performance of the IF/DC interconnect. The concept of the packaged down-converter is illustrated on the left inset of Fig. 7. Aside from the vertical feedthrough itself, the package consists of three multi-level blocks:

- The device block, where the quasi-optically coupled HEB mixer chip is mounted.
- The IF/DC block, where all the IF circuitry (MMIC IF LNA included) as well as dc-biasing networks and connectors are installed.
- The top lid, which is used to provide environmental, mechanical, and electromagnetic shielding for the components inside the package.

A photograph of the assembled module without cover is shown in the right inset of Fig. 7. The stacked module technique provides a volume reduction of 20 times with a corresponding mass reduction of 15x. The wide bandwidth performance is preserved at the expense of slightly lower sensitivity in this prototype version. A comparison of performance between the 2–D and 3–D down-converter implementations is

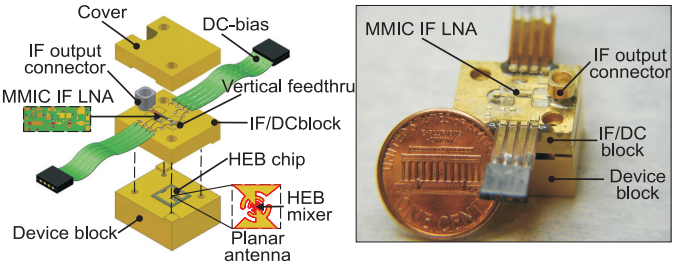


Fig. 7. Integrated receiver module with vertical IF interconnets: (left) concept and (right) photograph.

shown in Table II. For more details on the design considerations for this packaging approach the reader is referred to [6].

## IV. Conclusion

Following a series of previous papers by the authors, we have presented our most recent progress in the development of highly-packaged down-converters. We briefly describe how we have been able to accurately measure and model the small signal IF impedance of phonon-cooled HEB mixers over a wide IF frequency range and for more than one LO frequency. We have used parameters extracted from these measurements in combination with circuit models for the MMIC IF LNA to achieve the close and direct integration of the mixer/LNA combination. For this purpose, a compact, lumped-element matching circuit is proposed and implemented. We have accomplished a high degree of convergence between measurements and modeled performance as per our design methodology. Several integrated receivers for terahertz frequencies have been designed using this modeling approach and have been successfully tested, including what is believed to be the first 3-D terahertz receiver. The stacked module technique provides an outstanding volume and mass reduction while maintaining good electrical performance. The ultimate goal of this investigation was to make a large array a feasible architecture. We believe that a medium size array is now within reach.

## Acknowledgment

The authors would like to acknowledge Dr. S. Weinreb, Jet Propulsion Laboratory, for supplying the MMIC IF LNA chips.

TABLE II

Performance comparison between the 2-D and 3-D integration receiver implementations using mixer sample #C

| LO [THz] | Configuration | $T_{\mathrm{R,DSB}}$ [K] | $B_{\mathrm{eff}}$ [GHz] | $B_{\mathrm{N}}$ [GHz] |
|---|---|---|---|---|
| 0.694 | 2-D | 825 | 5.6 | 3.2 |
| | 3-D | 975 | 5.5 | 3.15 |
| 1.89 | 2-D | 3300 | 4.5 | 3.2 |
| | 3-D | 4200 | 4.6 | 3.0 |

## References

[1] S. Cherednichenko, M. Kroug, H. Merkel, P. Khosropanah, A. Adam, E. Kollberg, D. Loudkov, G. Goltsman, B. Voronov, H. Richter, and H.-W. Huebers, "1.6 THz heterodyne receiver for the far infrared space telescope." *Physica C*, vol. 372–376, pp. 427–431, 2002.

[2] F. Rodriguez-Morales, S. Yngvesson, E. Gerecht, N. Wadefalk, J. Nicholson, D. Gu, X. Zhao, T. Goyette, and J. Waldman, "A prototype focal plane array with HEB mixer elements and MMIC IF amplifiers." in *Proc. 15th Int. Symp. Space Terahertz Tech., Northampton, MA*, Apr. 2004, pp. 165–172.

[3] S. Weinreb, "SIS Mixer to HEMT Amplifier Optimum Coupling Network," *IEEE Trans. Microw. Theory Tech.*, vol. 35, no. 11, pp. 1067–1069, Nov. 1987.

[4] S. Padin, D. Woody, J. A. Stern, H. LeDuc, R. Blundell, C. Tong, and M. Pospieszalski, "An Integrated SIS Mixer and HEMT IF Amplifier," *IEEE Trans. Microw. Theory Tech.*, vol. 44, pp. 987–990, Jun. 1996.

[5] V. Koshelets, S. Shitov, A. Ermakov, L. Filippenko, O. Koryukin, A. Khudchenko, M. Y. Torgashin, P. Yagoubov, R. Hoogeveen, and O. Pylypenko, "Superconducting Integrated Receiver for TELIS," *IEEE Trans. Appl. Supercond.*, vol. 15, no. 2, pp. 960–963, Jun. 2005.

[6] F. Rodriguez-Morales, K. S. Yngvesson, D. Gu, J. Nicholson, K. Fu, and C. Chan, "Highly Packaged Terahertz Down-Converter Modules Using 3-D Integration," *IEEE Microw. Wireless Comp. Lett.*, In press, 2007.

[7] J. Kooi, J. Baselmans, J. Gao, T. Klapwijk, M. Hajenius, P. Dieleman, A. Baryshev, and G. de Lange, "IF Impedance and Mixer Gain of Hot-Electron Bolometers," *J. Appl. Phys.*, 101, 044511 (2007).

[8] F. Rodriguez-Morales, E. Gerecht, D. Gu, R. Zannoni, S. Yngvesson, N. Wadefalk, and J. Nicholson, "Performance Improvement of Integrated HEB-MMIC Receivers for Multi-Pixel Terahertz Focal Plane Arrays." in *Proc. 16th Int. Symp. Space Terahertz Tech., Goteborg, Sweden*, May 2005, pp. 246–250.

[9] F. Rodriguez-Morales, K. S. Yngvesson, N. Wadefalk, R. Zannoni, D. Gu, E.Gerecht, and J. Nicholson, "Optimal Coupling of NbN HEB THz Mixers to Cryogenic HEMT IF Low-Noise Amplifiers." in *Proc. 17th Int. Symp. Space Terahertz Tech., Paris, France*, May 2006.

[10] H. Ekstroem, B. Karasik, E. Kollberg, and K. S. Yngvesson, "Conversion Gain and Noise of Niobium Superconducting Hot-Electron Mixers," *IEEE Trans. Microw. Theory Tech.*, vol. 43, no. 4, pp. 938–947, Apr. 1995.

[11] B. Karasik and W. McGrath, "Microwave Transmission Technique for Accurate Impedance Characterization of Superconductive Bolometric Mixers," *Int J. IR and MM Waves*, vol. 20, no. 1, pp. 21–32, Jan. 1999.

[12] F. Rodriguez-Morales and K. S. Yngvesson, "Impedance and Bandwidth Characterization of NbN Hot Electron Bolometric Mixers," in *Proc. 14th Int. Symp. Space Terahertz Tech., Tucson, Az*, Apr. 2003, pp. 431–438.

[13] R. S. Nebosis, A. D. Semenov, Y. P. Gousev, and K. F. Renk, "Rigorous Analysis of Superconducting Hot-Electron Bolometer Mixer: Theory and Comparison with Experiment," in *Proc. 7th Int. Symp. Space Terahertz Tech., Charlottesville, VA*, Mar. 1996, pp. 601–613.

[14] H. Merkel, P. Khosropanah, P. Yagoubov, and E. Kollberg, "A Hot-Spot Mixer Model for Phonon-Cooled NbN Hot Electron Bolometric Mixers," *IEEE Trans. on Appl. Supercond.*, vol. 9, no. 2, pp. 4201–4204, Jun. 1999.

[15] H. Merkel, P. Khosropanah, S. Cherednichenko, K. S. Yngvesson, A. Adam, and E. Kollberg, "Gain and Noise of Phonon-Cooled Hot Electron Bolometers Using a Hot Spot Mixer Model," *IEEE J. Appl. Supercond.*, Sep. 2000.

[16] H. Merkel, P. Khosropanah, D. W. Floet, P. Yagoubov, and E. Kollberg, "Conversion gain and fluctuation noise of phonon-cooled hot-electron bolometers in hot-spot regime," *IEEE Trans. Microw. Theory Tech.*, vol. 48, no. 4, pp. 690–699, Apr. 2000.

[17] F. Rodriguez-Morales and S. Yngvesson, "Wide-Band Terahertz Mixers and Receivers: Modeling and Characterization," *Submitted to IEEE Trans. Microw. Theory Tech.*, 2007.

[18] F. Rodriguez-Morales, S. Yngvesson, R. Zannoni, E. Gerecht, D.Gu, N. Wadefalk, and J.Nicholson, "Development of Integrated HEB/MMIC Receivers for Near-Range Terahertz Imaging," *IEEE Trans. Microw. Theory Tech.*, vol. 54, no. 6, pp. 2301–2311, Jun. 2006.

[19] S. F. Al-sarawi, D. Abbott, and P. Franzon, "A Review of 3-D Packaging Technology," *IEEE Trans. Comp., Packag., Manufact. Technol. B*, vol. 21, no. 1, pp. 2–14, Feb. 1998.

[20] P. Monfraix, C. Schaffauser, M. Paillard, O. Veinder, and J. L. Cazaux, "3D Packaging for Space Application: Imagination and Reality," in *EGAAS 2005 Symp.*, Oct. 2005, pp. 173–176.

[21] M. Hauhe and J. Wooldridge, "High-Density Packaging of X-Band Active Array Modules," *IEEE Trans. Comp., Packag., Manufact. Technol. B*, vol. 20, no. 3, pp. 279–291, Aug. 1997.

[22] T. Barbier, F. Mazel, B. Reig, and P. Monfraix, "A 3D Wideband Package Solution using MCM-D BCB Technology for Tile TR Module," in *IEEE MTT-S Int. Microw. Symp. Dig.*, vol. 3, Jun. 1997, pp. 1551–1554.

# Sensitivity of an NbN hot electron bolometer based heterodyne receiver at 4.3 THz

P. Khosropanah, W.M. Laauwen, J.R. Gao, M. Hajenius, J.N. Hovenier, and T.M. Klapwijk

**Abstract— We have characterized a heterodyne receiver based on an NbN hot electron bolometer integrated with spiral antenna as mixer and a $CO_2$ pumped gas laser at 4.3 THz as local oscillator (LO). We succeeded in measuring the receiver output power, responding to the hot/cold load, as a function of bias voltage at optimum LO power. From the resulted receiver noise temperature versus the bias voltage, we found a DSB receiver noise temperature of 3500 K at a bath temperature of 4 K, which is a minimum average value. This is the highest sensitivity reported so far at frequencies above 4 THz.**

## I. Introduction

Hot electron bolometer mixers become the chosen technology for heterodyne receivers far above 1 THz. They have been used for the two highest frequency bands in the Heterodyne Instrument for Far Infrared (HIFI) on the Herschel Space Observatory, covering a frequency range of 1410-1910 GHz [1]. For future space missions, 2-6 THz high resolution spectroscopic surveys are highly desirable for astronomical and atmospheric studies. However, the performance of HEB mixers at frequencies above 3 THz, namely super-THz frequencies, has not been measured extensively and only few studies have so far been reported [2,3].

Our long-term research goal is to develop sensitive heterodyne receivers operating at super-THz frequencies using NbN HEBs as mixers and quantum cascade lasers (QCLs) as local oscillators [4,5]. To separate the problems associated with either HEBs or QCLs, we use a gas laser, commonly used in the laboratory, as a local oscillator at 4.3 THz to characterize the HEB mixers.

P. Khosropanah and W. Laauwen are with SRON Netherlands Institute for Space Research, Landleven 12, 9747 AD, Groningen, the Netherlands Corresponding author: phone: +31-(0)50-363-3465; fax: +31-(0)50-363-4033; e-mail: P.Khosropanah@sron.nl.

J.R. Gao and M. Hajenius are with SRON Netherlands Institute for Space Research, Sorbonnelaan 2, 3584 CA, Utrecht, the Netherlands and also with Kavli Institute of NanoScience, Faculty of Applied Sciences, Delft University of Technology, Lorentzweg 1, 2628 CJ, Delft, the Netherlands.

J.N. Hovenier and T.M. Klapwijk are with Kavli Institute of NanoScience, Faculty of Applied Sciences, Delft University of Technology, Lorentzweg 1, 2628 CJ, Delft, the Netherlands.

## II. HEB Mixer

The HEB used here is a 2 μm wide, 0.2 μm long and 5 nm thick NbN bridge on a high resistive Si substrate. We applied NbTiN/Au bilayer pads to contact the NbN bridge to a spiral antenna. Previously we have demonstrated excellent receiver sensitivities at 1.6, 2.5 and 2.8 THz using mixers with the same contact structures [5-7]. The HEB has a room temperature resistance of 80 Ω, a critical temperature of 10 K, and a critical current of 180 μA at 4.2 K. It is integrated with a spiral antenna, with a tight winding design close to the HEB. The antenna is circular polarized and has a very wide RF bandwidth allowing the detection of radiation up to 6 THz [8]. Fig. 1 shows an SEM micrograph of a similar HEB mixer. Details of device fabrication and DC characterization can be found elsewhere [9].

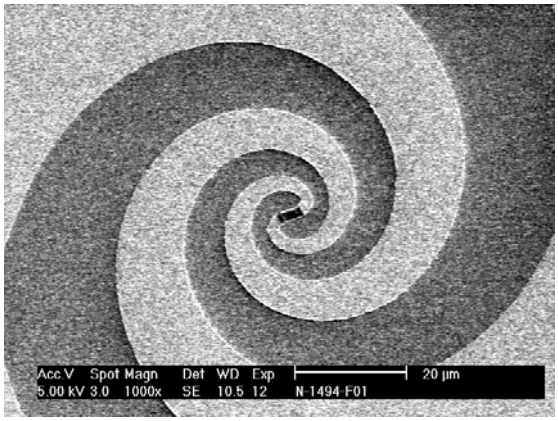


Fig 1. SEM micrograph of a spiral antenna coupled NbN HEB

## III. Heterodyne Measurement Setup

Fig. 2 shows a schematic view of the measurement setup. THz radiation is coupled to the mixer using a standard quasi-optical technique. The Si chip with the HEB is glued to the backside of an elliptical, anti-reflection coated Si lens. The coating on the lens is 14 μm thick Parylene C and optimized for 3.5 THz. Because of this, it improves the coupling efficiency only by about 10% at 4.3 THz in comparison to an uncoated one. The lens is placed in a metal mixer block, thermally anchored to the 4.2 K cold plate.

The local oscillator is a $CO_2$ pumped gas laser. The combination of the 9P34 line of the $CO_2$ laser and methanol in

the FIR laser gives about 3 mW of power at 4.3 THz (λ ≈70 μm). The laser beam is collimated with a HDPE lens and is further reflected to the HEB cryostat by a 3.5 μm thick Mylar beam splitter. The blackbody radiation from a slab of Eccosorb at 295 K (hot load) and 77 K (cold load) is used as a calibration source. This signal is combined with the laser beam by the beam splitter and passes through a 1 mm thick HDPE window at room temperature and a metal mesh heat filter (QMC Ltd.), mounted on the 4 K shield of the HEB cryostat.

The IF signal, resulting from mixing the hot/cold load signal with the LO, is amplified first using a cryogenic low noise amplifier and then room-temperature amplifiers. This signal is filtered at 1.4 GHz in a band of 80 MHz. The entire IF chain has a gain of 71 dB and a noise temperature of 7 K.

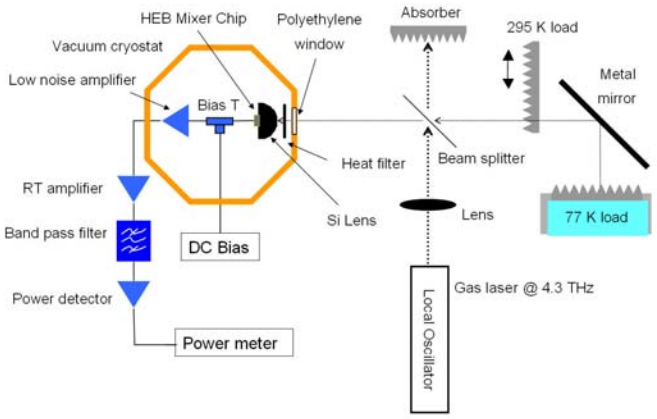


Fig 2. Measurement setup

## IV. Heterodyne Measurement Results

Fig. 3 shows a set of current-voltage curves of the HEB for different absorbed LO power levels. The optimum operating region, which gives the highest sensitivity is around 30-35 μA and 0.5-1.0 mV bias point. The optimum absorbed LO power is about 230 nW, determined by using the isothermal technique [10].

To obtain the receiver noise temperature we apply a standard Y-factor method, taking the ratio of the receiver output power responding to the hot/cold load. It is worthwhile to note that the equivalent temperature of a blackbody at such high frequencies is substantially different from its physical temperature. Using the Callen-Welton definition [11], at 4.3 THz the equivalent temperatures of a blackbody at 77 and 295 K are 118 and 307 K respectively.

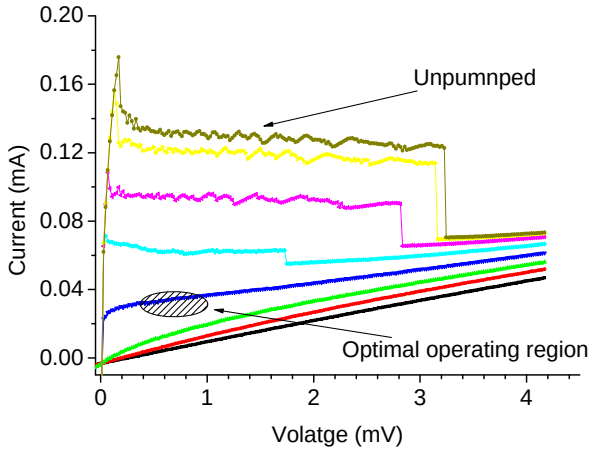


Fig 3. Current-voltage curves of the HEB mixer for different pumping level, taken at 4.2 K. The optimum operating point is around 0.5-1 mV and 30-35 μA where the absorbed LO power in HEB is about 230 nW.

Fig. 4 shows the measured receiver output power, responding to the hot/cold load, versus the bias voltage at optimum LO power. Fig. 5 gives the double sideband (DSB) receiver noise temperature, calculated using the data plotted in figure 4. If we focus on the noise temperature curves in Fig. 5, it is clear that the data is noisy. We attribute the noise to the fluctuations in the output power of the gas laser. It is known that the lasing in the cavity of a gas laser is sensitive to the fluctuations of temperature and gas pressure. Thus, stabilizing the gas lasers in general is cumbersome and therefore, it is difficult to record the IF output power versus bias voltage at constant LO. We succeeded in measuring such curves, suggesting that we have achieved reasonable power stability of the gas laser. However, the power is still not stable enough to accurately determine the Y-factor without averaging.

In our experiment we observed correlations between the fluctuations in the IF output power and those in the current of the HEB. The latter reflects the LO power fluctuations. To quantify the receiver sensitivity, we take the average value of measured Y factor and the receiver noise temperature at the optimum operating point. We found the highest Y-factor of 0.22 dB around 0.8 mV. This corresponds to a DSB receiver noise temperature of 3500 K in figure 5. To the best of our knowledge, this is the first published data, which shows the noise temperature of a HEB as a function of bias voltage using a gas laser as LO at super-THz frequencies and the value of 3500 K is the highest sensitivity reported beyond 4 THz in the literature [12].

We find the single sideband mixer conversion loss to be about 13 dB. In our case the total optical loss is estimated to be 5-6 dB in the optical path from the hot/cold load to the HEB, from which 1.7 dB is due to the cryostat window and 1 dB due to the air (at 40% relative humidity there is 4 dB/m loss in the air at 4.3 THz). This suggests that the receiver sensitivity can be improved by reducing these losses.

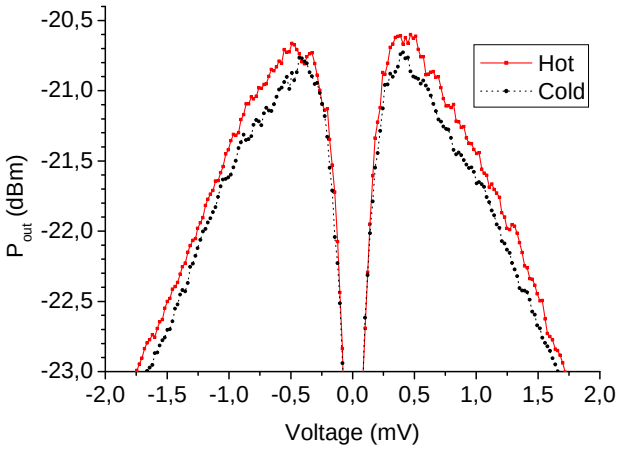


Fig.4. Receiver output power responding to the hot (295 K) and cold (77 K) load as a function of bias voltage at optimum LO power. The difference in $P_{out}$ between the two curves determines the receiver noise temperature. The fluctuations in the measured output power are caused by LO power fluctuations.

## V. Summary

In summary, we succeeded in characterizing a NbN HEB mixer at 4.3 THz using a $CO_2$ pumped gas laser as local oscillator. We measured the receiver output power, responding to hot/cold load, as a function of bias voltage of the HEB, which allows determining the receiver noise temperature at different bias voltages. The averaged lowest receiver noise temperature is 3500 K, which is uncorrected for any optical loss. Our experiment suggests that it is challenging to obtain accurate sensitivity data due to the power fluctuations of the gas laser at the super-THz frequencies. We believe that THz quantum cascade lasers can overcome this issue and have potential to replace currently used gas lasers.

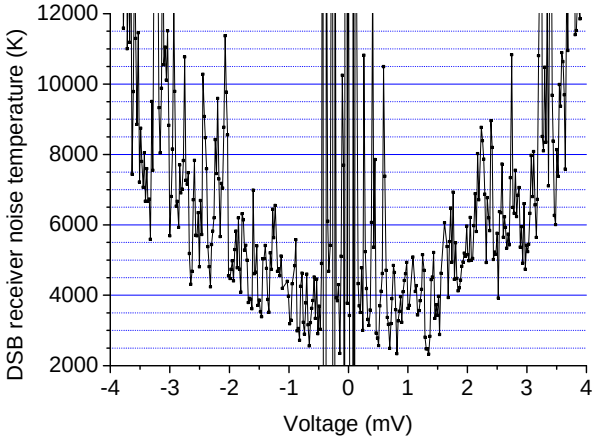


Fig. 5. DSB receiver noise temperature at optimum pumping level as a function of HEB bias voltage. The minimum receiver noise temperature is 3500 K, averaged and taken at 0.8 mV and 30 μA bias point. The fluctuations in the measured curve are caused by LO power fluctuations. The peaks near the zero voltage are due to unstable biasing area of the HEB and should be ignored. The LO frequency is 4.3 THz.

## Acknowledgment

We acknowledge P. van der Wal for helping us improving the performance of our gas laser, G.N. Gol'tsman and B. Voronov for providing the NbN film, and H. Hoevers and W. Wild at SRON for their support. The work is supported by the EU through RadioNet and INTAS.

## References

[1] S. Cherednichenko, P. Khosropanah, A. Adam, H. Merkel, E. Kollberg, D. Loudkov, G. Gol'tsman, B. Voronov, H. Richter, and H.-W. Hübers, "1.4-1.7 THz NbN hot electron bolometer mixers for the Herschel Space Observatory", in Proceedings of SPIE, vol. 4855, Millimeter and submillimeter detectors for astronomy, pp. 361-370, 2003.

[2] A. D. Semenov, H.-W. Hübers, J. Schubert, G. N. Gol'tsman, A. I. Elantiev, B. M. Voronov, and E. M. Gershenzon, "Design and Performance of the Lattice-Cooled Hot-Electron Terahertz Mixer", J. Appl. Phys. vol. 88, pp. 6758-6767, 2000.

[3] Y. B. Vachtomin, S. V. Antipov, S. N. Maslennikov, K. V. Smirnov, S. L. Polyakov, N. S. Kaurova, E. V. Grishina, B. M. Voronov, and G. N. Gol'tsman, "Noise temperature measurements of NbN phonon cooled hot electron bolometer mixer at 2.5 and 3.8 THz" Proceedings of the 15th International Symposium on Space THz Technology, Northampton, MA, 2004.

[4] J. R. Gao, J. N. Hovenier, Z. Q. Yang, J. J. A. Baselmans, A. Baryshev, M. Hajenius, T. M. Klapwijk, A. J. L. Adam, T. O. Klaassen. B. S. Williams, S. Kumar, Q. Hu, and J. L. Reno, "Terahertz heterodyne receiver based on a quantum cascade laser and a superconducting bolometer" Appl. Phys. Lett. vol 86, 244104-6, 2005.

[5] M. Hajenius, P. Khosropanah, J.N. Hovenier, J.R. Gao, T.M. Klapwijk, S. Dhillon, S. Barbieri, P. Filloux, C. Sirtori, A. Ritchie, and H.E. Beere, " THz heterodyne receiver based on a surface plasmon quantum cascade laser and a hot electron bolometer mixer" Proceedings of 17th International Symposium on Space-Terahertz Technology, 10-12 May 2006, Paris, France (in press).

[6] Z. Q. Yang, M. Hajenius, J. J. A. Baselmans, J. R. Gao, B. Voronov, and G. N. Gol'tsman, "Reduced noise in NbN hot electron bolometer mixers by annealing" Supercond. Sci. Technol. 19 (2006) L9-L12 (Rapid Com.).

[7] J.J.A. Baselmans, M.Hajenius, J.R. Gao, T.M. Klapwijk, P.A.J. de Korte, B. Voronov, and G. Gol'tsman, "Doubling of sensitivity and bandwidth in phonon cooled hot electron bolometer mixers", Appl. Phys. Lett, vol. 84: 1958, 2004.

[8] A. D. Semenov, H. Richter, H.-W. Hübers, B. Günther, A. Smirnov, K. S. Il'in, M. Siegel, and J. P. Karamarkovic, "Terahertz Performance of Integrated Lens Antennas With a Hot-Electron Bolometer", IEEE Tran. on MTT, vol. 55(2):239, 2007.

[9] M. Hajenius, J. J. A. Baselmans, J. R. Gao, T.M. Klapwijk, P. A. J. de Korte, B. Voronov and G. Gol'tsman, "Low noise NbN superconducting hot electron bolometer mixers at 1.9 and 2.5 THz", Supercond. Sci. Technol. 17, S224–S228, 2004.

[10] H. Ekström, B.S. Karasik, E.L. Kollberg, and K.S. Yngvesson. "Gain and noise of niobium superconducting hot-electron mixers", IEEE Tran. on MTT, 43(4):938, 1995.

[11] A.R. Kerr, "Suggestions for revised definitions of noise quantities, including quantum effects", IEEE Tran. on MTT. vol. 47:325, 1999.

[12] H.-W- Hübers, A. Semenov, H. Richter, M. Schwarz, B. Günther, K. Smirnov, G. Goltsman, B. Voronov, "Heterodyne receiver for 3-5 THz with hot electron bolometer mixer", in proceedings of SPIE, vol. 5498, Millimeter and submillimeter detectors for astronomy, pp. 579- 586, 2004.

# Stabilisation of a Terahertz Hot-Electron Bolometer mixer with microwave feedback control

Sergey Ryabchun[a], Cheuk-yu Edward Tong[a], Raymond Blundell[a], Robert Kimberk[a],

and Gregory Gol'tsman[b]

[a]Harvard-Smithsonian Center for Astrophysics, 60 Garden Street, Cambridge, MA 02138, USA

[b]Moscow State Pedagogical University, 29 Malaya Pirogovskaya Street, Moscow 119992, Russia

**ABSTRACT**

We report on implementation of microwave feedback control loop to stabilise the performance of an HEB mixer receiver. It is shown that the receiver sensitivity increases by a factor of 4 over a 16-minute scan, and the corresponding Allan time increases up to 10 seconds, as opposed to an open loop value of 1 second. Our experiments also demonstrate that the receiver sensitivity is limited by the intermediate frequency chain.

Keywords: hot-electron bolometer mixers, IF chain stability, Allan variance, Allan time.

## 1. INTRODUCTION

In radio astronomy, signals collected by a radio telescope are usually weak and the corresponding antenna temperature is much lower than the receiver temperature. Therefore, it is necessary to integrate the receiver output over a certain time interval in order to get a reasonable signal-to-noise ratio:

$$x(t,\tau) = \frac{1}{\tau}\int_{t}^{t+\tau} s(t')dt' , \tag{1}$$

where $s(t)$ is the receiver output (e.g. voltage from the power detector) and $\tau$ the integration time. However, if several such measurements of $x(t, \tau)$ are made, they in general will give different results, so one calculates the variance of $x(t, \tau)$ in order to determine how $x(t, \tau)$ changes in time:

$$\sigma^2(\tau) = \left\langle \left(x - \langle x \rangle\right)^2 \right\rangle = \left\langle x^2 \right\rangle - \langle x \rangle^2 . \tag{2}$$

The Allan variance is then defined as half the standard variance[1]:

$$\sigma_A^2(\tau) = \frac{1}{2}\sigma^2(\tau) . \tag{3}$$

Ideally, if there is only white noise in the system the signal-to-noise ratio will increase as the square root of the integration time[2]. This means that, given a receiver with a certain system noise temperature $T_{sys}$ and noise bandwidth $B$, one can reduce the uncertainty in the antenna temperature, $\Delta T$, by simply increasing the integration time:

$$\frac{\Delta T}{T_{sys}} = \frac{1}{\sqrt{B\tau}} . \tag{4}$$

In practice, however, one has to deal with at least two more types of noise: 1/f- (flicker) noise and drift noise. It can be shown[3] that if all of the above types of noise are present in the system, the Allan variance will be

$$\sigma_A^2(\tau) = \frac{a}{\tau} + b + c\tau^{\beta} . \quad (5)$$

The three terms in (5) represent white noise, 1/f-noise and drift noise respectively; the exponent $\beta$ in the drift noise term lies typically between 1 and 2[4]. Equation (5) reaches its minimum at what is called the Allan time, which marks the crossover from white noise to 1/f-noise and drift and is the maximum integration time for the receiver. Integrating longer than the Allan time will result in the worsening of the signal-to-noise ratio. Nor is it useful to integrate as long as the Allan time since doing so will not improve the signal-to-noise ratio much and will only result in the loss of the efficiency of observation. Plotting the Allan variance vs. integration time is a useful tool enabling one to estimate relative contributions of the three types of noise mentioned above and also determine the optimum integration time.

Currently, hot electron bolometer (HEB) mixers are detectors of choice for most terahertz heterodyne receivers because they offer a very low noise temperature, typically 1K/GHz[5], and require much less local oscillator (LO) power than their Schottky diode predecessors[6]. Unfortunately, most HEB receivers typically have an Allan time of less than 5 seconds[4], which is significantly shorter than that for SIS receivers operating below 1 THz[7] and competing Schottky diode based receivers.

In this paper we propose a microwave feedback control loop to compensate for local oscillator power fluctuations. The use of this feedback loop is shown to reduce the fluctuations of the intermediate frequency (IF) power of the receiver and increase the corresponding Allan time.

## 2. EXPERIMANTAL SETUP

Fig. 1 shows a schematic of the experimental setup. The HEB mixer element is installed into a half-height waveguide mixer-block mounted onto the cold plate of the liquid helium cryostat. A Gunn oscillator, operating at 90 GHz, followed

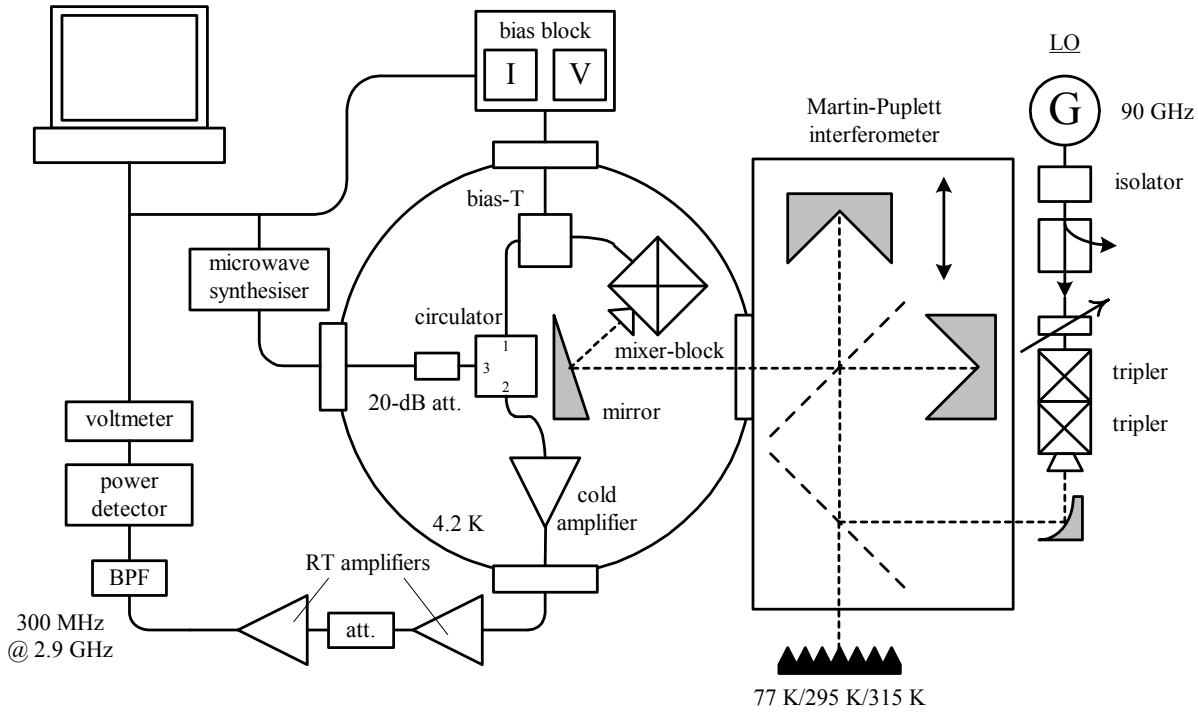


Fig.1: Schematic of the experimental setup.

by two solid state frequency triplers, provides local oscillator (LO) power at a frequency of 810 GHz. The signal and LO are combined in a Martin-Puplett Interferometer, pass through a 0.5-mm Teflon vacuum window and two Zitex G106 infra-red filters mounted onto the 77-K radiation shield and the cold plate respectively, and are finally directed into the corrugated feed horn of the mixer-block by a 30-degree offset parabolic mirror mounted on the cold-plate of the cryostat. A microwave synthesiser (HP83630A) serves as a remotely controllable microwave injection source when the receiver is operating with the feedback loop turned on. The output of this synthesiser is coupled to the HEB mixer via the 3rd port of the cold circulator through a 20-dB attenuator which reduces possible noise coming from outside the cryostat.

Since the frequency of the injected microwave signal is much lower than the LO frequency it will not introduce any spurious mixing tones. On the other hand, it should also be much higher than the mixer cut-off IF[8] so as not to interfere with the mixer IF output. We have selected 17 GHz for the microwave signal as this meets the above criteria and allows coupling the signal to the HEB element quite easily.

The IF output from the mixer passes through the bias-T and circulator to the cryogenic amplifier with a gain of 30 dB in the frequency range 2-4 GHz and then to a room temperature IF chain. The latter consists of two amplifiers with a gain of 26 dB in the frequency range 1-4 GHz. In noise temperature measurements the amplifiers are followed by a 2.4-3.6 GHz band-pass filter and the power meter HP436A. For stability measurements we use a 300-MHz band-pass filter centred at 2.9 GHz, a tunnel diode Herotek power detector loaded by a 120-Ω shunt resistor. The detector voltage is measured by the digital multimeter HP34401A.

## 3. EXPERIMENTAL RESULTS AND DISCUSSION

We used the standard Y-factor procedure to measure the DSB noise temperature of the receiver vs. bias voltage and current and thus determined the low-noise operating point. It was also possible to estimate the mixer gain at the same point:

$$G_M = \frac{T_{bath} + T_{HEMT}}{P(V_{bias} = 0)} \frac{P_{hot} - P_{cold}}{T_{hot} - T_{cold}}, \tag{6}$$

where $T_{\text{bath}} = 4.2$ K – the He bath temperature, $T_{\text{HEMT}} \sim 4$ K – the noise temperature of the cold amplifier; $P(V_{\text{bias}} = 0)$ is the IF chain output when the HEB mixer is not biased and the LO is turned off; $T_{\text{hot}} = 295$ K and $T_{\text{cold}} = 77$ K are hot and cold load temperatures respectively. Note, however, that (6) gives the mixer gain averaged over the output bandwidth.

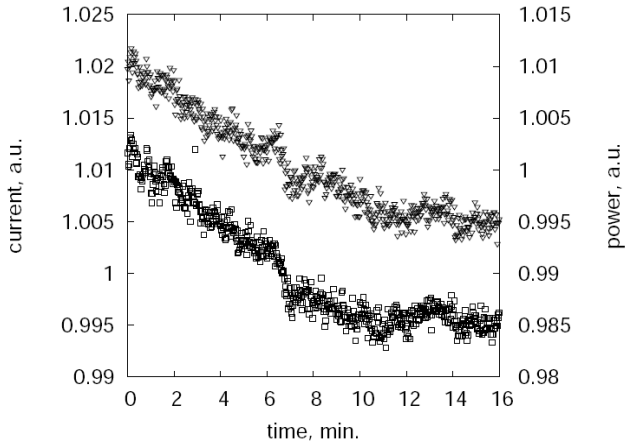


Fig. 2: Mixer current (squares) and IF power (triangles) vs. time with the feedback control turned off.

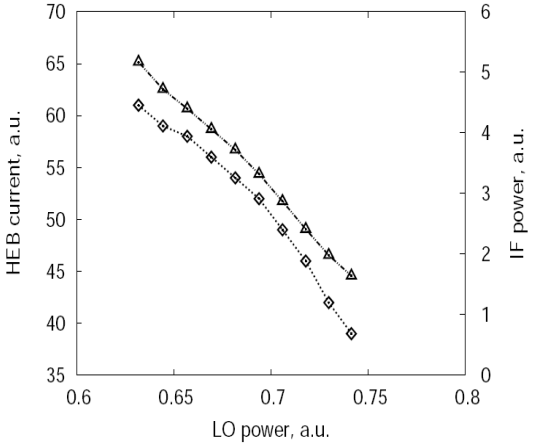


Fig. 3: Mixer current (diamonds) and IF power (triangles) vs. LO power

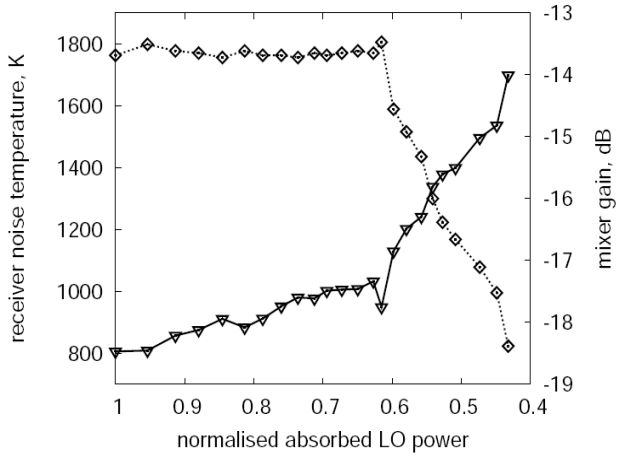


Fig. 4: Receiver noise temperature (triangles) and mixer gain (diamonds) vs. LO power normalised to the LO power level at the low-noise operating point.

In order to determine the stability of our receiver we fixed the bias voltage of the HEB mixer, set its current by adjusting the level of the LO power and then measured the operating current and IF output vs. time. As can be seen from fig. 2, both the mixer current and IF power fluctuate quite strongly and demonstrate very strong correlation as well. To check the latter we explored the dependence of the current and power on the level of LO drive near the low noise operating point. Fig. 3 shows that the dependence is almost linear, which suggests that the IF power is a linear function of the mixer current near the operating point. The last statement should not, of course, be taken at its face value since it is the LO drive, not the current that is the determining factor. However, if somehow it were possible to keep the operating point of the receiver fixed it might be possible to stabilise the IF power as well. This is the main idea behind our microwave feedback control loop.

Before implementing the microwave feedback scheme we needed to know the possible effect that microwave radiation might have on the performance of the HEB receiver in terms of its noise temperature and gain.

Once the low noise operating point was found, we reduced the LO drive level to increase the mixer current. The current was then restored to its original optimal value by injecting the appropriate amount of microwave radiation at 17 GHz. We then made a series of similar measurements, compensating for the decreasing LO power by increasing the

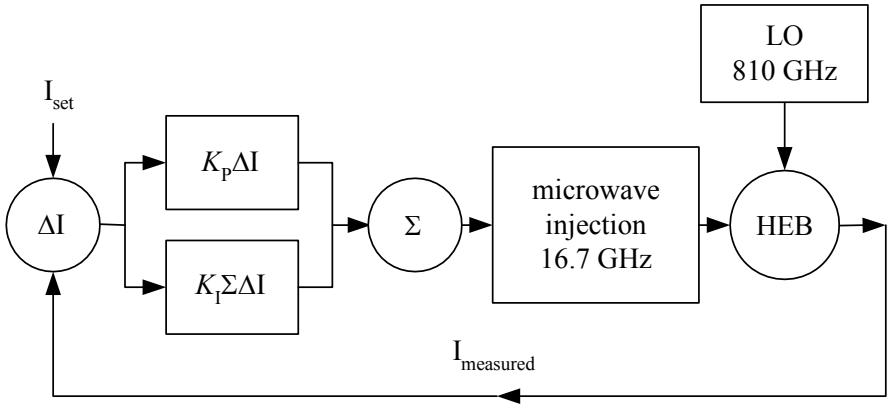


Fig. 5: Schematic of the feedback control loop

microwave injection at each step. In this way we derived the noise temperature and conversion gain as a function of terahertz LO drive normalised to the optimal LO drive level. The mixer bias voltage remained fixed in all measurements.

Fig. 4 summarises the results of our measurements. One can conclude that so long as the relative change of the LO power level is less than 10 % there is no significant degradation of the HEB receiver performance – the noise temperature and gain are practically unaffected by microwave radiation.

Our feedback loop (fig. 5) comprises proportional and integral terms: the mixer current is measured and compared to the preset value and the microwave power is then readjusted according to the formula:

$$P_{\mu wave}(t) = P_0 - K_P \cdot \Delta I(t - t_{sampl}) - K_I \cdot \sum_{t'=t_{sampl}}^{t'=t} \Delta I(t' - t_{sampl}), \quad (6)$$

$$\Delta I(t - t_{sampl}) = I_{meas}(t - t_{sampl}) - I_{set}, \quad (7)$$

where $P_0$ is the initial level of the microwave power at the synthesiser output, typically -10 dBm; $K_P$ is the proportional term coefficient, typically -0.1-0 dB/μA; $K_I$ is the integral term coefficient, typically -0.1 dB/μA; $I_{meas}(t)$ is the mixer current, $I_{set}$ is the preset value of the mixer current, $t_{sampl} \approx 30$ ms, the sampling interval.

Fig. 6 shows the mixer current and IF output vs. time with the feedback control loop turned on. Comparing fig. 2 (no feedback) and fig. 6, we see a marked improvement of both current and IF power stability. The calculated standard deviation of the IF power over a period of 16 minutes is 4 times as low as that for the open loop system. Fig. 7 presents the results of the Allan variance measurements. As is seen from the figure, in the case of the open loop system, the Allan time is about 1 second. Turning the feedback on suppresses the drift of the IF power and increases the Allan time up to 10 seconds. However, it can also be seen that the contribution from the IF chain becomes significant for integration times greater than a few seconds. This shows that the stability of our IF chain needs further improvement to allow full assessment of the potential of the microwave feedback loop.

## 4. CONCLUSIONS

We have developed and tested a microwave feedback control loop for stabilising the HEB receiver output. Our measurements show a four-fold improvement in the receiver stability when a feedback loop is operating. Additional experiments are underway to eliminate the contribution of the IF chain to the receiver instability. It has also been shown that the use of the microwave feedback loop does not cause any significant degradation of the HEB receiver performance.

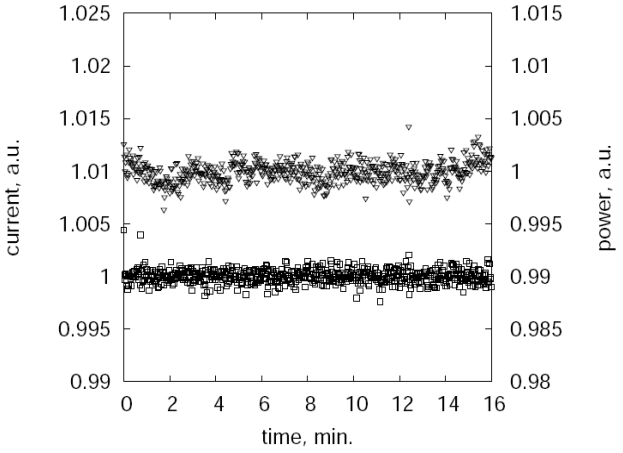


Fig. 6: Mixer current (squares) and IF power (triangles) vs. time with the feedback control turned on.

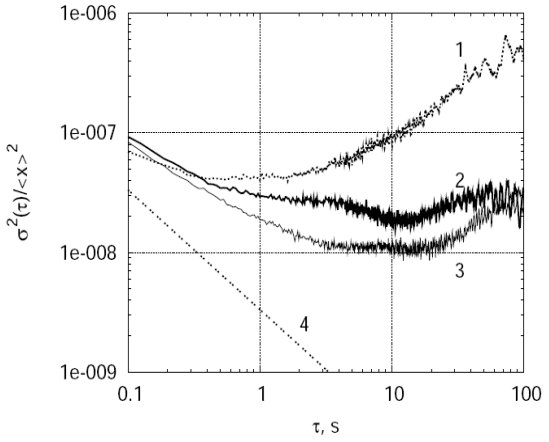


Fig. 7: Normalised system Allan variance: 1 – feedback turned off; 2 – feedback turned on; 3 – If chain; 4 – radiometer equation.

**REFERENCES**

[1] D.W. Allan, "Statistics of Atomic Frequency Standards," *Proc. IEEE* 54, 221 (1966).
[2] K. Rohlfs, T. L. Wilson. "Tools of Radio Astronomy", *Springer*, 3rd edition, 2000.
[3] R. Schieder, C. Kramer, "Optimization of Heterodyne Observation Using Allan Variance Measurements," *A&A* 373, 746-756, 2001.
[4] J.W. Kooi, J.J.A. Baselmans, A. Baryshev, R. Schieder, M. Hagenius, J.R. Gao, T.M. Klapwijk, B. Voronov and G. Gol'tsman, "Stability of Heterodyne Receivers," http://www.submm.caltech.edu/cso/receivers/papers/finalavjwk.pdf.
[5] A.D. Semenov, G.N. Gol'tsman and R. Sobolewski, "Hot-electron effect in superconductors and its applications for radiation sensors," *Supercond. Sci. Technol.* **15** R1-R16, 2002.
[6] Crowe, T.W.; Mattauch, R.J.; Roser, H.P.; Bishop, W.L.; Peatman, W.C.B.; Liu, X. "GaAs Schottky diodes for THz mixing applications", *Proc. IEEE*, vol. 80, no. 11, p. 1827-1841, 1992.
[7] J. W. Kooi, G. Chattopadhyay, M. Thielman, T. G. Philips and R. Schieder, "Noise Stability of SIS Receivers", http://www.submm.caltech.edu/papers/pdf/2000-03-irmm-sis_noise.pdf
[8] D. Meledin, C.-Y. E. Tong, R. Blundell, N. Kaurova, K. Smirnov, B. Voronov and G. Gol'tsman, "The Sensitivity and IF Bandwidth of Waveguide NbN Hot Electron Bolometer Mixers on MgO Buffer Layers over Crystalline Quartz," *Proc. of the 13th International Symposium on Space Terahertz Technology*, Cambridge, MA (USA), 2002.

# A High Performance Horn for Large Format Focal Plane Arrays

**G. Yassin[*], P. Kittara[+], A. Jiralucksanawong[+], S. Wangsuya[+], J. Leech[*] and Mike Jones[*]**

***We describe the design and performance of an easy to machine horn which exhibits excellent beam circularity and low cross polarisation over a relatively large bandwidth. No grooves are machined into the horn walls but, alternatively, flare angle discontinuities are generated along the horn profile. In other words, the horns will have several flare angles or sections instead of one. For example, if the horn consists of two flare angles, it could then be considered as a conventional Potter horn. As can be seen below, even with this simple design, excellent radiation patterns can be obtained over 15% bandwidth. The bandwidth could be further increased by adding more subsections with 30% bandwidth obtained when the profile is based on 4 sections. The operation of the horn is based on generating higher order modes at the correct amplitude ratio and phase with respect to the incident $TE_{11}$ mode in the circular waveguide, which is achieved by accurate determination of the magnitude and location of the flare steps. This in turn yields a field distribution at the horn aperture that has low sidelobes and cross polarization in the radiation pattern.***

***A key component in the design package is the optimization software that searches for the correct magnitude and location of the flare discontinuities. We have generated a software package based on the combination of modal matching, genetic algorithm (GA) and simplex optimization. The genetic code is first used to locate the proximity of the global minimum. The set of parameters obtained are then used as a starting point for the simplex method, which refines the parameters to the required accuracy. We shall illustrate our method by showing radiation patterns using two and three step discontinuities and also patterns for a spline profiled horn based on work by other investigators who used different optimization techniques.***

## 1. Introduction

High performance feeds are extensively used at millimetre and submillimetre wavelengths, in particular in astronomical instruments. Examples include the HARP array receiver on the James Clark Maxwell Telescope, the Atacama Large Millimetre Array (ALMA) and the newly emerging cosmic microwave background polarization experiments (CLOVER, EBEX and QUIET) [1], [2], [3]. All of these instrument projects intend to employ corrugated horns that offer excellent performance over a relatively large bandwidth. It is, however, evident that corrugated horns are time-consuming and expensive to fabricate, in particular when a large focal-plane array consisting of several hundred feeds is needed at submillimetre wavelengths. In this paper, we present the design of multi flare angled horns which are much easier to fabricate than corrugated horns. This type of horn provides an excellent option for many applications such as THz mixers and local

[*] Department of Physics, Oxford University, Denys Wilkinson Building, Keble Road , Oxford, OX1 3RH, UK.
[+] Department of Physics, Mahidol University, 272 Rama VI Road Bangkok 10400, Thailand.

oscillators, general purpose submillimetre telescope feeds and specialized CMB polarization experiments.

The principle of the new horn design may be considered as a generalisation of the Potter horn idea [4]. Conventionally, a Potter horn consisted of a conical horn with a single groove-step discontinuity at the horn throat whose dimensions were chosen in order to excite the $TM_{11}$ mode at a carefully selected amplitude (~16%) with respect to the amplitude of the incident $TE_{11}$ mode. This "dual-mode" was then made to propagate through a cylindrical "phasing section" to make the two modes arrive at the horn aperture in phase. The remarkable similarity in the sidelobe structure of the $TE_{11}$ and $TM_{11}$ modes resulted in sidelobe cancellations and a lowering of the cross polarization in the horn radiation pattern.

A simplified version of the conventional Potter horn was proposed by Pickett *et al*. [5]. The phasing section of the Potter horn is removed, resulting in a more compact and easier to machine horn. The phasing of the modes is now achieved during propagation through the flared horn section. In other words, the simplification is achieved by sacrificing one degree of freedom in choosing the horn dimensions.

An alternative method of exciting the $TM_{11}$ mode is a sudden change in the horn flare angle as shown in Fig. 1. Here a second section is formed by changing the flare angle when the horn radius is $r_1$, at an axial distance $L_1$ from the start of the horn.

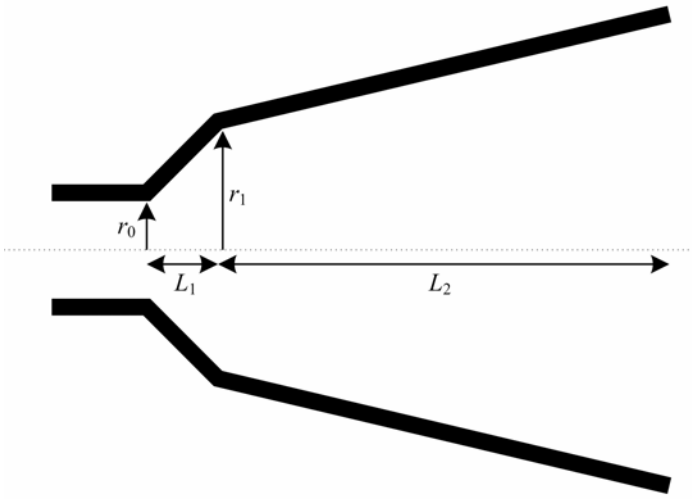


**Figure 1:** Geometry of the Potter horn with a flare angle discontinuity. $r_0$ is the radius of the circular waveguide. $r_1$ and $L_1$ are the radius and the length of the first conical section. $r_2$ and $L_2$ are the radius and length of the second conical section, respectively.

Although this method was reported previously [6], it was not thoroughly investigated or commonly used in conjunction with conical horns. Our simulations show that the pattern obtained with a flare-step potter horn is in fact superior to the pattern of a groove-step horn. The choice between the two types of horn could also depend on the method of fabrication. The availability of programmable lathes for precision machining makes the fabrication of the first type fairly straightforward, in particular if electroforming is used. If, on the other hand, the horn is machined from a split-block of metal then turning a single groove at the throat with a reasonably large flare angle is straightforward.

The conventional analysis of either type of Potter horn, which relied on an analytical method, assumed that only the $TE_{11}$ and $TM_{11}$ propagate to the horn aperture. This assumption, however, is not realistic, since higher order modes that are evanescent at the throat can later become oscillatory and carry energy to the aperture. Thus the analysis described in the original Potter horn papers cannot accurately predict the horn radiation patterns. Higher order modes can, however, be easily accounted for if the modal matching method [7, 8] is used to propagate the electromagnetic fields components numerically from the waveguide to the aperture. This method yields precise and fast converging solutions for the analysis of lossless horns with rectangular or cylindrical geometry.

Similarly, predicting the horn dimensions that yield optimum performance is not straightforward. Consequently, an optimization (minimization) technique is required to calculate the optimum horn parameters, for a required horn performance. In this paper, we shall describe a new technique of reliable and efficient minimization based on a genetic algorithm (GA) [9] combined with a downhill simplex technique. First the approximate position of the global minimum is found using the GA and then this is used as a starting point for the iterative simplex procedure which accurately locates the position of the minimum. The analysis is clearly not restricted to Potter horns but can be used to generate designs with a larger number of horn sections. Since our aim is to design easy to machine horns, we will mainly deal with flare rather the groove discontinuities.

## 2. Method of computation

### 2.1 The general scheme

The design method of the multi-flared angle horn is done by using a combination of analysis and synthesis packages. The analysis package is a modal matching routine that computes the radiation pattern and the electrical properties of a given horn geometry (e.g. cross-polarisation) and the synthesis package which consists of an optimisation routine that searches for a new improved horn design. We have written modal matching and genetic algorithm minimisation software and combined these into a single horn design package (***hornsynth***) with a graphical user interface.

Finding the optimum horn geometry that satisfies a pre-determined specification is done using a genetic algorithm (GA), which is a powerful computational method for solving optimization problems [10]. It employs a "natural selection" process which is similar to biological evolution. One usually begins by choosing a random set of parameters which form the *chromosomes.* A set of chromosomes is called a *population*. The *cost function* of the problem is then used to compute values corresponding to each chromosome (for example, the chromosome could be an array of the parameter set we want to optimise). Only half of the population, forming a subset $\{S_n\}$, comprising the *fittest* members (e.g. the ones that return the lowest values in the case of minimisation) is left to take part in forming the next generation while the "*weak*" members are discarded. The elected members of $\{S_n\}$ are then *paired* and allowed to produce *offspring* that form a new generation. The algorithm is motivated by the expectation that the new generation will be fitter than the old one and so this evolutionary process will eventually yield a solution consisting of the fittest population.

An important feature of the GA is that it avoids convergence to a local extremum by exploring the search space. However, searching for the final solution is very time consuming hence the GA is only used to find the global optimum. This output is then fed to a downhill simplex which is an efficient search iterative minimization algorithm for problems that do not have a very large number of variables.

### 2.2 Optimisation Criteria

The quality of the radiation pattern of a horn is normally characterised by several parameters, depending on the application. An antenna feed, for example, is expected to have good beam circularity (beamwidth independent on polarization), low cross polarization and sidelobes, good return loss and high beam efficiency, over a given bandwidth. Some of these properties are generally related. For example, good beam circularity is associated with low cross polarization level and high beam efficiency corresponds to low sidelobe level. However, considering that we are dealing with trade-offs between the quality of these parameters, we found it necessary to optimize several of them at the same time. Since the return loss of a smooth-walled horn is normally good we did not include it in the optimization parameters. Also, the beam efficiency was excluded since it requires a large number of time consuming integrations. We would like to emphasise, however, that different criteria can easily be incorporated into our software.

Based on the above discussion, we have chosen to optimize for beam circularity and cross polarization. The problem constraints included specifying the frequency band edges and the central frequency, in addition to geometry parameters, namely the waveguide radii at the flare steps and the value of the flare angles. These parameters were incorporated in the software using a quality function $\delta_f$ $(P)$ and a weighting function $W_f(P)$ for a given frequency $f$ where $P$ is the power level in the radiation pattern. The quality function was defined as

$$\delta_f^2 = (w_X)^2 \left[ \sum_{P=-1}^{P=-30} \left( \frac{\sigma_P}{\sigma_P^{av}} \right)^2 w_P \right]$$

where

$P$ = power level in dB,
$w_P$ = the absolute power, $\left(P = 10\log_{10} w_P\right)$,
$X$ = peak power of the cross polar in dB,
$w_X$ = absolute peak power in the cross polar, $\left(X = 10\log_{10} w_x\right)$,
$\sigma_P^E$ = width of the E-plane at the $P$ dB power level,
$\sigma_P^H$ = width of the H-plane at the $P$ dB power level,
$\sigma_P$ = the difference between the widths at $P$ dB, $\sigma_P = \left|\sigma_P^E - \sigma_P^H\right|$,
$\sigma_P^{av}$ = the average width, $\sigma_P^{av} = \left(\frac{\sigma_P^E + \sigma_P^H}{2}\right)$.

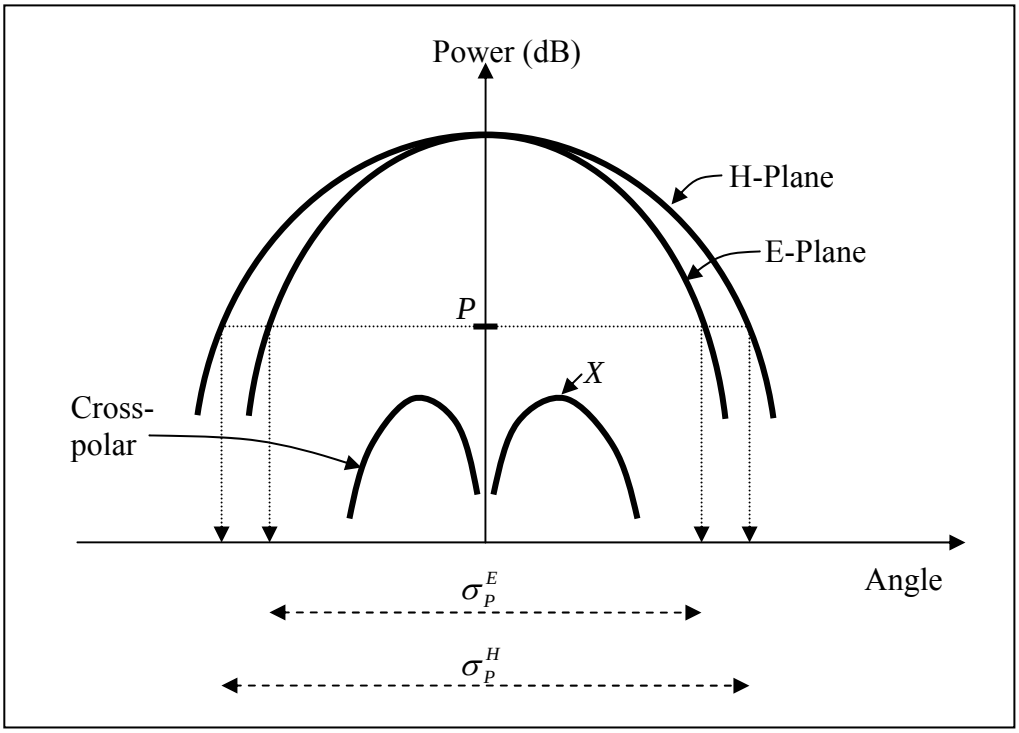


**Figure 2:** A sketch of radiation patterns and variables used in the quality function. When the cross-polarization is small and the beam is circular $\left(\sigma_P^E = \sigma_P^H\right)$, the quality function becomes small.

## 3. Computed radiation patterns

We start by simulating the radiation pattern of a dual flare angle (two section) horn that was designed using *hornsynth* optimisation. The centre frequency was chosen at 700 GHz and the parameters of the horn are given in Table 1. These parameters were then fed to the commercial software *corrug* in order to confirm the integrity of our design procedure. The beam patterns are shown in Fig. 3 – they exhibit excellent beam circularity and low cross polarisation levels over a bandwidth of 80 GHz. In fact the cross polarization level was approximately -30 dB across this bandwidth, reflecting our stringent criteria regarding cross polarization.

| | |
|---|---|
| Initial waveguide radius, $r_0$ | 0.1752 mm |
| Length of the 1st conical section, $L_1$ | 0.7163 mm |
| Radius of the 1st conical section, $r_1$ | 0.6145 mm |
| Length of the 2nd conical section, $L_2$ | 11.256 mm |
| Aperture | 1.500 mm |

**Table 1:** The geometry of the two-angle horn with an aperture of 3.5 wavelengths. The dimensions are scaled to the centre frequency 700 GHz. See Fig. 1 for the description of each dimension. The beamwidth of this horn is 12.4 degrees

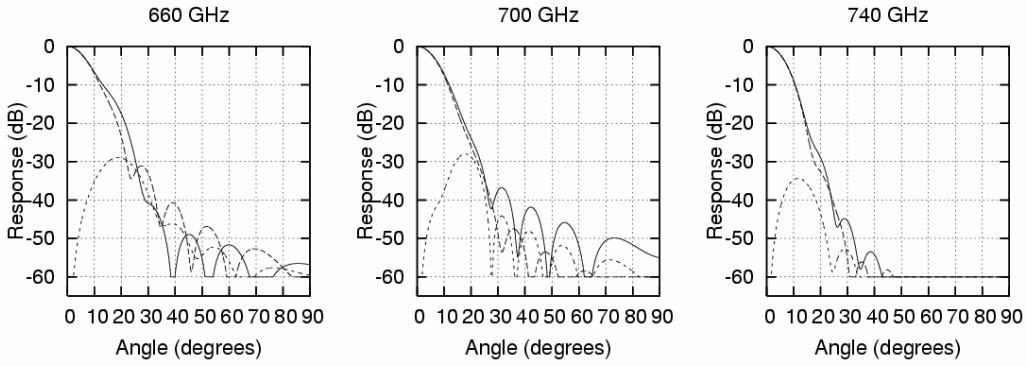


**Figure 3**: E-plane (solid line), H-plane (long dashes) and cross polar (short dashes) levels for the Potter horn consisting of two conical sections with a discontinuity in flare angle.

It is interesting to note that the radiation pattern obtained by a flare-step dual mode horn are significantly better than those obtained by the conventional groove-step Potter horn. This is because the ratio of the amplitudes $TM_{11}/TE_{11}$ at the discontinuity varies much more slowly with frequency in the first case. Also it seems that the amplitude of the inevitably excited higher order modes, in particular the $TE_{12,}$ is higher for the groove-step excitation.

The extension of the above ideas to a broadband design is clearly a multi-section horn, and perhaps to smooth the discontinuities into a profiled continuous curve if necessary. To this end we used hornsynth to generate a three-sectioned horn with the dimensions given in Table 2 and example radiation pattern given in Fig. 4.

*Results*

| | | | | |
|---|---|---|---|---|
| Waveguide (mm) | 0.200 | | | |
| | Begin R | Length | End R | Section |
| Section 1 (mm) | 2.00000E-1 | 4.85800E-1 | 4.88400E-1 | 49 |
| Section 2 (mm) | 4.88400E-1 | 3.98310E-1 | 5.95277E-1 | 30 |
| Section 3 (mm) | 5.95277E-1 | 7.88560E+0 | 1.200 | 110 |
| Error Fuction | 3.99830E-5 | 3.99830E-5 | | |

**Table 2**: Typical output of *hornsynth* showing the geometry of a three-section horn. The computed patterns are shown in Fig. 4.

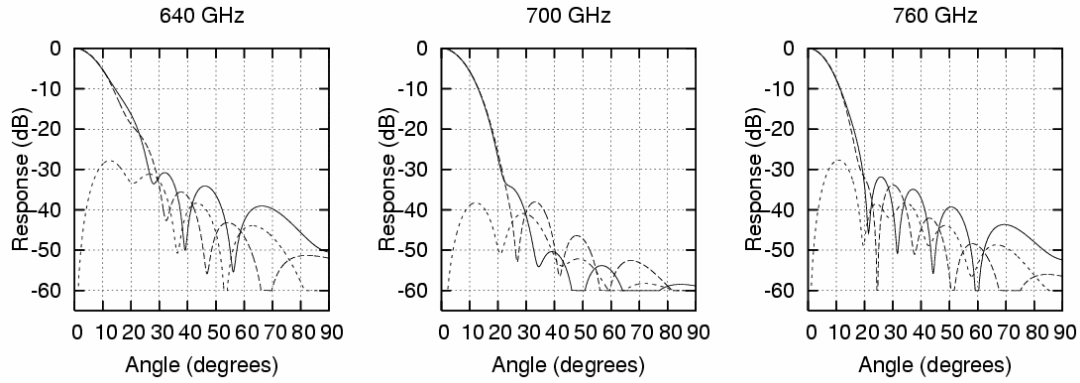


**Figure 4:** Radiation pattern for the three sections smooth-walled 700 GHz horn at 640 GHz (left), 700 GHz (middle) and 760 GHz (right).

Notice that excellent quality patterns with cross polarizations of below -30 dB are obtained over a bandwidth of 120 GHz. In fact, a cross polarization level below -25 dB was maintained across a bandwidth of 170 GHz which is remarkably broad, considering that only a three-section horn is used. Clearly, the bandwidth can be further increased by increasing the number of horn sections and we are expecting the bandwidth to exceed 30% for a 4-section horn.

From Fig. 4, it can also be seen that our patterns are diffraction limited with a beamwidth that is dependent on frequency. This feature may or may not be desirable depending on the application. For example, a telescope feed is usually designed to have high beam efficiency which is indeed given by our patterns. If on the other hand, a broad-band horn is required then this can also be obtained by imposing a higher flare angle to the second section. A broad band horn must have a phase error $\Delta > 0.4$ where

$$\Delta = \frac{r}{\lambda} \tan \frac{\vartheta_0}{2}$$

Where $r$ and $\vartheta_0$ are respectively the horn section radius and semiflare angle. In our case, the third section phase error is $\Delta \sim 0.1$ which yields a diffraction limited horn.

Finally it is instructive to compare our pattern with those obtained by Granet et al. [11], who generated a wide-band high performance horn by optimizing a spline-horn profile (Fig. 5).

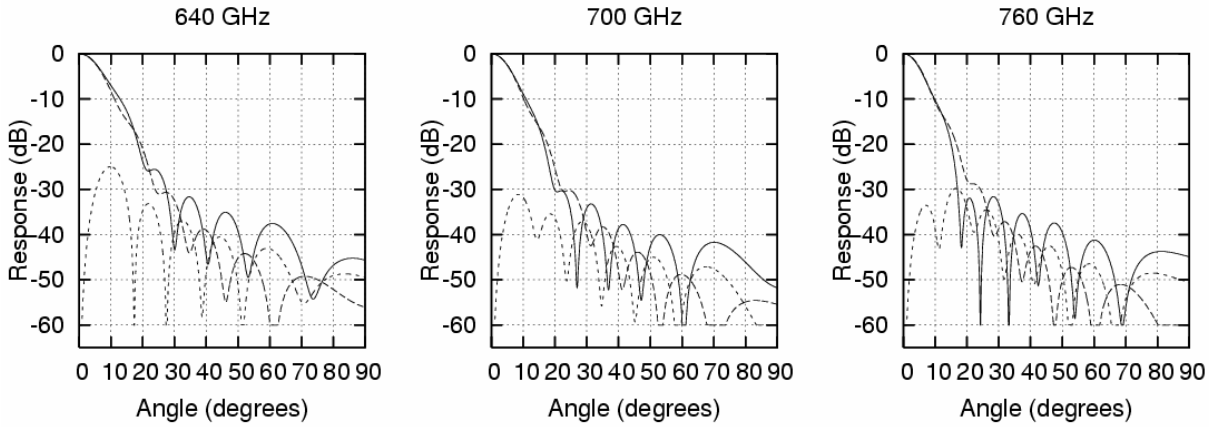


**Figure 5:** Radiation patterns of a 700 GHz spline horn computed using the method in [11].

The quality of the radiation pattern is similar in both cases with spline patterns being much less dependent on frequency and the three-sections pattern having better beam efficiency. The

differences between the horns can clearly be seen by comparing their profiles given in Fig. 6. We would like to emphasize that the spline horn used 6-optimization radii while we only used three.

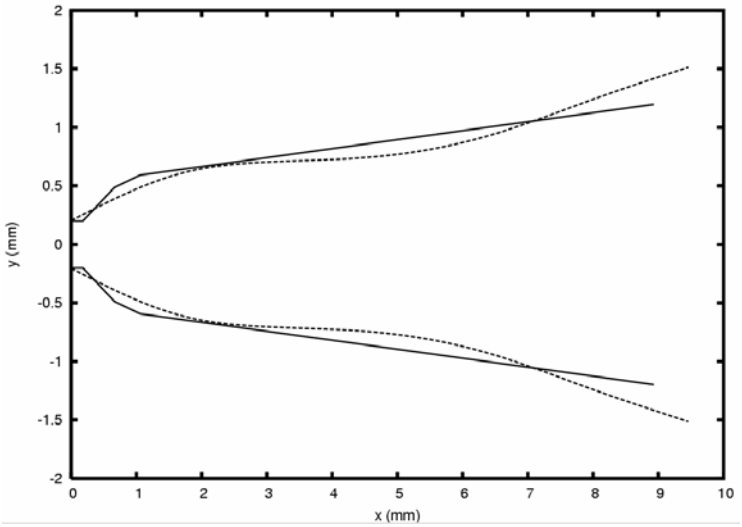


**Figure 6**: A comparison of the horn profiles for our 3-section horn and the horn reported in [11].

Finally, we present the computed return loss as a function of frequency for the three section horn (Fig. 7). As can be seen, the return loss is excellent (below -32 dB) across the operating bandwidth. The return loss shows less frequency dependence compared to a corrugated horn, since the return loss of a corrugated horn is determined by a $\sim \lambda/2$ deep groove at the horn throat.

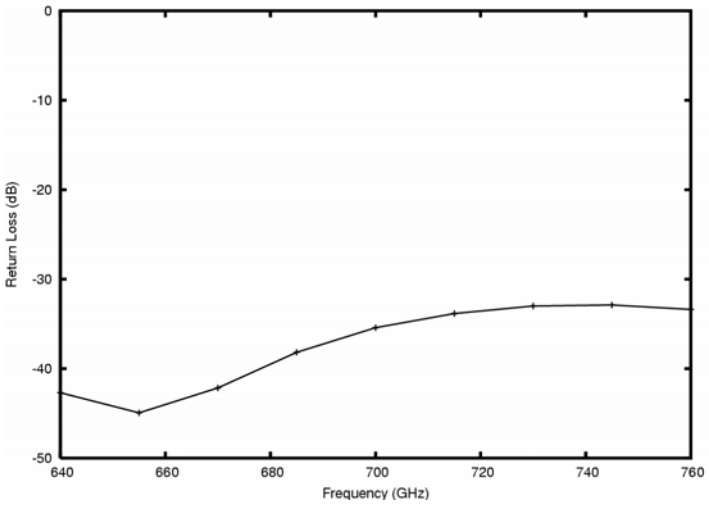


**Figure 7**: The computed return loss for the 3-section horn across the 640 to 760 GHz band.

## 4. Method of fabrication

Fabrication of smooth-walled horns is clearly easier than machining corrugated feeds. This becomes crucial at very high frequencies or one large arrays are required. For example, the focal plane arrays for millimetre or submillimetre wavelengths are now formed from horns that are fabricated individually. They are then mounted on metallic blocks that contain hundreds of detector channels. We are now proposing however to fabricate the whole array by drilling the horns into a block of aluminum using drill-bit tools that have the shape of the horn profile. Drilling the horns can be done using a standard mill and a high-speed steel tool. We have already fabricated a two-section 230 GHz Potter horn to test the precision of the method. Using the steel tool shown in Fig. 8, we drilled three horns using a mill into an aluminum block and then spit one of them into two halves in order to check the repeatability of the method and the accuracy of the surface finish.


**Figure 8**: The tool used for machining the two-section, 230 GHz horn.

Our measurements have shown that the surface finish and the accuracy near the flare discontinuities is sufficiently good to reproduce the theoretical predictions. Also, comparing the three horns that were fabricated using the same tool, did not reveal significant differences in the dimensions, although our measurements were accurate to within a micron.

## 5. Conclusion

We have presented a multi-section high performance horn design that has high beam circularity, low cross polarization and low sidelobe level. Each section is a smooth-walled conical horn with constant flare and no corrugations. The bandwidth of the horn depends on the number of sections

but 25% useful bandwidth can be obtained at 700 GHz using only three sections. Synthesis of the horn geometry is done using the software package *hornsynth* which we have written for this purpose which combines a minimization package using a genetic algorithm and a horn analysis package using the modal matching method. Fabrication of this horn at millimetre wavelengths can be obtained by drilling using a tool that has the shape of the horn into a block of aluminum. Our first attempt using a steel tool which cost £75 has demonstrated that several horns can be fabricated with identical dimensions and sufficiently good machining tolerances. Increasing the bandwidth requires more sectioning which in turn requires more computing time but the same fabrication effort. At lower frequencies, our method can still be used but it may be easier to use machining by a programmable lathe rather than drilling by a mill. Testing the RF performance of the horn is in progress.

## 6. References

1- Yassin, G. *et al* "CLOVER- Anovel instrument for measuring the CMB B-mode polarization, "*Proc. 15th Int Symp. On Space THz Tech.*., 2004.

2- Oxley, *et al*, "The EBEX experiment," *Proceedings of the SPIE* 5543, pp. 320-331, 2004.

3- Winstein, B., "QUIET: Goals and status," Proceedings of the 2nd Irvin cosmology conference, Bechman Centre, University of California, Irvin, CA, 2006.

4- Potter P., "A new horn antenna with suppressed sidelobes and equal beamwidth" *Microwave J.,* vol. 6, pp. 71-78, June 1963.

5- Pickett H., Hardy J. & Farhoomand J., 1984. Characterisation of a dual mode horn for submillimetre wavelengths. *IEEE Trans. Microwave Theory Tech*., MTT32(8), 936--937.

6- Cohn, S. B. "Flare angle changes in a horn as a mean of pattern control" *Microwave J.* pp. 41-46, Oct, 1970.

7- Kittara, P. "The development of a 700 GHz SIS mixer with Nb finline devices: nonlinear mixer theory, design techniques and experimental investigation " PhD Thesis University of Cambridge, 2002.

8- Olver A., Clarricoats P., Kishk A. & Shafai A. *Microwave horns and feeds.* IEEE press NY 1994.

9- Yang D. and Chung Y.C., (2002) "Genetic optimization of a corrugated conical horn antenna," *IEEE Trans. Antenna Propagat.*, pp. 342-344.

10- Randy, L. Haupt R.L. and Haupt S.E. (1998). *Practical Genetic Algorithms.* Willey & Sons, NY 1998.

11- Granet C., James G.L., Bolton R. and Moorey G., (2004) "A smooth-walled spline-profile horn as an alternative to the corrugated horn for wide band millimeter-wave applications," *IEEE Trans. Antenna Propagat.*, 52(3), pp. 848-85

# Measurement of a high-gain antenna at 650 GHz in a hologram-based CATR

A.V. Räisänen, J. Ala-Laurinaho, J. Häkli, A. Karttunen, T. Koskinen, A. Lönnqvist, J. Mallat, E. Noponen, A. Tamminen, M. Vaaja, and V. Viikari.
TKK Helsinki University of Technology, SMARAD/Radio Laboratory and MilliLab
P.O. Box 3000, FI-02015 TKK, Finland

## Abstract

A hologram-based compact antenna test range (CATR) at 650 GHz was designed, constructed, and used for testing the ADMIRALS RTO antenna of 1.5 m in diameter. The CATR is based on a 3.16-meter computer-generated amplitude hologram. Ordinary floor carpets with good absorbing and scattering properties were used as absorbers in the measurement room.

## Introduction

Functional prior-launch end-to-end tests of sub-millimeter wave antennas are vital for reliable satellite missions. However, testing of the electrically large reflector antennas is an extremely challenging task. The required far-field distance becomes easily very large at sub-millimeter wavelenghts. For example, the typical requirement $2D^2/\lambda$ gives about 9.8 km far-field distance for a 1.5 m antenna at 650 GHz. Therefore, far-field measurements are in practice impossible because of the atmospheric effects. Near-field measurements are technically very complicated and expensive requiring a high-accuracy scanner and a very stable RF-measurement system. Conventional compact antenna test range (CATR) measurements, although performed up to 500 GHz [1], are problematic due to high surface accuracy requirement of the reflectors; typical requirement is the surface accuracy better than $0.01\lambda$, corresponding to 4.6 μm at 650 GHz. In the hologram CATR, the needed plane wave is created with the use of a computer-generated binarized amplitude hologram [2]. The hologram pattern can be determined numerically by calculating the structure required to change the known input field (radiation pattern of the feed) into the desired output field (plane wave) [3]. The pattern is realized on a metal layer that is on top of a dielectric substrate. As a transmission type of element, the hologram planarity requirements are less stringent than those of a reflector. Thus, hologram CATR has a great potential in sub-millimeter wave antenna measurements [4,5,6,7].

## Design and construction of a hologram-based CATR for 650 GHz

We designed a hologram CATR, Figs. 1 and 2, aiming at 650-GHz tests of the Planck RFQM 1.5-m antenna. However, as the Planck RFQM was not available, we ended up using an alternative test object with the same antenna size, namely the ADMIRALS RTO from EADS Astrium. The hologram was made of three pieces, which were joined by soldering to form the final 3.16 m hologram. A proper illumination of the hologram was facilitated using a dual reflector feed system (DRFS) [8]. For quiet-zone testing, a plane-polar type scanner was designed with a linear stage allowing linear scans of about 2.5 m in four orientations: horizontal, vertical, and two diagonals. The measured peak-to-peak

planarity error of the scanner was about 0.3 mm. The scanner planarity was measured using a laser tracker twice during the measurement campaign and the measured quiet-zone phase was corrected accordingly. The antenna positioner was the same that was used during the previous RTO antenna measurements campaign at 322 GHz in 2003 [5,6].

The electrical instrumentation of the hologram CATR at 650 GHz was based on the AB Millimetre MVNA mm-wave network analyzer, and the transmitter and receiver procured from Virginia Diodes Inc. The measured dynamic range was about 27 dB in the quiet-zone field measurements. The measured dynamic range in the RTO antenna tests was about 74 dB with the same integration time as in the quiet-zone tests. A large amount of carpets, ca. 500 square meters, were used as radar absorbing material in the test site to prevent disturbing reflections. The measured reflectivity level was about –50 dB for the selected carpet material, Fig. 3 (please refer to [9,10] for the measurement method).

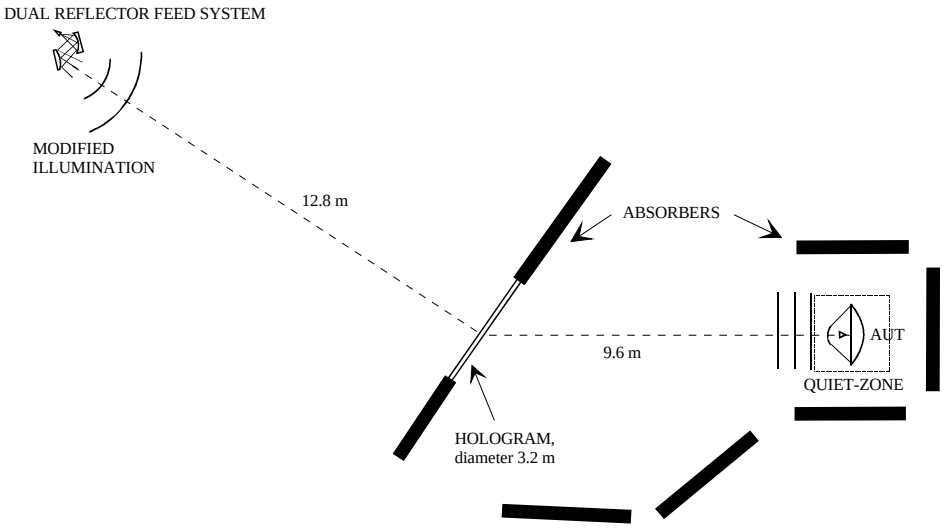


**Figure 1** – Layout of the hologram CATR. The dual reflector feed system is enlarged for clarity.

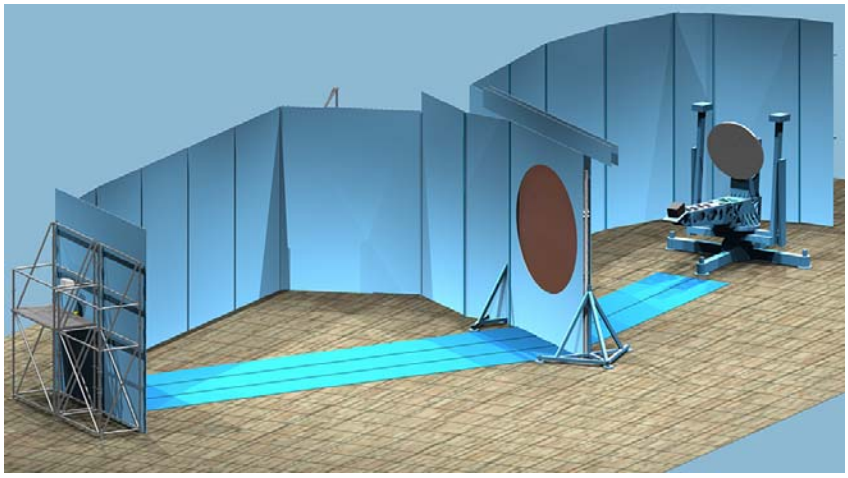

**Figure 2** – Artistic view of the 650 GHz hologram-based compact antenna test range.

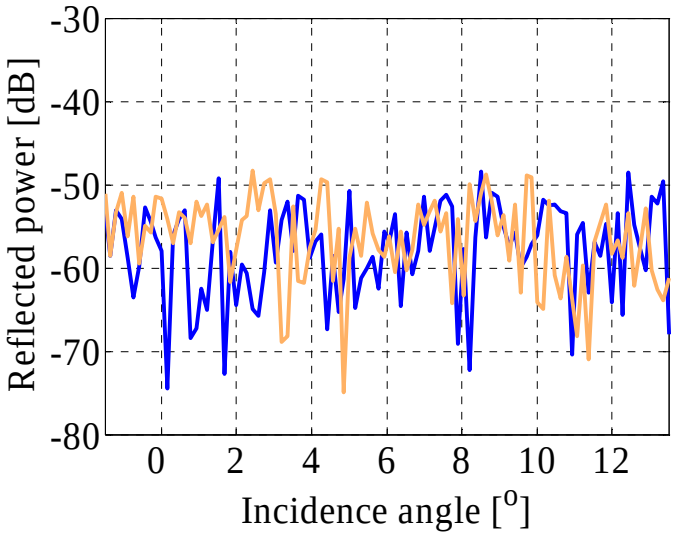


**Figure 3** – Measured radar reflectivity of a synthetic carpet at 650 GHz.

**Results**

The measured peak-to-peak amplitude deviations in the quiet-zone field were about 3 dB at each scanner orientation. The quiet-zone area in the vertical cut corresponding to the upper seam of the hologram had a slightly larger deviation. The typical measured amplitude ripple in the 2-meter diameter quiet-zone was of the order of 1.5–2 dB peak-to-peak. The peak-to-peak phase deviation was about 270 degrees in the whole quiet-zone area. The measured cross-polar level in the quiet-zone was below –20 dB compared to the co-polar level in the quiet-zone area. After evaluation of the quiet-zone field, its quality was concluded to be sufficient for antenna tests.

The ADMIRALS RTO test antenna was tested in the quiet zone described above. The horizontal (*H*-plane) pattern cut was measured in the angular range of –85°…+85° and the vertical (*E*-plane) cut in the range of –12.5°…+12.5°. Some results are shown in Fig. 4. The pattern cuts do not reveal any far-side lobes above the noise floor. The antenna pattern of the ADMIRALS RTO was simulated with GRASP software. The simulation model consisted of a physically measured reflector surface shape and an electrically measured feed pattern. The simulated antenna pattern corresponds well to the measured pattern. The range reflections were studied with the feed scanning APC [11] and spurious side lobes due to reflections were observed at around –6.3°, –3.7°, +3.9°, and +6.6° in the horizontal direction. The effect of the quiet-zone field on the measured antenna pattern was estimated with simulations. It was found that the realized quiet-zone field may cause 2 – 4 dB errors to the measured main beam.

**Conclusions**

A CATR based on a computer-generated hologram operating at 650 GHz designed, constructed, and used for testing a 1.5 m diameter reflector antenna. Ordinary floor carpets

with good absorbing and scattering properties were used as absorbers in the measurement room. The quiet-zone field was measured and optimized – the typical measured amplitude ripple in the 2-meter diameter quiet-zone was of the order of 1.5–2 dB peak-to-peak. Both horizontal (*H*-plane) and vertical (*E*-plane) cuts of the antenna pattern were measured.

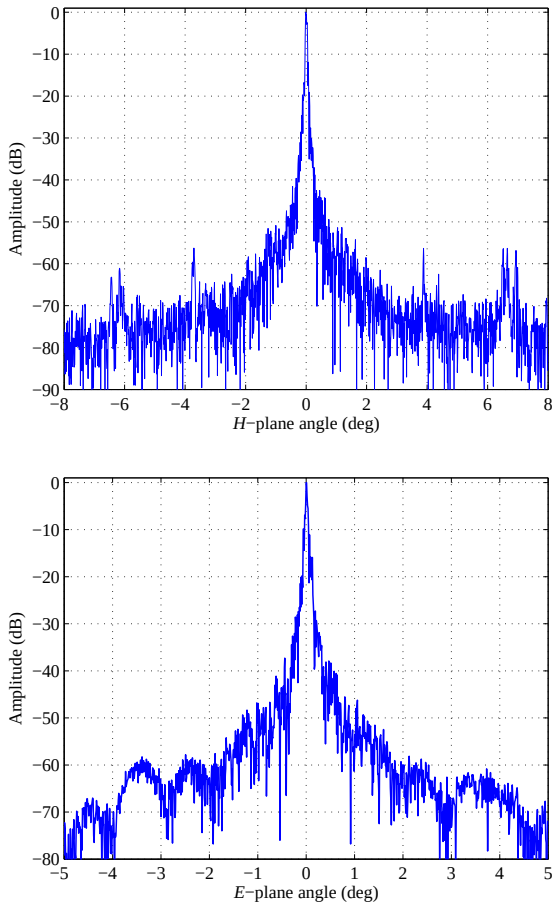


**Figure 4** – Measured antenna patterns at 650 GHz: horizontal pattern (upper), vertical pattern (lower).

## Acknowledgments

This work has been supported by the Academy of Finland and Tekes through the Centre-of-Excellence program, and by ESA through ESTEC Contract No. 19131/05/NL/LvH.

## References

1. J. Hartmann, J. Habersack, H.-J. Steiner, J. Lemanczyk, and P. de Maagt, “Calibration and verification measurements in compensated compact ranges up to 500 GHz,” in *Proc. of 23rd AMTA*, Denver, USA, Oct. 2001, pp. 377–382.
2. W.-H. Lee, “Computer-generated holograms: Techniques and applications,” pp. 121–231 in *Progress in Optics XVI*, E. Wolf (ed.), Elsevier, Amsterdam, 1978.

3. T. Hirvonen, J. Ala-Laurinaho, J. Tuovinen, A.V. Räisänen, "A compact antenna test range based on a hologram," *IEEE Trans. on Antennas and Propagation*, vol. 45, no. 8, pp. 1270-1276, 1997.
4. J. Ala-Laurinaho, T. Hirvonen, P. Piironen, A. Lehto, J. Tuovinen, A.V. Räisänen, U. Frisk, "Measurement of the Odin telescope at 119 GHz with a hologram type CATR," *IEEE Transactions on Antennas and Propagation*, vol. 49, no. 11, pp. 1264-1270, 2001.
5. A. Lönnqvist, T. Koskinen, J. Häkli, J. Säily, J. Ala-Laurinaho, J. Mallat, V. Viikari, J. Tuovinen, A. V. Räisänen, "Hologram-based compact range for submillimeter wave antenna testing," *IEEE Trans. on Antennas and Propagation*, vol. 53, no. 10, pp. 3151–3159, Oct. 2005.
6. J. Häkli, T. Koskinen, A. Lönnqvist, J. Säily, V. Viikari, J. Mallat, J. Ala-Laurinaho, J. Tuovinen, and A.V. Räisänen, "Testing of a 1.5 m reflector antenna at 322 GHz in a CATR based on a hologram," *IEEE Trans. on Antennas and Propagation*, vol. 53, no. 10, pp. 3142–3150, Oct. 2005.
7. T. Koskinen, A. Lönnqvist, J. Ala-Laurinaho, J. Säily, J. Häkli, J. Mallat, J. Tuovinen, A.V. Räisänen, "Experimental study on a hologram based compact antenna test range at 650 GHz," *IEEE Trans. on Microwave Theory Techniques*, vol. 53, no. 10, pp. 2999–3006, Sept. 2005.
8. J. Häkli, T. Koskinen, J. Ala-Laurinaho, and A.V. Räisänen, "Dual reflector feed system for hologram based compact antenna test range," *IEEE Trans. on Antennas and Propagation*, vol. 53, no. 10, pp. 3940–3948, Dec. 2005.
9. A. Lönnqvist, J. Mallat, A. V. Räisänen, "Phase hologram based compact RCS test range at 310 GHz for scale models," *IEEE Transactions on Microwave Theory and Techniques*, vol. 54, no. 6, part 1, pp. 2391- 2397, Jun. 2006.
10. A. Lönnqvist, A. Tamminen, J. Mallat, A. V. Räisänen, "Monostatic reflectivity measurement of radar absorbing materials at 310 GHz," *IEEE Transactions on Microwave Theory and Techniques*, vol. 54, no. 9, pp. 3486-3491, Sept. 2006.
11. V. Viikari, J. Häkli, J. Ala-Laurinaho, J. Mallat, A. V. Räisänen, "A feed scanning based APC technique for compact antenna test ranges," *IEEE Trans. on Antennas and Propagation*, vol. 53, no. 10, pp. 3160–3165, Oct. 2005.

# Near-Field beam measurements of corrugated horns for ALMA band 10

Y. Uzawa[1)], M. Sugimoto[1)], K .Kimura[2)], R. Nohara[2)], T. Manabe[2)], H. Ogawa[2)], Y. Fujii[1)], W.-L. Shan[3)], M. Kroug[1)], and S. Shitov[1)]

1) National Astronomical Observatory of Japan, 2-21-1 Osawa, Mitaka, Tokyo 181-8588, Japan
2) Osaka Prefecture University, 1-1 Gakuen-cho, Naka-ku, Sakai, Osaka 599-8531, Japan
3) Purple Mountain Observatory, 2 West Beijing Road, Nanjing,210008,China

For the receivers of the Atacama Large Millimeter and Submillimeter Array (ALMA), one of the requirements to achieve high sensitivity is to use good optics. Corrugated horns are widely used in the optics for highly sensitive receivers because of their good performance of high efficiency, low cross polarization, and so on. As well as those receivers, we consider to use a corrugated horn for the ALMA band 10 (787-950 GHz) receiver. To characterize the performance of fabricated horns experimentally, we developed a phase and amplitude antenna test system. The signal source consists of a W-band Gunn oscillator followed by a nonupler with an open waveguide probe on an X-Y-Z-θ translation stage. A corrugated horn is attached to a subharmonic Schottky diode mixer pumped by another W-band Gunn oscillator. Both Gunn oscillators are phase-locked to a single microwave reference at around 16 GHz, but on different sideband. The IF of 90 MHz is passed to a lock-in amplifier that measures phase and amplitude. Figure 1 shows preliminary results of the near field beam pattern (at 826 GHz) of a corrugated horn made by conventional electro-forming. The far-field beam pattern calculated from the phase and amplitude data showed good agreement with the theoretical one. The measurements at 860 and 896 GHz also showed symmetrical beam pattern as predicted. By using this system, we will test another corrugated horn made by direct machining suited for series production for the ALMA receivers.

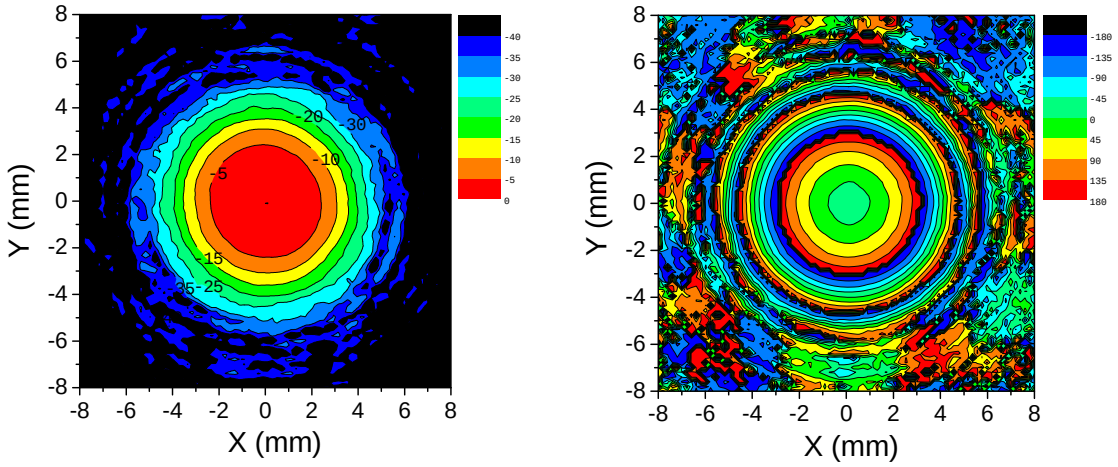


Fig. 1. Two dimensional amplitude (left) and phase (right) beam map of a corrugated horn. The amplitude contours are expressed in dB and the phase contours are shown in every 45 degree.

# Slot Antenna Array for CMB Polarization Detection

Goutam Chattopadhyay, Peter Day, Chao-Lin Kuo, James J. Bock, and Andrew E. Lange

Jet Propulsion Laboratory, California Institute of Technology
4800 Oak Grove Drive, Pasadena, CA 91109, USA.

## ABSTRACT

Cosmic Microwave Background (CMB) radiation contains the most valuable relic of the early universe. The details of the structure and evolution of the universe are believed to be encoded in the anisotropy of the CMB. It is believed that the direct evidence of the inflationary epoch – the rapid expansion of the universe after the Big Bang – lies in the traces of gravitational waves in the CMB, which manifests in the temperature anisotropy and polarization of the CMB. If inflationary gravitational waves do indeed exist, they will be the oldest relic of the universe, created 500,000 years before the CMB was emitted. The measurement of the CMB polarization – the B-mode polarization in particular – will be the indirect proof of the existence of the inflationary gravitational waves and will give insight into the epoch of inflation.

Cryogenic detectors currently in use for CMB instrumentation are sensitive enough to reach the photon noise limit which is governed by the photon arrival statistics and depends on the intensity of the background radiation. CMB space missions offer the opportunity to reach fundamental cosmic background limits, and therefore, further improvements in the detector sensitivity is not helpful. The only avenue available for improving the overall experimental sensitivity for a wide field survey is to increase the throughput, which simply corresponds to capturing more photons. The only way that will be possible is to increase the number of detectors. As a result, future CMB experiments are expected to require large focal planes with thousands of detectors.

For CMB experiments, the field of view of each detector is restricted in order to reduce the pickup of stray radiation. Currently, the collimation of the incoming beam is achieved using metal feedhorns. Though feedhorns have excellent performance, their mass, size, and expense make them unsuitable for large arrays. A highly desirable solution to these problems would be to fabricate monolithic array of antenna-coupled detectors on a planar substrate. In this paper, we describe a novel dual-polarization planar slot antenna array concept which produces quite a narrow (F/4) beam with no additional optical coupling elements such as substrate lens or micro-machined horns. The design, simulation, and preliminary measurement of the antenna array will be presented.

The research described herein was carried out at the Jet Propulsion Laboratory, California Institute of Technology, Pasadena, California, USA, under contract with National Aeronautics and Space Administration.

# CASIMIR: the Caltech Airborne FIR/Submm, High Resolution Heterodyne Spectrometer

Michael L. Edgar**, Andrew I. Harris[#], David W. Hawkins[+], Alexandre Karpov*, David Miller*, Kevin P. Rauch[#] & Jonas Zmuidzinas*

***Abstract*— CASIMIR, the Caltech Airborne Submillimeter Interstellar Medium Investigations Receiver, is a far-infrared and submillimeter heterodyne spectrometer, being developed for the Stratospheric Observatory For Infrared Astronomy, SOFIA. CASIMIR will carry out observations in the frequency range from 500 GHz up to 1.4 THz, with extremely high spectral resolution, of order $10^6$. Utilizing recent advances in SIS detector development, CASIMIR will cover this region of the spectrum with unprecedented sensitivity. CASIMIR is extremely well suited to observe the warm, ~100K, interstellar medium, particularly water lines, in both galactic and extragalactic sources. We present an overview of the instrument, its capabilities, systems and expected performance.**

**Keywords: heterodyne, spectrometer, FIR/submm, SOFIA**

## 1 INTRODUCTION

CASIMIR, the Caltech Airborne Submillimeter Interstellar Medium Investigations Receiver, is a far-infrared (FIR) and submillimeter, very high-resolution, heterodyne spectrometer. It is being developed as a first generation, Principal Investigator class instrument for the Stratospheric Observatory For Infrared Astronomy, SOFIA[1,2]. Observations with CASIMIR on SOFIA are expected to begin in 2010 and the instrument should be available to guest investigators soon after. It is anticipated SOFIA will eventually achieve a flight rate of up to 160 flights per year, with a lifetime of 20 years.

Initially, CASIMIR will cover a frequency range from 500 GHz up to 1.25 THz. A 1.4 THz band will be added soon after initial operations and the frequency coverage may eventually be expanded up to 2 THz. It will be capable of covering this range at a resolution of ~$10^6$.

** Contact Author: California Institute of Technology, MS 320-47
Pasadena, CA, 91125,USA
mick@submm.caltech.edu
* California Institute of Technology
# Department of Astronomy, University of Maryland
+ Owens Valley Radio Observatory, California Institute of Technology

The FIR/submm is extremely important for the investigation of both the galactic and extragalactic warm ($T$~100 K), interstellar medium. This material is heated by shock waves or UV radiation, phenomena that are often associated with star formation or other high energy events, e.g. supernovae or active galactic nuclei. This excited material then re-emits either as dust continuum radiation or gas line emission. CASIMIR will be able to utilize recent advances in the sensitivity of superconducting mixers to study the fundamental rotational transitions of many astronomically significant hydride molecules, which cannot be observed with ground based telescopes.

## 2 FREQUENCY BANDS

### *2.1 Initial Channels*

Four frequency channels will be available for initial observations. Table 1 shows a selection of significant spectral lines within these bands. It is expected that initial observations will concentrate on lines from this list. Almost all of these lines are completely unobservable from the ground.

### *2.2 Water*

As can be seen from Table 1, CASIMIR is particularly well suited to investigate the abundance and excitation of interstellar water, using a number of transitions of $H_2{}^{18}O$. While oxygen is the third most abundant element, its chemistry in interstellar clouds is poorly understood, since the atmosphere is opaque to many of its key species, such as O, $O_2$, $H_2O$, $H_3O^+$ and OH. Gas phase water also has an important role in the energy balance of molecular clouds due to radiative cooling or heating through FIR/submm rotational transitions[3]. Figure 1 shows the rotational energy levels for $H_2{}^{18}O$, indicating the large number of low excitation level transitions visible to CASIMIR. Figure 2 shows results from observations of the 547 GHz $H_2{}^{18}O$ line obtained on the Kuiper Airborne Observatory (KAO) and predictions of the line intensities that will be obtained for the same source with CASIMIR.

| Freq. Band GHz | Species | Line Freq. GHz | % Atmos. Trans. @12km |
|---|---|---|---|
| 500-600 | $H_2{}^{18}O$<br>CH<br>$NH_3$<br>CO | 547<br>532,536<br>572<br>576 | 81<br>98,97<br>94<br>80 |
| 700-800 | $H_2{}^{18}O$ | 745 | 82 |
| 900-1050 | $H_3O^+$<br>$CH_2$<br>NH<br>$H_2{}^{18}O$<br>CO | 985<br>946<br>975<br>995<br>1037 | 65<br>99<br>96<br>73<br>94 |
| 1050-1250 | $H_2{}^{18}O$<br><br>HF | 1137,1181<br>1189,1199<br>1232 | 70,75<br>87,81<br>30 |

Table 1. A list of selected significant species and lines that will be observed with the first 4 frequency bands of the CASIMIR instrument. The atmospheric transmissions shown are for typical SOFIA operating altitudes, ~4o,ooo ft. or 12 km. At the Caltech Submillimeter Observatory (CSO), on the summit of Mauna Kea at 4.1 km altitude, of all the lines shown, only two have an atmospheric transmittance more than 0%: CH (1%) and $CH_2$ (13%).

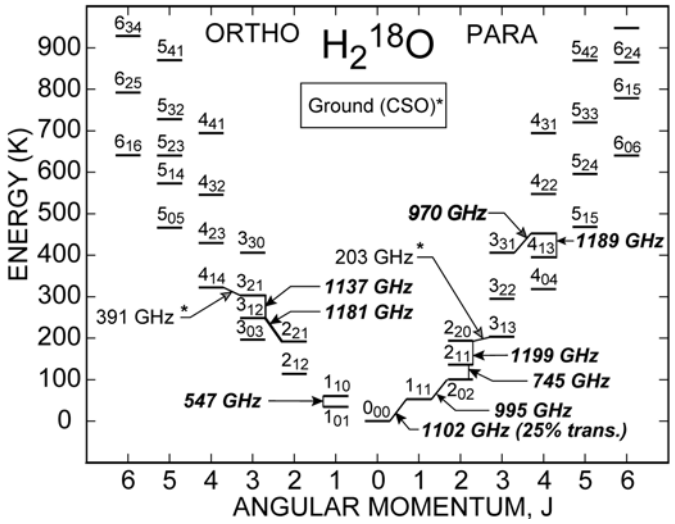


Figure 1. CASIMIR's coverage of the rotational energy levels of the $H_2{}^{18}O$ molecule. The first 4 bands of CASIMIR will be able to observe 9 transitions, including several low temperature lines, compared to only 2 relatively high energy transitions observable at the CSO, denoted by asterices.

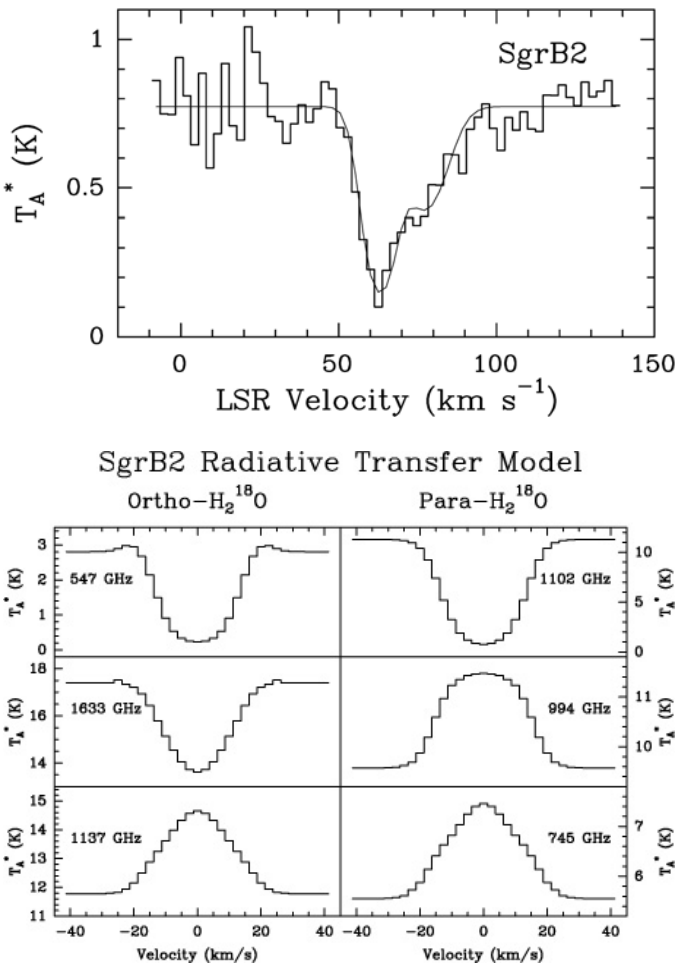


Figure 2. Comparison of $H_2{}^{18}O$ line sensitivities obtained with the Kuiper Airborne Observatory (KAO) and expected for CASIMIR. The top part of the figure shows 547 GHz observations of SgrB2, obtained on the KAO. The bottom part shows predicted performance for observations of SgrB2 with CASIMIR on SOFIA, for several lines. SgrB2 was modeled as a sphere, $n_{H2}(r) \sim r^{-2}$ and $T(r) \sim r^{-0.5}$, which matches existing CO, dust and $H_2{}^{18}O$ data.

### *2.3 1.4 THz Band and $H_2D^+$*

A 1.4 THz band is expected to be available soon after CASIMIR begins observations on SOFIA. This band will concentrate on the $H_2D^+$ 1370 GHz ground state line. The $H_2D^+$ ion is of particular interest, since it is the deuterated version of $H_3^+$, which is believed to be responsible for driving much of the chemistry of molecular clouds. The 372 GHz line for this species has now been detected from the ground in several protostellar cores with the CSO[4] and the APEX telescope[5], in the Atacama Desert. However, this line traces hot, dense gas, in which the chemistry is more complicated and the abundance is expected to be low. The 1370 GHz line is a better choice. The only previous search for this higher frequency line was made towards Orion, using the KAO, and resulted only in a tentative detection of an absorption feature[6].

## 3 RECEIVERS, LOCAL OSCILLATORS AND INTERMEDIATE FREQUENCY SYSTEM

### *3.1 Receivers*

The receivers for all of the first five CASIMIR bands, up to 1.4 THz, will be Nb/AlN/NbTiN Superconducting-Insulator-Superconducting (SIS), quasi-optically coupled, twin-slot mixers. These mixers and their development are discussed in detail elsewhere in these proceedings[7].

The ongoing development is expected to significantly reduce the noise temperatures compared to present receivers at these frequencies. It is expected that this development will achieve double side band (DSB) noise temperatures of the order of 3h**u**/kB for devices operating at less than 1 THz and 6h**u**/kB above.

It is also expected that the useful frequency range of SIS mixers may extended up to 1.6 THz.

### *3.2 Local Oscillators*

The Local Oscillators (LOs) for all bands are tunerless and use solid state devices exclusively. The 550 GHz and 1370 GHz LOs have already been acquired from Virginia Diodes[8]. The 1200 GHz was developed at JPL and is similar to the LO developed for the same frequency on the Herschel satellite[9]. The 750 and 1000 GHz LOs are under development by N. Erickson at the University of Massachusetts.

All bands are driven from a single, commercial microwave synthesizer at a frequency in the range 26-40 GHz. Any one of four bands can be selected via software at anytime during the flight, without mechanical adjustment or physical access to the instrument.

As shown in Figure 6, up to two LOs can be mounted directly to the side of the cryostat. The LO output is via a feedhorn. The output divergent beam is reflected through $90^{o}$ and converted into a ~f/10 converging beam, by an off-axis elliptical mirror, mounted directly below the feedhorn (see Figure 7). The beam passes through a window in the cryostat wall to a mylar beamsplitter mounted directly below the receiver elliptical mirror. The beamsplitter directs a portion of the LO signal power towards the cryostat cold work surface, combining it with the incoming, astronomical signal.

### *3.3 Intermediate Frequency System*

The intermediate frequency (IF) is the output signal from the mixer. For all bands on CASIMIR, the IF bandwidth is defined to be 4 GHz, centered on 6 GHz. This wide frequency range will allow observation of the broad lines from extragalactic sources.

The low noise amplifier in all bands is a Chalmers[10] design. It is a two-stage amplifier using InP transistors and has a minimum gain of 27 dB with a nominal noise temperature of 3 K. It is mounted on the cold work surface of the cryostat, at LHe temperature, and is connected to the mixer via a cryogenic isolator, which reduces ripple in the IF due to impedance mismatches.

The room temperature IF electronics consist of a 4-8 GHz amplifier module. This is an integrated unit developed under contract by CTT Inc.[11], containing a low noise amplifier, a voltage variable attenuator (VVA), band defining filter, power amplifier, a directional coupler for monitoring the IF power level, and a switch for setting the IF power zero level. An integrated isolator at the input of the module minimizes standing wave ripples between the cryostat and amplifier module. The nominal gain of the unit is 65 dB with a typical noise temperature of 300 K. The bandwidth defined by this unit is shown in Figure 3. A diode is connected to the monitor port for measuring the signal strength and adjusting the VVA to prevent the saturating internal amplifiers. These units are mounted directly to the side of the cryostat (see Figure 6) and are designed for fully automatic operation.

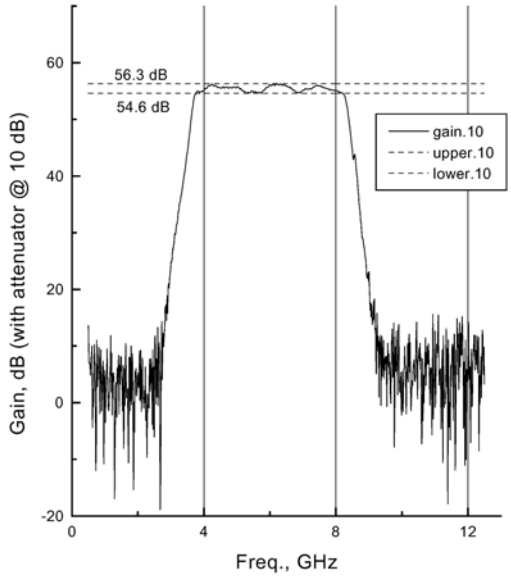


Figure 3. IF bandwidth defined by bandpass filter within the room temperature IF unit. At a typical operating point, with the VVA set for 10 dB attenuation, the IF unit demonstrates excellent uniformity, <+/- 1 dB, across the entire 4 GHz bandwidth.

## 4 MICROWAVE SPECTROMETERS

### *4.1 Wideband Analog Spectrometer (WASP2)*

The WASP2[12,13] was developed at the University of Maryland. It is an analog correlator spectrometer, which in contrast to other spectrometer types, analyzes the entire 4 GHz bandwidth as a whole, without splitting the IF into sub-bands. This approach will be more suitable for wide extragalactic spectral lines.

It is based on an analog correlator card, see Figure 4. Signals propogate in opposite directions along two delay lines. As WASP2 is configured as an autocorrelator, it is the same signal propogating along both lines. At fixed points, i.e. fixed phase lags, along the delay lines, there are taps at which a fraction of the signal from both lines are analog-multiplied together by active mixers. The resolution of this spectrometer is defined by the physical spacing of these taps. There are 16 taps, therefore 16 lags per card, which corresponds to a resolution of 33.6 MHz per channel. Observing at 1 THz, the resolution would be $R=3x10^4$ with a velocity resolution of 10 km/s.

The spectrometer contains 8 correlator cards, connected by cable delays, giving a total of 128 channels, continuously covering the full 4 GHz of the IF bandwidth. Due to practical considerations, only the top 110 channels are available to the user for spectroscopy, limiting the full bandwidth to 3.7 GHz.

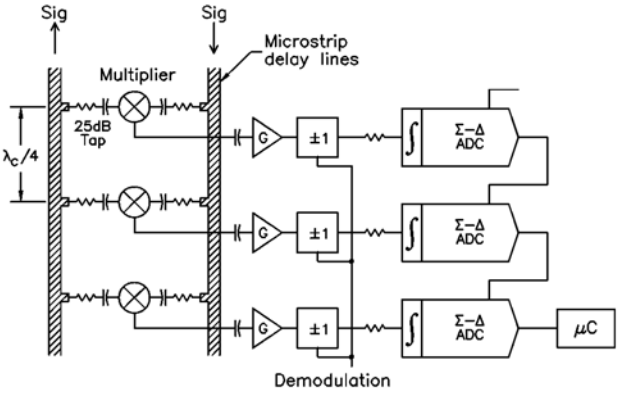


Figure 4. Schematic diagram of a part of the WASP analog correlator card.

### *4.2 High Resolution Digital Correlator, COBRA*

The COBRA[14,15] digital correlator was developed at the Owens Valley Radio Observatory (OVRO) to create a 4 GHz, 6-antenna, correlator system. The design was re-used to create an 8 GHz, 8-antenna, correlator for the University of Chicago SZA array, and the OVRO hardware was recycled to create a 1.5 GHz, 15-antenna, correlator system for the CARMA observatory. The COBRA boards are FPGA-based and use a 6U compact PCI form-factor.

A COBRA digitizer board contains two 1 GHz 2-bit samplers and four FPGAs, while a correlator board contains ten FPGAs.
Each FPGA contains 5,000 logic elements (LEs), and can be configured to calculate up to 32-lags across 500 MHz bandwidth data. Multiple FPGAs, and boards, can be cascaded to increase the number of lags calculated. For example, data from the dual samplers on a digitizer board can be fed to one or more correlator boards.
For CASIMIR's application, the COBRA hardware will be configured as an autocorrelator. Initially it will cover 2 GHz of the IF bandwidth, centered on 6 GHz. The 2 GHz IF is filtered into four 500 MHz bands, and downconverted to the digitizer input band from 500 MHz to 1 GHz. Each signal is then sampled at 1 GHz. The four sub-bands are processed by two digitizer boards and four correlator boards.

Each sub-band is processed using 2 FPGAs on the digitizer board and 10 FPGAs on a correlator board. The resulting power-spectrum has 384-channels, giving a resolution of ~1.3 MHz/channel. While observing at 1 THz, this would correspond to a resolution of $R=7.7x10^5$ and a velocity resolution of 0.4 km/s.

The channel resolution at 500 MHz can be improved by cascading the data through additional correlator cards, there are 320 lags per card.

The FPGAs on the digitizer board can also be used to implement digital (FIR) filtering Reducing the input bandwidth, reduces the parallelism required to processes the data, and increases the number of lags each FPGA can calculate (up to 64-lags). At CARMA, the input bandwidth can be reduced to as a low as 2 MHz. On CASIMIR, FIR filtering can be used to reduce the IF bandwidth from 500 MHz, to 250 MHz or 125 MHz. The mode changes can be made dynamically, take only a few seconds and could be carried out at any stage during the flight.

The CARMA observatory has revised the COBRA hardware, creating a new dual-purpose CARMA board. The board contains an 8-bit, dual-1GHz digitizer, and four FPGAs[16]. The digitizer can be operated as two 1GHz digitizers, or interlaced to operate as a single 2GHz digitizer. A CARMA digitizer board consists of a CARMA board populated with the digitizer components, and four 90,000LE FPGAs, while a CARMA correlator board is populated with four 130,000LE FPGAs, i.e., a CARMA correlator board contains 520,000LEs, whereas a COBRA correlator board contains 50,000LEs. The CARMA hardware offers an order-of-magnitude increase in resolution, and we hope it will be available for use during initial observations with CASIMIR.

## 5 INSTRUMENT CONFIGURATION AND STRUCTURE

The general layout of the CASIMIR instrument is shown in Figure 5. Two cryostats are mounted side by side on top of a box, which contains the relay optics, see Section 5.3.

Two 19-inch racks are mounted directly behind this box. All the critical electronics components are mounted in these racks, eg. the LO drive electronics and the microwave spectrometers. This ensures very short cable runs to the cryostat and prevents any differential rotation. All electronic systems for the

instrument are packaged as 19-inch bins, which will allow easy replacement of any unit.

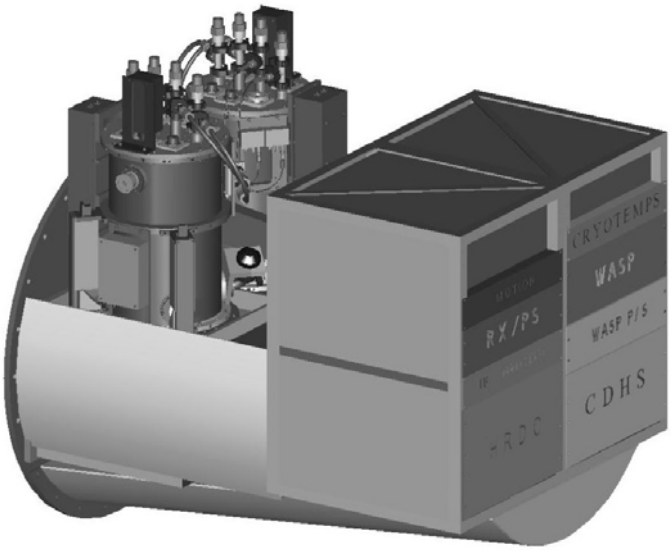


Figure 5. The CASIMIR instrument. The instrument is mounted to the telescope via the round flange at extreme left of the figure. This flange forms the pressure interface between the telescope cavity and the aircraft's cabin. The portion of the instrument shown is located in the cabin, with the observers. The telescope beam enters the instrument through the center of this round flange, about 150 mm below the bases of the cryostats. The instrument structure is constructed almost exclusively of aluminum. It is approximately 1.5 m long by 1 m square. It weighs approximately 550 kg, including 150 kg of electronics mounted in the racks, at the right of the figure. Approximately 150 kg more of ancillary electronics are located elsewhere in the aircraft cabin.

### *5.1 Cryostats*

The cryostats are of conventional design with $LN_2$ and LHe reservoirs. For frequencies below 1 THz, the mixers will operate at ~4 K. At higher frequencies, we will pump on the LHe reservoir to operate the receivers at ~ 2.5 K.

There will be two cryostats per flight and up to two frequency bands in each cryostat, so there will be up to four bands available per flight. Observations can be made with only one band at a time. Any one of the four bands can be selected at anytime during the flight. This selection is made by software alone, and does not require caging of the telescope, any mechanical adjustment or physical access to the instrument.

As shown in Figures 6 and 7, all the components specific to an individual frequency band are integrated directly onto the cryostat, eg. the LOs, IF systems and relay optics. All systems mounted elsewhere on the instrument are used for all of the bands. Therefore, changing the selection of the four bands which are to be used on a given flight only requires swapping cryostats, which could easily be carried out between flights. Also, any upgrades and improvements to the bands could be accomplished completely independent of the rest of the instrument. This will allow continuous upgrades to the frequency bands, throughout the life of the instrument.

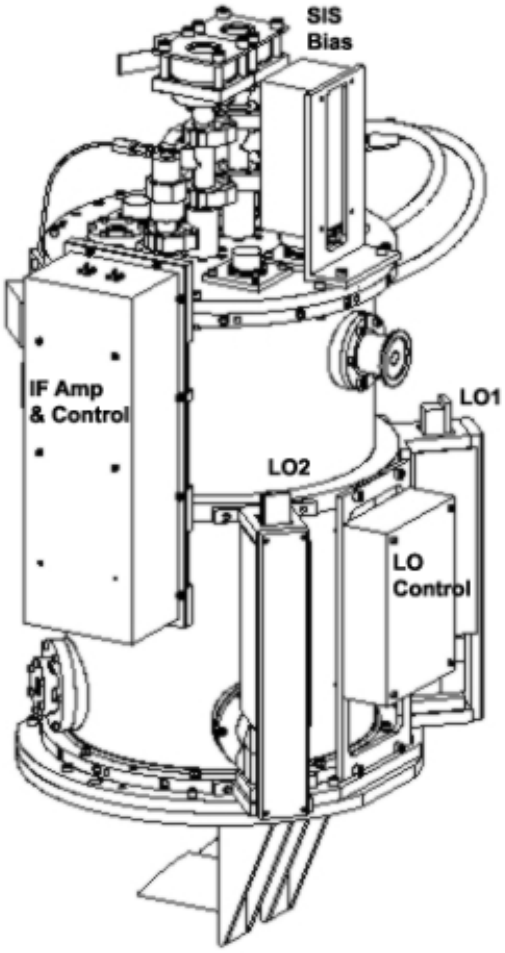


Figure 6 The CASIMIR Cryostat. The cryostat contains 5 liters each of $LN_2$ and LHe and has a 250 mm diameter cold-work-surface. This is the approximate, maximum, practical diameter for cryostats that can be used in the side-by-side configuration for SOFIA. It is 600 mm high and weighs ~40 kg. The LOs, IF system, receiver and LO bias electronics are mounted directly to the side of the cryostat. The electronics for the cryogenic amplifier bias and mixer electromagnet current are also mounted on the cryostat but are not shown in this view. The rather impressive array of plumbing fixtures on the top of the cryostat prevents the formation of ice plugs or the rupture of the cryogenic reservoirs. This design was required to obtain airworthiness certification of the cryostat by the Federal Aviation Administration. The two elliptical mirrors of the relay optics, mounted on the base of the cryostat, can be seen at the extreme bottom of the image.

### *5.2 Optics*

Figure 7 shows a schematic of the relay optics, which uses two off-axis elliptical mirrors to match the incoming telescope beam to the output beam of the mixer. Including the telescope, there are five mirrors at ambient temperature and one cryogenically cooled mirror, EM1, in the optical train.

This includes two plane mirrors, the fully reflective tertiary and a plane mirror in the Optics Box, see Figure 8.
The window in the base of the cryostat is the only pressure boundary in the optical path from the telescope. Therefore, this window and a lens in the mixer assembly are the only transmissive elements in the entire optical train from the telescope to the receiver.

The optical designs for all bands have an edge taper of 10 dB. Initially, SOFIA will have an oversize tertiary, which will produce an aperture efficiency of 0.64. A smaller tertiary may be available in the future, which will improve the aperture efficiency to 0.71. Main beam efficiency is calculated to be 0.77. The largest beam size is 0.8 arcmin, at 550 GHz.

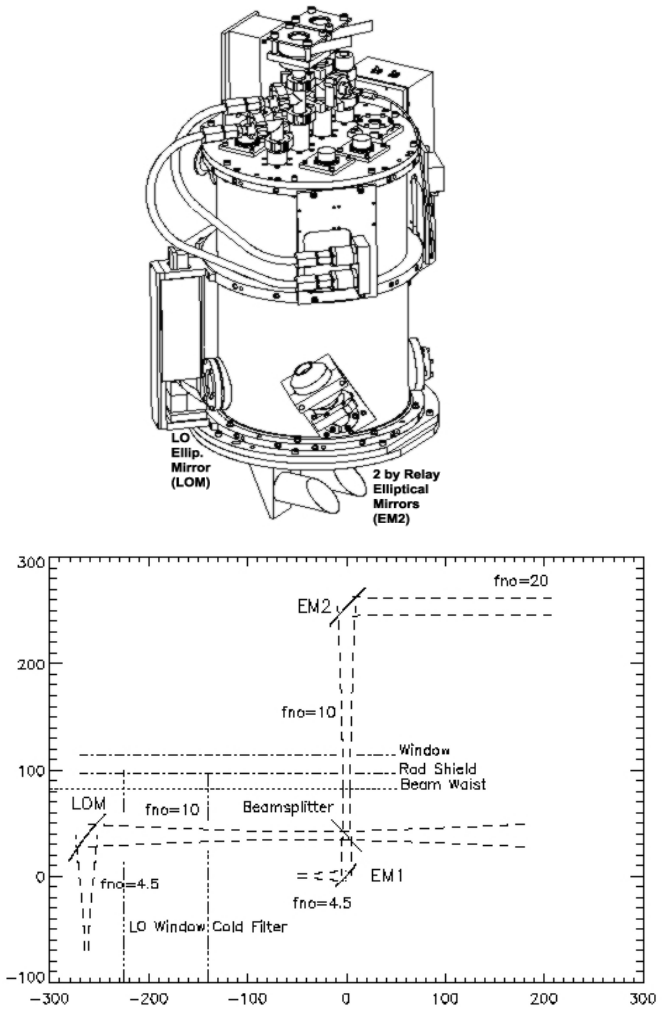


Figure 7 CASIMIR Relay and LO Injection Optics. The top image shows the location of the elliptical mirrors mounted on the cryostat. The bottom part of the image shows a schematic of the optics. In the lower image, the up down orientation is reversed and the units on the scale are mm, with the origin at the center of EM1, the elliptical mirror mounted on the cryostat cold-work surface. EM2 is the elliptical mirror mounted below the base of the cryostat, visible in the left image. EM2 is in the plane of the telescope beam, it converts the incoming, diverging f/20 telescope beam into an intermediate f/10 beam and reflects it through 90°, through a window in the base of the cryostat. LOM is the LO elliptical mirror, which matches the LO output beam to the incoming intermediate beam. EM1 converts the intermediate beam to a converging ~f/4.5 beam, which matches the output beam of the mixer.

### *5.3 Optics Box*

Figure 8 shows a 3D model of the Optics Box, which is the mount for the cryostats and contains all the optics common to all frequency bands. The central feature is a plane mirror, which can be commanded to rotate through +/- 180° in the plane of the telescope and up to +/-5° in tilt. This rotating mirror directs the telescope beam to one of the four elliptical mirrors mounted on the two cryostats, selecting the frequency band.

The calibration system consists of a chopper wheel at ambient temperature plus hot and ambient temperature loads. Moving the rotating mirror by ~180°, allows any of the frequency bands to be first illuminated with the sky signal and then the signal from a known temperature calibration load.

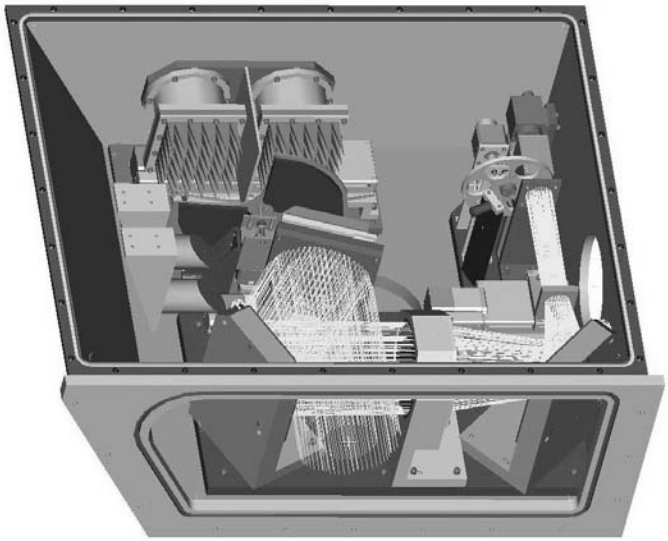

Figure 8 The Optics Box. The cryostats are bolted directly to the lid of this box, which has been removed for this image. The elliptical mirrors mounted on the base of the cryostats protrude trough an aperture in the lid and are located in the plane of the telescope beam. The two elliptical mirrors for one of the cryostats are shown in the left part of the image. The box forms part of the pressure interface between the aircraft cabin and the exteriorand wall thickness varies between 0.5 and over 0.75 in. The box interior is exposed directly to the telescope cavity, so that at altitude, the pressure inside is <200 Tr. The telescope beam enters from the front of the figure. In this image, the rotating mirror, at the center of the figure, directs the telescope beam to the optical boresight, at the far right rear corner. The calibration chopper wheel and the two loads are shown in the rear of the figure.

CASIMIR will use the fully reflective tertiary mirror on SOFIA's telescope. As a result, none of the observatory's guiding cameras will be able to image the telescope's focal plane. Therefore, we have included an optical boresight camera, inside the Optics Box, for alignment and

beamfinding. The boresight can also be used as a pupil imager by moving a biconcave lens into the optical path. The camera has a 6'x6' field of view and uses a 1024x1024 pixel, optical wavelength CCD. The rotating mirror also selects this camera.

Stepper motors are used to move all the optical components. All of these motors are mounted inside the Optics Box and are controlled remotely via software. There are only electronic feedthroughs mounted in the sides of the box, without any mechanical motions through the pressure boundary. Physical access to the Optics Box will not be required at any time during the flight.

## 6 CONCLUSIONS

CASIMIR is a FIR/Submm, heterodyne spectrometer for SOFIA. It is well suited for the studies of the warm (T~100K) interstellar medium, particularly water, measuring many significant lines unobservable from the ground. Initially, the instrument will cover 500 to 1250 GHz, with a 1.4 THz Band to be added soon after. Eventually the frequency coverage may be extended up to 2 THz. CASIMIR will have unprecedented sensitivity in this frequency region, due to recent advancement in SIS mixer design.

There will be up to 4 channels available per flight of the observatory. Any one of these channels can be selected at any time during the flight.

All bands will have an IF bandwidth of 4 GHz. A medium resolution ($R\sim3x10^4$) spectrometer will simultaneously cover this whole band. There will also be partial coverage of this band with very high resolution, up to $\sim10^6$.

The instrument design is extremely modular and will be able to continuously incorporate new hardware and accommodate future improvements in mixer, LO and microwave spectrometer technology, throughout the life of the observatory.

## 7 ACKNOWLEDGMENTS

Various subsystems of the CASIMIR instrument have been or continue to be developed by a number of people at several institutions: H. G. Le Duc, Micro Devices Lab, JPL (mixer fabrication), N. R. Erickson, U. Mass. (LOs), M. R. Haas, NASA Ames (optics), the Kosma I/O Team, U. of Koln and S. W. Colgan, NASA Ames (software), and S. Lin, Caltech/JPL (mechanical design). The development of CASIMIR is supported by NASA/USRA SOFIA Instrument Development Fund.

## REFERENCES

[1] S. C. Casey, "The SOFIA program: astronomers return to the stratosphere", *SPIE*, **6267**, 2006.

[2] E.E Becklin, A. G. G. M. Tielens & H. H. S. Callis, "Stratospheric Observatory for Infrared Astronomy (SOFIA)", *Mod. Phys. Lett. A*, **21**, 2551-2560, 2006.

[3] D. A. Neufeld & M. J. Kaufan, "Radiative Cooling of Warm Molecular Gas", *Ap. J.*, **418**, 263, 1993.

[4] C. Vastel, P. Caselli, C. Ceccarelli, T. Phillips, C. Wiedner, R. Peng, M. Houde & C. Dominik, "The distribution of ortho- $H_2D^+$ ($1_{1,0}$-$1_{1,1}$) in L1544: tracing the deuterization factory in prestellar cores", *Ap. J.*, **645**, 1198-1211, 2006.

[5] J. Harju, L. K. Haikala, K. Lehtinen, M. Juvela, K. Matilla, O. Miettinen, M. Dumke, R. Gusten, & L.-A Nyman, "Detection of $H_2D^+$ in a massive prestellar core in Orion B*", *A&A*, **454**, L55-58, 2006.

[6] R. T. Boreiko & A. L. Betz, "A search for the rotational transitions $H_2D^+$ at 1370 GHz and $H_3O^+$ at 985 GHz", *Ap. J. (Letters)*, **405**, L39-L42, 1993.

[7] A. Karpov, D. Miller, J. A. Stern, B. Bumble, H. G. Leduc & J. Zmuidzinas, "Development of THz SIS mixers for SOFIA", *these proceedings*, 2007.

[8] Virginia Diodes Inc., 979 Second St. S.E., Suite 309, Charlottesville, VA 22902-6172, USA.

[9] I. Mehdi, E. Schlect, G. Chattopadhyay & P. H. Siegel, "THz local oscillator sources: performance and capabilities", *SPIE*, **4855**, 435-446, 2003.

[10] N. Wadefalk, A. Mellberg, I. Angelov, M. E. Barsky, S. Bui, E. Choumas, R. W. Grundbacher, E. L. Kollberg, R. Lai, N. Rorsman, P. Starski, J. Stenarson, D. C. Streit & H. Zirath, "Cryogenic wide-band ultra-low-noise IF amplifiers operating at ultra-low DC power", *IEEE Trans. Microwave Theory Tech*., **51**, 1705-1711, 2003.

[11] CTT Inc., 3005 Democracy Way, Santa Clara, CA, 95054, USA.

[12] A. I. Harris & J. Zmuidzinas, "A wideband lag correlator for heterodyne spectroscopy of broad astronomical and atmospheric lines", *Rev. Sci. Instr.*, **72**, 1531-1538, 2001.

[13] A. I. Harris, "Heterodyne spectrometers with very wide bandwidth", *SPIE*, **4855**, 279-289, 2003.

[14] D. Hawkins, "COBRA digital correlator system", *SPIE.*, **4015**, 2000.

[15] D. W. Hawkins, D. P. Woody, B. Wiitala, J. Fredsti, & K. P. Rauch, "The CARMA Correlator", *SPIE*, **5498**, 567-578, 2004.

[16] K. P. Rauch & D. W. Hawkins, "Revised CARMA Correlator Design Considerations", CARMA Memo #28, 2004, (www.mmarray.org/memos/carma_memo28.pdf).

# STEAM-R (Stratosphere-Troposphere Exchange And climate Monitor Radiometer)

A. Emrich, Omnisys Instruments AB, Gruvgatan 8, 421 30 Göteborg, Sweden

ABSTRACT

The Stratosphere-Troposphere Exchange And climate Monitor radiometer, STEAM-R, is a Swedish national contribution to the PREMIER mission. This is specifically designed to provide accurate measurements of the global distributions of key target species in the UTLS. To achieve good vertical and horizontal resolution, it will utilise a small linear array of receivers, which will image different altitudes simultaneously backward along the satellite track, thereby providing unique information about the 2-D structure of the atmosphere in the orbital plane.

| Channel | | (1) UT/LS | (2) Stratosphere |
|---|---|---|---|
| Frequency | Lower sideband<br>upper sideband<br>Local oscillator | 324.0-332.0 GHz<br>343.8-351.8 GHz[18]<br>337.9 GHz | 488.25-492.25 GHz<br>500.25-504.25 GHz<br>496.25 GHz |
| Spectral resolution | | 10 MHz | 5 MHz |
| Lower FOV boundary at | | 5 km | 12 km |
| Upper FOV boundary at | | 28 km[19] | 35 km |
| Vertical sampling | | 1.5 km | 1.5 km |
| Horizontal sampling (along track) | | < 50 km | < 50 km |

Table 1. Baseline specifications of STEAM-R

The heterodyne array receivers are based on broad band sub-harmonically pumped planar Schottky diode mixers operating in the 320-360 GHz spectral range. A secondary alternative band can be measured in a time sharing mode using the same receiver by electronically selecting the frequency of the local oscillator (LO). The sub-mm channel in the frequency band 485-505 GHz will extend the measurements of O3, N2O, and H2O (Table 1) higher up in the stratosphere from 15 to 37 km, and above all will provide more sensitive measurements of ClO (ozone destruction) and HDO (D/H ratio, tracer for STE).

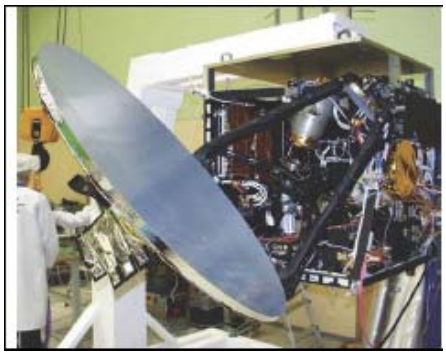

The signal originating from both sidebands is down-converted to an intermediate frequency (IF) in the range ~6-14 GHz. The IF signal is filtered, amplified and spectrally resolved using autocorrelation spectrometers that provide a instantaneous bandwidth of 8 GHz for the mm band and 4 GHz in the sub-mm band, with a spectral resolution of 10 MHz. The possibility of using side band separation mixers to achieve single sideband detection is under study. The use of frequency multipliers and power amplifiers to generate the LO will offer both simplification and increased reliability. Both bands share pre-optics and calibration targets. We expect the PREMIER radio telescope to be similar to the Odin telescope which is a shaped off axis Gregorian design. It will be constructed of carbon fibre composite material for thermal stability and have a surface accuracy better than 15 μm RMS, a factor of 2 less demanding than for Odin.

The STEAM-R instrument will be presented on system level and key subsystems will be described in detail.

# Laser Sideband Spectrometer: A new spectrometer concept with very large bandwidth

R. Schieder, O. Siebertz, F. Schloeder, P. Nagy

KOSMA, I. Physikalisches Institut, Universität zu Köln, Germany

**Abstract**

A new concept of a super wideband spectrometer is presented, which is based on phase-modulation of a single mode laser. The sideband spectrum is analyzed by means of a simple plane-parallel Fabry-Perot interferometer. A first prototype spectrometer has been built with a bandwidth of about 12 GHz and a resolution of 100 MHz. It has been demonstrated that the concept is viable and ready for further usage in very large IF-bandwidth heterodyne systems.

## Introduction

The trend to higher frequencies in heterodyne remote sensing causes high demand for larg bandwidth of the back-ends of such systems. Nowadays the typical bandwidth of a suitable back-end is of the order of 1 GHz, but the latest generation of heterodyne receivers has an IF bandwidth of 4 GHz or even more, like is used in the HIFI instrument of ESAs Herschel mission. On the other hand, the linewidth of pressure broadened atmospheric lines may reach values near 10 GHz so that back-ends with very large bandwidth are needed, while high resolution is not always required. The same is true for extragalactic signals when observing at frequencies of several THz. It is very difficult to achieve such large instantaneous spectrometer bandwidth with any present technology. There are a couple of different methods for large bandwidth, such as the analogue correlator (WASP), dedicated filterbanks, hybrid spectrometers based on correlator or acousto-optical methods (e.g. WBS in HIFI, see Poster P-14 on this conference), or recently, the introduction of a new Bragg-cell material for a broad band AOS [See paper 8-4 on this conference]. Nevertheless, none of these technologies have succeeded so far to provide access to very large instantaneous bandwidth in or above the 10 GHz range.

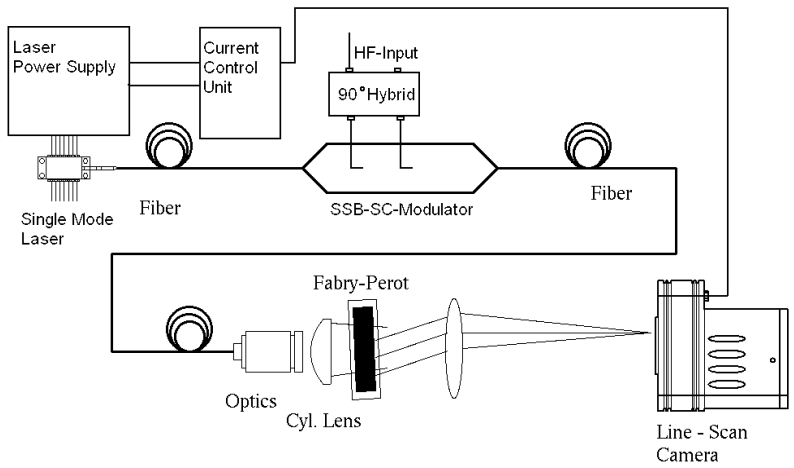


**Fig.1**

Scheme of the Laser Sideband Spectrometer. It consists of a single mode laser, an electro-optical phase-modulator and a custom made Fabry-Perot interferometer.

We have pursued a new idea for such instrument which is based on simple optical methods. The narrow line of a single mode laser is modulated by means of an electro-optical phase modulator. The generated sidebands contain all spectral information of the electric signal, which is driving the modulator. Consequently, it is natural to analyse the spectral distribution of the sidebands by means of a Fabry-Perot interferometer (FPI). Modulators are available with a bandwidth of more than 20 GHz, while the FPI is available as custom made item with nearly any bandwidth depending on the spacing of the mirrors in the device. With new coatings very high finesse in the range of a few hundred can be achieved so that spec-

trometers with reasonable numbers of resolution elements are accessible at practically any desired total bandwidth.

The principle of the Laser Sideband Spectrometer (LSS) is depicted in Fig.1. We use a near-IR laser at 1.55 µm wavelength and about 80 mWatts output power. The modulator is a single sideband modulator, which suppresses the initial laser carrier at the same time. Thus, real SSB operation is available. This is important, because with a DSP modulator, only half of the free spectral range (FSR) of the FPI would be available for the spectral analysis due to overlapping upper and lower sideband signals from successive orders of the FPI. The output of the modulator is then coupled to the FPI by special optics in order to obtain maximum efficiency (see below). The final imaging optics concentrates the signal light onto a linear diode array, which is controlled and processed by similar electronics as we use for our acousto-optical spectrometers as well.

**Concept analysis**

The plane-parallel Fabry-Perot interferometer needs some particular attention. As is immediately deducible from diffraction arguments and from walk-off problems within the interferometer, there is a minimum diameter D needed for a given free spectral range FSR and finesse F like

$$D \geq \sqrt{2 \cdot \lambda_{Laser} / FSR} \cdot F$$

For example, for a wavelength of $\lambda_{Laser}$ = 1.55 µm, a FSR of 0.5 $cm^{-1}$ (15 GHz) and a finesse of 200, the needed diameter is 5 cm! This means that very high accuracy for the fabrication of such FPI is required. A too small diameter causes sidelobe ringing of the signal and reduction of resolution. On the other hand, for such relatively high finesse, it is essential that extremely loss-free coatings are used. Otherwise, the throughput of the FPI, and therefore the efficiency of the optics become seriously reduced.

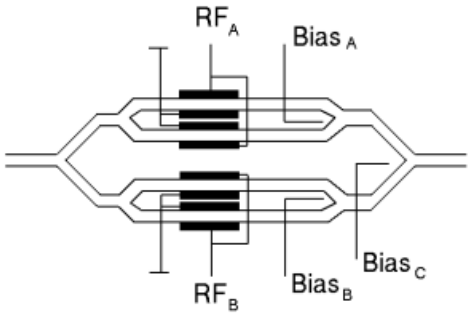


**Fig.2**

Scheme of the single sideband modulator. In the two sub-interferometers the laser carrier is suppressed to better than -20 dB. The two RF-inputs need to be phase shifted by π/2 by means of an RF hybrid. In the combining interferometer the two outputs are co-added with a phase delay of π/2. This can be controlled by a third dc-bias. For further details see text.

The principle of the modulator is shown in Fig.2. It consists of three different two beam interferometers, which can be tuned by means of separate dc voltages. In the two sub-interferometers the AC signal introduces a phase modulation of the laser light in both interferometer arms. The optical pathlength difference of these interferometers is set to $\lambda_{Laser}/2$ minimizing the laser carrier output to nearly zero level. This is important, because the wings of the FPI response to the strong laser carrier could add a severe background to the sideband signal resulting in additional and unwanted shot noise in the output of the spectrometer (see below). In order to explain the single sideband behaviour we need to use a bit of mathematics. The phase modulation with an IF frequency ω of the laser amplitude at frequency Ω in both arms of the first sub-interferometer can be described by:

$$A_1(t) = A_0 \cdot \exp\{i \cdot [\Omega \cdot t \pm u \cdot \cos(\omega \cdot t)]\} = A_0 \cdot \sum_{n=-\infty}^{\infty} (\pm i)^n \cdot J_n(u) \cdot \exp\{i \cdot [\Omega + n \cdot \omega] \cdot t\}$$

*u* is the modulation amplitude and the $J_n(u)$ are the integer Bessel-functions of order n. Due to the opposite sign of the modulation in both arms only odd contributions in the sum remain, when recombined at a pathlength difference of λ/2. In particular, the zero order carrier $J_0(u)$ is removed by this setting. The signal input to the second interferometer is phase shifted by 90 degrees. Therefore we have here:

$$A_1(t) = A_0 \cdot \exp\{i \cdot [\Omega \cdot t \pm u \cdot \sin(\omega \cdot t)]\} = A_0 \cdot \sum_{n=-\infty}^{\infty} (\pm 1)^n \cdot J_n(u) \cdot \exp\{i \cdot [\Omega + n \cdot \omega] \cdot t\}$$

Again, all even orders disappear after recombination in the sub-interferometer. The two interferometer output amplitudes are then co-added in the combining interferometer at 90 degrees phase shift (optical pathlength difference = λ/4), which multiplies the second amplitude by $exp[i \cdot \pi/2] = i$, so that all orders in the sum of both interferometer outputs disappear except for $n = 4k+1$ with $k = 0, \pm1, \pm2, \ldots$ The lowest order remaining is that for $n = 1$ ($k = 0$), which is the upper sideband. For a pathlength difference of -λ/4, the lower sideband is left. The sideband suppression is specified to better than 20 dB.

The higher order terms $J_{4k+1}(u)$, $k = \pm1, \pm2, \ldots$ are causing harmonic response of the modulator, and it is therefore essential to keep them small. The lowest term is $J_{-3}(u)$ which is for low modulation amplitude reduced in comparison to $J_1(u)$ by a factor of $u^2$, so that it is not difficult to avoid such contributions. At the same time, non-linearity due to compression should stay below 1% for a decent spectrometer, i.e. the value of $u$ should stay below 0.2, which corresponds to maximum phase amplitude of less than 3% of a wavelength. On the other hand, since for a broad band spectrum all frequency components contribute identically to the compression, it is possible to correct afterwards for linear response by software, when calibrating the deviation from linearity beforehand. Therefore it is still possible to operate at much higher modulation index than stated before. This helps to improve the efficiency of the system.

When analysing RF-signals by optical means, it is important to note that the shot noise might become the dominant problem. For example, if we consider a LSS with 15 GHz bandwidth and a finesse of 200, we have resolution element bandwidth of $\Delta_{1/2}$ = 15GHz/200 = 75 MHz. The radiometric noise level is determined by the fluctuation bandwidth (rms ~ $\sqrt{B_{FI}}$), which is in this case roughly 200 MHz ($B_{FI} = \pi \cdot \Delta_{1/2}$). On the other hand, the shot noise level is determined by the number N of photo-electrons per second (rms ~ $\sqrt{N}$). The shot noise should stay smaller than the radiometric noise for a suitable spectrometer so that we need at least $4 \cdot 10^8$ photo-electrons per second and pixel when assuming a noise dynamic range of the instrument of 10 dB for example. If we use 500 diodes of a diode array, the total optical power at the detectors must be larger than 0.4 μWatt. For a laser with 80 mWatt it requires an optical efficiency of about $10^{-5}$. This is well within the limits of linear operation of the modulator.

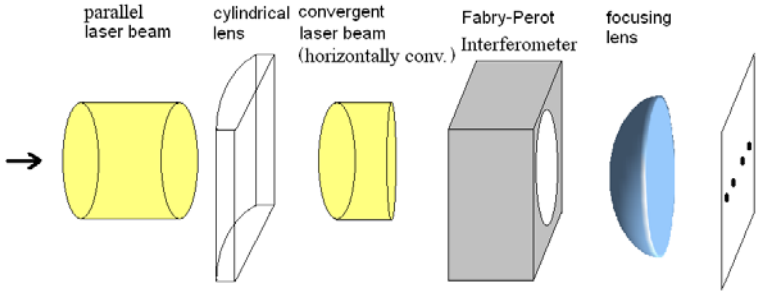


**Fig.3**

Layout of the LSS optics. The spectral distribution of the signal light is concentrated on a line matching the linear CCD.

It is also useful to design the coupling optics appropriately. In order to observe resonances for all sideband frequencies within the bandwidth of the spectrometer, the divergence of the incoming laser beam needs to be well defined. One finds that for a FPI with above defined parameters a minimum divergence of the laser beam of 0.7 degrees, when observing the spectrum in lowest FPI order. On the other hand, it is not desirable to waste signal light while generating rings of light as is normal for a FPI. Therefore we use an astigmatic light distribution as input to the FPI, which is achieved by inserting an additional cylindrical lens with large focal length. The situation is depicted in Fig.3. The horizontal beam divergence is adjusted for minimum divergence, so that in effect a linear cut through the image circles of the FPI is finally illuminated in the image plane at the CCD.

The frequency calibration of a FPI output is strongly non-linear. The frequency is a quadratic function of the distance from the optical axis of the FPI, i.e. the pixel number of the diode array. Therefore, resampling of the frequencies is essential. In order to avoid unfavourable losses in resolution, the optical resolution on the diode array is chosen for oversampling the spectrum accordingly. In combination with a suitable resampling procedure using a Gaussian weighting function one obtains a very linear frequency scale together with sufficient frequency resolution. The effect of the resampling is demonstrated in Fig.4.

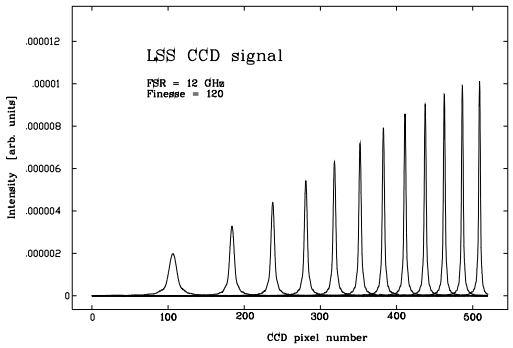


**Fig.4a**
Comb spectrum seen with the LSS before resampling. The non-linear frequency scale is very obvious.

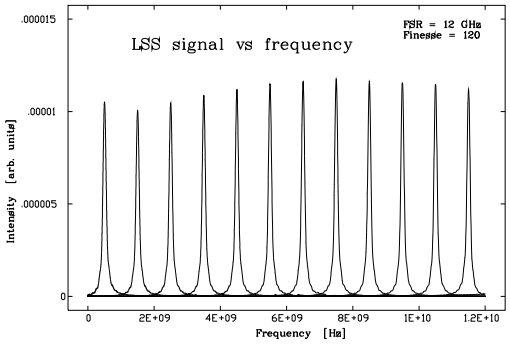


**Fig.4b**
Comb spectrum seen with the LSS after resampling. Note the modified power distribution.

## First Results

The prototype LSS is shown in Fig.5. The laser is located at the right on the base plate. The light is coupled to the modulator at the outer side of the back wall of the unit through a fiber, and its output is then brought into the unit back again by fiber. The emission from the fiber is then astigmatically formed as input to the FPI by the illuminating optics. Behind the FPI a simple imaging telescope is used illuminating the diode array.

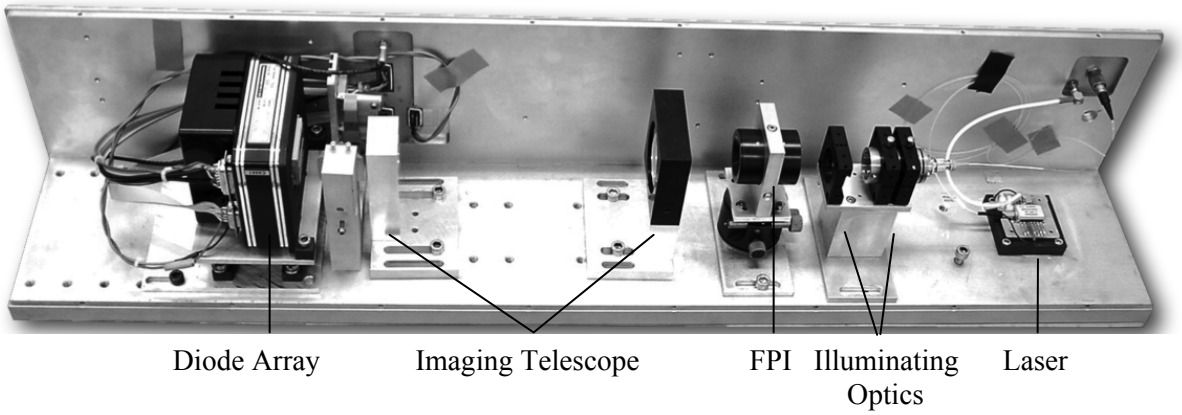


**Fig.5** Optics unit of the prototype LSS

It is important that the carrier suppression in the two sub-interferometers is efficient. To demonstrate this, Fig.6 shows spectra taken with and without proper biasing of the interferometers. The resolution function of FPIs, the Airy-functions, decrease with distance $\Delta x$ from center like $1/\Delta x^2$ so that extended wings of the laser carrier could lead to a strong background signal, which contributes to the shot noise of the detectors. This one must avoid, therefore, proper tuning of the interferometer bias is important.

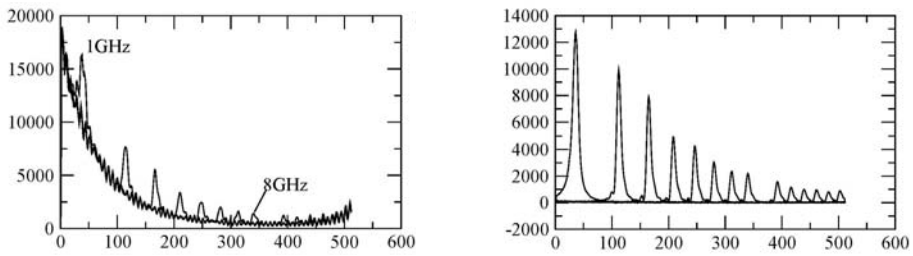


**Fig.6:** Demonstration of the carrier suppression in the two sub-interferometers. The lower frequencies (low pixel numbers) in the spectra are affected strongly by background, as is seen in the left plot..

The inevitable thermal drifts of laser and FPI resonance frequencies need a regulator in order to keep the spectral features at constant position on the diode array. For this, two pixels of the diode array are used, which detect the residual light of the carrier at two sides of its FPI resonance. By means of a differential amplifier, a regulator signal is derived which is fed to the laser current supply.

Fig.7 shows the output of an 18 GHz FPI with white noise input from a noise source after resampling. The bandpass is reasonably flat, and improvements are still possible by means of a RF-equalizer. This demonstrates that very large bandwidth is indeed obtainable.

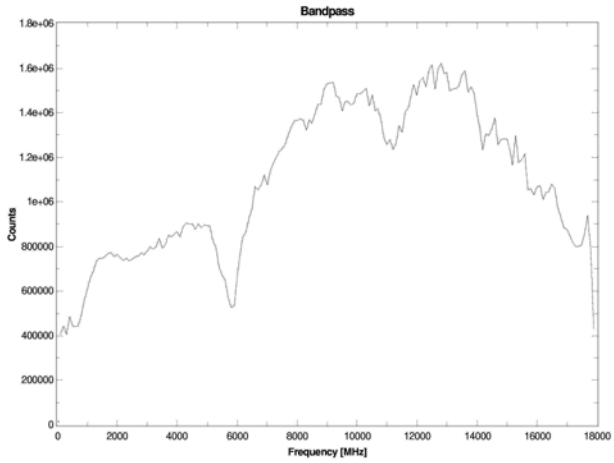


**Fig.7**

Bandpass of the LSS seen with an 18 GHz FPI and SSB modulator.

Finally, the stability of the spectrometer is most important. Since the LSS has large fluctuation bandwidth, the radiometric noise level is less than 10% of that of one of our standard AOSs. This means that the drift noise in the electronics as well as the amplitude stability of the laser must be more stable accordingly. This is a particular challenge for the instrument development. Fig.9 shows an Allan variance plot, as we have achieved so far. It is by now means perfect yet! The dependence on integration time like $1/\sqrt{t_{Int}}$ is somewhat surprising, and it seems to indicate that there is some noise contribution which follows approximately a $1/f^{1/2}$ spectral distribution, which we have not seen in other spectrometers. We believe that the laser is responsible for this behaviour, and we are presently improving the laser frequency and amplitude stability. We assume that in short time a fully qualified back-end is available, and we are hoping that a heterodyne receiver with 12 GHz IF bandwidth will become available for a realistic observing run.

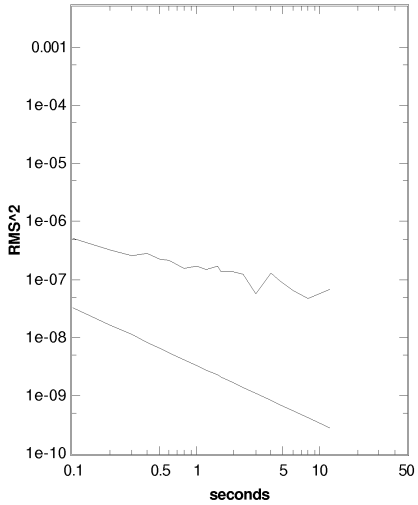


**Fig.8**

Allan variance plot of the LSS output. The slope indicates that there exists some unwanted instrumental noise of unknown origin. At longer integration times the drift noise starts to dominate. The figure indicates that the stability of the instrument still needs some improvement.

# A 3 GHz instantaneous bandwidth Acousto-Optical spectrometer with 1 MHz resolution

M. Olbrich, V. Mittenzwei, O. Siebertz, F. Schmülling, and R. Schieder
KOSMA, I. Physikalisches Institut, Universität zu Köln

***Abstract*— The design and implementation of a new broadband acousto-optical spectrometer is discussed. The device has an instantaneous bandwidth of 3 GHz, and a resolution and fluctuation bandwidth of 1 MHz / 1.4 MHz respectively. The backend has no platforming errors and a power linearity in the order of 0.1% over a noise dynamic range of 13 dB. With an Allan minimum time of better than 300 seconds, it is ideally suited for a large number of applications, including measurements that have broad lines like extragalactic sources or planetary atmospheres, as well as line surveys. Also, sources which require a large dynamic range of the receiver are well accessible due to the excellent linearity of the backend. The system includes its own temperature stabilization and can easily be mounted into a standard 19" rack.**

## I. Introduction

The exploration of the submm- and FIR frequency range for high resolution spectroscopy has produced large demand for wide band spectrometers, since the required bandwidth for the observation of Doppler-broadened atomic or molecular transitions scale with the frequency of the atomic or molecular lines. For example, extragalactic sources require sometimes about 600 km/sec velocity coverage, which corresponds to about 4 GHz bandwidth at frequencies near 2 THz. With new mixer technologies like Hot Electron Bolometers (HEB) it is now possible to achieve satisfying noise temperatures at these very high frequencies, and a new generation of observatories like SOFIA and Herschel will access this new spectral range in the near future. Similar, studies of pressure broadened lines of trace constituents in the Earth or other planetary atmospheres require large bandwidth as well in order to derive detailed abundance information in higher pressure regimes at lower altitudes. Particularly there the availability of very stable and reliable broadband spectrometers with high linearity is essential. In addition, line surveys will greatly benefit of high resolution large bandwidth backends.

When selecting a backend for a given instrument and observation one has to carefully balance the various advantages and disadvantages of different spectrometer technologies. Criteria should contain the resolution bandwidth, the fluctuation bandwidth (noise for a given resolution), power linearity, platforming effects of hybrid spectrometers, excess noise generated by the backend, and stability.

## II. Large Bandwidth AOS design

According to the basics of the acousto-optical principle the required optical aperture $\Delta x$ of a Bragg-cell for a given frequency resolution bandwidth $\delta\nu$ is defined by

$$\Delta x = V/\delta\nu$$

with V the velocity of the acoustic wave in the Bragg-crystal. The typical velocity of the acoustic shear wave in crystals like $LiNbO_3$ is about 3.5 mm/µsec. Consequently, the length of the illuminated acoustic field in the crystal has to be about 3.5 mm when considering a resolution near 1 MHz.

In order to provide sufficient acoustical power even at the end of the aperture, the acoustic attenuation should be sufficiently small. Since the damping constant of the acoustic field scales with $1/\nu^2$ ($\nu$ is the applied radio frequency), there is an upper limit for the maximum usable frequency for a given deflector material. For $LiNbO_3$ the damping constant is about $\delta$ = 3 mm (1/e length) at a frequency of 2.1 GHz, which is the center frequency of a typical 1 GHz bandwidth AOS. Therefore, at a frequency of, say, 5 GHz, the resulting 1/e length would reduce to about 0.5 mm, corresponding to a maximum resolution of about 7 MHz. This estimate shows that it is not possible to achieve a satisfying resolution together with a bandwidth of several GHz using the well established $LiNbO_3$ Bragg Cells.

Additionally, an increased bandwidth requires a larger angular spread of the acoustic waves in the crystal. Consequently, the overall efficiency becomes drastically reduced at large bandwidth. Since the acousto-optical efficiency $\eta$ depends strongly on the wavelength of the light source used in an AOS ($\eta \approx \lambda^{-2}$) one must also go to shorter laser wavelength for broadband AOS than the typically used laser diodes around 780 nm wavelength.

## III. Broadband AOS components and setup

As a consequence from the above discussion it is obvious that a large bandwidth device requires a new Bragg-Cell material and a short wavelength laser light source.

### A. *Bragg Cell*

In close collaboration with BAE Systems (UK) we developed a new Bragg-Cell where Rutile ($TiO_2$) is used for the first time as deflector material. Rutile has similar acoustical parameters like $LiNbO_3$ but it has a much lower acoustic attenuation. The most important acousto-optical properties are summarized and compared to the well established $LiNbO_3$ in the table below.

| | Rutile ($TiO_2$) | $LiNbO_3$ |
|---|---|---|
| Aperture time | 1 µs | 1 µs |
| Attenuation @ 2.1 GHz | 0.8 dB/µs | 4.9 dB/µs |
| 3 dB bandwidth | 3 GHz | 1.4 GHz |
| Center Frequency | 5.0 GHz | 2.1 GHz |
| Diffraction efficiency | max 2.3 % / W | ≥ 10 % / W |

The table shows the basic acousto-optical properties of Rutile compared to LiNbO3. Rutile data are kindly provided by Dr. Lionel Kent, BAE Systems (UK)

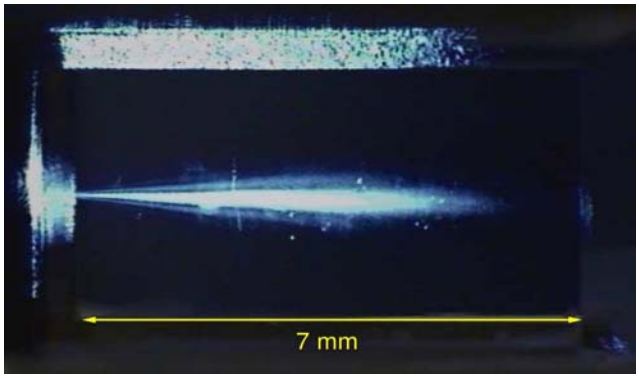


Schlieren-image of the acoustic wave in the Bragg-Cell

From the acousto-optical properties for Rutile it follows, that the new deflector can provide a bandwidth of at least 3 GHz with a resolution up to 1 MHz. To fully take advantage of these properties, the laser and the CCD have to be selected accordingly.

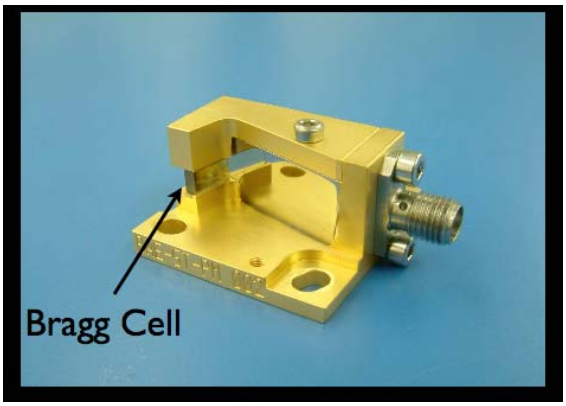


Photograph of the mounted Bragg Cell. The Bragg-Cell itself has a size of about 7 mm x 3 mm. Picture kindly provided by Dr. Lionel Kent, BAE Systems (UK)

### B. *CCD*

The deflected light from the Bragg-Cell should ideally be oversampled by a factor of two to allow efficient resampling in case the frequency axis of the backend has to be adapted or shifted for data analysis. The Fairchild CCD-191 has 6000 pixels, which exactly matches our requirements. Each pixel is 10x10µm square, the noise characteristics of the CCD allow a Noise Dynamic Range (NDR) of about 13 dB.

### C. *Laser*

As laser we use a commercially available, optically pumped diode laser system (OPS) from Coherent Inc (Sapphire 488-200). It is operating single mode at a wavelength of 488 nm. Its high output power of more than 100 mW, the very clean $TEM_{00}$ beam profile, and its high frequency and power stability make it a perfect light source for the BAOS.

### D. *Optical Setup*

It is evident that the large number of pixels together with the relative low optical efficiency of Rutile requires a careful optical design, even with a rather high laser output power in excess of 100 mW. The schematic setup of the BAOS is shown in the figure below.

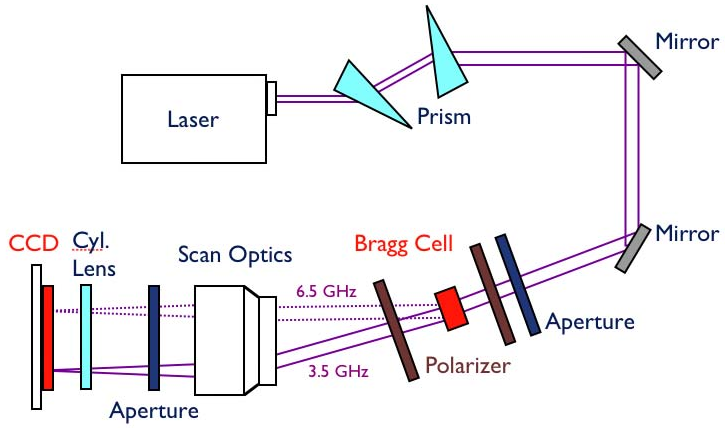


Schematic setup of the BAOS.

Two prisms expand the laser beam in horizontal direction to match the effective aperture of the Bragg-Cell. A polarizer in front of the bragg cell ensures the correct polarization angle for Rutile. Since the interaction with the shear wave in Rutile is anisotropic, the polarization of the diffracted light is changed with respect to the incident beam, a second polarizer behind the Bragg Cell is used to reduce the light scatter level. Additional apertures in the optical path further reduce the light scatter. To increase the optical throughput of the system, cylindrical lenses (focusing in vertical direction) are used in front of the deflector focusing the laser beam onto the sonic wave, and in front of the CCD.

The optical setup of an AOS requires a high temperature stability. This is because the Bragg-angle itself is temperature dependent, as well as the laser speckles, and the optical alignment of the instrument. Usually we use a chiller with a temperature regulator, but this is not very practical for varying field applications. Therefor with the BAOS we use a Peltier regulator, which stabilizes the temperature of the complete optics to about 0.1 K. The Peltier cooler is directly mounted on the box of the optics unit.

## IV. Test Results

The performance of the BAOS has been extensively measured and characterized in the laboratory and confirmed during a first run in the field. We present the most important test results that specify the resolution, linearity, and stability of the device.

### A. Frequency resolution

The resolution bandwidth of the BAOS is determined by the filter-curve. The measured value is about 1 MHz, the variation over the 3 GHz band is in the order of 10%. It is remarkable that the measured filtercurve is fully in agreement with numerical simulations that assume aberration-free optics. This proves that the quality of the laser beam, the optical components, and their alignment are „close to perfect“.

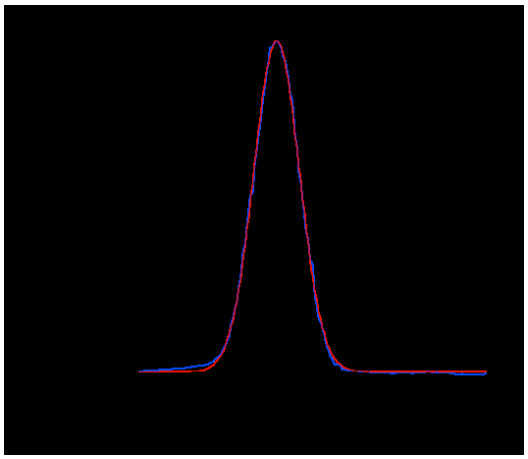

Sample filtercurve that has been recorded with a synthesizer step size of about 25 kHz. The blue line is the measured curve, the red line is a gaussian fit. The measured resolution bandwidth ($\delta_{res}$) is 0.93 MHz, the fluctuation bandwidth ($B_{fluc}$) is 1.31 MHz.

### B. Frequency linearity

As is well known from the theory of acousto-optical spectrometers, their response is slightly different from linear in frequency. However, this can easily be corrected by a resampling procedure. For this calibration measurements with known frequencies (a „comb“ signal) are needed. After correction the frequency precision is in the order of ±50kHz over the 3 GHz band.

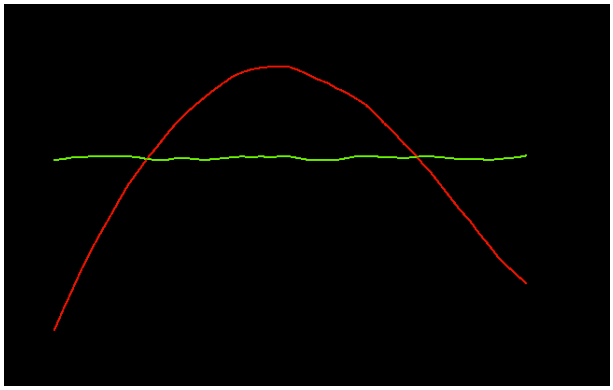

The deviation from a linear frequency scale (measured pixel positions - best linear fit, red curve) is in the order of ± 3MHz. The green curve shows the corrected data where the error has been reduced to about 50 kHz over the 3 GHz band.

### C. Power linearity

A common problem when using CCDs is their partly nonlinear response as function of the incident light. While deviations of a few percent are acceptable for many applications, AOSs need a linearity of better than 1% over the complete operating range. To ensure this we characterize the power linearity of our CCDs with a stabilized pulsed light source, which is used to illuminate the CCD for well defined periods of time. Once the non-linearity has been measured it can be corrected to a level near 0.1% during data analysis.

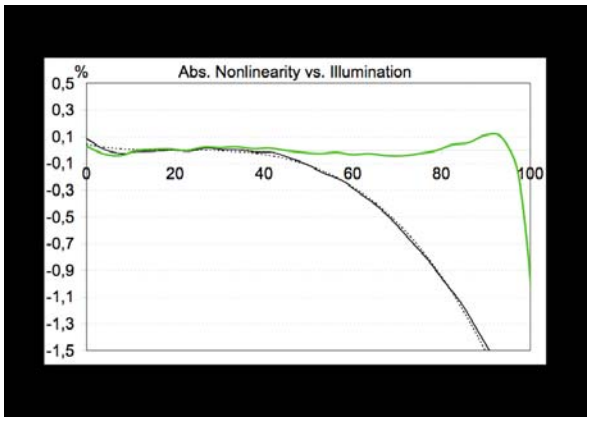


The figure shows the non-linearity of the Fairchild CCD-191. The black line is the measured non-linearity, the green curve is the corrected data. The corrected CCD has a non-linearity near 0.1% up to an illumination of about 95%.

### D. Stability

The stability of the instrument is determined by the Allan Variance. A typical Allan baseline plot is shown below. The straight line (blue) corresponds to the radiometric noise for a fluctuation bandwidth of 1.4 MHz. The reference value of 1.4 MHz is determined by the filter curve of the backend. The fact that for low integration times the variance of the baselines lies on to of the theoretical value shows that the BAOS does not contribute any noticeable noise to the measurement.

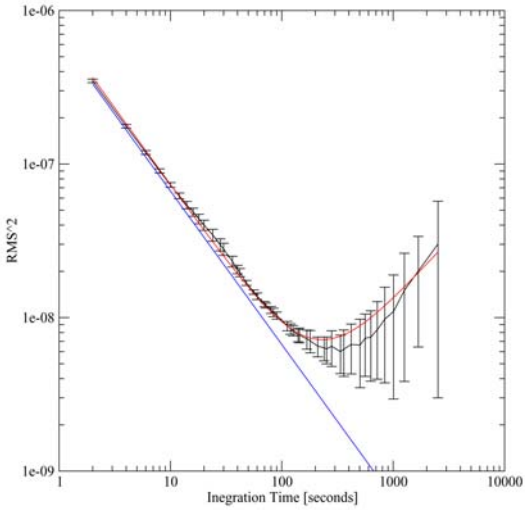


The Allan Baseline stability of the BAOS shows the variances of baselines for different integration times. The straight line (blue) is the radiometric noise for a fluctuation bandwidth of 1.4MHz.

Examples of the integrated baselines (sig-ref)/(ref-zero) are shown below. The top curve (red) corresponds to an integration time of two seconds and is pure radiometric noise without any noticeable instrument contribution. The lower curve (blue), which corresponds to a integration time of 2520 seconds, is completely dominated by the BAOS. From its shape it can be deduced that the excess noise is caused by laser speckles. The mid curve (green) is a typical baseline after 336 seconds integration time, which corresponds to the Allan minimum time in the above plot. Here the noise contains already some minor contributions from the laser speckles.

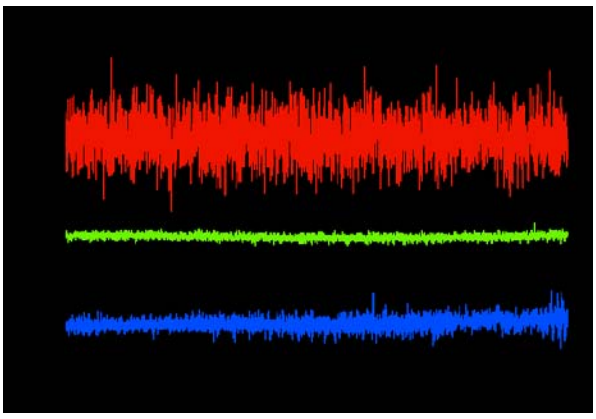

Sample baselines for various integration times. The upper curve (red) corresponds to a integration time of 2 seconds and is purely radiometric noise. The mid curve (green) corresponds to the Allan minimum time (here about 300 seconds) and has a RMS that is slightly higher than expected for radiometric noise. The bottom curve (blue) corresponds to 2520 seconds integration time and is completely dominated by laser speckles from the BAOS.

## V. Conclusion

The performance of the backend is summarized in the table below.

**BAOS specifications**

| | |
|---|---|
| Total bandwidth | 3 GHz |
| Number of valid frequency pixels | ≈ 5300 |
| Channel spacing | ≈ 560 kHz |
| Resolution bandwidth | ≈ 1.0 MHz |
| Fluctuation bandwidth | ≈ 1.4 MHz |
| Allan variance minimum time | > 300 sec |
| Noise dynamic range | ≈ 13 dB |
| Bandpass ripple | ≈ 4 dB |
| Frequency linearity | better 50 kHz after resampling |
| Power linearity | non-linearity < 1 % |

The spectrum below shows the „first light“ data taken in March 2007 with the KIRMA (Kiruna MW Radiometer) instrument in collaboration with U. Raffalski from the IRF, Kiruna, Sweden. It shows a 3 GHz spectrum of atmospheric Ozon lines around 210 GHz. The spectrum has been recorded with chop cycles of 5 seconds. The structure that is visible on the spectrum is caused by deficiencies of the frontend (compare the spectrum to the flat Allan baseline after 300 seconds), there is still some work to be done before the system can take full advantage of the BAOS.

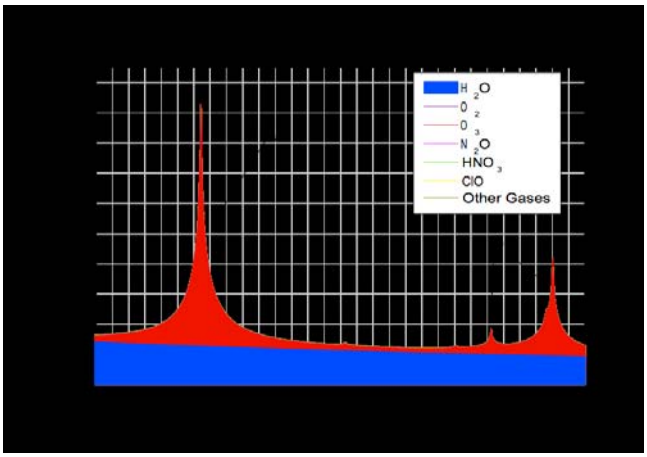


Model prediction of the Earth atmosphere at around 210 GHz. The blue underground is from water vapor in the atmosphere, the red lines are the expected Ozone emission features.

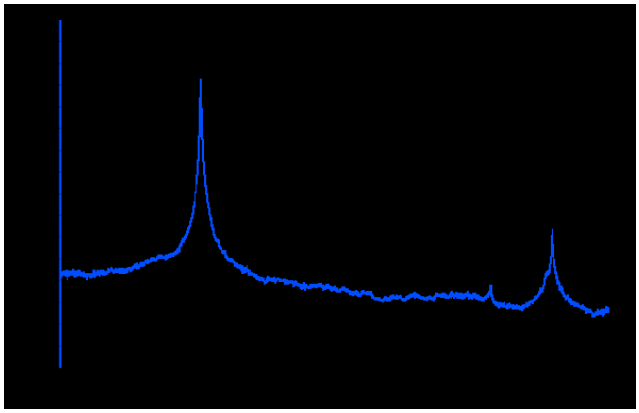

Sample Ozone spectrum at 210GHz observed with KIRMA and the BAOS.

## VI. ACKNOLEDGEMENTS

This work has been supported by the Deutsche Forschungsgemeinschaft (DFG) under special grant SFB 494.

# Correlators for (sub)mm radiometer applications

A. Emrich, S. Andersson
Omnisys Instruments AB, Gruvgatan 8, 421 30 Göteborg, Sweden

***ABSTRACT***

Two (sub)mm space interferometers are currently in various stages of development, the JPL GeoStar and the Omnisys/SES (ESA) GeoMS instruments. GeoStar is focused on the 53 and 183 GHz bands while 53, 89, 118, 155, 183, 340 and 380 GHz are considered for the GeoMS instrument but with 53 and 183 GHz as the core frequency bands. Omnisys is currently under contract to study cross correlators for both instruments and the results will be presented in this conference.

The autocorrelation spectrometer is one of 5 types of spectrometers being considered for space based (sub)millimetre heterodyne systems. The advantages of the digital autocorrelation spectrometer compared to Chirp Transform, Acousto Optical and Filterbank spectrometers are; stability, compactness, high reliability and variability in bandwidth and resolution. FFT spectrometers based on the latest generation of FPGA devices now promise a cost effective alternative for low to medium bandwidth applications with high resolution requirements. The Omnisys FFT spectrometers are presented in a separate poster.

Omnisys has designed and implemented several generations of autocorrelation chip sets and spectrometers. This range from the ODIN satellite spectrometers now in LEO to our current 8 GHz single chip spectrometer under development.

The ODIN chip set was a breakthrough at the time (1998). The power consumption was lowered by a factor of 50 compared to state of the art. Since then we have further improved the power consumption with a factor of 40, and we are now reaching 8 GHz of bandwidth for a single spectrometer chip.

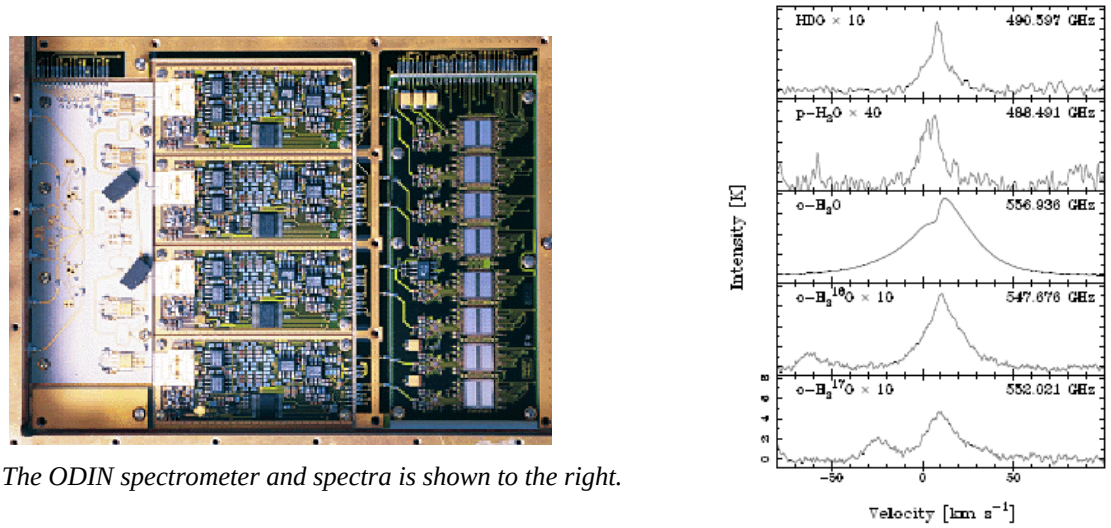


*Fig 1 The ODIN spectrometer and spectra is shown to the right.*

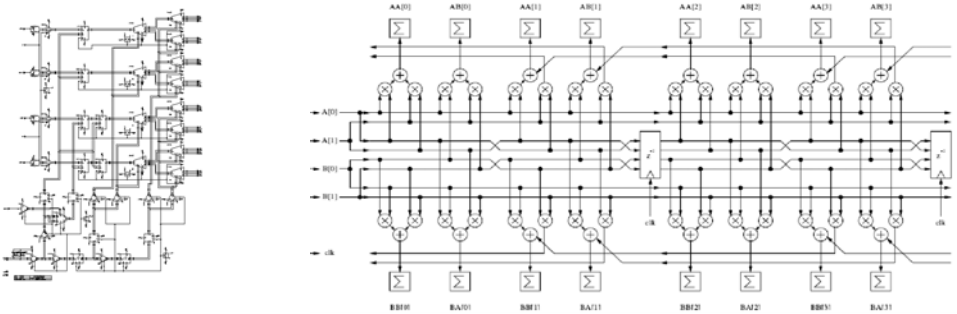

*Fig 2. Digitiser and correlator schematics for the 8 GHz / 1024 channel single chip spectrometer.*

Omnisys has now a tape out of a single chip spectrometer with 8 GHz bandwidth and 1024 channel resolution. The ADC is integrated on chip and can be configured for both real sampling as well as with complex sampling to facilitate an optimized IF downconverter architecture. This spectrometer can be configured for operation with 256, 512, 768 and 1024 channels. The maximum power consumption with 1024 channels at 8 GHz is estimated to be 2.8 W and with 256 channels, we will have a power consumption of about 1 W. Test results will be presented.

# The James Webb Space Telescope

Jonathan P. Gardner
NASA Goddard Space Flight Center

The scientific capabilities of the James Webb Space Telescope (JWST) fall into four themes. The End of the Dark Ages: First Light and Reionization theme seeks to identify the first luminous sources to form and to determine the ionization history of the universe. The Assembly of Galaxies theme seeks to determine how galaxies and the dark matter, gas, stars, metals, morphological structures, and active nuclei within them evolved from the epoch of reionization to the present. The Birth of Stars and Protoplanetary Systems theme seeks to unravel the birth and early evolution of stars, from infall onto dust-enshrouded protostars, to the genesis of planetary systems. The Planetary Systems and the Origins of Life theme seeks to determine the physical and chemical properties of planetary systems around nearby stars and of our own, and investigate the potential for life in those systems. To enable these for science themes, JWST will be a large (6.6m) cold (50K) telescope launched to the second Earth-Sun Lagrange point early in the next decade. It is the successor to the Hubble Space Telescope, and is a partnership of NASA, ESA and CSA. JWST will have four instruments: The Near-Infrared Camera, the Near-Infrared multi-object Spectrograph, and the Tunable Filter Imager will cover the wavelength range 0.6 to 5 microns, while the Mid-Infrared Instrument will do both imaging and spectroscopy from 5 to 28.5 microns. I review the status and capabilities of the observatory and instruments in the context of the major scientific goals.

# Clover – Measuring the CMB *B*-mode polarisation

**C. E. North**[1], P. A. R. Ade[2], M. D. Audley[3], C. Baines[4], R. A. Battye[4], M. L. Brown[3], P. Cabella[1], P. G. Calisse[2], A. D. Challinor[5,6], W. D. Duncan[7], P. Ferreira[1], W. K. Gear[2], D. Glowacka[3], D. J. Goldie[3], P. K. Grimes[1], M. Halpern[8], V. Haynes[4], G. C. Hilton[7], K. D. Irwin[7], B. R. Johnson[1], M. E. Jones[1], A. N. Lasenby[3], P. J. Leahy[4], J. Leech[1], S. Lewis[4], B. Maffei[4], L. Martinis[4], P. Mauskopf[2], S. J. Melhuish[4], D. O'Dea[3,5], S. M. Parsley[2], L. Piccirillo[4], G. Pisano[4], C. D. Reintsema[7], G. Savini[2], R. Sudiwala[2], D. Sutton[1], A. C. Taylor[1], G. Teleberg[2], D. Titterington[3], V. Tsaneva[3], C. Tucker[2], R. Watson[4], S. Withington[3], G. Yassin[1], J. Zhang[2]

***Abstract*— We describe the objectives, design and predicted performance of Clover, a fully-funded, UK-led experiment to measure the *B*-mode polarisation of the Cosmic Microwave Background (CMB). Three individual telescopes will operate at 97, 150 and 225 GHz, each populated by up to 256 horns. The detectors, TES bolometers, are limited by unavoidable photon noise, and coupled to an optical design which gives very low systematic errors, particularly in cross-polarisation. The telescopes will sit on three-axis mounts on a site in the Atacama Desert. The angular resolution of around 8′ and sky coverage of around 1000 deg$^2$ provide multipole coverage of $20<\ell<1000$. Combined with the high sensitivity, this should allow the *B*-mode signal to be measured (or constrained) down to a level corresponding to a tensor-to-scalar ratio of $r = 0.01$, providing the emission from polarised foregrounds can be subtracted. This in turn will allow constraints to be placed on the energy scale of inflation, providing an unprecedented insight into the early history of the Universe.**

## I. Introduction

Measurement of the cosmic microwave background (CMB) polarisation can provide information about the early universe not available from other observations alone. It will provide further constraints on cosmological parameters and break some of the existing degeneracies between them (see e.g. [1],[2]). The CMB fluctuations are polarised at about the 10% level. The polarisation field can be decomposed into two modes: the *E*-mode, a "grad-like" mode with even parity; and the *B*-mode, a "curl-like" mode with odd parity.

The primordial density perturbations which give rise to the large scale structure of matter in the Universe dominate the temperature anisotropies. These scalar perturbations generate only an *E*-mode polarisation with an r.m.s. of ~5 μK. The *E*-mode power spectrum and its correlation to the temperature power spectrum have been measured by several experiments

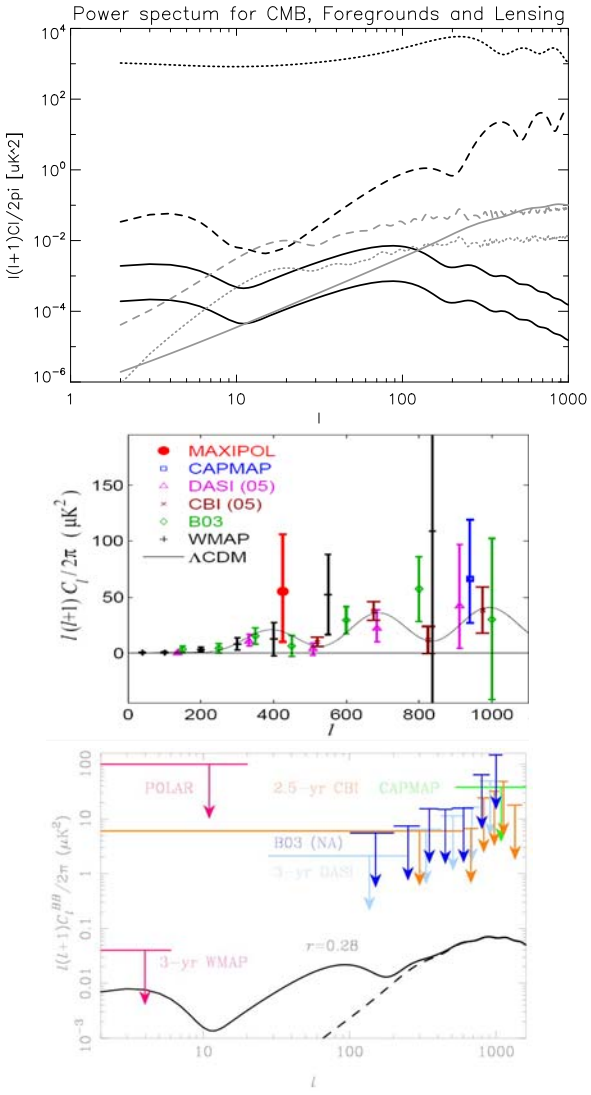


Figure 1: Top: Angular power spectrum of the CMB, showing the power in the spherical harmonics associated with multipole $l$ (where $l \approx 180°/\theta$). Shown are the temperature (black dotted), *E*-mode (black dashed) and *B*-mode (black solid; upper: $r = 0.1$, lower: $r = 0.01$) for the CMB. For comparison, we show the *B*-mode from weak gravitational lensing (grey solid), as well as galactic synchrotron (grey dashed) and thermal dust (grey dotted) emission at 100 GHz. The levels of the galactic emission are based on very simple models, so are for rough comparison only, and are calculated in regions of low emission. Bottom left: current *E*-mode power spectrum results compared with the ΛCDM model (from [5]). Bottom right: current limits on the *B*-mode power spectrum compared with a model for $r = 0.28$ (solid black line) and the weak lensing contamination (dashed line).

[1] Oxford Astrophysics, University of Oxford, UK
[2] School of Physics and Astronomy, Cardiff University, UK
[3] Cavendish Laboratory, University of Cambridge, Cambridge, UK
[4] School of Physics and Astronomy, University of Manchester, UK
[5] Institute of Astronomy, University of Cambridge, UK
[6] DAMTP, University of Cambridge, UK
[7] National Institute of Standards and Technology, USA
[8] University of British Columbia, Canada

This paper describes the current design for Clover, which is currently under review and may change in the future.

(e.g. [3],[4],[5]).

Theories of inflation predict the quantum generation of primordial gravitational waves and these propagated through the early universe, further polarising the CMB. These tensor perturbations cause both *E*-mode and *B*-mode signals, but at much lower level than the scalar perturbations. Measurement of the *B*-mode signal due to gravitational waves would allow direct measurement of the tensor-to-scalar ratio, *r*, the value of which can be linked directly to the energy scale of inflation. Measuring the value (or upper limit) of this would thus place constraints on inflationary theories.

Current measurements constrain *r* to less than 0.28 [6]. For $r = 0.01$, the *B*-mode signal is around 10 nK, so excellent control and knowledge of systematic effects is required for its detection.

Spurious *B*-mode signals are cause by both astrophysical and systematic effects. Astrophysical signals include extragalactic point sources, as well as diffuse galactic synchrotron and thermal dust emission. Weak gravitational lensing of the *E*-mode signal also causes spurious *B*-mode signal, which exceeds the primordial signal on small angular scales (see Figure 1).

Clover is a project intended to measure the *B*-mode polarisation of the CMB. It is a collaboration between the Universities of Oxford, Cambridge, Cardiff and Manchester. Detector readout technology is supplied by the University of British Columbia (UBC) and the National Institute of Standards and Technology (NIST). Clover will comprise three telescopes operating at central frequencies of 97, 150 and 225 GHz with 30% bandwidth. The spectral coverage is intended to allow separation of the CMB from the foreground contaminants. Each telescope will have a Compact Range Antenna optical system, which gives exceptionally low aberrations and cross-polarisation across a large focal plane. Each focal plane will be populated with arrays of polarimeters. Each pixel consists of a horn directly coupled to two transition edge sensor (TES) detectors, one for each polarisation. The polarisation of each pixel will be rotated so that each individual detector will independently measure the Stokes parameters, *I*, *Q* and *U*, removing the need for detector differencing. The TESs give background-limited sensitivity and can be manufactured in large quantities using lithographic techniques.

The science goals of Clover are:

- Measure *r*, for $r > 0.01$, by characterizing the *B*-mode polarisation power spectrum.
- Make sample-variance limited measurements of the temperature, *E*-mode and *T-E* cross-correlation power spectra over ~1000 deg$^2$.
- Measure the *B*-modes from weak gravitational lensing.
- Improve constraints on cosmological parameters.
- Determine or constrain the energy scale of inflation.
- Characterise the polarised Galactic foregrounds in regions of low emission.

TABLE 1
INSTRUMENT REQUIREMENTS

| Instrument Characteristic | Requirements |
|---|---|
| Stokes parameters measured | *I*, *Q* and *U* **at each detector** |
| Multipole range | $20 < l < 1000$ |
| Resolution | 8 arcmin |
| Sky area | 1000 deg$^2$ |
| Noise limit | Unavoidable photon noise |
| Detector NET at 97, 150, 225 GHz | 150, 225, 590 μKs$^{0.5}$ |
| Detector NEP at 97, 150, 225 GHz | 2, 4, 8 x $10^{-17}$ WHz$^{-0.5}$ |
| # Detectors at 97, 150, 225 GHz | 338, 504, 504 |
| Polarisation beam alignment | < 0.2% FWHM |
| Average beam ellipticity | < 0.85 |
| Differential eccentricity[a] | < 0.012 |
| Residual Q↔U rotation (cross-pol) | < 0.24° (< 1.4%) |
| Q,U loss (depolarization) | < 10% |
| Residual T→Q,U mixing (depolarization) | < 0.015% |
| Polarisation modulation efficiency | 90% |
| Absolute Calibration | 5% |

[a] Differential eccentricity is the difference in eccentricity between beams of the two orthogonal polarisations.

## II. INSTRUMENT DESCRIPTION

### A. Requirements

The ambitious science goals of Clover mean that the instrument requirements are very stringent. Some of the requirements are listed in Table 1. The particularly stringent optics requirements are the $Q \leftrightarrow U$ rotation (cross-polarisation), the differential eccentricity, and the residual $T \rightarrow Q,U$ mixing (instrumental polarisation).

### B. Optics

The Compact Range Antenna optical design of Clover [7] gives excellent cross-polarisation performance and low aberrations, as shown in Figure 3 for the 97 GHz. The large, flat focal plane means that the edge pixels have poorer performance than the central pixel, but these still meet the requirements given in Table 1. Sidelobes caused by diffraction around the mirrors are absorbed by the co-moving ground shield. The sidelobe at -50° (bottom panel of Figure

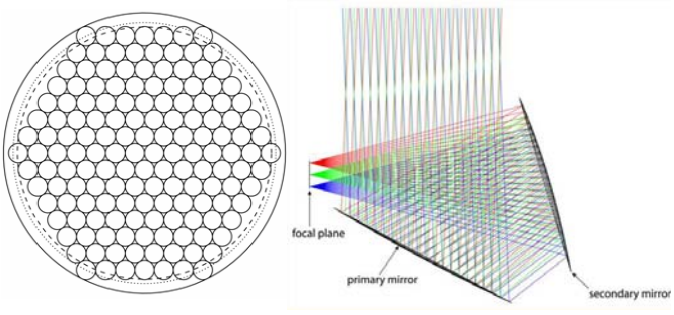


Figure 2: Left: layout of the 97 GHz hex-packed focal plane array. Right: optics ray diagram, showing the parabolic primary mirror, hyperbolic secondary mirror and the flat focal plane. The field of view of the whole array is around 2°.

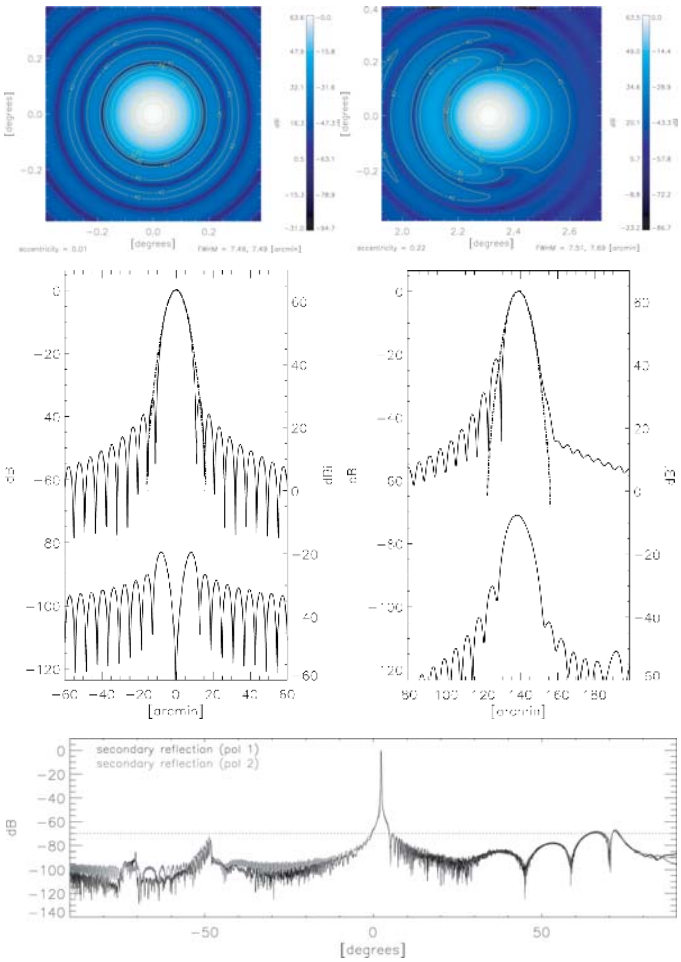


Figure 4: 97 GHz Optics performance. Top row: Beam maps of the central feed (left) and an edge feed (right). Middle row: Main beam cuts of the central feed (left) and an edge feed (right), showing the co-polar (top solid line), cross-polar (bottom solid line) and Gaussian approximation (dot-dashed line). Bottom: Far sidelobes of an edge pixel, up to 100° either side of the main beam for both polarisations.

3) is caused by an additional reflection off the secondary mirror.

The 97 GHz mirrors will both be around 1.8 m in diameter. The primary mirror has an offset parabolic shape, and the secondary mirror is an offset inverse (i.e. concave) hyperboloid.

### C. Polarimeter

Each pixel in the array comprises a single feed horn directly coupled to two TES detectors. Between the two will be an Orthomode Transducer (OMT), which splits the signal into two orthogonal polarizations. In front of the focal plane will be a single achromatic half-wave plate (AHWP) [8],[9]. This is a stack of three sapphire plates forming a birefringent layer. When rotated at angular speed $\omega$, the polarisation angle of the incoming radiation is rotated in such a way that the outputs of the two detectors are:

$$D_1(t) = I - Q\cos(4\omega t) - U\sin(4\omega t)$$
$$D_2(t) = I + Q\cos(4\omega t) + U\cos(4\omega t) \quad (1)$$

Rotating the AHWP ensures that each detector measures both $Q$ and $U$, modulated as shown in (1).

### D. Feed Horns

The requirement on the horns is that they have cross-polarisation below -30dB, sidelobes below -25dB and average return loss below -20dB. The chosen design is an electroformed, corrugated, Winston-like profile horn. At 97 GHz the horns have an aperture diameter of around 18 mm and a length of around 70 mm. At 150 and 225 GHz, the apertures are scaled by frequency to around 10 mm and 8 mm respectively. Measurements of prototype horns have shown excellent agreement to models, as shown in Figure 4.

### E. Orthomode Transducers

At 97 GHz, the OMT will be an electroformed turnstile junction OMT [10]. This design accepts circular waveguide input and outputs perpendicular polarisations into rectangular waveguide. Prototype measurements have confirmed that the OMT has better than -20dB return loss and below -40dB isolation between the two outputs (i.e. cross-polarisation). The rectangular waveguide outputs are coupled to the detector chips through a finline transition (see below).

At 150 and 225 GHz the OMT will be a cylindrical waveguide with four rectangular probes. Signals from opposite probes will be combined in planar circuitry and then connected directly to the TES detectors. This has the advantage that the rectangular probe OMT and TES detectors can be on the same chip. Simulations have predicted a return loss of -20dB and isolation of -60dB. Scale models are currently being designed and tested.

### F. Finline Transition

The rectangular waveguide output of the 97 GHz OMT is transformed into microstrip using a finline transition [11],[12]. The finline chip, which has a 225 μm thick silicon substrate, sits across the middle of the waveguide, supported in a groove. "Fins" of 500 nm thick superconducting niobium (Nb) are tapered in smoothly until they overlap, forming antipodal finline. The structure behaves as unilateral finline when the distance between the fins is much larger than the 400 nm of $SiO_2$ separating them.

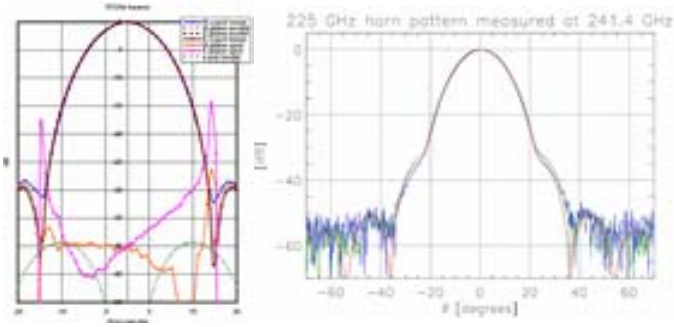


Figure 3: Measurements of prototype horns for 97 GHz (left) and 225 GHz (right) channels. Comparison to models is shown, with the data being indistinguishable from the models down to the -30dB level.

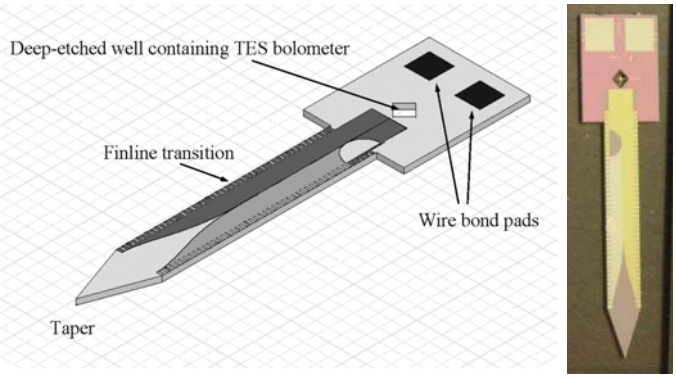


Figure 6: A schematic of the finline chip (left), and a photo of a prototype (right). The point at the end forms a transition from unloaded waveguide to waveguide loaded with Silicon. The TES detector sits in the diamond-shaped well at the end of the microstrip.

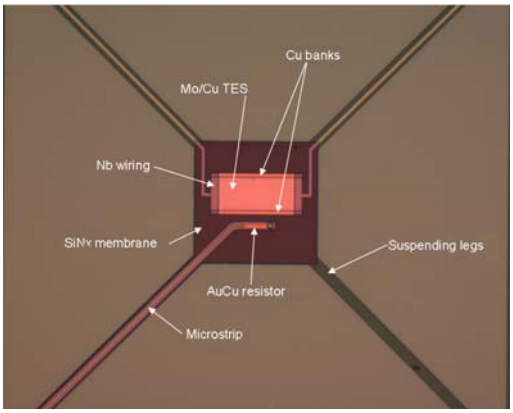


Figure 5: Schematic of the detector well, showing the microstrip terminating at the AuCu resistor and the Mo/Cu TES in the well. The nitrite suspension legs control the thermal conductance.

The transition from antipodal finline to microstrip is through a semicircular structure, where the outer edge of the top layer is brought in towards the centre (making the strip), then the inner edge of the bottom layer is brought out (forming the ground plane of the microstrip) (see Figure 6). Serrations of Nb sit in the waveguide groove to cut off other modes propagating in the waveguide. The 3 μm wide microstrip leads to a resistor on a $SiN_x$ membrane in the deep-etched well, seen as the diamond shape in Figure 6.

### G. Detectors and Readout

The Clover detectors are Mo/Cu TES bolometers [13] sitting on a 500 nm thick $SiN_x$ membrane in a 660 μm square well in the substrate. The Nb microstrip input is terminated in an AuCu resistor (see Figure 5). Thermal conductance to the thermal bath is controlled by four nitride legs. The critical temperature of the TESs' transition, between superconducting and normal behaviour, is about 190 mK (430 mK for 220GHz). They are cooled to 100 mK (230 mK for 225 GHz) in order to achieve the target NEPs (see Table 1). The chips are manufactured on Si wafers and cut into individual devices using Deep Reactive Ion Etching (DRIE) to ensure 100% cover of the focal plane. Prototype measurements have shown that the TES films are of high quality, and the devices have an electrical NEP close to the phonon noise level. While the thermal conductance of the nitride legs needs to be adjusted to achieve the required power handling, the prototype results show that the detectors have sharp resistance changes at the superconducting transition ($\alpha$=500 for $\log(R)=\alpha.\log(T)$) and fast rise times (1/*e* rise times of ~150 μs).

The readout and subsequent amplification is provided by a three-stage SQUID system. The MUX chips will all connect to Multi-channel electronics (MCE) supplied by UBC. The 32x1 multiplexer (MUX) chips supplied by NIST [14],[15],[16] lend themselves to linear arrangements of detectors. For this reason, the focal plane is split into rows, with 22 rows making up the 97 GHz focal plane. Each row of 16–20 detectors will be held in a single split block (see Figure 8).

### H. Cryogenics

The base temperature at which the detectors operate is reached by a three-stage (97 and 150 GHz) or two-stage (225 GHz) cryogenic system. The requirements on the cryogenic system are to provide 3 μW of cooling power at the base temperature. The temperature stability of the system must be 60 $nK/Hz^{0.5}$ with long-term stability of 3.5 μK over the 24 hour duty cycle. At 97 and 150 GHz, the system uses a CryoMech PT410 pulse tube cooler (PTC) to cool to 4 K, a closed-cycle He-7 sorption fridge down to 0.4 K, and a closed-cycle dilution refrigerator [17] to reach 100 mK. At 225 GHz there will again be a PT410 PTC, followed by a

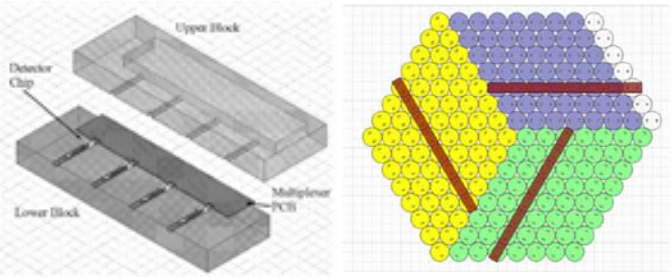


Figure 8: The design of the detector block at 97 GHz (left), and the concept behind the arrangement of the linear blocks in the focal plane (right). The two halves of the split block form the waveguide into which the finlines protrude.

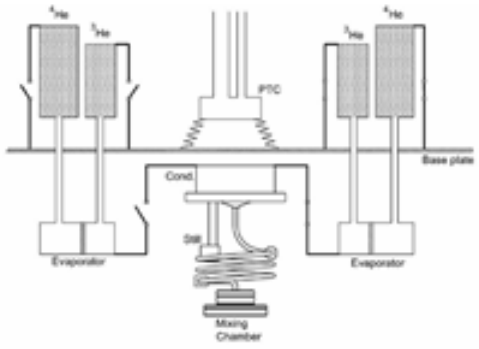


Figure 7: Schematic of the 97 GHz cryogenic system, showing the PTC (top middle), the sorption refrigerators (left and right), and the dilution refrigerator (bottom middle

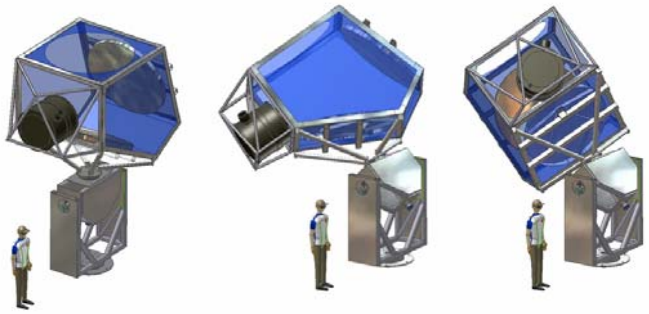

Figure 9: Three views of the 97 GHz mount showing its ability to rotate around three axes. The optical assembly, containing the 1.8 m mirrors, will be lined with an unpolarised absorber to reduce the effects of sidelobes.

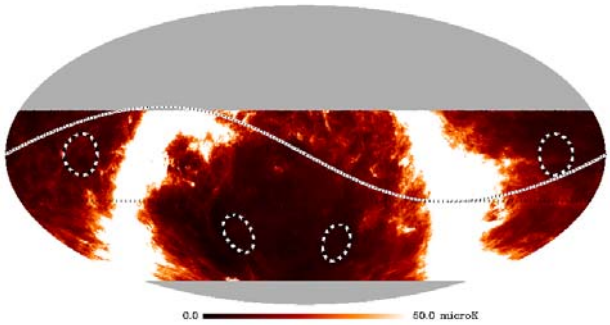


Figure 10: Mollweide projection of the sky in equatorial coordinates showing the Clover fields (black/white circles) relative to the site latitude (black line), the ecliptic plane (black/white dotted line) and the estimated galactic foreground emission at 97 GHz from toy models (greyscale).

He-10 sorption cooler to reach 250 mK. The closed-cycle nature means that there will be no cryogenic consumables. To reduce vibrations flexible stainless steel lines will lead to the PTC motor and expansion stage.

Band-pass and thermal filtering will be provided by a stack of metal-mesh filters. The maximum possible size of these filters (300 mm) is what limits the focal plane size, and hence the number of horns; this it the reason for the reduced number of horns at 97 GHz (169 rather than 202 at the higher frequencies).

### *I. Mount*

Each telescope will have its own mount, with the sizes roughly scaled with the frequency. The mount must be rotate fully in azimuth and reach elevations from 0–89.5°. As a further modulation of the polarisation signal, the mount will rotate the telescope around the optical axis. To move the science signals away from the atmospheric noise, the mount must be able to scan at speeds of at least 3 deg.s$^{-1}$ on the sky, and have sufficient acceleration to keep the turnaround time as low as possible (see below). The pointing accuracy must be 20 arcsec, with long-term tracking accuracy of 60 arcsec. The 97 GHz mount design (without counterweights for clarity) is shown in Figure 9.

## III. Site and Observations

Clover will be sited at Llano de Chajnantor, Chile, in the Atacama Desert. The high altitude (5080 m) places it above nearly half the atmosphere and most of the water vapour. The area is a popular one for millimetre and sub-millimetre experiments (e.g. ALMA, CBI, ACT, CCAT, etc.), as it is very dry and still accessible.

The latitude of the site (-23°) means that a good proportion of the sky is observable. Since contamination from Galactic foregrounds is a major issue for CMB *B*-mode experiments, the ability to select locations out of the galactic plane is vital. The required 1000 deg$^2$ of sky area is divided into four convex fields, spread roughly evenly in right ascension to maximise the observing efficiency throughout the year (see Figure 10).

In order to control the atmospheric noise as much as possible, Clover will perform fast constant-elevation scans over each field as it rises and falls each night. The observations will continue for two years, giving ~0.8 years of integration time needed to achieve the final required sensitivity.

Calibration for CMB polarisation experiments is particularly challenging, as there are few well-characterised, polarised, non-variable astronomical sources at mm wavelengths. Possible sources are extragalactic radio sources (e.g. Tau A) and planets (though planets are not highly polarised). While an absolute calibration of 5% should be possible from existing or planned data (e.g. WMAP, Planck), it is likely that characterisation of systematic effects will require additional calibration, possibly from an artificial source.

## IV. Data Analysis and Predictions

The fast detector speed and the large number of detectors mean that Clover will produce a very high volume of data. The usual data analysis procedures (e.g. deglitching, de-striping, etc.) will have to be applied to this data set in order to generate the final maps.

An additional challenge for *B*-mode experiments will be the removal of the foreground signals, particularly the galactic synchrotron and dust emission. The spectral coverage of Clover means that component separation should be possible, though it will probably require significantly more knowledge of the foregrounds than exists at the moment. For example, current data has a low signal-to-noise in the low emission areas of sky that we will target, and is either at too low a frequency (e.g. 1.4 GHz [18]) in the case of synchrotron emission or too high a frequency (e.g. 350 GHz [19] or 100 μm [20]) in the case of thermal dust emission. Much work is being done to make better predictions and observations of these signals (e.g. [21],[22]). Future all sky surveys at higher frequencies (e.g. CBASS at 5 GHz) will provide a lot of data on the synchrotron emission. This will also be at a frequency high enough to neglect Faraday rotation, which is a major problem when extrapolating from lower frequencies.

## SUMMARY

Clover has a unique instrument design which provides excellent control of systematic errors. This is required to complete the main science goal of characterising the CMB *B*-mode signal due to gravitational waves from inflation. The sensitivity will be good enough to measure or constrain the *B*-modes down to a level corresponding to a tensor-to-scalar ratio of $r = 0.01$, providing the polarised foreground emission can be subtracted.

The 97 GHz Clover telescope is in the final stages of the design phase, and is planned to be on the site towards the end of 2008, and will be installed, commissioned and tested over the following year. The 150 GHz instrument is planned to be shipped in mid-2009 and the 225 GHz in late 2009.

## ACKNOWLEDGMENT

Clover is funded by the Science and Technology Facilities Council. CEN acknowledges a STFC studentship.

## REFERENCES

[1] W. Hu, M. White, 1997, *A CMB Polarization Primer*, New Ast., **2**, 323

[2] A. Challinor, 2005, *Constraining fundamental physics with the cosmic microwave background*, arXiv:astro-ph/0606548v1

[3] J. M. Kovac, E. M. Leitch, C. Pryke, J. E. Carlstrom, N. W. Halverson, W. L Holzapfel, 2002, *Detection of Polarization in the Cosmic Microwave Background using DASI*, Nature, **420**, 722

[4] J. L. Sievers, C. Achermann, J. R. Bond, et al., in press, *Implications of the Cosmic Background Imager Polarization Data*, arXiv:astro-ph/0509203v2

[5] J. H. P. Wu, J. Zuntz, M. E. Abroe, et al., in press, *MAXIPOL: Data Analysis and Results*, arXiv:astro-ph/0611392

[6] D. N. Spergel, R. Bean, O. Doré, et al., in press, *Wilkinson Microwave Anisotropy Probe (WMAP) Three Year Results: Implications for Cosmology*, arXiv: astro-ph/0603449v2

[7] G. Yassin, P. K. Grimes, S. B. Sorenson, 2005, Proc. of the 16th Int. Symp. on Space Terahertz Technology, Gothenburg, Sweden

[8] G. Savini, G. Pisano, P. A. R. Ade, 2006, *Achromatic half-wave plate for submillimeter instruments in cosmic microwave background astronomy: modeling and simulation*, Applied Optics, **45**, 35, 8907–8915.

[9] G. Pisano, G. Savini, P. A. R. Ade, V. Haynes W. K. Gear, 2006, *Achromatic half-wave plate for submillimeter instruments in cosmic microwave background astronomy: experimental characterization*, Applied Optics, **45**, 27, 6982–6989

[10] G. Pisano, L. Pietranera, K. Isaak, L. Piccirillo, B. R. Johnson, B. Maffei, S. Melhuish, 2007, *A Broadband WR10 Turnstile Junction Orthomode Transducer*, IEEE Microwave and Wireless Components Letters, **17**, 4, 286–288

[11] C. E. North, G. Yassin, P. K. Grimes, 2006, *Rigorous Analysis and Design of Finline Tapers for High Performance Millimetre and Submillimetre Detectors*, Proc. of the 17th Int. Symp. on Space Terahertz Technology, Paris, France, in press

[12] G. Yassin, S. Withington, M. Buffey, K. Jacobs, S. Wulff, 2000, *A 350 GHz SIS Antipodal Finline Mixer*, IEEE Trans. on Microwave Theory and Techniques, **48**, 662

[13] M. D. Audley, R. W. Barker, M. Crane, et al., 2006, *Prototype finline-coupled TES bolometers for CLOVER*, Proc. of the 17th Int. Symp. on Space Terahertz Technology, Paris, France, arXiv:astro-ph/0608285v1

[14] Reintsema, C.D, J. Beyer, S.W. Nam, S. Deiker, G.C. Hilton, K. Irwin, J. Martinis, J. Ullom,L.R. Vale, M. MacIntosh 2003, *A Prototype System for Time-Domain SQUID Multiplexing of Large-Format Transition-Edge Sensor Arrays*, Review of Scientific Instruments, **74**, 4500

[15] Chervenak, J.A., K.D. Irwin, E.N. Grossman, J.M. Martinis, C.D. Reintsema, and M.E. Huber 1999, *Superconducting multiplexer for arrays of transition edge sensors*, Applied Physics Letters, **74**, 4043—4045

[16] P.A.J. de Korte , J. Beyer , S. Deiker, G.C. Hilton, K.D. Irwin, M. MacIntosh , S.W. Nam, C.D. Reintsema, L.R. Vale and M.E. Huber 2003, *Time-Division SQUID Multiplexer for Transition-Edge Sensors, Review of Scientific Instruments*, **74**, 3807

[17] G. Teleberg, S. T. Chase, L. Piccirillo, 2006, *A miniature dilution refrigerator for sub-Kelvin detector arrays*, Proceedings of SPIE, **6275**, 62750D

[18] L. La Porta, C. Burigana, W. Reich, P. Reich, 2006, *An angular power spectrum analysis of the DRAO 1.4 GHz polarization survey: implications for CMB observations*, A&A, **455**, 2, L9 – L12

[19] N. Ponthieu, J. F. Macías-Pérez, M. Tristram, P. Ade, A. Amblard, et al., 2005, *Temperature and polarization angular power spectra of Galactic dust radiation at 353 GHz as measured by Archeops*, A&A, **444**, 327–336

[20] D. P. Finkbeiner, M. Davis, D. J. Schlegel, 1999, *Extrapolation of Galactic Dust Emission at 100 Microns to Cosmic Microwave Background Radiation Frequencies Using FIRAS*, ApJ, **524**, 2, 867–886

[21] C. Burigana, L. La Porta, W. Reich, et al., 2006, *Polarized Synchrotron emission*, Proc. of CMB and Physics of the Early Universe, Ischia, Italy, arXiv:astro-ph/0607469v1

[22] E. Carretti, G. Bernardi, S. Cortiglinoi, 2006, *B-mode contamination by synchrotron emission from 3-yr Wilkinson Microwave Anisotropy Probe data*, MNRAS, **373L**, 93C

# ESPRIT – A Far-Infrared Space Interferometer

W. Wild[a,d,*], Th. de Graauw[a,c], A. Baryshev[a,d], J. Baselmans[a], A. Bos[b], J.R. Gao[a,e], A. Gunst[b], F. Helmich[a,d], R. ter Horst[b], B. Jackson[a], V.P. Koshelets[f,a], P. Maat[b], J. Noordam[b], P. Roelfsema[a,d], L. Venema[b], N. Whyborn[a], and P. Yagoubov[a]

[a] SRON Netherlands Institute for Space Research, POBox 800, 9700 AV Groningen, the Netherlands
[b] ASTRON, Dwingeloo, POBox 2, 7990 AA, Dwingeloo, the Netherlands
[c] Leiden Observatory, POBox 9513, 2300 RA Leiden, the Netherlands
[d] Kapteyn Astronomical Institute, University of Groningen, 9700 AV Groningen, the Netherlands
[e] Kavli Institute of Nanoscience, Delft University of Technology, Lorentzweg 1, 2628 CJ Delft, NL
[f] Institute of Radio Engineering and Electronics, Russian Academy of Science, Mokhovaya 11, 125009, Moscow, Russia.

## ABSTRACT

In the far-infrared (FIR) / THz regime the angular (and often spectral) resolution of observing facilities is still very restricted despite the fact that this frequency range has become of prime importance for modern astrophysics. ALMA (Atacama Large Millimeter Array) with its superb sensitivity and angular resolution will only cover frequencies up to about 1 THz, while the HIFI instrument for ESA's Herschel Space Observatory will provide limited angular resolution (10 to 30 arcsec) up to 2 THz. Observations of regions with star and planet formation require extremely high angular resolution as well as frequency resolution in the full THz regime. In order to open these regions for high-resolution astrophysics we propose a heterodyne space interferometer mission, ESPRIT (Exploratory Submm Space Radio-Interferometric Telescope), for the Terahertz regime inaccessible from ground and outside the operating range of the James Webb Space Telescope (JWST). This interferometer will use coherent detectors in the range 0.5 to 6 THz on six free-flying telescopes and a distributed correlator.

**Keywords:** Submillimeter wave receivers, Interferometry, Space mission, Space Instrumentation, Radio astronomy, FarInfrared, Submillimeter.

## 1. INTRODUCTION

The study of star and planet formation is one of the prime topics in modern astrophysics. Important questions include the physical conditions for star-formation to occur, the evolution of circum-stellar disks, the decoupling of dusty proto-planetary regions from the gas, and the chemistry that leads to the pre-biotic conditions of early Earth-like planets. In addition, current research concerns the question what role star-formation, and in particular starbursts, play in external galaxies and how this interacts with the general interstellar medium.

The phenomena connected to star and planet formation are best studied in the far-infrared/Terahertz regime (0.5 THz to several THz). This wavelength range holds the most important spectral signatures of the material (atoms, ions, molecules) as it is processed. The low extinction at these long wavelengths allows unique observations of details of the star formation process, in particular during its early phases, when these regions are completely obscured by the surrounding dust.

The Earth atmosphere severely limits the possibility to observe at THz frequencies from ground-based observatories. ALMA will cover the atmospheric windows at very high angular resolution up to about 1 THz which is the limit for observations even from high-altitude sites (with the exception of a few small atmospheric windows around 1.3 and 1.5 THz accessible only from the very best sites on Earth).Astronomical observations above 1 THz need to be done from space. However, all past, current and planned missions have limited angular resolution. The relatively small ratios of aperture diameter to wavelength, like for example in ISO, Spitzer Space Telescope and Herschel, provide only angular resolutions of the order of 5 arcsec in the 100μm region. This does not match the 0.1 arcsec resolution which is required for these studies. In order to achieve the required angular resolution, to investigate for example the distribution of key molecules in a circum-stellar disk, application of interferometer techniques in space is the only way forward. At the same time, high spectral resolution is required to measure the chemical composition, the dynamics and other physical conditions. In particular, studies of water and other hydrides, are of prime interest for the star formation process.

* W.Wild@sron.rug.nl; phone +31-(0)50-363 4074.

A mission concept that combines all these capabilities is uniquely suited to address these questions: a free-flying, 6 element, far-infrared imaging interferometer using heterodyne detection: ESPRIT – the Exploratory Submm sPace Radio-Interferometric Telescope. Here we will present the ESPRIT mission concept including science goals, configuration aspects, the needed receiver, local oscillator and correlator technology as well as cooling and system considerations.

## 2. MISSION CONCEPT

### 2.1 ESPRIT baseline design

Table 1 gives the main characteristics of ESPRIT. The 6-element interferometer with 15 baselines will be in a free-flying configuration with precise metrology to determine the exact position of each satellite. The array will fly in a constantly moving configuration filling the u-v plane (see below). In a preliminary trade-off between signal strength, primary beam size and practical considerations, it appears that a 3.5 to 4 meter diameter of the primary mirrors would satisfy the overall mission goals.

Table 1. The main characteristics of ESPRIT

| *Item* | *Value (at 100 μm / 3 THz when no wavelength / frequency is specified)* | *Goal* | *Satisfies Science requirement* |
|---|---|---|---|
| # of telescopes | 6 (15 baselines) | >6 | Sensitivity |
| Telescope design | 3.5m off-axis | 4m off-axis | |
| Configuration | Free-flying 3-D | | |
| Projected baselines | 7 – 200 – 1000m | | Spatial resolution |
| Frequencies | Several ranges between 0.5 and 6 THz | | Spectral coverage |
| Spectral resolution | 1 km/s | 0.1 km/s | Spectral resolution |
| Field-of-view | 6 arcseconds | | |
| Angular resolution | <0.02 arcseconds | | Spatial resolution |
| Pointing accuracy | 0.3 arcseconds | | |
| Image dynamic range | >100 | | Image quality |
| Spectral dynamic range | >1000 | | Image quality |
| T(sys) | <1000K | | Sensitivity |
| Mixer technology | SIS/SIR up to ~1.5 THz<br>HEB > 1.5 THz | | Wavelength coverage |
| IF bandwidth | 4 GHz | 8 GHz | Velocity coverage |
| Local Oscillators | FFO for SIR channels<br>Multiplier chain up to ~2-3 THz<br>QCL > 2-3 THz | | Wavelength coverage |
| Correlator | Distributed with base -bands | | |
| Metrology | <1 micrometer (total in all directions) | | |
| Cooling | Mixers < 4K, ambient telescope (70K) | | Sensitivity |

From ground-based interferometer experience it is evident that in order to get an acceptable imaging capability one needs a minimum of 6 antenna elements. Each antenna will be equipped with a number of heterodyne receivers – possibly small arrays - covering selected ranges between 0.5 and 6 THz (600μm to 50μm). The exact choice of frequencies will depend on the scientific priorities, and the number of receivers as well as pixels for the arrays will depend on technical limitations (mass, size, cooling power, correlator etc.).

A distributed correlator seems to be the most practical solution for this mission. Pointing requirements are proportional to the diffraction diameter and are roughly a factor of 10 more stringent than is being provided today in ESA's space missions. An important point is the aim to have all six satellites put into space with a single launch. A telescope design with subreflectors that unfold after leaving the launch vehicle in space would make this feasible. ESPRIT is preferably situated in the Sun-Earth Lagrange point L2 about 1.5 million km from Earth because of thermal stability.

### 2.2 Interferometer considerations

The six satellites of ESPRIT will be positioned in space in a three dimensional configuration to avoid collision danger (Fig. 1). By combining the down converted and digitized signals of the elements in a correlator a set of complex visibilities are obtained corresponding to different locations in the sky Fourier transform plane. Thus by Fourier transforming these visibilities an image of the sky is obtained. Different configurations are being studied. A simple radial

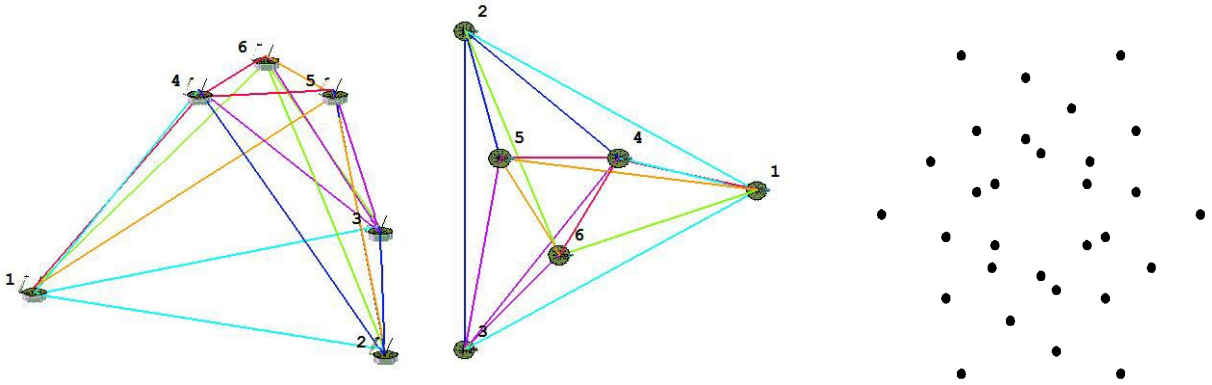


Figure 1. Three-dimensional instantaneous ESPRIT array configuration (left) and corresponding instantaneous coverage of the UV-plane (right).

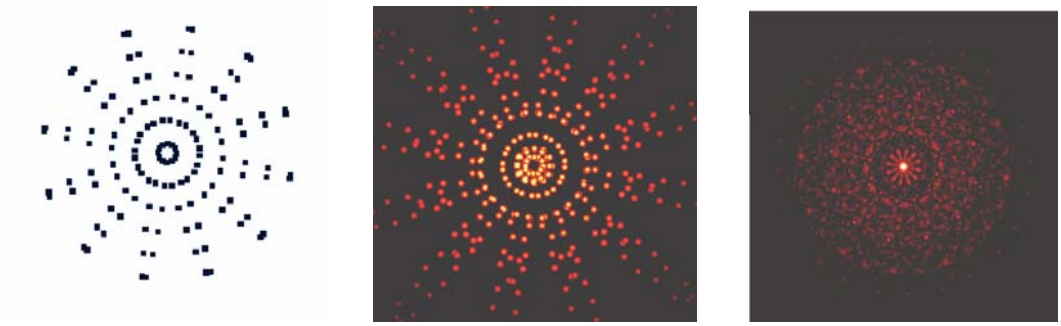

Figure 2. One example of a possible ESPRIT array configuration which rotates while it expands and contracts. Left: Motion of ESPRIT elements. Middle: Resulting u-v coverage. Right: Synthesized beam.

expansion and contraction of the array does not yield a high-quality beam, whereas a combined movement of radial expansion together with overall rotation of the array results in a more uniform u-v coverage and thus a "better" synthesized beam (Fig. 2). Clearly more detailed studies will have to determine the best strategy for positioning and moving the individual satellites.

It is anticipated that ESPRIT will make use of small ion thrusters like FEEPs (Field-Emission Electric Propulsion). Due to weight and power constraints it will not be possible to move the satellites very quickly. Therefore the thrust and duration of each thrust period determines the velocity each telescope will get and thus limits the number of instantaneous configurations, within one observing run for a particular source. Likely it will typically take several days before the array has expanded from its smallest configuration to its full size of around 1 kilometer.

## 3. SCIENTIFIC AIMS

ESPRIT will be able to address one of the major themes of modern astrophysics: the formation and evolution of stars and planetary systems. In particular the indirect detection of more than 100 Jupiter-like extra-solar planets has enforced these

studies and the development of missions. Although Spitzer and JWST will address these subjects in detail, there is a clear missing link in these studies. This concerns mainly the epoch before the objects are becoming strong IR emitters. And Herschel, although the largest space telescope planned for the FIR, will have a too modest angular resolution (ranging from 6 to 40 arcsec) for unraveling the star/planet formation process.

The most critical and unique spectral lines for studying this process are from $H_2O$, $H_3O^+$, OI, $C^+$, $N^+$, CH, OH, $CH^+$, and their isotopes including their deuterations. ESPRIT will trace the movements and spatial distribution of the ionic and molecular material and its specific components, from cold dark pre-stellar clouds through the final stages of star formation process. In particular measuring the distribution of water in the pre-stellar clouds and proto-planetary nebulae and disks is crucial, not only for its unique diagnostics but also for assessing the cloud's thermal conditions during its evolution.

Similar observations of circum-stellar material of evolved stars are most relevant for understanding the evolution of extra-solar planetary systems. In this sense the detection by SWAS of circum-stellar water vapor towards the evolved carbon-rich star IRC10216 is very interesting [1]. The most plausible explanation for the presence of the amount of detected water vapor is evaporation of ice on Kuiper Belt type objects by the central star. ESPRIT will have sufficient sensitivity to detect in detail many of these objects.

The facility will be the high-frequency/short-wavelength complement of the ground-based ALMA, without any atmospheric attenuation and disturbance in phase and transmission. It will be a follow-up mission of ISO-LWS, SWAS, ODIN, SIRTF, ASTRO-F, Herschel-PACS and -HIFI and of MIRI on JWST. Nevertheless, with the rapid development and increase of observing capabilities of ground-based and space/airborne facilities it will be important to update the scientific case.

## 4. HETERODYNE DETECTION AND ITS IMPLICATIONS

ESPRIT will use the heterodyne detection technique in order to achieve a very high spectral resolution. In general, interferometers can either use coherent (heterodyne) or incoherent (direct) detection. Each type of detection scheme has its own advantages and disadvantages. Here we will point out a number of advantages for a heterodyne interferometer which will make a space mission of such an interferometer easier than a direct detection interferometer.

Coherent (heterodyne) detection advantages include: high spectral resolution is easily achieved, the output (IF) signal can be copied/split and amplified without adding noise, and spectral analysis can be done with digital correlators without noise penalty or need of optical delay lines. In the particular case of a FIR interferometer, the heterodyne technique offers the following advantages:

- **Ambient temperature (~90 K) telescopes and optics can be used.** This aspect leads to lower system complexity and increased mission life time (if the detector cooling can be guaranteed over long time periods). It probably also allows lower launch mass. All these points should lead to lower mission cost. For an interferometer with direct detection, cooled optics is mandatory in order to reduce the background. A heterodyne instrument can operate with uncooled optics.
- **Very high spectral resolution.** Many science goals in far-IR astronomy demand very high spectral resolution (see also Section 3) which in the case of heterodyne detection is not determined by the receiver but the backend. Typically resolutions of $10^6 - 10^7$ are achieved.
- **Large coherence length.** Due to the smaller signal bandwidth, a heterodyne interferometer has a large coherence length (up to several tens of meters). This means two things: Simple (electronic) delay line compensation can be used (for example in the correlator), a very precise, real-time optical/RF path-length compensation is not required, and the metrology requirements are less demanding. Instead of precise, sub-micron *control* of the relative positions of the telescopes, only *knowledge* of the positions is required. In principle, the slow drifting of the telescopes (dynamic configuration) could even be used to fill the u-v plane during observations.
- **Number of telescopes.** For a heterodyne interferometer, the correlation is done after detection and amplification of the signal. This means that the signal can be "multiplied" in as many copies as needed. As a consequence, the number of antennas for a heterodyne space array is not limited by the signal itself but rather by other considerations such as launch mass. This is different for a direct detection interferometer. Since the signal has to be correlated before detection, only a limited number of antennas can be used because the available signal power needs to be divided for correlation.

This, together with other typical heterodyne characteristics, makes a heterodyne interferometer relatively simple as compared to a direct detection interferometer. Table 2 summarizes some of the differences between the two types of interferometers.

Table 2. Comparison of interferometers using direct or heterodyne detection.

| *Item* | *Direct detection* | *Heterodyne detection* |
|---|---|---|
| Correlation | Pre-detection (requires precision optical delay line) | Post-detection (requires electronic delay) |
| Signal bandwidth | Large (few 10s to 100s of GHz) | Small (4-16 GHz) |
| Background reduction | Cooled telescopes and optics needed (~4 K) | Telescopes and optics at ambient temperature (~90 K) |
| Spectral resolution | Low (max. few x $10^3$) | High (>$10^6$) |
| Velocity resolution | Low (~100 km/sec) | High (<1 km/sec) |
| Metrology | Accurate position control needed | Accurate position knowledge sufficient |
| Coherence length | Small (<< 1 micron) | Large (>> 1mm to 150m) |
| Number of telescopes | Limited due to signal division for correlation | Unlimited due to post-detection correlation |
| Detectors | Need improved detectors with NEP ~$10^{-20}$ W/√ Hz | Present and novel detectors approaching quantum limit |

# 5. FOCAL PLANE INSTRUMENTATION

## 5.1 Heterodyne Receivers

The focal plane instrumentation to be used for ESPRIT will consist of cryogenic heterodyne receivers of the type in use at many ground-based submm observatories and to be used for SOFIA and Herschel-HIFI [2]. Two types of mixer technology are envisaged: from 0.5 to about 1.3 or 1.5 THz SIS mixers offer best sensitivity, and above 1.5 THz up to 6 THz HEB mixers are the best choice. Both types of mixer have been space qualified (up to 1.9 THz) for Herschel-HIFI and will be flown in 2008 (see next section).

ESPRIT will cover as many spots in the frequency range from 0.5 to 6 THz as possible within the technical limitations (such as volume, mass, cooling capacity etc.). In addition, a low frequency channel (80…200 GHz) is considered for phase calibration. Since the astronomically observable velocity width scales inversely with the observing frequency for a given IF bandwidth, a large IF bandwidth of the receiver is important at THz frequencies. For example, a 4 GHz IF bandwidth corresponds to only 200 km/sec at 6 THz, and an 8 GHz IF bandwidth still provides only 400 km/sec velocity coverage.

The performance of a heterodyne front-end is largely determined by three components in the system: the mixer, the local oscillator (LO), and the IF amplifier chain.

- Mixer: The noise and gain of the mixer dominate the sensitivity of a high-frequency heterodyne receiver (especially for a space-based instrument that is not affected by an atmosphere or cryostat windows). The mixer may also limit one or both of the RF tuning range and IF bandwidth of the receiver.
- LO: The LO must provide sufficient power to drive the mixer (typically 10's of μW), must be spectrally pure, and must be stable. The tuning range of the LO is also critical to the tuning range of the receiver.
- Cryogenic IF amplifier: The noise contribution of the IF amplifier chain (especially the first stage "pre-amp") can be an important part of the total system noise, while its bandwidth may limit the overall receiver IF bandwidth.

In the following sections we will discuss the present status of these components and the required development / improvements for ESPRIT.

Table 3. Space qualified heterodyne technology for HIFI-Herschel

| | Bands 1 to 5 | Bands 6L and 6H |
|---|---|---|
| Mixer type | SIS | HEB |
| Frequency | 0.48-1.25 THz | 1.4 – 1.9 THz |
| IF | 4 – 8 GHz | 2.4 – 4.8 GHz |
| Local oscillator | Multiplier chain | Multiplier chain |
| Sensitivity | 3 - 5 hν/k | ~10 -15 hν/k |
| Status | Space qualified | Space qualified |

### 5.2 Mixers and local oscillators up to 2 THz

SIS and HEB mixers as well as multiplier chain local oscillators have been developed and space qualified for Herschel-HIFI covering the range up to 2 THz, with a 4 and 2.4 GHz IF bandwidth, respectively. Table 3 and Figure 3 give an overview. During the last few years the multiplier chain LO development for HIFI has progressed significantly. For details on the status of high-frequency multiplier chain LOs see e.g. [3]-[5]. For ESPRIT some development in the areas of noise temperature and IF bandwidth would be required. The sensitivity of the interferometer depends to a large extent on the front end noise with the mixer being the most important element. Mixer noise temperatures have improved significantly over the past years, in particular for SIS mixers, and it is desirable that continued development further decreases the mixer noise. Concerning HEB mixers, improvement of the mixer noise is required for ESPRIT.

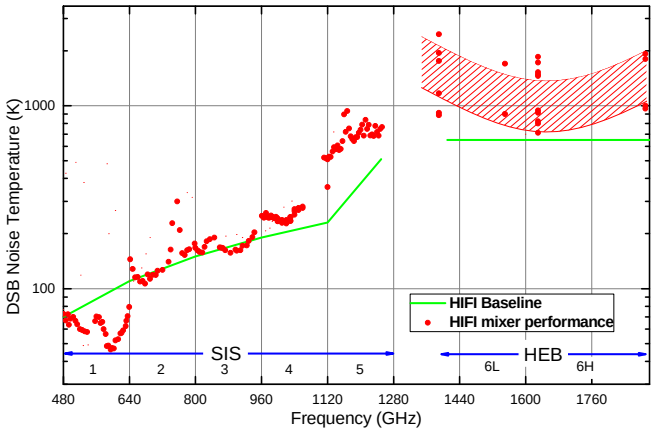


Figure 3. DSB noise temperatures of the HIFI mixers integrated into the Focal Plane Unit (Bands 1-5: SIS; Bands 6L and 6H: HEB), Apr 2006.

For ESPRIT an IF bandwidth of up to 8 GHz (or even more) is desirable. Extending the IF bandwidth of the SIS mixers is possible, 8 GHz has been achieved up to 720 GHz [6], [7]. However, reaching 8 GHz IF bandwidth for the HEBs needs more development work. For both types of mixers a development to integrate mixers and pre-amp could simplify the instrument. Another development, the use of superconducting integrated receivers (SIR) with the (flux flow) local oscillator located on the same chip as the mixer, as is developed by Koshelets et al. [8], could lead to more compact receivers. At present a SIR channel at 650 GHz is being integrated into the balloon-based atmospheric mission TELIS (Terahertz and submm limb sounder, see Yagoubov et al. [9] and reference therein) for which a first flight is scheduled for November 2007. Figure 4 shows the chip containing all major elements of a heterodyne receiver. Based on the results of this development, the SIR could become an interesting option for some of the ESPRIT frequency channels with the corresponding advantages in terms of mass, size, and lower system complexity.

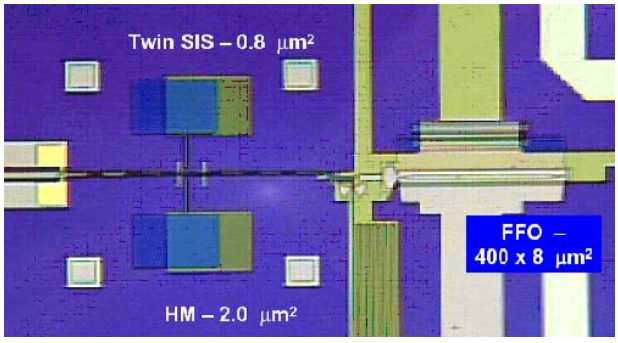


Figure 4. Microscope photograph of the central part of the SIR chip (field of view is about 1.5 mm by 1.0 mm). All main elements of the Integrated Receiver (double-dipole twin SIS mixer, Flux Flow Oscillator and Harmonic Mixer) are present.

### 5.3 Mixers and local oscillators above 2 THz

Above 2 THz a number of HEB systems have been demonstrated in the lab by various groups, but none has been used for astronomical observations due to a lack of suitable (space) platforms. All of these systems have been operated at specific frequencies with a small tuning range (due to the use of a laser LO) and fairly low IF bandwidth (typically 2-3 GHz, or less). The highest demonstrated frequency is 5.3 THz. Figure 5 shows reported noise temperatures with best values around 8-10 hv/k. For ESPRIT, both a larger IF bandwidth and lower noise temperatures will be needed. An extension of the IF bandwidth (ideally 8 GHz) and improved sensitivity (to ~ 3 hv/k) will require development work. Note that the drop in demonstrated sensitivities at 3 THz is due to the bulk of developments to-date being aimed at receivers for 2.5 THz or less – it does not reflect a limitation of the HEBs themselves.

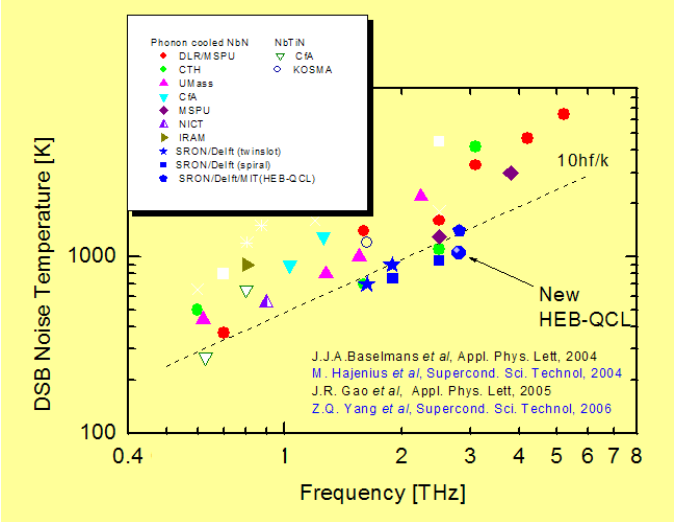


Figure 5. State-of-the-art DSB noise temperatures of HEB mixers from 0.6 to 5.3 THz. Best results correspond to about 8 hv/k (compilation by Gao et al. and Huebers). Recently, a HEB-QCL system has reached 1050 K at 2.84 THz [11].

The Local Oscillator development for Herschel-HIFI has pushed the operation of multiplier chains driven by high-power millimeter-wave sources to 2 THz. With some effort this could probably be extended to 3 THz. Coming from the mid-IR side of the spectrum, the recent successful development of Quantum Cascade Lasers (QCL) has opened up the possibility for heterodyne receivers operating at 6 THz (=50µm). QCLs have been demonstrated in CW operation in the THz range from 2.1 to 4.7 THz with output powers of several hundred µW to tens of mW (an HEB mixer only requires ~0.5 to 1 µW of LO power). The tuning range is on the order of 10 GHz and thus quite limited. The line-width of a QCL is small - 30 kHz has been measured. These characteristics make QCLs interesting THz local oscillators. Recently, a heterodyne receiver at 2.8 THz using an HEB mixer and QCL local oscillator has been demonstrated for the first time [10], and a receiver noise temperature of 1050K has been measured at 2.84 THz [11]. For a THz heterodyne receiver system issues like phase-locking, tuning range and stability need to be considered and investigated. Furthermore, since the QCL chips are very small (millimeter size) and fairly compact integrated systems could be developed possibly containing many QCL chips for one mixer, to overcome the tuning range limitation.

### 5.4 IF amplifiers

Existing cryogenic IF amplifiers provide bandwidths of up to 8 GHz (with discrete elements) or beyond (with MMIC-based designs) with very good noise temperatures (below 5 K). For HIFI, IF amplifiers in the 4-8 and 2.4-4.8 GHz ranges have been space qualified. For ESPRIT, existing designs may be either used directly or modified to accommodate a different IF range, depending on the exact IF range and bandwidth requirements. Integration of the first IF amplifier with the mixer might reduce system complexity.

# 6. CORRELATOR DESIGN

## 6.1 Distributed correlator

For ESPRIT a distributed correlator implementation is proposed. In this concept each satellite has a correlator on board resulting in several advantages. Redundancy prevents the occurrence of a single point of failure. Furthermore, distributing the correlator over all satellites has the advantage that all satellite can be identical (resulting in cost savings). There are a number of ways to distribute the correlator. For ESPRIT the baseline design splits the total band of 4 GHz up in 6 pieces with analog filters. To sample the bands of 667 MHz an A/D converter sample rate of about 1.4 GHz is required per baseband.

Since the satellites are moved to different positions in a 3D space, delay compensation is necessary. The delay compensation can be implemented by means of electrical delay lines. This requires the knowledge of satellite locations at micrometer precision. Furthermore, the rate of the delay compensation depends on the stability and velocity of the satellites.

The key items determining the dimensions of the ESPRIT correlator include: (1) Number of antennas, (2) Number of polarizations, (3) Total bandwidth, (4) Total number of spectral channels, and (5) Number of bits.

## 6.2 Data rates in the correlator

The correlator is distributed over all six satellites in the current baseline concept, meaning that each satellite is responsible to correlate 1/6 of the total bandwidth. Hence, each satellite transports 5/6 of the bandwidth to the other satellites and receives one baseband from all the other satellites. The total data rate, which is transmitted by each satellite, is 26.7Gbps (two polarizations assumed) and the total data rate received by each satellite is 26.7Gbps as well. The reason for doing the correlation in space is to save on the downlink budget. After correlation the data is reduced significantly, the factor depending on the integration time. We estimate that for the ESPRIT baseline configuration the total output data rate will be in the order of 1 Mb/s.

## 6.3 Current Technology

To give an idea of the size of the ESPRIT correlator, the ALMA correlator design (i.e. without the current enhancement) [12] and Omnisys correlator [13] are used for comparison (only the digital part is considered). The ALMA correlator is a ground based crosscorrelator while the correlator of Omnisys is an autocorrelator for space applications. An overview of all three correlators is given in Table 4. It can be seen that – concerning the number of correlations – the proposed ESPRIT correlator is about a factor 114 smaller than the ALMA correlator, if the same architecture is used. The ESPRIT correlator will be 32 times larger than the Omnisys correlator.

Table 4. Key numbers of the ESPRIT, ALMA and Omnisys correlators

| | **ESPRIT** | **ALMA** | **Omnisys** | **ESPRIT/ALMA** | **ESPRIT/Omnisys** |
|---|---|---|---|---|---|
| Antennas | 6 | 64 | 1 | | |
| Polarizations | 2 | 2 | 1 | | |
| # of correlations | 72 | 8192 | 1 | 0.01 | 72.0 |
| Bandwidth (GHz) | 4 | 8 | 4 | 0.50 | 1.0 |
| # of lags | 1024 | 512 | 4096 | 2.00 | 0.3 |
| Number of bits | 2 | 2 | 1.5 | 1.00 | 1.8 |
| **Total scale factor** | | | | **0.01** | **32.0** |

Projecting the power of the ALMA and Omnisys correlator to the ESPRIT correlator results in a first order total power estimation of about 600 W, to be distributed over 6 ESPRIT elements. Furthermore, the Omnisys correlator weighs 600 grams [13]. Based on this, we estimate in the first order about 30 kg for the ESPRIT correlator (taking into account a more complex architecture). This mass is also distributed over 6 ESPRIT elements. Clearly, these estimates will have to be refined in a more detailed study, but they nevertheless indicate that the ESPRIT correlator would stay within a reasonable power and mass budget.

In principle the digital correlator design can be developed with current technology for ground based systems. However, the required operation power and mass should be minimized for this space application. The two steps to be taken are: development of a distributed correlator (communication and synchronization needs to be correctly dealt with), and mass and power optimization as well as space qualification of this distributed cross correlator.

# 7. COOLING

The cooling requirements for ESPRIT can be divided in several components like telescope cooling, detector cooling and everything in between. It is beyond the scope to provide a complete overview of the ESPRIT cooling and a careful system study is mandatory. However, the requirements of a number of key system components can be considered.

## 7.1 Telescope cooling requirements

While older FIR space telescopes relied on liquid Helium for the cooling of the telescope to suppress the telescope's own background, newer ones rely on passive cooling, as is the case for the Herschel telescope. The advantage is clear: since the telescope dish doesn't have to fit in the helium cryostat it can be larger, such that the size of the telescope dish is now mainly determined by the mass of the dish itself and the space available in the launch vehicle. Cooling of the Herschel telescope (3.5m) is done passively by radiating heat away into cold deep space. Although it is not yet certain what the final temperature of the telescope will be, studies show that it will be close to 70-80K. Note that due to the heterodyne nature of HIFI, it is the least susceptible of the Herschel instruments to the telescope background radiation. This advantage is also available to ESPRIT, so an 80K dish is sufficient. Since it is assumed that the ESPRIT telescope will be similar in size to that of Herschel, very similar passive cooling is needed.

## 7.2 Front-end optics cooling requirements

The front end optics for ESPRIT is expected to be at a similar temperature as the telescope dish. Due to the heterodyne nature of ESPRIT, thermal background and stray-light problems are not expected, but standing waves may occur if parallel surfaces exist within the light paths. Detailed quasi-optical modeling would show whether and how standing waves could be avoided, even at temperatures of 70-80K. Note that for Herschel-HIFI the Focal Plane temperature of 15K is sufficient to keep the background low, and although some parallel surfaces do exist within HIFI, the standing wave amplitudes are within reasonable bounds.

## 7.3 Front-end electronics cooling requirements

The SIS and HEB mixers will need to be cooled to 4K or below (with dissipation powers of much less than a mW each), while the IF pre-amplifiers will need to be cooled to at least 20K (dissipation ~ 8mW per pre-amp). The second-stage IF amplifiers may be heat-sunk to the passively cooled front-end optics, at about 70-80 K (dissipation ~ 10 mW per amplifier).

Table 5. Cooling Requirements for ESPRIT front-ends

| **Temperature level** | **One receiver with 2 mixers and LO** | |
|---|---|---|
| Between 30 K and 120 K | LO (QCL) | 2.5 W |
| 70 K | 2 Amplifiers | 20 mW |
| 20 K | 2 Pre-amplifiers | 16 mW |
| 4.2 K | 2 Mixers | 0.5 mW |
| | Parasitics | 1 mW |

The local oscillators (multiplier chain and/or QCL) may require active cooling, with operating temperatures between 30 and 120K. The QCLs will have power dissipations on the order of 1 W.

An overview of the cooling requirements for the ESPRIT THz receivers is given in Table 5 for observations at one frequency with dual polarization (i.e. using two mixers per interferometer element). These estimates apply only to the active channels (the instrument will likely operate with 1 or 2 active channels and several inactive channels at any one time) and do not include the mechanical support structure of the cryostat. A more detailed thermal design is needed to evaluate the overall heat-loads in the cryostat, front-end, and cable harnesses.

In order to achieve a long life time of ESPRIT, the active cooling of the front-end electronics to 4 K will require the use of mechanical, sorption/Joule-Thompson or similar coolers. The thermal stability of this 4K temperature level may also form an important aspect of the cooler design.

While a study needs to be conducted to show the exact figures for passively cooling the telescope and the optical bench, the real technology step lies in space-qualifying coolers such as now developed e.g. at the University of Twente (Netherlands) and elsewhere. Since the cooling of the front-ends is critical, this should receive early attention, but it should also be noted

that many space missions require similar technology, and studies dedicated to the cooling of these missions will provide the necessary knowledge for ESPRIT.

The bias and control electronics for the front-end electronics can be located with the other warm electronics. If it is defined as part of the front-end, the 2nd LO (which down converts individual sub-bands of the 4-8 or 4-12 GHz IF band to a common lower-frequency base band that is then sampled in the correlator) can also be located with the other warm electronics.

## 8. SYSTEM CONSIDERATIONS

Heterodyne interferometers provide, due to the long coherence length, a large degree of freedom in positioning and moving the dishes in terms of the path difference. Thus, the proposed six-element free-flying interferometer can be configured in three dimensions, avoiding collision danger. However, to limit the complexity of the metrology for measuring the distance between elements, we consider having the elements in two planes with three mirrors in each plane as a viable baseline. An example of such a 3D configuration along with the instantaneous u-v coverage is shown in Figure 1. As pointed out before, our preference is for a distributed correlator in which each of the six elements houses its own correlator. Thus, the design for all six elements can be the same, which reduces costs, and has built-in redundancy. Furthermore, the power requirements are shared between the elements for the most notorious power-hungry element of the system.

The launch configuration for the elements is made small by folding the deployable boom secondary support structures into the cavities of the off-axis telescopes. Conceptual designs indicate that all six elements could be fitted into a cylinder 10–11 m high and four meter in diameter and could be launched on a single rocket.

### 8.1 The metrology subsystem

The metrology subsystem will provide accurate information on the distances between satellites. In principle two distance measures per satellite are enough, but to obtain sufficient redundancy three metrology links will be required. An accuracy of approximately 1 to 5 micrometer in the distance determination is required. Positions should be recorded continuously, also during movements of the satellites. Most likely, the metrology subsystem will utilise an optical system based on laser beams. The information from the coarse positioning system (part of time and phase distribution subsystem) can be used for additional position clarification as well as for aiming the beams between the satellites. The metrology information is then used in the global central geometrical model (like in ALMA or SMA) to provide the fringe stopping phases. This accurate position information should be recorded with every data frame.

### 8.2 Navigation, pointing and propulsion

The most stringent navigation requirements are for relative satellite movements to allow for fringe-stopping. Secondary are the requirements related to the low levels of thrust that are required for continuous on-the-fly operation as contrasted to the relatively large demand in satellite repositioning capabilities needed for the core operation of the interferometer, i.e. image quality. The high angular resolution places significant requirements on the pointing accuracy. However, these pointing requirements can be met using today's technology. One should note, that an inertial navigation system may be required which is likely accurate enough to reinforce the coarse GPS because of the stable space conditions.

### 8.3 Central control and earth communications

Many of the satellite and observatory control functions are fulfilled by a main computer. Most of these functions are well understood as they apply to any satellite mission; however there are a few issues which deal specifically with the interferometer nature of ESPRIT. Firstly based on the coarse and fine metrology signals, the central computer should always know the relative positions of the satellites for use in the central geometrical model for the array, which is to be updated (continuously) during an observation. The phase corrections should be computed for each satellite relative to a common virtual phase centre. These phase corrections are then used to stop the fringes either in correlator or in LO subsystem. Since the metrology system has its own time cycle, the positions of satellites should be (continuously) interpolated between known points using a dynamic model of the array element movements and information on velocity and acceleration of the satellite (aided by extrapolation of past movements). The phase closure relations should also be used to constrain the element positions provided the signal to noise ratio is good enough.

## 9. SENSITIVITY CALCULATIONS

The ESPRIT baseline design is for six interferometer elements and a diameter of at least 3.5 m for each element to achieve the desired sensitivity. Thus, the collecting area for each element is >10 $m^2$. The use of small mixer arrays, if LO power and correlator capacity permitted, could compensate the small primary beam size. In using the ALMA sensitivity calculator [14]

ESPRIT sensitivity results were obtained which are given below in Table 6. With expected levels of molecular line brightness in the order of 10 K, we can expect from ESPRIT a large set of interesting observations.

Table 6. Sensitivity calculations for ALMA, and for ESPRIT with 6 telescopes with 3.5 m primaries and 15 baselines.

| **Parameters:** | **Units** | **ALMA** | **ESPRIT** |
|---|---|---|---|
| Central Frequency (Wavelength) | GHz (μm) | 650 (461) | 3000 (100) |
| Velocity Resolution | km/s (MHz) | 1 (2.2) | 1 (10) |
| Angular Resolution | arcsec | 0.1 | 0.1 |
| Baseline | m | 900 | 200 |
| Jy per K ratio | mJy/K | 3.4 | 74 |
| Tsys | K | 1326 | 1000 |
| Cont. flux density | mJy | 0.13 | 16.7 |
| Cont. Brightness | K | 0.04 | 0.2 |
| Line flux density | mJy | 8.07 | 333 |
| Line brightness | K | 2.33 | 4.5 |

Assumed integration times are 3600 secs.

## 10. CONCLUSION

We have presented a concept for a far-infrared space interferometer consisting of 6 free-flying elements, each with a 3.5m telescope, heterodyne receivers in the range 0.5 to 6 THz, and part of the distributed correlator. Such a space interferometer allows addressing fundamental question of modern astrophysics in the field of star and planet formation. Issues concerning the configuration, detectors, detector cooling, correlator, and the system were presented and discussed.

## REFERENCES


1. Melnick, G.J., Neufeld, D.A., Ford, K.E.S., et al. “Discovery of water vapour around IRC +10216 as evidence for comets orbiting another star”, Nature 412, p. 160, 2001.
2. De Graauw, Th., Helmich, F.P. et al., “Herschel-HIFI: the heterodyne instrument for the far-infrared”, in Pilbratt, G.L., et al. (eds), Proc. of *The Promise of the Herschel Space Observatory,* 12-15 Dec 2001, Toledo, Spain, ESA-SP460, pp. 45-51, 2001.
3. J. Ward et al., “Local Oscillators from 1.4 to 1.9 THz”, Proc. of the 16th Int. Symposium on Space THz Technology, Chalmers Technical University, Gothenburg, Sweden, May 2-4, 2005.
4. G. Chattopadhyay, E. Schlecht, J. Ward, J. Gill, H. Javadi, F. Maiwald, and I. Mehdi, "An All Solid-State Broadband Frequency Multiplier Chain at 1500 GHz," IEEE Transactions on Microwave Theory and Techniques, vol. 52, no. 5, pp. 1538-1547, May 2004.
5. A. Maestrini, J. Ward, J. Gill, H. Javadi, E. Schlecht, G. Chattopadhyay, F. Maiwald, N. R. Erickson, and I. Mehdi, "A 1.7 to 1.9 THz Local Oscillator Source, IEEE Microwave and Wireless Components Letters," vol. 14, no. 6, pp 253-255, June 2004.
6. A. Baryshev, E. Lauria, R. Hesper, T. Zijlstra, and W. Wild, "Fixed-tuned waveguide 0.6 THz SIS mixer with wide band IF," in: R. Blundell and E. Tong (Eds.), Proc. of the 13th Int. Symposium on Space THz Technology, Havard University, Cambridge, MA, USA, March 26-28, 2002, pp. 1-10.
7. R. Hesper et al., “Design and development of a 600-720 GHz receiver cartridge for ALMA Band 9”, Proc. of the 16th Int. Symposium on Space THz Technology, Chalmers Technical University, Gothenburg, Sweden, May 2-4, 2005, pp. 110-115.
8. Koshelets et al., “Superconducting Submm Integrated Receiver with Phase-Locked Flux-Flow Oscillator for TELIS”, Proc. of the 16th Int. Symposium on Space THz Technology, Chalmers Technical University, Gothenburg, Sweden, May 2-4, 2005, pp. 276-281.
9. P.A. Yagoubov, et al., "550-650 GHz spectrometer development for TELIS”, Proc. of the 16th Int. Symposium on Space THz Technology, Chalmers Technical University, Gothenburg, Sweden, May 2-4, 2005.
10. Gao, J.R., et al., “Terahertz heterodyne receiver based on a quantum cascade laser and a superconducting bolometer”, App. Phys. Lett. 86, p. 244104, 2005.
11. M. Hajenius, P. Khosropanah , J.N. Hovenier, J.R. Gao, T.M. Klapwijk, S. Dhillon, S. Barbieri, P. Filloux, C. Sirtori, D.A. Ritchie and H.E. Beere, Proc. of the 17th Int. Symposium on Space THz Technology, ISSTT 2006, in Paris, France.
12. Escoffier. R.P., Comoretto, G., Webber, J.C., Baudry, A., Broadwell, C.M., Greenberg, J.H., Treacy, R.R., Cais, P., Quertier, B. and Gunst, A.W., "The ATACAMA Large Millimeter Array Correlator", URSI 2005, New Delhi, October, 23-29, 2005.
13. Emrich, A., Integrated submillimeter system, Internal report, Omnisys Instruments AB, Sweden.
14. http://www.eso.org/projects/alma/science/bin/sensitivity.html

# The "Millimetron" project, a future space telescope mission.

G.N. Gol'tsman and "Millimetron" collaborators.

Astro Space Senter of Lebedev Physical Institute, RAS

The goal of the Millimetron project is to develop a space observatory operating in the millimeter, sub-millimeter and infrared wavelength ranges using a 12-m actively cooled telescope in a single-dish mode and as an interferometer with the space-ground and space-space baselines (the later after the launch of the second identical space telescope). The Millimetron's main reflector and other optics will be cooled down to 4K thus enabling astronomical observations with super high sensitivity in MM and subMM (down to nanoJansky level). Heterodyne observations in an interferometer mode at frequencies 0.1-1 THz will provide super high angular resolution. The main instruments, planned to be installed are wide-range imaging arrays, radiometers with spectrometers and polarimeters, VLBI heterodyne receivers, and Mikelson type interferometer devices. Wide-range MM and subMM imaging arrays and spectrometers will be based on a superconducting hot electron direct detectors with Andreev mirrors operating at 0.1 K. Such detectors are the best candidates to reach the noise equivalent power level of $10^{-19}$-$10^{-20}$ W/√Hz. Heterodyne receivers will be both SIS based superconducting integrated receiver with flux-flow oscillator as LO (0.1-0.9 THz range) and HEB based receivers using multiplied Gunn oscillator as LO for 1-2 THz range and quantum cascade lasers as LO for 2-5 THz range. For observations in middle IR region there will be installed large arrays of superconducting single photon detectors, providing imaging with very high dynamic range and ultimate sensitivity.

# Wideband AlN-based SIS devices for frequencies around 700 GHz

C. F. J. Lodewijk, T. Zijlstra, D. N. Loudkov, T. M. Klapwijk, F. P. Mena, and A. M. Baryshev

***Abstract*—We report results on SIS tunnel junctions based on AlN tunnel barriers grown with plasma nitridation from a remote inductively coupled plasma source. Results for the noise temperature are shown and compared to $AlO_x$ results in a ALMA Band 9 mixer. The parameters for $AlO_x$ devices are RnA=25 Ωμm$^2$ with a normal state resistance of 25 Ω and an optimized tuning circuit. For the AlN devices we have RnA = 2.9 Ωμm$^2$ (Jc=71kA/cm$^2$), A=0.36 μm$^2$, $V_{gap}$=2.77 mV, and Rsg/Rn = 14. The data for AlN devices with a not yet optimized tuning circuit show comparable noise temperatures and a flat noise response.**

***Index Terms*—AlN tunnel barriers, heterodyne, nitridation, SIS mixers.**

## I. Introduction

THE use of AlN tunnel barriers instead of $AlO_x$ barriers in superconducting tunnel junctions alleviates the problem of tuning out the capacitance and promises to provide an increased band coverage [1]. Although the specifications for Band 9 (602 to 720 GHz) of the atmospheric window at the Atacama Large Millimeter Array (ALMA) can be met with $AlO_x$, an intrinsically wider band coverage would be beneficial. High critical current-density (low specific resistance) tunnel-junctions are needed to achieve this larger bandwidth. $AlO_x$ barriers have an upper limit [2] of 15 kA/cm$^2$ (a lower limit of 15 Ωμm$^2$), beyond which excessive sub-gap leakage emerges.

After the initial introduction of AlN [3], various groups have reported successful use of AlN tunnel barriers for mixers at frequencies up to 900 GHz [4], [5]. However, most of the techniques to nitridize aluminium, forming the thin AlN-layer, have shown poor process control and substantial scatter in the achieved current densities [6]. Recently, we have developed a process based on plasma nitridation from a remote inductively coupled plasma source, leading to an excellent degree of control [7].

Manuscript received April 27, 2007. This work was supported by NanoImpuls, the Dutch Research School for Astronomy (NOVA), the Dutch Organisation for Scientific Research (NWO) and the European Southern Observatory (ESO).

C. F. J. Lodewijk, T. Zijlstra, D. N. Loudkov and T. M. Klapwijk are with the Kavli Institute of Nanoscience, Faculty of Applied Sciences, Delft University of Technology, Lorentzweg 1, 2628 CJ Delft, The Netherlands.

F. P. Mena and A. M. Baryshev are with the SRON Netherlands Institute for Space Research and Kapteyn Astronomical Institute, University of Groningen, Landleven 12, 9747 AD Groningen, The Netherlands.

## II. AlN tunnel barrier growth

Unlike thermally grown $AlO_x$, AlN is formed in a nitrogen plasma with a mixture of chemically active species of various energies. It is energetically favorable for Al and $O_2$ to react into $Al_2O_3$, whereas it is not favorable for Al and $N_2$ to form AlN. The latter reaction needs extra energy, which is provided by the plasma.

Most barriers to date have been grown in a parallel plate reactor in which the aluminum is in direct contact with the plasma. Very high current-densities (54 kA/cm$^2$) have been reached in barriers deposited by reactive sputter deposition [8]. An alternative nitridation-method has been introduced by Kaul *et al.* [9], where a Kaufmann ion source is used to generate a controlled ion flux.

We use an inductively coupled plasma source [10], for which we have chosen to work in the range of high pressures ($2 \times 10^{-3}$ mbar to $1 \times 10^{-1}$ mbar), in order to have a low energy of the ions. At these higher pressures, the fraction of atomic nitrogen is expected to be large [11], while the energies are as low as a few eV. The substrate is placed on a chuck with a distance with respect to the plasma source, which can be varied from 10 cm to 30 cm. Optionally, the chuck may be DC powered and it can rotate about the height axis.

The AlN barrier is created by first depositing in the usual way a thin (~7 nm) layer of Al on top of Nb in a process chamber. Without breaking the vacuum, the substrate is then transferred to a dedicated nitridation chamber. Subsequently, the Al is exposed to the nitrogen plasma for several minutes, producing a layer of AlN.

## III. DC results and process parameters

The devices are fabricated on a quartz substrate. All metal layers are deposited by magnetron sputtering in a Kurt Lesker system. First, a Nb monitor layer is deposited, after which a ground plane pattern is optically defined. Subsequently, a bilayer of Nb/Al is deposited, which is nitridized, followed by a top electrode of Nb. The lateral dimensions of the multilayer of Nb/Al/AlN/Nb are patterned by lift-off. Junctions are defined by e-beam lithography with a negative e-beam resist (SAL-601) layer and etched with a $SF_6/O_2$ reactive ion etch (RIE) using the AlN as a stopping layer. The junction resist pattern is used as a self-aligned lift off mask for a dielectric layer of $SiO_2$. A Nb/Au top layer is deposited and Au is etched with a wet etch in a $KI/I_2$ solution using an optically defined mask. Finally, using an e-beam defined top wire mask pattern,

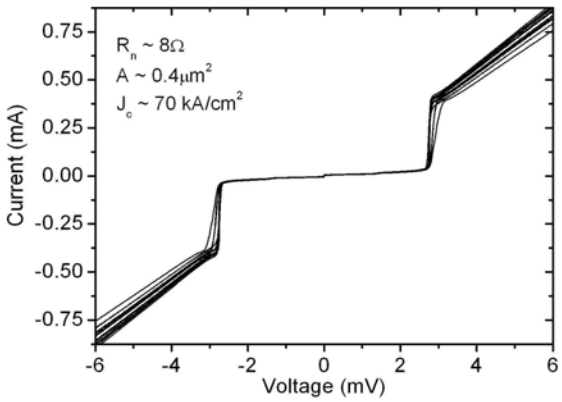


Fig. 1. Current-voltage characteristics of a typical batch of Nb/AlN/Nb junctions. Junction area is about 0.4 μm$^2$, resulting in a normal resistance, $R_n$, of 8 Ω (critical current density ~70 kA/cm$^2$). The Josephson current has been suppressed with a magnetic field. The scatter in $R_n$ is caused by variation in the junction area.

the layer of Nb is etched with a $SF_6/O_2$ RIE, which finishes the fabrication process.

A set of current-voltage (*IV*) characteristics of a typical batch of SIS devices is shown in Fig. 1. The Josephson current of each junction has been suppressed with a magnetic field. The e-beam defined junction areas $A_j$ are about 0.4 μm$^2$, while the normal resistance $R_n$ is about 8 Ω. This gives a resistance times area product $R_nA$ of ~ 3 Ωμm$^2$ (critical current density $J_c$ ~ 70 kA/cm$^2$). The scatter in the $R_n$ of the devices originates in a variation in $A_j$. For the observed scatter of ~9% around the mean, the linear uncertainty in the junction definition, which results after reactive ion etching, is about 30 nm.

We have made several batches, varying the nitridation time $t_N$ from 9 to 60 minutes. About half of the batches has been made with a low position of the chuck (30 cm distance to the plasma source) in the nitridation chamber, the other half with a higher position (15 cm distance to the plasma source).

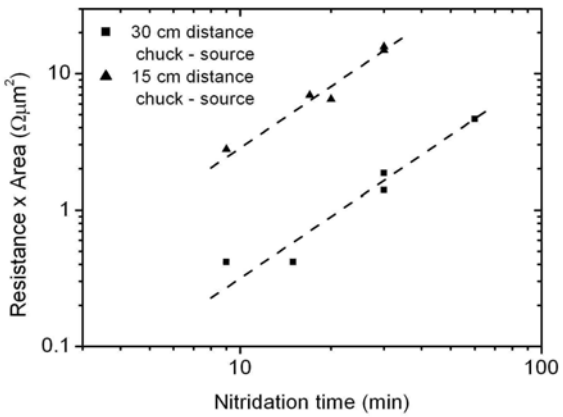


Fig. 2. $R_nA$ product as a function of nitridation time, $t_N$, for nine different fabricated batches. The squares represent data for a 30 cm chuck-source distance, whereas the triangles indicate a 15 cm chuck-source distance. Dashed lines indicate a dependence $R_nA \propto t_N^{1.5}$, with different prefactors for the two chuck positions.

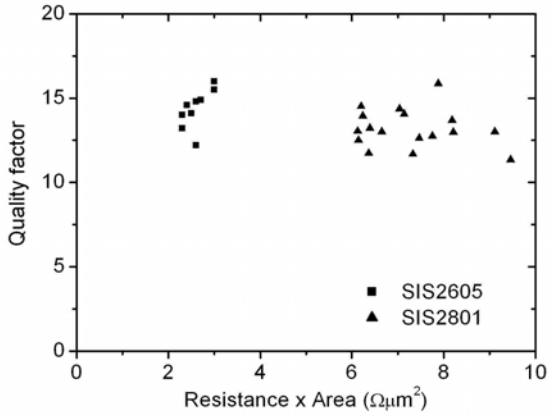


Fig. 3. Quality factor as a function of $R_nA$ product for two batches of Nb/AlN/Nb junctions. The apparent scatter in $R_nA$ within a batch is related to a scatter in junction area.

In Fig. 2, we plot the $R_nA$ product of the batches as a function of $t_N$ for the large chuck-source distance (squares) and for the small chuck-source distance (triangles). The dashed lines indicate a dependence $R_nA \propto t_N^k$, with $k = 1.5$.

Obviously, there is a systematic dependence on nitridation time, indicating a well-behaving process control. By varying the nitridation time and the chuck position, we can realize any desired $R_nA$ value between 0.5 Ωμm$^2$ and 10 Ωμm$^2$.

As shown in Fig. 2, we reach $R_nA$ products as low as ~0.4 Ωμm$^2$, corresponding to a $J_c$ of 420 kA/cm$^2$. For such high current densities, heating effects decrease the superconducting gap voltage of the junction in the form of back-bending. Up to about 100 kA/cm$^2$, this effect is not yet visible.

The quality factor $Q$, defined as $R_{sg}/R_n$, where $R_{sg}$ is the subgap resistance, gives an indication of the amount of subgap leakage through the tunnel barrier. For the curves in Fig. 1, $Q$ varies from 10 to 15. The quality factor as a function of $R_nA$ product has been plotted in Fig. 3 for two different batches.

From Fig. 3, it is evident that $Q$ is higher than 10 for all devices down to those with a $R_nA$ of at least 2.5 Ωμm$^2$ (80 kA/cm$^2$). The variation in the $R_nA$ within a batch is related to uncertainties in determining $A_j$: we multiply the measured $R_n$ of a device with the design value of the area. Since there is scatter in the actual value of $A_j$, reflected in a variation of $R_n$, the plotted $R_nA$ value shows the same scatter.

## IV. RF EVALUATION

All devices incorporate a multisection Nb/$SiO_2$/Nb microstripline, which tunes out the capacitance of the SIS junction. The transmission efficiency of a device is evaluated using a Fourier Transform Spectrometer (FTS) by measuring the changes in the DC current produced by the incoming light for a chosen bias voltage, selected to be close to the gap voltage.

An AlN-based SIS device is mounted onto a waveguide backpiece designed for Band 9 (600 GHz to 720 GHz) of ALMA. The device has the following parameters: $R_n$=8.1Ω, $A_j$=0.36μm$^2$, $Q$=14. The microstripline of this device had been

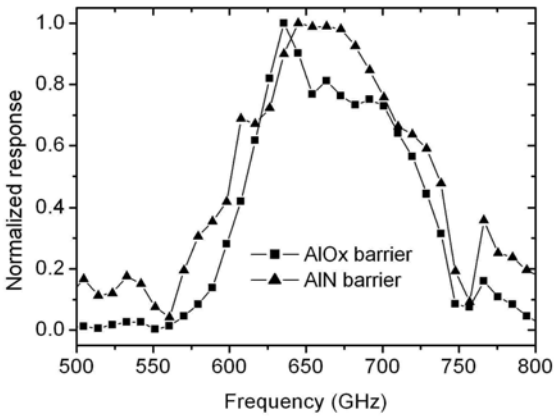


Fig. 4. Normalized photoresponse of two devices, measured with a Fourier Transform Spectrometer (FTS). The triangles are for a device with an AlN tunnel barrier and a non-optimized tuning circuit, whereas the squares show a typical result for an $AlO_x$ based SIS with an optimized tuning circuit. Minima in the response are due to water absorption.

designed for $R_n$=25Ω and $A_j$=0.25μm$^2$. The FTS data for a AlN tunnel barrier, taken at a temperature of 4.2K, are shown in Fig. 4 (triangles). Note that the FTS setup is operated in air. In the same graph, a typical FTS result for an $AlO_x$ based SIS device with an optimized tuning circuit for its parameters $R_n$=25Ω and $A_j$=1.0μm$^2$ is shown.

Obviously, the bandwidth for the AlN based device is larger, despite of the fact that it does not have an optimized tuning circuit. The difference becomes more obvious when the minima due to the water absorption are taken into account, in particular around 560 GHz and 750 GHz.

It is interesting to analyze what one would expect for AlN devices with an optimized tuning circuit. The transmission efficiency, calculated following Ref. 1, for the AlN device of Fig. 4 is shown in Fig. 5 with a full line. The parameters of the actual device have been used. For comparison, the FTS data are shown by triangles. The dashed line shows a calculation of the transmission efficiency for the same SIS junction parameters, but with an optimized tuning circuit. It is evident

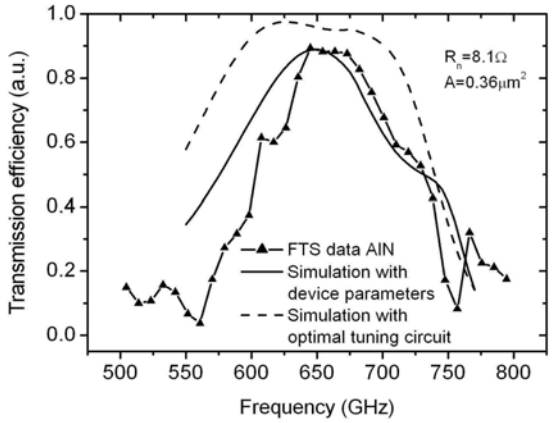


Fig. 5. FTS response of an AlN device (triangles), compared to the simulation (full line), with the non-optimized tuning circuit. The scale for the data is adjusted to match the maximum of the simulation. The dashed line shows the expected response for the same device with an optimized tuning circuit.

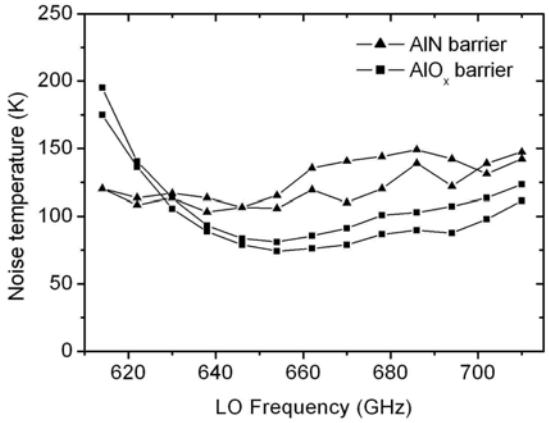


Fig. 6. Uncorrected DSB noise temperature of a SIS mixer with an AlN tunnel barrier (triangles) and the best result obtained for a SIS with an $AlO_x$ tunnel barrier (rectangles), in the frequency range of ALMA Band 9.

that future devices with an optimized circuit will lead to considerable improvement.

The same AlN based device has been mounted in a standard ALMA Band 9 test cartridge. The noise temperature of the mixer, the accompanying optics and the IF chain [12] has been measured using the standard Y-factor method. The resulting uncorrected DSB noise temperatures at different frequencies are presented in Fig. 6 with triangles. In the same graph, the best results obtained with $AlO_x$ based SIS devices are shown with rectangles.

The noise temperature for the AlN device is considerably flatter over the whole range of ALMA Band 9 and compares well with the best results obtained with $AlO_x$.

## V. Conclusion

We have used a new method for AlN tunnel barrier growth, with which we can realize critical current densities of over 100 kA/cm$^2$. This new method has good process control and reproducibility. Using newly fabricated Nb/AlN/Nb junctions in devices for ALMA Band 9, we have achieved a better bandwidth coverage and a flat noise temperature. By making AlN SIS devices that have an optimized tuning circuit, we expect both bandwidth coverage and noise temperature to improve further.

## Acknowledgment

The authors would like to thank O. Noroozian for help with the modeling and B. de Lange and G. Gerlofsma for technical assistance.

## References

[1] C.F.J.Lodewijk, O. Noroozian, D.N. Loudkov, T. Zijlstra, A.M. Baryshev, F.P. Mena, and T.M. Klapwijk, "Optimizing superconducting matching circuits for Nb SIS mixers operating around the gap frequency," *IEEE Trans. Applied Superconductivity*, to be published.

[2] R. E. Miller, W. H. Mallison, A. W. Kleinsasser, K. A. Delin, and E. M. Macedo, "Niobium trilayer Josephson tunnel junctions with ultrahigh critical current densities," *Appl. Phys. Lett.*, Vol. 63, 1423 (1993).

[3] T. Shiota, T. Imamura and S. Hasuo, "Nb Josephson junction with an $AlN_x$ barrier made by plasma nitridation," *Appl. Phys. Lett.*, Vol. 61, 1228 (1992).

[4] J. Kawamura, D. Miller, J. Chen, J. Zmuidzinas, B. Bumble, H. G. LeDuc, and J. A. Stern, "Very high-current-density Nb/AlN/Nb tunnel junctions for low-noise submillimeter mixers," *Appl. Phys. Lett.*, Vol. 76, 2119 (2000).

[5] J. W. Kooi, J. Kawamura, J. Chen, G. Chattopadhyay, J. R. Pardo, J. Zmuidzinas, T. G. Phillips, B.Bumble, J. Stern, and H. G. LeDuc, "A low noise NbTiN-based 850 GHz SIS receiver for the Caltech submillimeter observatory," *Int. J. IR and MM waves*, Vol. 21, 1357 (2000).

[6] B. Bumble, H. G. LeDuc, J. A. Stern and K.G. Megerian, "Fabrication of Nb / AI-N, / NbTiN Junctions for SIS Mixer Applications," *IEEE Trans. Applied Superconductivity*, Vol. 11, 76 (2001).

[7] T. Zijlstra, C. F. J. Lodewijk, ..., D. N. Loudkov, T. M. Klapwijk, "High current-density aluminum-nitride tunnel barriers grown by plasma nitridation from a remote plasma source," in preparation.

[8] Z. Wang, A. Kawakami, and Y. Uzawa, "NbN/AlN/NbN tunnel junctions with high current density up to 54 $kA/cm^2$," *Appl. Phys. Lett.*, Vol. 70, 114 (1997).

[9] A. B. Kaul, A. W. Kleinsasser, B. Bumble, H. G. LeDuc and K. A. Lee, *J. Mater. Res.*, "Aluminum nitride tunnel barrier formation with low-energy nitrogen ion beams," Vol. 20, 3047 (2005).

[10] M. Weiler, K. Lang, E. Li, J. Robertson, "Deposition of tetrahedral hydrogenated amorphous carbon using a novel electron cyclotron wave resonance reactor," *Appl. Phys. Lett.*, Vol. 72, 1314 (1998).

[11] T. Czerwiec, F. Greer, and D.B. Graves, "Nitrogen dissociation in a low pressure cylindrical ICP discharge studied by actinometry and mass spectrometry," *J. Phys. D: Appl. Phys.*, Vol. 38, 4278 (2005).

[12] A. Baryshev, E. Lauria, R. Hesper, T. Zijlstra, and W. Wild, ALMA memo 429.

# 100 GHz sideband separating mixer with wide IF band

D. Maier, D. Billon-Pierron, J. Reverdy, and M. Schicke

***Abstract*—A sideband separating SIS mixer with a 4–12 GHz IF band and covering the RF frequency range of 80 to 116 GHz has been developed. First junctions have been fabricated and tested as DSB mixers resulting in good and flat noise temperatures over RF and IF bands.**

***Index Terms*—sideband separating mixer, SIS mixer, wide IF band**

## I. Introduction

A sideband separating mixer for 100 GHz based on single-ended DSB mixers and an RF waveguide quadrature coupler has been developed. A schematic view of the mixer is shown in Figure 1. The two DSB mixer units are connected at their inputs and outputs to quadrature hybrids. The LO signal is split and applied in-phase to the two mixers through –23dB injection couplers. Since upper and lower sideband signals undergo different phase shifts, they appear separately at the two outputs of the IF quadrature hybrid [1].

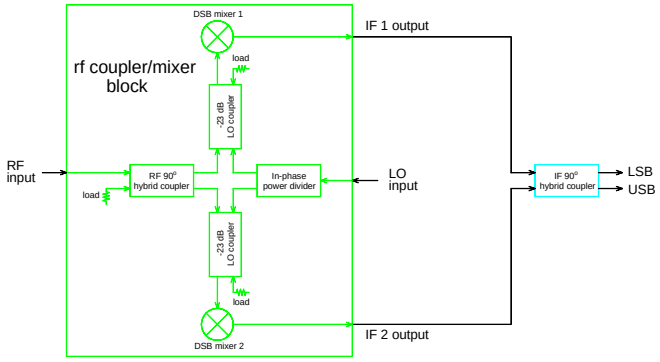


*Figure 1. Schematic view of the sideband separating mixer.*

## II. 2SB mixer assembly

The RF 90° hybrid coupler, the two –23 dB LO couplers and the in-phase power divider as well as the two mixer blocks have been integrated into one E-plane split-block as shown in Figure 2. So, the 2SB mixer assembly consists of this combined RF coupler/mixer block and a commercially available IF 90° hybrid coupler. The IF outputs of the mixers are connected via semirigid cables to the inputs of the IF quadrature coupler.

D. Maier, D. Billon-Pierron, J. Reverdy, and M. Schicke are with the Institut de RadioAstronomie Millimétrique, 300, rue de la piscine, 38406 St. Martin d'Hères, France (phone: +33476824900; fax: +33476515938; e-mail: maier@iram.fr).

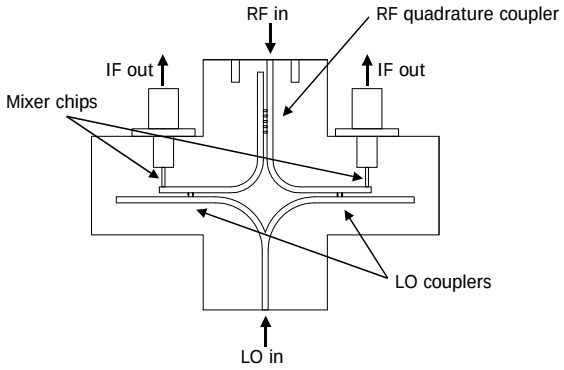


*Figure 2. RF coupler/mixer block realized as E-plane splitblock.*

### A. RF quadrature coupler

The RF quadrature coupler has been realized as branchline coupler [2]. The dimensions of the slots have been optimized using CST Microwave Studio [3]. The results of the simulations are shown in Figure 3.

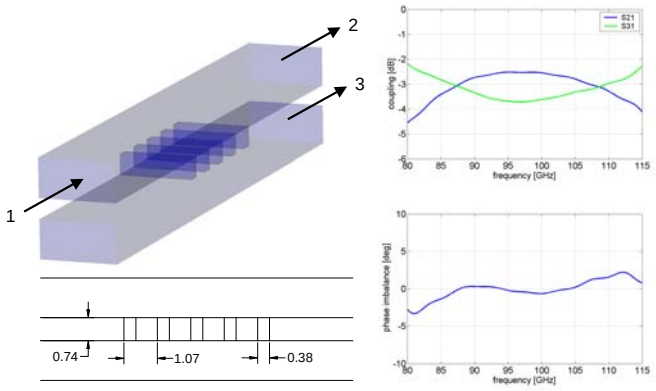


*Figure 3. RF quadrature coupler.*

### B. LO coupler

In order to decrease the noise contribution of the LO system, we decided to use a -23 dB LO coupler. With such a coupler we expect a noise contribution of 1.5 K compared to 6 K of a normally used –17 dB coupler. Just like the RF quadrature coupler the LO coupler has been realized as branchline coupler, but only with two slots.

## III. DSB MIXER

### A. RF design

The essential part of the mixer is a series array of superconductor-insulator-superconductor (SIS) tunnel junctions, which is deposited together with a supercon-ducting circuit onto a quartz substrate. This circuit comprises the antenna providing a full-height waveguide to suspended microstrip transition, the RF choke and the actual tuning circuit whose role is to compensate the junction capacitance and matching to the antenna impedance. Figure 4 shows the layout of one individual mixer chip with a size of 0.6 × 4.5 × 0.08 $mm^3$. These devices are fabricated by IRAM's SIS group [4].

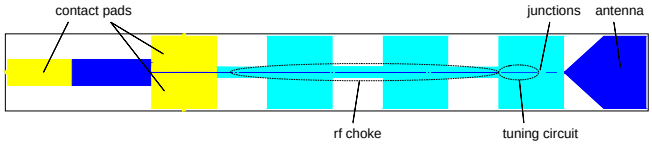


*Figure 4. Layout of the mixer chip.*

The mixer chip is placed in a channel perpendicular to the waveguide axis and stretches only partly across the waveguide as can be seen in Figure 5. The full-height waveguide to microstrip transition is provided by an antenna structure that has been optimized using CST Microwave Studio [3]. The resulting antenna impedance is slightly capacitive, but its real part is almost constant over the operating frequency range (see Figure 6).

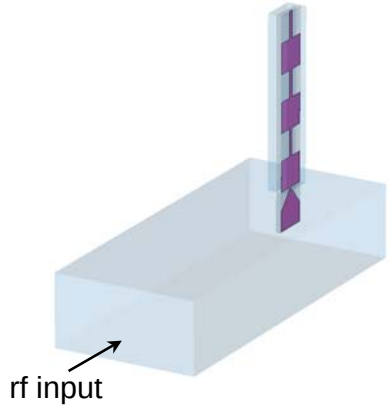


*Figure 5. Full-height waveguide to microstrip transition.*

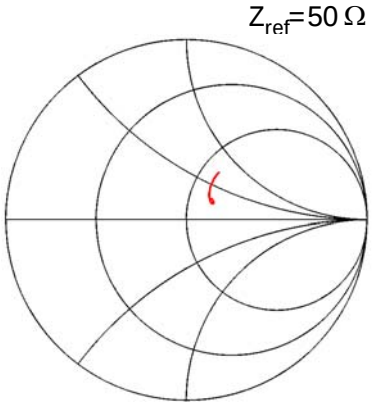


*Figure 6. Antenna driving point impedances for frequencies between 80 and 116 GHz. Smith chart is normalized to 50 Ω.*

A superconducting tuning circuit has been developed and optimized using Sonnet [5] and ADS [6]. Figure 7 shows a picture of the tuning structure. The equivalent circuit is shown in Figure 8.

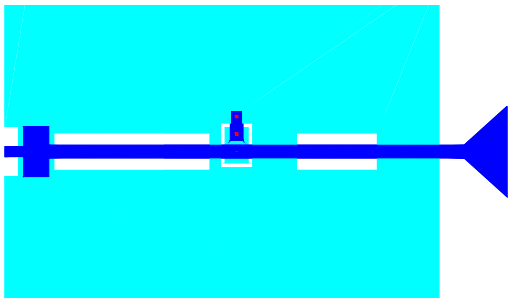

*Figure 7. Tuning circuit of baseline design.*

The design employs three junctions of size 1.5×1.5 $mm^2$ in series of which two are placed on an island structure. Although this adds a small series inductance to the junction array, the whole structure remains capacitive. This capacitance is compensated by a parallel inductance consisting of a coplanar waveguide followed by a capacitance providing the virtual ground to RF. Matching to the antenna impedance is achieved with a structure that can be viewed either as a CLCPW λ/4-transformer or as a discrete L-C transformer.

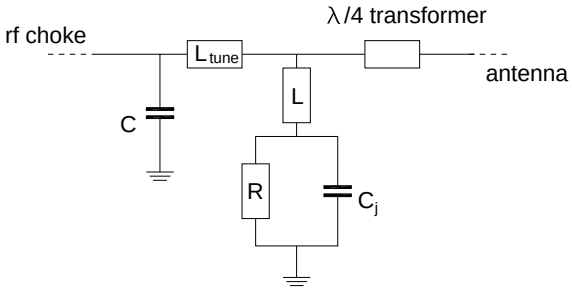


*Figure 8. Equivalent circuit of the tuning structure.*

IRAM's standard fabrication process for SIS junctions includes anodization for better isolation [4]. Since in this design two junctions are placed on an isolated island, they cannot be anodized and so the standard process cannot be used. In order to limit the risk of the development of a process without anodization, a second design based on the standard process has been made. In this design the array consists only of two junctions of size 1.2×1.2 $mm^2$. The short to ground has been realized with a large area junction. The order of the different layers is inverted compared to the baseline design. A small line connects the large junction to mass, so that both junctions can be anodized. The characteristics of the two junction array in the backup design have been chosen to equal those of the three junctions array in the baseline design so that tuning and matching to the antenna impedance are almost the same for the two designs.

The achieved matching to the junction is quite homogenous over the whole frequency range for both designs as can be seen by the junction's embedding impedances plotted in the Smith chart in Figure 9. The red line in the Smith chart delimits the region of impedances for which we expect unconditionally stable behaviour. The power coupled to the junction lies above 96% (see Figure 10).

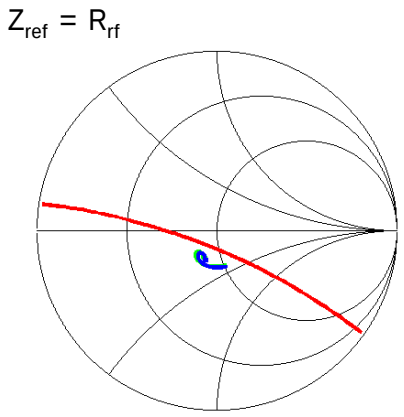


*Figure 9. Embedding impedances of the junctions for baseline (green) and backup (blue) design. The red line delimits the region of unconditionally stable behaviour. Smith chart is normalized to the junction's RF impedance.*

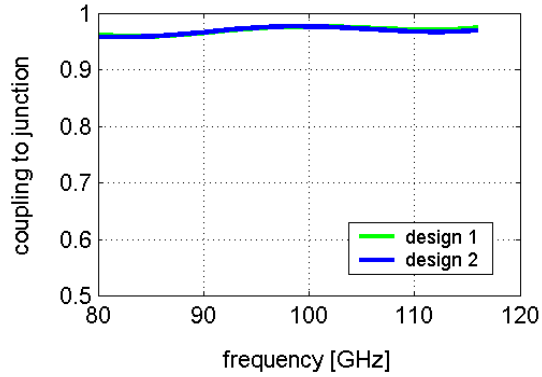


*Figure 10. Fraction of power coupled to the junctions for both designs.*

### B. Noise measurements

First wafers have been fabricated having a very low yield and bad homogeneity of chips of design 1. No chips of design 2 could be fabricated so far. Figure 11 shows a photograph of the 3 junctions array of a design 1 mixer chip, which has been tested as DSB mixer.

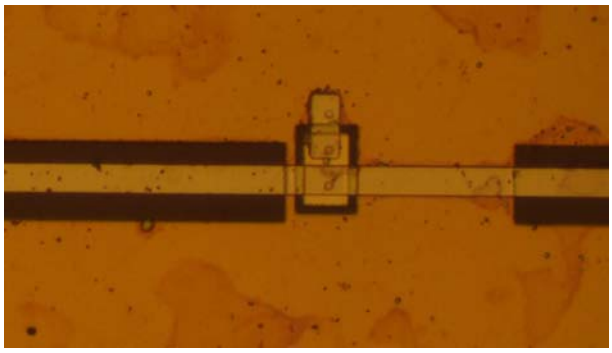

*Figure 11. Photograph of the 3 junctions array of design 1.*

Although in the final design the junctions are directly mounted into the integrated coupler/mixer block without prior testing, mixer blocks have been fabricated to be able to validate the mixer design by DSB mixer tests. Figure 12 shows a mixer chip mounted in the DSB mixer block for testing. On the right-hand side the IF output of the mixer is connected via bond wires to a 50Ω line.

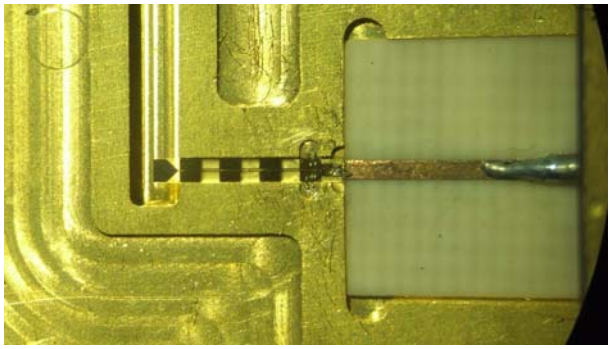

*Figure 12. Photograph of mixer chip mounted in the DSB mixer block.*

An example of a DSB noise measurement for $f_{LO}$ = 100 GHz and an IF band of 4 to 12 GHz is shown in Figure 13. It can be seen that the three junctions in series behave like one single junction.

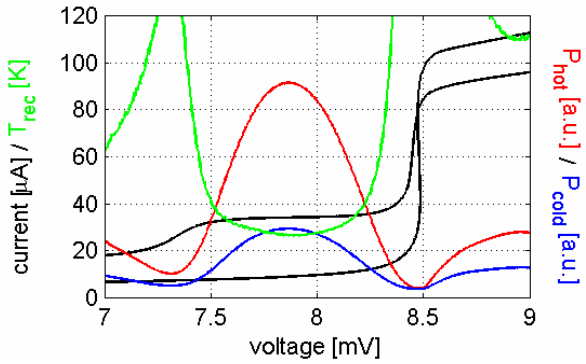


*Figure 13. Example of noise measurement for $f_{LO}$ = 100 GHz and $f_{IF}$ = 4-12 GHz.*

Noise measurements have been carried out first for an IF band of 4 to 8 GHz. The result is shown in Figure 14 represented by the blue curve. When changing the IF chain to 4–12 GHz, the noise increases by ~6 K due to the higher noise of the HEMT amplifier [7] (green curve in Figure 14). Since these measurements have been made with a –17 dB LO coupler these results will improve by around 4.5 K when changing to the initially foreseen LO coupler with –23 dB coupling.

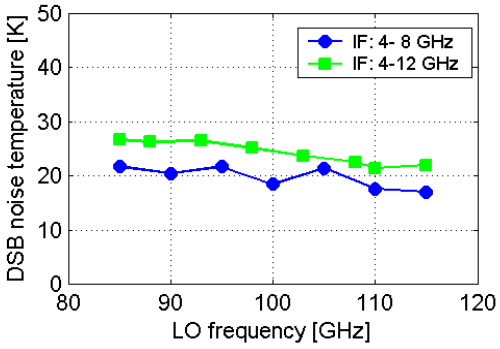


*Figure 14. DSB noise measurements integrated over 4 to 8 GHz and 4 to 12 GHz IF band.*

Noise temperatures as a function of the IF frequency are shown in Figure 15. Apart from the point at 4 GHz where the cryogenic isolator is not working correctly noise curves are flat over the IF band.

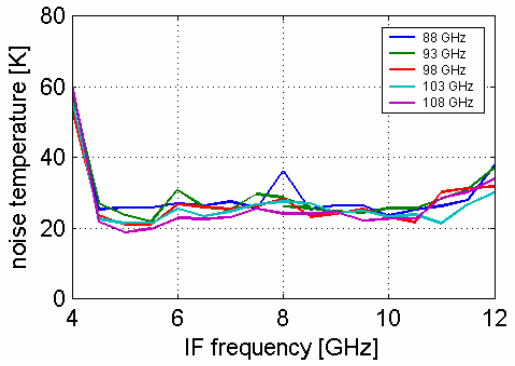


*Figure 15. Noise temperatures as a function of the IF frequency.*

## IV. Conclusions

A sideband separating mixer for the RF frequency range of 80 to 116 GHz has been designed. First junctions have been characterized as DSB mixers for LO frequencies from 85 to 115 GHz and an IF band of 4 to 12 GHz achieving integrated noise temperatures between 22 and 27 K. The DSB mixer design could thus be validated for signal frequencies between 77 and 123 GHz. The design also covers the IF band of 4 to 12 GHz as can be seen by the flat noise curves as function of IF frequency.

## Acknowledgements

This work has been supported by the European Union through the RadioNet program.

## References

[1] S. A. Maas, *Microwave mixers.* Artech House, Inc., 1986

[2] S.M.X. Claude, C.T. Cunningham, A.R. Kerr, and S.-K. Pan, "Design of a Sideband-Separating Balanced SIS Mixer Based on Waveguide Hybrids," *ALMA Memo 316*, 2000

[3] CST Microwave Studio, Bad Nauheimer Str. 19, D-64289 Darmstadt, Germany

[4] I. Péron, P. Pasturel, and K.F. Schuster, "Fabrication of SIS junctions for space borne submillimeter wave mixers using negative resist e-beam lithography," IEEE Trans. Applied Superconductivity, Vol. 11, pp. 377-380, March 2001

[5] Sonnet Software, 100 Elwood Davis Road, North Syracuse, NY 13212

[6] Advanced Design System, Agilent EEsof EDA

[7] J.D. Gallego Puyol, F. Colomer, I.L. Fernández, and A. Barcia, in 3rd RadioNet Annual Report

# SuperCam : A 64 pixel superheterodyne camera

**Christopher Groppi[1,7], Christopher Walker[1], Craig Kulesa[1], Dathon Golish[1], Patrick Pütz[1,6], Paul Gensheimer[1], Abby Hedden[1], Shane Bussmann[1], Sander Weinreb[2,3], Glenn Jones[3], Joseph Barden[3], Hamdi Mani[3], Tom Kuiper[2], Jacob Kooi[3], Art Lichtenberger[4], Thomas Cecil[4], Gopal Narayanan[5]**

1: University of Arizona, 2: NASA Jet Propulsion Laboratory, 3: California Institute of Technology, 4: University of Virginia, 5: University of Massachussetts, 6: Universität Zu Köln, 7: National Science Foundation Astronomy and Astrophysics Postdoctoral Fellow

**Abstract— We report on the development of *SuperCam*, a 64 pixel, superheterodyne camera designed for operation in the astrophysically important 870 μm atmospheric window. *SuperCam* will be used to answer fundamental questions about the physics and chemistry of molecular clouds in the Galaxy and their direct relation to star and planet formation. The advent of such a system will provide an order of magnitude increase in mapping speed over what is now available and revolutionize how observational astronomy is performed in this important wavelength regime.**

***SuperCam* is constructed by stacking eight, 1x8 rows of tunerless, SIS mixers. The SIS junctions use SOI (Silicon on Insulator) technology, with beamleads for device positioning and IF and ground electrical connections. The mixer modules are fabricated using a Kern MMP-2522 micromilling machine purchased specifically for this task. The IF output of each SIS device is directly connected to a low-noise, broadband MMIC amplifier module integrated into the mixer block. The instantaneous IF bandwidth of each pixel is 2 GHz, with a center frequency of 5 GHz. An IF processor constructed of eight 8-channel modules provides IF amplification, total power monitoring and baseband downconversion. A spectrum of the central 250 MHz or 500 MHz of each IF band is provided by the Omnisys real-time FFT spectrometer system, based on Xilinx Virtex 4 FPGAs. This spectrometer can operate in either 32 channel mode (500 MHz/channel) or 64 channel mode (250 MHz/channel). Local oscillator power is provided by a Virginia Diodes solid-state multiplier chain whose output is divided between the pixels with a matrix of waveguide power dividers. The mixer array is cooled to 4K by a closed-cycle cryostat with two cryocoolers. *SuperCam* will reside at the Cassegrain focus of the 10m Heinrich Hertz telescope (HHT) with a dedicated re-imaging optics system.**

**All subsystems of *SuperCam* have completed the development stage, and are undergoing testing. We present test results for the *SuperCam* LNA modules, integration of LNAs in a test mixer, IF processor performance, spectrometer performance, cryogenic system verification, and end-to-end measurements of the IF chain and backend. Results from the fabrication, construction and testing of prototype SOI mixers, in both single pixel and 8 pixel versions will be shown. We will enter the final fabrication stage in early 2007, with expected completion in late 2007. Science operations are expected to begin in Spring, 2008.**

***Index Terms*—Submillimeter heterodyne array**

## I. Introduction

SuperCam will operate in the astrophysically rich 870μm atmospheric window, where the HHT has the highest aperture efficiency of any submillimeter telescope in the world and excellent atmospheric transmission more than 40% of the time. The proposed Superheterodyne Camera (SuperCam) will be an 8x8, integrated receiver array fabricated using leading-edge mixer, local oscillator, low-noise amplifier, cryogenic, and digital signal processing technologies.

SuperCam will be several times larger than any existing spectroscopic imaging array at submillimeter wavelengths. The exceptional mapping speed that will result, combined with the efficiency and angular resolution achievable with the HHT, will make SuperCam the most uniquely-powerful instrument for probing the history of star formation in our Galaxy and the distant Universe. SuperCam will be used to answer fundamental questions about the physics and chemistry of molecular clouds in the Galaxy and their direct relation to star and planet formation. Through Galactic surveys, particularly in CO and its isotopomers, the impact of Galactic environment on these phenomena will be realized. These studies will serve as "finder charts" for future focused research (e.g. with ALMA) and markedly improve the interpretation, and enhance the value of numerous contemporary surveys.

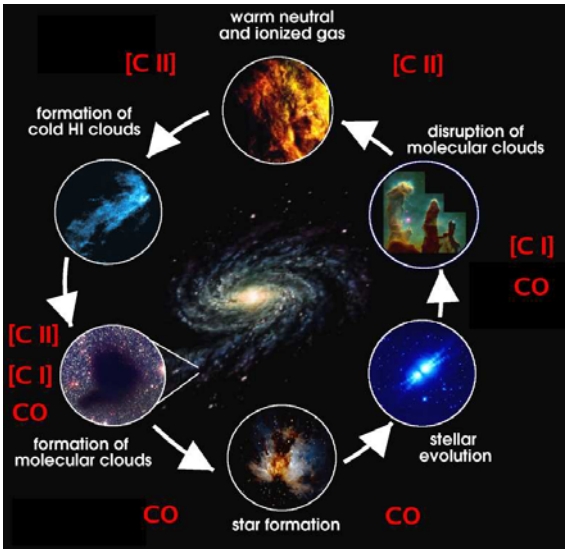


Figure 1: Life cycle of the ISM

Manuscript received May 31, 2007. This work is supported by the National Science Foundation Major Research Instrumentation Program, grant number AST-0421499.

## II. SuperCam Science

From the Milky Way to the highest-redshift protogalaxies at the onset of galaxy formation, the internal evolution of galaxies is defined by three principal ingredients that closely relate to their interstellar contents:

- The transformation of neutral, molecular gas clouds into stars and star clusters (star formation).
- the interaction of the interstellar medium (ISM) with the young stars that are born from it, a regulator of further star formation.
- the return of enriched stellar material to the ISM by stellar death, eventually to form future generations of stars.

The evolution of (the stellar population of) galaxies is therefore determined to a large extent by the life cycles of interstellar clouds: their creation, starforming properties, and subsequent destruction by the nascent stars they spawn. The life cycle of interstellar clouds is summarized pictorially in Figure 1. Although these clouds are largely comprised of neutral hydrogen in both atomic and molecular form and atomic helium, these species are notoriously difficult to detect under typical interstellar conditions. Atomic hydrogen is detectable in cold clouds via the 21 cm spin-flip transition at 1420 MHz, but because the emission line is insensitive to gas density, cold (T~70K) atomic clouds are not distinguishable from the warm (T~8000K) neutral medium that pervades the Galaxy. Furthermore, neither atomic helium nor molecular hydrogen ($H_2$) have accessible emission line spectra in the prevailing physical conditions in cold interstellar clouds. Thus, it is generally necessary to probe the nature of the ISM via rarer trace elements. Carbon, for example, is found in ionized form ($C^+$) in neutral HI clouds, eventually becoming atomic (C), then molecular as carbon monoxide (CO) in dark molecular clouds. The dominant ionization state(s) of carbon accompany each stage of a cloud's life in Figure 1. In general, however, only global properties can be gleaned from the coarse spatial resolution offered by studies of external galaxies. Therefore detailed interstellar studies of the widely varying conditions in our own Milky Way Galaxy serve as a crucial diagnostic template or "Rosetta Stone" that can be used to translate the global properties of distant galaxies into reliable estimators of star formation rate and state of the ISM.

## III. SuperCam Instrument Description

### A. Instrument Design

Unlike all other millimeter/submillimeter arrays composed of individual mixers and discrete components, SuperCam has a high degree of integration. Well conceived, efficient packaging is essential to the successful implementation of large format systems. The enormous complexity of even a small discrete system suggests a more integrated approach for larger systems. At the heart of the array is an 8x8 integrated array of low-noise mixers. The array mixer contains first stage, low-noise, MMIC IF amplifier modules with integrated bias tees. A single solid-state source provides local oscillator power to each array mixer via a waveguide corporate power divider and a simple silicon etalon. Below we discuss SuperCam's key components.

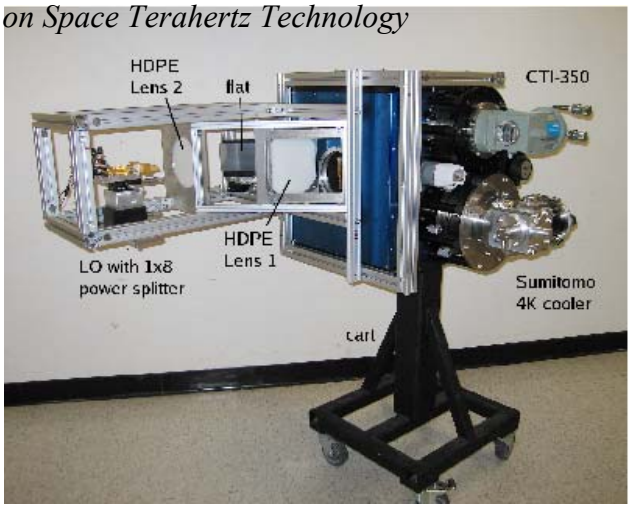


Figure 2: The SuperCam cryostat and optics

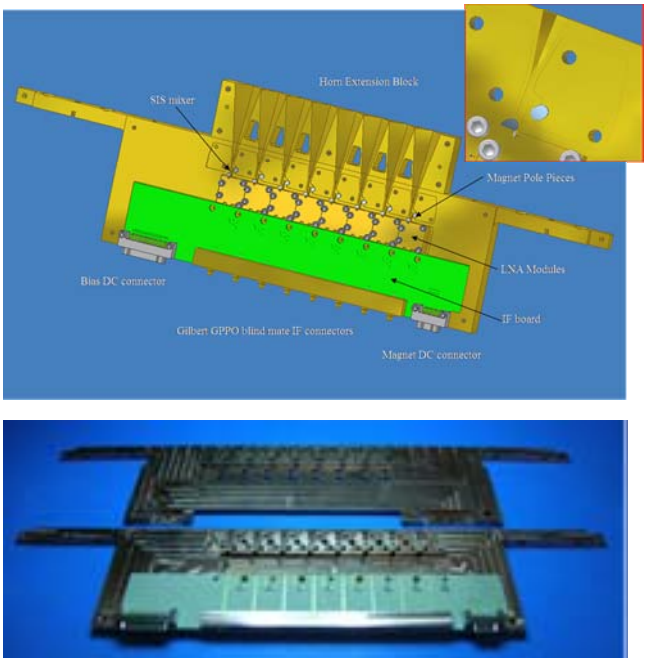


Figure 3: 3D CAD model of an open mixer array module (top) and a completed tellurium copper mixer block with IF board installed (bottom).

#### 1) Cryogenics

The SuperCam cryostat with attached LO optics is shown in Figure 2. The cryostat was constructed by Universal Cryogenics in Tucson, Arizona, USA. Light from the telescope enters the cryostat through a 127 mm diameter AR coated, crystalline quartz vacuum window and passes through an IR blocking filter on the 40 K radiation shield before illuminating the 4 K mixer array. SuperCam uses a Sumitomo SRDK-415D cryocooler. The cooler has 1.5 W of thermal capacity at 4.2 K and 45W at 40K with orientation-independent operation. The operating temperature of the cryocooler is stabilized by the addition of a helium gas pot on the 2nd stage. A CTI cryogenics CTI-350 coldhead supplements the cooling of the 40K shield, and provides 12K heatsinking for the 64 stainless

steel semi-rigid IF cables. The addition of this second coldhead permits the use of moderate lengths of standard coaxial cable while maintaining low heat load at 4K. Measurements using resistive heaters positioned in the cryostat at the location of the IF amplifiers verify that the cryogenic system has adequate performance, with an expected load capacity margin of ~50%.

*2) Mixer Array*

We are developing a compact, sensitive, 64 pixel array of SIS mixers optimized for operation in the 320-360 GHz atmospheric window. The two dimensional, 8x8 array will be composed of eight, 1x8 subarrays. The array mixers utilize SIS devices fabricated on Silicon-On-Insulator (SOI) substrates, with beam lead supports and electrical contacts. The waveguide probe and SIS junction are based on an asymmetric probe design currently in use at the Caltech Submillimeter Observatory in their new facility 350 GHz receiver. The measured DSB noise temperature of this receiver (40 K) is excellent and essentially frequency independent across the band. The 1x8 mixer subarrays will be constructed from tellurium copper using the splitblock technique. Stainless steel guide pins and screws are used to ensure proper alignment and good contact between parts. Figure 3 shows a photograph of a prototype tellurium copper 1x8 mixer array fabricated at the University of Arizona using a Kern MMP micromilling machine. This block meets all design specifications, with 3 µm dimensional accuracy for all waveguide circuits. A diagonal feedhorn extension block is bolted to the front of the mixer array assembly, extending the diagonal horns to 11mm aperture size. This eliminates the need for dielectric lenses and their associated manufacturing and alignment difficulties. The energy in the horn passes through a 90° waveguide bend before reaching the device. The waveguide environment is designed around full height rectangular waveguide, with a fixed quarter wave backshort. The SIS device is suspended above the suspended stripline channel via eight small beamlead supports. Both the hot and ground beamleads are tack-bonded with a wirebonder to the MMIC module input pad and block, respectively. The mixer blocks are fabricated at the University of Arizona using a Kern MMP micromilling machine purchased for this project. This numerically controlled mill can fabricate structures to micron accuracy with a high level of automation. A SuperCam 1x8 module can be produced in ~8 hours of machine run time, using only a single set of micro end mills per block half. The machine's 24 position tool changer allows a complete block to be fabricated with minimal user intervention during the machining process. Integrated workpiece and tool metrology systems, along with sophisticated computer aided manufacturing (CAM) software result in high part yield. Verification of fabricated parts though a high precision measurement microscope and 3D interferometric microscope insure dimensional accuracy and waveguide surface finish are within design tolerances.

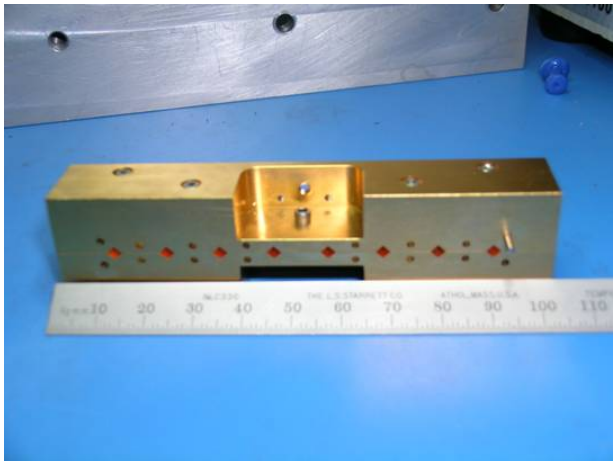

Figure 4: SuperCam 8-way LO power divider. The divider is based on a corporate array of E-plane y-splitters.

*3) Local Oscillator*

With an array receiver, LO power must be efficiently distributed among pixels. Depending on the mechanical and optical constraints of the array, a balanced distribution can be achieved using quasioptical techniques or waveguide injection. With the quasioptical approach, dielectric beam splitters or holographic phase gratings are used to divide the LO energy between array pixels. The quasioptical approach works well for modest sized arrays. However, for the large format system being proposed here, the size of the required quasi-optical

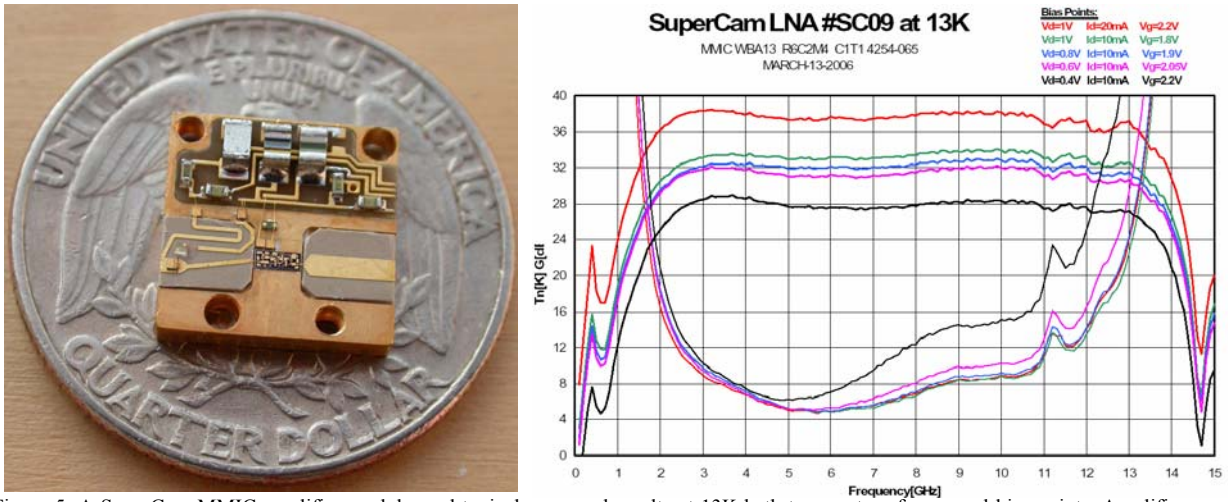


Figure 5: A SuperCam MMIC amplifier module, and typical measured results at 13K bath temperature for several bias points. Amplifier noise remains low for bias powers as low as 8 mW. Gain remains above 30 dB.

power splitter and diplexer become prohibitive. Therefore we have chosen to use a hybrid waveguide/quasioptical LO power injection scheme. The LO power for the array will be provided by a single solid-state, synthesizer-driven source available from Virginia Diode Inc. The active multiplier chain consists of a high power solid-state amplifier followed by a series of tunerless broadband multipliers. The output of the multiplier is coupled to an eight-way waveguide corporate power divider with splitblock machineable waveguide twists. Each of the eight outputs provides the drive power for a 1x8 subarray via an identical 8 way corporate divider with diagonal waveguide feedhorn outputs. Figure 4 shows a prototype 1x8 power divider designed to power a single 1x8 mixer row. The final 64 way power divider will consist of 9 copies of this circuit, with a different block footprint. An extended diagonal horn array similar to the mixer horn extension blocks then matches the LO beams to the mixers through a Gaussian beam telescope comprised of two large dielectric lenses. A silicon etalon diplexer is used to inject the LO power. This diplexer consists of a precisely polished silicon plate which acts as a fixed tuned Fabry-Perot etalon. This technique can couple 70% of the available LO power and over 99% of the sky power into the mixers, with no moving parts and simple optical alignment. As SuperCam is designed to spend extended periods of time tuned to a single frequency, this simple technique is preferred over more complicated tunable diplexers. A set of diplexers will allow tuning to any line of interest by switching silicon plates. This scheme ensures uniform LO power in each beam since the waveguide path lengths are identical for each beam. In addition, the waveguide feedhorns provide well controlled and predictable LO power distribution and coupling to each mixer. Accounting for conduction and surface roughness losses, we expect this 64-way network to add an additional 2dB of LO power loss compared to a lossless divider.

Figure 6: SuperCam IF processor system for two SuperCam rows (16 channels).

*4) IF/Bias Distribution System*

The IF outputs from the SIS devices are bonded directly to the input matching networks of low-noise, InP MMIC amplifier modules located in the array mixers. These amplifier modules have been designed and fabricated by Sander Weinreb's group at Caltech. The IF center frequency of the array is 5 GHz. The MMIC chip is contained in an 11mm x 11mm amplifier module that contains integrated bias tees for the SIS device and the amplifier chip. The module achieves noise temperature of ~5 K consuming 8 mW of power at 4K. The first 10 amplifier modules are complete., with all components necessary to complete all the modules finished. An example is shown in figure 5, with measured gain and noise data at 8 mW power dissipation. We have integrated an amplifier module into a single pixel SIS mixer and have verified that the amplifier module operates as expected. Allan varience times and mixer noise temperatures are unchanged within the measurement errors compared to a similar mixer used with an external commercial LNA and isolator. Similar tests have been performed with a single pixel mixer with beamlead devices, which will be described in section IV.

In addition to the LNA modules, the Caltech group has designed and constructed a warm IF system for SuperCam that will condition the IF signal for use with the SuperCam Array Spectrometer (figure 6). This IF system consists of a single large microwave printed circuit board with 8 channels of signal conditioning mounted in a modular chassis. The module contains a 5 GHz gain stage, switchable filters for both 250 MHz and 500 MHz bandwidth modes, baseband downconversion and baseband amplification. These modules have been extensively tested for stability and noise performance. Their stability is sufficient to avoid increasing the allen time of the array spectrometer, while adding less than 1K to the receiver noise temperature.

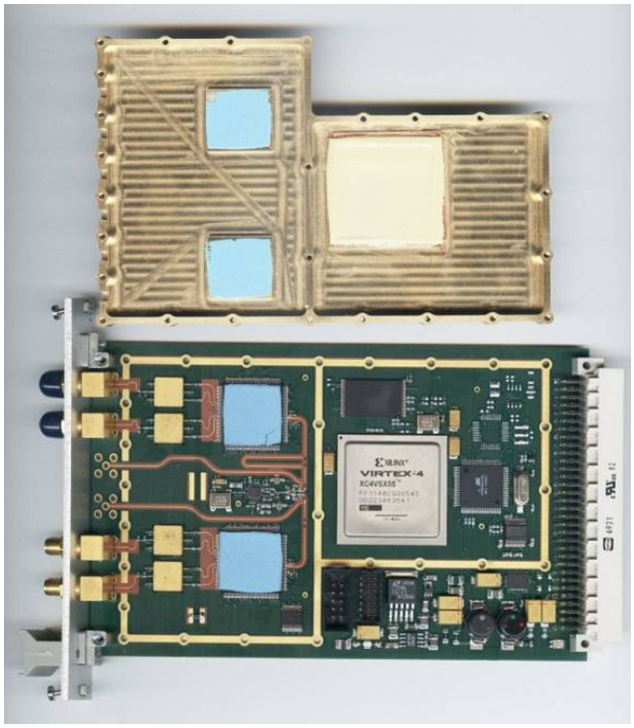


Figure 7: SuperCam FFT spectrometer board from Omnisys AB. This 3U board can process 4 500 MHz bandwidth IF signals or 2 1 GHz bandwidth IF signals at 250 kHz resolution.

*5) Array Spectrometer*

The SuperCam spectrometer will deliver 64 channels at 250 MHz/channel with 250 kHz resolution, or 32 channels at 500 MHz with 250 kHz resolution. The system will be capable of resolving lines in the coldest clouds, while fully encompassing the Galactic rotation curve. The system is easily extendible to deliver 64 500 MHz bandwidth channels or 32 1 GHz bandwidth channels. This leap in spectrometer ability is driven

by the rapid expansion in the capabilities of high speed Analog to Digital Converters (ADCs) and Field Programmable Gate Arrays (FPGAs). The SuperCam spectrometer, built by Omnisys AB of Sweden, is based on a real-time FFT architecture. High speed ADCs digitize the incoming RF signal at greater than 10 bits resolution, preventing any significant data loss as with autocorrelation based schemes. Then, a large, high speed FPGA performs a real time FFT on the digitized signal and integrates the resulting spectrum. In our board architecture, 4 ADCs feed a single Xilinx Virtex 4 FPGA on each spectrometer board (shown in figure 7). This single board can process 4 500 MHz IF bandwidth signals or two 1 GHz IF bandwidth signals at 250 kHz resolution. Only recently has Xilinx released FPGAs fast enough and large enough to accommodate the firmware capable of this task. These systems are fully reconfigurable by loading new firmware into the FPGAs. In addition, the spectrometer can be easily expanded to increase bandwidth. We have received 8 boards capable of processing 64x250 MHz, 32x 500 MHz or 16x1GHz IF signals. In the 64x250 MHz mode, we power combine two IF signals into one spectrometer input. Stability testing shows the spectrometer is capable of delivering a spectroscopic Allan time in excess of 600s.

*6) Optics*

The existing secondary mirror of the Heinrich Hertz Telescope provides a f/13.8 beam at the Nasmyth focus. The clear aperture available through the elevation bearing prevents the possibility of a large format array at this position. To efficiently illuminate a large format array like SuperCam, the telescope focus must fall within the apex room located just behind the primary. A system of re-imaging optics transforms the f number of the telescope to f/5. Since the physical separation between array elements in the instrument focal plane scales as $2f\lambda$, lower f/#'s serve to reduce the overall size of the instrument. The reimaging optics are composed of a hyperbola and an ellipse with two flat mirrors. All the reimaging optics can be mounted on a single optical breadboard and left in the apex room. The cryostat and optics frame have been designed using finite element analysis to minimize gravitational deflection, and the calculated deflections have been fed into the tolerancing of the optical design. The optical system was initially designed and optimized with Zemax, and was then verified by BRO research using their ASAP physical optics package. The system's efficiency exceeds 80% for all pixels, and has been verified to be robust to alignment and fabrication tolerances.

## IV. Laboratory Testing

For testing the SuperCam mixer design in the laboratory, we have designed two single pixel mixers. The first design uses an existing SIS junction design from the DesertStar 7-pixel array [7], but incorporates the Caltech designed MMIC module. This work has been reported in other papers [12,13]. We determined that the SIS receiver with integrated MMIC amplifier worked as well as a receiver with a separate connectorized amplifier and cryogenic amplifier, and resulted in no heating effects at the SIS device from the close proximity of the amplifier. We later designed a second single pixel amplifier (shown in figure 8) that is an exact copy of a single pixel of the 1x8 mixer array design discussed in section III.2. This mixer was designed to test the self-aligning beam-lead-on-SOI SIS devices that will be used in the SuperCam array, as well as the compact, low power electromagnet, MMIC amplifier module and extended diagonal feedhorn. The first batch of SIS junctions suffered from curling caused by a stressy oxide layer which made them difficult to mount, but successful testing was still possible. Lab results from the first device mounted are also shown in figure

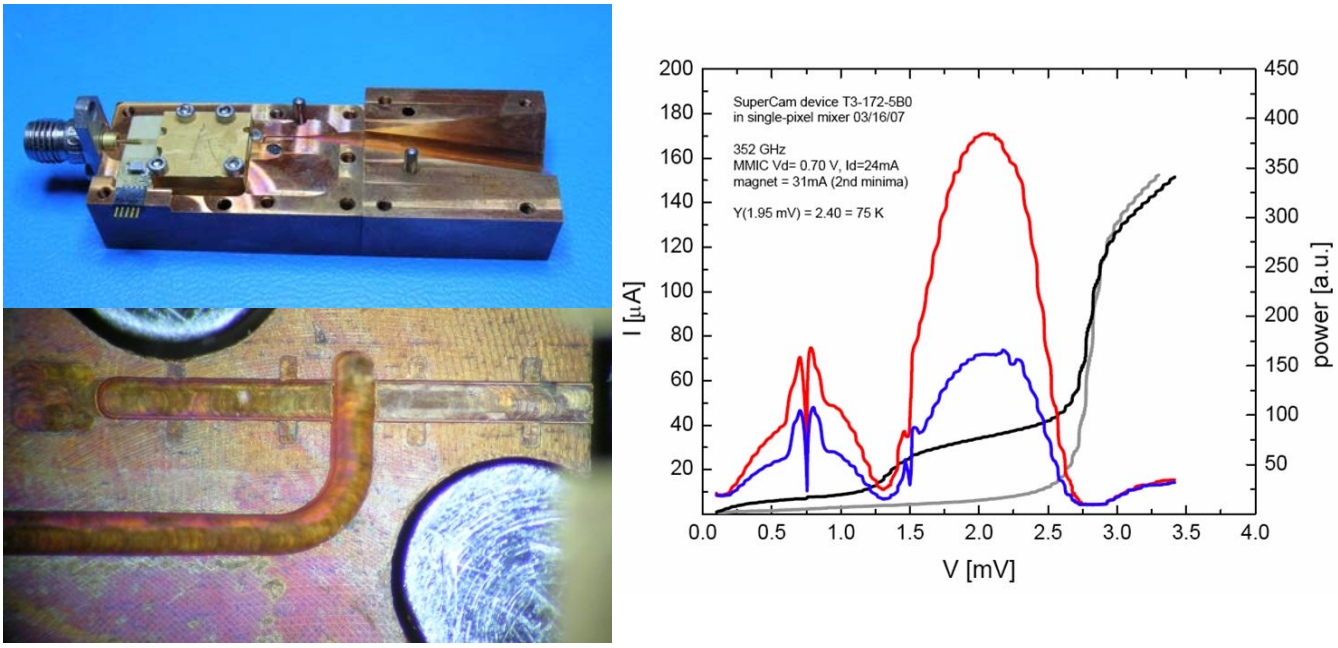


Figure 8: Single pixel test mixer with extended diagonal horn, LNA module and IF board (top left), a closeup of the device waveguide environment (bottom left), and a representative IV curve and hot/cold total power curve (right).

8. We achieved an uncorrected DSB noise temperature of 75K, and verified efficient operation of the electromagnet. Since these tests, a second batch of SIS devices has been delivered with the curling problem eliminated. This will facilitate rapid, self aligned mounting if the devices. With further optimization, we expect to be able to achieve the 60K receiver noise temperature predicted by the SIS device simulations.

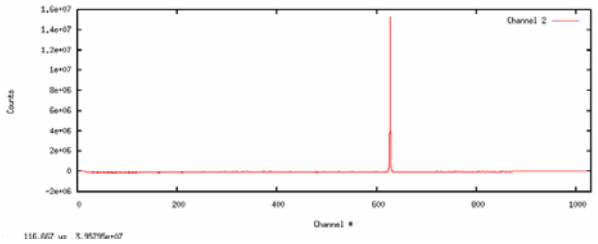


Figure 9: Spectrum from an end to end test of SuperCam prototype hardware.

In addition to measurement of these test mixers, we have also conducted an end to end test using prototype components of the complete SuperCam system. In this test, we used a line injector to detect a simulated spectral line using a single pixel test mixer with MMIC LNA module, a prototype IF processor module and an Omnisys FFT spectrometer board. The spectrum produced via this measurement is shown in figure 9.

## V. Conclusion

We are constructing SuperCam, a 64-pixel heterodyne imaging spectrometer for the 870 μm atmospheric window. A key project for this instrument is a fully sampled Galactic plane survey covering over 500 square degrees of the Galactic plane and molecular cloud complexes. This $^{12}$CO(3-2) and $^{13}$CO(3-2) survey has the spatial (23") and spectral (0.25 km/s) resolution to disentangle the complex spatial and velocity structure of the Galaxy along each line of sight. SuperCam was designed to complete this survey in two observing seasons at the Heinrich Hertz Telescope, a project that would take a typical single pixel receiver system 6 years of continuous observing to complete. Prototypes of all major components have been completed and tested. The first 1x8 mixer row has been fabricated, and is now undergoing testing. We expect to complete fabrication and testing of the focal plane in 2007, with operations on the telescope to begin in 2008.

## References

[1] R.B. Bass, J.C. Schultz, A.W. Lichtenberger (University of Virginia); C. Walker (University of Arizona); J. Kooi (CalTech), "Beam Lead Fabrication Using Vacuum Planarization", submitted to Proceedings of the Fourteenth International Symposium on Space THz Technology, May 2003.

[2] Carpenter, J. M., Snell, R. L., & Schloerb, F. P. 1995, "Star Formation in the Gemini OB1 Molecular Cloud Complex", ApJ, 450, 201

[3] Dame, T. M. et al. 1987, "A composite CO survey of the entire Milky Way", ApJ, 322, 706

[4] Dame, T. M., Hartmann, D., & Thaddeus, P. 2001, "The Milky Way in Molecular Clouds: A New Complete CO Survey", ApJ, 547, 792

[5] Gillespie, A. R. & Phillips, T. G., 1979, "Array Detectors for Millimetre Line Astronomy", A&A, 73, 14.

[6] Goldsmith, P., in "Quasioptical Systems", pub. IEEE Pressm 184.

[7] Groppi, C. E. et al. 2003, "DesertSTAR: a 7 pixel 345 GHz heterodyne array receiver for the Heinrich Hertz Telescope", SPIE, 4855, 330

[8] J.W. Kooi, C.K. Walker, and J. Hesler, "A Broad Bandwidth Suspended Membrane Waveguide to Thin Film Microstrip Transition", 9th Int. Conference on Teraherz Electronics, 15th - 16th October 2001.

[9] Sakamoto, S., Hasegawa, T., Hayashi, M., Handa, T., & Oka, T. 1995, "The Five College Radio Astronomy Observatory CO Survey of the Outer Galaxyî" ApJS, 100, 125

[10] Simon, R., Jackson, J. M., Clemens, D. P., Bania, T. M., & Heyer, M. H. 2001, "The Structure of Four Molecular Cloud Complexes in the BU-FCRAO Milky Way Galactic Ring Survey", ApJ, 551, 747

[11] E. Schlecht, G. Chattopadhyay, A. Maestrini, A. Fung, S. Martin, D. Pukala, J. Bruston, and I. Mehdi, "200, 400, and 800 GHz Schottky diode substrateless multipliers: Design and Results," 2001 IEEE, MTT-S International Microwave Symp. Digest, Phoenix, Az, pp. 1649-1652, May 2001.

[12] Walker, C. K., Groppi, C., d'Aubigny, C., Kulesa, C., Hungerford, A., Jacobs, K., Graf, U., Schieder, R., & Martin, C., 2001, PoleSTAR: A 4-Pixel 810 GHz Array Receiver for AST/RO, "Proceedings of the 12th International Symposium on Space Tera- Hertz Technology", San Diego, CA, Eds. Mehdi & McGrath, JPL.

[13] Groppi, C.E., Walker, C.K., Kulesa, C., Puetz, P., Golish, D., Gensheimer, P., Hedden, A., Bussmann, S., Weinreb, S., Kuiper, T., Kooi, J., Jones, G., Bardin, J., Mani, H., Lichtenberger, A., Narayanan, G. *SuperCam, a 64- Pixel Superheterodyne Camera,* Proceedings of the 17th International Symposium on Space Terahertz Technology, 2006.

[14] Puetz, P., Hedden, A., Gensheimer, P., Golish, D., Groppi, C., Kulesa, K., Narayanan, G., Lichtenberger, A., Kooi, J., Wadefalk, N., Weinreb, S., Walker, C., *345 GHz Prototype SIS Mixer with Integrated MMIC LNA*, Int. J. Infrared Milli. Waves, 27, 1365, 2006.

# Upgrades to the CSO Heterodyne Facility Instrumentation: A 280-420 GHz Wide IF band Rx and beyond....

Jacob Kooi
California Institute of Technology

The facility receivers of the CSO are in the process of being replaced by broadband (no-tuners), wide IF (4-8 GHz) state-of-the-art versions. The standard version will use a balanced mixer input, simplifying the LO input and canceling LO amplitude noise. Design and fabrication of the many individual components, e.g. mixers, low noise amplifiers, SIS junctions, optics etc. is now complete. A second style mixer, a 2 element balanced correlation receiver with one pixel on-source and one pixel off-source, has also been delivered. This instrument will be constructed after the facility receivers are upgraded.

To demonstrate the technology, and to facilitate extended baseline observations with the SMA (eSMA), a tunerless 280-420 GHz DSB single-ended receiver (Barney) has recently been deployed at the CSO. At the heart of the mixer is a high current density AlN SIS tunnel junction and a novel waveguide-to-thinfilm microstrip transition that affords unprecedented tunerless RF bandwidth. The IF bandwidth of the new receivers is 4-8 GHz, though in principal IF bandwidth's up to 12 GHz are possible.

The presentation discusses a number of supporting technologies, and concludes with recent results obtained from 'Trex'; the 280-420 GHz wide IF bandwidth technology demonstration receiver.

# Superconducting Integrated Spectrometer for TELIS

Valery P. Koshelets, Andrey B. Ermakov, Pavel N. Dmitriev, Lyudmila V. Filippenko, Andrey V. Khudchenko, Nickolay V. Kinev, Oleg S. Kiselev, Alexander S. Sobolev, Mikhail Yu. Torgashin

*Institute of Radio Engineering and Electronics (IREE), Russia*

Pavel A. Yagoubov, Ruud W.M. Hoogeveen, and Wolfgang Wild

*SRON Netherlands Institute for Space Research, the Netherlands*

We report on the results of developing a single-chip superconducting integrated receiver which is the key element of the 500 -650 GHz spectrometer for the Terahertz Limb Sounder (TELIS) balloon project. TELIS is a collaborative European project to develop a three-channel heterodyne balloon-based spectrometer for measuring a variety of atmospheric constituents of the stratosphere. The Superconducting Integrated Receiver (SIR) comprises in one chip a planar antenna integrated with an SIS mixer, a superconducting Flux Flow Oscillator (FFO) acting as Local Oscillator (LO) and a second SIS harmonic mixer (HM) for the FFO phase locking.

As a result of the FFO design optimization a free-running linewidth between 9 and 1.5 MHz has been measured in the frequency range 500 – 710 GHz resulting in phase-locking of 35 to 95 % of the FFO power correspondingly. A new generation of the SIR devices with improved FFO performance and optimized interface between FFO and SIS/HM has been developed and comprehensively tested; all required TELIS parameters were demonstrated. Phase–locked FFO operation over entire SIR channel frequency range has been realized, spectral resolution below 1 MHz has been confirmed by gas cell and CW signal measurements. An uncorrected double side band (DSB) noise temperature about 200 K has been measured with the phase-locked FFO. The intermediate frequency bandwidth 4-8 GHz has been realized. To ensure remote operation of the phase-locked SIR several procedures for its automatic computer control have been developed and tested.

To overcome temperature constraints and extend operation frequency of the all-Nb SIR we have developed and studied Nb-AlN-NbN-Nb circuits with a gap voltage Vg up to 3.7 mV and extremely low leakage currents (Rj/Rn > 30). Based on these junctions integrated microcircuits comprising FFO and harmonic mixer have been designed, fabricated and tested; the radiation from such circuits has been measured at frequencies up to 700 GHz. Employment of NbN electrode does not result in the appearance of additional noise. For example, FFO linewidth as low as 1 MHz was measured at 600 GHz, that allows us to phase lock up to 92 % of the emitted by FFO power and realize very low phase noise about –90 dBc. Preliminary results demonstrated uncorrected DSB noise temperature of the Nb-AlN-NbN SIR below 250 K at frequencies of primary TELIS interest around 500 and 600 GHz. We expect that Nb-AlN-NbN-Nb device will be used for the first qualification TELIS flight that is scheduled on April 2007.

The work was supported in parts by the RFBR projects 06-02-17206, the ISTC project # 3174, NATO SfP Grant 981415, and the Grant for Leading Scientific School 7812.2006.2

# New Results on Microwave and Terahertz Detection Using Metallic Single-Walled Carbon Nanotubes

Sigfrid Yngvesson, Kan Fu, Richard Zannoni, Fernando Rodriguez-Morales, John Nicholson, Stephan Adams, Chak Chan, Alexander de Geofroy, Eric Polizzi and Joerg Appenzeller

*Abstract*— **At the ISSTT2006, we presented experimental results for a new microwave (~ 1GHz) direct and heterodyne detector based on metallic Single-Walled Carbon Nanotubes (m-SWNTs). We now report on microwave detection in several different contact configurations, and the methods used to fabricate these. One such configuration is a log-periodic toothed terahertz antenna with which we have now (soon after the conference) detected terahertz radiation from laser sources up to 1.63 THz. We also report on *ab-initio* simulations relevant for interpreting the experimental data. We argue that exploring the properties of single m-SWNTs at terahertz should be very fruitful.**

## I. Introduction

Single Wall Carbon Nanotubes (SWNTs) have been proposed for use of in many new types of electronic devices [1]. SWNTs can be either metallic or semiconducting [2]. One device that is being researched is the Carbon Nanotube Field Effect Transistor (CNT-FET) [3], [4] which employs semiconducting CNTs (s-SWNTs). Applications have also been proposed to detectors for microwave or terahertz frequencies. Schottky barriers exist at the contacts of semiconducting SWNTs [5], [6], and were fabricated and analyzed for use as terahertz detectors by Manohara *et al.* [7]. Experimental results were recently published by Rosenblatt *et al.* [8] demonstrating detection of microwaves up to 50 GHz, as well as by Pesetski *et al.* [9] who measured heterodyne detection with flat frequency-dependence up to 23 GHz. These references ([7]-[9]) all used the s-SWNT-FET configuration. Itkis et al. published results on a Near IR bolometric detector employing a CNT film in which it is likely that the metallic CNTs were most active. A similar bolometric CNT film detector was demonstrated at 94 GHz by Tarasov et al. [11]. Metallic SWNTs (m-SWNTs) have considerable potential for detector applications, and one of us (SY) recently proposed a very fast terahertz detector based on the hot electron bolometric (HEB) effect [12,13]. In the present paper we report experimental results for a device that uses an m-SWNT for detecting microwaves up to 12 GHz, as well as terahertz radiation up to 1.6 THz. In its microwave operation the device described here functions both as a direct (DC output) detector and as a heterodyne detector (difference frequency output up to at least 200 MHz). In this paper we will discuss the experimental results, the possible detection mechanisms involved, as well as relevant *ab-initio* simulations.

S. Yngvesson, K. Fu, R. Zannoni, J. Nicholson, S. Adams, A. de Geofroy, and E. Polizzi are with the Department of Electrical and Computer Engineering, University of Massachusetts, Amherst, MA 01003-9292.

F. Rodriguez-Morales was with the Department of Electrical and Computer Engineering, University of Massachusetts, Amherst, MA 01003-9292; he is now with the Center for Remote Sensing of Ice Sheets (CReSIS), University of Kansas, Lawrence, KS 66045.

C. Chan was with Holyoke Community College, Holyoke, MA; He is now with the Department of Electrical and Computer Engineering, University of Massachusetts, Amherst, MA 01003.

J. Appenzeller was with the IBM T.J. Watson Research Center, PO Box 2128, Yorktown Heights, NY 10598, USA. He is now with the Dept. of Electrical and Computer Engineering, Purdue University Birck Nanotechnology Center, West Lafayette, IN 47907-20575.

This work was supported by a grant for Nanoscale Exploratory Research from the National Science Foundation (ECS-0508436).

## II. Experimental Methods and Results

### A. Initial Experimental Procedures

SWNTs used in our study were grown using laser ablation [14]. They have diameters between 0.6 nm and 1.5 nm, and were contacted either at the IBM T.J. Watson Research Center, or at UMass/Amherst. In the IBM process they were spun from solution onto a p+-doped silicon substrate covered with 100 nm of silicon oxide. Contact strips of width 350 nm were made with 20 nm of Ti followed by 100 nm of Au, and were connected to 80 μm x 80 μm contact pads. The length of the tubes between contacts is known to be in the range of 300 nm to 500 nm.

In the UMass process, CNTs were also first spun onto doped silicon substrates. We used an available mask that produced long metal contact strips with different spacings from 4 to 8 μm and contact pads that could be wire-bonded.

In all subsequent microwave experiments the chip was placed in a small copper enclosure (with a metallic cover) to isolate it from external radiation, see Figure 1 for an example. The contact pads were connected by wire bonds to (1) a microstrip transmission line that was in turn connected to a standard coaxial connector installed in the side of the enclosure; and (2) the ground plane of the enclosure. The silicon substrate was left electrically insulated in order to minimize parasitic reactances. The assembly was placed in a liquid helium vacuum dewar and pumped to a good vacuum for at least one day in order to remove most of the surface contaminations on the CNT. A well shielded stainless steel coaxial cable makes the sample accessible from the outside of

the dewar. We used a programmable DC power supply (Keithley) to provide a voltage source bias to the device through the coaxial cable. The DC supply measured the DC voltage and current, and these were read by a computer for further processing. Microwave sources (Agilent) were also fed to the coaxial cable, and different sources (DC and microwave) were separated through the use of commercial bias tees.

### *B. I-V-Curves and Microwave Detection*

It is well-known that Ti/Au contacts yield a contact resistance that is usually quite high and strongly dependent on the nanotube diameter [15]-[17]. The devices used in our study had contact resistances that were in the range of a few hundred kΩ to a few MΩ. It is also known that the conductance of such

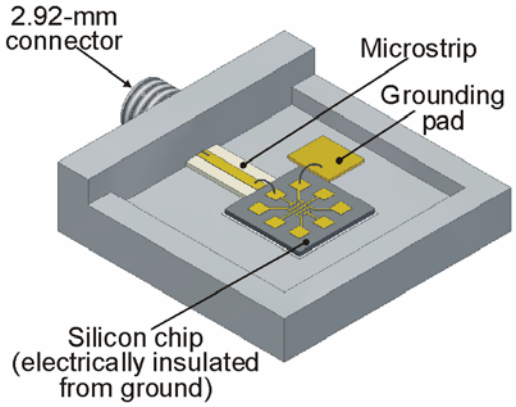


Figure 1. The experimental fixture used in this work.

CNTs shows a "zero-bias anomaly" [17-19], i.e. the differential conductance (dI/dV) plotted as a function of bias voltage (V) shows a dip at low values of V with a width of about +/- 400 mV. This presents a nonlinearity in the IV-curve (Figure 2; for an IBM device) that we exploited for microwave detection.

The zero-bias anomaly "dip" is also evident from the additional plot of dI/dV in Figure 2. This dip deepens as the temperature is decreased (the curves shown in Figure 2 were taken at 77K). At larger voltages the IV-curve shows a linear dependence between current and bias with a slight decrease in dI/dV for the highest voltage range. Except for the zero-bias anomaly, the IV-curve can thus be assumed to be due to a (roughly) constant contact resistance, that is weakly dependent on the temperature. Evidence from other metallic CNTs [4] indicates that the electrons have mean free paths of about 1μm; thus in our shortest tubes they travel ballistically from contact to contact. The zero-bias anomaly is usually ascribed to the very strong electron-electron Coulomb interactions in one-dimensional conductors that necessitates treating the electrons as a collective, plasmon-like, medium known as a "Luttinger liquid" ("LL") [17]. Tunneling from the contacts into the LL is suppressed at low temperatures, which explains why the conductance approaches zero. It has been suggested that the behavior of the conductance in the entire temperature range from 4 K to 300 K can be better explained as being due to a combination of effects, the LL effect, and that of interfacial barriers at the contacts [18]. The LL effect is expected to be important only in the lowest temperature range.

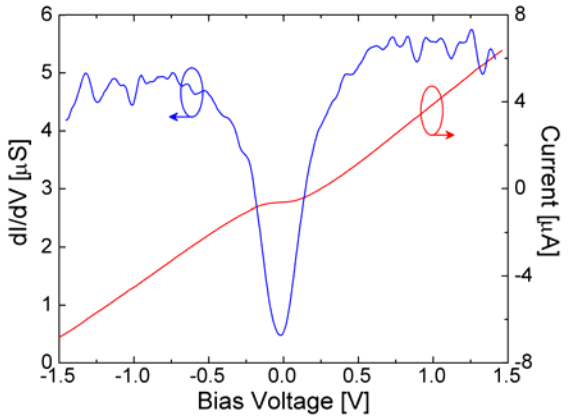


Figure 2. Measured IV-curve for a SWNT from IBM at 77 K (right scale); dI/dV based on the IV-curve (left scale).

As made clear in the paper mentioned above [18], a complete understanding of the contacts between the one-dimensional m-SWNTs and a 3-D metal is not yet available.

UMass devices with Ti/Au contacts were also fabricated with IV-curves similar to that in Figure 2. In a different process, we placed CNTs on top of Ti/Au contacts, and then added a further Pd contact metalization on top of the CNTs. This resulted in a much lower contact resistance, and an IV curve that was curved in the opposite direction, see Figure 3. The increased resistance at higher bias voltages is known to be due to optical phonon emission that requires a minimum electron energy of about 160 meV [4,19,20].

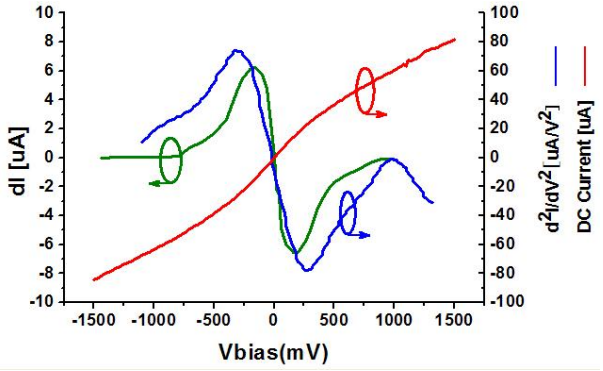


Figure 3. IV curve 77K (red) for CNT contacted with low resistance Pd contacts at UMass. The detected current change (ΔI) (green) is compared with $d^2I/dV^2$ (blue).

As microwaves were applied to the SWNT at 77K, we recorded a change in the device DC current (ΔI), and plotted this versus DC bias voltage (Figure 3). Similar recordings were also obtained for the IBM tubes, as reported earlier [21,22]. This recording was done by measuring the voltage across a series resistance with a lock-in amplifier, while square wave modulating the microwave source. The DC power supply was still configured as a voltage source. As shown in Figure 3, the detected current change varies with the bias voltage in the same way as $d^2I/dV^2$, the second-order derivative of the IV-curve. We can then interpret the detection

process as a standard microwave detection process [23]. Theory and experiment agree quantitatively within 3dB. Heterodyne detection was demonstrated [21,22], and the microwave reflection coefficient (S11) was measured with an automatic network analyzer, as also reported in [21,22]. The detector response is flat to 900 MHz, and then falls off with the microwave frequency at about 12 dB per octave, consistent with a microwave model that was derived based on the S11 measurements. The modeling makes clear that the main factor that limits the frequency response is the very high doping of the silicon substrate used in all early measurements, as well as the large capacitance from the contact pads to the doped substrate.

### *C. Recent Experimental Procedures.*

In order to explore the new detection process at higher frequencies we next fabricated devices on substrates that are insulating: sapphire and silicon-on-sapphire (SOS). Both of these substrates show good transmission up to high terahertz frequencies. New lithography masks were also designed and fabricated, with new contact configurations, see Figure 4: (1) Coplanar waveguides (CPW); and (2) Log-periodic toothed antennas, similar to designs we have previously used with NbN HEB mixers. The intention was to place CNTs across the narrow gaps at the center of these structures. The CPW mask has two parts, one for the center conductor and one for the outer conductors. These two parts of the mask can be adjusted in the lithography process resulting in different gap widths. The log periodic antenna has a gap of about 6 μm.

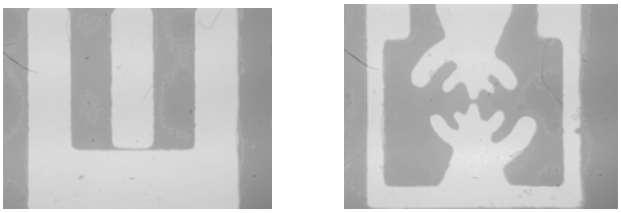

**(a)** **(b)**

Figure 4. Contact patterns for the new masks: (a) Coplanar waveguide; (b) Log-periodic antenna.

Each mask contains a large number of patterns of the types shown in Figure 4 (a) and (b) to maximize the probability of obtaining a CNT across the small gaps as they are spun on the substrates. The yield of tubes with acceptable IV-curves was found to be lower than when using contacts consisting of long, narrow strips, but several contacted tubes were found. The method of spinning the tubes onto the contacts in this case proved to result in unreliable contact performance, and few detection measurements were performed. The one shown in Figure 3 represents an exception, but in this case the contacts were improved by evaporating Pd on top of the CNTs.

Recently we have developed a much improved method for placing CNTs across the contacts, namely dielectrophoresis (DEP) [24-27]. In this method, an RF voltage (typically 5-10 V RMS, 5 MHz) is applied across a pair of electrodes, after a drop of a solution containing the CNTs is placed over the contacts. In our case, the CNTs were suspended in Isopropyl alcohol [25] and then ultra-sonicated for 10 minutes. The result of the DEP is that CNTs migrate in the solution toward the contacts, and then become attached to the contacts. It has also been observed that nearby contacts that experience a floating RF potential can attract CNTs [26]. The procedure typically takes only a few minutes. The DC resistance is being monitored as the DEP proceeds and the process is stopped when a desired IV-curve has been obtained. If a somewhat longer time is used a large number of CNTs will be collected on the contacts, with a typical minimum resistance of 500 Ω. In this case it is possible to gradually burn CNTs by using a higher voltage (DC or pulsed). We have implemented the DEP procedure for both contact patterns in Figure 4. One advantage is that the substrate need not contain many patterns, one is sufficient. Another advantage is that when the applied voltage has a frequency of 5 MHz or above metallic SWNTs are preferentially selected [24]. We assume that if a few s-SWNTs are also contacted in parallel with the m-SWNTs, their resistance is high enough that it can be neglected (no gate voltage is applied).

### *D. Recent Experimental Results – Microwave and Terahertz Detection*

We have measured microwave detection in m-SWNTs placed by DEP and find similar results to the previous microwave experiments. One difference is that the detection persisted to higher frequencies, about 12 GHz. This was expected since we are now able to employ non-conducting substrates (sapphire and SOS) as mentioned above. A photograph of the fixture we use for the measurements is shown in Figure 5. This fixture was adapted from one previously used for NbN HEB mixers. The device chip in this case is SOS with dimensions 6 x 6 mm. Bond wires (3-4 mm long) are used to connect between a microstrip transmission line and the contact pads of the antenna. The bond wires have enough inductance to explain fall-off of the frequency response for microwave detection. The CPW structure has been tested in a microwave probe system, and this will be used to further extend the frequency response at microwave frequencies.

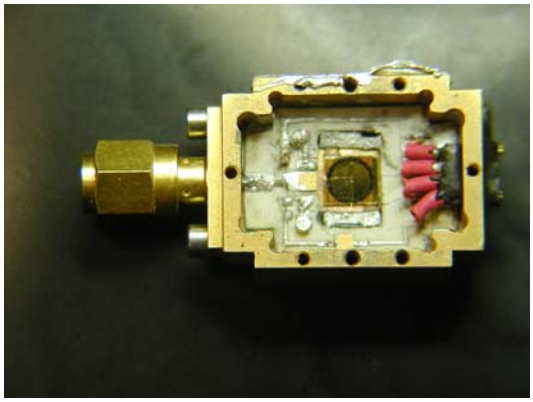

Figure 5. The fixture used for recent measurements of MW and terahertz detection in m-SWNTs. The device is biased through the SMA connector. The silicon lens located on the opposite side of the SOS substrate can be seen through this substrate.

A 4 mm diameter ellipsoidal silicon lens was attached with purified bees wax to the substrate for quasi-optical coupling to the antenna as discussed in [12,13]. Note that the dielectric constant of sapphire is a close match to that of silicon. The device was biased through a 100 kΩ sensing resistor that configured the Keithley supply as a voltage source. A lock-in amplifier was connected across that resistor in a balanced mode through two further 100 kΩ resistors in order to record the detected change in current through the device. The same fixture can then be used for both microwave and terahertz detection. Terahertz radiation was introduced through the silicon lens from a terahertz gas laser that has a typical output power of 2-5 mW. The laser was modulated at 1 kHz by inserting an acousto-optic modulator after the $CO_2$ pump laser. The modulator also provided the reference voltage for the lock-in amplifier.

Using this configuration we have now for the first time (soon after the conference) demonstrated detection at terahertz frequencies in a CNT. Three different frequencies were used (wavelength in μm is given in parenthesis): 0.694 THz (432); 1.04 THz (287); 1.63 THz (184); the IV-curve at 77 K is first displayed below in Figure 6.

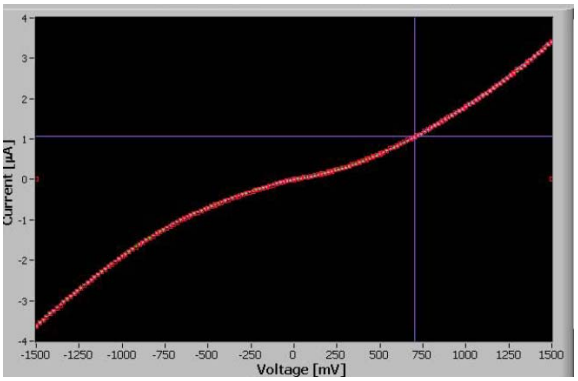


Figure 6. IV-curve for a device placed with DEP on the substrate shown in Figure 5.

The detected voltage on the lock-in amplifier is plotted versus the bias voltage in Figure 7 when the 432 μm line was used as input. The input power was 2.3 mW, measured on a Scientech power meter. The noise level was of the order of 4-5 μV, except for the highest bias voltages (near 1.5 V) where an increase in the 1/f noise from the CNT was evident. The S/N at the optimum bias point thus is about 25. These are preliminary data, but clearly show that the m-SWNT detects the terahertz radiation both at 300 K and at 77 K. Re-alignment of the laser produced slightly different responsivities, but all features were reproducible.

The highest frequency for which we obtained detection was 1.63 THz (184 μm), see Figure 8. We also attempted detection at 2.54 THz (118 μm) but were not successful so far. Two different (perpendicular) polarizations were employed, and it is not yet clear what the significance of the different responses for different polarizations is.

The bias voltage dependence of the detector response to terahertz radiation does not have a simple $d^2I/dV^2$ dependence, as it did for microwave detection (see Figure 3). We discuss different processes that may be responsible for the detection in section III. Much further work is clearly needed to identify the detection process(es) that actually occur(s). It is also noteworthy that the terahertz responsivity of the detector at this stage of the investigation is about the same at 300 K (~ 1.2 V/W) as it is at 77 K (2 V/W). The responsivities are uncorrected for the optical losses in the dewar window and the silicon lens (~3-4 dB). The same device has a microwave responsivity of 73 V/W at 300 K, a typical value for microwave responsivity. The largest microwave responsivity measured is 600 V/W, at 77 K, for the device with the IV-curve as given in Figure 3. Future work will also explore use of lower temperatures than 77 K, for which we earlier found a much larger responsivity at microwaves [12,13].

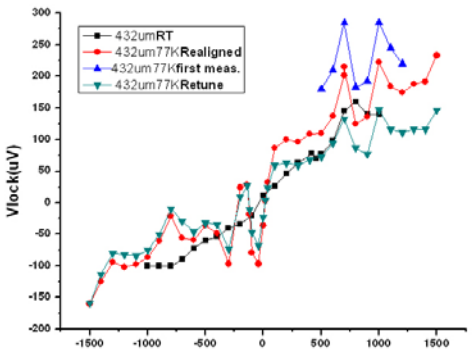


Figure 7. Detected voltage on the lock-in amplifier when the laser line at 432 μm was used.

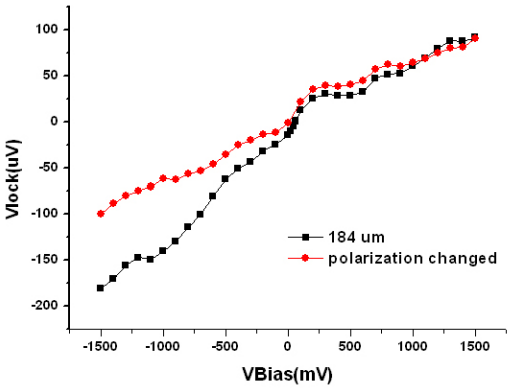


Figure 8. Detected voltage on the lock-in amplifier with an input frequency of 1.63 THz.

## III. PREDICTED TERAHERTZ RESPONSE FOR M-SWNTS

A single m-SWNT can be modeled as shown below in Figure 9, based on the work of P.Burke and others [28]. The contents of the "cell" are meant to be repeated periodically. The periodically repeated cells model a transmission line with a propagation velocity of about 2.4 x $10^8$ cm/s. The physical process this models is the plasmon mode we discussed in Sec. II.B. Based on this model one finds that the m-SWNT has a very large kinetic inductance ($L_K$), as well as a quantum capacitance ($C_Q$). The kinetic inductance of a single m-SWNT was recently measured with microwave network analyzer

techniques, confirming a major aspect of the above model [29].

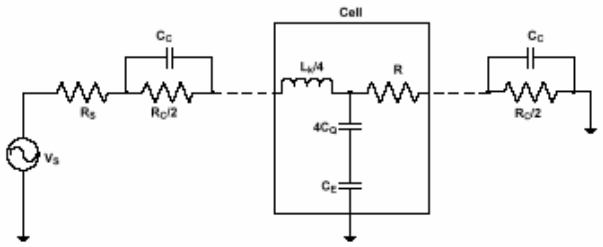


Figure 9. Circuit model for an m-SWNT.

The contact resistance ($R_C$) is typically large as also discussed in Sec. II.B, and often represents most of the measured DC resistance. $R_C$ has a capacitance in parallel ($C_C$), however, and if $C_C$ is large enough then $R_C$ will be shunted and have a negligible effect at terahertz frequencies. We can then distinguish two types of cases:

CASE A (CNT nonlinearity): If the contact impedance is small, we see mainly the m-SWNT proper, and a reasonable fraction of the terahertz power will be absorbed in the tube, provided that its ohmic resistance is not too high.

CASE B (contact nonlinearity): In this case the contact resistance dominates the total impedance, as clearly occurs at microwave frequencies.

We have simulated the circuit in Figure 9 for CASE A and find the result shown in Figure 10. The m-SWNT was assumed to be 1 μm long and the plasmon wave shows a half-wave resonance at 1.2 THz. There is a second resonance at a much lower frequency due to a lumped circuit combination of the kinetic inductance and the contact capacitance.

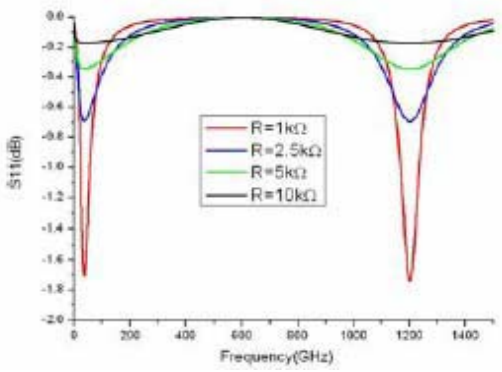


Figure 10. Simulated S11 response of a 1 μm long m-SWNT fed from a 100 Ω source (the LP antenna). Values assumed for the circuit in Figure 9 are $R_C/2$ = 20 kΩ, $C_C$ = 10 fF, $L_K$ = 4 nH [28], $C_E$ = 50 aF [28] and $4C_Q$ = 400 aF [28].

The CNT can be well matched to the antenna for the lower values of CNT resistance, which are expected to occur at lower temperatures. At room temperature the matching can be improved by designing a matching network, as shown in [13].

We have also simulated CASE B, and shown that excellent matching can be obtained at the lower terahertz frequencies. We can thus conclude that it is possible to efficiently absorb terahertz radiation in an m-SWNT. In CASE A we expect that the detection may occur due to HEB effects, as discussed earlier [11,12,21,22]. The responsivity will depend on the temperature dependence of the resistance, which can be quite substantial at the lower temperatures. CASE B has already been demonstrated at microwave frequencies, and further work will show to how high frequencies this process will be effective.

## IV. AB INITIO SIMULATION OF METALLIC CARBON NANOTUBES

We have mentioned above that our theoretical understanding of m-SWNT properties such as contact resistance and capacitance, as well as transport properties, is quite limited at the present time. Reliable and accurate quantum simulations of CNTs are needed to clear up our understanding of many experimental issues and characterize our devices. These are being performed by the group of Professor Eric Polizzi.

In [30], we have achieved electron transport simulations of CNT-FETs based on Non-Equilibrium Green's Functions (NEGF). The results obtained have highlighted the huge influence of 3D electrostatics on the 1D CNT and the role of defects (vacancies and charged impurities) in altering nanotube transistor device characteristics from the ballistic transport limit.

In order to allow an accurate physical description of the contacts with the reservoirs, one needs to resort *to ab-initio* atomistic approaches such as density functional theory (DFT). For numerical reasons, *ab-initio* transport calculations are usually limited to isolated regions of the carbon nanotube close to the metal contacts or possible defects. An *ab-initio* atomistic description of the electron transport in the entire carbon nanotube, however, could provide important insights on electronic properties of the device while considering arbitrary length, chirality, diameters, etc. . . This type of "bottom-up" simulation is still a formidable task and we are making use of innovative numerical modeling strategies to realize this goal efficiently.

For *ab-initio* type calculations, as compared to other traditional methods, mesh techniques (such as the finite element method- FEM) present significant advantages which have been reviewed in [31]. For a 100 nm long CNT composed of ~10,000 atoms, one may typically obtain a Hamiltonian matrix size of $10^8$. Within our real-space mesh framework, we have, however, been able to reduce the computational cost of the transport simulations by introducing novel strategies such as: sub-band decompositions, and preconditioning strategies for solving the resulting linear systems via iterative methods. We have then recently applied these techniques for *ab-initio* electronic structure calculations for a CNT. Our preliminary results are summarized in Figure 11. We also performed the calculation of the electron density.

In the future we plan to increase the level of sophistication of our model by introducing the following aspects:

1. A rigorous treatment of the CNT contacts.
2. A non-ballistic quantum transport model including phase-breaking dissipation processes (*e.g.*, electron-phonon scattering).
3. A time-dependent transport regime by adapting the transient simulation approach proposed in [32].

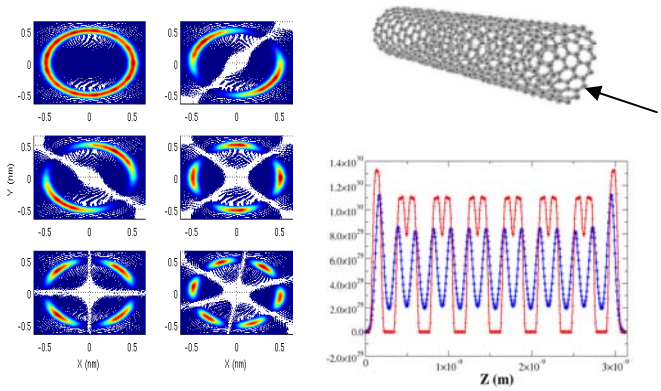


Figure 11. Preliminary results obtained using *ab-initio* electronic structure calculations of CNT and a real space mesh technique (FEM). On the left, the figures represent the first six modes at a given cross section of a (13,0) tube. On the right we choose to represent the variation of the electron density along the z direction starting from a given (x,y) atom node at the first cross section. The red cross curve is obtained using a semi-classical Thomas-Fermi approximation while the blue star curve represents the result of the quantum simulation. The length of the nanotube tube has been set at 3nm for the purpose of illustrating a simple case.

Ref. [32] studied non-quasi-static effects (NQSE) in CNT transistors. The NQSE are equivalent to the kinetic inductance ($L_K$) and quantum capacitance ($C_Q$) we introduced in Sec. III. This reference found that for CNT-FETs the intrinsic response can be accurately calculated *without* taking the NQSE into account, up to about 2 THz. One reason $L_K$ can be neglected is that the fastest CNT-FETs are very short (~ 10nm). The difference in the present project is that we are experimentally studying configurations for which NQSE's are emphasized, and that measurements of such effects can be performed (see above), partly because parasitic effects have been minimized, which is not possible for CNT-FETs. Our continued *ab-initio* simulations will study in detail the device characteristic responses (I-V-curve, conductance, capacitance, inductance, etc…) to different excitations that may alter the terahertz experimental data such as defects, vacancies, charge impurities, and other distortions.

## V. CONCLUSIONS

We have reported new results on microwave detection and the first detection of terahertz radiation in m-SWNTs. The path now lies open for further studies combining microwave and terahertz measurements with *ab-initio* simulations that explore the high-frequency properties of this unique medium.

## REFERENCES

[1] P.L. McEuen, M. S. Fuhrer, and H. Park, IEEE Trans. Nanotechnol, **1**, 78 (2002).
[2] R. Saito, G. Dresselhaus, and M.S. Dresselhaus, *Physical Properties of Carbon Nanotubes* (Imperial College Press, London, 1998).
[3] Y.-M. Lin, J. Appenzeller, J. Knoch, and Ph. Avouris, IEEE Trans. Nanotechnol. **4**, 481 (2005).
[4] A. Javey, J. Guo, D.B. Farmer, Q. Wang, D. Wang, R.G. Gordon, M. Lundstrom, and H. Dai, Nano Lett. **4**, 447 (2004).
[5] S. Heinze, J, Tersoff, R. Martel, V. Derycke, J. Appenzeller, and Ph. Avouris, PRL **89**, 106801 (2002).
[6] J. Appenzeller, J. Knoch, V. Derycke, R. Martel, S. Wind, and Ph. Avouris, PRL **89**, 126801 (2002).
[7] H.M. Manohara, E.W. Wong, E. Schlecht, B.D. Hunt, and P.H. Siegel, Nano Lett. **5**, 1469 2005.
[8] S. Rosenblatt, H. Lin, V. Sazonova, S. Tiwari, and P.L. McEuen, Appl. Phys. Lett. **87**, 153111 (2005).
[9] A. A. Pesetski, J.E. Baumgardner, E. Folk, J. Przybysz, J. D. Adam, and H. Zhang, Appl. Phys. Lett., **88**, 113103 (2006).
[10] M.E. Itkis, F.Borondics, A.Yu, R.C. Haddon, Science **312**, 314 (2006).
[11] M. Tarasov, J. Svensson, L. Kuzmin, and E. E. B. Campbell, Appl.Phys.Lett., **90**, 163503 (2007).
[12] K.S. Yngvesson, Appl. Phys. Lett. **87**, 043503 (2005).
[13] K.S. Yngvesson, 16th Intern. Symp.Space Terahertz Technol., Gothenburg, Sweden, May 2005.
[14] A. Thess, R. Lee, P. Nikolaev, H. Dai, P. Petit, J. Robert, C. Xu, Y.H. Lee, S.G. Kim, A.G. Rinzler, D.T. Colbert, G.E. Scuseria, D. Tomanek, J.E. Fischer, and R.E. Smalley, Science **273,** 483 (1996).
[15] Z. Chen, J. Appenzeller, J. Knoch, Y.-M. Lin, and Ph. Avouris, Nano Lett. **5**, 1497 (2005).
[16] W. Kim, A. Javey, R. Tu, J. Cao, Q. Wang, and H. Dai, Appl. Phys. Lett. **87**, 173101 (2005).
[17] M. Bockrath, D.H. Cobden, J. Lu, A.G. Rinzler, R. E. Smalley, L. Balents and P. L. McEuen, Nature **397**, 598 (1999).
[18] Th. Hunger, B. Lengeler, and J. Appenzeller, Phys. Rev. B, **69**, 195406 (2004).
[19] Z. Yao, C.L. Kane, and C. Dekker, Phys. Rev. Lett. **84**, 2941 (2000).
[20] A. Javey, J. Guo, M. Paulsson, Q. Wang, D. Mann, M. Lundstrom, and H. Dai, Phys. Rev. Lett. **92**, 106804-1 (2004).
[21] K.S. Yngvesson, F. Rodriguez-Morales, R. Zannoni, J. Nicholson, M. Fischetti and J. Appenzeller, 17th Intern. Symp. Space Terahertz Technol., Paris, May 2006.
[22] F. Rodriguez-Morales, R. Zannoni, J. Nicholson, M. Fischetti, K. S. Yngvesson, and J. Appenzeller, Appl. Phys. Lett., **89**, 083502 (2006).
[23] K.S. Yngvesson, *Microwave Semiconductor Devices* (Kluwer Academic Publishers, Norwell, MA, 1991).
[24] R. Krupke and F. Hennrich, Adv. Engin. Materials, 7, 111 (2005).
[25] N. Peng, Q. Zhang, J. Li, and N. Liu, JAP **100**, 024309(2006).
[26] L. Dong et al., J.Phys.Chem. **109**,13148 (2005).
[27] Z-B. Zhang, X-J. Liu, E.E.B. Campbell, and S-L. Chang, JAP, **98**, 056103 (2005).
[28] P.J. Burke, IEEE Trans. Nano Technol. **1**, 129 (2002).
[29] J. J. Plombon, K. P. O'Brien, F. Gstrein, V. M. Dubin, and Y. Jiao, Appl. Phys. Lett., **90**, 063106 (2007).
[30] N. Neophytou, D. Kienle, E. Polizzi, M. P. Anantram, Appl. Phys. Lett. **88**, 242106 (2006).
[31] T. Beck, Rev. of Modern Phys., **72**, p1041, (2000).
[32] L. Latessa, A. Pecchia, and A. Di Carlo, IEEE Trans. Nanotechn, **6**, 13 (2007).

# Detection of 0.5 THz radiation from $Bi_2Sr_2CaCu_2O_8$ single crystals using a superconducting integrated receiver

I. E. Batov, X. Y. Jin, S. V. Shitov, Y. Koval, P. Mueller, and A. V. Ustinov

*Physikalisches Institut III, University of Erlangen-Nuremberg*
*Erwin-Rommel-Str. 1, D-91058 Erlangen, Germany*

Josephson junctions utilizing high-temperature superconductors were considered as promising candidates for terahertz oscillators, but experimental demonstrations of their performance are still lacking. The most promising devices that have been proposed so far are based on intrinsically layered $Bi_2Sr_2CaCu_2O_8$ single crystals, which consist of natural stacks of Josephson tunnel junctions.

We report on detection of electromagnetic radiation at about 500 GHz from current-biased intrinsic $Bi_2Sr_2CaCu_2O_8$ single crystal Josephson junctions[1]. We used two silicon lenses to quasi-optically couple radiation from our samples to an integrated superconducting heterodyne receiver. The samples were prepared in a step-like geometry, by defining a mesa in the shape of bow-tie antenna using electron beam lithography and argon ion milling on the upper surface of the crystal. The microwave radiation was detected by a low-noise all-superconducting heterodyne receiver. The receiver consists of an SIS mixer integrated on the single chip with a superconducting flux-flow oscillator acting as a local oscillator[2].

From our data we can identify the emission of individual intrinsic Josephson junctions from a stack consisting of over 100 junctions. The estimated maximum Josephson radiation power which reached the receiver antenna was about 1 pW. We suppose that the possibility of mutual phase locking of a large number of stacked junctions strongly depends on several factors such as spread in junction parameters, heating effects, and presence of an external magnetic field. For their frequency locking, series-connected junctions biased by the same current need to have a very small spread in resistances. This requirement seems hard to achieve even in very uniform stacks due to unavoidable resistance changes induced by the dissipated heat.

[1] I. E. Batov, X. Y. Jin, S. V. Shitov, Y. Koval, P. Mueller, and A. V. Ustinov, *Appl. Phys. Lett.* **88**, 262504 (2006).
[2] V. P. Koshelets and S. V. Shitov, *Supercond. Sci. Technol.* **13**, R53 (2000),

# Logarithmic Growth of $AlN_x$ Barriers in Nb/Al–$AlN_x$/Nb Tunnel Junctions

Akira Endo, Takashi Noguchi, Matthias Kroug, and Tomonori Tamura

***Abstract*—The growth rate of ultra-thin $AlN_x$ films during low energy plasma nitridation has been studied by measuring the normal state resistance-area product ($R_NA$) of Nb/Al–$AlN_x$/Nb Superconductor-Insulator-Superconductor junctions. The barriers were formed by nitridizing the surface of Al films with an rf plasma discharge of $N_2$ gas diluted to 10% with He. The reaction was started smoothly by adopting a "two-step-ignition" technique. Junctions with $R_NA = 10^0$–$10^6$ Ω·μm$^2$ were fabricated by this process. A power law relationship between $R_NA$ and nitridation time was found to hold across the whole range of the measured $R_NA$ values. This implies that the physical thickness of the $AlN_x$ layer obeys a logarithmic growth law.**

**Index Terms—Submillimeter wave mixers, Superconducting device fabrication, Superconductor-insulator-superconductor devices**

## I. Introduction

Ultra-thin films of aluminum nitride ($AlN_x$) have been proved to serve as excellent tunnel barriers for Superconductor-Insulator-Superconductor (SIS) junctions with normal state resistance-area products ($R_NA$) less than 10 Ω·μm$^2$ [1, 2]. Such low-$R_NA$ SIS junctions are essencial in the development of broadband and high-sensitivity SIS mixers for astronomical observations in the submillimeter-terahertz range. While classical aluminum oxide ($AlO_x$) barrier SIS junctions begin to suffer from large leakage current below $R_NA$ = 20 Ω·μm$^2$, $AlN_x$ barrier SIS junctions can have $R_NA$ < 1 Ω·μm$^2$ with still decent quality, e.g., $R_{sg}/R_N > 10$ [1]. This can be understood as a result of the lower barrier height of $AlN_x$ barriers compared to $AlO_x$ barriers ($\phi_{AlNx} < 0.9$ eV [3], $\phi_{AlOx} < 2$ eV [4]).

While there have been a number of studies reporting successful fabrication of high quality $AlN_x$ barriers with low $R_NA$ by rf plasma nitridation [1, 5–11], controlling the $R_NA$ is a problem. This is because the nitridation of aluminum requires a plasma process which involves many free parameters, such as nitridation time, substrate temperature, rf power, dc voltage, $N_2$ pressure and flow rate, etc. The dependence of the $R_NA$ product on these parameters has been studied by several authors [7–10, 12]. Among these parameters, the reported nitridation-time dependence of $R_NA$ differs from one study to another. While pioneering studies applied linear fits to their data ($R_NA \propto t_N$) [5, 6], subsequent studies have reported exponential relations ($R_NA \propto e^{kt_N}$) [13, 14], or peculiar relations involving plateaus [8, 9]. Meanwhile, no theory has been established which predicts the growth rate of the thickness of the $AlN_x$ layer during low energy plasma nitridation. Thus the relation between the $R_NA$ and nitridation time has been elucidated neither experimentally nor theoretically, and therefore the search for the appropriate process parameters involves a considerable amount of trial and error.

In this work, we fabricated many Nb/Al–$AlN_x$/Nb SIS junctions using a composite plasma of $N_2$ and He. By comparing their $R_NA$ and nitridation time, we investigated the rate and mechanism of the growth of $AlN_x$ barriers.

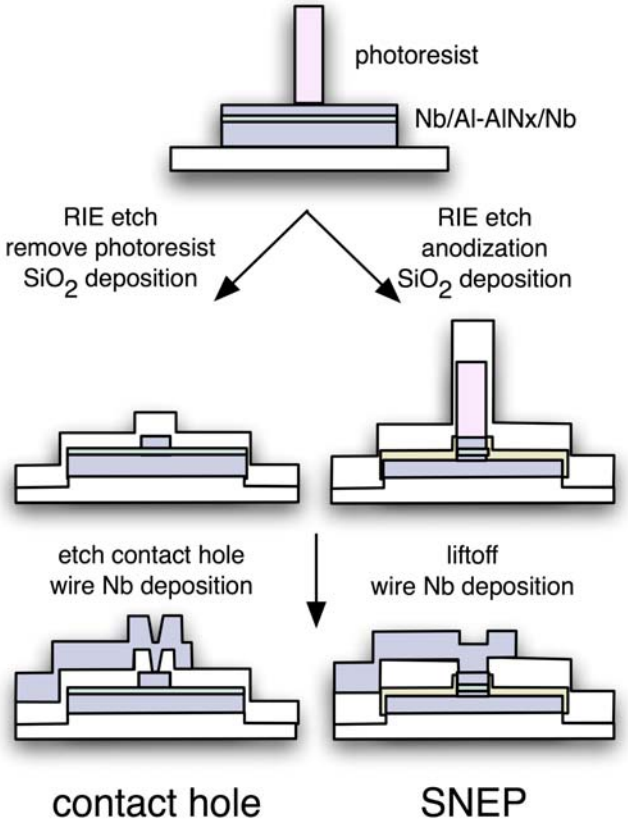


Fig. 1. Schematic diagram of the two kinds of fabrication processes.

## II. Fabrication of Nb/Al –$AlN_x$/Nb SIS Junctions

The junctions were prepared using either the standard Selective Nb Etching Process (SNEP) [15] or a contact-hole

Manuscript received May 1, 2007. This work was supported in part by the Japan Society for the Promotion of Science (JSPS) for Young Scientists.

A. Endo, T. Noguchi, M. Kroug, and T. Tamura are with the National Astronomical Observatory of Japan, Osawa 2-21-1, Mitaka, Tokyo, 181-8588, Japan (telephone: +81-422-34-3870, e-mail: akira.endo@nao.ac.jp).

A. Endo is also a JSPS research fellow at the Institute of Astronomy, University of Tokyo, 2-21-1 Osawa, Mitaka, Tokyo 181-0015, Japan.

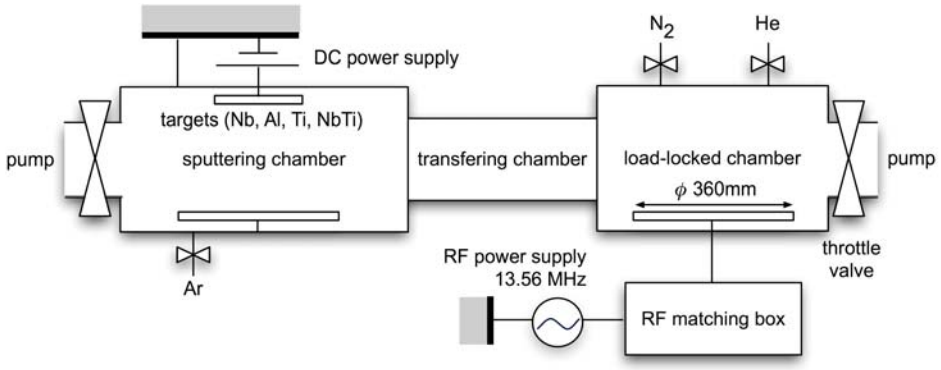


Fig. 2. Setup of the sputtering machine.

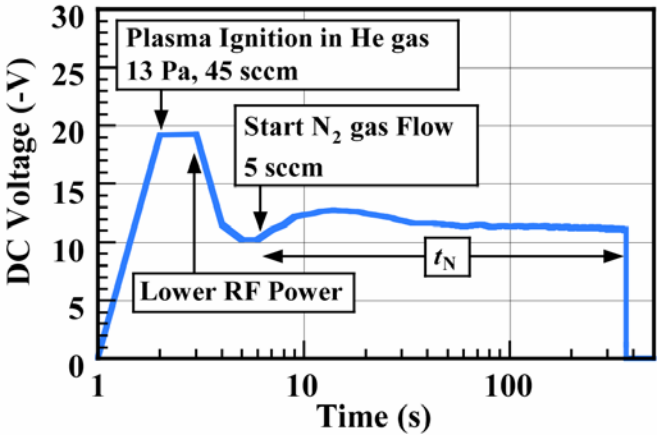


Fig. 3. DC voltage as a fuction of time during a typical nitridation process.

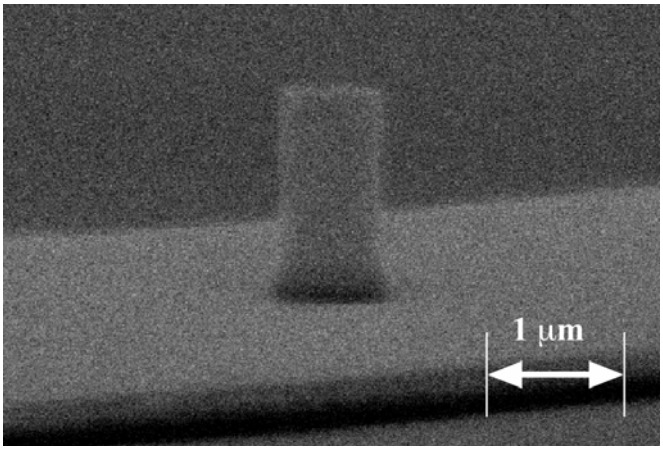


Fig. 4. SEM image of an SIS junction after RIE etching with photoresist on top. The designed diameter of the junciton was 0.8 μm.

process. The sequences of these processes are described in Fig. 1. The wafers were made of fused quartz, 35 mm in diameter and 300 μm thick. The structures of the Nb/Al–AlNx/Nb trilayers were defined by a liftoff pattern made by the Canon FPA-3000 i5+ i-line stepper. The trilayers were deposited in the ULVAC CS200 ET sputtering machine, a schematic diagram of which is presented in Fig. 2. The typical background pressure in the sputtering chamber was $1 \times 10^{-5}$ Pa. The lower Nb electrode had a thickness of 200 nm and a compressive stress of 0.2–0.8 GPa. Its resistivity at room temperature was ~18 Ω·μm$^2$. The thickness of the Al layer was ~10 nm.

The nitridation of the Al films were performed in the load-locked chamber of the sputtering machine. The wafer was placed directly on the electrode that creates the rf discharge, so that the reactive nitrogen ions are accelerated by the dc potential and reach the wafer. The rf power during the process was kept at the lowest possible level that the generator can supply (1 W), in order to realize the slowest and softest (i.e., low energy) nitridation condition as possible. However, a larger rf power (6 W) was needed to ignite the plasma at the beginning of the process. In order to avoid any reaction that could take place during this unstable and high-energy phase, we adopted the following sequence which we call the "two-step-ignition" technique [14]:

1) Ignition of the plasma in pure He with a large power of 6 W.
2) Reduce the power to 1W which is suitable for the process.
3) Introduce nitrogen into the chamber to start the reaction.

An example of the dc voltage at the electrode as a function of time during the nitridation process is presented in Fig. 3. The nitridation time ($t_N$) was defined as the time from introducing nitrogen till turning off the power. Using a mixture of $N_2$ and He not only allows one to adopt the method mentioned above, but also enables one to control the dc voltage and the $N_2$ partial pressure independently by adjusting the $N_2$/He ratio. In other words, the density and the momentum of the nitrogen ions can be reduced simultaneously, which should benefit in realizing a slow and low energy process. The composition of $N_2$ was set to 10% by adjusting the flow rate of the two gases. The total pressure was 13 Pa. While we used Ar as the solvant gas in our former work [14], we used He this time to reduce any damage of the barrier caused by etching.

After the nitridation, the upper Nb electrode was deposited to a thickness of 100 nm. An example of the photoresist pattern for junction definition is presented in Fig. 4. The junctions were round and had diameters ranging from 0.4 to 4 μm. The upper Nb electrode was etched by a $CF_4$ + 3%$O_2$ plasma in an RIE etcher. The lower electrode and the Nb wire layer (400 nm) were separated by 270 nm of $SiO_2$.

## III. Results and Discussion

### A. DC I-V Characteristics

Examples of dc *I-V* curves of SIS junctions with various $R_NA$ products are presented in Fig. 5. The normal-state resistance ($R_N$) and the sub-gap resistance ($R_{sg}$) were measured at 4 and 2 mV, respectively. The leakage current began to increase at $R_NA \leq 20\ \Omega{\cdot}\mu m^2$, which was similar to our previous work using Ar to dilute the $N_2$ plasma [14]. It was also found that the optimum sputtering time for the Al layer to achieve the smallest leakage current and largest gap voltage [16] was about half of what was optimum in the previous study. We speculate that a considerable amount of Al was etched by the Ar ions during the nitridation in the previous study, which reduced the final thickness of the Al–$AlN_x$ bilayer.

In this study, we define the term "calibrated normal-state resistance" ($R_{N,c}$) as the normal resistance after subtracting the sub-gap current portion from the dc *I-V* curve. We will refer to the $R_{N,c}A$ product rather than the nominal $R_NA$ product when we discuss the dependence of the resistivity or physical thickness of the barrier on the nitridation time, because the thickness of the barrier correlates exponentially only with the tunnel current, and not with the leakage current that goes through the pinholes.

### B. Dependence of $R_{N,c}A$ on Nitridation Time

The dependence of $R_{N,c}A$ on the nitridation time is presented in the form of a log-log plot in Fig. 6, along with data collected from literature [5–8, 13, 14]. Critical current density values in literature were converted to $R_{N,c}A$ by applying the theoretical BCS relation: $J_CR_{N,c}A=\pi\Delta/2e$. Our results are well fitted by a straight line that streches across nearly six orders of magnitude in $R_{N,c}A$, which implies that there is a power law relationship between $R_{N,c}A$ and $t_N$ as follows:

$$R_{N,c}A = 6.5\times10^{-6}\,t_N^{3.9}\ \Omega{\cdot}\mu m^2, \quad (1)$$

where $t_N$ is the nitridation time in s. It is also possible that the experiments by previous studies presented in Fig. 6 also follow certain power laws, but were not noticed because the data was collected for no more than 3 orders of magnitude in $R_{N,c}A$. Nevertheless, if we fit every result with a power law of the form $R_{N,c}A = Ct_N^k$, we observe that the power law index $k$ has a range of $0.5 \leq k \leq 3.9$. It is interesting that the data from our prior experiment using Ar as a solvent gas yields $k = 1.8$, which is considerably smaller compared to the He process, even though the total pressure, gas composition ratio and the applied power were kept the same. This implies that the species of the solvent gas has a significant effect on the growth rate of the $AlN_x$ layer. It should also be noted that the process of this work is one of the slowest to approach 10 $\Omega{\cdot}\mu m^2$, which is favorable in controlling the $R_NA$ at this range. The growth of the physical thickness of the $AlN_x$ layer ($d_{AlNx}$) can be studied by converting $R_{N,c}A$ to $d_{AlNx}$. The relation between $R_{N,c}A$ and the thickness of $AlN_x$ barriers has been studied in the range of $R_NA = 1$–$1000\ \Omega{\cdot}\mu m^2$ for reactively sputtered $AlN_x$ barriers [3], and is roughly

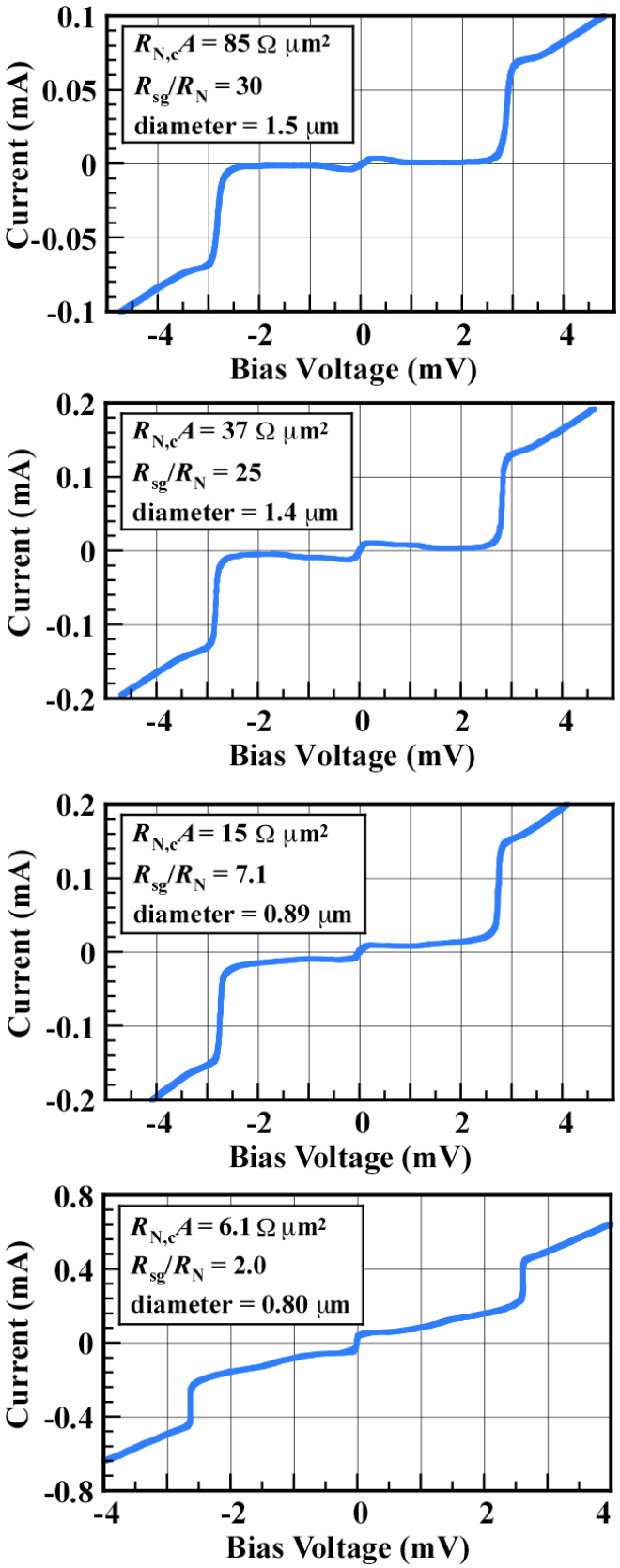


Fig. 5. DC *I-V* characteristics of junctions with various $R_{N,c}A$ products.

$$d_{AlN_x} = [0.20\log(R_{N,c}A) + 1.0]\ \text{nm}, \quad (2)$$

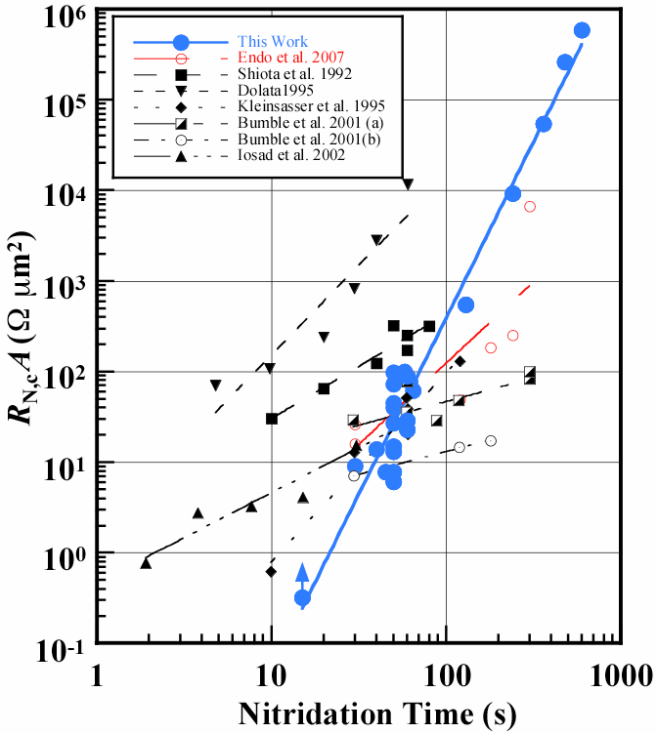


Fig. 6. Dependence of $R_{N,c}A$ on nitridation time. Data from literature are plotted together. Each data point of our data represents the average of about 20 junctions on each wafer. The arrow shows that the data point is a lower limit, for the $R_{N,c}A$ could not be sufficiently corrected for the large leakage current. The lines are least square fits to each set of data.

where $R_{N,c}A$ is in units of $\Omega\cdot\mu m^2$. If we assume that this relation holds up to $R_NA = 10^6\ \Omega\cdot\mu m^2$, and that sputtered and plasma-nitridized $AlN_x$ have the same barrier height, the $R_{N,c}A$ v.s. $t_N$ relation presented in Fig. 6 can be converted into a growth curve of the $AlN_x$ layer as shown in Fig. 7. The growth is well fitted by the following logarithmic curve, presented as a solid curve in the figure:

$$d_{AlN_x} = [0.36\log(t_N) - 0.17]\ \text{nm}, \quad (3)$$

where $t_N$ is again in units of s. The trend of the growth curve is consistent with the growth curve observed by an in-situ ellipsometric observation [17], which observed the nitridation to saturate at a certain thickness. However, we find that the logarithmic growth continues beyond $R_NA = 10^6\ \Omega\cdot\mu m^2$ or $d_{AlNx}$ = 2 nm, and that it is probably difficult to realize a process in which the nitride growth completely stops at the range of our interest: $R_NA \sim 10^1\ \Omega\cdot\mu m^2$.

Finally, we discuss the kinetics governing the growth of $AlN_x$ barriers during low energy rf plasma nitridation. As seen in Fig. 6, we found the nitride layer to grow according to a logarithmic law. Such a behavior is observed for example when thin Al films are oxidized at room temperature or below, and is theoretically explained by migration of the metal cations [18, 19]. On the other hand, a parabolic curve ($d_{AlNx}$ □ $t_N$) also fits our data fairly well as shown by a broken curve in Fig. 6. Such parabolic growth laws are observed in reactions with relatively high energy, for example thermal oxidation of metals at temperatures around $10^3$ K, and are theoretically explained by thermal diffusion [20–22]. In fact, Iosad *et al.* [8, 9] have carefully considered the energy of various species in the nitrogen plasma, and concluded that

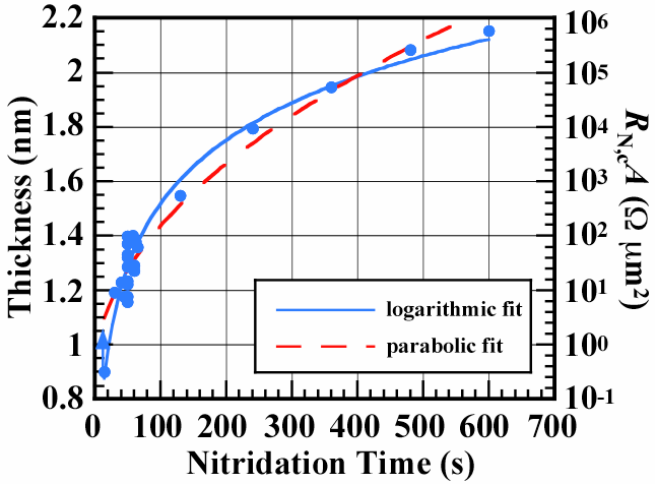


Fig. 7. Fig. 6 replotted, with the tunnel resistivity ($R_{N,c}A$) converted to the thickness of the nitride. The solid and broken curves are logarithmic and parabolic least square fits, respectively.

thermal diffusion of nitrogen is the dominant mechanism in the nitridation of the Al films. They estimated the power density of the nitrogen ions reaching their substrate chuck to be 5–9 $W\cdot m^{-2}$ from direct Langmuir probe measurements. This value is similar to the upperlimit in our system (10 $W\cdot m^{-2}$), assuming that all of the applied rf power is uniformly dissipated on the driven electrode. Though our data is marginally better fitted by a logarithmic curve, additional experiments are definitely necessary to make a conclusion on the mechanism dominating the growth of the $AlN_x$ barriers.

## IV. Conclusion

We fabricated Nb/Al–$AlN_x$/Nb SIS junctions by plasma nitridation of Al, using $N_2$ gas diluted with He. SIS junctions with decent quality can be fabricated using this process. There is a power law relationship between the $R_NA$ and $t_N$ that holds across $R_NA = 10^0$–$10^6\ \Omega\cdot\mu m^2$. This implies that the physical thickness of the $AlN_x$ barrier obeys a logarithmic growth law. These results will contribute to controlling the $R_NA$ of $AlN_x$ barrier SIS junctions.

## Acknowledgment

A. Endo thanks Shin'ichiro Asayama, Yoshinori Uzawa, and Wenlei Shan for technical advice and helpful discussions.

## References

[1] M. Y. Torgashin, V. P. Koshelets, P. N. Dmitriev, A. B. Ermakov, L. V. Filippenko, and P. A. Yagoubov, *IEEE Trans. on Appl. Supercond.* 17 (2007), to be published.

[2] C. F. J. Lodewijk, T. Zijlstra, D. N. Loudkov, T. M. Klapwijk, F. P. Mena, and A. M. Baryshev, *Proc. of the 18th Int. Symp. on Space THz Tech.* (2007), to be published.

[3] Z. Wang, H. Terai, A. Kawakami, and Y. Uzawa, *Appl. Phys. Lett.* 75, 701 (1999).

[4] S. Tolpygo, E. Cimpoiasu, X.Liu, N. B. Simonian, Y. A. Polyakov, J. E. Lukens, and K. K. Likharev, *IEEE Trans. Appl. Supercond.* 13, 99 (2003).

[5] T. Shiota, T. Imamura, and S. Hasuo, *Appl. Phys. Lett.* 61, 1228 (1992).

[6] A. Kleinsasser, W. Mallison, and R. Miller, *IEEE Trans. Appl. Supercond.* 5, 2318 (1995).

[7] B. Bumble, H. G. LeDuc, and J. A. Stern, *Proc. of the 9th Int. Symp. on Space THz Tech.* pp. 295–304 (2001).

[8] N. N. Iosad, A. B. Ermakov, F. E. Meijer, B. D. Jackson, and T. M. Klapwijk, *Supercond. Sci. Tech*. 15, 945 (2002).
[9] N. N. Iosad, M. Kroug, T. Zijlstra, A. B. Ermakov, B. D. Jackson, M. Zuiddam, F. E. Meijer, and T. M. Klapwijk, *IEEE Trans. Appl. Supercond*. 13, 127 (2003).
[10] P. N. Dmitriev, I. L. Lapitskaya, V. Filippenko, A. B. Ermakov, S. V. Shitov, G. V. Prokopenko, S. A. Kovtonyuk, and V. P. Koshelets, *IEEE Trans. Appl. Supercond.* 13, 107 (2003).
[11] M. J. Wang, *Proc. of the 5th Workshop on Submillimeter-Wave Reciever Technologies in Eastern Asia* p. 91 (2004).
[12] B. Bumble, H. G. LeDuc, J. A. Stern, and K. G. Megerian, *IEEE Trans. Appl. Supercond.* 11, 76 (2001).
[13] R. Dolata, M. Neuhaus, and W. Jutzi, *Physica C* 241, 25 (1995).
[14] A. Endo, T. Noguchi, T. Matsunaga, and T. Tamura, *IEEE Trans. Appl. Supercond.* 17 (2007), to be published.
[15] M. Gurvitch, M. A. Washington, and H. A. Huggins, *Appl. Phys. Lett*. 42, 472 (1983).
[16] T. Imamura and S. Hasuo, *J. Appl. Phys*. 66, 2173 (1989).
[17] T. W. Cecil, R. M. Weikle, A. R. Kerr, and A. W. Lichtenberger, *IEEE Trans. Appl. Supercond*. 17 (2007), to be published.
[18] N. Cabrera and N. F. Mott, *Rep. Prog. Phys*. 12, 163 (1948).
[19] F. P. Fehlner and N. F. Mott, *Oxidation of Metals* 2, 59 (1970).
[20] B. E. Deal and A. S. Grove, *Journal of Applied Physics* 36, 3770 (1965).
[21] C. Wagner, *Corrosion Science* 9, 91 (1969).
[22] R. H. Doremus, *J. Appl. Phys*. 95, 3217 (2004).

# Monolithic Millimeter-wave and Submillimeter-wave Integrated Circuit (MMIC and S-MMIC) Testing Capabilities at JPL up to 500 GHz

Lorene Samoska, A. K. Fung, Todd C. Gaier, W. R. Deal, V. Radisic, X.B.Mei, and R. Lai
*Jet Propulsion Laboratory, California Institute of Technology, Pasadena, California 91109 USA*
*Northrop Grumman Corporation, Redondo Beach, CA USA*

Over the years, our group has been developing on-wafer and waveguide testing capabilities for MMIC amplifiers, oscillators, transistors, and diode circuits up to 500 GHz. In this work, we outline the present state-of-the-art in terms of on-wafer *S*-parameter measurements, on-wafer noise figure measurements, and on-wafer power measurements up to 350 GHz for a variety of MMIC and new Submillimeter-wave MMIC (S-MMICs) chips. The first S-MMIC chips are described in Reference [1] and were tested at JPL and fabricated at NGST, and include single stage HEMT amplifiers with 2.5 dB of gain at 300 GHz. Figure 1a, below, shows the on-wafer full 2-port vector network analyzer test set used for the measurements up to 325 GHz.

Several years ago we reported the state-of-the-art in HEMT doubler technology up to 320 GHz using on-wafer test equipment outside of its recommended frequency range, which resulted in large uncertainty in measured power data [2]. Today, together with GGB Industries and OML Laboratories, we have developed the submillimeter-wave test sets to measure noise figure and power data to within 1 dB of accuracy on-wafer. Below in Figure 1b is a photograph of our on-wafer noise figure test set, capable of less than +/- 1 dB accuracy up to 270 GHz.

In this work, we will describe the key components required for the measurements, highlight recent test results on MMIC and S-MMIC chips, and plans for future wafer probing up to 500 GHz.

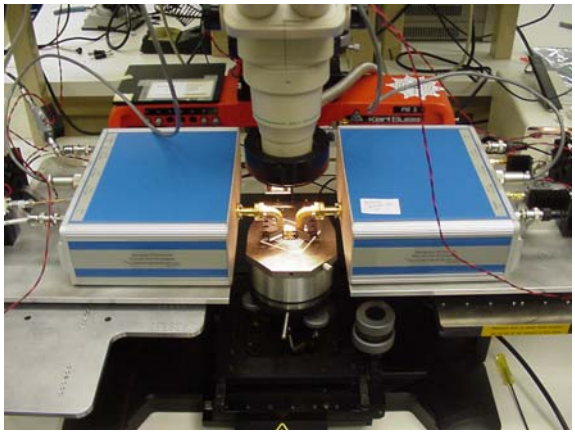

Figure 1a. On-wafer *S*-parameter test set up to 325 GHz.

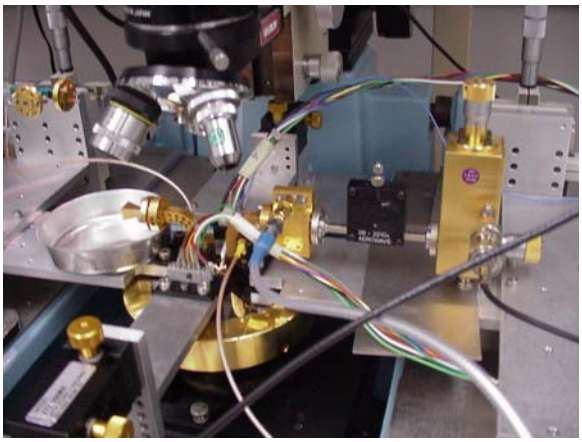

Figure 1b. On-wafer noise figure test set at 270 GHz.

[1] "Demonstration of a Sub-MillimeterWave Integrated Circuit (SMMIC) using InP HEMT with a 35-nm Gate," W. R. Deal, S. Din, V. Radisic, J. Padilla, G. Mei, W. Yoshida, P. Liu, J. Uyeda, M. Barsky, T. Gaier, A. Fung, L. Samoska, and R. Lai, *28th IEEE Compound Semiconductor Integrated Circuit Symposium Digest*, San Antonio, TX, November, 2006.
[2] "Advanced HEMT MMIC Circuits for Millimeter-wave and Submillimeter-wave Power Sources," Lorene Samoska, Jean Bruston, and Alejandro Peralta, *Proceedings of the Far Infrared, Millimeter, and Submillimeter-wave Detector Workshop*, Monterey, CA, April 1-3rd, 2002.

*This work was carried out in part at the Jet Propulsion Laboratory, California Institute of Technology, under a contract with the National Aeronautics and Space Administration. This work was also supported in part by the DARPA SWIFT Program and Army Research Laboratory under the ARL Contract no. W911QX-06-C-0050.*

# A 675 GHz FMCW Radar with Sub-Centimeter Range Resolution

**Goutam Chattopadhyay, Ken B. Cooper, Robert J. Dengler, Erich Schlecht, Anders Skalare, Imran Mehdi, and Peter H. Siegel**

Jet Propulsion Laboratory, California Institute of Technology
4800 Oak Grove Drive, Pasadena, CA 91109, USA.

Remote sensing systems operating in the submillimeter spectrum using heterodyne techniques hold great promise for concealed weapons detection, surveillance, and planetary exploration. Here we describe a novel versatile system at 675 GHz capable of high range-resolution radar operation, broadband coherent active imaging, and high resolution spectroscopic studies.

In this paper we describe the system architecture, performance requirements, and preliminary results of the novel all-solid-state radar system with spectroscopic imaging capability operating at 675 GHz. By using the frequency-modulated continuous-wave (FMCW) technique over a bandwidth of 18 GHz, this submillimeter radar is capable of a range resolution below one centimeter. Using a scanning single-pixel transceiver with a modest aperture size and output power, the radar is capable of generating detailed three-dimensional images of concealed targets at stand-off distances of many meters. Our measurements also suggest that the FMCW range-gating technique can reduce clutter noise when acquiring spectroscopic information of target substances. With anticipated improvements in performance and cost, THz radar technology with 3-D imaging and spectroscopic capability may become an effective tool for a variety of national security, civil, and scientific applications.

The research described herein was carried out at the Jet Propulsion Laboratory, California Institute of Technology, Pasadena, California, USA, under contract with National Aeronautics and Space Administration.

# Operation of a Monolithic Planar Schottky Receiver Using a THz Quantum Cascade Laser

Mark Lee, Albert D. Grine, and Michael C. Wanke
*Sandia National Laboratories, Albuquerque, NM, USA*

Peter H. Siegel and Robert J. Dengler
*California Institute of Technology and Jet Propulsion Laboratory, Pasadena, CA, USA*

Terahertz heterodyne receivers using Schottky diode mixers are desirable because they require no cryogenic cooling, have intermediate frequency (IF) bandwidths ≥ 20 GHz, and can deliver usefully low noise performance. However, to achieve optimal conversion gain and noise temperature, Schottky receivers operating in the THz range require at least several milliwatts of continuous local oscillator (LO) power. For this reason, the most common THz LO source used for Schottky receivers is the $CO_2$-pumped molecular gas laser. Of clear interest is the possibility of replacing the tube-based molecular gas laser with a solid-state THz LO source capable of pumping a Schottky mixer. To date the only solid-state source capable of producing > 1 mW of continuous wave power above ~ 2 THz is the quantum cascade laser (QCL). THz QCLs have been shown to work as good LO sources for superconducting HEB mixers, [1] which require significantly less LO power than Schottky mixers. Frequency down-conversion has also been accomplished using two QCL lines and a point-contact Schottky diode.[2]

We will report on the operation of a monolithic planar Schottky diode receiver using a THz QCL. The Schottky mixer consists of a Ti/Pt/Au anode contacting a GaAs membrane and is packaged into a waveguide block with an integral horn antenna. The details of the mixer design, construction, and packaging are described in Refs. 3 and 4. At 2.5 THz, the minimum noise temperature of the packaged receiver was about 11,000 K. Although the design of the receiver was optimized for 2.5 THz, good responsivity and measurable noise temperature were obtained for this receiver at frequencies up to 3.1 THz. Using the 2.9 THz deuterated methanol line from a molecular gas laser, the receiver showed a noise temperature of ~ 30,000 K, using 6 mW of LO power in a 25 mm diameter Gaussian beam coupled to the receiver input mirror.

Preliminary measurements using a 2.8 THz surface-plasmon guided QCL in place of a molecular gas laser have been made. The QCL emitted a total power of ~ 2 mW in a non-Gaussian divergent beam. After collecting and collimating this beam using an off-axis paraboloid mirror, there was insufficient LO power coupled to the receiver input mirror to generate a measurable noise temperature. However, the receiver did show that when the QCL was driven past a threshold current bias, its output split into two modes spaced 12.8 GHz apart, generating a clear 12.8 GHz IF signal in the receiver. The width of this IF signal indicated that the linewidth of the free-running QCL emission was ≤ 10 kHz. We will present further studies on receiver operation with better coupling of QCL light and higher power QCLs.

Sandia is a multiprogram laboratory operated by Sandia Corporation, a Lockheed Martin Company, for the United States Department of Energy's National Nuclear Security Administration under contract DE-AC04-94AL85000.

---

[1]H.-W. Hübers, *et al*., Optics Express **13**, 5890 (2005)
[2]S. Barbieri, *et al*., Optics Lett. **29**, 1632 (2004)
[3]P. H. Siegel, *et al*., IEEE Trans. Microwave Theory & Tech. **47**, 596 (1999)
[4]M. C. Gaidis, *et al*., IEEE Trans. Microwave Theory & Tech. **48**, 733 (2000)

# Influence of Schottky Diode Modelling Under Flat-Band Conditions on the Simulation of Submillimeter-Wave Mixers

José V. Siles[1], Jesús Grajal[1] and A. di Carlo[2]

[1]Dep. de Señales, Sistemas y Radiocomunicaciones, Universidad Politécnica de Madrid,
E.T.S.I. Telecomunicación, Ciudad Universitaria s/n, 28040 Madrid, Spain,
e-mail: {jovi, jesus}@gmr.ssr.upm.es, tel: +34 91.336.73.58
[2]Dip. di Ingegneria Elettronica, Universitá degli Studi di Roma "Tor Vergata",
Via del Politecnico 1, 00133 Roma, Italy
e-mail: aldo.dicarlo@uniroma2.it

***Abstract* — Flat-band conditions are usually reached in submillimeter-wave Schottky diode-based mixer operation. Numerical drift-diffusion (DD) models with conventional boundary conditions, which are based on the thermionic emission theory, do not correctly predict the behaviour of Schottky diodes under flat-band conditions so mixers performance cannot be accurately estimated. We employ a Monte Carlo simulator to analyze the performance of GaAs Schottky diodes in this operation regime. The results are employed for the refinement of DD model in the epitaxial layer. This new model is able to accurately predict the performance of submillimeter-wave mixers.**

## I. INTRODUCTION

Harmonic balance simulators employing numerical physics-based models for Schottky diodes have shown very good results for the analysis and optimization of submillimeter-wave multipliers [1] and they might represent the best alternative for the design and optimization of Schottky mixers at millimeter and submillimeter-wave bands. These mixers usually reach the flat-band operation regime. Thus, an accurate modelling of the diodes under these conditions [2] is required.

When employing traditional drift-diffusion diode models to simulate Schottky mixers at and beyond flat-band voltages, important discrepancies appear between measurements and simulations. These discrepancies consist of an anomalous increase in the simulated conversion loss when flat-band voltages are reached (Fig. 1). Thus, physics-based drift-diffusion Schottky models must be refined in order to correctly simulate submillimeter-wave mixers. For this task, a deeper understanding of the transport phenomena through the Schottky barrier is required.

We have analyzed the response of typical Schottky diodes employed for submillimeter-wave applications by means of a Monte Carlo (MC) simulator [3]. We have found an excellent agreement between drift-diffusion results and Monte Carlo results below flat band conditions for different physical parameters as the charge concentration, the electric field and the electron velocities. However, beyond flat-band voltages, important differences appear due to non-local transport phenomena [4]. Monte Carlo results will be employed for the refinement of the DD model for GaAs Schottky diodes under flat-band conditions. The aim of this work is to provide an accurate numerical modelling for Schottky diodes beyond flat-band. This is a key point for an accurate analysis of the performance of Schottky diode-based mixers at millimeter and submillimeter-wave bands.

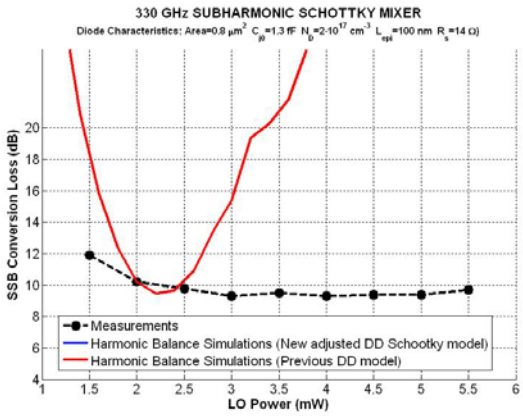


Fig. 1: Comparison between measurements and simulations (including drift-diffusion Schottky diode models) for a 330 GHz SHP mixer fabricated at the Observatory of Paris [5].

## II. DESCRIPTION OF THE SIMULATION TOOLS

### *a. Mixer CAD Tool*

The numerical CAD tool employed in this work couples a external circuit simulator with a physics-based drift-diffusion (DD) model of the Schootky diode by means of multi-tone Harmonic Balance (HB) techniques [6]. The Almost Periodic Fourier Transform (APFT) is utilized to perform the time-to-frequency transforms. Thus, no assumptions are made regarding the LO and RF power levels.

The Schottky diode DD model accounts for the most important transport phenomena at the interface: barrier lowering, tunnelling, velocity saturation.

### *b. Monte Carlo simulator for Schottky diodes*

Our Monte Carlo (MC) simulator has been developed at the "Tor Vergata" University in Rome (Italy) [3]. It consists of a band structure with three valleys at the conduction band (the central valley 'Γ' and the two

satellite valleys 'L' and 'X'), and three valence bands (heavy-holes, light-holes and spin-orbit). Spherical constant-energy surfaces are assumed and non-parabolicity correction factors are applied for the calculations [3].

The following scattering events are included in the MC simulator: acoustic phonon interaction, polar-optical phonon interaction, electron-plasmon interaction, impurity scattering, electron-hole scattering, intervalley scattering and impact ionization.

## III. SCHOTTKY DIODE MODELLING UNDER FLAT-BAND CONDITIONS

### *a. Focusing the problem*

In order to focus the problem concerning the anomalous increase of the simulated conversion loss of Schottky mixers, we firstly compared the I-V curves obtained with DD simulation and MC simulation for a Schottky diodes with similar characteristics to the one employed in the 330 GHz mixer [5]. The Schottky diodes analysed in this section has the following parameters: A 90 nm epilayer with doping concentrations varying from $1{\cdot}10^{16}$ $cm^{-3}$ to $1{\cdot}10^{18}$ $cm^{-3}$, anode area of 0.9 $\mu m^2$, and a $4{\cdot}10^{18}$ $cm^{-3}$ doping in the substrate (the length of the substrate has been reduced to 30 nm to speed up the MC simulations).

It can be appreciated in Fig. 2 that an early saturation of DC current occurs according to DD results when compared to MC results. However, for DC voltages below flatband (~0.95 V) both simulation results agree very well. It has been also checked that the increase in the simulated conversion loss of the 330 GHz mixer (Fig. 1) starts at the LO power for which the peaks of the voltage swing in the diodes reach flat band voltages.

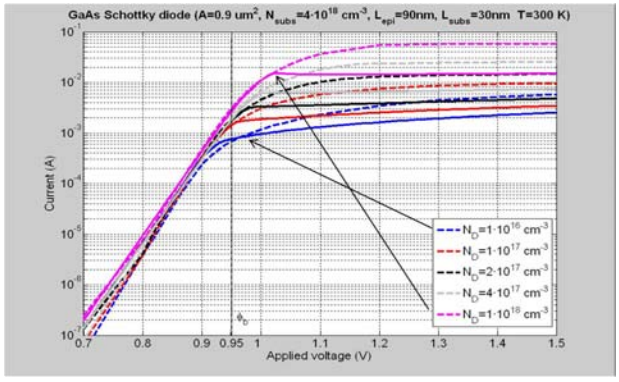


Fig. 2: Schottky diode I-V curves as a function of epilayer doping obtained by Monte Carlo simulation (dashed lines) and drift-diffusion simulation (solid lines). $\phi_b$ represents the ideal Schottky barrier height.

The DD results for the internal distributions of the Schottky diodes are also in a big disagreement with MC results beyond flat band voltages. In Fig. 3 it can be noticed that an important increment in the electron concentration is predicted by MC in the vicinity of the Schottky contact under flatband conditions. On the contrary, DD predicts a homogeneous increment of the electron concentration throughout the epilayer. Discrepancies between MC and DD can be also appreciated in Fig. 4 for the electric field profiles.

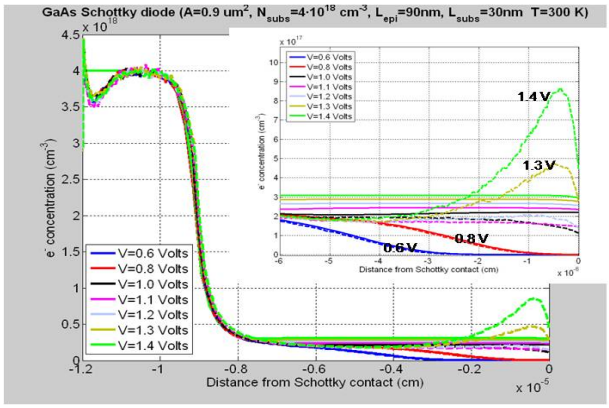


Fig. 3: Doping concentration as a function of the distance to the Schottky contact at different bias voltages. Monte Carlo simulations (dashed lines) and drift-diffusion simulations (solid lines). Epilayer doping is $N_D=2{\cdot}10^{17}$ $cm^{-3}$.

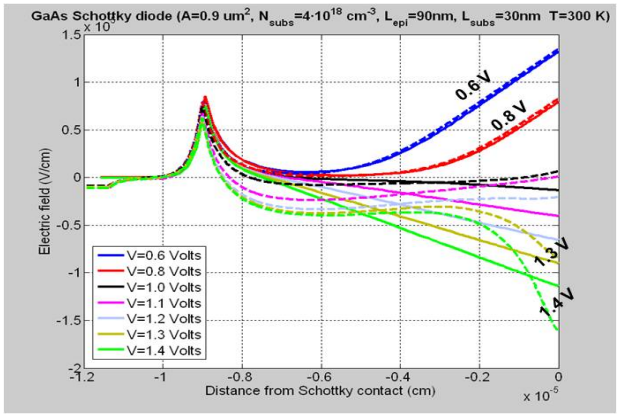


Fig. 4: Electric field as a function of the distance to the Schottky contact at different bias voltages. Monte Carlo simulations (dashed lines) and drift-diffusion simulations (solid lines). Epilayer doping is $N_D=2{\cdot}10^{17}$ $cm^{-3}$.

### *b. Analysing the problem*

The study of the internal distributions (electron velocities, electron distributions, populations of different valleys, electric field profiles, etc.) by means of MC simulation give us a physical insight on the limitations of DD and the modifications to be included in the DD formulation to overcome some of these limitations, especially at the Schottky contact.

Figure 5 shows a peak in the velocities predicted by the MC simulator just after reaching flat-band conditions. This peak does not appear in DD simulations.

The physical justification of this velocity overshoot can be deduced from Monte Carlo simulations (M. Lundstrom in [4]): When flatband voltages are reached, electron

population in the Γ valley grows as the electric field increases and electrons gain energy rapidly. The maximum occupation in the Γ valley corresponds to the peak of velocity (Figs. 5 and 6), and the dominant scattering mechanism is the optical phonon scattering. However, when electrons exceed a certain energy (0.3 eV for GaAs), intervalley scattering starts to dominate and the occupation in the satellite valleys (L and X) rises. Hence, velocity drops because of the higher effective mass of electrons in these valleys.

An analogous effect occurs for the recombination velocity at the Schottky contact. MC results showed a recombination velocity twice higher than that shown in Fig. 5. This is due to the hemi-maxwellian velocity distribution in the vicinity of the Schottky junction [7]. The classical phormula for the recombination velocity given by Crowell and Sze [8], typically used in drift-difussion models, does not predict either the increment of the electron velocity by a factor of 2, or the existence of the velocity peak.

The last analysis performed consisted of comparing the mobility curves obtained with both MC and DD models. Fig. 7 shows the mobility near the Schottky junction for different doping levels. It can be noticed that MC and DD results agree well below flatband voltages (corresponding to positive electric fields in Fig. 7). However, beyond flatband, the MC mobility drops at higher electron fields due to the peak in the average electron velocity. Furthermore, the field-dependent mobility depends on the distance to the Schottky junction as shown in Fig. 8.

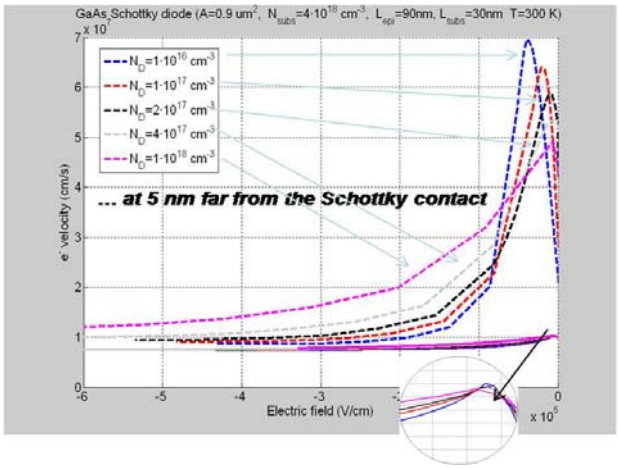


Fig. 5: Electron velocity as a function of the electric field for different epilayer dopings. Monte Carlo simulations (dashed lines) and drift-diffusion simulations (solid lines). Electric field is negative beyond flatband.

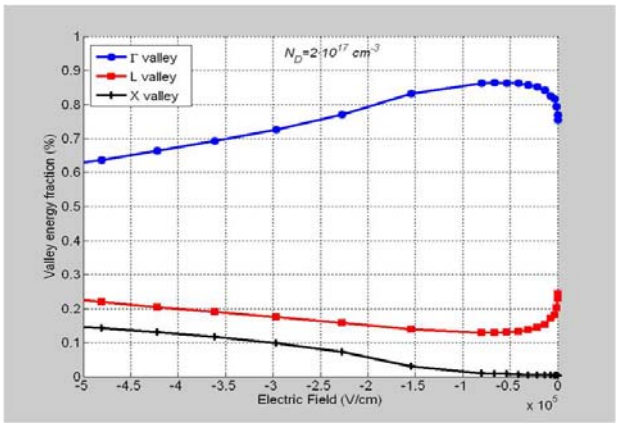


Fig. 6: Valley population (obtained by Monte Carlo simulations) as a function of the electric field. Epilayer doping is $N_D=2\cdot10^{17}$ $cm^{-3}$.

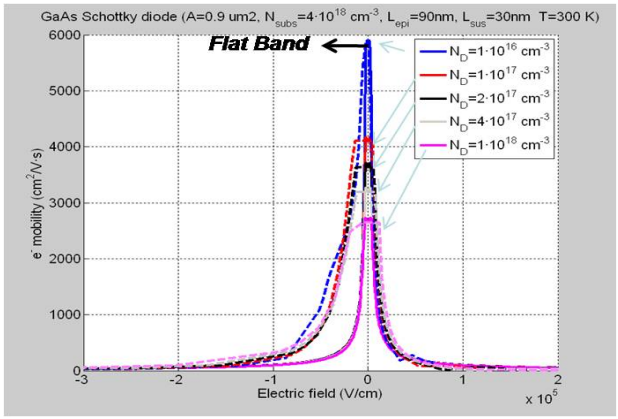


Fig. 7: Electron mobility as a function of the electric field for different epilayer dopings. Monte Carlo simulations (dashed lines) and drift-diffusion simulations (solid lines). Electric field is negative beyond flatband.

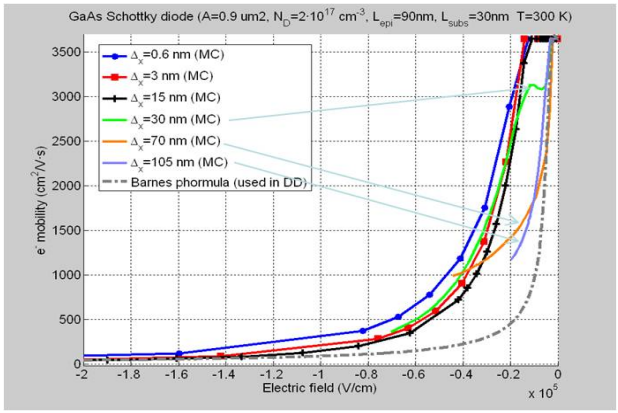


Fig. 8: Monte Carlo electron mobility as a function of the electric field and the distance to the Schottky contact. Results are compared with the traditional DD mobility (Barnes phormula [9]).

*c. Solving the problem*

The last step of this work was to refine our DD Schottky diode model by using the MC results previously discussed. A new recombination velocity at the Schottky contact, obtained from MC simulations, was defined in order to take into account that effect of the intervalley transitions. Also, a new field-dependent mobility characteristic as a function of the doping level, the distance to the Schottky contact and the epilayer length has to be set in the DD model. The most accurate modeling should define a different mobility at each position in the Schottky diode. However, it is enough to define two regions in the epilayer. The regions are indicated in Fig. 9. The first region is characterized by an almost constant electric field for a given voltage, and therefore, the mobility in this region can be assumed to be constant. In the second region close to the Schottky contact, the mobility predicted by MC is far from the mobility expression given by Barnes [9] (see Fig. 8). The field-dependent mobility characteristic to be used in DD is derived from MC results by assuming a negligible effect of diffusion (that is, drift velocity is dominant and velocity can be written as the product of mobility and electric field). Next, this mobility is slightly tuned to improve the agreement between MC and DD internal distributions.

Further analyses are being carried out to obtain a general rule for automatic segmentation of the epilayer for which different mobility characteristics are employed.

The results after the corrections on the DD model are shown in Figs. 9 and 10. The early saturation of the current that was shown in Fig. 2 is also corrected and the new I-V curves obtained with the adjusted DD model match pretty well the MC results.

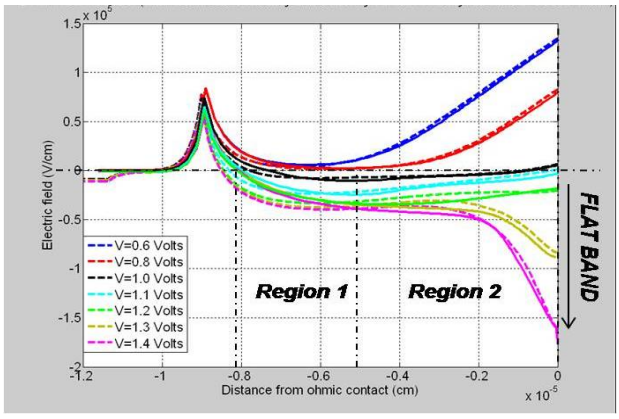


Fig. 9: Electric field as a function of the distance to the Schottky contact at different bias voltages. Monte Carlo simulations (dashed lines) and drift-diffusion simulations (solid lines). Epilayer doping is $N_D=2\cdot10^{17}$ cm$^{-3}$.

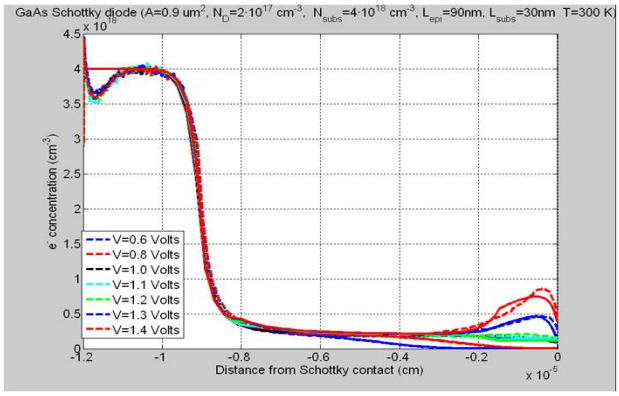


Fig. 10: Doping concentration as a function of the distance to the Schottky contact at different bias voltages. Monte Carlo simulations (dashed lines) and drift-diffusion simulations (solid lines). Epilayer doping is $N_D=2\cdot10^{17}$ cm$^{-3}$.

## III. 330 GHz SHP MIXER SIMULATION

Harmonic Balance simulations of the 330 GHz SHP Schottky mixer described in [5] were performed with the new DD model for the Schottky diode. The Schottky diode employed in the design and fabrication of the mixer is the *SD1T7-D20* from the University of Virginia. The characteristics of this diode (provided by the University of Virginia) can be found in [5]: An epitaxial layer of 100 nm, an anode area of 0.9 μm$^2$, an epilayer doping of $2\cdot10^{17}$ cm$^{-3}$, a built-in potential of 0.72 Volts, a zero junction capacitance of 1.3 fF and a series resistance of 11-15 Ω.

The DC analysis of the diode showed a series resistance of 14 Ω and a 1.3 fF zero junction capacitance, $C_{j0,}$ that are in good agreement with the nominal values specified by the University of Virginia. The optimum impedances employed in the simulation were optimized at a 1.5 mW LO power in absence of parasitics: $Z_{RF}=77+j\cdot138$ Ω and $Z_{LO}=142+j\cdot 238$ Ω. These values are very close to those considered in [5]: $Z_{RF}=83+j\cdot53$ Ω and $Z_{LO}=147+j\cdot207$ Ω. A 100 Ω IF output impedance has been considered in both the fabrication and the simulation of the 330 GHz mixer. This value is optimum for the antiparallel-diode pair according to [5], and agrees with the result provided by the IF impedance optimization performed with our CAD tool. The parasitic capacitance of the fabricated mixer is 5 fF according to [5]. The optimum impedances (when $C_p$ is considered) that are predicted by our CAD tool ($Z_{RF}=5+j\cdot56$ Ω and $Z_{LO}=4+j\cdot120$ Ω) are very different to those employed in the fabrication of the 330 GHz mixer so we have considered that the parasitic capacitance was no tuned out in the results presented in [5]. In order to make possible the comparison, the quasi-optical losses (0.7 dB) and the losses in the IF circuit and SMA connectors (2.5 dB) predicted in [5] have been added to the simulation results.

Taking into account all these considerations, the new results are provided in Fig. 11. The adjusted DD model eliminates the anomalous increase in the conversion loss that occurred with the previous model when flatband

voltages were reached. As a consequence, new simulation results are in a very good agreement with measurements, certifying the validity of the correction done.

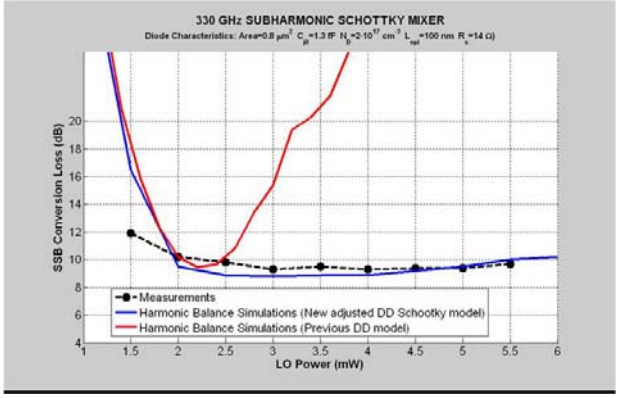


Fig. 11: Comparison between measurements and HB simulations with the new adjusted DD Schottky model for the 330 GHz SHP mixer.

## IV. CONCLUSION

Limitations of present DD models for Schottky diodes operating above flatband voltages have been presented in this work. Mixer designs based on these models are not accurate enough, and, therefore, a refinement of DD models is necessary.

Monte Carlo models can be used for a better understanding of the physics inside Schottky diodes. However, mixer design including MC models is not viable due to the high computational cost. Hence, circuit simulation with refined DD models offers a very good trade-off between accuracy and computation time for submillimeter-wave mixer design, as the agreement between measurements and simulations for a 330 GHz SHP mixer shows.

This work is part of an effort to establish a numerical CAD tool for the design and optimization of millimetre-wave and submillimeter-wave circuits based on Schottky diodes and HBV diodes including accurate physical models for the semiconductor devices.

## ACKNOWLEDGEMENT

This work was supported by the Spanish National Research and Development Program under project number TEC2005-07010-C02-01/TCM.

The authors wish to thank Dr. B. Thomas (*Rutherford Appleton Laboratory*, UK), and Dr. A. Maestrini (*L'Observatoire de Paris*, France), for providing all the data and measurements corresponding to the 330 GHz SHP Schottky mixer.

## REFERENCES

[1] J. Grajal, J.V. Siles, and V. Krozer, E. Sbarra, and B. Leone "Performance evaluation of multiplication chains up to THz frequencies," *in proc. 29th Internatinal Conference on Infrarred and Millimeter Waves and 12th International Conference on THz Electronics*, pp.197-198, September 2004.

[2] I. Mehdi, P.H. Siegel, and J. East "Improved millimeter-wave mixer performance analysis using a drift diffusion capacitance model," *1991 IEEE MTT-S Digest*, June 1999.

[3] C. Jacoboni and P. Lugli, " *The Monte Carlo method for semiconductor devices*, Springer-Verlag Wien New York, 1989.

[4] M. Lundstrom, "Fundamentals of carrier transport (Second edition)," *Cambridge University Press*, 2000.

[5] B. Thomas, A. Maestrini, and G. Beaudin, "A low-noise fixed tuned 300-360-GHz sub-harmonic mixer using planar Schottky diodes," *IEEE Microwave and Wireless Components Letters*, vol. 15, no. 12, pp. 865-867, December 2005.

[6] J.V. Siles, J. Grajal, V. Krozer, and B. Leone, "A CAD tool for the design and optimization of Schottky diode mixers up to THz frequencies," *16th International Symposium on Space Terahertz Technology*, May 2005.

[7] J. Adams, and T.-W. Tang, "A revised boundary condition for the numerical analysis of Schottky barrier diodes," *IEEE Electron Device Letters*, vol. 7, no. 9, pp. 525-527, September 1986.

[8] C.R. Crowell, and S.M. Sze, "Current transport in metal semiconductor barriers," *Solid-State Electron.*, vol. 9, pp. 1035-1047, 1966.

[9] J.J. Barnes, and R.J. Lomax, "Finite-element simulation of GaAs MESFET's with lateral doping profiles and submicron gates," *IEEE Transactions on electron Devices.*, vol. 23, no. 9 pp. 1042-1048, September 1976.

# Progress towards an integrated 380 GHz planar Schottky diode heterodyne receiver on single substrate

Bertrand Thomas, Byron Alderman, John Spencer,
Dave Matheson, and Peter de Maagt.

*Abstract*— : **We report on the design, build and characterisation of an integrated submillimetre wave receiver featuring a 380 GHz sub-harmonic mixer and a 190 GHz frequency doubler on a single quartz based microstrip circuit. The integrated circuit uses two separate planar Schottky diode components to perform the doubling and 2nd harmonic mixing. Measurement results give best double sideband mixer noise temperatures of 1625 K at 372 GHz, and a corresponding mixer conversion loss of 8 dB. The measured instantaneous RF bandwidth extends from 368 GHz to 392 GHz, in good agreement with simulations. This work represents the first demonstration of a single substrate integrated mixer/multiplier at submillimetre wavelengths.**

***Index Terms*— Submillimetre wave receiver, integrated mixer/multiplier, planar Schottky diodes.**

## I. Introduction

Submillimetre receiver arrays are expected to enhance the capabilities of future airborne and space-borne atmospheric limb sounding instruments. For example, Schottky diode based heterodyne array instruments will not only allow observations with greater sensitivity than single pixel sounders, but will also provide vertically and horizontally resolved information on global distributions of key species in the Earth's upper troposphere and lower stratosphere (e.g., the STEAM-R concept [1]). One way of avoiding difficulties associated with local oscillator (LO) generation and injection in an array of receivers is to integrate the mixer and LO provision within each pixel; in principle this will allow reduced size, mass and power consumption, and an easily extendable array concept. Here we investigate the integration of a subharmonic mixer with a frequency doubler based on planar Schottky diodes, since this is the method generally used to provide the local oscillator signal in a sub-millimetre receiver.

Manuscript received May 1, 2007. This work has been carried out at the Space Science & Technology Department of the Rutherford Appleton Laboratory and was funded in part by the European Space Agency under contract number 16142/02/NL/EC.

B.Thomas, B.Alderman, J. Spencer and D. Matheson are with the Rutherford Appleton Laboratory, Chilton Didcot, OX11 0QX Oxfordshire, UK (contact phone: 1235-446343; fax: 1235-445848; e-mail: b.thomas@rl.ac.uk).

P. de Maagt is with the ESA/ESTEC, Keplerlaan 1, Postbus 299, 2200 AG Noordwijk, the Netherlands.

Due to the efficient and mature modelling techniques for planar Schottky diode devices at submillimetre wavelengths, coupled with the monotonic increase in available computing power, mixer and multiplier circuits which were previously designed and packaged independently are now being incorporated in a single housing [2]. However, no mixer/multiplier device integrated on a single circuit carrier has been reported so far in the submillimetre wave domain. We report here for the first time the development of an integrated 380 GHz sub-harmonic mixer/doubler using a single quartz substrate.

## II. 380 GHz integrated mixer/multiplier design architecture

The 380 GHz integrated mixer/doubler design concept features a balanced doubler stage and a sub-harmonic mixer stage in a single circuit, as illustrated in Fig.1. The integrated circuit performs the second harmonic mixing between the output LO signal of the doubler stage and the RF input signal of the mixer stage. The main advantage of using a balanced diode configuration is the possibility of decoupling the input matching circuit for the fundamental frequency, circa 95 GHz, and the RF input matching circuit without additional filtering elements, as shown in Fig.1. This is due to the natural input and output mode separation of a balanced configuration, further detailed in [3]. The reduced dimensions of the microstrip channel help to prevent the third and fifth harmonics, generated by the doubler diodes in a parasitic TE mode, from propagating towards the mixer diodes. The fourth harmonic, generated in a quasi-TEM mode, is strongly rejected by the RF low-pass filter as it falls into the RF frequency band. In the selected approach, each series pair of the balanced doubler diodes can be biased independently from the sides of the input waveguide, rather than from the central microstrip line usually used in balanced doubler architectures [4]. A bond wire is used to provide both a DC ground for the doubler diodes and an IF ground for the sub-harmonic mixer diodes via the central microstrip line. Its length is set as a quarter wavelength at the LO frequency in order to affect minimally its propagation. The bond wire does not significantly disturb the RF matching circuit since the RF signal is already attenuated strongly by the low pass filter at this point.

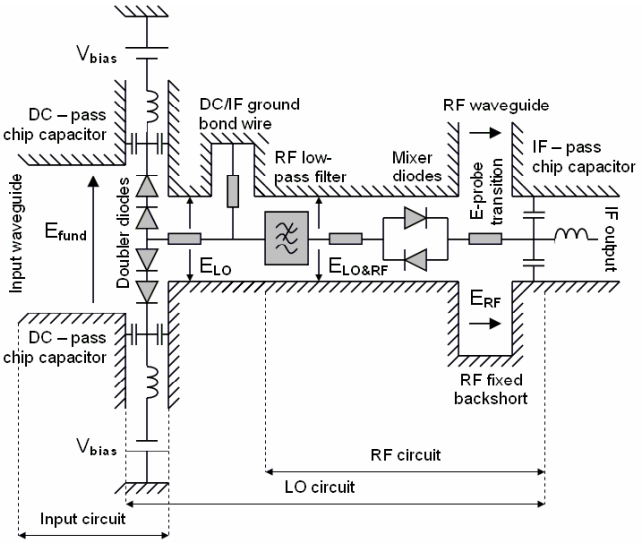


Fig.1. Schematic diagram of the integrated receiver. RF input is from 370 to 390 GHz, whereas the fundamental input frequency is about 95 GHz.

The design methodology uses a combination of linear/non-linear circuit simulations (Agilent ADS [5]) to optimize and compute the performances of the circuit, and 3D EM simulations (Ansoft HFSS [6]) to model accurately the diodes and waveguide structures.

As a first step, the electrical models for the doubler and mixer diodes are linearised around their optimum operating point. The electrical parameters of the doubler's VDI SB6T4-R1 varactor diodes [7] are a series resistance of $R_s = 5\ \Omega$, saturation current $I_{sat}$ = 146 pA, a zero voltage capacitance $C_{jo}$ = 42 fF, an ideality factor $\eta = 1.2$, a built-in potential $V_{bi} = 0.83$ V and an anode diameter d = 6 µm. An additional linear capacitance corresponding to approximately 4% of $C_{jo}$ is introduced in parallel to the non-linear plate capacitance of the junction to include the edge effect [8]. Considering an available input power of 9 mW at 95 GHz and a bias voltage of -3 V per diode, an ideal input embedding impedance of $Z_{in}$ = 8.5 + j.68, and an output embedding impedance of $Z_{out}$ = 13 + j.34 at a frequency of 190 GHz is found for a single barrier.

For the subharmonic mixer, the electrical parameters of VDI's SC1T9-D20 diodes used are a series resistance $R_s$ = 10 Ω, a zero voltage junction capacitance of $C_{jo}$= 2.5 fF, saturation current $I_{sat}$ = 30 fA, ideality factor η=1.25 and built-in potential $V_{bi}$ = 0.73 V. Considering an optimum LO power level of 1.5 mW, a set of non-linear simulations gives an ideal embedding impedances of approximately $Z_{RF}$ = 47+j.46 at RF frequencies and $Z_{LO}$ = 63+j.121 at LO frequencies. The IF load impedance is set to 100 Ω.

In a second step, each part of the circuit is modelled electromagnetically with HFSS, and imported in ADS for further optimisation. In order to retrieve the S-parameters at the level of each Schottky barrier in the doubler and mixer devices, micro-coaxial probe ports are introduced [9]. A simple low-pass filter is required to prevent the RF signal from leaking into the doubler stage and to transmit the LO signal to the mixer stage. Single layer chip capacitors (model Tcap® from DLI [10]) with minimum dimensions of 254 µm x 254 µm x 76 µm are used to present a shunt resonance at fundamental and LO frequencies for the doubler stage, allowing independent DC bias to be applied to each branch. On the mixer stage, a similar chip capacitor is reduced in size using a dicing saw in order to present a shunt resonance at LO and RF frequencies, allowing the transmission of the IF signal to the output.

The circuit is optimized for best coupling of the fundamental signal to the doubler diodes, the LO signal from the output of the doubler stage to the mixer stage, and the RF signal to the mixer diodes. As an example, the total coupling efficiency between the doubler and the mixer diodes is presented in Fig. 2. It is obtained by summing the individual coupling efficiencies between each of the doubler diodes and mixer diodes, and is estimated to be between 60 % and 70%, from 186 GHz to 196 GHz. The simulated RF input return losses of mixer circuit stage are given in Fig.3, showing a predicted RF bandwidth extending at least from 370 GHz to 390 GHz.

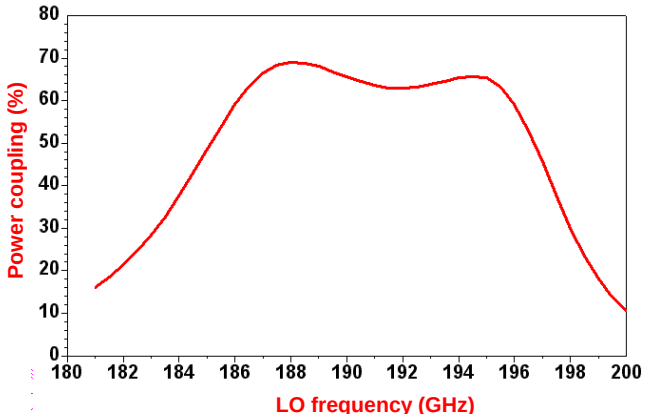


Fig.2. Predicted coupling efficiency between the doubler and the mixer stages at LO frequencies.

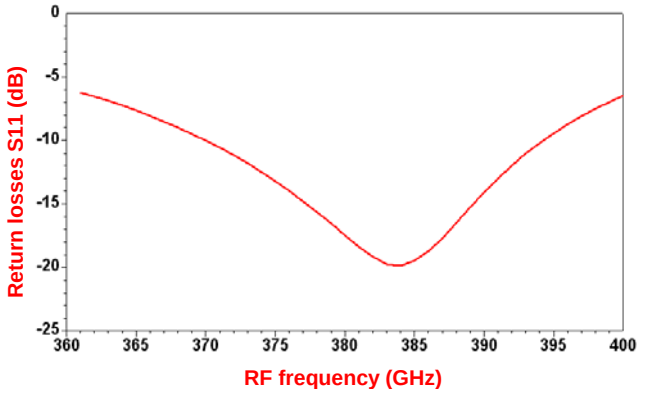


Fig.3. Predicted waveguide return losses in as a function of RF, assuming 60 mW of input power at the fundamental frequency.

## III. 380 GHz INTEGRATED MIXER/MULTIPLIER FABRICATION

The integrated circuit includes an anti-parallel pair of planar Schottky diodes (ref. SC1T9-D20 from VDI) for the 380 GHz sub-harmonic mixing part, and an anti-series array of 4 planar Schottky Varactor diodes (ref. SB6T4-R1 from VDI) for the multiplier part. The latter component has originally six Schottky devices. However, one diode at each extremities is removed to produce the configuration shown in Fig. 4, which

reduces the amount of input power required. Both mixing and multiplying diodes components are flip-chip mounted onto a single quartz based microstrip circuit. The quartz substrate is cut into the required "T" shape using a precision dicing saw. This geometry is needed to accommodate the different dimensions of the two Schottky devices and to prevent higher order modes, as described above, from propagating inside the circuit.

Then, the quartz based circuit is mounted inside the lower half of the split-block and connected via beamleads to the three ceramic chip capacitors, as shown in Fig.4. Gold bond wires are then contacted to the circuit using a conductive silver-epoxy glue as a final step of the mounting procedure.

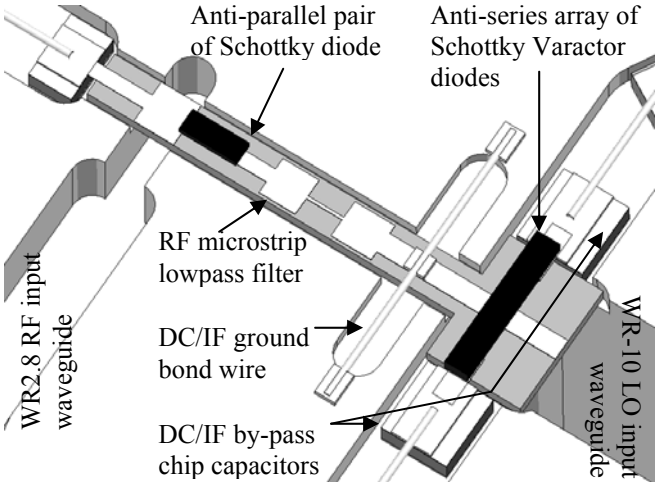


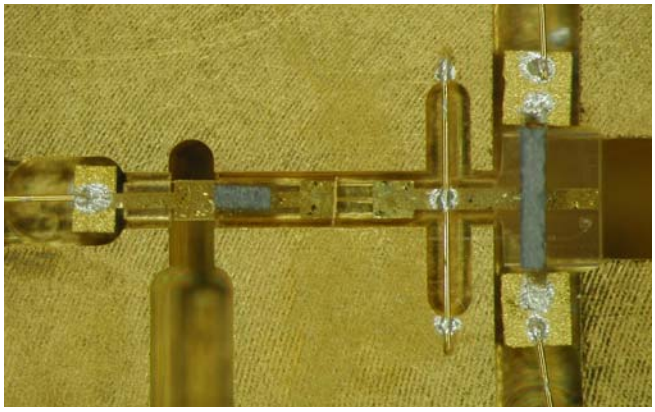

Fig.4. Top: labelled schematic of the integrated design and, bottom, a photograph of the circuit after mounting into the lower half of the split metal block

The assembled 380 GHz block shown in Fig.5 includes two SMA DC bias ports, a K-type IF output connector (right hand side), a WR-10 input flange for the fundamental input signal (not visible, on the left-hand side), and an integrated diagonal RF horn antenna [11] with aperture visible on the front of the block. The IF microstrip-to-K connector transition is designed to present low insertion losses from DC up to 40 GHz.

Fig.5. Photograph of the final integrated mixer/multiplier assembled block.

## IV. Test of the Integrated 380 GHz Receiver

For testing, the 380 GHz integrated mixer/multiplier is driven by a BWO whose output power is controlled by a separate rotary vane attenuator. In order to maximize the matching at the fundamental frequency, an E/H tuner is inserted after variable attenuator. Both DC bias lines to the doubler stage are connected to a stabilized low noise DC power supply. The IF signal is amplified by a low noise amplifier chain, with a noise figure of 1.4 dB, which included a filter with a pass band between 2.5 GHz and 3.5 GHz. The output power of the amplifier chain is measured using an HP 8481D diode power sensor.

Test results presented in Fig.6, show the double side band (DSB) receiver noise temperature, DSB mixer noise temperature and DSB mixer conversion losses as functions of four times the fundamental signal frequency. The best DSB receiver noise temperature obtained is 2330 K at an RF frequency centred at 372 GHz, corresponding to a DSB mixer noise temperature of 1625 K and DSB mixer conversion losses of 8 dB. The measured conversion losses are between 1.2 dB and 2.5 dB above the predicted ones. The 3 dB conversion losses bandwidth extends from a RF centre frequency from 368 GHz to 392 GHz, apart from degradation in performances around 380 GHz, due to a lack of LO power delivered to the mixer stage. This could arise from a drop of power from the BWO at the fundamental frequency as it has been observed by a measurement of the output power of the BWO at this frequency, and/or a resonance in the LO matching circuit at 190 GHz.

Despite the possibility to bias independently each branch of the doubler diodes array, it is noticed that the performances are optimum when both branches are biased with the same voltage, with equal resulting DC currents, giving an indication that the power coupled to the diodes is well distributed between both branches.

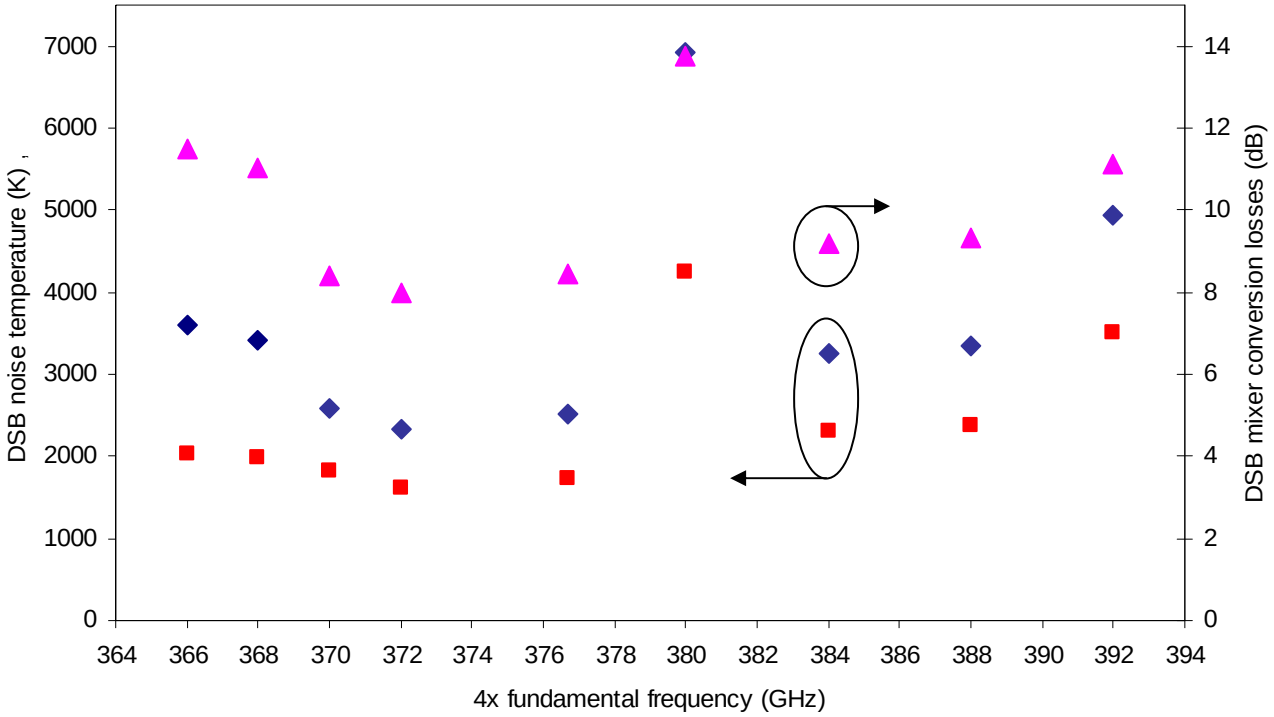


Fig.6. Measured double sideband performance of the 380 GHz integrated mixer/multiplier as functions of the RF frequency. The IF band extends from 2.5 to 3.5 GHz. The bottom red squares show the DSB mixer noise temperature, the middle blue diamonds show the DSB receiver noise temperature and the top pink triangles show the DSB mixer conversion losses.

## I. Conclusion

The first operation of an integrated sub-millimetre wave receiver featuring a doubler and a sub-harmonic mixer stage on a single substrate is reported. Over nearly all of the designed RF bandwidth, conversion losses between 8 and 10 dB and DSB noise temperatures between 1625 and 3000 K were measured. These agree relatively well with the simulation. An observed degradation in performance at 380 GHz is attributed to a loss in LO power delivered to the mixer stage. The device demonstrates that it is possible to couple efficiently the output signal of a doubler stage to a sub-harmonic mixer circuit when both are mounted on the same microstrip quartz-based circuit.

## Acknowledgements

The authors wish to acknowledge Dr. Alain Maestrini and the LERMA department at the Observatory of Paris for their help and support during the test campaign. We thank Professor Tom Crowe, University of Virginia/ VDI for the supply of high quality diodes.

This research has been funded by ESA under contract number 16142/02/NL/EC

## References

[1] U. Klein, C.C. Lin, J. Langen and R. Meynart, "Future Satellite Earth Observation Requirements in Millimetre and Sub-Millimetre Wavelength Region", *Proceedings of the 4th ESA workshop on Millimetre-Wave Technology and Applications*, Espoo, Finland, 15-17 February 2006.

[2] D. Porterfield, J. Hesler, T. Crowe, W. Bishop, and D. Woolard, "Integrated Terahertz Transmit/Receiver Modules", proceedings of the 33rd European Microwave Conference, Munich, Germany, 2003.

[3] N. Erickson, "High Efficiency Submillimeter Frequency Multipliers", IEEE MTT-Symposium Digest, 1990.

[4] D. Porterfield, T. Crowe, R. Bradley, and N. Erickson, " A high-power fixed-tuned millimetre-wave balanced frequency doubler", IEEE Trans. on MTT, Vol.47, No.4, April 1999.

[5] Advanced Design System 2005A, Agilent Technologies, 395 Page Mill Road, Palo Alto, CA 94304, USA.

[6] High Frequency Simulation Software, V10, Ansoft Corporation, 225 West Station Square Drive, Suite 200, Pittsburgh, PA 15219, USA.

[7] Virginia Diodes Inc., http://www.virginiadiodes.com

[8] J.T. Louhi and A.V. Raisanen, "On the modeling of optimization of Schottky Varactor frequency multiplier at submillimeter wavelengths", IEEE Trans. On MTT, Vol. 43, No. 4, April 1995.

[9] J. Hesler, W.R. Hall , T.W. Crowe, R.M. Weikle, B.S. Deaver, Jr., R.F. Bradley and S-K. Pan, "Fix-Tuned Submillimeter Wavelength Waveguide Mixers Using Planar Schottky-Barrier Diodes", *IEEE Trans. MTT,* **45**, pp. 653-658, 1997.

[10] Dielectric Laboratories Inc. http://www.dilabs.com

[11] J. Johansson and N.D. Whyborn, "The Diagonal Horn as a Submillimeter Wave Antenna", *IEEE Transactions on Microwave Theory and Techniques*, Vol. 40, No. 5, pp.795-800, May 1992.

# First Wideband 520-590 GHz Balanced Fundamental Schottky Mixer

Erich Schlecht, John Gill, Robert Dengler, Robert Lin, Ray Tsang, and Imran Mehdi

Jet Propulsion Laboratory, California Institute of Technology, Pasadena, CA 91109, USA

***Abstract* — We report on the design and performance of a novel broadband, biasable, balanced fundamental 520-590 GHz fix-tuned frequency mixer that utilizes planar Schottky diodes. The suspended stripline circuit is fabricated on a GaAs membrane mounted in a split waveguide block. The chip is supported by thick beam leads that are also used to provide precise RF grounding, RF coupling and DC/IF connections. At room temperature, the mixer has a measured DSB noise temperature of 2200 K at the low end of the band, and less than 4000 K across the design band.**

***Index Terms* — Submillimeter wave mixers, Schottky diode mixers, Submillimeter wave diodes.**

## I. Introduction

There is a demand for mixers operating in the submillimeter band between 300 and 1200 GHz for atmospheric remote sensing spectroscopy. Near term missions that might use such mixers include a proposal for water detection observations on Mars, and measurements of middle atmosphere trace gases and gas dynamics on Venus. Schottky submillimeter and Terahertz sensors would be ideal for future proposed missions to Europa and Titan as well.

We have designed, fabricated and tested a variation of the crossbar type of balanced mixer. In this mixer, the waveguides are rotated so that they are both cut in the E-plane by the block split.

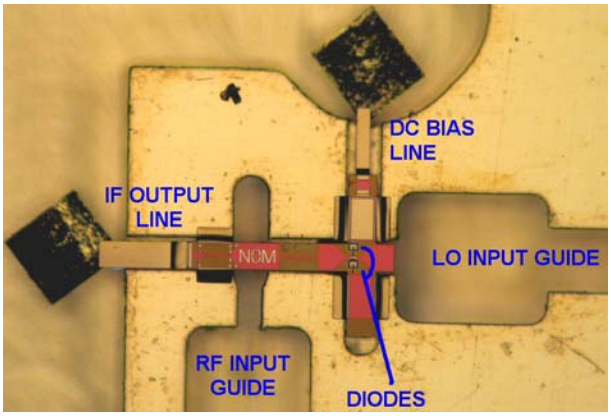


Fig. 1. Balanced mixer mounted in block.

## II. Design and Fabrication

The mixer was designed using a combination of commercial software packages and a harmonic balance simulator developed at JPL to allow advanced diode properties such as undepleted epi-layer electron heating to be included in the analysis. The passive portion of the circuit is analyzed with a combination of linear circuit simulators and Ansoft HFSS.

The design itself starts with an optimization of the diode size and terminating impedances, based on the available LO pump power. Then the circuit is designed using a combination of HFSS and linear circuit simulators The completed circuit inside the waveguide block is shown in Fig. 1.

The mixer was fabricated using JPLs planar membrane beam lead process, and the blocks were fabricated from brass using precision machining techniques.

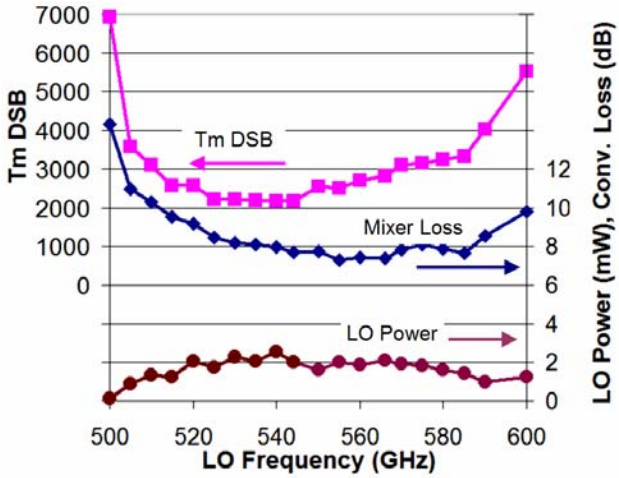


Fig. 2. Mixer performance variation with LO frequency.

## III. Mixer Measurements

The mixers' performance is measured using an automatic Y-factor system specifically assembled for mixers. The measured performance of the mixer as a function of LO frequency is shown in Fig. 2. These measurements were taken at the LO power levels as shown. They cover the design bandwidth from 530 to 590 GHz, and indicate the wide RF bandwidth of the mixer.

## IV Conclusion

This work presents a description and measured results of a very widely tunable balanced Schottky mixer. As far as the authors know, it is the first of its type in this frequency range.

# High-Performance Negative Differential Resistance Oscillators and Combiners

H. Eisele[1], Y.-R. Wu[2], R. Kamoua[3], and G. I. Haddad[2]

[1] Institute of Microwaves and Photonics, School of Electronic and Electrical Engineering
University of Leeds, Leeds LS2 9JT, United Kingdom

[2] Solid-State Electronics Laboratory, Department of EECS
University of Michigan, Ann Arbor, Michigan 48109-2122, USA

[3] Department of Electrical and Computer Engineering
Stony Brook University, Stony Brook, NY 11794-2350, USA

**Abstract**

Many emerging systems applications at submillimeter-wave frequencies critically depend on the availability of compact, reliable, and efficient sources of radiation with substantial amounts of power. Negative differential resistance (NDR) devices, such as GaAs tunnel-injection transit-time diodes [1] and InP Gunn devices [2] have been the most successful approach to fundamental oscillators. To exploit the favorable material parameters of GaN, such as the high breakdown electric fields, the relatively low dielectric constant, and, most importantly, the high electron drift velocity, a novel tunnel-injection transit-time device was proposed recently [3]. It uses the unique tunneling properties from piezoelectric and spontaneous polarization effects in GaN/AlGaN heterojunctions [3]. Its performance potential was initially evaluated with simulations using a hydrodynamic device model [4] and excellent performance characteristics were predicted around 160 GHz and 320 GHz [3]. The validity of the hydrodynamic model at higher submillimeter-wave frequencies is questionable. Therefore, an energy-momentum model was employed more recently together with refined GaN material parameters and heterojunction intraband-tunneling injection characteristics. These simulations predicted RF output power levels (and corresponding dc-to-RF conversion efficiencies) of more than 25 mW (> 2%) at 260–360 GHz and more than 5 mW (> 1%) at 350–490 GHz for operating active-layer temperatures well below 600 K.

Power combining is a well-known method if power levels higher than those of a single oscillator are needed in systems applications. Its viability and strong performance potential with milliwatts of output power was demonstrated for the first time at submillimeter-wave frequencies using InP Gunn devices [4]. In these initial experiments [4], the performance of the in-line waveguide combiner was limited by the fixed spacing between the two oscillators. More recently, waveguide washers were used to adjust the spacing and get closer to the optimum phase relationships at the fundamental and second-harmonic frequencies of the InP Gunn devices in the two cavities. Initial experiments already yielded a performance improvement of 25% and combined power levels of more than 7.5 mW with corresponding combining efficiencies of more than 85% were measured at 280 GHz. These experiments together with earlier experiments at lower frequencies indicate that this a very promising method to increase the output power levels from various NDR devices at submillimeter-wave frequencies including the GaN-based devices described above.

**References**

[1] H. Eisele, "355-GHz Oscillator with GaAs TUNNETT Diode," *Electronics Letters*, vol. 41, no. 6, 2005, pp. 329–331.

[2] H. Eisele, "InP Gunn Devices for 400–425 GHz," *Electronics Letters*, vol. 42 no. 6, 2006, pp. 358–359.

[3] H. Eisele, M. Singh, Y.-R. Wu, J. Singh, and G. I. Haddad, "AlGaN/GaN Heterostructure Transit-Time Devices: A Novel Device Concept for Submillimeter-Wave Sources," *Proceedings of the 16th International Symposium on Space Terahertz Technology*, May 2–4, 2005, Gothenburg, Sweden.

[4] H. Eisele and R. Kamoua, "High-Performance Oscillators and Power Combiners with InP Gunn Devices at 260–330 GHz," *IEEE Microwave and Wireless Components Letters*, vol. 16, no. 5, 2006, pp. 284–286.

## Registered Participants at ISSTT 2007

| | | | |
|---|---|---|---|
| Tarun | Bansal | SRON | t.bansal@tudelft.nl |
| Rami | Barends | Delft University of Technology | r.barends@tnw.tudelft.nl |
| Andrey | Baryshev | SRON/RuG/NOVA | andrey@sron.rug.nl |
| Jochem | Baselmans | SRON | J.Baselmans@sron.nl |
| Eric | Becklin | USRA/UCLA | becklin@astro.ucla.edu |
| Dominic | Benford | NASA / GSFC | dominic.benford@nasa.gov |
| Raymond | Blundell | Smithsonian Astrophysical Observatory | rblundell@cfa.harvard.edu |
| Faouzi | Boussaha | LERMA | faouzi.boussaha@obspm.fr |
| Eric | Bryerton | NRAO | ebryerto@nrao.edu |
| Tomas | Bryllert | Chalmers University of Technology | bryllert@chalmers.se |
| Rick | Campbell | Cascade Microtech | kk7b@ieee.org |
| Sean | Casey | USRA/SOFIA | scasey@mail.arc.nasa.gov |
| Goutam | Chattopadhyay | JPL | Goutam.Chattopadhyay@jpl.nasa.gov |
| Sergey | Cherednichenko | Chalmers University of Technology | serguei.cherednichenko@mc2.chalmers.se |
| Jay | Chervenak | NASA GSFC | James.A.Chervenak@nasa.gov |
| Ken | Cooper | JPL | Ken.B.Cooper@jpl.nasa.gov |
| Thomas | Crowe | VDI / UVa | TomVDI@earthlink.net |
| Gert | de Lange | SRON | gert@sron.rug.nl |
| Robert | Dengler | JPL | Robert.J.Dengler@jpl.nasa.gov |
| Pieter | Dieleman | SRON Netherlands Institute for Space Research | P.Dieleman@sron.rug.nl |
| Simon | Doyle | Cardiff University | simon.doyle@astro.cf.ac.uk |
| Jack | East | The University of Michigan | jeast@eecs.umich.edu |
| Michael | Edgar | Caltech | mick@submm.caltech.edu |
| Heribert | Eisele | University of Leeds | h.eisele@leeds.ac.uk |
| Anders | Emrich | Omnisys | ae@omnisys.se |
| Akira | Endo | Tokyo Univ. / NAOJ | akira.endo@nao.ac.jp |
| Jian-Rong | Gao | SRON/TU Delft | J.R.Gao@tnw.tudelft.nl |
| Jiansong | Gao | Caltech | jiansong@caltech.edu |
| Jonathan | Gardner | NASA GSFC | jonathan.p.gardner@nasa.gov |

| | | | |
|---|---|---|---|
| Jason | Glenn | University of Colorado | jglenn@casa.colorado.edu |
| Paul | Goldsmith | JPL | Paul.F.Goldsmith@jpl.nasa.gov |
| Gregory | Goltsman | Moscow State Pedagogical University | goltsman@mspu-phys.ru |
| Paul | Grimes | Oxford University | pxg@astro.ox.ac.uk |
| Christopher | Groppi | University of Arizona | cgroppi@as.arizona.edu |
| Bruno | Guillet | GREYC (CNRS UMR 6072) | bruno.guillet@greyc.ensicaen.fr |
| Jeffrey | Hesler | VDI | hesler@virginiadiodes.com |
| Ronald | Hesper | SRON/University of Groningen | hesper@sron.rug.nl |
| Niels | Hovenier | TUDelft | j.n.hovenier@tnw.tudelft.nl |
| Heinz-Wilhelm | Hübers | DLR | heinz-wilhelm.huebers@dlr.de |
| Volker | Hurm | Fraunhofer IAF | volker.hurm@iaf.fraunhofer.de |
| Karl | Jacobs | KOSMA | jacobs@ph1.uni-koeln.de |
| Hamid | Javadi | JPL | Hamid.H.Javadi@jpl.nasa.gov |
| Willem | Jellema | SRON Netherlands Institute for Space Research | W.Jellema@sron.nl |
| Cecile | Jung | Observatoire de Paris | cecilejung@yahoo.fr |
| Boris | Karasik | JPL/Caltech | boris.s.karasik@jpl.nasa.gov |
| Alexandre | Karpov | Caltech | karpov@submm.caltech.edu |
| Pourya | Khosropanah | SRON | p.khosropanah@sron.rug.nl |
| Jacob | Kooi | Caltech | kooi@caltech.edu |
| Valery | Koshelets | Institute of Radio Engineering and Electronics | valery@hitech.cplire.ru |
| Shwetank | Kumar | Caltech | shwetank@caltech.edu |
| Leonid | Kuzmin | Chalmers University | leonid.kuzmin@mc2.chalmers.se |
| Gene | Lauria | Arizona Radio Observatory | glauria@as.arizona.edu |
| Mark | Lee | Sandia National Laboratories | mlee1@sandia.gov |
| Roger | Lee | JPL | Roger.A.Lee@jpl.nasa.gov |
| Jamie | Leech | Oxford University | jxl@astro.ox.ac.uk |
| Roland | Lefèvre | Paris Observatory | roland.lefevre@obspm.fr |
| Robert | Lin | Jet Propulsion Laboratory | Robert.H.Lin@jpl.nasa.gov |
| Chris | Lodewijk | Delft University of Technology | C.F.J.Lodewijk@TUDelft.nl |

| | | | |
|---|---|---|---|
| Denis | Ludkov | TU Delft | d.ludkov@tudelft.nl |
| Alain | Maestrini | Observatoire de Paris | alain.maestrini@obspm.fr |
| Doris | Maier | IRAM | maier@iram.fr |
| Frank | Maiwald | JPL | Frank.W.Maiwald@jpl.nasa.gov |
| Hiroshi | Matsuo | NAOJ | h.matsuo@nao.ac.jp |
| James | McGuire | Optical Research Associates | frankm@opticalres.com |
| Imran | Mehdi | Jet Propulsion Laboratory | imran@merlin.jpl.nasa.gov |
| Denis | Meledin | Chalmers University of Technology | denis.meledin@chalmers.se |
| Patricio | Mena | SRON | mena@sron.rug.nl |
| Harald | Merkel | October Biometrics AB | harald.merkel@mc2.chalmers.se |
| David | Miller | California Institute of Technology | davem@submm.caltech.edu |
| Raquel | Monje | Onsala Space Observatory, Chalmers University of Technology | raquel@oso.chalmers.se |
| TETSUO | MORI | INFRARED LIMITED | mori@infrared.co.jp |
| Dmitry | Morozov | Cardiff University | Dmitry.Morozov@astro.cf.ac.uk |
| Harvey | Moseley | NASA/GSFC | Harvey.Moseley@nasa.gov |
| Bret | Naylor | Caltech | naylor@submm.caltech.edu |
| Omid | Noroozian | California Institute of Technology | omid@caltech.edu |
| Chris | North | University of Oxford | cen@astro.ox.ac.uk |
| Francois | Pajot | IAS - Orsay | francois.pajot@ias.u-psud.fr |
| Alejandro | Peralta | JPL | Alejandro.Peralta@jpl.nasa.gov |
| Chiara | Portesi | INRIM | portesi@inrim.it |
| David | Pukala | JPL | dpukala@mail.jpl.nasa.gov |
| Patrick | Pütz | Steward Obs. / KOSMA | ppuetz@as.arizona.edu |
| Simon | Radford | Caltech | sradford@caltech.edu |
| Antti | Raisanen | TKK | antti.raisanen@tkk.fi |
| George | Reiland | Univ. of Arizona - ARO | greiland@as.arizona.edu |
| Frank | Rice | Caltech | rice@its.caltech.edu |
| Christophe | Risacher | European Southern Observatory (ESO) | crisache@eso.org |
| Fernando | Rodriguez | UMass Amherst | frodrigu@ecs.umass.edu |

| | | | |
|---|---|---|---|
| John | Rogers | Optical Research Associates | frankm@opticalres.com |
| Michela | Romanini | Kapteyn Astronomical Institute, University of Groningen | romanini@astro.rug.nl |
| Sergey | Ryabchun | Harvard-Smithsonian Center for Astrophysics | sryabchu@cfa.harvard.edu |
| Daryoosh | Saeedkia | University of Waterloo | daryoosh@maxwell.uwaterloo.ca |
| Lorene | Samoska | JPL | Lorene.A.Samoska@jpl.nasa.gov |
| Virendra | Sarohia | JPL | virendra.sarohia@jpl.nasa.gov |
| Celeste | Satter | JPL | satter@jpl.nasa.gov |
| Rudolf | Schieder | University of Cologne | schieder@ph1.uni-koeln.de |
| Erich | Schlecht | JPL | Erich.T.Schlecht@jpl.nasa.gov |
| Frank | Schmülling | University Cologne / KOSMA | schmuelling@ph1.uni-koeln.de |
| Alexei | Semenov | DLR | alexei.semenov@dlr.de |
| Wenlei | Shan | Purple Mountain Observatory | shawn@mwlab.pmo.ac.cn |
| Shengcai | Shi | Purple Mountain Observatory | scshi@mail.pmo.ac.cn |
| Sergey | Shitov | NAOJ / IREE | s.shitov@nao.ac.jp |
| Peter | Siegel | JPL | Peter.H.Siegel-104099@jpl.nasa.gov |
| Jose V. | Siles | Technical University of Madrid | jovi@gmr.ssr.upm.es |
| Anders | Skalare | JPL | Anders.Skalare@jpl.nasa.gov |
| Robert | Stachnik | JPL | robert.a.stachnik@jpl.nasa.gov |
| Matthew | Sumner | Caltech | sumner@caltech.edu |
| Bertrand | Thomas | RAL | b.thomas@rl.ac.uk |
| Edward | Tong | Harvard-Smithsonian CfA | etong@cfa.harvard.edu |
| lai | tran | jpl | lynskies@hotmail.com |
| Charlotte | Tripon-Canseliet | UPMC-LISIF | charlotte.canseliet@lisif.jussieu.fr |
| Alexey | Ustinov | University of Erlangen-Nuremberg | ustinov@physik.uni-erlangen.de |
| Yoshinori | Uzawa | National Astronomical Observatory of Japan | y.uzawa@nao.ac.jp |
| Josip | Vukusic | Chalmers University of Technology | vukusic@chalmers.se |
| Hui | Wang | Observatoire de Paris | hui.wang@obspm.fr |
| John | Ward | JPL | John.S.Ward@jpl.nasa.gov |
| Sander | Weinreb | Caltech | sweinreb@caltech.edu |

| | | | |
|---|---|---|---|
| Wolfgang | Wild | SRON | W.Wild@sron.rug.nl |
| Pavel | Yagoubov | SRON | p.a.yagoubov@sron.rug.nl |
| Ghassan | Yassin | University of Oxford | ghassan@astro.ox.ac.uk |
| Stephen | Yates | SRON | s.yates@sron.nl |
| Sigfrid | Yngvesson | UMass/Amherst | yngvesson@ecs.umass.edu |
| Jonas | Zmuidzinas | Caltech | jonas@caltech.edu |